TECHNISCHE UNIVERSITÄT DARMSTADT

Institut für Elektrische Energiewandlung

Motor Development for Electrical Drive Systems

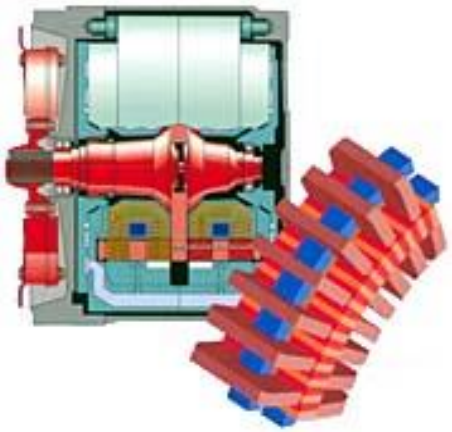

(1) (2) (3)

Sources*: (1) Voith, Heidenheim, Germany; (2) ELIN EBG Motoren GmbH, Weiz, Austria; (3) Siemens AG, Germany*

Issue SS 2017

Prof. Dr.-Ing. habil. Dr. h.c. Andreas Binder

Oral examination to lecture „Motor Development for Electric Drive Systems“

Examination questions (10 min. per each question):

Rotating permanent magnet drives - synchronous servo-drives:

1) How is the magnetic operating point of the motor determined at no-load operation? How will this operating point be shifted at load and by temperature change?
2) Draw some typical *B(H)*-characteristics of permanent magnets and explain them.
3) Sketch and describe the operating characteristics of the PM synchronous motor with rotor position control.
4) How can field weakening be realized for PM machines?
5) Explain the operating mode of block-current commutated PM synchronous machines! Why is this motor type called “brushless DC”-drive?
6) Explain the sinus-commutated operating mode of PM synchronous machines! Name the differences to block-commutation and indicate some advantages and disadvantages!
7) Explain the structure of rotors with surface mounted and buried magnets! What does flux concentration mean? How is it realized?
8) Describe the structure of a position-controlled PM servo drive. Name some application domains.
9) What does “*q*-current operation” mean? Explain it with help of the phasor diagram. How does the torque generation at this operation mode look like (Explain it with the air gap field)?
10) Describe the danger of demagnetization of permanent magnets through the stator field at load / overload!
11) Which electromagnetic and mechanic parameters are essential for design of high-speed drives with high utilization of active mass?

PM-linear drives:

1) How are PM linear drives built? Give an overview of the variety of different configurations.
2) Discuss the tangential and normal force density of PM linear motors and give some typical numerical values, depending on type of motor cooling!
3) Name typical values for the acceleration, the speed, the movement distances of PM linear machines! Why is the efficiency of linear machines lower than the efficiency of rotating machines?
4) Name the basic components of a typical PM linear drive. Sketch the structure of the complete drive system!

PM high-torque drives:

1) What characteristics do synchronous machines with high pole count have and when are they used?
2) Why is the active mass of PM synchronous machines with high pole count relatively smaller for a given torque, compared with machines with low pole count (e.g. 2 pole machine) ?
3) Describe the basic ideas of modular synchronous machines. What is a tooth wound armature winding?
4) Which are the advantages and disadvantages of modular synchronous machines? Where are they used?
5) How does the transversal flux machine operate in principle? For which application domains is it well suitable?
6) Describe the basic characteristics of the transversal flux machine. Which loss components are most dominant?
7) Sketch different structures of transversal flux machines and name the advantages and disadvantages of them!

Switched reluctance drives:

1) Describe the motor and inverter design, and the operation modes of switched reluctance drives!
2) What are the advantages and disadvantages of the switched reluctance drive, compared to traditional rotating field machines?
3) Explain the torque generation of the switched reluctance machine on the basis of the variation of phase inductance at rotor rotation!
4) Sketch the "maximum torque vs. speed"-curve of the switched reluctance drive and explain the particular speed sections!
5) Why is for switched reluctance machines a high saturation aimed to get high machine utilization ? Explain the principle by means of the "flux linkage –current"-characteristic for different rotor positions!
6) Explain the causes of torque ripple generated by switched reluctance machines!
7) Why do switched reluctance machines tend to generate electromagnetically excited acoustic noise? Describe the mechanism of this effect! With which dominant frequency does this noise generation occur?
8) Name typical application domains for switched reluctance drives, and the reasons why they are used.

Synchronous reluctance motors:

1) Describe the stator and rotor design and the operation modes of synchronous reluctance motors! Which parameters are significant for torque generation?
2) Draw the phasor diagram of the synchronous reluctance machine in motor operation ! Explain the main parameter load angle, phase angle, voltage and current !
3) The synchronous reluctance machine is supplied by fixed stator voltage and frequency: Sketch the torque's dependency on load angle ϑ at neglected stator resistance and give the formula. How does the stator resistance change the torque curve?
4) Sketch rotor structures of the synchronous reluctance motor for increased ratio X_d/X_q !
5) Name typical application domains for synchronous reluctance motors, and the reasons why they are used. Why are synchronous reluctance motors built and used only in lower power range ?

PM synchronous machines with rotor cage:

1) Describe the stator and rotor design of a PM synchronous machine with rotor cage. Give applications, where these motors are used!
2) Explain the flux concentration effect and sketch possible rotor configurations! What is the concentration factor?
3) Give the characteristic "torque vs. load angle" for a grid-operated PM synchronous machine with buried rotor magnets! What condition is necessary for minimum magnet strength?
4) Discuss the peculiarities of the starting characteristic "torque vs. speed" of grid-operated PM synchronous machines with rotor cage!
5) Describe the synchronization process of the line-started PM synchronous machine with rotor cage! What is the critical slip?

Grid-operated asynchronous machines with squirrel-cage rotor – standard motors:

1) Explain the dependence of motor efficiency and the efficiency maximum at variable load!
2) Name the basic components of standard asynchronous motors! What is "standardized" at these motors and up to which shaft height?
3) Sketch the speed-torque characteristic of squirrel-cage asynchronous motors by mains supply with fixed voltage and frequency! What are "torque classifications"?
4) What are the main loss groups in line-operated squirrel-cage asynchronous machines? How do they influence the operational behaviour?

5) Explain the physical nature of asynchronous space harmonic torque! How is this additional torque component generated? How it is influencing motor performance?
6) What are space harmonics of air gap flux density? Give an overview on ordinal numbers (formula) of stator and rotor field harmonics in squirrel-cage asynchronous machines!
7) Why do cage rotors of grid-operated asynchronous machines have skewed bars?
8) Explain the appearance of inter-bar currents and inter-bar current losses in cage rotors. How do these losses depend on inter-bar resistance and slot number ratio Q_s/Q_r?
9) How are rotor time harmonic currents generated in line-fed asynchronous machines? How do they contribute to so-called additional losses?
10) Why do synchronous space harmonic torque components appear? How does this additional torque component change the speed-torque characteristic of the asynchronous machine?
11) Explain the generation of magnetic noise in asynchronous machines at line–operation! Explain the physical background step by step from the magnetic air gap field to the sound pressure waves in air!
12) What are "slot harmonic" flux density waves? Give an example! Why do different slot number ratios Q_s/Q_r have significant influence on the stimulation of magnetic noise?

Inverter-fed standard induction machines:

1) Explain the operational behaviour (maximum torque-speed curve, voltage speed-curve, power-speed curve) of inverter-fed standard- induction machines without and with influence of the stator winding resistance!
2) Sketch the steady state torque-speed characteristic (thermal limit of motor winding) of the variable-speed asynchronous drive with shaft-mounted fan cooling! Explain the particular speed sections!
3) Discuss the operational mode (maximum torque-speed curve, voltage speed-curve, power-speed curve) of standard induction machines with "steep" and "flat" voltage-frequency characteristic! Explain, why the same motor with flat characteristic can deliver a higher (how many times?) power!
4) Explain the field-weakening operation of inverter-fed asynchronous machines! How is the field-weakening realized? Why is the field-weakening used? What natural limitations in torque-speed range exist at field-weakening?
5) Name the loss components in inverter-fed asynchronous machine with shaft-mounted fan! How do they change with variable stator frequency? What effect has the variable speed (variable loss) on the steady state torque-speed characteristic concerning thermal limits?

Induction machines, designed especially for inverter operation:

1) How can field weakening range (= constant power range) be extended by serial and parallel switching of the windings?
2) What methods of creating a wide field weakening range do you know? What typical field weakening range (= constant power range) is possible? Give applications!
3) How is the shaft-height defined? With which methods can a significant increase of power per shaft-height be obtained in inverter-fed special induction machines, compared to standard induction machines?
4) Sketch maximum torque-speed curve, voltage speed-curve, power-speed curve of an inverter-fed induction motor with external fan cooling!
5) What is the difference between "field-oriented control" and operation with "U/f- characteristic"?
6) Name some special features of induction machines, which are designed especially for inverter-operation! In what way do they differ from the standard induction machines?

Effects in asynchronous machines, caused by inverter-operation:

1) Why do additional time harmonic currents occur both in stator and rotor winding in asynchronous machines at inverter supply? Which are the dominating frequencies, if the inverter is operated with pulse-width modulated inverter output voltage?
2) Explain the reasons for additional losses in asynchronous machines at inverter supply!
3) How is a "pulsating torque" component generated in asynchronous machines at inverter supply? Name the dominant frequency! Why may this oscillating torque be harmful in some application cases?
4) Why are space harmonic additional torque components (asynchronous and synchronous harmonic torque) generally insignificant at inverter supply?
5) Why does inverter supply lead to an additional electromagnetic noise generation? Which frequency and pulsation mode of the motor housing are dominating?
6) Why can the time harmonic content of current in asynchronous machines be obviously reduced with fast-switching IGBT voltage DC link converter?
7) Which parasitic effects occur due to fast-switching IGBT voltage DC link converter in asynchronous machines and in the motor cables?
8) Explain the appearance of an increased motor terminal voltage at inverter supply, caused by voltage wave reflections!
9) Why will the "first" coil of each motor phase be the most highly charged with voltage stress at inverter supply with fast-switching IGBTs?

Rotor balancing:

1) What is "unbalance" of a rotor defined? How is this unbalance disturbing motor operation? How is its effect encountered by the balancing procedure in principle?
2) Define the static and dynamic unbalance by means of a simple rotor model and give the formulas for their definition! How do both unbalance modes manifest at motor operation?
3) What is meant by "rigid body balancing"? Describe the configuration of a balancing machine and its function!
4) Describe the difference between a rigid and an elastic rotor! Explain the natural bending frequencies and their influence on the oscillatory behaviour of rotor and on the balancing process?
5) How can be estimated the magnitude of unbalance by a vibration measurement of an (electrical) machine?
6) Give a quantitative measure which describes the quality of balancing of a rotor? How is it defined? Give examples (numerical values) for different applications!

Contents

Literature

Mohan, N. et al: Power Electronics, Converters, Applications and Design, John Wiley & Sons, 1995

Miller, T.: Switched Reluctance Motors and their Control, Clarendon Press, Oxford, 1993

Gieras, J.: Permanent Magnet Motor Technology, Wiley, 2000

Hendershot, J.: Design of brushless Permanent-magnet motors, Clarendon Press, Oxford, 1993

Hindmarsh, J.: Electrical Machines and their Application, Pergamon Press, 1991

Fitzgerald, A. et al: Electric machinery, McGraw-Hill, 1992

Salon, S.: Finite Element Analysis of Electrical Machines, Kluwer academic press, 1995

Boldea, I.: Reluctance synchronous machines and drives, Clarendon Press, Oxford, 1996

Parasiliti, F.; Bertoldi, P. (ed.): Energy Efficiency in Motor Driven Systems, Springer, Berlin-Heidelberg, 2003

Amin, B.: Induction Motors, Springer, Berlin, 2001

Dubey, G. K.: Fundamentals of Electrical Drives, Narosa Publishing House, New Delhi, 2000

Boldea, I., Nasar, S.A.: Electric drives, CRC Press, Boca Raton, 1999

Binder, A.: Elektrische Maschinen und Antriebe, Springer, Berlin-Heidelberg, 2012

Binder, A.: Elektrische Maschinen und Antriebe - Übungsbuch, Springer, Berlin-Heidelberg, 2012

The Greek alphabet:

$A\ \alpha$	Alpha	$B\ \beta$	Beta	$\Gamma\ \gamma$	Gamma	$\Delta\ \delta$	Delta
$E\ \varepsilon$	Epsilon	$Z\ \zeta$	Zeta	$H\ \eta$	Eta	$\Theta\ \vartheta$	Theta
$I\ \iota$	Jota	$K\ \kappa$	Kappa	$\Lambda\ \lambda$	Lambda	$M\ \mu$	My
$N\ \nu$	Nye	$\Xi\ \xi$	Xi	$O\ o$	Omicron	$\Pi\ \pi$	Pi
$P\ \rho$	Rho	$\Sigma\ \sigma$	Sigma	$T\ \tau$	Tau	$Y\ \upsilon$	Ypsilon
$\Phi\ \varphi$	Phi	$X\ \chi$	Chi	$\Psi\ \psi$	Psi	$\Omega\ \omega$	Omega

List of symbols

a	-	number of parallel branches of winding in AC machines, BUT: Half of number of parallel branches of armature winding in DC machines:
A	A/m	current layer
A	m^2	area
b_s, b_r	m	slot width (Stator, Rotor)
b_p	m	pole width
B	T	magnetic flux density
d_E	m	penetration depth
d_{si}	m	inner stator diameter
E	V/m	electric field strength
f	Hz	electric frequency
F	N	force
g	-	integer number
h	m	height
H	A/m	magnetic field strength
I	A	electric current
j	-	imaginary unit
J	A/m^2	electric current density
J	kgm^2	polar momentum of inertia
J	Vs/m^2	magnetic polarization
k	-	ordinal number of time harmonics
k_d	-	distribution factor
k_p	-	pitch factor
k_w	-	winding factor
l	m	axial length
L	H	self inductance
m	-	number of phases
M	H	mutual inductance
M	Nm	torque
M_b	Nm	asynchronous break down torque
M_{p0}	Nm	synchronous pull out torque
M_s	Nm	shaft torque
M_1	Nm	starting torque
n	1/s	rotational speed
N	-	number of turns per phase
N_c	-	number of turns per coil
p	-	number of pole pairs
P	W	power
q	-	number of slots per pole and phase
Q	-	number of slots
R	Ohm	electric resistance
s	-	slip
s	m	distance
t	s	time
T	s	time constant, duration of period
U	V	electric voltage
U_p	V	back EMF, synchronous generated voltage
$\ddot{u}_I$	-	current transforming ratio
$\ddot{u}_U$	-	voltage transforming ratio

v	m/s	velocity
V	A	magnetic voltage
V	m^3	volume
W	J	energy
W	m	coil width
x	m	circumference co-ordinate
X	Ohm	reactance
X_d, X_q	Ohm	direct and quadrature reactance
z	-	total number of conductors
Z	Ohm	impedance
α	rad	firing angle
δ	m	air gap width
φ	rad	phase angle
Φ	Wb	magnetic flux
Ψ	Vs	magnetic flux linkage
κ	S/m	electric conductivity
μ	-	ordinal number of rotor space harmonics
μ	Vs/(Am)	magnetic permeability
μ_0	Vs/(Am)	magnetic permeability of empty space ($4\pi \cdot 10^{-7}$ Vs/(Am))
ν	-	ordinal number of stator space harmonics
ξ	-	„reduced“ conductor height
η	-	efficiency
ϑ	°C	temperature
Θ	A	ampere turns
τ_Q, τ_s, τ_r	m	slot pitch (stator, rotor)
τ_p	m	pole pitch
ω	1/s	electric angular frequency
ω_m, Ω_m	1/s	mechanical angular frequency

Subscripts

av	average
b	asynchronous break down
c	coil
d	direct, DC, distribution, dissipation
e	electric
f	field
Fe	iron
h	main-
i	induced
in	input
k	short circuit-
mag	magnetising, magnetic
m	mechanical
max	maximum
N	rated
out	output
p	pole, pitch
q	quadrature

Q	slot
r	rotor
s	stator
s	shaft
syn	synchronous
w	winding
δ	air gap
σ	leakage
0	no load
1	starting (*s* = 1 with induction machine)

Notation

i	small letters: instantaneous value (e.g.: electric current)
I	capital letters: r.m.s. or DC value (e.g.: electric current)
X, *x*	capital letter: value in physical units e.g. reactance in Ω, small letter: per unit value
$\underline{I}$	underlined: complex values
	amplitude
	related to stator side winding
Re(.)	real part of ...
Im(.)	imaginary part of ...

Literature (“classical” papers)

[1] LLOYD,M.R.: Development in Large Variable Speed Drives, ICEM Proceedings, 1992, Manchester, p.7-11
[2] ARKKIO,A.: On the Choice of the Number of Rotor Slots for Inverter-Fed Cage Induction Motors, ICEM Proceedings, 1992, Manchester, p.366-370
[3] NEUHAUS,W.; WEPPLER,R.: Einfluss der Querströme auf die Drehmomentenkennlinie polumschaltbarer Käfigläufermotoren, ETZ-A 88, 1967, H.3, p.80-84
[4] BINDER,A.: Vorausberechnung der Betriebskennlinien von Drehstrom-Kurzschlussläufer-Asynchronmaschinen mit besonderer Berücksichtigung der Nutung, Diss. TU Wien, 1988
[5] WEPPLER, R.: Ein Beitrag zur Berechnung von Asynchronmotoren mit nichtisoliertem Käfig, Archiv f. Elektrotechn. 50, 1966, p.238-252
[6] SEINSCH,H.-O.: Oberfelderscheinungen in Drehfeldmaschinen, B.G.Teubner, Stuttgart, 1992
[7] WEPPLER,R.; NEUHAUS,W.: Der Einfluss der Nutöffnungen auf den Drehmomentenverlauf von Drehstrom-Asynchronmotoren mit Käfigläufern, ETZ-A 90, 1969, p.186-191
[8] Moritz,W.D., RÖHLK,J.: Drehstrom-Asynchron-Fahrmotoren für elektrische Triebfahrzeuge, Ele.Bahnen 50, 1979, H.3, p.65-71
[9] HUTH,G.: Entwicklungstendenzen und Realisierungsmöglichkeiten bei AC-Hauptspindelantrieben, ETG-Fachberichte, 1987, Offenbach, p.243-25
[10] KLEINRATH,H.: Ersatzschaltbilder für Transformatoren und Asynchronmaschinen, e&i 110, 1993, H.2, p.68-74
[11] KLEINRATH,H.: Stromrichtergespeiste Drehfeldmaschinen, Springer-Verlag, Wien, 1980
[12] Motorenkatalog M11: Drehstrom-Niederspannungsmotoren, Käfigläufermotoren, SIEMENS AG, 1990
[13] BENECKE,W.: Temperaturfeld und Wärmefluss bei kleineren oberflächengekühlten Drehstrommotoren mit Käfigläufer, ETZ-A 87, 1966, H.13, p.455-459
[14] PFAFF,G.: Regelung elektrischer Antriebe I, Oldenbourg Verlag, München, 1990, 4.Aufl.
[15] Antriebskatalog SIMODRIVE 611(HS/AM-Module), Siemens AG,1991
[16] LINK,U.: Efficient Control Methods for PWM Voltage Source Inverters, ICEM Proc., 1992, Manchester, p.928-932
[17] Gertmar,L. et al.: Rotor design for inverter-fed high speed induction motors, EPE-Proc. 1989, Aachen, p.51-56
[18] HÜGEL,H.; SCHWESIG,G.: Neues Stromregelverfahren für Drehstrom-Asynchronmotoren, antriebstechnik 30, 1991, H.12, p.36-42
[19] BAYER,K.-H.: TRANSVEKTOR-Regelung - Ein Regelprinzip für Drehstromantriebe, Glasers Annalen 104, 1980, H.8/9, p.291-298
[20] ANDRESEN,E.Ch. et al.: Fundamentals for the design of high speed induction motor drives with transistor inverter supply, EPE Proc., 1989, Aachen, p.823-828
[21] KLAUTSCHEK,H.; SPETH,F.: Mit Mikroprozessoren in hohe Leistungsbereiche der Antriebstechnik, Energie & Automation, 11, 1989, H.2, p.30-32
[22] BRAUN,M.: Tendenzen und Perspektiven bei Umrichtern, etz 114, 1993, H.17, p.1058-1059
[23] LORENZ,L.: MOS-Controlled Power Semiconductor Components for Voltages from 50V to 2000V, EPE Journal 2, 1992, H.2, p.77-84
[24] BOYS,T.; HANDLEY,P.G.: Spread spectrum switching: Low noise modulation technique for PWM inverter drives, IEE Proc.-B 139, 1992, H.3, p.252-260
[25] STEFANOVIC,V.R.: Industrial AC Drives Status of Technology, EPE Journal 2, 1992, H.1, p.7-23
[26] GREEN,T.C; WILLIAMS,B.W.: Derivation of Motor Line-Current Wave Forms from the DC-Link Current of an Inverter, IEE Proc.B 136, 1989, H.4, p.196-203
[27] HAUN,A.: Vergleich von Steuerverfahren für spannungseinprägende Umrichter zur Speisung von Käfigläufermotoren, Diss. TH Darmstadt, 1992
[28] KLAUSECKER,K.;SCHWESIG,G.: Drehstromhauptspindelantriebe: digital geregelt und hochdynamisch, Energie&Automation 9, 1987, H.1, p.28-29
[29] GICK,B. et al.: Kommunikation bei Antrieben, etz 112, 1991, H.17, p.906-918
[30] GRIEVE,D.W.; MC SHANE,I.E.: Torque Pulsations on Inverter Fed Induction Motors
[31] HEUMANN,K.: Grundlagen der Leistungselektronik, Teubner, Stuttgart, 1985
[32] BINDER,A. et al.: Motor design with large air gap for centrifugal blood pumps using rare-earth magnets, Archiv f. Elektrotechn. 73, 1990, p.261-269
[33] DEMEL,W. et al.: Block- und sinusförmige Speisung von bürstenlosen SERVODYN-Motoren für Werkzeugmaschinen und Handhabungsgeräte, ETG-Fachberichte 1988, Offenbach, p.49-60
[34] LEHMANN,R.: Technik der bürstenlosen Servoantriebe, 1.Teil, Elektronik 21, 1989, p.96-101
[35] MÜHLEGGER,W., RENTMEISTER,M.: Die permanenterregte Synchronmaschine im Feldschwächbetrieb, e&i 109, 1992, H.6, p.293-299
[36] HENNEBERGER,G.; SCHLEUTER,W.: Servoantriebe für Werkzeugmaschinen und Industrieroboter, etz 110, 1989, H.5, p.200-205; H.6/7, p.274-279

[37] HUTH,G.: Grenzkennlinien von Drehstrom-Servoantrieben in Blockstromtechnik, etz-Archiv 11, 1989, H.12, p.401-408
[38] PILLAY,P.; KRISHNAN,R.: An investigation into the torque behaviour of a brushless DC drive, IEEE-IAS, 1988, p.201-207
[39] SCHRÖDER,M.: Einfach anzuwendendes Verfahren zur Unterdrückung der Pendelmomente dauermagneterregter Synchronmaschinen, etz-Archiv 10, 1988, H.1, p.15-18
[40] NEROWSKI,G. et al.: New Permanent-Field Synchronous Motor with Integrated Inverter, ICEM-Proc., Boston, 1990, p.124-131
[41] MENKE,K.: Gut verpackt - Drehstromantriebe für Verpackungsmaschinen, drive&control 4, 1993, p.7-8
[42] BEINHORN,R.; GEKELER,M.: Kostengünstiges Positionieren mit bürstenlosen Servoantrieben, antriebstechnik 30, 1991, H.3, p.84, 90, 91
[43] Antriebskatalog SIMODRIVE 611 (Drehstrom-Vorschubantriebe), Siemens AG, 1989
[44] FEUSTEL,H.P.: Bürstenlose Antriebe bis 130kW, elektroanzeiger 45, 1992, H.9, p.46-50
[45] Werkstoffkatalog Selten-Erd-Magnetwerkstoffe (VACODYM, VACOMAX); Vacuumschmelze GmbH, 4/88
[46] BÖNING,W.(Hrsg.): HÜTTE-Elektrische Energietechnik, Bd.1: Maschinen, Abschn. Elektrische Entwurfsrechnung, Springer, Berlin, 1978
[47] RUSSENSCHUCK,S.: Mathematische Optimierung permanenterregter Synchronmaschinen mit Hilfe der numerischen Feldberechnung, Diss., TH Darmstadt, 1990
[48] KLEINRATH,H.: Kennlinienberechnung und Entwurf von Schenkelpolsynchronmaschinen mit Erregung durch Permanentmagnete, E&M 82, 1964, H.10, p.489-500
[49] VOLKRODT,W.: Eigenschaften eines neuartigen Synchronmotors mit Erregung durch Bariumferritmagnete, Diss. TH Braunschweig, 1960
[50] VOLKRODT,W.: Polradspannung, Reaktanzen und Ortskurve des Stromes der mit Dauermagneten erregten Synchronmaschine, ETZ-A 83, 1962, H.16, p.517-522
[51] VOLKRODT,W.: Ferritmagneterregung bei größeren elektrischen Maschinen, Siemens Zeitschrift 49, 1975, H.6, p.368-374
[52] BAUSCH,H. et al.: Anlauf von Reluktanzmotoren mit geblechtem Läufer, ETZ-A 85, 1964, p.170-173
[53] BINDER,A.: Untersuchung zur magnetischen Kopplung von Längs- und Querachse durch Sättigung am Beispiel der Reluktanzmaschine, Archiv f. Elektrotechn. 72, 1989, p.277-282
[54] SCHROEDER,J.W.: Beitrag zum Vergleich zwischen Reluktanz- und MERRILL-Motor, ETZ-A 89, 1968, H.10, p.230-233
[55] KURSCHEIDT,P.: Theoretische und experimentelle Untersuchung einer neuartigen Reaktionsmaschine, Diss RWTH.Aachen, 1961
[56] SCHMIDT,A.: Beitrag zur Berechnung der Reluktanzmaschine, Diplomarbeit, TU Wien, Inst. f. ele. Masch. u. Antriebe, 1987
[57] LAWRENSON,P.J.; GUPTA,S.K.: Developments in the performance and theory of segment-rotor reluctance motors, Proc. IEE 114, 1967, H.5, p.645-653, correspondence in: Proc. IEE 115, 1968, H.9, p.1283-1285, Proc. IEE 117, 1970, H.12, p.2271-2272
[58] KAMPER,M.J.; TRÜBENBACH,R.A.: Vector Control and Performance of a Reluctance Synchronous Machine with a Flux Barrier Rotor, ICEM Proc., Manchester, 1992, p.547-551
[59] TAEGEN,F. et al.: Elektromagnetisches Geräusch von Reluktanzmaschinen mit segmentiertem Läufer, Archiv f. Elektrotechn. 73, 1990, p.253-260, p.293-298
[60] NAGRIAL,M.H.; LAWRENSON,P.J.: Optimum steady-state and transient performance of reluctance motors, ICEM Proc., Lausanne, 1984, p.321-324
[61] BOLDEA,I. et al.: Distributed Anisotropy Rotor Synchronous Drives - Motor Identification and Performance, ICEM Proc., Manchester, 1992, p.542-546
[62] HOPPER,E.: Geschalteter Reluktanzmotor als robuste Alternative, Elektronik 26, 1992, p.72-75
[63] LAWRENSON,P.J.: Switched reluctance drives: a perspective, ICEM Proc., Manchester, 1992, p.12-21
[64] RIEKE,B.: Untersuchungen zum Betriebsverhalten stromrichtergespeister Reluktanzantriebe, Diss. Hochschule der Bundeswehr, München, 1981
[65] AMIN,B.: Structure of High Performance Switched Reluctance Machines and their Power Feeding Circuitries, ETEP 2, 1992, H.4, p.215-221
[66] CAMERON,D.E. et al.: The Origin and Reduction of Acoustic Noise in Doubly Salient Variable-Reluctance Motors, IEEE-IAS 28, 1992, p.1250-1255
[67] MOGHBELLI,H. et al.: Performance of a 10HP-Switched Reluctance Motor and Comparison with Induction Motors, IEEE-IAS 27, 1991, H.3, p.531-538
[68] OMEKANDA,A. et al.: Quadratic hybrid boundary integral equation-finite element method applied to magnetic analysis of a switched reluctance motor, ICEM Proc., Manchester, 1992, p.499-502
[69] AUERNHAMMER,E. et al.: Kompaktere Gleichstromantriebe durch Leistungssteigerung, etz, 1992, H.21, p.1342-1349
[70] GROSS,H. (Hrsg.): Elektrische Vorschubantriebe für Werkzeugmaschinen, Siemens AG, München, 1981

[71] PRETZENBACHER,R.; FANGMEYER,H.: Ohne Stau zum Ziel - Antriebstechnik für Kabelfertigung, drive&control 10, 1993, H.4, p.10-11
[72] REICHE,H.: Objektive Bewertung der Kommutierungsgüte - ein Beitrag zur Entwicklung des Gleichstromantriebes, Elektrie 46, 1992, H.7, p.344-346
[73] GABSI,M.K. et al.: Calculation and measurement of commutation currents in DC machines, Electric machines and power systems 17, 1989, p.167-182
[74] PARSLEY,G.M.J. et al.: Factors Affecting the Prediction of Commutation Limits for a DC Machine under Varying Speed and Load Conditions, Trans. of the SA Institute of Electrical Engineers, 1992, p.171-176
[75] VOITS,M.: Tuning durch Digitaltechnik, Elektronik 7, 1991, p.97-102
[76] LAUER,L.: Digitalisiertes Stromrichterkonzept für Gleichstromantriebe, antriebstechnik 30, 1991, H.11, p.62-66
[77] HENTSCHEL,E. et al.: Beanspruchung der Wicklungsisolierung von Drehstrommaschinen, etz 114, 1993, H.7, p.1074-1077
[78] HELLER,B.; VEVERKA,A.: Stoßerscheinungen in elektrischen Maschinen, VEB Verlag Technik, Berlin, 1957
[79] DEISENROTH,H.; TRABERT,Ch.: Vermeidung von Überspannungen bei Pulsumrichterbetrieb, etz 114, 1993, H.17, p.1060-1066
[80] SCHMID,W.: Pulsumrichterantriebe mit langen Motorleitungen, AGT 4, 1992, p.58-64
[81] KAUFHOLD,M.; BÖRNER,G.: Langzeitverhalten der Isolierung von Asynchronmaschinen bei Speisung mit Pulsumrichtern, Elektrie 47, 1993, H.3, p.90-95
[82] BUNZEL,E.; GRASS,H.: Spannungsbeanspruchung von Asynchronmotoren im Umrichterbetrieb, etz 114, 1993, H.7/8, p.448-458
[83] FEICHTINGER,P.; GOSS,W.: Rechnergestützte Diagnose am Bus - kontinuierliche Überwachung von Gleichstromantrieben, drive&control 2, 1992, p.28-29
[84] Wälzlager-Katalog "Präzisions-Schrägkugellager", SNFA, 4.Aufl., Leonberg, Deutschland
[85] Wälzlager-Katalog "Wälzlager für Werkzeugmaschinen", NSK (Nippon Seiko), 1991, Pr.Nr.G124, Ratingen, Deutschland
[86] Wälzlager-Katalog "Kugellager, Rollenlager", NSK, 1988, Kat.Nr.D1100, Ratingen, Deutschland
[87] HOFMANN,R. et al.: Wer gut schmiert...- Fett erobert den High-Speed-Bereich, Konstruktionspraxis 21, 1991, H.8, p.12-14
[88] RENTZSCH,H.: Elektromotoren - Electric Motors, ABB-Fachbuch, 4.Aufl., 1992, ABB-Drives AG, Turgi, Schweiz
[89] LINGENER,A.: Auswuchten - Theorie und Praxis, Verlag Technik GmbH Berlin, 1992
[90] ECK,B.: Ventilatoren, Springer, Berlin, 1971, 5.Aufl.
[91] BINDER,A.: Additional losses in converter-feds uncompensated D.C.motors - their calculation and measurement, Archiv f. Elektrotechn. 74, 1991, p.357-369
[92] TAEGEN,F.: Zusatzverluste von Asynchronmaschinen, Acta Technika CSAV, 1968, H.1, p.1-31
[93] JORDAN,H. et al.: Ein einfaches Verfahren zur Messung der Zusatzverluste in Asynchronmaschinen, ETZ-A 88, 1967, H.23, p.577-583
[94] JORDAN,H.: TAEGEN,F.: Experimentelle Untersuchungen der lastabhängigen Zusatzverluste von Käfigläufermotoren im reverse rotation test, E&M 85, 1967, H.1, p.11-17
[95] SCHÄFER,G.: Pendelmomente bei permanenterregten, bürstenlosen Servoantrieben, ihre Ursachen und meßtechnische Bestimmung, ETG-Fachberichte 22, Offenbach, 1988, p.109-118
[96] DREYFUS,L.: Eine Methode zur experimentellen Ermittlung des BLONDEL'schen Koeffizienten der Gesamtstreuung für Drehstrommotoren, E&M 39, 1921, H.13, p.149-151
[97] RENTZSCH,H.: Luftströmungsgeräusche in elektrischen Maschinen, ETZ-A 82, 1961, H.24, p.792-798
[98] FERENCZ,G.: Alles geregelt - Erfassen und Messen von Drehzahlen bei Antrieben mit Hilfe von Tachogeneratoren, Maschinenmarkt, Würzburg 97, 1991, p.46-50
[99] WILHELMY,L. et al.: Drehzahl-Istwertaufnehmer: Longlife oder bürstenlos?, etz 110, 1989, H.5, p.246-247
[100] BOYES,G.S.: Synchro and Resolver Conversion, 1980, Memory Devices Ltd., Surrey, United Kingdom
[101] Katalog "Resolvers", Moore Reed and Company Ltd., 1979, Walworth, Andover, Hampshire, United Kingdom
[102] SCHRÖDL,M.; STEFAN,T.: New Rotor Position Detector for Permanent Magnet Synchronous Machines Using the "Inform"-Method, ETEP 1, 1991, H.1, p.47-53
[103] CARDOLETTI,L. et al.: Indirect position detection at stand-still for brushless DC and step motors, EPE Proc. 1989, Aachen, p.1219-1222
[104] SATTLER,Ph.-K.; STÄRKER,K.: Estimation of speed and pole position of an inverter fed permanent excited synchronous machine, EPE Proc., 1989, Aachen, p.1207-1212
[105] BINNS,K.J. et al.: A self-commutating PM machine with implicit rotor position sensing using search coils, ICEM Proc., Boston, 1990, p.53-56

[106] BINNS,K.J. et al.; Implicit rotor position sensing using motor windings for a self-commutating permanent-magnet drive system, IEE Proc.B 138, 1991, H.1, p.28-34
[107] BRUNSBACH,B.-J. et al.: Lagegeregelte Servoantriebe ohne mechanische Sensoren, Archiv f. Elektrotechn. 76, 1993, p.335-341
[108] BRUNSBACH,B.-J.; HENNEBERGER,G.: Einsatz eines Kalman-Filters zum feldorientierten Betrieb einer Asynchronmaschine ohne mechanische Sensoren, Archiv f. Elektrotechn. 73, 1990, p.325-335
[109] PANDA,S.K.; AMARATUNGA,G.A.J.: Waveform detection technique for indirect rotor-position sensing of switched reluctance motor drives, IEE Proc.B 140, 1993, H.1, p.80-96
[110] SCHRÖDL,M.: Sensorless Control of Induction Motors at low Speed and Standstill, ICEM Proc., Manchester, 1992, p.863-867
[111] ENGEL,U.; JORDAN,H.: Über pendelmomentbildende Sättigungsfelder in Drehstrom-Asynchronmaschinen, ETZ-A 94, 1973, H.1, p.1-3
[112] REICHERT,K.; NEUBAUER,R.; REICHE, H.; BERG, F.: Elektrische Antriebe energieoptimal auslegen und betreiben, RAVEL-Broschüre, Bern, 1993 (Eidgen. Drucksachen- u. Materialzentrale, Best.Nr.724.331d)
[113] URGELL; J.J.; REGIS, A.: A new spindle drive: High power-to-weight and low speed through magnetic flux control, GEC Alsthom Techn. Review 6 (1991), p.67-74
[114] GAILLARD, G.; REGIS, A.; FAGE, P.: Moteur synchrone adpaté pour marcher à puissance constante et commande pour ce moteur, Europ. Patentamt, Patent Nr.0 378 162 A1 (1990), zurückgezogen 1994, (Fa.Parvex, Dijon, Frankreich)
[115] CUENOT, A.; PETITBOULANGER, A.: Moteur synchrone comportant des aimants insérés dans un rotor, Europ. Patentamt, Patent Nr.0 695 018 A 1(1995) (Fa.Parvex, Dijon, Frankreich)
[116] HENZE, M.: Standard-Asynchronmotor mit integriertem Frequenzumrichter, antriebstechnik 35 (1996), H.11, p.36/39
[117] PAUSTIAN, R.: Drehstrommotoren mit integriertem Frequenzumrichter für Pumpenantriebe, antriebstechnik 35 (1996), H.8, p.40/41
[118] STEINBECK, L.: Innovation durch Integration - SIMOVERT COMBIMASTER, der Frequenzumrichter im Motor, drive&control (1995), H.3, p.20-21
[119] BÄHR, H.: Gemeinsam noch stärker - 2BH7, der intelligente ELMO-G Verdichter mit integriertem Frequenzumrichter, drive&control (1996) H.2, p.6-7
[120] KIZLER, A.: Evolution im Motorenbau - ROTEC - progressive Motoren für Umrichterbetrieb von 0.5kW bis 300kW, drive&control (1996) H.1, p.14-15
[121] RICHTER, E.; CALO FERREIRA, A.; RADUN, A.V.: Testing and performance analysis of a high speed, 250kW switched reluctance starter generator system, Proc. ICEM 1996, Vigo, Vol.3, p.364-369
[122] LUTZ, J.F.: Selecting pole count for permanent magnet motor designs, Proc. ICEM 1996, Vigo, Vol.2, p.3675-380
[123] WEH, H.: Permanentmagneterregte Synchronmaschinen hoher Kraftdichte nach dem Transversalflusskonzept, etzArchiv 10 (1988), H.5, p.143-149
[124] WEH, H.; HOFFMANN, H.; LANDRATH, J.: New permanent magnet excited synchronous machine with high efficiency at low speeds, Proc. ICEM 1988, Pisa, p.35-40
[125] VOITH Transversalflussmotoren - Grundlagen, Werbeprospekt Fa.Voith G1320 4.92 (1992)
[126] VOITH Transversalflussmaschine - Entwicklung eines elektrischen Einzelradantriebes für Citybusse der Zukunft, Werbeprospekt Fa.Voith G1401 d 5.95 (1995)
[127] KOLLETSCHKE, H.-D.: Die modulare Dauermagnetmaschine - Aufbau und Eigenschaften, Diss. Techn. Univ. der Bundeswehr Neubiberg b. München, 1987
[128] BAUSCH, H.; KOLLETSCHKE, H.-D.: A novel polyphase multipole permanent-magnet machine for wheel drive applications, Proc. ICEM 1984, Lausanne, p.591-594
[129] TAEGEN, F.; KOLBE, J.: Drehmomente und Geräusche der modularen Dauermagnetmaschine, Archiv f. Elektrotechnik 77 (1994), p.391-399
[130] STILLMAN, H.: IGCT2 – Megawatt-Halbleiterschalter für den Mittelspannungsbereich, ABB Technik 3 (1997), p.12-17
[131] LEMP, D.: Realisierung eines asynchronen Antriebs mit direkter Fluss- und Drehmomentregelung, Diss. TH Darmstadt, 1997, Verlag Shaker, Deutschland
[132] Pelloloa, M.; Perala, S.; Bryfors, U.: ACS600-Antriebe mit direkter Drehmomentregelung, ABB Technik 6 (1997), p.31-39
[133] Wissenswertes über Frequenzumrichter, Handbuch, Danfoss A/S, 1997
[134] Binder, A.: Motor- und Kabelbelastung durch Umrichter, in: Reichert, K. (Hrsg.): Messen von Betriebsparametern elektrischer Antriebe, RAVEL-Broschüre, 1996, p. 48-52
[135] BINDER, A.; SCHREPFER, A.: Bearing Currents in Induction Machines due to Inverter Supply, Proc. ICEM 1998, Istanbul, p.586-591
[136] BINDER, A.: Measures to cope with a.c. motor insulation stress due to IGBT-inverter supply, Proc. PEVD, Nottingham, 1996, p.569-574

[137] GREUBEL, K.; HELBIG, F.; HEINEMANN, G.; PAPIERNIK, W.: Einsatz von Linearantrieben zur Herstellung von Konturenwirkware, ETG-Fachbericht 79, 1999, p.461-470
[138] SCHNURR, B.; WINKLER, W.: Lineare Direktantriebe: Neue Möglichkeiten im Werkzeugmaschinenbau, ETG-Fachbericht 79, 1999, p.449-460
[139] STÖLTING, H.-D.; BEISSE, A.: Elektrische Kleinmaschinen, Teubner, Stuttgart, 1987
[140] N.N.: Stepping motors and associated electronics, Philips Data Handbook: Components and Materials, Book C17, Philips Export B.V., Eindhoven, Netherlands, 1986
[141] N.N.: Drei-Phasen-Schrittmotoren und Leistungsansteuerungen, Katalog Berger-Lahr, Juni 1994
[142] RUMMICH, E. (Hrsg.): Elektrische Schrittmotoren und -antriebe, expert-Verlag, Band 365, Ehringen/Böblingen,1992
[143] KENJO, I.: Stepping motors and their microprocessor controls, Oxford Press, 1984

German-English translation of important technical items

a	-	Anzahl paralleler Wicklungs-zweige bei Drehfeldmaschinen, aber: HALBE Anzahl paralleler Wicklungszweige bei Gleichstrom-maschinen	number of parallel winding branches of poly-phase machines, however: HALF of the number of parallel winding branches of dc machines
A	A/m	Strombelag	electric loading
A	m^2	Fläche	area
b_s, b_r	m	Nutbreite (Stator, Rotor)	slot width (stator, rotor)
b_p	m	Polschuhbreite	width of pole shoe
b_{Stab}	m	Stabbreite	width of bar
B	T	magnetische Induktion (Flussdichte)	magnetic induction (flux density)
c_d, c_q	-	Feldfaktoren der Längs-, Quer-achse	field factors of d-(direct) and q-(quadrature) axis
$c_{,g}$	Nm/rad	Ersatzfederkonstante der Synchronmaschine	equivalent spring constant of a synchronous machine
d_{si}	m	Bohrungsdurchmesser	bore diameter
D	As/m^2	elektrische Verschiebung (elektrische Flussdichte)	electric displacement (electric flux density)
E	V/m	elektrische Feldstärke	electric field density
f	Hz	elektrische Frequenz	electric frequency
F	N	Kraft	force
g	-	ganze Zahl	integer
h	m	Höhe	height
H	A/m	magnetische Feldstärke	magnetic field density
I	A	elektrische Stromstärke	electric current
j	-	imaginäre Einheit	imaginary unit
J	A/m^2	elektrische Stromdichte	electric current density
J	kgm^2	polares Trägheitsmoment	moment of inertia
k	-	Ordnungszahl	ordinal number
k_d	-	Zonenfaktor	distribution factor
k_K	-	Leerlauf-Kurzschluss-Verhältnis	no load - short circuit ratio
k_p	-	Sehnungsfaktor	pitch factor
k_R, k_L	-	Stromverdrängungsfaktoren	current displacement factors
k_R	$V \cdot s/A$	Proportionalitätskonstante der Reaktanzspannung	proportional constant of the reactance voltage
k_w	-	Wicklungsfaktor	winding factor
K	-	Anzahl der Kommutatorsegmente	number of collector segments
l	m	Länge (axial)	length (axial)
L	H	Selbstinduktivität	self inductance
m	-	Strangzahl	number of phases
M	H	Gegeninduktivität	mutual inductance
M	Nm	Drehmoment	torque
M_b	Nm	asynchrones Kippmoment	asynchronous breakdown torque
M_{p0}	Nm	synchrones statisches Kippmoment	synchronous, steady-state break-down torque
M_s	Nm	Kupplungsmoment, Wellenmoment	shaft torque

M_1	Nm	Anfahrmoment	breakaway torque
n	1/s	Drehzahl	motor speed
N	-	Windungszahl je Strang	number of windings per phase
N_c	-	Spulenwindungszahl	number of windings per coil
p	-	Polpaarzahl	number of pole pairs
P	W	Leistung	power
q	-	Lochzahl (Nuten pro Pol und Strang)	number of slots per pole and phase
Q	-	Nutenzahl	number of slots
R	Ohm	elektrischer Widerstand	electric resistance
s	-	Schlupf	slip
s	m	Weglänge	distance
t	s	Zeit	time
T	s	Zeitkonstante	time constant
u	-	Spulenseiten je Nut und Schicht	number of coils per slot and layer
U	V	elektrische Spannung	electric voltage
U_p	V	Polradspannung	synchronous internal voltage
$\ddot{u}$, $\ddot{u}_U$	-	Übersetzungsverhältnis (Spannungsübersetzungsverhältnis)	ratio (voltage ratio)
$\ddot{u}_I$	-	Stromübersetzungsverhältnis	current ratio
v	m/s	Geschwindigkeit	velocity
V	A	magnetische Spannung	magneto-motive force (“magnetic voltage”)
V	m^3	Volumen	volume
W	J	Energie	energy
W	m	Spulenweite	coil width
x	m	Umfangskoordinate	circumferential coordinate
X	Ohm	Reaktanz	reactance
X_d, X_q	Ohm	Längs-, Querreaktanz	d-, q-reactance
y	-	Weite einer Spule, gezählt in Nutteilungen	width of a coil in numbers of slots
z	-	gesamte Leiterzahl	total number of conductors
Z	Ohm	Impedanz	impedance
α_e	-	äquivalente Polbedeckung	pole pitch factor
α	rad	Zündwinkel	firing angle
α_Q	rad	Nutenwinkel (elektrischen Grad)	slot angle (electric degrees)
γ	rad	Umfangswinkel (elektrische Grad)	circumferential angle (electric degrees)
δ	m	Luftspalt	air-gap
φ	rad	Phasenwinkel	phase angle
Φ	Wb	magnetischer Fluss (Scheitelwert)	magnetic flux (peak value)
Ψ	Vs	magnetische Flussverkettung (Scheitelwert)	magnetic flux linkage (peak value)
κ	S/m	elektrische Leitfähigkeit	electric conductivity
μ	-	Ordnungszahl	ordinal number
μ	Vs/(Am)	magnetische Permeabilität	magnetic permeability
μ_0	Vs/(Am)	magnetische Permeabilität des Vakuums ($4\pi \cdot 10^{-7}$ Vs/(Am))	magnetic permeability of vacuum ($4\pi \cdot 10^{-7}$ Vs/(Am))

ν	-	Ordnungszahl	ordinal number
ξ	-	„reduzierte“ Leiterhöhe	“reduced” conductor height
η	-	Wirkungsgrad	efficiency
ϑ	rad	Polradwinkel (elektrische Grad)	load angle (electric degrees)
Θ	A	elektrische Durchflutung	Ampere-turns
σ	-	BLONDEL´scher Koeffizient der Gesamtstreuung, Streuziffer	BLONDEL’s leakage coefficient
σ_o	-	Streuziffer der Oberfelderstreuung	leakage coefficient of harmonic leakage
τ_c	m	Kommutatorstegteilung	collector segment pitch
τ_Q, τ_s, τ_r	m	Nutteilung allgemein bzw. Stator- und Rotornutteilung	slot pitch in general, stator / rotor slot pitch
τ_p	m	Polteilung	pole pitch
ω	1/s	elektrische Kreisfrequenz	electric angular frequency
Ω	1/s	elektrische Winkelgeschwindigkeit	electric angular speed
ω_m, Ω_m	1/s	mechanische Winkelgeschwindigkeit	mechanic angular speed

Indizes / Subscripts

a		Anker	armature
av		Mittelwert	average value
b		Bürste, asynchrones Kippen	brush, asynchronous breakdown
c		Spule, Kommutator	coil, collector
com		Kommutierungs-	collector
C		Koerzitiv-	coercive
d		direct (längs), dc (Gleichgröße), Zone (distribution), Verluste (dissipation)	direct, dc (direct current), phase (distribution), losses (dissipation)
D		Dämpferwicklung in der Längsachse	damper winding in direct axis
e		elektrisch, äquivalent	electric, equivalent
f		Feld	field
Fe		Eisen	steel
h		Haupt-	mutual / magnetising
i		induziert	induced
in		zugeführt	fed -
k		Kurzschluss-	short circuit -
m		Magnetisierungs-, magnetisch	magnetising -, magnetic
m		mechanisch	mechanical
m		maximal	maximum
N		Nenn	rated
out		abgegeben	delivered
o		Oberfelder	harmonics
p		Pol, Polrad, Sehnung	pole, rotor (synchronous machine), pitch
q		quer	quadrature
Q		Dämpferwicklung in der Querachse	damper winding in the quadrature axis

Q		Nut	slot
r		Rotor	rotor
R		Reaktanz- (Gleichstrommaschine), Remanenz, Reibung	reactance (DC machine), remanence, friction
s		Stator	stator
s		Welle	shaft
sch		schalt	switching
syn		Synchron	synchronous
sh		Shunt	shunt
v		Vorwiderstand	external resistance
w		Wicklung	winding
W		Wendepol	commutating
δ		Luftspalt	air-gap
σ		Streu-	leakage
0		Leerlauf	no load
1		Anfahrpunkt (*s* = 1 bei Asynchronmaschine)	breakaway (*s* = 1 with asynchronous machines)
Notationen / Notations			
i		Kleinbuchstabe: z.B.: elektrische Stromstärke, Augenblickswert	lower case letter: e.g.: electric current, instantaneous value
I		Großbuchstabe: z.B.: elektrische Stromstärke, Effektivwert oder Gleichstrom-Wert	upper case letter: e.g.: electric current, rms or dc value
X, x		Großbuchstabe: z.B. Reaktanz, Kleinbuchstabe: z.B. bezogene Reaktanz (p.u. -Wert)	upper case letter: e.g. reactance, lower case letter: e.g. normalised reactance (p.u.-value)
$\underline{I}$		unterstrichen: komplexe Größen	underlined: complex values
$\hat{I}$		Spitzenwert, Amplitude	peak value, amplitude
I'		auf Ständerwicklungsdaten umgerechnet	as seen from the stator winding
X', X''		transiente, subtransiente Reaktanz	transient, subtransient reactance
$\underline{I}^*$		konjugiert komplexer Wert von $\underline{I}$	conjugated complex value of $\underline{I}$
Re(.)		Realteil von ...	real part of ...
Im(.)		Imaginärteil von ...	imaginary part of ...

1. Permanent magnet synchronous machines as “brushless DC drives”

1.1 Basic principle of brushless DC drives

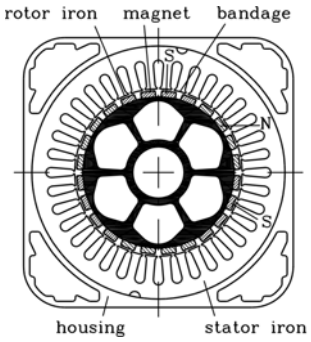

Fig. 1.1-1: Cross section of six-pole PM synchronous machine (*Siemens AG*)

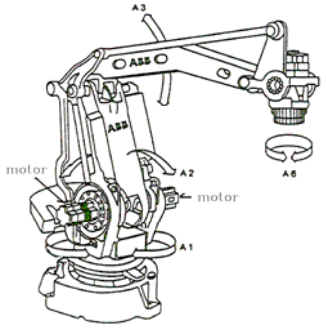

Fig. 1.1-2: Robot with four degrees of freedom (axes A1, A2, A3, A6) for loading goods: 160 kg lifting force, 1200 cycles per hour (=3 s per cycle), continuous operation. Brushless DC drives visible on the sides of the axes joints (*ABB, Sweden*).

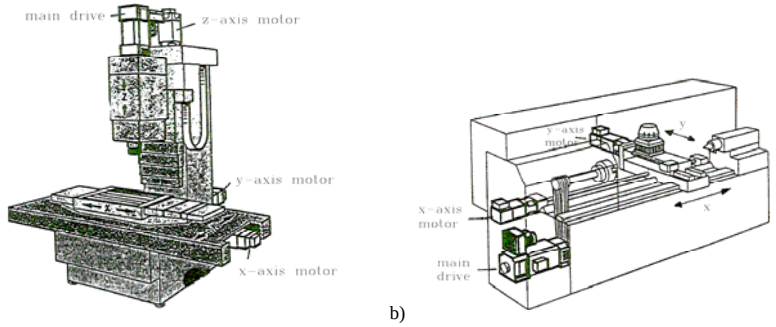

Fig. 1.1-3: Tooling machines for milling with main drive (usually AC induction motor or PM synchronous drive) and a) 3 and b) 2 brushless DC servo drives for positioning the tool (*Siemens AG*).

Synchronous machines, fed by PWM inverters, which allow field oriented motor control, behave like DC machines and not like line-fed synchronous machines. No pull-out torque exists and no oscillation of rotor. The inverter acts like the commutator of the DC machine, the stator three-phase AC winding like the DC armature winding of the DC rotor and the magnetostatically excited rotor of the synchronous machine corresponds with the magneto-statically excited DC stator. Therefore this kind of synchronous machine is called **"brushless DC drive"**, as – unlike in DC machines - no brushes are necessary. Usually a rotor position sensor is used to determine rotor flux orientation, which is necessary for field oriented control. **Permanent magnet rotor** excitation allows rotor flux generation without any excitation losses, thus gaining high efficiency and low temperature rise. Stator PWM voltage generates three phase AC current system in stator winding, the coils of which are distributed

in stator slots. These AC winding currents with a time shift of one third of a period between each two currents generate along with the distributed three-phase winding a **travelling air gap magnetic field**, which drags the rotors synchronously. Fig.1.1-1 shows the cross section of a typical three phase, six-pole PM synchronous motor with rare earth rotor permanent magnets, 36 stator slots and $q = 2$ slots per pole and phase.
These brushless DC drives are widely used, such as robot drives (Fig.1.1-2) or in tooling machines (Fig.1.1-3 a, b). Their features are low torque ripple (typically below 2 %) for smooth movements at low speed ("servo drive function"), high overload capability for fast acceleration (typically 4-times overload for short period of time e.g. a few seconds), no additional cooling system ("self cooling") and high degree of protection ("totally enclosed machine").

1.1.1 Basic function of PM synchronous machine

A magnetic field H is excited along a closed loop C in empty space according to *Ampere´*s law (1.1.1-1) by the enclosed ampere-turns $N \cdot I = \Theta$, where I is the electric current and N is the number of turns in series of the electric conductor.

$$\oint_C \vec{H} \bullet d\vec{s} = N \cdot I = \Theta \qquad (1.1.1\text{-}1)$$

Fig.1.1.1-1 shows an example where two different conductors with two different currents I_1 and I_2 form the total ampere-turns. The so-called magnetic flux density B is proportional to the field strength H.

$$B = \mu_0 H \qquad \mu_0 = 4\pi \cdot 10^{-7}\,\mathrm{Vs/(Am)} \qquad (1.1.1\text{-}2)$$

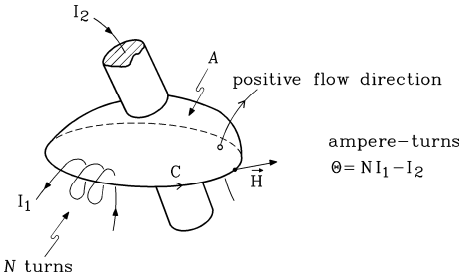

Fig.1.1.1-1: *Ampere´*s law: A magnetic field H is excited along a closed loop C in empty space by the enclosed ampere-turns Θ . In this example two different conductors with two different currents I_1 and I_2 form the total ampere-turns (*A. Prechtl, Springer, Wien*).

In Fig.1.1.1-2 is shown one phase, called U, of a distributed winding with $q = 3$ coils in series per pole and phase. The coil sides are placed in slots, the connection of coil sides by winding overhangs is not depicted. If the coils are excited by a current, according to (1.1.1-1) a field is excited, which generates a magnetic flux. As the magnetic flux per pole Φ penetrates iron parts and air gap, the flux density in the air gap and in the iron is determined by the geometric cross sections A_δ, A_{Fe}, where the flux passes by.

$$B_\delta = \Phi / A_\delta, \qquad B_{Fe} = \Phi / A_{Fe} \tag{1.1.1-3}$$

With material law for air and iron

$$B_\delta = \mu_0 \cdot H_\delta, \qquad B_{Fe} = \mu_{Fe} \cdot H_{Fe} \tag{1.1.1-4}$$

we get the magnetic field strength, which is determined by *Ampere´*s law (1.1.1-1). With $\mu_0 = 4\pi \cdot 10^{-7}$ Vs/(Am) and assuming instead of real ratio $\mu_{Fe}/\mu_0 \approx 2000...5000$ in unsaturated state the theoretically ideal iron with $\mu_{Fe} \to \infty$ the magnetic field strength H_{Fe} in the iron parts is zero.

$$H_{Fe} = B_{Fe} / \mu_{Fe} \to 0 \tag{1.1.1-5}$$

From *Ampere´*s law for a closed flux line *C* around a stator slot (with its ampere-turns Θ_Q), which contains the sections δ and s_{Fe} in air gap and iron parts, thus crossing the air gap from stator (subscript *s*) to rotor (subscript *r*) we get

$$\oint_C \vec{H} \bullet d\vec{s} = H_{Fe,s} \cdot s_{Fe,s} + H_{Fe,r} \cdot s_{Fe,r} + H_{\delta,right} \cdot \delta + H_{\delta,left} \cdot \delta = \Theta_Q \quad . \tag{1.1.1-6}$$

The values $H_{\delta,right}$, $H_{\delta,left}$ denote the field strength left and right of one slot in the air gap. With H_{Fe} = 0 and the **"magnetic voltage" ("magnetmotive force" MMF)** for air gap

$$V_\delta = H_\delta \cdot \delta \tag{1.1.1-7}$$

the air gap flux density B_δ is directly proportional to MMF:

$$B_\delta = \mu_0 V_\delta / \delta \quad . \tag{1.1.1-6}$$

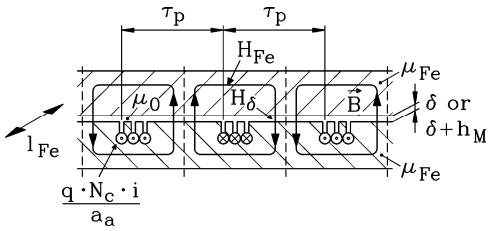

Fig. 1.1.1-2: Generation of flux lines by distributed winding system (here only one phase U depicted, q = 3, N_c turns per coil, a_a parallel coil groups, so current in one coil is i/a_a)

In Fig.1.1.1-3 for a distributed three-phase winding with q = 2 slots per pole and phase the slot ampere turn distribution is shown for time steps t = 0, t = T/12 and t = T/6, where $T = 1/f_s$ is the AC current period with f_s stator frequency of AC sinusoidal currents. Defining positive direction of H_δ from stator to rotor, and applying (1.1.1-6) to each slot along co-ordinate x, the MMF distribution in air gap is

$$\oint_C \vec{H} \bullet d\vec{s} = H_{\delta,right} \cdot \delta - H_{\delta,left} \cdot \delta = \Delta V_\delta(x) = \Theta_Q(x) \quad . \tag{1.1.1-9}$$

Starting at an arbitrary position x, where H_δ is zero, a step-like MMF distribution is generated by the distributed winding. At each slot the MMF distribution changes according to the local slot ampere turns Θ_Q, stepping up, if $\Theta_Q > 0$, and stepping down, if $\Theta_Q < 0$. Slot width is neglected, therefore the change of stator field at the slot ampere turns is stepwise with step height proportional to instantaneous slot ampere turns. According to (1.1.1-8) the MMF distribution coincides with air gap flux density distribution B_δ, as long as $\mu_{Fe} \to \infty$. Thus the air gap field B_δ is a step-like function of circumference co-ordinate x.

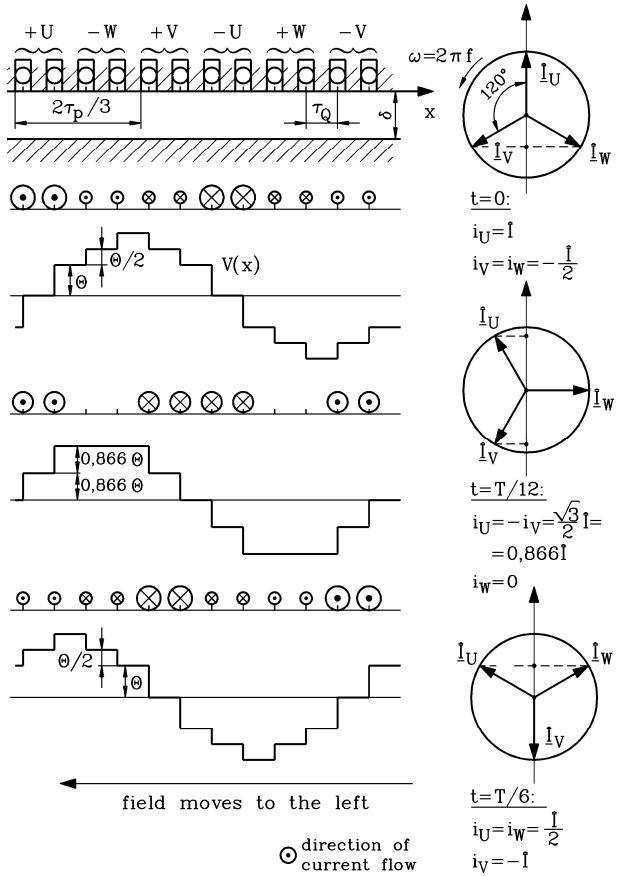

Fig. 1.1.1-3: Generation of travelling air gap field by sinusoidal three phase current system (q = 2)

Regarding the time steps t = 0, t = T/12 and t = T/6, one recognizes that the air gap flux density distribution B_δ is travelling to the left with the speed $v_{syn} = 2 \cdot f_s \cdot \tau_p$. It may be shown by *Fourier* analysis of this flux density distribution, that **the fundamental space harmonic**, which is sinusoidally distributed, keeps its shape unchanged during travelling,

whereas the step-like flux density distribution changes shape during travelling, as can be seen from Fig.1.1.1-2. Speed of this fundamental travelling sine wave is also

$$v_{syn} = 2 \cdot f_s \cdot \tau_p \quad , \qquad (1.1.1\text{-}10)$$

where **pole pitch** τ_p is half of the wave length of this fundamental sine wave. In rotational machines this velocity is the wave surface velocity at the stator bore, therefore rotational speed of this fundamental wave is

$$n_{syn} = \frac{f_s}{p} \quad . \qquad (1.1.1\text{-}11)$$

This stator travelling wave acts on the rotor magnets with a magnetic dragging force, this moving the permanent magnet rotor synchronously with the same speed $n = n_{syn}$. Thus the machine is acting as a **motor**. If the rotor is turned by external source, it will induce in the stator winding a voltage due to the moving rotor magnets, thus causing a changing flux linkage of stator coils. This induced voltage u_p may generate a current in the stator loaded winding; - the machine is in generating mode **(generator)**.

Conclusions:
A three-phase winding with distributed coils with their coil sides placed in slots is called distributed winding. When fed with current, this distributed winding excites a step-like air gap flux density distribution with north and south poles. Width of the poles is called pole pitch. The fundamental harmonic of this step-like distribution has wavelength equal to two pole pitches. If the coils of the three phases U, V, W of the distributed winding are spaced by $2\tau_p/3$ *and are fed by sinusoidal three-phase current with* $2\pi/3$ *phase shift, the air gap flux density is travelling (rotating) with synchronous speed.*

1.1.2. Permanent magnet technology

a) Permanent magnet properties:
The elements Fe, Ni and Co show **ferromagnetic** behaviour, that means they consist of randomly distributed elementary permanently magnetized regions. If these elements are exposed to an external magnetic field *H*, these "elementary" magnets turn parallel to this external field and create an own magnetic polarization *J*. This polarization amplifies the external field, yielding a resulting magnetic flux density

$$B = \mu_0 H + J \quad . \qquad (1.1.2\text{-}1)$$

Permanent magnets always consist of these elements Fe, Ni or Co and other elements, which are necessary to increase coercive field. The most widely used permanent magnet materials are
- AlNiCo,
- Ba-Ferrite and Sr-Ferrite,
- Rare earth magnets SmCo and NdFeB.

Magnetization of rare earth permanent magnetic material in external field H_M is shown in Fig.1.1.2-1 along the dotted "virgin" curve. When all "elementary" magnets are in parallel

with the external field, the maximum value $J_M = J_s$, the so-called **saturation** of polarization, is reached. The corresponding necessary flux density

$$B_M = \mu_0 H_s + J_s \qquad (1.1.2\text{-}2)$$

is huge (about 3.5 T ... 4 T). When the external field is switched off, *J* decreases along the upper branch of the closed $J_M(H_M)$ loop and reaches $J_M(H_M{=}0) = J_R = B_R$, the so-called **remanence** flux density. With inverse field H the permanent magnet is demagnetized completely at H_{CJ}. At the coercive field strength H_{CB} the resulting flux density B_M vanishes.

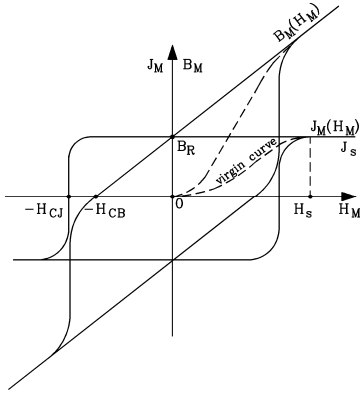

Fig.1.1.2-1: Hysteresis loop $J_M(H_M)$ and $B_M(H_M)$ of a rare earth permanent magnet

The inclination of the $B_M(H_M)$-loop is ca. $1.05\,\mu_0$ according to (1.1.2-1). Therefore modern rare earth magnets behave in an external magnetic field like air with a relative permeability of nearly unity.

b) Design of magnet dimensions:
In permanent magnet motors the magnets are often fixed on the rotor surface (Fig.1.1-1). The air gap δ between stator and rotor and the stator and rotor iron have to be magnetized by the magnets. Let us assume that the iron permeability is infinite ($\mu_{Fe} \to \infty$), then according to $B_{Fe} = \mu_{Fe} H_{Fe}$ and a given flux density the iron magnetic field H_{Fe} is zero. Thus *Ampere´s* law yields for the resulting magnetic field of the surface mounted magnets with magnet height h_M according to Fig.1.1.2-2 with *C* as the closed loop of the *B* flux lines:

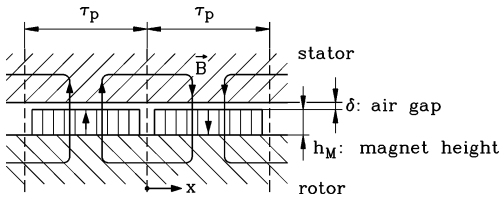

Fig.1.1.2-2: Magnet field of surface mounted permanent magnet (no electric current in stator winding)

$$\oint_C \vec{H} \bullet d\vec{s} = 2(H_\delta \delta + H_M h_M) = \Theta = 0 \qquad (1.1.2\text{-}2)$$

As the magnetic flux Φ of the magnets has to be constant in the machine and the cross section of flux in air gap and in the magnets is the same $A_M = A_\delta$, one gets

$$\Phi = B_M A_M = B_\delta A_\delta \qquad (1.1.2\text{-}3)$$

and therefore $B_M = B_\delta$. With (1.1.2-2) the relation between the air gap flux density and field strength within the magnet is

$$\boxed{B_\delta = \mu_0 H_\delta = -\mu_0 \frac{h_M}{\delta} H_M = B_M} \quad . \qquad (1.1.2\text{-}4)$$

This linear expression with negative inclination has to be combined with the hysteresis loop of the magnet $B_M(H_M) = B_\delta(H_M)$. The crossing of the straight line (1.1.2-4) with the loop in the second quadrant of the *B*-*H*-plane yields the operation point *P* of the magnet with a resulting flux density B_δ, which is lower than the remanence B_R, showing that the magnet is demagnetized by the air gap, but this demagnetization is reversible. The operating region of the magnet is the second quadrant. With **increased temperature** the remanence and coercive field are decreasing (Fig.1.1.2-3), yielding reduced air gap flux density according to operation points P_1 to P_4. It has to be noted that above a certain relatively high temperature (***Curie*-temperature**) the ferromagnetism vanishes completely in Fe, Ni, Co and therefore also the permanent magnet behaviour.

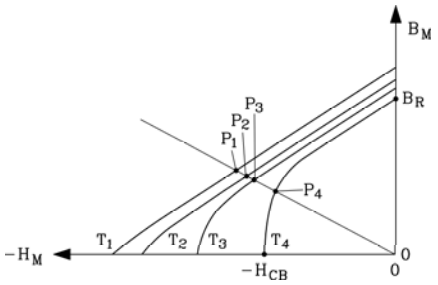

Fig.1.1.2-3: Reversible demagnetization of permanent magnet by air gap. The operating region of the magnet is the second quadrant. With increased temperature the remanence and coercive field is decreasing, yielding reduced air gap flux density according to operation points P_1 to P_4.

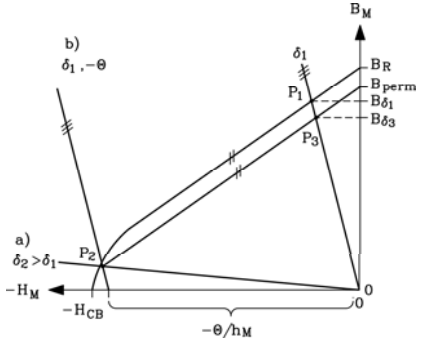

Fig.1.1.2-4: Irreversible demagnetization of permanent magnet a) by increased air gap $\delta_1 < \delta_2$, b) by external opposite field $-\Theta/h_M$, reaching an operating point P_2 below the "knee" of the hysteresis loop.

If the air gap is increased significantly e.g. by removing the rotor from the stator, the inclination of the straight line (1.1.2-4) is decreased. The operation point may be shifted from P_1 to P_2 below the "knee" of the hysteresis loop (Fig.1.1.2-4a). When air gap is reduced again e.g. by putting the rotor again into the stator, the operation point moves on a parallel line below the hysteresis loop. The remanence B_R is reduced to the so-called **permanence** B_{perm},

the magnet is demagnetized partially, but irreversibly. The air gap flux density according to operation point P_3 is lower than before in point P_1.
If in Fig.1.1.2-2 an additional amount of ampere turns Θ per pole is introduced in stator slots (which means that stator winding is carrying current), we get

$$\oint_C \vec{H} \bullet d\vec{s} = 2(H_\delta \delta + H_M h_M) = 2\Theta \qquad (1.1.2\text{-}5)$$

$$B_\delta = \mu_0 H_\delta = -\mu_0 \cdot (H_M - \Theta / h_M) \cdot \frac{h_M}{\delta} = B_M \qquad (1.1.2\text{-}6)$$

The straight line is shifted by the stator ampere turns to the left in case of negative ampere turns (Fig.1.1.2-4b). In that case the magnet is demagnetized by the stator self field of the stator ampere turns. If the ampere turns are positive, their field increases the permanent magnet field. The first case is critical, because like in Fig.1.1.2-4a again danger of irreversible demagnetization exists.

Conclusions:
The magnet must not be operated below the "knee" of the hysteresis loop to avoid irreversible demagnetization.

In order to avoid irreversible demagnetization the height of magnet h_M has to be large enough to reduce the shift of the straight line in Fig.1.1.2-4b to keep the crossing point P_2 well above the knee of the hysteresis loop.

Therefore the **design of dimensions of permanent magnets** with a given *B*(*H*)-loop depend for a given temperature on the following rules:
1. For a given air gap δ the magnetic flux Φ is determined by a proper height h_M to reach a sufficient air gap flux density B_δ and by a proper magnet cross section A_M to get the wanted flux $\Phi = B_\delta \cdot A_M$.
2. To withstand a given stator field excited by the ampere turns Θ the "knee" of the hysteresis loop has to be located at a value $|H| > |\Theta / h_M|$, again requiring a certain magnet height h_M.

Example 1.1.2-1:
For given B_R and H_{CB} of six different permanent magnet materials
(1) AlNiCo, (2) rare earth NdFeB, type A for 70°C, (3) NdFeB, type B for 180°C,
(4) rare earth Sm_2Co_{17} for 350°C, (5) Ba-ferrite, (6) composite rubber/Ba-ferrite magnet
according to Table 1.1.2-1 (Fig.1.1.2-6b) the same air gap flux Φ and the same demagnetization limit against given Θ is wanted. How has magnet height h_M and cross section A_M to be chosen ?
Conditions are $A_M = \Phi / B_\delta \sim 1/B_R$ and $|h_M| > |\Theta / H_{knee}| \sim 1/H_{CB}$. We consider for AlNiCo the value $A_0 = A_M$ and $h_0 = h_M$ as 100%. Then the geometry and the volume $V_M = h_M A_M$ for the other magnets is as given in Table 1.1.2-1.

at 20°C	AlNiCo	NdFeB, A	NdFeB, B	Sm_2Co_{17}	Ba-ferrite	rubber ferrite
B_R / T	1.3	1.4	1.2	0.95	0.4	0.24
H_{CB} / kA/m	90	1100	900	710	270	175
A_M/A_0	*1*	*0.93*	*1.08*	*1.36*	*3.25*	*5.4*
h_M/h_0	*1*	*0.08*	*0.1*	*0.13*	*0.33*	*0.51*
V_M/V_0	*1*	*0.076*	*0.11*	*0.18*	*1.08*	*2.8*

Table 1.1.2-1: Comparison of different magnetic material for the same flux and demagnetizataion limit

Conclusions:
Rare earth magnets allow for the same flux and the same demagnetization limit a much smaller magnetic volume of only about 10%, which yields compact PM motors, but it is expensive. Cheap PM motors with ferrite magnets need nearly the same amount of magnets as AlNiCo. Motors with AlNiCo need relatively long magnets, whereas ferrite magnets without flux concentration methods have a rather low air gap flux density below 0.4 T.

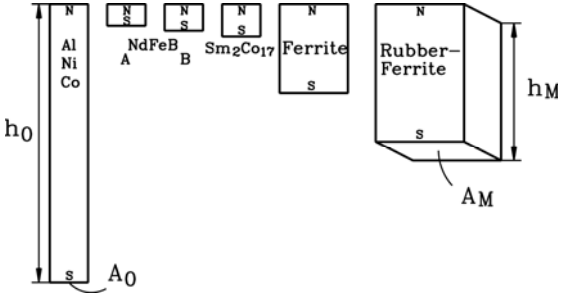

Fig.1.1.2-5: Comparison of influence of material properties on magnetic design for (1) AlNiCo, (2) rare earth NdFeB, type A for 70°C, (3) NdFeB, type B for 180°C, (4) Sm_2Co_{17}, (5) Ba-ferrite, (6) composite rubber-ferrite

Example 1.1.2-2:
Magnetic *B(H)*-loops for (Fig.1.1.2-6)
a) 1: Soft magnetic material (e.g. iron) compared with 2: permanent magnet characteristic
b) Second quadrant for permanent magnets: (1) AlNiCo, (2) anisotropic Ba-ferrite, (3) rare earth magnet Sm_2Co_{17} (for 350°C), (4) rare earth magnet NdFeB (for 180°C)

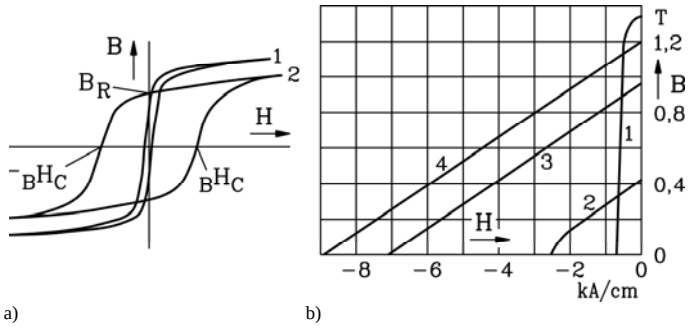

a) b)

Fig.1.1.2-6: *B(H)*-characteristics: a) (1) Soft magnetic material, (2) PM magnet, (b) PM magnets: Second quadrant at 20°C; (1) Al-Ni-Co, (2): Ba-Ferrit, (3): Sm_2Co_{17} (ϑ_{max} = 350°C) (4): NdFeB (ϑ_{max} = 180°C)

c) Surface-mounted permanent magnets on rotors:

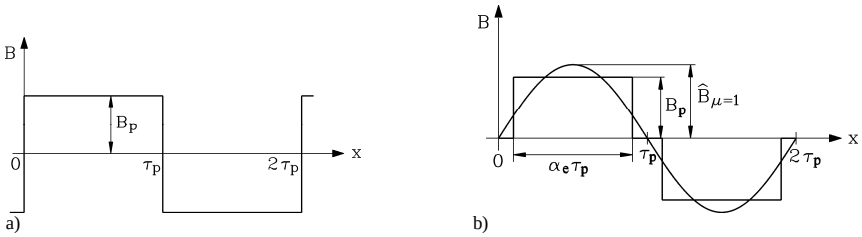

Fig.1.1.2-7: No-load air gap magnetic flux density a) with pole coverage ratio $\alpha_e = 1$, and b) with $\alpha_e < 1$

The **no-load** condition of an electric machine means that stator current is zero. Rotor magnets produce a rectangular shaped magnetic flux density profile (Fig.1.1.2-7a) with an amplitude given by (1.1.2-4). If some magnets are omitted, the pole coverage ratio is $\alpha_e < 1$; thus a pole gap exists (Fig.1.1.2-7b).
Under **load**, the feeding inverter impresses a stator current distribution, which should yield maximum torque for a given current amplitude. According to the electromagnetic *Lorentz*-force F_c on a current-carrying conductor (current *I*) with length *l*

$$\vec{F}_c = \int_0^l I \cdot (d\vec{s} \times \vec{B}) \qquad (1.1.2\text{-}7)$$

we get for right angle between straight conductor and constant flux density vector *B*

$$F_c = I \cdot B \cdot l \quad . \qquad (1.1.2\text{-}8)$$

Thus for maximum force $F = \sum F_c$ (and therefore maximum torque) of all current-carrying conductors in stator winding the currents of the three phases must flow per pole in the same direction to add to a total resulting force. For a three-phase winding this is achieved by moving the stator travelling field synchronously with rotor magnets and keeping the rotor position relative to the stator travelling field so, that positive ampere turns are opposite of rotor north pole and negative ampere turns are opposite of rotor south pole. Therefore a rotor position sensor is necessary to tell the inverter the appropriate current phase angle for impressing stator current. In Fig.1.1.2-8 the current distribution for maximum torque is shown along with force generation.

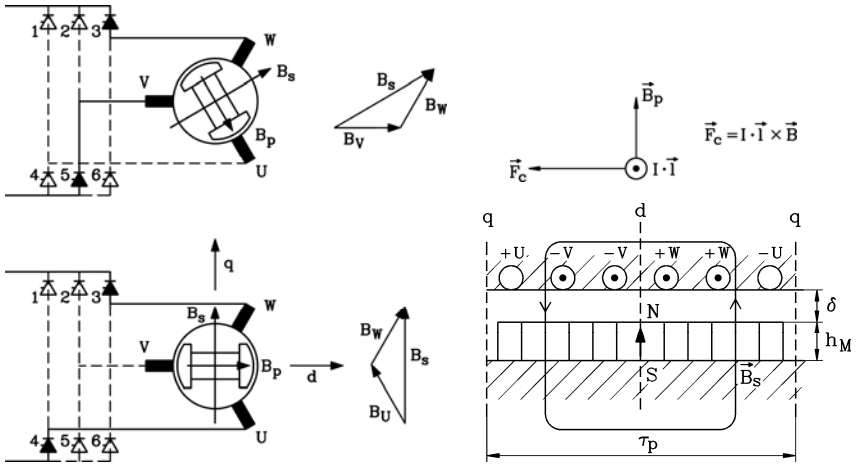

a) b)

Fig.1.1.2-8: How to get maximum force (torque) for given ampere turns: By rotor position sensing the inverter (a) impresses the current so that its stator field B_s is perpendicular to rotor PM field B_p. Then stator currents are with one polarity under north pole of PM magnets (b), and with opposite polarity under south pole, thus generating maximum tangential force.

The stator magnetic field, which is excited by the stator ampere turns, rises linear with co-ordinate x from the centre axis of the magnets (d-axis), as can be seen from *Ampere´*s law (Fig.1.1.2-9). Assuming the magnets passive permeability as μ_0, we get

$$\oint_C \vec{H} \bullet d\vec{s} = 2 \cdot H_{\delta,s} \cdot (\delta + h_M) = 2 \cdot A \cdot x \quad \Rightarrow \quad H_{\delta,s} = \frac{A}{\delta + h_M} \cdot x \quad . \qquad (1.1.2\text{-}9)$$

In (1.1.2-5) we assumed that the ampere turns are equally distributed along the stator circumference, resulting in an average "current layer"

$$A = \Theta / \tau_p = \frac{2 \cdot m \cdot N_s \cdot I_s}{2p \cdot \tau_p} \qquad . \qquad (1.1.2\text{-}10)$$

The superposition of stator and rotor field gives a reduction of magnetic field on the trailing edge of the PM pole with danger of demagnetization. So, current must stay below the demagnetization limit.

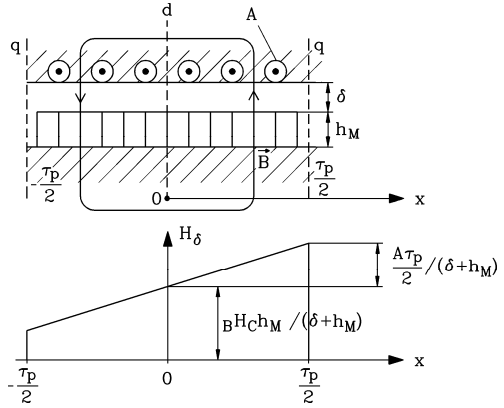

Fig.1.1.2-9: Air gap magnetic flux density for one pole under load

Conclusions:
Under load surface mounted rotor magnets experience danger of demagnetization at the trailing pole edge.

1.1.3 Torque generation in PM machines with block and sine wave current operation

Torque can be calculated from total *Lorentz*-force (1.1.2-10) (with stator inner diameter d_{si})

$$M_e = F \cdot d_{si} / 2 \qquad (1.1.3\text{-}1)$$

or from **internal (air gap) power**

$$P_\delta = 2\pi \cdot n_{syn} \cdot M_e \qquad . \qquad (1.1.3\text{-}2)$$

Internal power is given by product of rotor **induced voltage** in stator winding

$$U_i = U_p \qquad (1.1.3\text{-}3)$$

("back EMF", EMF = electromotive force, which of course is no "force", but a voltage !) and stator current.

$$p_\delta(t) = u_{pU}(t) \cdot i_U(t) + u_{pV}(t) \cdot i_V(t) + u_{pW}(t) \cdot i_W(t) \qquad (1.1.3\text{-}4)$$

Two different modes for torque generation are distinguished:

- block current feeding ("block commutation" of current),
- sine wave current feeding ("sine wave commutation" of current).

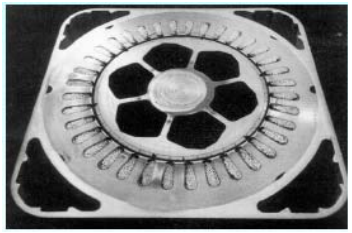

a) (*Siemens AG, Germany*)

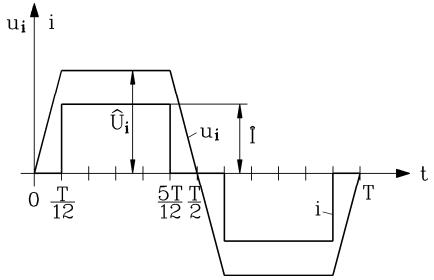

b)

Fig.1.1.3-1: Block current feeding: a) Cross section of PM synchronous machine with 100% pole coverage ratio, b) trapezoidal no-load stator phase voltage (back EMF); block shaped current impressed in phase with back EMF

With **block current feeding** the rotor has surface mounted magnets with 100% pole coverage ratio, yielding rectangular shaped air gap magnetic flux density. This distribution yields trapezoidal no-load stator induced voltage (back EMF, Fig.1.1.3-1), when stator slots or rotor magnets are skewed by one stator slot pitch. For this purpose, the stator winding consists of coils with coil span W equal to pole pitch τ_p. Therefore, simple single layer three phase winding can be used.

If block stator currents are impressed by inverter with 120° pulse width and 60° gap in phase with back EMF, the internal power according to (1.1.3-4) is contributed at each moment by only two of the three phases. The third phase always yields zero power (Fig. 1.1.3-2).

Usually stator winding for inverter operation is star-connected. With phase current block amplitude $\hat{I}$ and phase back EMF amplitude $\hat{U}_p$ torque amplitude is

$$M_e = \frac{2 \cdot \hat{U}_p \cdot \hat{I}}{2 \cdot \pi \cdot n} \quad . \qquad (1.1.3\text{-}5)$$

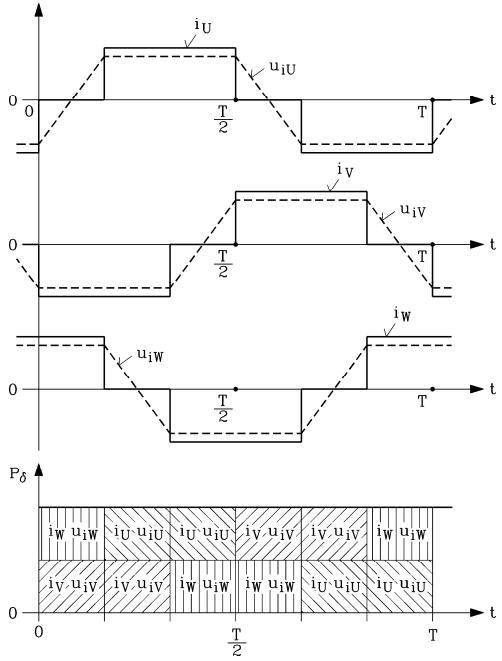

Fig.1.1.3-2: Torque generation with block current feeding, calculated via internal power. A smooth torque without any ripple is theoretically produced with contribution of two phases at each moment

With **sine wave current feeding** the rotor has surface mounted magnets with typically 85% pole coverage ratio, yielding 85%-block shaped air gap magnetic flux density with gaps of 15% in between. If a two-layer star-connected chorded winding with coil span $W < \tau_p$ is used with number of coils per pole and phase $q > 1$ is used, the induced no-load voltage is nearly sinusoidal (Fig.1.1.3-3).
If sine wave stator currents are impressed by inverter in phase with this sinusoidal back EMF, the internal power according to (1.1.3-4) is constant for each moment. Each phase contributes one third of the total power.

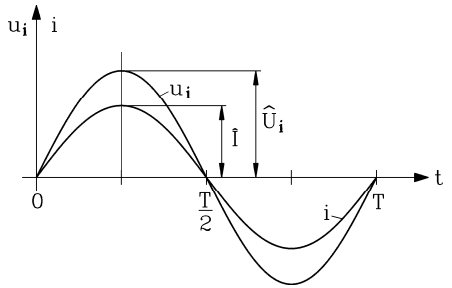

Fig.1.1.3-3: Torque generation with sine wave current feeding: Sinusoidal phase current is impressed by inverter in phase with sinusoidal back EMF, resulting in pulsating power per phase, but smooth constant power and torque for all three phases.

$$p_\delta(t) = \hat{U}_p \cos(\omega t)\cdot \hat{I}\cos(\omega t) + \hat{U}_p \cos(\omega t - 2\pi/3)\cdot \hat{I}\cos(\omega t - 2\pi/3) + \\ + \hat{U}_p \cos(\omega t - 4\pi/3)\cdot \hat{I}\cos(\omega t - 4\pi/3) \qquad (1.1.3\text{-}6)$$

By use of

$$\cos\alpha\cdot\cos\beta = \frac{1}{2}\cdot\left[\cos(\alpha+\beta)+\cos(\alpha-\beta)\right]$$

we get

$$p_\delta(t) = \frac{\hat{U}_p\hat{I}}{2}\cdot\left[\cos(2\omega t)+1\right] + \frac{\hat{U}_p\hat{I}}{2}\cdot\left[\cos(2\omega t - \frac{4\pi}{3})+1\right] + \frac{\hat{U}_p\hat{I}}{2}\cdot\left[\cos(2\omega t - \frac{8\pi}{3})+1\right]$$

and with

$$\cos(\lambda) + \cos(\lambda - \frac{4\pi}{3}) + \cos(\lambda - \frac{8\pi}{3}) = 0$$

finally the time-independent internal power (m = 3: number of phases)

$$p_\delta(t) = m\frac{\hat{U}_p\hat{I}}{2} = const. \qquad (1.1.3\text{-}7)$$

and the **electromagnetic torque**

$$\boxed{M_e = \frac{(3/2)\cdot\hat{U}_p\cdot\hat{I}}{2\cdot\pi\cdot n}} \quad . \qquad (1.1.3\text{-}8)$$

Conclusions:
Both block and sine wave commutated PM machines deliver (theoretically) constant torque, if phase currents are impressed in phase with back EMF.

1.1.4 Induced no-load voltage ("back EMF") in PM machines

a) Block commutation principle:
The flux linkage of one coil (N_c: number of turns per coil, l_{Fe}: length of stator iron stack) with coil span equal to pole pitch (= unchorded coil) is

$$\psi_c(t) = N_c\cdot l_{Fe}\cdot\int_0^{\tau_p} B_\delta(x,t)\cdot dx \quad . \qquad (1.1.4\text{-}1)$$

According to Fig.1.1.4-1 this flux linkage is changing linear from positive maximum to negative maximum in linear way, when the rotor moves one pole pitch. This leads to triangular change of coil flux linkage, when rotor is moving on, leading to rectangular shape of induced coil voltage according to *Faraday´*s law

$$u_i = -d\psi/dt \quad \Rightarrow \quad u + u_i = R\cdot i \quad \Rightarrow \quad u = R\cdot i + d\psi/dt \qquad (1.1.4\text{-}2)$$

with induced voltage amplitude per coil

$$\hat{U}_{i,c} = 2N_c\cdot\nu\cdot B_\delta\cdot l_{Fe} = 2N_c\cdot 2f\tau_p\cdot B_\delta\cdot l_{Fe} \quad . \qquad (1.1.4\text{-}3)$$

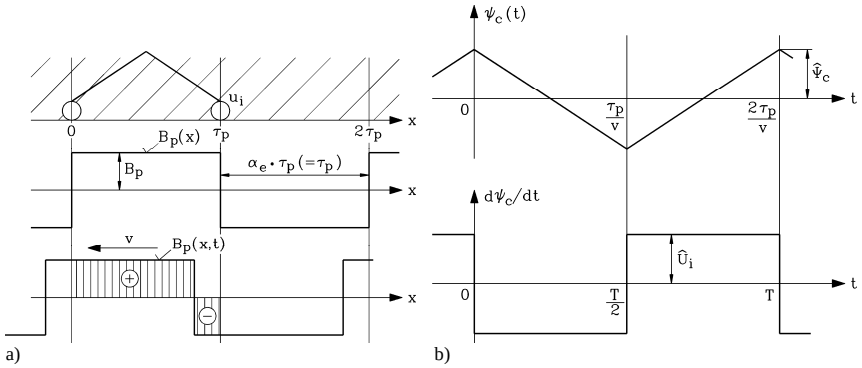

Fig.1.1.4-1: Rectangular air gap flux density distribution (a) leads to triangular flux linkage time function, causing (b) rectangular shaped induced coil voltage dψ/dt

Conclusions:
For an unchorded (= full pitched) coil the shape of spatial distribution of air gap flux density is identical with the time function of the corresponding induced coil voltage.

If the stator coil sides (or rotor magnets) are skewed by one coil pitch, the change of flux density is changed from rectangular to trapezoidal. Therefore also induced voltage has the same shape. If q coils are in series per phase and pole (= coil group), they add to series voltage again of trapezoidal shape with 120° constant voltage and 60° linear voltage change (Fig.1.1.4-2). With $N_s = p\cdot q\cdot N_c/a$ windings per phase in single layer winding we get from (1.1.4-3) the voltage amplitude per phase

$$\hat{U}_i = 2N_s\cdot\nu\cdot B_\delta\cdot l_{Fe} = 2N_s\cdot 2f\tau_p\cdot B_\delta\cdot l_{Fe} \quad . \qquad (1.1.4\text{-}4)$$

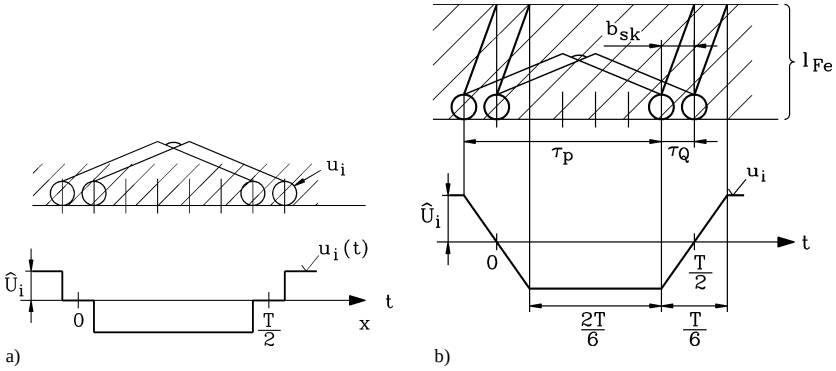

Fig.1.1.4-2 a, b: Coil group with q coils (here: q = 2), a) unskewed coils: the induced back EMF is step-like, when being induced by rectangular air gap flux density distribution, b) coils skewed by one slot pitch yield a trapezoidal back EMF

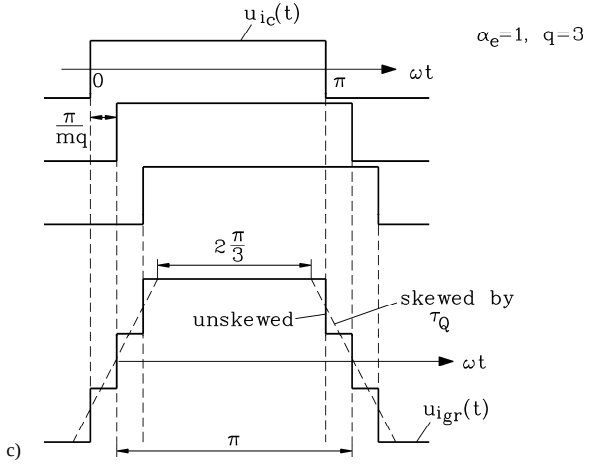

Fig.1.1.4-2c: Coil group with q = 3 coils: unskewed coils: the induced back EMF is step-like, but coils - skewed by one slot pitch - yield a trapezoidal back EMF

b) Sine wave commutation principle:

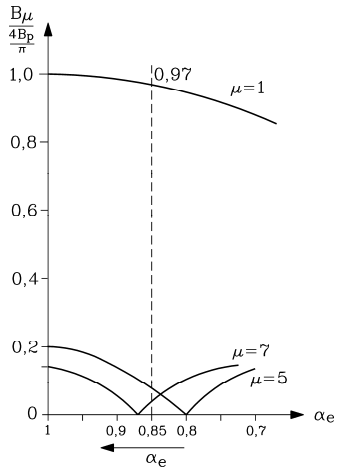

Fig.1.1.4-3: Influence of α_e on the rotor flux density amplitudes: At α_e = 0.85 the fundamental amplitude is reduced by 3%, but 5th and 7th harmonic are reduced drastically.

The air gap flux density distribution – depending on rotor co-ordinate x_r - may be expanded into a *Fourier*-series with only odd ordinal numbers μ due to the symmetry of north and south pole

$$B_\delta(x_r) = \sum_{\mu=1}^{\infty} B_{\delta,\mu} \cdot \cos(\mu\pi x_r / \tau_p), \qquad \mu = 1, 3, 5, 7, ... \qquad (1.1.4\text{-}5)$$

with amplitudes

$$B_{\delta,\mu} = \frac{4 \cdot B_\delta}{\pi \cdot \mu} \cdot \sin(\mu \cdot \alpha_e \cdot \pi/2) \quad . \qquad (1.1.4\text{-}6)$$

In Fig.1.1.4-3 the influence of α_e on the amplitudes shows, that at α_e = 0.85 the fundamental amplitude is reduced by 3%, but 5th and 7th harmonic are reduced considerably.

With moving rotor the relationship between stator and rotor co-ordinate $x = x_s$ and x_r is

$$x_s = x_r + v_{syn} \cdot t = x_r + 2 f \tau_p t \qquad (1.1.4\text{-}7)$$

and therefore

$$B_{\delta,\mu}(x,t) = B_{\delta,\mu} \cdot \cos(\frac{\mu x \pi}{\tau_p} - \mu \cdot \omega \cdot t) \quad , \mu = 1, 3, 5, 7, ... \quad . \qquad (1.1.4\text{-}8)$$

If the coil span is smaller than one pole pitch, the coil flux linkage of the remaining 5th and 7th harmonic can be further reduced, if the ratio W / τ_p is chosen appropriately. With (1.1.4.-1) and (1.1.4-3) we get

$$\psi_{c\mu}(t) = N_c l_{Fe} \int_{-W/2}^{W/2} B_{\delta,\mu}(x,t) \cdot dx = N_c \cdot \frac{2}{\pi} \cdot \frac{\tau_p}{\mu} l_{Fe} B_{\delta\mu} \cdot \sin(\mu \cdot \frac{W}{\tau_p} \cdot \frac{\pi}{2}) \cdot \cos(\mu\omega t) \,. \qquad (1.1.4\text{-}9)$$

Compared with unchorded coil $W = \tau_p$, we get a reduction of flux linkage by the **pitch factor**

$$k_{p\mu} = \sin(\mu \cdot \frac{W}{\tau_p} \cdot \frac{\pi}{2}) \quad . \qquad (1.1.4\text{-}10)$$

Example 1.1.4-1:
Three-phase winding with 6 slots per pole, thus q = 2 slots per pole and phase. Coil span reduced by one slot pitch, resulting in W / τ_p = 5/6. Reduction of flux linkage is very strong for 5th and 7th harmonic.

μ	1	3	5	7	9	11	13
$k_{p\mu}$	0.966	-0.707	0.259	0.259	-0.707	0.966	0.966

Table 1.1.4-1: Reduction of coil flux linkage due to chording W / τ_p = 5/6.

So harmonics with higher ordinal number will induce stator voltage with increased frequency μf, but can be reduced by appropriate chording. A further reduction of these higher harmonics occurs due to the fact, that with q > 1 several coils per pole and phase are connected in series. There is a phase shift $\alpha_{Q\mu}$ between the voltages of adjacent coils due the coil displacement by the slot pitch τ_Q, which increases with increasing ordinal number.

$$\alpha_{Q\mu} = \mu \cdot \pi \cdot (\tau_Q / \tau_p) \qquad (1.1.4\text{-}11)$$

Therefore the resulting series voltage of the coil group is smaller than the algebraic sum of voltage per coil.

Example 1.1.4-2:
Three-phase winding, 9 slots per pole, q = 3 coils per pole and phase.
$\alpha_{Q\mu=1} = \alpha_Q = \pi \cdot (\tau_Q / \tau_p) = \pi / 9 \leftrightarrow 180° / 9 = 20°$

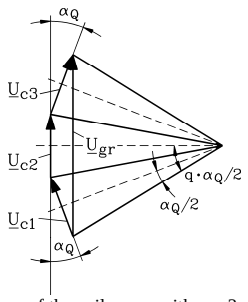

Fig.1.1.4-4: The resulting series voltage u_{gr} of the coil group with q = 3 coils is smaller than the algebraic sum of voltage per coil u_c.

The ratio of resulting series voltage $U_{i,gr,\mu}$ versus algebraic sum of coil voltages $U_{i,c,\mu}$ is according to Fig.1.1.4-4 the so-called **distribution factor $k_{d,\mu}$:**

$$k_{d,\mu} = \frac{\hat{U}_{i,gr,\mu}}{q\hat{U}_{i,c,\mu}} = \frac{2\sin\left(q\frac{\alpha_{Q,\mu}}{2}\right)}{q \cdot 2\sin\left(\frac{\alpha_{Q,\mu}}{2}\right)} = \frac{\sin\left(\mu\frac{\pi}{2m}\right)}{q \cdot \sin\left(\mu\frac{\pi}{2mq}\right)} \qquad (1.1.4\text{-}12)$$

μ	1	3	5	7	9	11	13
$k_{d\mu}$	0.960	0.667	0.218	-0.177	-0.333	-0.177	0.218

Table 1.1.4-2: Reduction of coil flux linkage due to coil group arrangement q = 3.

So, the resulting effect of harmonics, decreasing with ordinal number, and of chording and coil group arrangement, being summarized in the **winding factor**

$$k_{w,\mu} = k_{p,\mu} \cdot k_{d,\mu} \quad , \qquad (1.1.4\text{-}13)$$

can be given for the induced voltage with (1.1.4-2) as

$$u_{i\mu}(t) = \mu\omega \cdot N_s \cdot k_{w\mu} \cdot \frac{2}{\pi} \cdot \frac{\tau_p}{\mu} l_{Fe} B_{\delta\mu} \cdot \sin(\mu\omega t) = U_{i\mu} \cdot \sin(\mu\omega t) \quad , \qquad (1.1.4\text{-}14)$$

where $N_s = 2p \cdot q \cdot N_c / a$ is the number of windings per phase of two-layer winding. If the stator winding is **star connected**, the third harmonic voltages in all three phases U, V, W are IN phase and IDENTICAL:

$$\begin{aligned} u_{U3}(t) &= U_3 \cdot \cos(3\omega t) \\ u_{V3}(t) &= U_3 \cdot \cos(3(\omega t - 2\pi/3)) = U_3 \cdot \cos(3\omega t) = u_{U3}(t) \\ u_{W3}(t) &= U_3 \cdot \cos(3(\omega t - 4\pi/3)) = U_3 \cdot \cos(3\omega t) = u_{U3}(t) \end{aligned} \qquad (1.1.4\text{-}15)$$

Therefore the line-to-line voltages show NO 3rd harmonic component:
$u_{UV3}(t) = u_{U3}(t) - u_{V3}(t) = u_{U3}(t) - u_{U3}(t) = 0$
and so on for all phases. Further, no current of 3rd harmonic can occur, as according to *Ohm´s* law the current per phase is proportional to the phase impedance $\underline{Z}_3$ and phase voltage $\underline{U}_3$ and according to *Kirchhoff´s* second law the sum of all currents in the star node must be zero.

$$\underline{I}_3 = \underline{U}_3 / \underline{Z}_3 \quad \Rightarrow \quad \underline{I}_{U3} + \underline{I}_{V3} + \underline{I}_{W3} = 3\underline{I}_3 = 0 \quad \Rightarrow \quad \underline{I}_3 = 0 \qquad (1.1.4\text{-}16)$$

Thus, by star connection, the 3rd current harmonic and all other current harmonics with ordinal numbers, divisible by factor 3, and all corresponding line-to-line voltages are suppressed. So, the ordinal numbers 3, 9, 15, ... vanish.

In addition, **skewing** by the distance b_{sk} reduces flux linkage and therefore induced voltage further by the so-called **skewing factor** (which is not derived here)

$$\chi_\mu = \sin(S_\mu)/S_\mu \qquad S_\mu = \frac{\mu\pi b_{sk}}{2\tau_p} \quad . \qquad (1.1.4\text{-}17)$$

Example 1.1.4-3:
Six pole machine, rotor speed 1500/min
Stator: Three-phase winding, 5/6 chorded coils, q = 2 coils per pole and phase
Rotor: Surface permanent magnets, 85% pole coverage ratio
Magnets skewed by one stator slot pitch $\frac{\pi b_{sk}}{2\tau_p} = \frac{\pi}{12} \leftrightarrow 15°$

Ordinal Number	Stator frequency	Flux density	Winding Factor	Skewing factor	Induced phase voltage	Induced line-line voltage
μ	μf	$B_{\delta\mu}$	$k_{w\mu}$	$\chi_{skew,\mu}$	$U_{i\mu}$	$U_{i\mu,LL}$
1	75 Hz	100 %	0.933	0.989	100 %	100 %
3	225 Hz	-26.1 %	-0.50	0.900	12.73 %	0
5	375 Hz	7.9 %	0.067	0.738	0.42 %	0.42 %
7	525 Hz	1.2 %	-0.067	0.527	0.05 %	0.05 %
9	675 Hz	-6.0 %	0.50	0.300	0.98 %	0
11	825 Hz	8.0 %	-0.933	0.090	0.73 %	0.73 %

Table 1.1.4-3: Spectrum of induced voltages for six pole machine, rotor speed 1500/min, three-phase winding, 5/6 chorded coils, q = 2 coils per pole and phase, 85% pole coverage ratio, skew one slot pitch

Table 1.1.4-3 shows that the amplitudes of induced voltages of higher harmonics are below of 1 % of fundamental voltage and can therefore be neglected.

Conclusions:
Due to pole coverage ratio less than unity, chording of coils, arrangement of coils in coil groups, skewing of coils and star connection the back EMF is nearly sinusoidal, although air gap flux density is not.

Example 1.1.4-4:
Motor designed for sine wave commutation: Measured no-load voltage in generator mode (back EMF), machine driven by external motor (Fig.1.1.4-5). The back EMF (no-load voltage) is nearly sinusoidal due to “filter effect” of stator winding, although the rotor has

surface mounted magnets with 85% pole coverage. *Fourier* analysis shows that higher harmonics (here: 5th order: $f = 5f_s$ = 167 Hz) are very small, compared with fundamental f_s = 33.5 Hz.

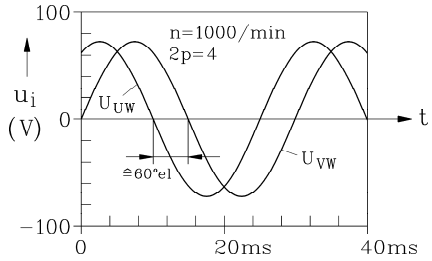

Fig.1.1.4-5: Measured no-load voltage line-to-line of a 4 pole brushless DC motor, designed for sine wave commutation, at 1000/min, showing nearly ideal sine wave back EMF (Data: M_N = 1.3 Nm, n_N = 6000/min)
Fourier-Analysis of no-load voltage: μ = 1: 33.5 Hz, 74.8 V
μ = 5: 167 Hz, 0.34 V
Other amplitudes are negligible !

1.1.5 Equivalent circuit of PM synchronous machine

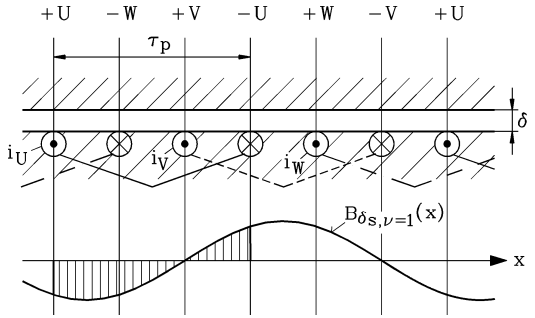

Fig.1.1.5-1: Distributed stator winding excites air gap flux density. Fundamental of this flux density induces back into stator winding, thus linking phases U, V, W, generating a self- inductance L_h, which is equal for all three phases (here is shown flux linkage with coil of phase U)

The stator field B_s – excited by the stator currents – contains a fundamental sine wave, which can be easily calculated with (1.1.5-2), if a constant magnetically active air gap δ_{res} is assumed. With surface mounted magnets we get this magnetically active air gap as the sum of mechanical air gap δ, bandage height h_B and the height of magnets h_M, as modern rare earth magnets behave in an external magnetic field like air with a relative permeability of nearly unity.

$$\delta_{res} = \delta + h_B + h_M \qquad (1.1.5\text{-}1)$$

Sine wave amplitude $B_{\delta s,1}$ of stator field for stator current I_s (rms):

$$B_{\delta s,1} = \frac{\mu_0}{\delta_{res}} \cdot \frac{\sqrt{2} \cdot m_s \cdot N_s \cdot k_{ws} \cdot I_s}{\pi \cdot p} \quad . \qquad (1.1.5\text{-}2)$$

The flux per pole is

$$\Phi = \frac{2}{\pi} \cdot \tau_p \cdot l_{Fe} \cdot B_{\delta s,1} \quad , \qquad (1.1.5\text{-}3)$$

yielding a self-induced voltage per phase

$$U_{s,s} = \frac{\omega_s}{\sqrt{2}} \cdot N_s \cdot k_{ws} \cdot \Phi \quad , \qquad (1.1.5\text{-}4)$$

which can be expressed by the main inductance

$$\boxed{L_h = \frac{U_{s,s}}{\omega_s \cdot I_s} = \mu_0 \cdot (N_s \cdot k_{ws})^2 \cdot \frac{2m_s}{\pi^2 \cdot p} \cdot \frac{\tau_p l_{Fe}}{\delta_{res}}} \quad . \qquad (1.1.5\text{-}5)$$

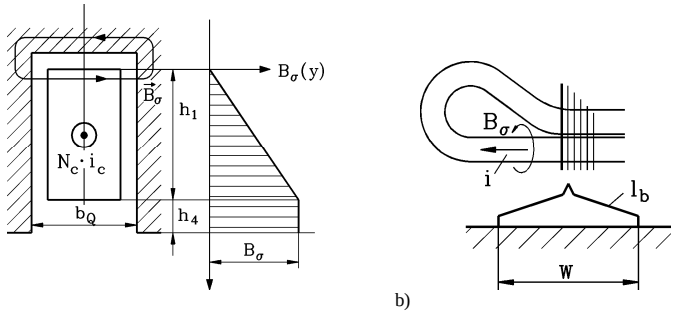

Fig.1.1.5-2: Schematic drawing of stray flux lines: a) Slot leakage flux, rising linear from bottom to top of slot according to *Ampere´*s law, b) leakage flux density of winding overhangs

Additional **stray flux** in the **slots** $L_{\sigma Q}$ and in the **winding overhangs** $L_{\sigma b}$ (Fig.1.1.5-2) and the **self-inductance of the higher *Fourier* harmonics** $L_{\sigma o}$ of the step-like air gap flux density distribution have to be considered in addition as so called **stray (or leakage) inductance** $L_\sigma = L_{\sigma Q} + L_{\sigma b} + L_{\sigma o}$, yielding finally the so-called **synchronous self inductance**

$$\boxed{L_d = L_h + L_\sigma} \quad . \qquad (1.1.5\text{-}6)$$

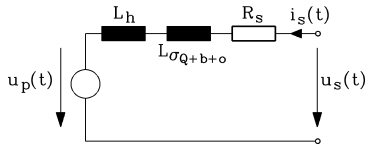

Fig.1.1.5-3: Equivalent circuit per phase of synchronous PM machine

Along with the stator resistance per phase R_s and the back EMF u_p we get the equivalent circuit per phase Fig.1.1.5-3.

$$u_s(t) = R_s \cdot i_s(t) + L_d \frac{di_s(t)}{dt} + u_p(t) \qquad (1.1.5\text{-}7)$$

Considering only fundamental harmonics of voltage and current, we may use complex phasors $\underline{U}_s$, $\underline{U}_p$ and $\underline{I}_s$, leading us to complex phasor diagram Fig.1.1.5-4a. Field oriented operation demands current in phase with back EMF, thus getting phasor diagram Fig.1.1.5-4b. Current phasor is then directed into *q*-axis and is therefore called ***q*-axis current** I_q. We assume here that inductivity for *d*-axis and *q*-axis is identical ($L_d = L_q = L_s$).

$$\Rightarrow \underline{U}_s = R_s \underline{I}_s + j\omega L_d \underline{I}_s + \underline{U}_p \ , \quad \Rightarrow \underline{U}_p = j\omega \underline{\Psi}_p / \sqrt{2} \qquad (1.1.5\text{-}8)$$

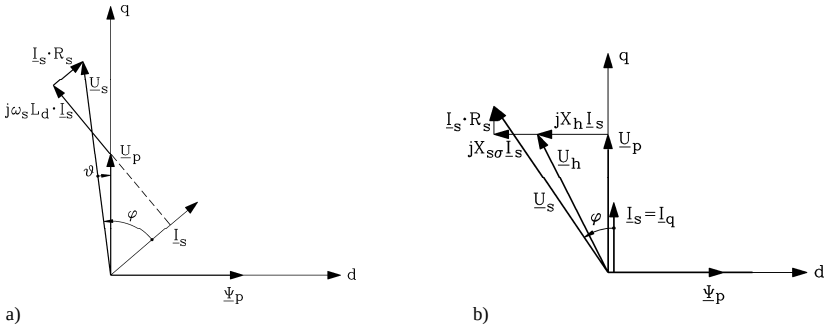

Fig.1.1.5-4: Phasor diagram per phase of synchronous PM machine at operation with sinusoidal voltage and current: a) for arbitrary current phase shift, b) for field-oriented control with current **in phase** with back EMF U_p ("brushless DC drive")

1.1.6 Stator current generation

Stator current is impressed by dc link voltage inverter via B6-bridge switching inverter (Fig. 1.1.6-1).

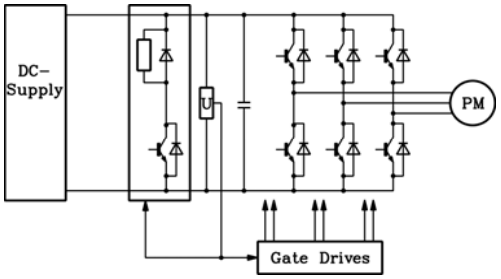

Fig.1.1.6-1: DC link voltage source inverter with switching transistors and free-wheeling diodes

For simplification we consider two legs of the inverter, e.g. feeding phase U and V in series, while phase W is switched off. For that instant, the dc link voltage is connected to the two phases via two switches, which are represented in Fig.1.1.6-2a by one switch and one resulting winding inductance L_s and phase resistance R_s. During that short time of operation the back EMF is considered constant, so that we get with $u_{s,LL} = U_d$, $u_{p,LL} = U_{p,LL}$

$$U_d - U_{p,LL} = L_s \cdot di_s / dt + R_s \cdot i_s \quad . \qquad (1.1.6\text{-}1)$$

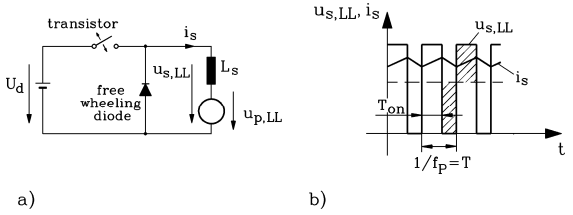

Fig.1.1.6-2: a) Equivalent switching scheme of DC link voltage source inverter, connected to the two phases with switching transistor and free-wheeling diode, b) Current ripple and chopped inverter voltage

Neglecting the resistance we get (1) a linear rise of current, when the switch is closed, and (2) a linear decrease of current, when the switch is opened. During that time the current continues to flow through the free-wheeling diode. Thus we get a current with a ripple (Fig.1.1.5-2b).

$$(1):\ U_d - U_{p,LL} \approx L_s \cdot di_s / dt \qquad (2):\ -U_{p,LL} \approx L_s \cdot di_s / dt \qquad (1.1.6\text{-}2)$$

Considering that in reality this are two switches in series, switching in alternating mode, the ripple frequency f_P is twice the switching frequency f_c of the switches. The current controller governs the transistor switches within a hysteresis band Δi_{Hyst} to get either a block shape of the phase current (Fig.1.1.6-3a) for *block commutation* or within a sine wave band for *sinusoidal operation* (Fig.1.1.6-3b).

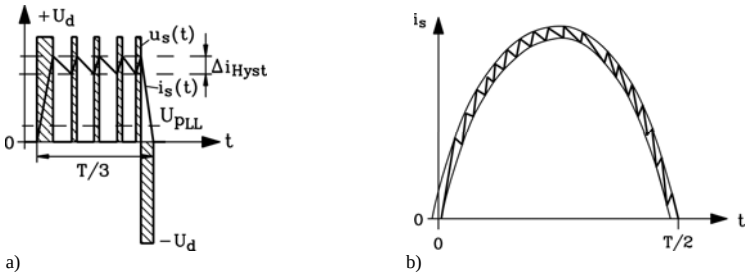

Fig.1.1.6-3: Hysteresis band controller for a) block commutation, b) sine wave commutation

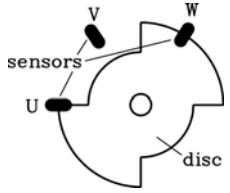

Fig.1.1.6-4: A rotor disc and three stator-fixed sensors U, V, W, spaced by 120°/*p* (*p*: number of pole pairs), are sufficient for rotor position sensing for block commutation (here: $2p = 4$)

A rotor position sensor is used to check rotor position, thus giving information of the phase shift of the induced rotor voltage. Thus it is possible to impress stator phase currents IN PHASE with the induced rotor voltage. For *block commutation* only the beginning and the end of each current block per half period must be known, therefore a simple sensor like in

Fig.1.1.6-4 for a four-pole motor may be used. An iron disk with two omitted parts for the south poles and two parts in between for the north poles is fixed to the rotor. Magnetic sensors, fixed in the stator, sense a change in magnetic field, as the disc rotates, when a change from N-pole to S-pole and vice versa occurs. This can be related to the zero crossings of the trapezoidal induced back EMF and is used to demand the impressed block stator currents in phase with the voltage.

For *sine wave commutation* rotor position must be known at every moment to generate the appropriate sine wave current in phase with sine wave induced back EMF, as frequency might change at every moment due to changed speed. Therefore resolvers or incremental encoders are necessary to measure rotor position. This is much more expensive, but by counting the increments in given time on gets immediately rotor speed for the speed controller, whereas with block commutation one needs an additional speed sensor, because at low speed the 2*p* increments of the disk are too few to get a good value for speed.

Conclusions:
Hysteresis current controller impresses stator current either with block or sine wave commutation in phase with back EMF, using the information of a rotor position sensor.

1.1.7 Operating limits of brushless DC drive

With induced voltage (back EMF)

$$\hat{U}_p = \omega_s \cdot \Psi_p = 2\pi n \cdot p \cdot \Psi_p \qquad (1.1.7\text{-}1)$$

we see that electromagnetic torque is directly proportional to current, if stator current is in phase with back EMF.

$$\boxed{M_e = \frac{(3/2)\cdot \hat{U}_p \cdot \hat{I}}{2\cdot\pi\cdot n} = \frac{3}{2}\cdot p \cdot \Psi_p \cdot \hat{I}_q} \qquad (1.1.7\text{-}2)$$

At stand-still we get the torque M_0 (**zero speed torque**), which in steady-state condition is limited by the temperature rise in the winding due to the stator copper losses

$$P_{Cu} = 3\cdot R_s \cdot I_s^2 \quad , \qquad (1.1.7\text{-}3)$$

where I_s is the r.m.s-value. Please note that at zero speed stator frequency is zero, thus yielding dc currents in the three phase windings. Usually smaller brushless dc drives are operated without any fan in self-cooling condition. Thus the total losses P_d define the steady state temperature rise $\Delta\vartheta$ in the winding according to the thermal heat transfer coefficient α at the surface A of the machine.

$$P_d = \alpha \cdot A \cdot \Delta\vartheta \qquad (1.1.7\text{-}4)$$

At zero speed the total losses are given only by $P_d = P_{Cu}$. With rising speed friction and windage losses P_{fr} occur in addition with iron losses $P_{Fe,s}$. These losses are due to flux change in stator iron stack with stator frequency f_s, which is causing hysteresis and eddy current losses $P_{Hy,s}$ and $P_{Ft,s}$. Therefore the iron stack consists of laminated iron with insulated iron

sheets of typically 0.5 mm thickness to suppress eddy current in iron. Iron losses are proportional to stator iron mass $m_{Fe,s}$, stator flux density in iron teeth and yoke, and to materials coefficients $k_{Hy,s}$, $k_{Ft,s}$, considering size of *B(H)*-hysteresis loop and conductivity and thickness of iron sheets.

$$P_{Fe,s} = P_{Hy,s} + P_{Ft,s} \sim m_{Fe,s} \cdot B_{Fe,s}^2 \cdot (k_{Hy} \cdot f_s + k_{Ft} \cdot f_s^2) \qquad (1.1.7\text{-}5)$$

The rotor iron is not induced by the stator fundamental flux wave, as it is rotating synchronously with the rotor. But higher space harmonics, which contribute to the step-like shape of air gap flux density distribution, are rotating much slower, therefore inducing the rotor, causing additional eddy current losses in rotor magnets and rotor iron back $P_{M+Fe,r}$. Further, non-sinusoidal current causes additional flux change in rotor
- due to the current ripple with switching frequency, caused by PWM and
- due to the block shaped current when using block commutation.

With rising speed therefore total losses increase to

$$P_d = P_{Cu} + P_{Fe,s} + P_{fr} + P_{M+Fe,r} \quad , \qquad (1.1.7\text{-}5)$$

so current must be reduced to keep total losses and therefore winding temperature rise constant. Thus with rising speed steady state torque has to be reduced, leading to rated torque M_N at rated speed n_N, which is smaller than torque M_0 at zero speed.

At high speed the inductive voltage drop $\omega_s L_d I_s$ and the back EMF $U_p = \omega_s \cdot \Psi_p / \sqrt{2}$, rising linear with speed, are much bigger than the ohmic voltage drop $R_s I_s$, therefore R_s is neglected (see phasor diagram 1.1.7-1). With rising speed and constant torque (or current) the stator phase voltage U_s which is the fundamental harmonic of the PWM stator voltage pattern, must therefore rise linear with frequency.

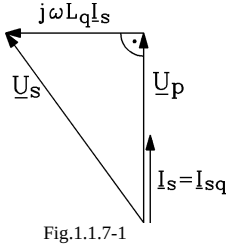

Fig.1.1.7-1

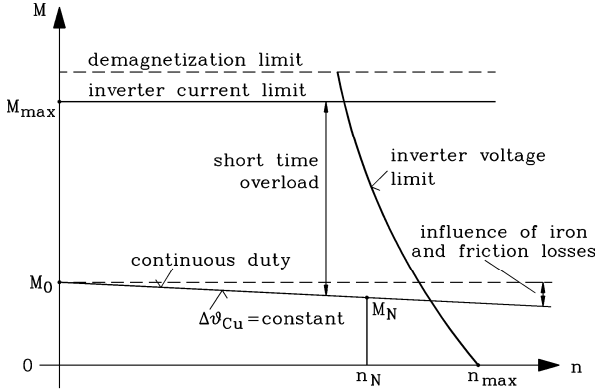

Fig.1.1.7-2

Fig.1.1.7-1: Phasor diagram per phase of synchronous PM machine at high speed with neglected stator resistance; field-oriented control with current in phase with back EMF, no saliency assumed $L_d = L_q$

Fig.1.1.7-2: Speed-torque curve limit for synchronous PM machine with field-oriented control (current in phase with back EMF)

$$U_s = \omega_s \cdot \sqrt{\Psi_p^2 / 2 + (L_d I_s)^2} \qquad (1.1.7\text{-}6)$$

When inverter maximum voltage $U_{s,max}$ is reached, it is only possible to increase speed by reducing stator current according to *Pythagoras´* law for triangles with right angle:

$$I_s = \frac{1}{\omega_s L_d} \cdot \sqrt{U_{s,max}^2 - (\omega_s \Psi_p / \sqrt{2})^2} \qquad (1.1.7\text{-}7)$$

The relationship (1.1.7-7) $I_s(n)$ is called **"voltage limit"**. At maximum speed we get $U_{s,max} = \omega_{s,max} \cdot \Psi_p / \sqrt{2}$ and therefore current is theoretically zero.

$$\boxed{n_{max} = \frac{U_{s,max}}{2\pi \cdot p \cdot \Psi_p / \sqrt{2}}} \qquad (1.1.7\text{-}8)$$

In reality, friction and windage losses create a certain torque demand even at no-load, maximum speed, so maximum speed is a little bit lower than (1.1.7-8), thus allowing a small current to flow to generate the required electromagnetic torque to overcome windage and friction.

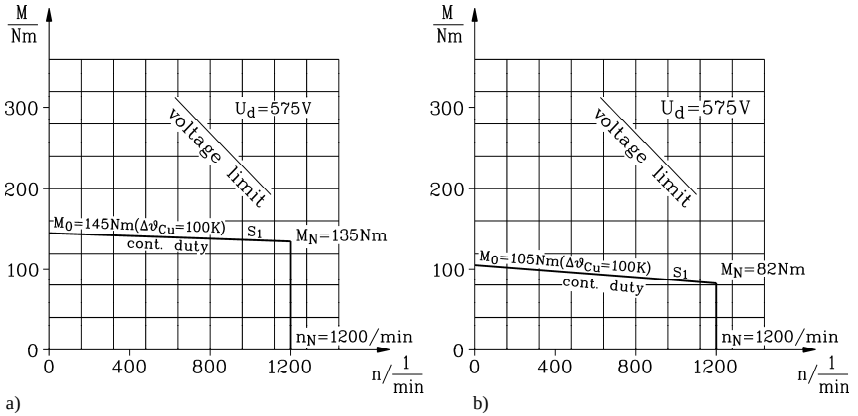

Fig.1.1.7-3: Measured speed-torque curve limit for 6-pole synchronous PM machine, shaft height 132 mm, with field-oriented control a) for cooling with external fan, thus getting increased output torque, b) for self-cooling (no fan)

In Fig.1.1.7-2 the limits of a brushless DC drive are given:
- **Steady state torque** is given by temperature limit of insulation material of stator winding. Please note that an increase of 10 K steady state temperature leads to reduction of insulation material life time by about 50 % (*Montsinger´s* rule). It decreases from M_0 at n = 0 down to M_N by n_N. Typical temperature limit according to IEC 34-1 is 105 K for insulation material of insulation class F and 125 K for class H with ambient temperature of 40°C.
- Increased torque for accelerating and braking is only possible for short time operation. During that time temperature rises according to thermal time constant T_{th} of the motor winding, but has to stay below the above noted temperature limit. So **dynamic torque** overload operation up to about $4M_0$ is only possible for several seconds.

- Maximum torque is limited by maximum current, which is given by the **inverter current limit**. As thermal time constant of power transistors is very short (in the range of several ms), short time current is already steady state condition for inverter power semiconductors.
- **Demagetization limit:** Inverter current limit must be below the critical motor current which would cause irreversible demagnetization of the hot rotor magnets (typically at 150°C).
- Balancing of rotor and (for high speed application) centrifugal rotor forces demand a **mechanical maximum speed limit**, which must be above rated speed n_N, and may be also above n_{max} of (1.1.7-8).
- The above described **voltage limit** shows maximum possible overload torque at high speed.

Concerning **thermal limit** at low and medium speed copper losses in stator winding are dominating over iron, friction, windage and additional losses. For the same stator geometry with identical winding and with identical magnet material and magnet height both sine wave and block commutated motors show the same thermal performance; that means: For the same copper losses we get the same output power.

The following comparison is therefore done at *q*-current operation for identical stator resistance per phase R_s and identical magnetic air gap flux density at no-load B_p. From (1.1.2-4) we get for flux density in air gap at no-load

$$B_\delta = -\mu_0 \frac{h_M}{\delta} H_M = B_M \qquad (1.1.7\text{-}9)$$

and with linear PM material curve in the second quadrant

$$B_M = B_R + \mu_M H_M, \qquad \mu_M = B_R / H_{CB} \qquad (1.1.7\text{-}10)$$

finally

$$B_p = B_\delta = \frac{(h_M / \mu_M) \cdot B_R}{(\delta / \mu_0) + (h_M / \mu_M)} \quad . \qquad (1.1.7\text{-}11)$$

PM machine	*Block commutation (B)*	*Sine wave commutation (S)*
Air gap flux density amplitude	$B_\delta = B_p$	$B_{\delta,1} = \frac{4B_p}{\pi} \cdot \sin\left(\frac{\alpha_e \pi}{2}\right)$
Back EMF	$\hat{U}_{pB} = 2N_s \cdot 2f\tau_p \cdot B_p \cdot l_{Fe}$	$\hat{U}_{pS} = 2\pi f \cdot N_s \cdot k_w \cdot \frac{2}{\pi} \tau_p l_{Fe} B_{\delta,1}$
Stator copper losses	$P_{Cu} = 2 \cdot R_s \cdot \hat{I}_{sB}^2$	$P_{Cu} = (3/2) \cdot R_s \cdot \hat{I}_{sS}^2$
Air gap power	$P_{\delta B} = 2 \cdot \hat{U}_{pB} \cdot \hat{I}_{sB}$	$P_{\delta S} = (3/2) \cdot \hat{U}_{pS} \cdot \hat{I}_{sS}$

Table 1.1.7-1: Comparison of block and sine wave commutated motors

For equal copper losses the current ratio is $\hat{I}_{sS} / \hat{I}_{sB} = 2/\sqrt{3}$ and therefore the ratio of air gap power, which can be transmitted into mechanical output power

$$\frac{P_{\delta S}}{P_{\delta B}} = \frac{(3/2) \cdot \hat{U}_{pS} \cdot \hat{I}_{sS}}{2 \cdot \hat{U}_{pB} \cdot \hat{I}_{sB}} = \frac{\sqrt{3} \cdot 2}{\pi} \cdot k_w \cdot \sin\left(\frac{\alpha_e \pi}{2}\right) \quad . \qquad (1.1.7\text{-}12)$$

Example 1.1.7-1:
For typical values (winding factor k_w = 0.933, pole coverage ratio α_e = 0.85) is derived: $P_{\delta S} / P_{\delta B} = 1.00035$ .Thus, equal thermal utilization of both motor types yields identical output power, but 15 % lower amount of necessary magnet material for sine wave commutation.

Example 1.1.7-2:
If the inverter current limit is fixed to $I_{s,max}$ for both commutation principles, which of block or sine wave commutated motor delivers the higher (short term) torque ?

Answer: $$\frac{M_{e,S}}{M_{e,B}} = \frac{P_{\delta S}}{P_{\delta B}} = \frac{(3/2)\cdot \hat{U}_{pS}\cdot \hat{I}_{s,\max}}{2\cdot \hat{U}_{pB}\cdot \hat{I}_{s,\max}} = \frac{\sqrt{3}\cdot 2}{\pi}\cdot k_w \cdot \sin\left(\frac{\alpha_e \pi}{2}\right)\cdot \frac{\sqrt{3}}{2}$$

For typical values k_w = 0.933 and $\alpha_e = 0.85$ we get $\frac{M_{e,S}}{M_{e,B}} \cong \frac{\sqrt{3}}{2} = \frac{1}{1.15}$.

Conclusions:
The block commutated motor is able to deliver at the SAME current amplitude 15% higher maximum torque, whereas for the same copper losses the thermal steady state torque for block and sine wave commutated PM machine is equal.

1.1.8 Torque ripple of brushless DC motors

a) No-load torque ripple:
According to Fig.1.1.8-1 at no-load with zero current the flux of the rotor magnets exerts a tangential magnetic pull on the sides of the stator teeth, dragging the rotor into an equilibrium position. This position occurs periodically along the stator circumference with stator slot pitch as period. This stator-slot frequent magnetic tangential pull F yields with the stator diameter d_{si} the **no-load cogging torque** .

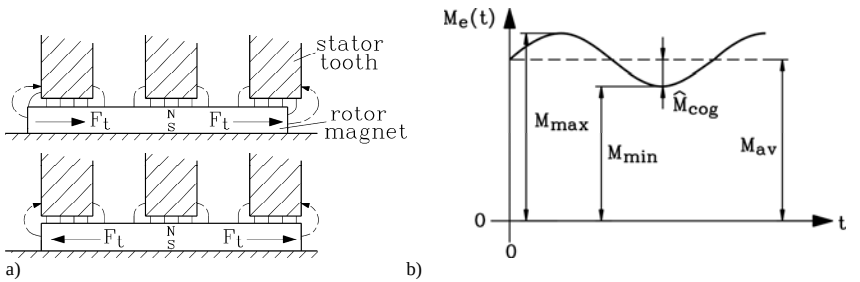

Fig.1.1.8-1: Cogging torque M_{cog}: a) No-load (i_s = 0): above: unaligned position: rotor tangential magnetic pull F_t on stator tooth sides generates no-load cogging torque, below: aligned position: sum F_t = 0, no cogging torque, b) Load cogging torque as function of time, quantification of torque ripple from measured torque time function (e.g. measured with strain gauge torque-meter)

By
- reducing the slot openings s_Q (so-called semi-closed stator slots),
- skewing either stator slots or rotor magnets by one stator slot pitch,
- use of special stator windings with non-integer number of slots per pole and phase q,
- shifting of e.g. 2 rotor poles by a quarter of stator slot pitch each

and other measures the cogging torque amplitude $\hat{M}_{cog}$ can be reduced.

- Unequal air gap along circumference,
- slightly different position of rotor magnets,
- slightly different magnetization per pole

and other deviations from ideal condition are the reason that the cogging torque does not vanish, but can in practice only be reduced to a minimum of typically below 1% of stand-still torque M_0 in best case.

b) Load torque ripple in block commutated brushless DC machines:
At load under ideal trapezoidal back EMF and ideal block shaped current no additional torque ripple will occur. In practice this is not possible, because
- the current cannot change suddenly from zero to peak and vice versa, but shows a certain finite rise time t_r, which is determined by the stator winding inductance and the current controller time constant,
- the radial magnetic flux density distribution in air gap does not change polarity in q-axis suddenly, but also with a certain slope (thus B_δ distribution is deviating from ideal rectangular shape), which is determined by the two-dimensional flux distribution in air gap especially with large air gaps and big magnet heights,
- the rotor position sensor is not aligned perfectly with the d-axis, causing slight position errors.

In Fig.1.1.8-2 and Fig.1.1.8-3a the slightly trapezoidal shape of block current i due to finite rise time t_r is shown along with ideally assumed back EMF u_p. From

$$m_e(t) = \left(u_{p,U}(t)\cdot i_U(t) + u_{p,V}(t)\cdot i_V(t) + u_{p,W}(t)\cdot i_W(t)\right)/(2\pi n) \qquad (1.1.8\text{-}1)$$

the torque is derived, showing considerable ripple with frequency of the current changes, which occur in all three phases with six time fundamental frequency. So a load torque ripple with $f = 6\cdot f_s$ is dominating.

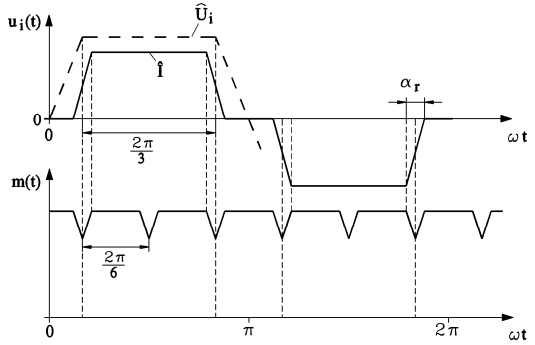

Fig.1.1.8-2: Block commutated brushless DC motor: Generation of load torque ripple due to block current commutation with finite current rise time t_r

In Fig 1.1.8-3b it is assumed alternatively, that the current wave form is ideal block current, but the back EMF trapezoidal slope is slightly increased due to deviation of air gap flux density distribution from ideal rectangular shape. Again a load torque ripple with $f = 6\cdot f_s$ is dominating. Fig.1.1.8-4 shows the measured shape of block commutated current. At low speed and therefore low frequency f_s block time $t_{Block} = T/3 = 1/(3f_s)$ is long enough to generate nearly ideal block current.

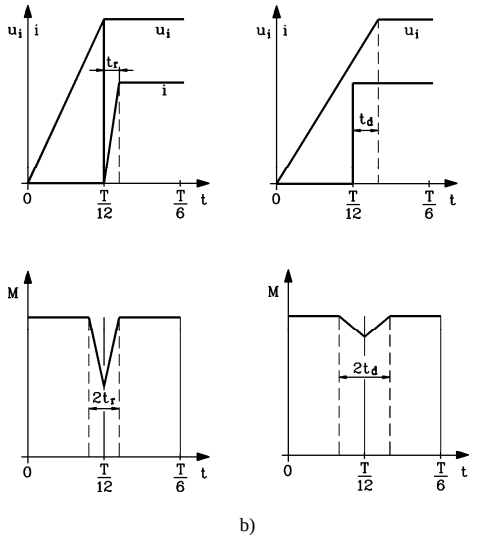

Fig.1.1.8-3: Two typical reasons for load torque ripple with block commutated brushless DC motors, generating load torque ripple with six times fundamental frequency: a) deviation of block current from ideal shape (finite rise time t_r), b) deviation of trapezoidal back EMF from ideal shape (slope increased by t_d)

With rising speed duration of blocks t_{Block} gets shorter due to increased frequency, thus revealing the time constant of the PI-current controller at the beginning of each block and the current ripple due to hysteresis control. Situation gets worse with further increasing speed, as back EMF amplitude $\hat{U}_p$ rises with speed, thus reducing the voltage span to impress current quickly. So ratio of current rise time versus block time t_r/t_{Block} decreases rapidly with rising speed.

$$L_s \cdot di_s/dt + R_s i_s = U_d - \hat{U}_p \quad \Rightarrow \quad L_s \cdot di_s/dt \approx U_d - \hat{U}_p \quad \Rightarrow$$

$$\Rightarrow \quad t_r \approx \frac{L_s \cdot \hat{I}_{Block}}{U_d - \hat{U}_p} \qquad (1.1.8\text{-}2)$$

So with rising speed the deviation of current from ideal block shape increases, causing an increased load torque ripple at high speed.

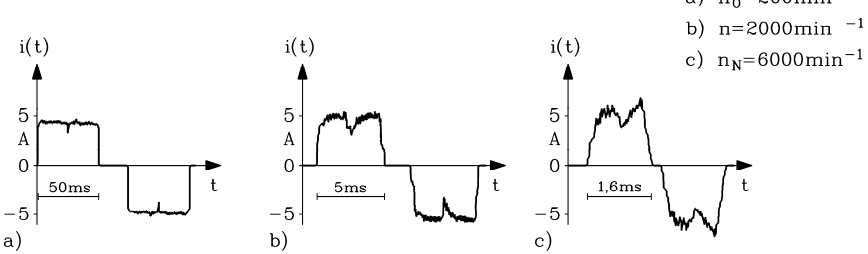

Fig.1.1.8-4: With increased speed the deviation of current from ideal block shape increases, causing an increase of load torque ripple amplitude

At the voltage limit, which occurs at high speed, the current blocks are so short when compared with current rise time, that no longer hysteresis control of current is possible. The voltage is only switched on (to U_d) and switched off (to zero) per half period. Along with the time constant $T_e = L_s/R_s$ the current consists of sections with exponential function like depicted in Fig. 1.1.8-5a. As current is directly proportional to torque via constant PM flux, the current ripple causes a considerable torque ripple again with a dominating harmonic content of six time fundamental frequency (Fig.1.1.8-5b).

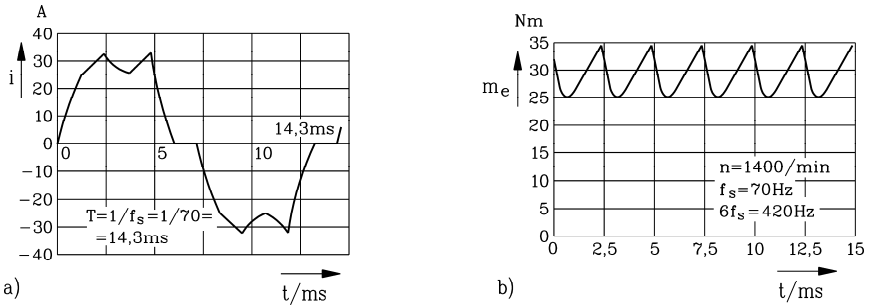

Fig.1.1.8-5: High speed operation at voltage limit: a) The current is no longer of block shape, but its shape is determined by remaining difference U_d-U_p and the electric time constant T_e of the winding, b) corresponding torque ripple with ripple frequency $6f_s$

Example 1.1.8-1:

Quantification of per unit torque ripple $\hat{w}_M$ (Fig.1.1.8-1b) from measured torque time function is:

$$\hat{w}_M = \frac{\hat{M}_{cog}}{M_{av}} \cong \frac{(M_{max} - M_{min})/2}{(M_{max} + M_{min})/2} = \frac{M_{max} - M_{min}}{M_{max} + M_{min}} \qquad (1.1.8\text{-}3)$$

Example 1.1.8-2:

Measured current shape and torque ripple of a six-pole block commutated brushless DC motor for robot drive at very low speed 20/min (Fig.1.1.8-6). As back EMF is nearly zero, the total voltage U_d = 560 V is usable to impress block current, which has a very long block time of 1/3 s.

$$f_s = n \cdot p = (20/60) \cdot 3 = 1\text{Hz} \qquad \Rightarrow \qquad t_{Block} = 1/(3f_s) = 333\,\text{ms}$$

Therefore block current shape is almost ideal, resulting in a load torque ripple of

$$\hat{w}_M = \frac{\hat{M}_{cog}}{M_{av}} = \frac{(M_{max} - M_{min})/2}{M_0} = 3.4\%$$

Example 1.1.8-3:

Typical increase of load torque ripple of a block commutated brushless DC motor:

n = 20/min: $\hat{w}_M = 3.4\%$ (Fig.1.1.8-6)

n = 1400/min: $\hat{w}_M = 16.7\%$ (Fig.1.1.8-5b)

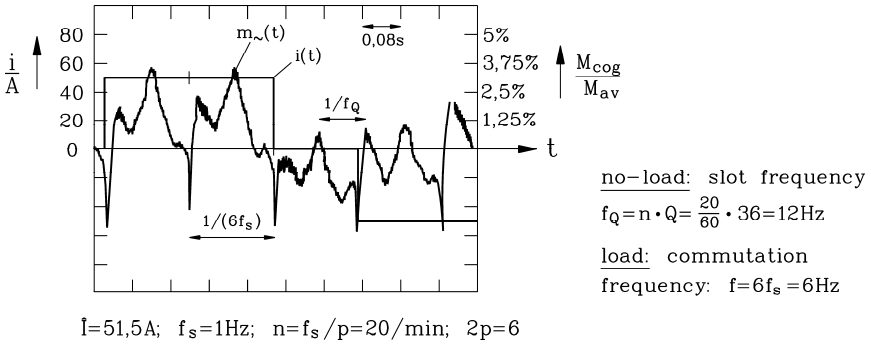

Fig.1.1.8-6: Measured block current and corresponding torque ripple (measured with strain gauge torque-meter) at very low speed 20/min

c) Load torque ripple in sine wave commutated brushless DC machines:
As current changes sinusoidal, the sudden current changes of block commutated machines, which are difficult to realize especially at increased speed, do not occur. Further, the air gap flux density distribution does not need to be of ideal rectangular shape, as only the fundamental of the air gap flux is used for force generation. Due to the sinusoidal wave form of both back EMF and current, a position error of the position sensor results only in a reduction of torque due to a phase shift between sinus current and sinus back EMF, but not in an increased torque ripple. So, the load torque ripple of sine wave commutated machines is much smaller than of block commutated machines. Good sine wave commutated brushless DC drives show a total current ripple (no-load and load) of $\hat{w}_M < 1\%$.

Example 1.1.8-4:
Comparison of *Fourier* analysis of torque ripple at rated torque and very low speed 20/min for a) block commutated 6-pole motor and b) sine wave commutated 8-pole motor (Fig.1.1.8-7). The harmonic content of a) shows a dominating 6th harmonic in torque ripple, which in b) is very small. Thus with a) in best case a load torque ripple at very low speed of about $\hat{w}_M \approx 3...4\%$ can be achieved, whereas with b) lower values $\hat{w}_M < 1\%$ are possible.

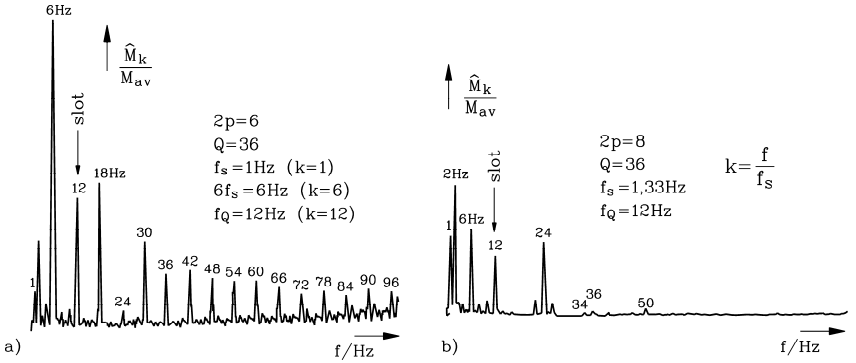

Fig.1.1.8-7: Measured *Fourier* spectrum of torque ripple of a) block commutated and b) sine wave commutated brushless DC machine (ripple measured with strain gauge torque-meter at very low speed 20/min)

Conclusions:
The sine wave commutated motor has a lower load dependent torque ripple than the block commutated brushless DC drive.

1.1.9 Significance of torque ripple for motor and drive performance

a) Torsion resonance:
A drive system consists typically of the motor (rotor inertia J_M) and driven load (rotary inertia J_L) with usually an elastic coupling (torsion spring coefficient c) in between (Fig.1.1.9-1).

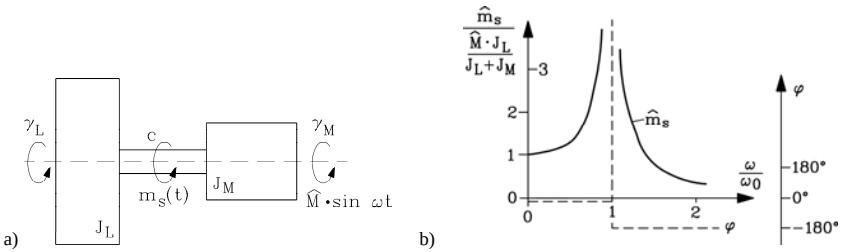

Fig.1.1.9-1: Torsion resonance: a) Rotor of motor coupled to rotating load via an elastic coupling, b) Shaft torque amplitude, excited by air gap cogging torque

Let us assume that a cogging torque with e.g. dominant frequency $k = 6$ (block commutated brushless DC drive)

$$m_{e,c}(t) = \hat{M} \cdot \sin(\omega t), \qquad \omega = k \cdot (2\pi \cdot n \cdot p) \tag{1.1.9-1}$$

acting in addition to the motor torque, which causes the speed n. For evaluating the oscillating shaft torque m_s at the coupling the torque equation for both rotor bodies with their oscillation angles γ_M, γ_L yields

$$J_L \ddot{\gamma}_L - m_s = 0 \quad , \quad J_M \ddot{\gamma}_M + m_s = m_{e,c} \quad , \quad m_s = c \cdot (\gamma_M - \gamma_L) \tag{1.1.9-2}$$

or with

$$\ddot{\gamma}_L = m_s / J_L \quad , \quad \ddot{\gamma}_M = (m_{e,c} - m_s)/J_M \quad \Rightarrow \quad \ddot{\gamma}_M - \ddot{\gamma}_L = -\left(\frac{1}{J_M} + \frac{1}{J_L}\right) m_s + \frac{m_{e,c}}{J_M} \tag{1.1.9-3}$$

finally the system differential equation (with abbreviation $\gamma = \gamma_M - \gamma_L$)

$$\ddot{\gamma} + \frac{c \cdot (J_M + J_L)}{J_M \cdot J_L} \cdot \gamma = \frac{m_{e,c}}{J_M} \quad . \tag{1.1.9-4}$$

Solution for exciting torque ripple (1.1.9-1) yields for the torsion vibration angle γ and for the oscillating shaft torque m_s :

$$\gamma(t) = \frac{\hat{M}}{J_M} \cdot \frac{1}{\omega_o^2 - \omega^2} \cdot \sin(\omega t) \ , \qquad m_s(t) = c \cdot \gamma(t) = \frac{\hat{M}}{J_M} \cdot \frac{c}{\omega_o^2 - \omega^2} \cdot \sin(\omega t) \tag{1.1.9-5}$$

If the frequency of the cogging torque $f = \omega/(2\pi)$ equals the **torsion resonance frequency** of the drive system

$$f_0 = \omega_0/(2\pi) = \frac{1}{2\pi}\cdot\sqrt{c\cdot\frac{J_M + J_L}{J_M \cdot J_L}} \quad , \qquad (1.1.9\text{-}6)$$

the shaft torque – in spite of the small cogging torque amplitude $\hat{M}$ - gets **infinite**, as no damping is assumed. In that case the coupling will break **("torsion resonance").**

Conclusions:
It must be avoided that the dominant cogging torque frequency excites the torsion resonance of the drive system. This can be achieved by designing the drive with a stiff coupling (c: high value) to stay with cogging torque frequency below the resonance.

At low speed n the cogging torque frequency $f = \omega/(2\pi) = k\cdot n\cdot p$ is also low: $\omega << \omega_0$. Therefore the oscillating shaft torque at low speed is

$$m_s(t) \cong \frac{\hat{M}}{J_M}\cdot\frac{c}{\omega_0^2}\cdot\sin(\omega t) = \frac{\hat{M}\cdot J_L}{J_L + J_M}\cdot\sin(\omega t) \qquad (1.1.9\text{-}7)$$

directly proportional to the cogging torque in the motor air gap. In measurement systems for cogging torque therefore a load machine is coupled to the test motor with additional inertia disc to get $J_L >> J_M$ in order to get $m_s(t) \cong m_{e,c}(t)$. Thus a torquemeter in the coupling – measuring shaft oscillating torque – also directly measures the cogging torque (e.g. like in section 1.1.8).

b) Speed ripple:
Due to cogging torque an additional speed ripple Δn is superimposed to constant speed

$$n(t) = n + \Delta n(t) \quad , \qquad (1.1.9\text{-}8)$$

bringing difficulty for smooth positioning in tooling machinery such as grinding, milling, polishing etc., as the surface of the working piece gets a slight ripple, which is clearly visible with the eye, when observing the reflected light from the surface.

$$\Delta n(t) = \dot{\gamma}_M(t)/(2\pi) \qquad (1.1.9\text{-}9)$$

$$\ddot{\gamma}_M(t) = \frac{m_e(t) - m_s(t)}{J_M} = \frac{\hat{M}}{J_M}\cdot\left(1 - \frac{c/J_M}{\omega_o^2 - \omega^2}\right)\cdot\sin(\omega t) \qquad (1.1.9\text{-}10)$$

$$\Delta n(t) = \dot{\gamma}_M(t)/(2\pi) = -\frac{\hat{M}}{2\pi\cdot\omega\cdot J_M}\cdot\left(1 - \frac{c/J_M}{\omega_o^2 - \omega^2}\right)\cdot\cos(\omega t) \qquad (1.1.9\text{-}11)$$

Staying below the resonance $\omega << \omega_0$, we observe that especially at low speed the speed ripple amplitude, expressed as percentage of actual speed, increases with DECREASING speed:

$$\left|\frac{\Delta n}{n}\right| = \left|\frac{\hat{M}}{(2\pi)^2\cdot k\cdot p\cdot n^2\cdot J_M}\cdot\left(1 - \frac{c/J_M}{\omega_o^2 - \omega^2}\right)\right| \approx \frac{\hat{M}}{(2\pi)^2\cdot k\cdot p\cdot n^2\cdot(J_L + J_M)} \sim \frac{1}{n^2} \qquad (1.1.9\text{-}12)$$

Note, that due to operation well below resonance the result could have also been obtained by considering a very stiff coupling between motor and load ($c \to \infty \;\Rightarrow\; \gamma_M = \gamma_L$), getting a much simpler differential equation:

$$(J_L + J_M)\cdot\ddot{\gamma}_M = \hat{M}\cdot\sin(\omega t) \;\Rightarrow\; \Delta n(t) = -\frac{\hat{M}}{2\pi\cdot\omega\cdot(J_L + J_M)}\cdot\cos(\omega t) \qquad (1.1.9\text{-}13)$$

Conclusions:
Especially at low speed the torque ripple leads to considerable speed ripple, when compared with actual speed. Therefore servo drive applications with positioning tasks are sensitive to torque ripple, demanding low cogging torque amplitudes.

1.2 Brushless DC drive systems

Brushless DC drive systems are positioning drives of utmost accuracy with very smooth torque at low speed as so called servo drives. A high overload capability for fast acceleration yields a high dynamic performance. A motor as electromechanical energy conversion actuator, a positioning measurement system, a power electronic system for motor feeding and a control system for motion control comprise the basic elements for a high performance brushless DC servo drive system.

The whole drive is usually connected to an electronic bus system such as
- PROFIBUS (Process Field Bus),
- Drivecom-Bus (Interbus-S),
- SERCOS-Interface,
- CAN-Bus (Controller Area Network),
- ASI (Actor-Sensor-Interface) or others.

1.2.1 Block commutated drives

According to Fig. 1.2.1-1 a block commutated drive system consists of
- a permanent magnet motor with three phase, single layer winding, skewed slots and 100% pole coverage ratio for the rotor magnets,
- a simple rotor position sensor with rotor disc according to pole number,
- a brushless DC tachometer for speed measurement,
- an encoder with high resolution for precise positioning,
- a voltage source inverter system with power transistors and speed and current control, implemented in a micro-computer system and motor current measurement devices such as shunts or DC transformers with *Hall*-sensors,
- a motion control system, which is implemented in a second microcomputer and allows position control, but also different motion control such as special velocity profiles according to the needs of the driven load.

Often the motion control due to the modern powerful microcomputer systems is nowadays implemented in the inverter itself.

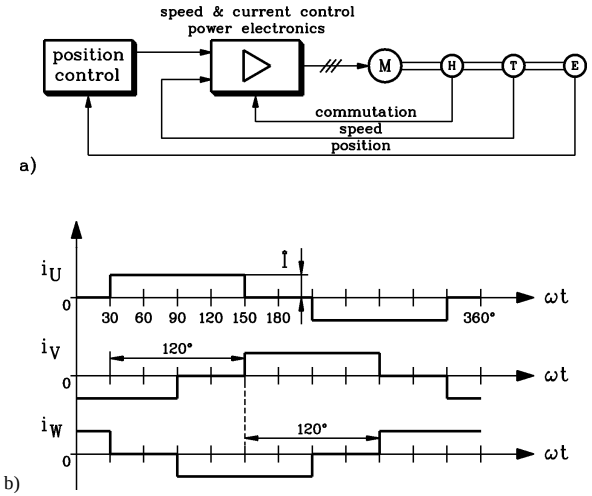

Fig.1.2.1-1: Brushless DC servo drive system for block commutated permanent magnet machines
a) Drive components: M: motor, H: rotor position sensor, T: tachometer, E: encoder. The motor control and power electronic device comprises also the current measurement system.
b) Shape of the three-phase block commutated motor currents

Brushless DC tachometers are small PM machines with the rotor mounted to the rotor of the PM motor, and the stator fixed in the end-shield of the PM motor. The trapezoidal no load back EMF of the tachometer is rectified by an additional six-phase inverter, cutting off the linear parts of the voltage time function, thus considering only the constant part of the trapezoidal voltage. Thereby a constant DC voltage is derived, which is proportional to the PM flux the tachometer and to rotor speed. As it is always a positive voltage also for reversal speed, by considering the phase sequence U-V-W-U-... or U-W-V-U-... of the tachometer phase voltages the direction of rotation is recognized.

Hysteresis control of block current is done by switching on and off DC link voltage.

The advantages of the block commutated PM servo drive are
- a cheap rotor position and rotor speed sensor,
- a cheap motor winding and
- a 15% higher overload at given inverter current limit than sine wave commutated drives.

Disadvantages are
- an extra encoder for accurate drive positioning,
- a higher minimum torque ripple of about 2% ... 4% at low speed,
- increased additional losses in the motor due to extra eddy currents especially in the rotor due to the rapid chance of stator flux during stator block current commutation.

Therefore for highest performance the sine wave commutated drive is preferred, but is more expensive.

1.2.2 Sine wave commutated drives

According to Fig. 1.2.2-1 a sine wave commutated drive system consists of

- a permanent magnet motor with three phase, double layer winding (or special single layer winding with non-integer *q*), skewed slots and 80%...85% pole coverage ratio for the rotor magnets,
- a high resolution rotor position sensor such as optical encoder or magnetic resolver, which acts also speed sensor and sometimes as position sensor for precise positioning,
- a voltage source inverter system with power transistors and speed and current control, implemented in a micro-computer system and motor current measurement devices such as shunts or DC transformers with *Hall*-sensors,
- a motion control system, which is implemented in a second microcomputer and allows position control, but also different motion control such as special velocity profiles according to the needs of the driven load.

Often the motion control due to the modern powerful microcomputer systems is nowadays implemented in the inverter itself.

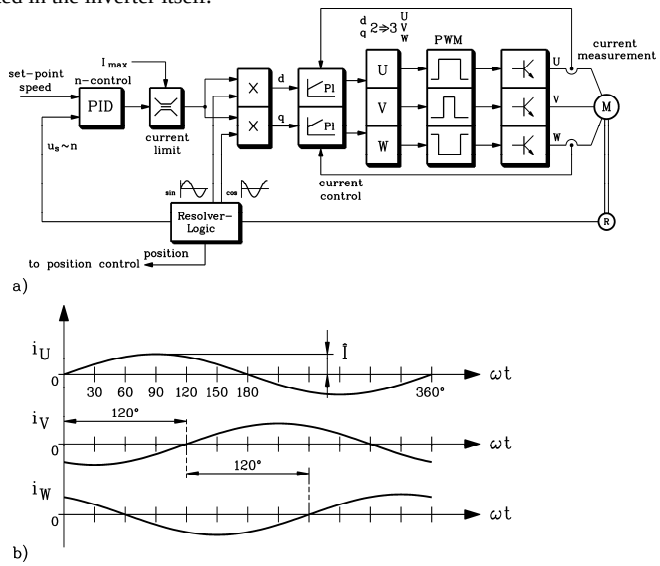

Fig.1.2.2-1: Brushless DC servo drive system for sine wave commutated permanent magnet machines
a) Drive components: M: motor, R: rotor position and speed sensor (e.g. resolver). The motor control and power electronic device comprises also the current measurement system.
b) Shape of the three-phase block commutated motor currents

From the measured three phases of the stator current by mathematical operation in the microcomputer the current per phase is decomposed into *q*-component in phase with back EMF and *d*-component with a 90° phase shift. For servo drive application only the torque generating *q*-component is used, whereas the *d*-component is set to zero ("***q*-current operation**"). From the two components I_d and I_q by transformation the actual set point values of the three phase sinusoidal currents in U, V, W are calculated and impressed by pulse-width (PWM) modulated stator voltage. For fixed current the fundamental voltage of the PWM voltage pattern U_s changes with speed *n*: $U_s \sim n$.

The advantages of the sine wave commutated PM servo drive are
- a 10% ... 15% reduced amount of magnets for given steady state torque,
- a very low torque ripple below 1%,

- reduced additional losses at high speed,
- reduced torque ripple sensitivity to misalignment of rotor position sensor.

Disadvantages are
- an expensive encoder for current commutation and speed measurement,
- a more expensive stator winding, if two layer winding is used,
- a 15% lower overload capability for given inverter current limit when compared with block commutation,
- a more complex mathematical model for motor control.

Conclusions:
Brushless DC PM servo drive systems with block current commutation offer a simple motor control and are usually cheaper due to simple winding and rotor position sensing, but at lower performance in terms of low load-dependent torque ripple and low losses at high speed. Sine wave operated drives show the best servo performance and are therefore nowadays used as standard high performance servo drives.

1.3 High speed PM machines

1.3.1 How to increase power of a given machine ?

With increased speed the output power of the motor can be increased considerably, as power rises for constant torque linear with speed.

$$P = 2\pi \cdot n \cdot M \qquad (1.3.1\text{-}1)$$

Note, that electromagnetic torque is given by the total amount of *Lorentz*-forces F on the stator conductors (total number of stator conductors: z)

$$M_e = z \cdot F \cdot (d_{si}/2) = z \cdot I_s \cdot B_\delta \cdot l_{Fe} \cdot (d_{si}/2). \qquad (1.3.1\text{-}2)$$

Considering the sinusoidal distribution of flux density gives a factor $1/\sqrt{2}$ for overall mean torque, as well as we have to consider the distributed winding. Therefore not all z conductors act at the same time with same current, which has to be considered by winding factor k_w, as explained in Section 1.1. Along with the definition of **current loading**

$$A = \frac{z \cdot I_s}{d_{si} \cdot \pi} \qquad (1.3.1\text{-}3)$$

the **electromagnetic torque** of an electric machine is determined by

$$\boxed{M_e = \frac{\pi}{2\sqrt{2}} \cdot k_w \cdot A \cdot B_\delta \cdot (d_{si}^2 \cdot l_{Fe})} \quad . \qquad (1.3.1\text{-}4)$$

The motor torque rises with square of bore diameter and linear with iron stack length. **Electromagnetic utilization *C*** (“***Esson´*s number**”) of electric machines is (inner) apparent machine power S versus speed and “bore volume” (factor $\pi/4$ neglected in that definition)

$$C = \frac{(S/n)}{d_{si}^2 l_{Fe}} \quad . \qquad (1.3.1\text{-}5)$$

For field oriented PM motors inner power is $P_\delta = 2\pi n M_e$. Thus we get with (1.3.1-4), (1.3.1-5)

$$\boxed{C = \frac{\pi^2}{\sqrt{2}} \cdot k_w \cdot A \cdot B_\delta} \quad , \qquad (1.3.1\text{-}6)$$

which is also true for other AC rotating machines.

Conclusions:
For raising power output of a given motor, either speed can be raised or current load and flux density.

Due to **iron saturation** the air gap flux density amplitude cannot be raised much above 1 T, as in the teeth, where flux fringing leads to increased flux density by about factor 2, already about 2 T flux density occurs, which is above the saturation limit of about 1.7 ... 1.8 T. Current loading can be increased by increasing the current (or the number of conductors), but this also means increased losses in the stator. Therefore high current loading is only possible for intensive cooling, and is therefore limited, too.

Example 1.3.1-1:
Low speed machines:
a) Totally enclosed PM servo motor with self cooling (without any fan): 40.5 Nm, 1000/min
   A = 145 A/cm, B_δ = 0.65 T, d_{si} = 154 mm, l_{Fe} = 175 mm, k_w = 0.933
   C = 1.0 kVAmin/m^3, P_δ = 4.24 kW
b) High torque PM motor with water jacket cooling: 737 Nm, 600/min
   A = 611 A/cm, B_δ = 0.8 T, d_{si} = 280 mm, l_{Fe} = 200 mm, k_w = 0.866
   C = 4.9 kVAmin/m^3, P_δ = 46.32 kW

Example 1.3.1-2:
c) High speed machine: PM motor with water jacket cooling: 12 Nm, 24000/min
   A = 225 A/cm, B_δ = 0.7 T, d_{si} = 90 mm, l_{Fe} = 90 mm, k_w = 0.933
   C = 1.7 kVAmin/m^3, P_δ = 30.0 kW

Conclusions:
With only 70% higher electromagnetic utilization C the motor c) has about 7 times higher output power than motor a), as speed is increased by factor 24.

Nevertheless, for operation at high speed several constraints have to be considered:
- high centrifugal forces acting on rotor and magnets
- increased bearing wear
- increased motor frequency, thus increased iron, friction, windage and additional losses
- increased inverter power.

1.3.2 Flux weakening with negative *d*-current

Several applications need for broader speed range a constant output power, e.g. tooling machines need a constant cutting power – given by technological demands of the cutting

process - in order to get good results. Nevertheless this cutting power is needed at high speed to get a quick cutting process ("**HSC – high speed cutting**"). In Fig.1.3.2-1 the power demand is shown. Above rated speed n_N the power is kept constant. The torque therefore decreases with 1/*n*, thus the motor is oversized at high speed, but not at low speed, where full torque is required. In order not to oversize the expensive inverter, the inverter power reaches its maximum voltage at rated speed. Below rated speed, for maximum torque the current limit of the inverter is used, as torque in field-oriented controlled PM machines is proportional to current.

$$M \sim \Psi_p \cdot I_s \qquad I_s = I_q, I_d = 0 \tag{1.3.2-1}$$

At speed **above rated speed** the back EMF rises further, as it is directly proportional to speed:

$$U_p \sim \Psi_p \cdot n \tag{1.3.2-2}$$

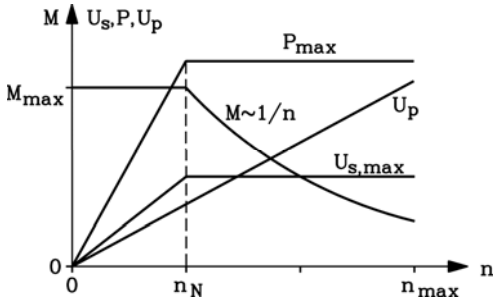

Fig.1.3.2-1: Variable speed, constant power operation, showing maximum required torque, stator voltage and back EMF

In order to avoid "voltage limit" due to I_q-operation and to reach much higher speed, a negative *d*-current component I_d is added, as is shown in the phasor diagrams of Fig.1.3.2-2.

Example 1.3.2-1:
Operation of PM synchronous motor with flux weakening (Fig.1.3.2-2): Voltage limit of inverter $U_{s,max} = U_N$ (=100%), inverter current limit $I_{s,max} = 2I_N$ (= 200% of rated value). Synchronous reactance $x_d = X_d/Z_N = 0.33$ p.u.; $Z_N = U_N/I_N$, $U_p/U_N = 0.7$ at rated speed.

	Voltage u_s	Current i_s	*d*-axis i_{sd}	*q*-axis i_{sq}	Power	Speed *n*	cosφ
a)	0.8	1.0	0	1.0	P_N	n_N	0.89 ind
b)	1.0	2.0	0	2.0	$2P_N$	n_N	0.7 ind
c)	1.0	1.5	**-0.8**	1.2	$2P_N$	$1.67n_N$	0.98 ind
d)	1.0	1.7	**-1.6**	0.5	$2P_N$	$4n_N$	0.89 **cap**

Table 1.3.2-1: Electric data of variable speed PM motor with flux weakening (p.u.-values: $u_s = U_s/U_N$, $i_s = I_s/I_N$)

At rated speed, rated torque (Fig.1.3.2-2a) the field oriented control as described in Section 1.1 is used with only *q*-current operation. For overload torque at rated speed the stator voltage has to be increased to $U_{s,max}$ as well as the current to inverter its current limit $I_{s,max}$, still as a *q*-current (Fig.1.3.2-2b). For further speed increase the rising back EMF has to be reduced by an additional voltage drop at stator reactance $X_s = \omega_s L_{sd}$ (Fig.1.3.2-2c). According to

$$I_s = \sqrt{I_q^2 + I_d^2} \tag{1.3.2-3}$$

an additional (negative) *d*-current component means a necessary reduction of I_q. This is possible, as the torque demand in the constant power range decreases. As long as the decrease of *q*-current balances the increased demand of negative *d*-current component, the inverter is able to supply the needed current. In Fig.1.3.2-2d at $n = 4n_N$, the back EMF is 4 times higher than at rated speed, but the required torque only $M_{max}/4$. Therefore only $I_q = I_{s,max}/4$ ($= 0.5I_N$) is needed, leaving 96.8% of inverter current limit for flux weakening component I_d.

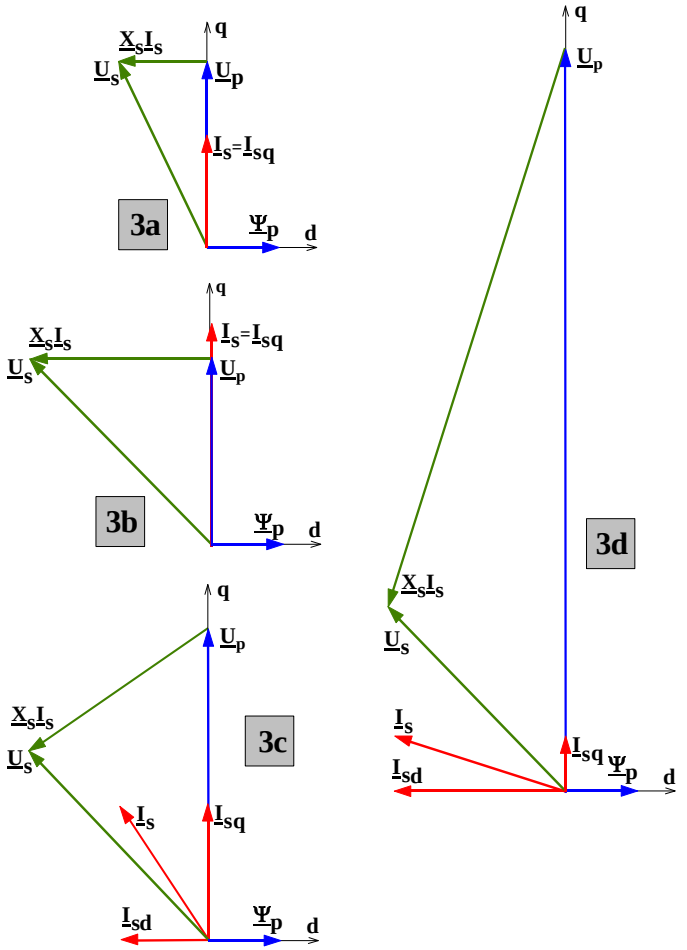

Fig.1.3.2-2: Phasor diagrams of PM machine with field weakening (stator resistance R_s neglected):
a) rated speed, rated torque,
b) rated speed, overload torque,
c) speed at 170% rated speed, decreased torque, flux weakening by negative I_d-current,
d) very high speed (400%) can only be reached by strong field weakening; nearly the whole current consists of flux weakening component I_d, whereas torque-producing component I_q is very small.

Is an infinite maximum speed in any case possible ? At very high speed torque demand is so small, that we may neglect it. In the same way due to $U_p >> U_{s,max}$, we may neglect $U_{s,max}$. Looking on phasor diagram Fig.1.3.2-2d, one gets the necessary field weakening current as

$$I_{s,d} \cong U_p / X_s = \Psi_p / L_s = \Psi_p / L_d \quad , \qquad (1.3.2\text{-}4)$$

which must be smaller than the inverter current limit:

Demand: $\boxed{I_{s,d,\max} < I_{s,\max}}$ (1.3.2-5)

As long as the synchronous *d*-axis inductance L_d is big enough, or the permanent magnet flux linkage with stator winding Ψ_p is small enough, so that the necessary field weakening current is smaller than the inverter current limit, then speed can be raised further.

The necessary field weakening current for infinitely high speed is determined according to (1.3.2-4) by the **short circuit current** $I_{s,k}$ of the machine, which can be measured, when the machine is driven as a generator and short-circuited at the motor terminals.

$$I_{s,k} = U_p / \sqrt{R_s^2 + X_s^2} \cong U_p / X_s = \Psi_p / L_s = \Psi_p / L_d \qquad (1.3.2\text{-}6)$$

Conclusions:
By impressing a negative d-current component it is possible to reduce the increased back EMF at high speed, thus weakening the resulting air gap flux. This allows much higher speed operation than with pure q-current operation. If the short-circuit current of the PM machine is smaller than the inverter current limit, an infinite field weakening is theoretically possible.

Example 1.3.2-2:

Motor of Example 1.3.2-1: $I_{s,k} \cong U_p / X_d$, thus $\frac{I_{s,k}}{I_N} \cong \frac{U_p / U_N}{X_d / Z_N} = \frac{0.7}{0.33} = 2.12 > 2.0$. The short circuit current is bigger than the current limit, therefore there is an upper speed limit, where the necessary *d*-component of current reaches inverter current limit.

Example 1.3.2-3:
Two PM motors A and B are compared with different voltage drop and different back EMF, but the same inverter voltage and current limit $U_{s,\lim}$ and $I_{s,\lim}$. Numbers are given in per unit-values of $U_{s,\lim}$ and $I_{s,\lim}$, e.g. $u_s = U_s / U_{s,\lim}$, $i_s = I_s / I_{s,\lim}$.

$$I_{s,k} / I_{s,\lim} = i_{s,k} = U_p / (X_s I_{s,\lim}) \qquad (1.3.2\text{-}7)$$

PM machine	A	B
$U_p/U_{s,\lim}$ at n_N	0.6	0.8
$X_s I_{s,\lim}/U_{s,\lim}$ at n_N	0.8	0.6
$U_{s,\lim}$ at n_N	$\sqrt{0.6^2 + 0.8^2} = 1$	$\sqrt{0.8^2 + 0.6^2} = 1$
Short circuit current $I_{s,k}$	$0.6/0.8 = 0.75 < 1$	$0.8/0.6 = 1.33 > 1$
Field weakening ?	Unlimited	Limited

Table 1.3.2-2: Comparison of two different PM machines concerning field weakening

Motor B has only a limited flux weakening range, whereas this range for motor A is unlimited (Fig.1.3.2-3).

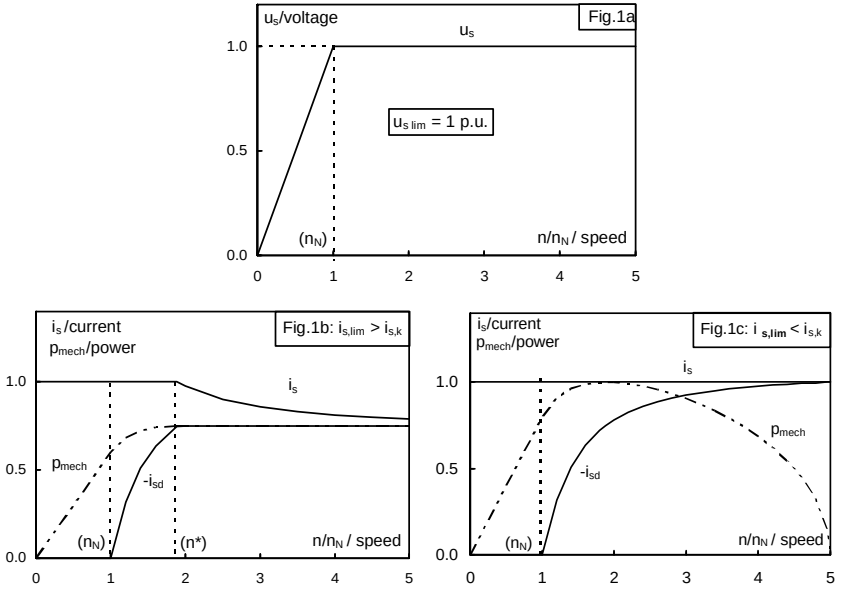

Fig.1.3.2-3: Comparison of two different PM machines concerning field weakening: above: Voltage characteristic of inverter with voltage limit, below left: Motor A with inverter current limit $i_{s,\lim} > i_{s,k}$, below right: Motor B with inverter current limit $i_{s,\lim} < i_{s,k}$

1.3.3 Rotor configurations for flux weakening

a) Surface mounted magnets:
As the permeability of rare earth magnets is nearly μ_0, the magnet height h_M (and the bandage thickness d_B) add to the mechanical air gap δ for the resulting magnetic air gap. According to Section 1.1.5 main inductance L_h is rather low, so resulting *d*-axis inductance L_d is also low, yielding a rather big short circuit current. So surface mounted magnet machines have only a limited field weakening range of typically 1:2.

b) Buried magnets:
With buried magnets (Fig.1.3.3-1) an additional iron bridge covers the magnets. So stator field weakening flux passes only mechanical air gap δ and then stays mainly in the iron bridge. Therefore *d*-axis inductance L_d is much bigger, yielding a lower short circuit current and thus a lower *d*-current demand for flux weakening. Therefore with given inverter current limit much higher field weakening ratios are possible e.g. 1:5.

Conclusions:
For field weakening with negative d-current component a big d-axis inductance is recommended to keep the current low. This inductance is bigger with rotors with buried magnets instead of surface mounted magnets.

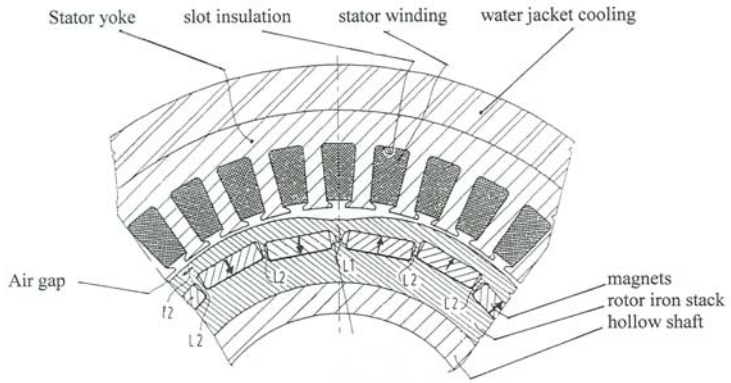

Fig.1.3.3-1: Cross section of a high speed permanent magnet rotor with hollow shaft for good flux weakening conditions; L1: gap between N- and S-magnets, L2: gap between magnets of same polarity, l2: width of iron bridge, critical for mechanical reasons, *Parvex*

1.3.4 Applications: Tools machinery and electric cars

In **tooling machinery** high speed with constant power is needed for "high speed" cutting (Fig.1.3.4-1), milling, grinding.

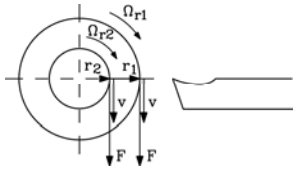

Fig.1.3.4 -1: Cutting: Constant cutting force F and velocity v demands for smaller diameters $2r$ increased speed Ω_r, but reduced torque $M = F.r$, thus constant power $P = F.v$

Special so-called **spindle drives** are used for turning the work piece. They consist of inverter-fed high speed induction motor or permanent magnet synchronous motor drive, often with water jacket cooling for the stator iron stack. Surface speed of the rotor lies in the range of 100 ... 200 m/s (!). The advantage of the PM rotor is that losses in the rotor are small, whereas in induction motors the rotor slip losses in the squirrel cage heat not only the rotor, but also the working piece. Inevitably, thermal expansion occurs, which gives rise to errors in geometric dimensions of the working piece. Nowadays high-end demands lie in the region of some microns, so tooling process is very sensitive to thermal expansion.

Example 1.3.4-1:

Motor	Maximum speed	Constant Power
A	30 000/min	4.5 kW
B	12 000/min	27 kW

Table 1.3.4-1: Typical rated data of hi-speed PM spindle drives

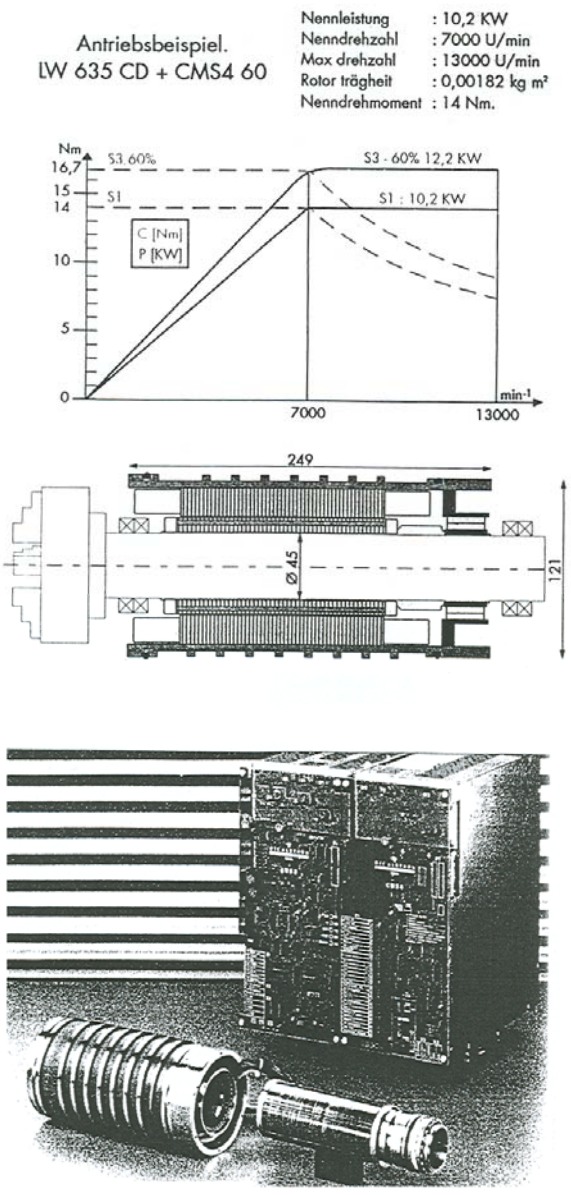

Fig.1.3.4 -2: Example of a permanent magnet synchronous spindle drive (10.2 kW, max. speed 13000/min, with hollow shaft) for cutting, *Parvex*
Rated power: 10.2 kW, rated speed: 7000/min, maximum speed: 13000/min, rotor inertia: 0.00182 kgm^2, rated torque: 14 Nm, short time overload torque: 16.7 Nm, overload power: 12.2 kW

With increasing maximum operating speed the rotor outer diameter $d_r \cong d_{si}$ of the motor has to be reduced to keep the rotor surface speed $v_{max} = d_r \cdot \pi \cdot n_{max}$ and thus the centrifugal forces constant. Therefore with rising maximum speed the power of motors decreases.

$$d_{si} \sim \frac{1}{n_{max}}: \quad P = 2\pi \cdot n_{max} \cdot M_e = 2\pi \cdot n_{max} \cdot \frac{\pi}{2\sqrt{2}} \cdot k_w \cdot A \cdot B_\delta \cdot (d_{si}^2 \cdot l_{Fe}) \sim 1/n_{max} \qquad (1.3.4\text{-}1)$$

In **electric or hybrid-electric cars** the demanded propulsion power (e.g. 30 ... 40 kW for small sized cars) should also be delivered by very small motors, as there is not much space aboard for driving components. Most of the space is occupied by batteries. Therefore inverter-fed induction motors or PM motors must operate at high speed to get the power out of the speed, keeping the torque and thus the motor diameter small. Usually operation up 10000/min is used along with a gear, which reduces speed to the wheel rotational speed. Note that motor in electric traction must sustain $1.25 n_{max}$ for 2 min. as over-speed stress during final motor test at manufacturer.

Example 1.3.4-2:
Medium sized car: 1400 kg mass, tire diameter D = 0.6 m, gear ratio i = 8, motor maximum speed n_{max} = 10000/min. How big is car maximum speed ?

$$v_{car,max} = D \cdot \pi \cdot n_{max} / i = 0.6 \cdot \pi \cdot (10000/60)/8 = 39.3\,\text{m/s} = 141\ \text{km/h}$$

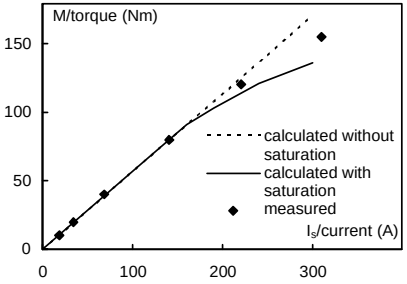

a)

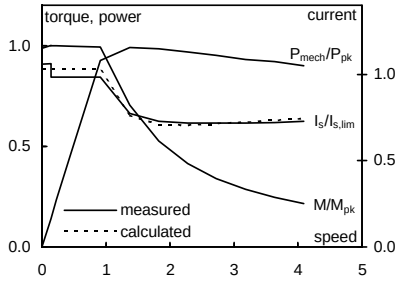

b)

c)

Fig.1.3.4 -3: Propulsion for electric car: a) Torque-Current-Characteristic for propulsion motor, b) Measured torque-speed drive characteristic at 132V DC, $M_{pk} = 156 Nm, P_{pk} = 35 kW, I_{s,\lim} = 315 A$, (inverter) c) Prototype of fuel cell powered cars NECAR (New Electric Car) of *DaimlerChrysler* with electric drive system

Example 1.3.4-3: (Fig.1.3.4-3)
Typical electric data of motor for small sized car: outer diameter d_s = 200 mm, overall length 400 mm, battery voltage 132 V = DC link voltage of inverter, inverter current limit 400 A

a) constant rated torque 65 Nm between zero and rated speed n_N = 2200/min
b) overload torque 156 Nm for short time operation
c) constant power 15 kW rated speed n_N = 2200/min and max. speed n_N = 10000/min
d) overload power 30 kW for short time operation

1.3.5 Additional losses at high speed

The following loss groups of PM synchronous motors have been already discussed in 1.1.7 and are essential for heating of stator copper winding and insulation and of rotor magnets and bandage fixing. Considering frequency $f = n \cdot p$, we get:

No-load losses:
a) **Iron losses**:

$$P_{Fe} \sim B^2 \cdot f^x \sim B^2 \cdot n^x \quad , \qquad (1.3.5\text{-}1)$$

x = ca. 1.8, considering eddy-current and hysteresis losses

b) **Friction losses** at the rotor surface (and in the bearings):

$$P_{fr} \sim d_r \cdot l_{Fe} \cdot n^y \qquad (1.3.5\text{-}2)$$

y = 2 ... 3, depending on rotor and stator surface condition

Load losses:
c) **Armature winding losses** (copper losses):

$$P_{Cu} = 3 \cdot R_s \cdot I_s^2 \qquad (1.3.5\text{-}3)$$

d) **Additional losses** in rotor magnets and rotor iron:

$$P_{M+Fe,r} = f(n,\ \text{current shape}) \sim I^2 \cdot n^z \qquad (1.3.5\text{-}4)$$

z = ca. 1.5 ... 2, depending on rotor geometry and stator current shape.

With high speed motors the loss groups a), b) and d) dominate, and therefore special care must be taken for motor design. Low loss iron sheets with only 1 W/kg losses at 1 T, 50 Hz may reduce iron losses. **Sine wave current** operation is superior to **block current operation** yielding lower additional losses. The reason is that *Fourier*-analysis of block shaped current yields additional current harmonics (amplitudes I_k) with high frequencies $f_k >> f_s$, which excite additional magnetic field in air gap. These flux density waves have the same number of poles like the stator field of sine wave fundamental current I_s, but they rotate with increased speed $n_k = f_k / p$ and therefore induce in rotor massive conductive parts like magnets or rotor iron back harmful eddy currents.

Conclusions:
At high speed the frequency dependent iron, friction and additional losses dominate over the copper losses. For high speed sine wave current operation should be used instead of block current, as the additional losses are much lower.

Example 1.3.5-1:
30 kW PM-Motor, 24 000/min, 2*p* = 4 (Fig.1.3.5-1):
Measured losses a) at ideal sine wave operation from medium frequency synchronous generator, b) at voltage six step operation, causing increased current harmonics I_k

- Fundamental frequency $f = n \cdot p = (24000/60) \cdot 2 = 800\,\text{Hz}$
- Harmonic frequencies $f_k = f \cdot k: \quad k = 6: f_6 = 6 \cdot 800 = 4800\,\text{Hz}$

$$k = 12: f_{12} = 12 \cdot 800 = 9600\,\text{Hz}$$

Due to the 4.8 kHz and 9.6 kHz current component at inverter operation the massive rotor iron is induced with these frequencies, causing big eddy current flow there. Efficiency is still high enough, but the rotor is heated up above 150°C, where the glass fibre bandage loses its mechanical stability. Therefore an additional filter is needed between inverter and motor to suppress the current harmonics. Another solution is to use a laminated rotor iron back to reduce the eddy currents.

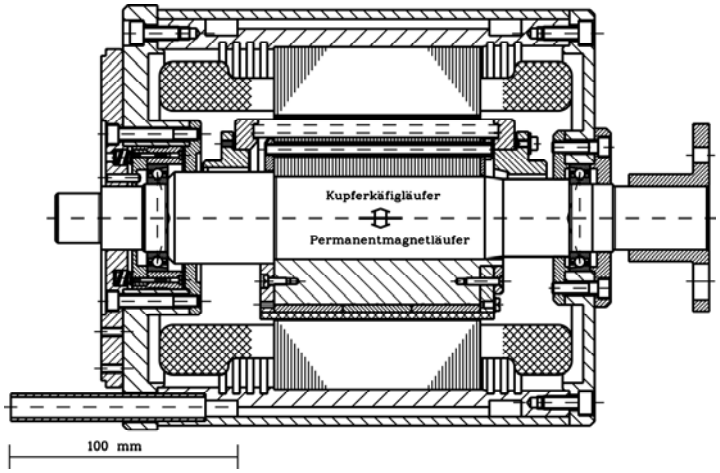

Fig.1.3.5-1: Cross section of four pole high speed AC motor 30 kW, 24 000 /min, identical stator with 36 slots, two-layer winding and water jacket cooling. Upper half: Induction machine with copper squirrel cage rotor, lower half: Synchronous machine with surface-mounted Sm_2Co_{17}-Magnets and glass fibre bandage, d_r = 90 mm, $v_{max} = d_r \cdot \pi \cdot n_{max} = 113\,\text{m/s}$

Permanent magnet synchronous motor: magnets h_M = 3.5 mm, d_B = 2.8 mm, δ = 0.7 mm		
Fundamental voltage, current, power factor	*Ideal sine wave operation*	*Voltage six step inverter operation*
$U_{s,(1)}$ (line to line), I_s, $\cos\varphi_{(1)}$	301 V, 67.4 A, 0.89	309 V, 71.9 A, 0.84
Motor output power P_{out}	30 144 W	30 159 W
P_{Fe}	560 W	560 W
P_{fr}	440 W	440 W
$P_{Cu,s}$	430 W	522 W
$P_{M+Fe,r}$	50 W	520 W
Efficiency	95.3 %	93.65 %

Tabelle 1.3.5-1: Measured losses in permanent magnet synchronous motor with massive rotor iron back

1.4 Linear PM machines

1.4.1 Application of high performance linear PM motors

Linear movements are often needed in production systems such as positioning drives in tooling machines, packaging machines etc. This linear movement can be done either by:

a) rotating position controlled servo motors (such as the PM brushless DC drive) with a change from rotating to linear movement by **mechanical elements** such as belts, toothed bars, screw ball spindles, chains etc. (Fig.1.4.1-1).
b) by **electric linear position controlled servo motors** without any mechanical link between motor and moved working piece (Fig.1.4.1-2). Therefore this is called a **direct drive**.

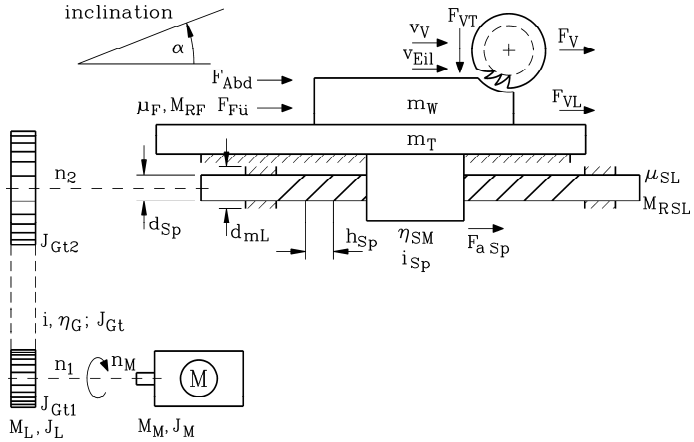

Fig.1.4.1-1: Linear movement of a table (mass m_T) with a working piece (mass m_W) during a milling process. A rotating servo motor *M* with belt gear (gear ratio *i*) drives a screw ball spindle, which converts rotating movement into linear movement.

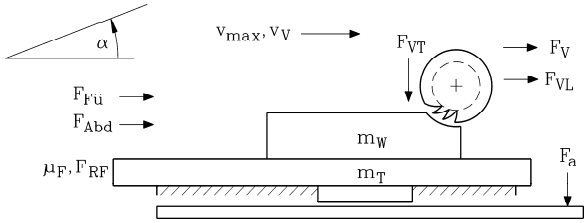

Fig.1.4.1-2: A linear PM servo motor moves a working table for milling process

Advantages of direct drive with linear motors:
- direct drive, therefore no play between mechanical parts such as teeth of gear,
- less mechanical components with their typical steel elasticity lead to less vibration resonance frequencies (increased stiffness of mechanical system)
- less number of resonance frequencies especially in the low frequency region (typically below 100...200 Hz) allow higher gain of position controller, leading to higher dynamic response of controlled system,

- increased dynamic performance of controller leads to smaller process and shape errors e.g. during milling or grinding and allows reduction of time for manufacturing,
- less mechanical components lead to reduced mechanical wear,
- increased stiffness often leads to reduced vibration.

Disadvantages of direct drive:
- Linear motors are more expensive than the conventional solution.
- As motor is directly connected to working piece, special cooling systems must prohibit the heating of the working piece by the motor losses.

The increased accuracy of processing and the reduced process time usually justify the use the linear motor.

Example 1.4.1-1:
Cutting process: Comparison of manufacturing accuracy for conventional positioning of cutting edge and working piece versus linear motor positioning.
a) linear motor, direct drive,
b) conventional system with screw ball spindle
Moved mass of working piece: 1.2 t, velocity: 4m/min. The out-of-roundness of a circular shape of 300 mm diameter is
a) only 0.4 µm, whereas with
b) due the clearance of the balls in the screw it is 5 µm.

Conclusions:
Compared with conventional systems for generating linear movement, the position controlled linear motor yields increased accuracy of processing and reduced process time, thus often justifying the use of the linear motor.

1.4.2 Basic elements of linear PM motors

In Section 1.1.1 a travelling field was excited by a three-phase current system and a distributed winding. This linear distributed winding is housed in the slots of the so-called *primary part* and can be used to drag a *secondary part.* Depending on the type of the secondary part we distinguish different kinds of linear AC motors.
a) **Synchronous permanent magnet linear motor:** Secondary carries permanent magnets with north and south poles
b) **Synchronous reluctance linear motor:** The secondary is a toothed iron structure constituting magnetized north and south poles by the travelling field of the primary.
c) **Asynchronous linear motor:** The secondary carries a conductive rail or a linear conductive cage, where the travelling wave of the primary induces currents, which generate a dragging force with the field of the primary part.
Version a) is superior to b), because for the same primary current a bigger thrust force is generated. Version a) is also superior to c), because there are nearly no losses in secondary.

Synchronous permanent magnet linear motor:
- *Primary part:* Linear distributed three phase winding, fed by a frequency converter, current commutation depending on the position of the secondary (**brushless DC operation** either with block or sine wave commutation)

- *Secondary part:* Usually surface mounted rare earth magnets, covered by non-magnetic steel sheet for protection, and to allow wiping off magnetic debris from secondary´s surface in an easy way.
- The moved part (primary or secondary) is running in a linear sliding system or in linear roller ball system.

Two different basic configurations are used:
- *Long stator linear motor:* The long primary (stator) part is usually fixed. The short secondary part is moving along the primary. Advantage is that only a small amount of (expensive) rare earth magnets is needed, and that the motor cables are also fixed.
- *Short stator linear motor:* The short primary part is moved along the fixed long secondary part. Advantage is that the distributed winding is short, thus yielding smaller armature winding losses. Therefore this type of motor is preferred nowadays.

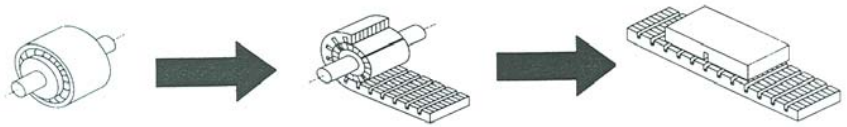

Fig. 1.4.2-1: Basic principle of a linear PM motor: “Unrolling” a rotating PM synchronous motor leads to the (long stator) linear motor

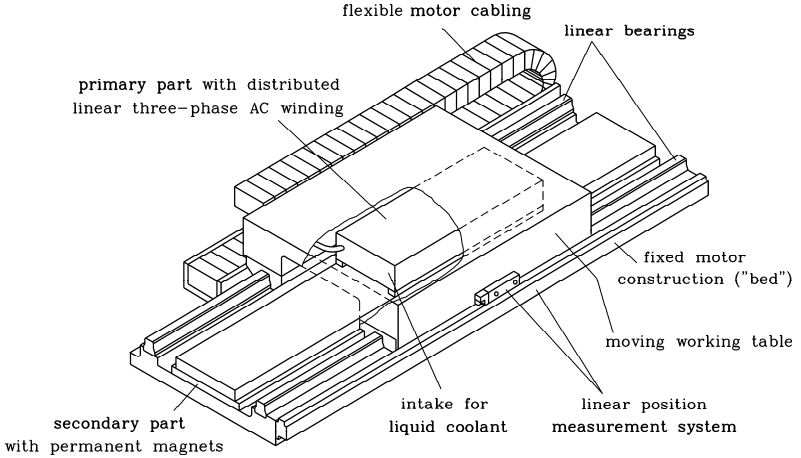

Fig. 1.4.2-2: Main elements of short stator PM linear synchronous motor

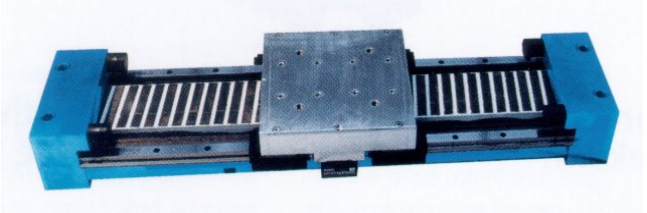

Fig. 1.4.2-3: Short stator PM linear synchronous motor (*Oswald*), skewed PM rows are visible.

Example 1.4.2-1:
Speed of travelling wave (Acc. to section 1.1.1): $v_{syn} = 2 f_s \tau_p$

a) **TRANSRAPID** high speed magnetically levitated train: Long stator linear synchronous motor with electric excitation of the moving secondary, which is the train cabin: pole pitch 258 mm, max. frequency 270 Hz, maximum speed: **139.3 m/s = 500 km/h**
b) **PM short stator linear motor** for tooling machinery: pole pitch 40 mm, max. frequency 125 Hz, maximum speed: **10 m/s = 36 km/h = 600 m/min**
c) **Rotating PM servo motor** (six poles, 120 mm rotor diameter): Rotor surface speed = speed of rotating field: pole pitch 63 mm, max. frequency 150 Hz, maximum surface speed: **18.9 m/s**, corresponding with rotational speed **3000/min**

Example 1.4.2-1:
Maximum acceleration of linear motors:

a) **TRANSRAPID:** For personnel transportation maximum acceleration of typically 1 m/s^2 is recommended.
b) **PM short stator linear motor** for tooling machinery: self acceleration up to 600 m/s^2 is possible.

Conclusions:
The maximum speed of position controlled linear motors e.g. in tooling machines is rather low, when compared with rotor surface speed of rotating machines or compared with special high speed applications of linear drives. On the other hand, the acceleration of linear motors is rather high, yielding high dynamic performance.

1.4.3 Forces and acceleration with linear PM motors

a) Thrust force:
As already explained in 1.1.2 and 1.3.1, the travelling primary current distribution – caused by a three-phase sinus current system - exerts tangential *Lorentz*-forces on the secondary surface magnets with their air gap flux density B_p. The force $F_c = I_s \cdot B_p \cdot l$ per conductor (r.m.s. *q*-current I_s per conductor) adds – over all conductors *z* – to the total tangential thrust $F_t = \sum F_c$. Considering the sinusoidal distribution of flux density with the *Fourier* fundamental field amplitude $B_{p,1} = B_{\delta,1}$ gives a factor $1/\sqrt{2}$ for overall mean thrust force, applying a distributed winding adds the fundamental winding factor k_w. Again using the **current loading (current layer) *A* as total ampere-turns per motor length** $2p \cdot \tau_p$

$$A = \frac{z \cdot I_s}{2p \cdot \tau_p} \quad , \qquad (1.4.3\text{-}1)$$

we get

$$F_t = \frac{k_w}{\sqrt{2}} \cdot z \cdot I_s \cdot B_{\delta,1} \cdot l = \frac{k_w}{\sqrt{2}} \cdot A \cdot B_{\delta,1} \cdot A_{mot} = f_t \cdot A_{mot} \quad , \qquad (1.4.3\text{-}2)$$

where f_t is the **tangential thrust per "active motor surface" A_{mot}**

$$A_{mot} = 2p \cdot \tau_p \cdot l \quad . \qquad (1.4.3\text{-}3)$$

b) Normal force:
The magnetic flux density in the air gap B_δ is the sum of magnet flux density B_p and the primary flux density B_s and exerts a magnetic pull F_n between the surfaces of primary and secondary, which is perpendicular to the tangential force direction. This magnetic pull is calculated with ***Maxwell* stress f_n**, acting on the motor surface A_{mot}. With the resultant sinusoidal field wave amplitude $B_{\delta,1}$ the average stress along the circumference is ½ of maximum value.

$$f_n = \frac{1}{2} \cdot \frac{B_{\delta,1}^2}{2\mu_0} \qquad (1.4.3\text{-}4)$$

$$F_n = f_n \cdot A_{mot} \qquad (1.4.3\text{-}5)$$

In rotating machines with ideal constant air gap, meaning that the rotor is ideally placed in the centre of the stator bore, this magnetic pull is completely balanced, yielding no total normal force on the rotor. But in **single sided linear motors** this magnetic pull must be coped by the linear bearings of the moving secondary. Therefore not only single sided, but also **double sided linear motors** are used, where this rather big magnetic pull is balanced.

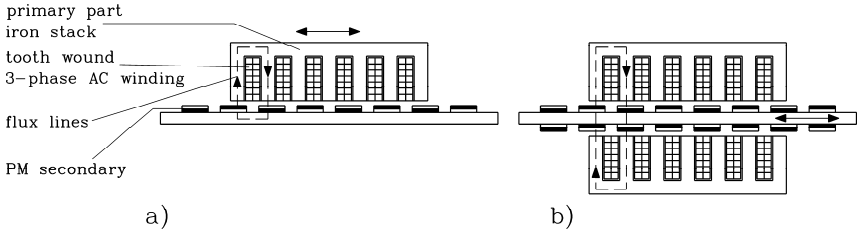

Fig. 1.4.3-1: Linear PM synchronous motors: a) single sided, short stator, b) double sided, short stator

Example 1.4.3-1:
Single sided linear motor: Tangential and normal force:
Usually B_s is much smaller than B_p, so we assume $B_{\delta,1} \cong B_{p,1} = 0.7$ T; winding factor $k_w = 0.93$
a) Normal force per motor surface: *Maxwell* stress: $F_n/A_{mot} = B_{\delta,1}^2/(4\mu_0) = 9.8$ N/cm^2
b) Tangential force per motor surface: *Lorentz* thrust:
The current loading depends on the permissible temperature rise of the winding, which in steady state condition is depending on the kind of cooling.

Steady state current loading and tangential thrust:

Cooling of primary	Direct air cooling	Indirect water jacket cooling
Current loading *A*	400 A/cm	1000 A/cm
Lorentz thrust f_t	1.8 N/cm^2	4.5 N/cm^2
Ratio f_n/f_t	5.4	2.2

Short time overload S3-25%, 1 s cycle time (= 0.25 s overload, 0.75 s no-load, periodically)

Cooling of primary	Indirect water jacket cooling
Current loading *A*	2000 A/cm
Lorentz thrust f_t	9 N/cm^2
Ratio f_n/f_t	1.1

Example 1.4.3-2:
Mechanical loading of linear bearings:

- Steady state thrust force demand: 17 000 N,
- single sided linear motor, water jacket cooling: f_t = 4.5 N/cm^2 (= 45000 N/m^2)
- necessary motor surface: $A_{mot} = F_t / f_t = 17000/45000 = 0.38$ m^2,
- motor primary mass and mass of moving cables for feeding the winding: m_{mot} = 220 kg
- mass of table and working piece: $m_{\mathrm{W+T}}$ = 1500 kg

Weight force	Magnetic pull
$(m_{W+T} + m_{mot}) \cdot g = 16870$ N	$f_n \cdot A_{mot} = 37050$ N

The magnetic pull is more than 4 times bigger than the weight force and would demand very strong linear bearings. Therefore this (big) linear motor would only be realized as double sided version. In that case the tangential force is doubled, and the normal force cancelled.

Conclusions:
In single sided linear motors the normal force exceeds the tangential force by a factor 5. Big linear motors therefore have to be built double sided.

c) Acceleration:
As the weight of the transported working piece may vary, often the so-called **self acceleration** a with maximum thrust $F_{\mathrm{t,max}}$ is used as typical value for characterizing the **dynamic performance** of linear motors. In that case only motor primary mass and motor cables m_{mot} have to be moved.

$$a = F_{t,\max} / m_{mot} \qquad (1.4.3\text{-}6)$$

Example 1.4.3-3:
- Single sided motor of Example 1.4.3-2: m_{mot} = 220 kg, steady state thrust force: 17 000 N
- Maximum thrust: 200% of steady state value

$a = F_{t,\max} / m_{mot} = 34000/220 = 155$ m/s^2

1.4.4 Features of linear PM motors

a) Cooling of linear motors for tooling machinery application:
Only a very small thermal expansion of the working piece is allowed to achieve high accuracy of the manufacturing process in the micron region. Therefore the motor winding is often cooled with a water jacket, **using two cooling systems**. The **power cooler** is directly mounted on the primary iron stack and takes off 85% of the total primary losses. On top of this cooler a **precision cooler** is mounted with controlled coolant flow, taking away 15% of total losses and keeping the changing of the table surface temperature of the linear drive within $\Delta\vartheta$ = 2 K (!). So the working piece, mounted on the table, sees only a change in temperature of 2 K.

Example 1.4.4-1:
Working piece: main dimension: l = 400 mm at 20°C
At 22°C (when motor is hot) the additional length is $\Delta l = l \cdot \alpha_\vartheta \cdot \Delta\vartheta$

Material of working piece	Aluminium	Iron
Linear expansion coefficient	$\alpha_\vartheta = 23.8 \cdot 10^{-6}$ / K	$\alpha_\vartheta = 12.0 \cdot 10^{-6}$ / K
Δl	19 μm	10 μm

b) Minimization of thrust force ripple:
The same measures as to minimize torque ripple, as explained in 1.1.8, are used. In addition, the influence of the ends of the short primary iron stack on force ripple has to be considered.

(i) No-load force ripple (current is zero):
- Minimization of **magnetic cogging** due to slot openings
  1) Skewing of magnets or of slots,
  2) Optimization of the ratio slot opening vs. slot pitch,
  3) Use of fractional slot windings such as tooth wound windings (see Section 1.5.2)
- Minimization of **magnetic cogging** due to both ends of primary iron stack **("end effect")**
  1) Skewing of primary iron stack ends,
  2) Optimization of the ratio iron stack length vs. pole pitch,

(ii) Additional force ripple at loaded motor (current flow in winding):
- Operation with sine wave commutated currents instead of block commutated currents
- star connection of three phase primary winding cancels current harmonics with 3-times multiples of basic frequencies 3f_s, 6f_s, 9f_s, ...

The influence of (i) is dominating in case of sine wave operated motors. The thrust force ripple is usually below 2% of the steady state thrust force in high quality linear motors.

c) Features of linear PM synchronous motors with indirect liquid cooling:
(i) Maximum thrust:
Single sided motor: 5...8 N/cm^2. Self acceleration (without cable mass): 150...300m/s^2.
Double sided motor: The thrust force F_{t} is doubled at the same thrust per motor surface $F_{\mathrm{t}}/A_{\mathrm{mot}}$, as the motor surface A_{mot} is doubled. Related to the motor surface of a single sided motor $A_{\mathrm{mot}} = 2p\tau_{\mathrm{p}}l_{\mathrm{Fe}}$ this means a doubling of f_{t} : 10...16 N/cm^2. If the secondary is moved, then the moved mass is the same as with single sided motor, but thrust is doubled. So self-acceleration is increased by 200%, reaching values of 600 m/s^2.
(ii) Steady state thrust:
It is typically 50% of maximum thrust, so the overload capability is 200%.
(iii) Maximum speed: up to 600m/min = 36 km/h
(iv) Position control: Resolution of the position: With modern linear optical position sensors a resolution of 1 nm is possible. Accurate repeatability for control is less; for controlled operation steps of 0.5 µm are possible for linear precision drive systems.
(v) Efficiency at maximum speed: Depending on speed typically 60% to 70%, thus rather low when compared to rotating PM synchronous motors (typically up to 95%). The reason for this is the rather low velocity of moving part, which determines the rather low output power and therefore low efficiency.

Example 1.4.4-2:
Comparison of a linear and a rotating six pole PM synchronous motor:

	Linear motor	*Rotating motor*
		d_{r} = 120 mm, l_{Fe} = 37 mm
Motor surface A_{mot}	140 cm^2	140 cm^2
Rated speed	120 m/min	1500/min ($\leftrightarrow v$ = 565 m/min)
Tangential force $F_t = A_{mot} f_t$	630 N	630 N
Frequency f_s	16 Hz	75 Hz
Output power $P_{out} = F \cdot v$	1260 W	5930 W
Input power $P_{in} = P_{out} + P_{Cu}$	1585 W	6255 W
Efficiency $\eta = P_{out} / P_{in}$	**79.5%**	**94.8%**

Assumption: Identical cooling system (water jacket cooling), current loading A and air gap flux density B_δ , thus identical steady state specific thrust f_t = 4.5 N/cm^2, and identical copper winding losses P_{Cu} = 325 W. Further losses are neglected.

Note: The same linear motor, operated only at 60m/min with the same force and the SAME losses, produces only 630 W output power and therefore only 66% efficiency (Fig.1.4.4-1).

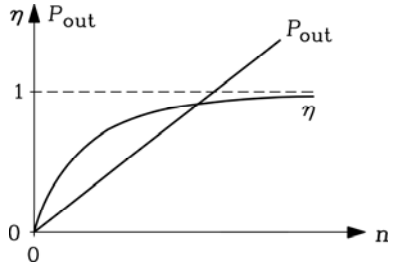

Fig.1.4.4.-1: With constant tangential force (or torque) and constant losses the output power P_{out} decreases linear with rotational speed n (or linear speed v), causing a decrease of the efficiency η

1.5 High torque machines

Variable speed inverter- fed rotating AC direct drives avoid the gear between motor and load, thus avoiding additional noise, oil lubrication of gear and gear maintenance. On the other hand the motor now must turn with the same speed as the load and must also generated the load torque. In many cases such as electric traction (electric cars, trains, ships) the load, which is the wheel set or the propeller, need a rather low rotational speed, but rather big torque. The same is true for wind mills, big turning roasting ovens in the cement industry, grinding mills for coal and ore mining, but also for tooling industry e.g. for co-ordinate tables. The **big torque** requires a big rotor diameter, as torque increases with the square of diameter, but only linear with axial length. Thus, these so-called **hi-torque motors** are of a disc-like shape. In order to minimize the motor mass, these motors are often integrated within the system, e.g. the outer diameter of a cylindrical turning oven bears the rotor active mass of the motor. So the **inactive mass** (bearings, shaft, end shields) may be avoided. In order to mimimize the **active mass** (iron stack, winding, magnets) a **high pole count 2*p* with a small pole pitch τ_p** is aimed. Thus a big bore diameter d_{si} for a big torque is realized, but only a small flux per pole Φ is needed.

$$d_{si} = 2p\tau_p / \pi \qquad (1.5\text{-}1)$$

$$\Phi = (2/\pi)\cdot\tau_p \cdot l \cdot B_\delta \qquad (1.5\text{-}2)$$

Due to the small flux per pole the yoke height h_y of stator and rotor iron back may be small, still ensuring that the yoke flux density B_y stays below the saturation limit of about 1.7 T. By this, active iron masses may be kept small, e.g. the yoke masses m_y are small due to low yoke height.

$$B_y = \frac{\Phi}{2\cdot h_y \cdot l} \qquad (1.5\text{-}3)$$

$$m_y \cong 2p\cdot h_y \cdot \tau_p \cdot l \cdot \gamma_{Fe} \qquad (1.5\text{-}4)$$

The air gap must be kept above a minimum value to avoid mechanical problems, so it cannot be reduced in the same way as pole pitch. Therefore, the stator main inductance of the armature winding (see section 1.1.5) is decreasing due to the reduced ratio of pole pitch vs. air gap.

$$L_h = \mu_0 \cdot (N_s \cdot k_{ws})^2 \cdot \frac{2m_s}{\pi^2 \cdot p} \cdot \frac{\tau_p l_{Fe}}{\delta} \sim \frac{\tau_p}{\delta} \quad . \qquad (1.5\text{-}5)$$

If induction motors were used as high torque motors, the magnetizing current to excite the magnetic air gap field, which is limited by the main inductance, would increase significantly, causing additional copper losses and an increased inverter size. Therefore, usually **PM synchronous motors** are used as hi-torque motors, where small pole pitches may be realized and the air gap is magnetized by the magnets.

Conclusions:
Hi-torque drives avoid mechanical gear and can be integrated into the whole system. Using a high pole count allows reduction of active motor mass, but must be realized as PM synchronous machine to keep losses low.

1.5.1 Hi-torque motors with conventional distributed winding

Starting a design of a high-torque motor from the basic brushless DC motor principle, explained in section 1.1, with distributed three-phase stator winding and surface mounted rotor magnets, we can evaluate the possible mass reduction by increasing the pole count with the following considerations.
Keeping **current load** A, **flux density** B, the rotor diameter and axial length and thus motor torque constant, **by increasing the pole count** by the ratio $x = p_2/p_1 > 1$

- the flux per pole is reduced by 1/x due to decrease of pole pitch,
- the yoke heights are reduced likewise,
- the winding overhangs are shortened by 1/x due to reduced pole pitch.

Thus, both copper and iron mass are reduced. The demagnetizing stator field on the rotor magnet´s trailing edge due to the stator current load, which is given by (see section 1.1.2)

$$H_{\delta,s}(x = \tau_p/2) = \frac{A\cdot\tau_p}{2(\delta + h_M)} \qquad (1.5.1\text{-}1)$$

has to be kept constant. We see that with decreased pole pitch also the magnet height may be reduced, thus decreasing the mass of the expensive magnets. Please note, that the ratio of material costs per mass unit for iron/copper/rare earth magnets is typically 1/2/30 !

But there are also some **disadvantages** due to the increased pole count:

- For the same speed the frequency has to be increased by x due to $v_{syn} = 2f_s\tau_p$, causing increased iron losses according to $P_{Fe} \sim m\cdot f^2 \sim (1/x)\cdot x^2 = x$. So the use of expensive, low loss iron sheets might be necessary, if higher speeds are also needed. Thus high-torque motors are especially **well suited for low speed**.

- Motors are of **special kind and usually expensive**, as the manufactured numbers are low. So often the use of a standard motor with gear is a cheaper investment, which has to be compared with higher maintenance costs.

Example 1.5.1-1:
Calculation of mass reduction of an 8- and 16-pole PM synchronous motor for a torque of 70 Nm, 100 A, brushless DC operation with sine wave commutation, stator water jacket cooling. The main data of both motors A and B are identical: torque M, speed n, stator phase voltage and current U and I; current loading A, air gap flux density B_p = 0.67 T, winding current density J = 12 A/mm^2; air gap δ, q = 2 slots per pole and phase.

Motor B is derived from motor A by simply increasing the number of poles. So the cross section of the slot arrangement per pole pitch remains the same, e.g. the same tooth breadth b_d and tooth length l_d, the same copper wire cross section q_{Cu} and the same yoke height h_y. Pole pitch is the same, too; thus the length of the winding overhangs l_b remains constant, but bore diameter d_{si} increases by a factor of 2, the number of turns N and slot number Q_s increase likewise. Due to constant pole pitch magnet height h_M must be kept constant. Due to the increased diameter, but constant torque, motor B may be much shorter than motor A in axial length l_{Fe}.
By utilizing the following rough equations

Torque $M \sim A \cdot B_p \cdot d_{si}^2 \cdot l_{Fe}$ Yoke mass $m_y \sim d_{si} \cdot h_y \cdot l_{Fe}$

Teeth mass $m_d \sim Q_s \cdot b_d \cdot l_d \cdot l_{Fe}$ Copper mass $m_{Cu} \sim q_{Cu} \cdot N \cdot 2(l_{Fe} + l_b)$

Winding resistance $R_s \sim N \cdot 2(l_{Fe} + l_b) / q_{Cu}$

we note the following ratios for motor B vs. motor A:

Pole count:	$2p_B/2p_A$ = 2/1
Bore diameter:	d_{siB}/d_{siA} = 2/1
Stator slot number:	Q_{sB}/Q_{sA} = 2/1
Number of winding turns per phase:	N_B/N_A =2/1
Axial iron length:	l_{FeB}/l_{FeA} =1/4 .

The actual motor parameters (Table 1.5.1-1) can be checked with the above noted equations.

Motor	***A***	***B***	***Changes***
Pole count	*8*	*16*	+100%
Q_s	48	96	+100 %
d_{si} / mm	95	190	+100 %
L_{Fe} / mm	305	76	-75 %
R_s / mOhm	25	19	-25 %
NdFeB magnet mass / kg	1.25	0.79	-36 %
Iron active mass: yoke, teeth/ kg	17.2	8.3	-50 %
Copper mass / kg	3.1	2.3	-25 %

Table 1.5.1-1: Active masses of two motors A and B for the same electric data, same cross section per pole pitch, but with different pole count

The increase of pole count by factor 2 decreases the iron mass by 50 %, copper mass and resistance by 25 % due to non-changing winding overhangs. Magnet mass is decreased by only 36%, as increased surface speed (factor 2) demands a thicker fixing bandage, as centrifugal force increases by factor 4. A thicker bandage increases the magnetically active air gap and requires therefore a slightly increased magnet height to get the same air gap flux density.

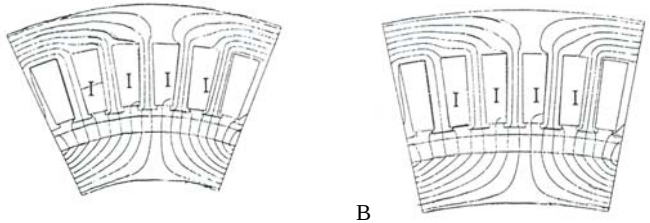

Fig.1.5.1-1: View of one pole cross section of motor A and B with numerical field calculation with Finite Element Method for rated torque 70 Nm: Motor A: 8 poles (M 1.15:1), Motor B, 16 poles (M 1:1). Brushless DC operation with $I_s = I_q$, $I_d = 0$. Current flowing in marked slots ($i_U = 0$, $i_V = -i_W = I$).

The motor of example 1.5.1-1 already has a rather small slot pitch

$$\tau_Q = \frac{d_{si}\pi}{Q_s} \qquad (1.5.1\text{-}2)$$

of $\tau_Q = 95 \cdot \pi / 48 = 6.2$ mm, which is a lower limit for manufacturing windings in slots. In order to increase the pole count for fixed pole pitch, instead of q = 2 only q = 1 slot per pole and phase could be used, leading to a lower limit of pole pitch with conventional distributed windings of about 20 mm. Usually, the manufacturing of such small slots is already very expensive. Therefore, the tooth-wound winding, constituting a **modular synchronous machine**, is used for small pole pitches.

Conclusions:
Considerable active mass reduction is possible with high pole count PM machines used for high torque, low speed. Three slots per pole is the minimum for conventional three-phase distributed windings, defining the minimum pole pitch for high pole count.

1.5.2 Modular synchronous machines

a) Basic principle of tooth-wound winding:
Conventional distributed windings allow minimum pole pitches with one slot per pole and phase. Nevertheless still a crossing of the coils of phase U, V, W in the winding overhang is necessary. With two-layer form wound coils, made of copper wire with rectangular cross section, this crossing is possible, but expensive, and therefore mainly used for high power machines. With cheap single layer winding, often used with round wire copper, this crossing needs additional space in the winding overhangs, this increasing the length of copper wire and the stator resistance (Fig.1.5.2-1a). This can be avoided, if each coil is wound around one single tooth (so-called "**tooth coils**"). The winding overhangs are very short, decreasing the resistance significantly. Moreover, each tooth with its coil can be fabricated separately as a **"module"** and put together afterwards to form the stator **("modular" synchronous machine**). At minimum in three-phase systems, three coils per pole pair, constituting the 3 phases U, V, W, are necessary (Fig.1.5.2-1b). Thus, the number of slots per pole and phase is a non-integer value. Therefore this winding is a so-called **"fractional slot winding",** whereas windings with integer value q like q = 1 in Fig.1.5.2-1a are called **integer slot windings**.

$$q = Q/(2p \cdot m) = 3/(2 \cdot 3) = 1/2 \qquad (1.5.2\text{-}1)$$

In Fig.1.5.2-1 the MMF distribution $V(x) = H_\delta(x)\delta$ and the corresponding flux density distribution $B_{\delta,s}(x)$ is shown for the moment, when the phase currents are $i_U = 0$, $i_V = -i_W$. This distribution is symmetrical to x-axis in case of integer slot winding (Fig.1.5.2-1b), but asymmetric in case of fractional slot winding (Fig.1.5.2-1a).

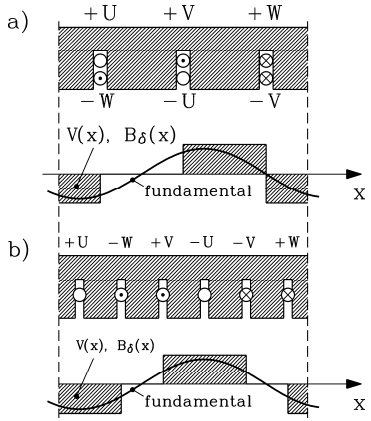

Fig.1.5.2-1: Magnetic flux density distribution and fundamental in a constant air gap: a) fractional slot winding q = ½, b) Integer slot winding q = 1, current flowing in marked slots ($i_U = 0$, $i_V = -i_W = I$).

b) Air gap space harmonics:
Fourier-analysis therefore yields a spectrum of travelling waves with different wave lengths

$$\lambda_\nu = 2\tau_p / |\nu| \qquad (1.5.2\text{-}1)$$

and MMF amplitudes $V_{s,\nu}$ and flux density amplitudes $B_{\delta,s,\nu}$, which are decreasing with rising ordinal number ν. In the symmetric case only odd values ν occur, whereas in the asymmetric case both odd and even values occur. Due to the three phase system (m = 3) no values occur, which are divisible by factor 3.

Integer slot winding: $\nu = 1 + 2m \cdot g \quad g = 0, \pm 1, \pm 2, \pm 3, \ldots \quad \nu = 1, -5, +7, -11, +13, \ldots$

Fractional slot winding: $q = q_Z / q_N, q_N \neq 1,\ \nu = 1 + 2m \cdot g / q_N \quad g = 0, \pm 1, \pm 2, \pm 3, \ldots$
For $q_N = 2 : \nu = 1, -2, +4, -5, +7, -8, +10, -11, +13, \ldots$

The sign of the ordinal number denotes the direction of rotation. As all waves are exited by stator current, oscillating with frequency f_s, the wave speed is

$$v_\nu = \lambda_\nu \cdot f_s = \frac{2\tau_p}{\nu} \cdot f_s \qquad (1.5.2\text{-}2)$$

Thus waves with negative ν rotate counter-clockwise, whereas waves with positive ν rotate clockwise. The fundamental wave $\nu = 1$ is the one, which produces the tangential force with the rotor magnet flux wave of the same wave length. For basic motor understanding, as done so far, the consideration of the fundamental space harmonic is sufficient. The other waves, so-called **space harmonics**, produce no constant tangential force with the permanent magnet flux

distribution, as they are moving slower with increasing ordinal number, whereas the rotor permanent magnet flux distribution rotates with synchronous speed only. Thus, additional **oscillating parasitic torque** is generated, which has been discussed already in 1.1.8 as load torque ripple. We have to conclude that the amount of oscillating torque may increase with fractional slot winding due to the increase of space harmonics. The magnetic pull of these space harmonics is also oscillating and might cause the stator and rotor construction to vibrate. Usually the cylindrical shell-like stator yoke and housing is less stiff than the rotor and more sensitive to vibrations. The vibrations may compress and decompress the surrounding air, thus generating acoustic sound ("**magnetic noise**"). Furthermore, the space harmonics, running asynchronously with respect to the rotor, may induce eddy currents in the conductive magnets and iron back, thus generating **additional rotor losses** even at ideal sinusoidal current supply.

Conclusions:
With tooth-wound coils of the modular synchronous machine a low stator resistance and a small pole pitch for high pole count is achieved at the expense of asymmetric stator air gap flux density distribution, which may give rise to additional load torque ripple, magnetic noise and additional rotor losses.

c) Use of modular machines to increase pole count:
The big advantage of modular machines is that the pole pitch may be decreased even further **without the need of reducing slot pitch**. In Fig. 1.5.2-3a the case for q = ¼ is shown, that means that three stator slots are opposed by 4 rotor magnet poles. The stator coil arrangement and therefore the MMF distribution is the same as for q = ½ (Fig.1.5.2-3b), but now the rotor pole pitch does not fit with the wave length of the stator wave ν = 1, but for ν = -2. That means that the rotor will rotate synchronously not with the stator fundamental wave, but with the first space harmonic, thus a 50% speed and in counter-clockwise direction. The fundamental will generate a pulsating torque with the rotor magnets, which has to be sustained.

Example 1.5.2-1:
Gearless direct drive with 28 poles for light rail vehicles such as metros (Fig.1.5.2-2)

Rated output power P_N per motor	250 kW
Rated/maximum rotational speed n_N per wheel set	398 /min / 772 /min
Rated torque M_N per wheel set: low vs. maximum speed	6000 Nm / 3094 Nm
DC link voltage U_d	750 V
Rated phase voltage U_N (rms), sine-wave	338 V
Overall outer /inner diameter d_a / d_{si}	390 mm / 282 mm
Air gap + bandage: $\delta + d_B$	1.34 mm
Pole pitch τ_p & magnet height h_{mag} & stack length l_{Fe}	31.64 mm & 7 mm & 975 mm

Two different designs with tooth-wound coils are shown in Fig. 1.5.2-3: q = 1/4 and q =1/2.

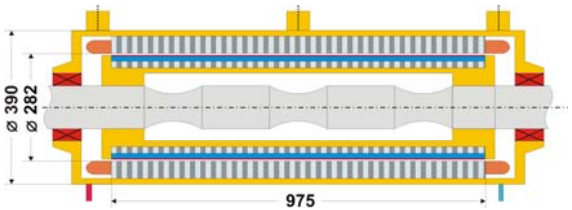

Fig.1.5.2-2: Cross section of a direct drive modular synchronous machine with the rotor directly mounted on the axle shaft of a metro wheel set

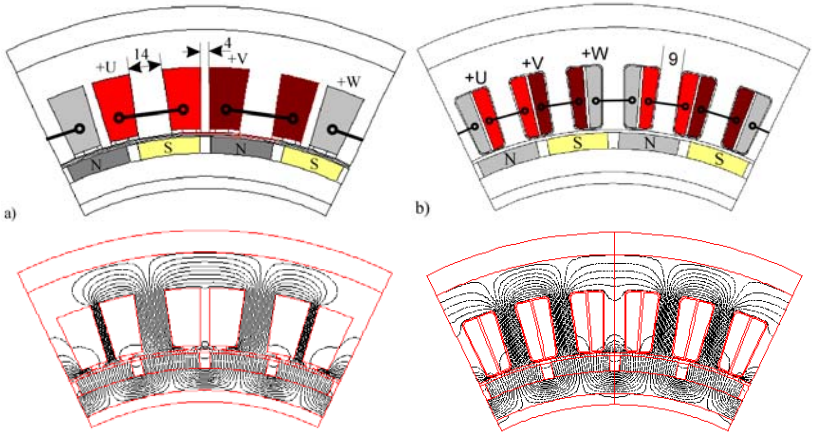

Fig.1.5.2-3: Modular synchronous machine: Numerically calculated magnetic flux density distribution at no-load (current is zero) for 2 pole pairs of PM synchronous machines with tooth-wound fractional slot winding:
a) q = ¼ (with 4 mm narrow inter-tooth to separate tooth coils), b) q =1/2 (no inter-tooth used)

The wave length of the stator fundamental defines the **basic scheme** of a stator winding arrangement. This can be repeated periodically, e.g. four times. With the number of z_S = 7 basic schemes we get in Fig.1.5.2-3a $7 \cdot 3 = 21$ slots and $4 \cdot 7 = 28$ poles. Per basic scheme in Fig.1.5.2-3 the number of slots and rotor poles differs by one. This configuration is often used to design modular synchronous machines. For this case we get the number of poles by

$$2p = z_S \cdot (Q_M \cdot m + 1) \quad , \qquad (1.5.2\text{-}3)$$

with Q_M being the number of slots per module.

d) Application of modular motors:
The fractional slot winding with tooth-coils is used not only for high torque rotating machines, but also extensively for linear PM motors and for standard PM brushless DC servo drives. The main feature is that the rotor has surface mounted magnets. Due to this fact the magnetically active air gap $\delta_{res} = \delta + d_B + h_M$ is rather big, yielding only very small space harmonic amplitudes:

$$B_{\delta s,\nu} = \mu_0 \cdot \frac{V_{s,\nu}}{\delta_{res}} \qquad (1.5.2\text{-}4)$$

In induction machines with their small air gap the space harmonic amplitudes would be rather big, causing big additional harmonic currents in the short circuited rotor winding with big additional losses. Therefore, these fractional slot windings have to be used very carefully only with those rotor configurations, where the influence of space harmonics is kept small.

Example 1.5.2-2:
Wheel-hub motor for military vehicle (Fig.1.5.2-4)
An outer rotor construction is chosen to be fixed directly to the wheel. A big torque is needed to accelerate the vehicle from stand-still. Therefore, a modular synchronous machine is well suited. For increased safety a five phase system is chosen, feeding the five winding legs from

five independent single-phase inverters. If one of the phases fails, the other four will still produce a travelling field to drive the rotor, even when starting from stand still. Please note, that a three phase system with one phase failed will not produce a travelling field any longer, but only a pulsating air gap field: So no starting from stand still is possible in case of a failure.

Number of basic schemes: $z_S = 2$, number of slots per module: $Q_M = 1$,
number of phases: m = 5 (a ... e); number of slots: $Q_s = z_S \cdot m \cdot Q_M = 10$
number of poles: $2p = z_S \cdot (Q_M \cdot m + 1) = 2 \cdot (1 \cdot 5 + 1) = 12$

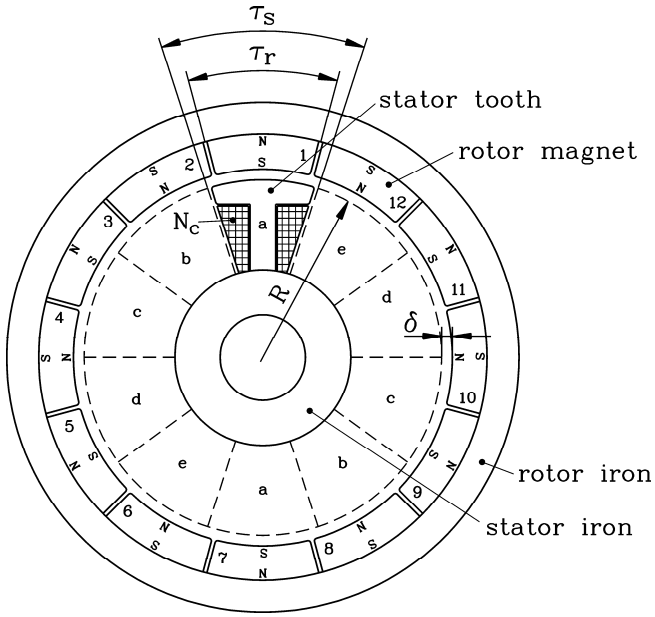

Fig.1.5.2-4: Modular outer rotor synchronous motor as a wheel hub drive, operated with 5 phases a, b, c, d, e (*PhD thesis Kolletschke, Uni Bundeswehr, Munich*)

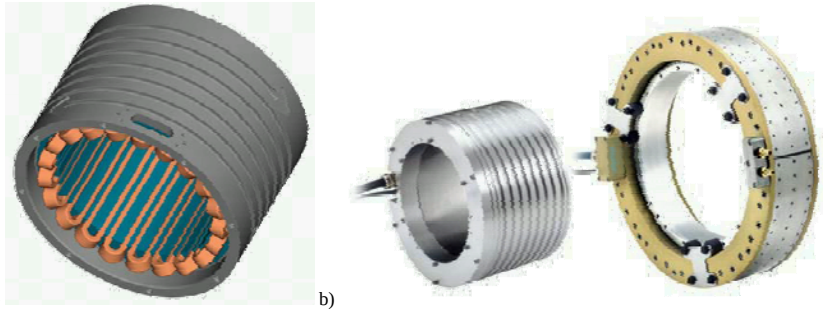

Fig.1.5.2-5: High torque motor with tooth-wound coils: a) stator with tooth coils, b) complete motor with water jacket cooling (Note spiral slot in stator housing for water flow), *Siemens AG, Germany*.

1.5.3 Transversal flux machines

a) Basic arrangement of machine components:
Increasing the pole count at a limited motor diameter is possible by designing each stator phase as a ring coil, lying in the axial planes of the motor. Each phase is independent. The flux of each ring coil flows in perpendicular (transversal) direction to rotational direction of rotor, calling this kind of machine **transversal flux machine**, whereas the conventional machines with flux lines lying in the axial plane are **longitudinal flux machines.** In Fig.1.5.3-1 the stator ring coil of one phase is shown along with U-shaped stator yoke elements – spaced by two pole pairs - to guide the ring coil flux towards the air gap. The rotor consists in the most simple case of surface mounted magnets, but arranged in two rows per ring coil ("twin row arrangement") to fit with the stator flux from the U-yokes. The rotor flux is guided by iron components beneath the magnets from one row to the other. The polarity of magnets of the twin row is opposite.

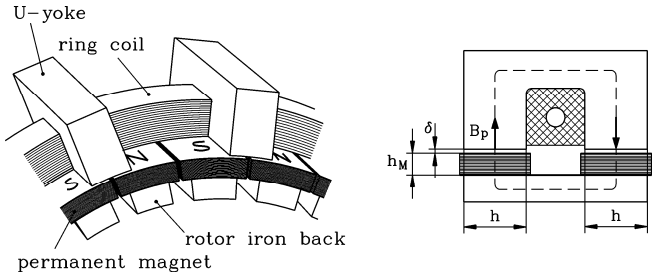

Fig.1.5.3-1: Transversal flux machine, basic arrangement of one phase (left), stator ring coil flux in U-yokes, excited by permanent magnets (right) (*H. Weh, TU Braunschweig, Germany*)

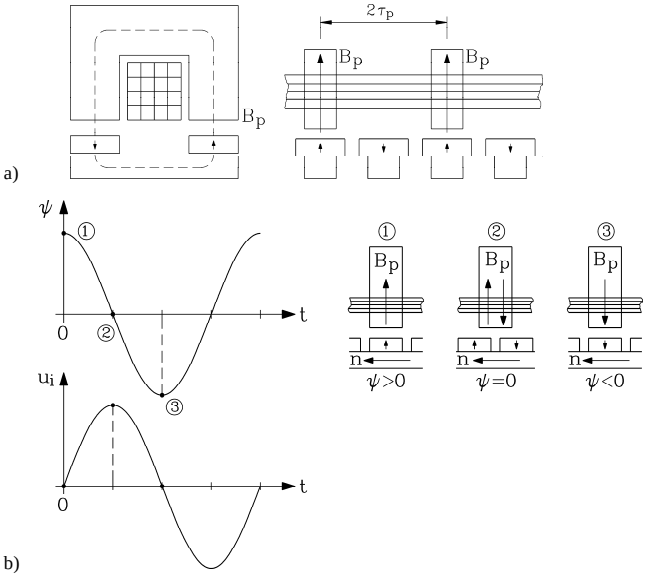

Fig.1.5.3-2: Transversal flux machine: a) no-load permanent magnetic flux linkage with stator ring coil of one phase, b) changing flux linkage ψ induces back EMF u_i

b) Transversal flux machine as generator at no-load:
We assume the current in the stator coil to be zero. The rotor permanent magnet flux is linked to the stator coil via the U-yokes (Fig.1.5.3-2). If the rotor is turned mechanically, the rotor magnets are moving from *d*-position (where the magnets are under the U-yoke pole face) to *q*-position, where the flux linkage with the stator winding is zero. If first in *d*-position, N-poles in the left magnet row were under the left U-yoke side, and therefore S-poles in the right magnet row under the right U-yoke side, then this is reversed in the next *d*-position. After moving by one pole pitch next *d*-position is reached; the left magnet row has the S-poles underneath the U-yoke and the right magnet row therefore the N-poles. Thus the flux linkage of ring coil is reversed. The reversal of the flux linkage repeats with turning rotor. The change of flux linkage induces a back EMF u_p in the stator ring coil: $u_i = -d\psi/dt = -N_s \cdot d\Phi/dt = -u_p$ with the frequency $f_s = n \cdot p$ (N_s : number of turns per stator ring coil).

In order to generate a three phase voltage system, three ring coils are necessary and three twin magnet rows. By shifting the magnets (or the U-yokes) by $2\tau_p/3$, the phase shift of the three induced phase voltages u_p is 120° each. In general, if *m* ring coils are used and the shift of U-yokes or magnets is $2\tau_p/m$, we get a *m*-phase voltage system with phase shift $360°/m$. A special case is *m* = 2, where 2 ring coils are used. U-yokes must be shifted by $2\tau_p/4$ to get two voltage with phase shift $360°/4 = 90°$, because phase shift $360°/2 = 180°$ yields only phase opposition.

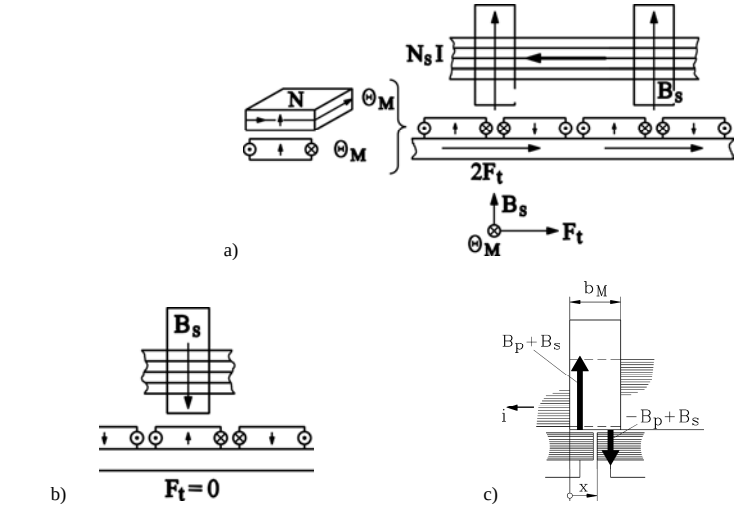

Fig.1.5.3-3: Tangential force generation in a transversal flux machine: For a better understanding the permanent magnets are depicted as electrically excited ring coils. (a) *q*-position: maximum force generation, (b) *d*-position: no force generation, (c) superposition of rotor and stator magnetic field B_p and B_s in the U-yokes

c) Motor operation:
When an external voltage u_s is supplied to the ring coil, a current flows in the ring coil, which excites the stator field B_s (Fig.1.5.3-1). The rotor magnets may be thought as electrically excited coils with an equivalent ampere-turns $\Theta_M = h_M \cdot H_{CB}$, generating the same flux density B_p as the magnets. Then with *Lorentz´*s law we get a tangential force

$$F_{t,M} = \Theta_M \cdot B_s \cdot h \qquad (1.5.3\text{-}1)$$

per pole magnet per row, when the magnet is in *q*-position, meaning that the gap between two adjacent pole magnets is centred under the U-yoke pole face. In *d*-position the magnetic equivalent ampere-turns are outside of the stator field, and no force is generated. In the stator coils flows the AC current with a frequency $f_s = n \cdot p$. At *q*-position maximum current must occur, whereas in *d*-position the current can be zero. This is the already discussed *q*-current operation of brushless DC machines. After movement of the rotor by one pole pitch, negative current amplitude with the rotor magnet of opposite polarity again produces positive tangential force (Fig.1.5.3-4). Thus the force pulsates with double stator frequency.

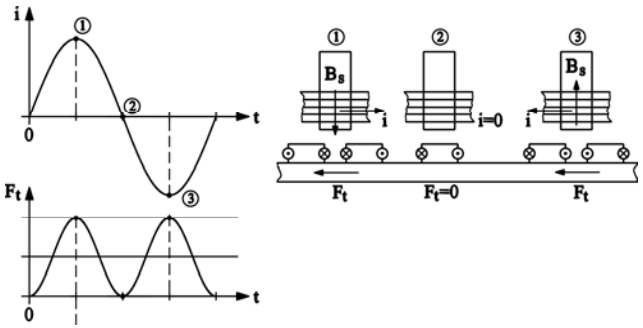

Fig.1.5.3-4: AC current produces positive (pulsating) tangential force in one phase of a transversal flux machine

This can also be understood by considering the internal power of one coil, which is determined by back EMF and current:

$$p_\delta(t) = u_p(t) \cdot i(t) = \hat{U}_p \sin(\omega_s t) \cdot \hat{I}_s \sin(\omega_s t) = \frac{\hat{U}_p \hat{I}_s}{2} \cdot \left(1 - \cos(2\omega_s t)\right) = v_{syn} \cdot F_t(t) \quad (1.5.3\text{-}2)$$

As in any single phase system, power and therefore force is consisting of an average value and an oscillating part with twice frequency. As the ring coils-magnet systems of the other phases operate with voltage and current phase shifted by $2\pi/m$, the total tangential rotor force is constant, given by the sum average force values per phase, whereas the oscillating parts are cancelling.

$$F_t = \frac{m \cdot \hat{U}_p \hat{I}_s}{2 \cdot v_{syn}} \qquad M_e = F_t \cdot (d_{si}/2) = \frac{p}{\omega_s} \cdot m \cdot U_p I_s \qquad (1.5.3\text{-}3)$$

Thus torque has the same formula as at conventional PM machines. As the stator field also induces a voltage $\omega_s L_s I_s$ due to self-induction in the ring coil, where L_s is the inductance of the coil, we finally get –along with the resistive voltage drop - the voltage equation for each ring coil, which is the same as with conventional PM synchronous machines. Thus we understand that the transversal flux machine is a special kind of PM synchronous machine, which delivers maximum torque if it is operated with a position sensor as a brushless DC drive with sine wave commutated *q*-current.

$$\boxed{\underline{U}_s = R_s \underline{I}_s + jX_s \underline{I}_s + \underline{U}_p} \qquad (1.5.3\text{-}4)$$

In Fig.1.5.3-3c the superposition of stator and rotor field in U-yoke is shown. On the left side the flux is increased to $B_s + B_p$, on the right side it is decreased to $B_s - B_p$. So the left side will saturate strongly, thus limiting the total flux density and the power output of the machine. Tangential force generation can also be understood by considering this resulting magnetic field. On the left side in the U-yoke it is increased, on the right side decreased. So the tangential magnetic force on the left side is bigger than on the right side, therefore a tangential magnetic pull will drag the rotor from left to right. This is the same result as with consideration of *Lorentz*-force on magnetic equivalent ampere-turns in Fig.1.5.3-3a.

Conclusions:
The transversal flux machine is a special kind of PM synchronous machine with a high pole count, as no slots are necessary. As coil cross section and flux cross section lie in perpendicular planes (transversal arrangement), the coil cross section may be increased without influencing the magnetic flux path. This is a big advantage compared to longitudinal machines. There, increase of coil cross section means increase of slot area, thus reducing tooth area, where magnetic flux is passing. Narrower teeth mean increased tooth flux density and increased iron saturation. Therefore the flux must be reduced to avoid extensive saturation. Hence in longitudinal machines areas for flux and current flow are dependent from each other, whereas in transversal flux machines they can be chosen independently.

d) Rotor magnetic flux concentration:
Instead of using surface mounted magnets, it is possible to use buried magnets in order to increase air gap flux density and to reduce permanent magnet material (Fig.1.5.3-5). So we get a symmetric arrangement, which allows a double sided ring coil arrangement. Hence the tangential force is generated twice, thus doubling the torque.

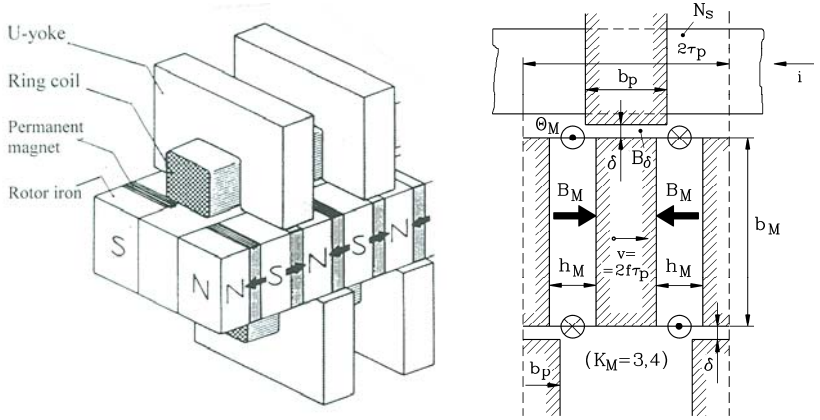

Fig.1.5.3-5: Magnetic flux concentration inside the rotor of a transversal flux machine in order to increase the air gap flux density and to allow a double sided ring coil arrangement (left); schematic of flux concentration with main dimensions (right) (*H. Weh, TU Braunschweig, Germany*)

Theoretical flux concentration is given by the ratio of both permanent magnet surfaces versus the pole pitch surface:

$$\Phi = 2 \cdot B_M \cdot (b_M \cdot h) = B_\delta \cdot \tau_p \cdot h \quad \Rightarrow \quad k_M = \frac{B_\delta}{B_M} = \frac{2b_M}{\tau_p} > 1 \qquad (1.5.3\text{-}5)$$

So magnet breadth b_M must be at least bigger than half the pole pitch to get flux concentration inside the air gap. By using *Ampere´*s law for assumed $\mu_{Fe} \to \infty \ (\Leftrightarrow H_{Fe} = 0)$ at no-load (current is zero) we get

$$\oint_C \vec{H} \bullet d\vec{s} = 2 \cdot (2H_\delta \cdot \delta + H_M \cdot h_M) = 0 \quad \Rightarrow \quad B_\delta = \mu_0 H_\delta = -\mu_0 \frac{h_M}{2\delta} \cdot H_M \ . \qquad (1.5.3\text{-}6)$$

Combining it with the $B_M(H_M)$-characteristic of the permanent magnet in the second quadrant

$$B_M = \mu_M H_M + B_R \quad , \qquad (1.5.3\text{-}7)$$

we finally get with (1.5.3-5) for no-load air-gap flux density $B_\delta(I = 0) = B_p$:

$$\boxed{B_\delta = \frac{B_R}{\frac{1}{k_M} + \frac{\mu_M \cdot 2\delta}{\mu_0 \cdot h_M}}} \quad . \qquad (1.5.3\text{-}8)$$

In Fig.1.5.3-6 a 2D numerical field calculation is shown for *d*- and *q*-position of the rotor to calculate real flux concentration. Left, in *d*-position, current and force are zero. So we get the conditions assumed for the derivation of (1.5.3-8). But we see that a considerable part (23%) of the rotor permanent magnet flux is leaving the rotor downwards, thus reducing the flux available for concentration. Only 77% of magnet breadth b_M delivers its flux to the upward air gap. Hence the concentration factor decreases: $k_M = 0.77 \cdot 2b_M / \tau_p$.

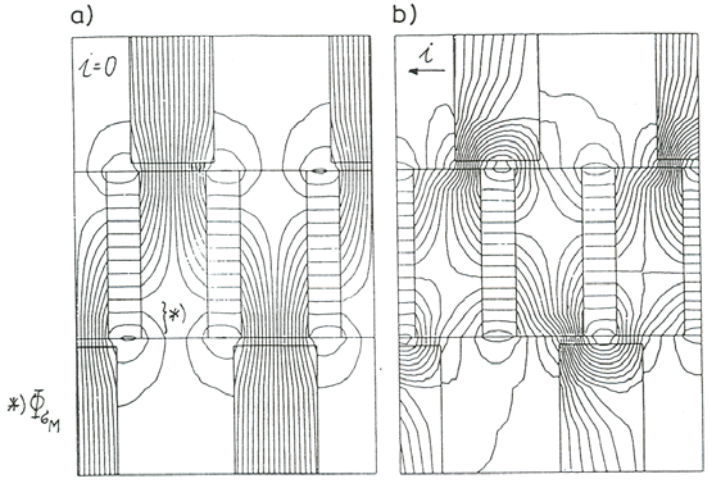

Fig.1.5.3-6: Real flux concentration (2D numerical field calculation): left: *d*-position of rotor: stator current and tangential force is zero, (right) *q*-position, maximum current and force

Example 1.5.3-1:
Theoretical increase of the air gap-flux density by flux concentration for the following data:

$h_M / \delta = 4$, $\mu_M / \mu_0 = 1.05$, B_R = 1.1 T.

	No flux concentration	*Flux concentration No stray flux*	*Flux concentration Stray flux 23%*
Concentration factor k_M	1	3.4	$0.77 \cdot 3.4 = 2.6$
$B_\delta(I = 0) = B_p$	0.72 T	1.34 T (+85%)	1.21 T (+68%)

By using a concentration factor of 3.4, an increase of the air gap flux density by a factor of 1.85 is theoretically possible. Considering 2D rotor stray flux of 23% of PM flux, this concentration increase is reduced to factor 1.68.

Possible flux increase is limited, because under load the stator field B_s is added in the U-yoke. The total flux density then should not exceed 2.0 T to avoid extensive iron saturation. The flux line pattern of Fig.1.5.3-6 leads again to understanding of force generation by considering the magnetic pull. Imagining the flux lines as elastic rubber strings, in *d*-position this pull is symmetric to left and right side, yielding total force value zero. In *q*-position the pull on rotor on left side of U-yokes is bigger than on right side. Thus a total tangential force exists, moving the rotor to the right.

e) Electromagnetic utilization of transversal flux machines:
Now we want to calculate power output of a simplified single sided transversal flux machine. We assume the pole width of the U-yoke b_P equal to the pole pitch τ_p and neglect the magnet height h_M. Then the flux density $B_\delta(I = 0) = B_p$ in *d*-position (Fig.1.5.3-7a, time t = 0) is constant along the pole pitch, yielding the pole flux

$$\Phi_p = B_p \cdot (h \cdot \tau_p) \quad . \qquad (1.5.3\text{-}9)$$

The flux is linked to the ring coil p times (in p U-yokes), yielding a flux linkage $\Psi = p \cdot N_s \cdot \Phi_p$. This maximum flux linkage decreases linear, when the rotor is moving and is zero in *q*-position ($t = T/4$) and negative maximum at $t = T/2$. *Faraday´*s law yields for induced voltage $u_i = -d\psi / dt$ a rectangular oscillating induced voltage, oscillating with $\omega_s = 2\pi f_s$ ($T = 1/f_s$), with the amplitude (Fig.1.5.3-7b)

$$\hat{U}_i = \frac{2 \cdot \Psi}{T/2} = p \cdot N_s \cdot 2 f_s \tau_p \cdot 2h \cdot B_p \quad . \qquad (1.5.3\text{-}10)$$

Considering the voltage fundamental $\hat{U}_{i(1)} = k_1 \cdot \hat{U}_i = U_p \cdot \sqrt{2}$ (here: $k_1 = 4/\pi$) according to *Fourier* analysis as ideal sinus back EMF, the internal power of transversal machines with *q*-current operation $I_s = I_q$ is derived:

$$P_\delta = m \cdot U_p I_s = m \cdot k_1 \cdot pN_s \cdot 2 f_s \tau_p \cdot 2h \cdot B_p \cdot I_s \cdot \sqrt{2} \quad . \qquad (1.3.5\text{-}11)$$

As with longitudinal flux machines in Section 1.3, we consider the power per speed $n = f_s / p$ and active rotor volume (*Esson´*s number *C*), which is proportional to torque per rotor volume. Rotor volume is (neglecting $\pi/4$) given as $d_{si}^2 l_{Fe}$. With $d_{si}\pi = 2p\tau_p$ and $l_{Fe} = m \cdot 2h$ for all m phases we get

$$C = \frac{P_\delta}{n \cdot d_{si}^2 l_{Fe}} = \frac{\pi^2}{\sqrt{2}} \cdot \frac{N_s I_s}{2\tau_p} \cdot k_1 B_p \qquad (1.3.5\text{-}12)$$

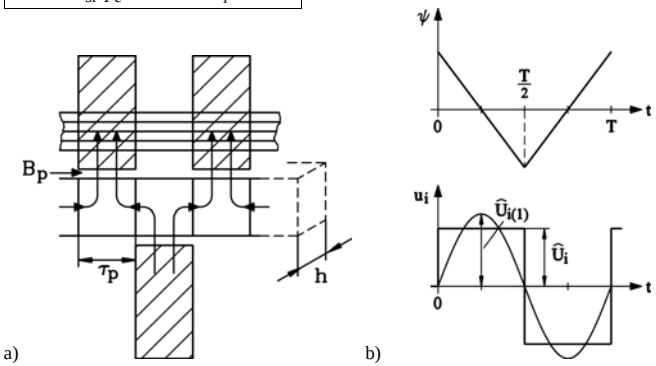

Fig.1.5.3-7: Ideal transversal flux machine: a) Permanent magnet flux linkage of the ring coil at *d*-position of the rotor (time $t = 0$), b) changing of the flux linkage, when the rotor is moving, induced rectangular shaped coil voltage and its fundamental

Comparing this with C for longitudinal machines (section 1.3.1) $C = \frac{\pi^2}{\sqrt{2}} \cdot k_w \cdot A \cdot B_\delta$ we see: The concentrated ring coil of a transversal flux machine (TFM) has the winding factor $k_W = 1$, and we can take $k_1 B_p$ as equivalent amplitude of a sinusoidal distributed flux density to get an ideal sine wave back EMF. Most interesting is that for the transversal flux machine we have to take the **current loading**

$$A = \frac{N_s I_s}{2\tau_p} \text{ (single sided TFM)}, \quad A = \frac{2N_s I_s}{2\tau_p} \text{ (double sided TFM)} \qquad (1.3.5\text{-}13)$$

As the ring coil with its ampere-turns $N_s I_s$ passes all U-yokes, which are distanced by $2\tau_p$, the current loading per U-yoke is $N_s I_s/(2\tau_p)$, thus explaining the result (1.3.5-12) easily. When comparing A of TFM with that one of the longitudinal flux machine (LFM) (Section 1.3.1)

$$A = \frac{z \cdot I_s}{d_{si} \cdot \pi} = \frac{2m \cdot N_s \cdot I_s}{2p\tau_p} \qquad (1.3.5\text{-}14)$$

we see, that for LFM all phases contribute, whereas for TFM each phase acts independently. Most important is, that with the increase of pole count and simultaneous decrease of pole pitch the current loading and therefore motor output power remains constant for the LFM, but not for the TFM. As A for the TFM does not depend on the pole count, with decreasing pole pitch (= increasing pole count) current loading increases and thus the internal power, too. This can be easily understood. Tangential force per pole magnet $F_{t,M} = \Theta_M \cdot B_s \cdot h$ is added to the total force summing all force contributions of U-yokes. So, with an increasing number of poles and therefore increasing number of all U-yokes we increase force and therefore torque and power.

$$F_t = \sum F_{t,M} = m \cdot p \cdot \Theta_M \cdot B_s \cdot 2h \qquad (1.3.5\text{-}14)$$

Of course, by reducing the pole pitch at a very small pole pitch (below about 20 mm) also the magnet height has to be reduced (Fig.1.3.5-6), so B_p decreases, and the motor loses power. Thus we get an optimum for the pole pitch of theoretically 10 ... 15 mm (Fig.1.3.5-8), which is derived by numerical field calculation.

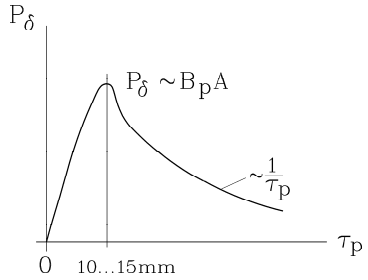

Fig.1.5.3-8: Increase of power of a TFM at a given motor diameter and length by increasing the pole count (decreasing the pole pitch τ_p) with a theoretical optimum pole pitch at about 10 ... 15 mm

Example 1.5.3-2:

Steady state internal power of single sided small 2-phase TFM (bore diameter $d_{si} = 167$ mm):

Data: $2p = 30$, $\tau_p = 17.5$ mm, $\delta = 0.8$ mm, $h = 28$ mm, $h_M = 6.5$ mm, $b_M = 18$ mm, $m = 2$, $\mu_M/\mu_0 = 1.05$, $B_R = 1.095$ T, stray flux: 30%, $k_1 = 1.07$, $N_s = 22$
indirect cooling of the ring coil, current density: 4.6 A/mm^2, nominal current $I_s = 95$ A
speed $n = 900$/min

a) Internal power:

$$f_s = n \cdot p = (900/60) \cdot 15 = 225\,\text{Hz}$$

$$k_M = \frac{2b_M \cdot (1-0.3)}{\tau_p} = \frac{2 \cdot 18 \cdot (1-0.3)}{17.5} = 1.44$$

$$B_p = \frac{B_R}{\frac{1}{k_M} + \frac{\mu_M \cdot 2\delta}{\mu_0 \cdot h_M}} = \frac{1.095}{\frac{1}{1.44} + \frac{1.05 \cdot 2 \cdot 0.8}{6.5}} = 1.15\,\text{T}$$

$$\hat{U}_i = p \cdot N_s \cdot 2 f_s \tau_p \cdot 2h \cdot B_p = 15 \cdot 22 \cdot 2 \cdot 225 \cdot 0.0175 \cdot 2 \cdot 0.028 \cdot 1.15 = 167.3\,\text{V}$$

$$\hat{U}_{i(1)} = k_1 \cdot \hat{U}_i = 1.07 \cdot 167.3 = 179\,\text{V}$$

$$P_\delta = m \cdot U_p I_s = 2 \cdot (179/\sqrt{2}) \cdot 95 = 24\,\text{kW}$$

c) Steady state utilization of a TFM:

$$A = \frac{N_s I_s}{2\tau_p} = \frac{22 \cdot 95}{2 \cdot 1.75} = 600 \text{ A/cm}$$

$$C = \frac{\pi^2}{\sqrt{2}} \cdot A \cdot k_1 B_p = \frac{\pi^2}{\sqrt{2}} \cdot 60000 \cdot (1.07 \cdot 1.15) = 515000\,\text{Ws/m}^3 = 8.6\,\text{kVAmin/m}^3$$

Compared to the results of longitudinal flux machines, Example 1.3.1-1b) we get 75% higher utilization.

Conclusions:

The transversal flux machine has a high torque per volume ratio, if the pole count is high, yielding an optimum pole pitches of typically 10...15 mm. Thus the TFM is well suited for low

speed, high torque applications as direct drive. Utilization can be increased by a factor of about 2 compared to longitudinal flux machines.

f) Performance and technology of transversal flux machines:
In order to judge the technical value of transversal flux machines, one has to regard:
- electromagnetic performance, concerning power output and losses
- manufacturing (motor technology)
- inverter rating.

Electromagnetic performance:
- **No-load losses:** The U-yokes experience iron losses due to changing flux linkage. The numerically calculated flux plots show rather big stray flux already at no-load. With a rotating rotor this flux causes already at **no-load** eddy currents in metallic parts, such as end shields, cooling ducts, and in those ring coil copper wires, which are adjacent to the air gap. Eddy currents act along with this stray flux as an eddy current brake and reduce the possible shaft torque. In the rotor the PM flux has to change direction to the upper and lower U-yoke with stator frequency, causing additional eddy current losses in rotor iron and rotor magnets. These losses are dominating over friction losses.
- **Load losses:** At **load** the stator field adds to the stator iron losses and rotor magnet and iron losses, whereas the resistive losses in the ring coils are small. The ring coils are very compact and therefore have a low *ohmic* resistance.
- Tangential force usually per phase is not pulsating with an ideal sine, so over all phases the force and torque ripple is not cancelling totally, leading to a **torque ripple** with the frequency $f = 2p \cdot n \cdot m$. At the same time a radial magnetic pull between U-yokes and the rotor occurs, which is also pulsating with that frequency, causing radial vibrations of the stator and rotor, which might lead – especially in case of mechanical resonance with the natural frequency of the stator housing – to considerable **magnetic noise**.

Motor technology:
- Flux concentration and **buried rotor magnets** are necessary to increase flux density in the air gap, which is possible up to 1.5 T, as no tooth-slot-structure will cause further fringing. Only under load the additional stator flux in the U-yoke must be considered. The **composite rotor** consists of different components: laminated iron, permanent magnets, glass fibre construction to fix the magnet rows to the shaft and glue to fix the magnets. Due to different thermal expansion coefficients the rotor is mechanically sensitive to large changes in temperature.
- Rotor iron between the magnets must be laminated, as the permanent magnet flux is pulsating between upper and lower U-yokes (see Fig.1.5.3-6).
- Each phase is an electrically and mechanically **independent** module. So power may be increased by stacking more modules on one shaft. On the other hand, the pulsating forces of each single phase are acting on the rotor fixation, which must endure this stress.
- As the TFM has many poles, the stator frequency is rather high, if higher speed range is wanted. With frequencies up to 2000 Hz the U-yokes must be manufactured of **very low loss iron sheet** (0.1 mm thickness). As flux is not rotating within the sheets, low loss Hi-B-transformer iron sheets with losses of only 0.3 W/kg (at 1 T, 50 Hz) may be used. Another possibility is the use of the rather new material **"soft magnetic composite",** which is a pressed structure of small iron grains, insulated by plastic encapsulation. Thus eddy currents are suppressed very well, but due to the plastic content the permeability is rather low (typical values $\mu < 500\mu_0$).

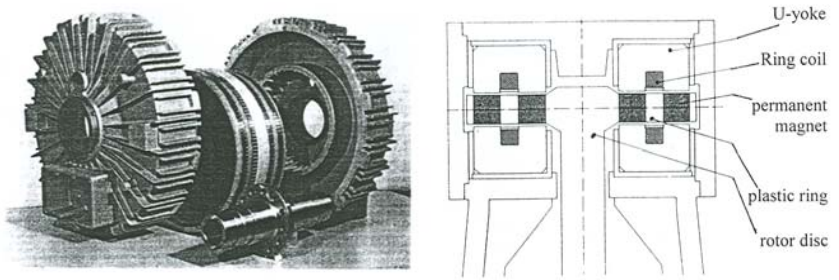

Fig.1.5.3-9: Two phase prototype TFM (Univ. *Brunswick*, Prof. *Weh*): motor components and cross section

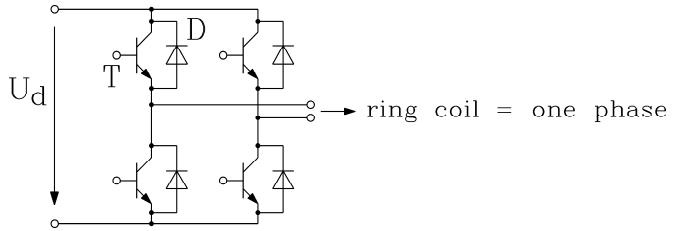

Fig.1.5.3-10: Two phase TFM demands a full bridge per phase

Inverter technology:
- In order to simplify the rotor construction, only **three and two phase machines** are used. Three phase machines allow the use of conventional IGBT voltage source inverters (six IGBTs, six free-wheeling diodes on the motor side) with brushless DC current control. A rotor position sensor is needed. For two phase machines special inverters are necessary: Each phase is supplied by a full bridge inverter with 4 IGBTs and 4 free-wheeling diodes (Fig.1.5.3-10), which is more expensive than in three phase case. Upper and lower half bridge are chopping phase shifted, thus reducing the transistor switching frequency by factor 2 for a given pulse frequency at the coil terminals.
- At low speed the **inverter is chopping** the DC link voltage with a fixed switching frequency. With increased speed only **six step mode** (for three phases) or **four step mode** (for two phases) switching is applied, reducing the switching losses in the IGBTs. The back EMF is usually rather sinusoidal and dominates at elevated speed. So even with six or four step mode (= block shaped terminal voltage) the motor current is rather sinusoidal.
- **Flux weakening** for increased speed is possible by impressing I_d current. With a buried magnet rotor the inductance of the stator coil is rather big, as the air gap between the U-yoke and the rotor may be kept small (< 1 mm). Hence the short circuit current is in the order of the rated current. So the necessary *d*-component of current for flux weakening can be easily supplied by the inverter.
- Due to the big stator inductance the **power factor** of the machine is rather low between 0.5 and 0.7. Hence the inverter needs a bigger current rating especially at low speed.

Conclusions:
Rated current and short circuit current are nearly equal; the motor is flux weakened without overrating of the inverter. The power factor of about 0.75 is rather low due to the rather big inductance.

g) Applications:
Transversal flux machines are up to now not widely used. Small three phase motors exist as **servo drives** for positioning (Fig.1.5.3-13), but due to the strong curvature of the rotor at the small dimensions of about 100...150 mm outer diameter considerable stray flux reduces the power output. So the utilization of these motors is not bigger than of conventional longitudinal flux PM motors. Interesting applications for the TFM may be as direct drives in electric vehicles, street cars, trains, ships and wind-mills, where an increased motor diameter allows a high machine utilization. **Prototypes** have been built for several of these applications:

- Three phase wheel-hub motors for street cars with about 45 kW power,
- 500 kW prototype gearless drive for the ICE 3 high speed train,
- Direct drives for city busses, where a diesel engine powers a TFM generator at constant speed and optimum efficiency with minimized exhaustion and environmental pollution. The generator feeds inverters, which supply a wheel hub TFM for propelling the bus.
- Other projects deal with smaller motors for electric driven air planes, electric car drives, and larger ones with wind mill generators.

Example 1.5.3-3:
Variable speed drive system for a City-Bus (*Voith*-Company, *Heidenheim, Germany*)
Transversal motor:
n_{max} = 2500/min, M_{max} = 1050 Nm, f_{max} = 1375Hz, steady state output power 57 kW, Outer diameter 420 mm, mass 115 kg, 300 V DC link voltage, high pole count 2p = 66, two phase system m = 2

Base speed range: Constant torque	0...750/min	725 Nm steady state 1050 Nm overload
Constant power range	750...2500/min	725...218 Nm steady state

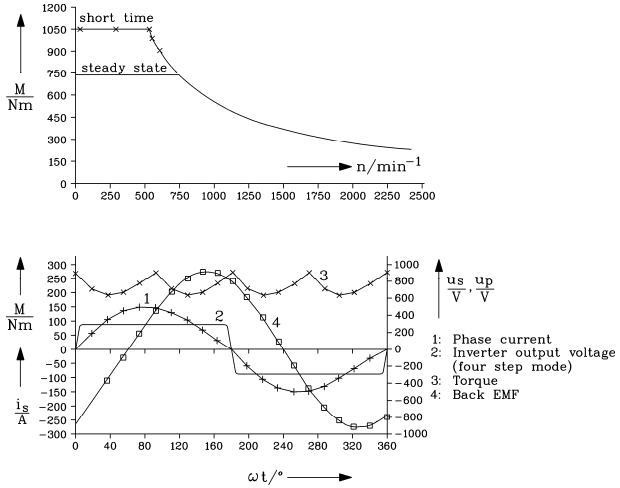

Fig.1.5.3-11: 57kW TFM calculated electric characteristic for a city bus drive system (*Voith, Germany*). Upper diagram: Steady state and overload torque vs. speed, lower diagram: Current, back EMF, torque and inverter output voltage at maximum speed. The torque ripple due to non-sinusoidal current visible with 4-times stator frequency 5.5 kHz; per unit torque ripple 17%

$$f_{s,max} = n \cdot p = (2500/60) \cdot 33 = 1375\,\text{Hz}$$

Rated power: $P = 2\pi mM = 2\pi \cdot (750/60) \cdot 725 = 57\,\text{kW}$

Back EMF amplitude at rated / maximum speed: $\hat{U}_p = 285\,\text{V}$ / $\hat{U}_{p,max} = 950\,\text{V}$

Stator inductance: L_s = 0.5 mH

Four step operation in flux weakening range: rectangular stator voltage with DC link voltage as amplitude has a *Fourier*-fundamental $\hat{U}_{s(1)} = (4/\pi) \cdot U_d = (4/\pi) \cdot 300 = 380\,\text{V}$(rms: 270 V)

Rated current (losses neglected): $I_s = I_{sqN} = \underline{141\text{ A}}$: $P_\delta = m \cdot U_p I_s = 2 \cdot (285/\sqrt{2}) \cdot 141 = 57\,\text{kW}$

Current at maximum speed: peak 168 A, r.m.s.: $168/\sqrt{2} = 119\,\text{A}$

q-current at max. speed: $I_{sq} = 141 \cdot (750/2500) = 42.3\ \text{A}$

d-current at max. speed: $I_{sd} = \sqrt{I_s^2 - I_{sq}^2} = \sqrt{119^2 - 42.3^2} = 111\,\text{A}$

Short circuit current (resistance neglected): $I_{s.k} = U_p/(\omega_s L_s) = \underline{158}\ \text{A}$

Fundamental voltage at rated speed and load: $U_{s(1)} = \sqrt{U_p^2 + (\omega_s L_s I_{sqN})^2} = 270\,\text{V}$

Power factor at rated load: $\cos\varphi_{(1)} = P_\delta/(mU_{s(1)}I_{sqN}) = 57000/(2 \cdot 270 \cdot 141) = \underline{0.75}$

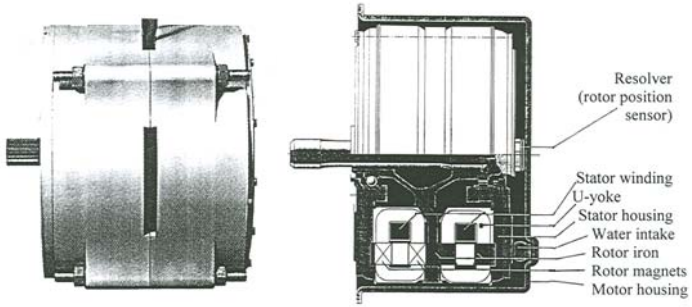

Fig.1.5.3-12: Transversal flux motor with indirect water cooling (left), cross section (right) for a city bus drive system (*Voith, Germany*)

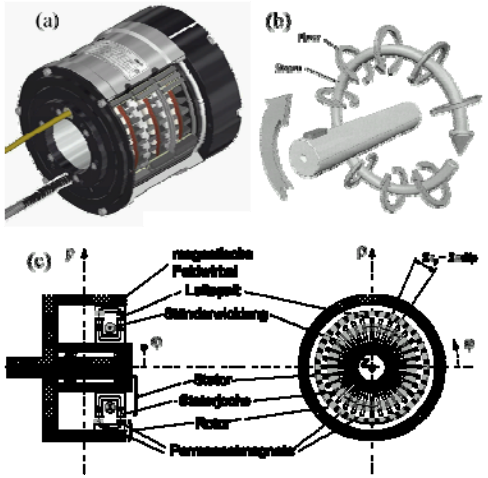

Fig.1.5.3-13: Three phase small transversal flux motor with outer rotor as servo drive: a) motor cut view, b) ring coil with flux linkage, c) cross section, d) axial cross section (*Landert, Switzerland*)

2. Reluctance motors

2.1 Switched reluctance drives

2.1.1 Basic function

Stator and rotor of switched reluctance machines consist of different number of teeth and slots, e.g.: stator: 8 teeth, rotor: 6 teeth (Fig.2.1.1-1). Stator teeth bear tooth coils, which are connected in *m* different phases. Usually three phases are used for medium power motors.

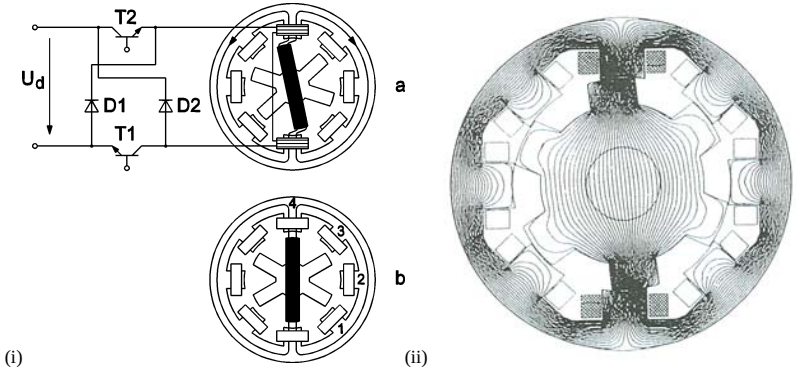

Fig. 2.1.1-1: Two pole, four phase switched reluctance machine (cross section): (i) Phase "4" is energized by a H-bridge inverter, fed from DC link U_d. The magnetic pull of the flux lines drags the next rotor teeth into aligned position with the energized stator teeth, thus creating a torque (*E. Hopper, Maccon, Germany*), (ii) numerical field calculation shows the flux pattern with energized phase "4" (Motor data: outer stator diameter: 320 mm, air gap: 1 mm, iron stack length: 320 mm, shaft diameter: 70 mm, coil turns per tooth: 10, current per turn: 10 A DC), (Source: *A. Omekanda*).

The rotor teeth contain no winding, so it is a very robust construction. Each phase winding is energized independently from the next. By using a rotor position sensor, that phase is chosen to be energized, which may pull the next rotor tooth into an aligned position (Fig.2.1.1-1; Phase "4"). In Fig.2.1.1-1 the flux lines show a tangential and a radial direction. Thus magnetic pull is both tangential to generate torque and radial, attracting the stator teeth versus the rotor teeth (radial pull). When the rotor is in an aligned position for phase "4", it is switched off, and phase "1" is energized to generate torque.

Thus it is sufficient to impress **unipolar** current (= block shaped current of one polarity) into the coils, as the magnetic pull is independent of the sign of the current flow. By switching one phase after the other in that mode, the rotor keeps turning and explains the name "switched" reluctance motors (**motor mode**). The flux lines try to pass through the iron teeth with their high permeability ($\mu_{Fe} >> \mu_0$) and avoid the slot region. We say: The iron teeth have a low magnetic resistance, and the slots a big one. This rotor structure of high and low magnetic resistance is called a **reluctance** structure. By switching the phases, the rotor moves stepwise, therefore this principle is also used for small reluctance stepper motors, but then without a position sensor to get a cheap drive. With position sensor the rotor movement is completely controllable. No pull-out at overload is possible, as long as the inverter is able to impress current. Speed can be measured by using the rotor position sensor as a speed sensor. Thus, a variable speed drive is easily realized **(speed control**). By measuring the current, its amplitude may be controlled by chopping the DC link voltage with PWM.

In Fig.2.1.1-1 the switching on/off sequence of the phases "1", "2", "3", "4", "1", ... gives clockwise rotation, whereas "4", "3", "2", "1", "4", ... gives **counter-clockwise rotation**.

If the rotor is driven mechanically and the stator coils are energized when the rotor moves from aligned to unaligned position, then the magnetic pull is **braking** the rotor. As the rotor movement causes a flux change in the stator coils, a voltage is induced, which along with the stator current gives generated electric power, which is fed to the inverter (**generator mode).**

The switched reluctance (SR) machine Fig.2.1.1-1 is a 2-pole, 4-phase machine, as each of the phases excites one N- and S-pole (notation: per pole pair: 8/6-stator/rotor teeth). In Fig.2.1.1-2 the cross section of a 4-pole, 3-phase machine is shown. Each of the 3 phases excites 2 N- and 2 S-poles (notation: per pole pair: 6/4-stator/rotor teeth).

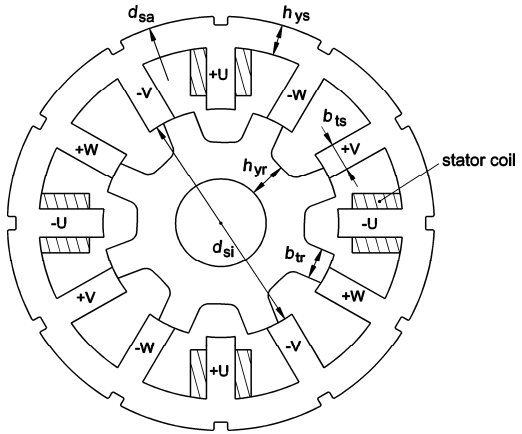

Fig.2.1.1-2: Cross section of a totally enclosed, air cooled 4-pole SR machine, 7.5 kW, 1500/min, motor current (rms): 12 A, stator outer/inner diameter: 210 / 120.9 mm, air gap: 0.45 mm

As teeth numbers of stator and rotor must be different, usually the number of rotor teeth is chosen smaller than the stator teeth number: $Q_r < Q_s$. Stator teeth number is

$$Q_s = 2p \cdot m \qquad (2.1.1\text{-}1)$$

and rotor teeth number is often chosen as

$$Q_r = Q_s - 2p \qquad (2.1.1\text{-}2)$$

Example 2.1.1-1:
Stator and rotor teeth numbers
a) Three phase machine: per pole pair ($2p = 2$): $m = 3$:
$Q_s = 2p \cdot m = 2 \cdot 3 = 6$, $Q_r = Q_s - 2p = 6 - 2 = 4$
So for higher number of pole pairs the 6/4 arrangement is repeated p-times at the motor circumference. In Fig.2.1.1-2 a four pole machine yields 12/8 as teeth numbers.
b) Four phase machine: per pole pair ($2p = 2$): $m = 4$:
$Q_s = 2p \cdot m = 2 \cdot 4 = 8$, $Q_r = Q_s - 2p = 8 - 2 = 6$ (Fig.2.1.1-1)

From Figs.2.1.1-1 and 2.1.1-2 we see, that the motors can start from any position, as there are always some rotor and stator teeth non-aligned and will exert a tangential magnetic pull, when the corresponding coils are energized. Note: For 2-phase machines self-starting is not possible from any rotor position (Fig.2.1.1-3a). By putting a step into the rotor tooth surface, the rotor will be asymmetric and then self-starting again is possible (Fig.2.1.1-3b).

Example 2.1.1-2:
Stator and rotor teeth numbers, two phase machine: per pole pair ($2p = 2$): $m = 2$:
$Q_s = 2p \cdot m = 2 \cdot 2 = 4,\ Q_r = Q_s - 2p = 4 - 2 = 2$
Self starting is only assured, if some special asymmetry is put into the machine e.g. **asymmetric rotor teeth**, additional permanent magnet in one stator tooth etc.

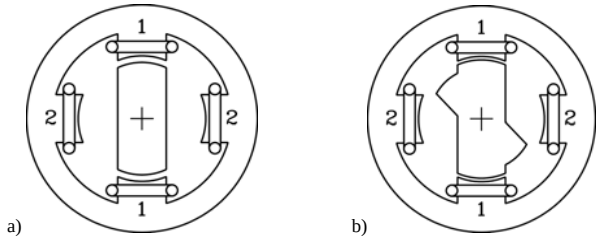

Fig.2.1.1-3: Cross section of a two phase, two pole SR Machine: a) a symmetric rotor cannot start from an aligned position (phase 1), when phase 2 is energized, a total tangential magnetic pull is zero, b) Phase 2 exerts a magnetic pull on the **asymmetric rotor**, which is therefore self-starting

2.1.2 Flux linkage per phase

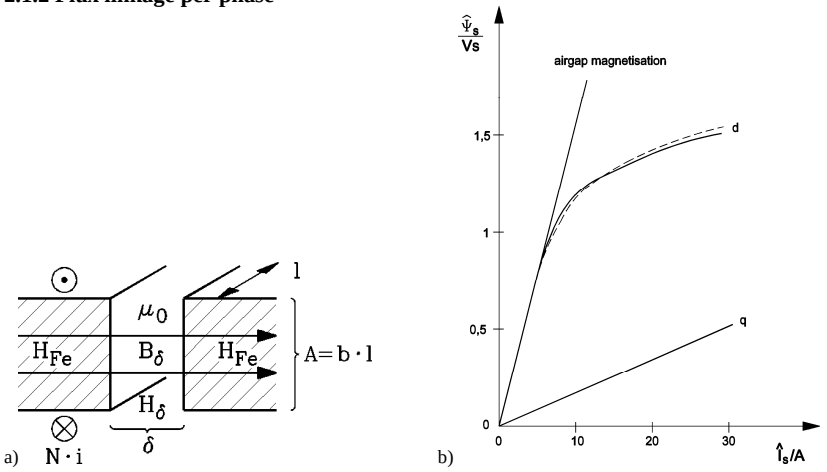

Fig.2.1.2-1: Flux linkage: a) Magnetic field in the air gap between stator and rotor iron, excited by a tooth coil (closed flux lines, not depicted here), b) Flux linkage of 7.5 kW 12/8-motor (Fig.2.1.1-2) in *d*- and *q*-axis (full line: measured at 50 Hz, sinusoidal voltage, dotted line: calculated)

The magnetic flux Φ in the air gap is the same as in iron, if the coil stray flux is neglected.

$$\Phi = A \cdot B_\delta = A \cdot B_{Fe} \ \Rightarrow\ B_\delta = B_{Fe} \qquad (2.1.2\text{-}1)$$

The flux linkage with the tooth coil ($N = N_c$: number of turns per coil) is given by

$$\Psi = N \cdot \Phi = N_c \cdot A \cdot B_\delta \qquad \text{with } A = b \cdot l \qquad (2.1.2\text{-}2)$$

with the permeability of iron and air according to μ_{Fe} and μ_0.

$$H_{Fe} = \frac{B_{Fe}}{\mu_{Fe}}, \quad H_\delta = \frac{B_\delta}{\mu_0} \qquad (2.1.2\text{-}3)$$

*Ampere´*s law yields the field strength H along the air gap and iron path:

$$\oint_C \vec{H} \bullet d\vec{s} = H_\delta \cdot \delta + H_{Fe} \cdot s_{Fe} = N_c \cdot i \qquad (2.1.2\text{-}4)$$

Thus we get

$$B_\delta = \frac{\mu_0 \cdot N_c \cdot i}{\delta + s_{Fe} \cdot (\mu_0 / \mu_{Fe})} \qquad (2.1.2\text{-}5)$$

And the **self inductance per coil** as:

$$L_c = \frac{\Psi}{i} = \frac{N_c \cdot A \cdot B_\delta}{i} = \frac{\mu_0 \cdot N_c^2 \cdot A}{\delta + s_{Fe} \cdot (\mu_0 / \mu_{Fe})} = \mu_0 \cdot N_c^2 \cdot \frac{b}{\delta \cdot k_s} \cdot l = \mu_0 \cdot N_c^2 \cdot \lambda \cdot l \qquad (2.1.2\text{-}6)$$

The self inductance is defined by the square of the number of turns and by the "geometric parameter":

$$\lambda = \frac{b}{\delta \cdot k_s} \qquad \text{with} \quad k_s = 1 + (s_{Fe} / \delta) \cdot (\mu_0 / \mu_{Fe}) \qquad (2.1.2\text{-}7)$$

Conclusions:
With an increasing air gap the inductance is decreasing. In case of ideally unsaturated iron ($\mu_{Fe} \to \infty$) the ***saturation factor*** *$k_s = 1$. With an increasing current i the flux increases and iron saturation occurs: μ_{Fe} decreases and k_s increases. Thus the coil inductance $L_c(i)$ decreases with an increasing current.*

The inductance per phase includes all coil inductances along with the stray flux in the slots and the winding overhangs. If all coils per phase are connected in series, the total number of turns is $N = 2p \cdot N_c$. The inductance $L = 2p \cdot L_c$ is biggest in aligned position (***d*-position**), as the flux lines then only have to cross the small air gap δ. In the unaligned position a rotor slot opposes a stator tooth, thus the air gap increases and is equal to the slot depth (***q*-position**). In that case the inductance is smallest. Thus the inductance varies with moving rotor between L_d and L_q.

Conclusions:
The inductance depends on current and rotor position $L(i, \gamma)$.

Fig. 2.1.2-1b shows the flux linkage depending on the coil current for different rotor positions. At low current no saturation occurs and assuming $\mu_{Fe} >> \mu_0$, the factor $k_s = 1$. Then the characteristics are linear rising. With beginning saturation $k_s > 1$ the curves are bent ("saturation region"). In *d*-position the air gap is $\delta_d = \delta$, and in *q*-position the air gap is equal to rotor tooth length $\delta_q = \delta + l_{dr}$. Therefore the *q*-axis flux linkage is much smaller than the flux of *d*-axis. *In order to get a big torque the difference between d-axis and q-axis flux linkage must be very big, as shown in Section 2.1.4.*

$$\Psi = N \cdot A \cdot B_\delta = \mu_0 \cdot \frac{N^2}{2p} \cdot i \cdot \frac{b}{\delta \cdot k_s} \cdot l \qquad (2.1.2\text{-}8)$$

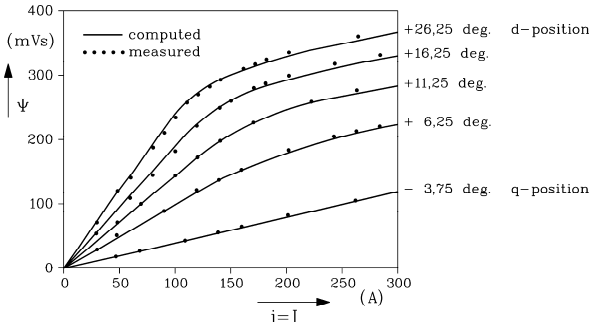

Fig.2.1.2-2: Flux linkage for different rotor positions, calculated with Finite Element numerical field calculation for motor of Fig.2.1.1-1b, compared with measurement

2.1.3 Voltage and torque equation

Each phase is fed independently from an H-bridge, which is considered here as a voltage source *u*. Each phase has a resistance *R* and an inductance *L*. With a big current the excited flux is so big that the iron in teeth and yokes is saturating. Rotor movement is described by the **rotor position angle** γ, leading to the rotor angular speed

$$\Omega_m = d\gamma / dt \quad . \qquad (2.1.3\text{-}1)$$

The flux linkage per phase is given by the inductance

$$\psi(\gamma, i) = L(\gamma, i) \cdot i \qquad (2.1.3\text{-}2)$$

and without saturation: $L(\gamma)$, leading to

$$\frac{d\psi}{dt} = L \cdot \frac{di}{dt} + i \cdot \frac{dL}{d\gamma} \cdot \frac{d\gamma}{dt} \quad , \qquad (2.1.3\text{-}3)$$

and the **voltage equation** is

$$u = R \cdot i + \frac{d\psi}{dt} = R \cdot i + L \cdot \frac{di}{dt} + i \cdot \frac{dL}{d\gamma} \cdot \Omega_m \qquad (2.1.3\text{-}4)$$

with the **"rotational induced voltage"** (where γ is considered in mech. degrees)

$$u_i = i \cdot \frac{dL}{d\gamma} \cdot \Omega_m \quad , \qquad (2.1.3\text{-}5)$$

which may be regarded as **back EMF**. The electric input power p_e per phase has to balance the change of the stored magnetic energy W_{mag}, the resistive losses and the internal p_δ, which is converted into mechanical output power. Here we neglect the stator iron losses.

$$p_e = p_{Cu} + \frac{dW_{mag}}{dt} + p_\delta \quad . \qquad (2.1.3\text{-}6)$$

The magnetic energy per phase and its derivative are

$$W_{mag} = \frac{L(\gamma, i) i^2}{2} \quad \Rightarrow \quad \frac{dW_{mag}}{dt} = i \cdot L \cdot \frac{di}{dt} + \frac{1}{2} \cdot i^2 \cdot \frac{dL}{d\gamma} \cdot \Omega_m \qquad (2.1.3\text{-}7)$$

By multiplying the voltage equation with the current these different parts of the power balance are determined.

$$p_e = u \cdot i = R \cdot i^2 + i \cdot L \cdot \frac{di}{dt} + i^2 \cdot \frac{dL}{d\gamma} \cdot \Omega_m \qquad (2.1.3\text{-}8)$$

Comparing (2.1.3-6), (2.1.3-7), (2.1.3-8) we get the **internal power**

$$p_\delta = \frac{1}{2} i^2 \cdot \frac{dL}{d\gamma} \cdot \Omega_m \qquad (2.1.3\text{-}9)$$

and finally the **electromagnetic torque** without considering iron saturation

$$\boxed{M_e = p_\delta / \Omega_m = \frac{1}{2} i^2 \cdot \frac{dL}{d\gamma}} \quad . \qquad (2.1.3\text{-}10)$$

2.1.4 SR machine operation at ideal conditions

In Fig.2.1.4-1 the change of the inductance is shown, which may be considered almost linear as the overlapping region of stator and rotor tooth is decreasing linear, when the rotor is moving along the angle α (here considered in mechanical degrees: 1 rotor revolution = 2π). Stator and rotor tooth width b_{ds} and b_{dr} correspond with the circumference angles α_s and α_r. For $Q_s > Q_r$ a stator tooth is usually smaller than a rotor tooth, hence there is an angle $\tilde{\alpha} = |\alpha_s - \alpha_r|$, where the complete stator tooth width is facing either a rotor tooth or a rotor slot opening. In that region the stator inductance will not change. By impressing ideal constant current $i = \hat{I}$ into the considered phase during the movement of the rotor from an unaligned to an aligned position only for the section α, motor torque is produced.

$$M_e = \frac{1}{2} i^2 \cdot \frac{dL}{d\gamma} = \frac{1}{2} \hat{I}^2 \cdot \frac{L_d - L_q}{\alpha} \qquad (2.1.4\text{-}1)$$

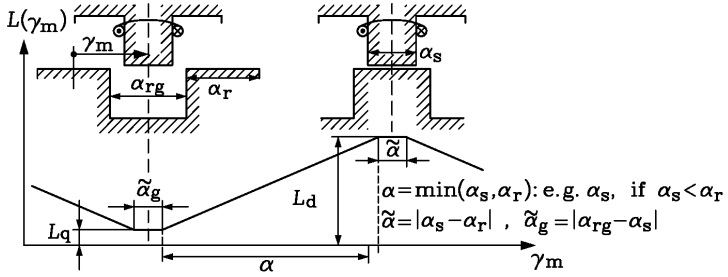

Fig.2.1.4-1: Change of stator inductance during rotor movement

Conclusions:
In order to get a big torque the difference between d-axis and q-axis flux linkage (inductance) must be very big, ***which holds true for all kinds of reluctance machines.*** *The sign of the current polarity does not influence the sign of the torque, so* ***unidirectional*** *current feeding is sufficient. This corresponds with the fact that the direction of magnetic pull does not depend on the polarity of flux density. If no saturation occurs, torque rises with the* ***square*** *of current.*

In order to ensure a big *d*-axis and a small *q*-axis inductance to get maximum torque, the air gap δ must be vary small and the rotor slot depth rather big. Further, the stator tooth width α_s must be smaller than the rotor slot opening $2\pi/Q_r - \alpha_r$, so that the stator tooth in the *q*-position is completely facing a rotor slot to get a minimum inductance.

$$\alpha_s \le \frac{2\pi}{Q_r} - \alpha_r \quad \text{mech. degrees} \qquad (2.1.4\text{-}2)$$

If unidirectional current is energizing the coil, when the rotor moves from aligned to unaligned position, we get negative torque **(generator mode).**

$$M_e = \frac{1}{2} i^2 \cdot \frac{dL}{d\gamma} = \frac{1}{2}\hat{I}^2 \cdot \frac{L_q - L_d}{\alpha} < 0 \qquad (2.1.4\text{-}3)$$

In motor mode the induced voltage is positive (Fig.2.1.4-2b), and in generator mode it is negative. Thus with positive current we get positive internal power in motor mode, fed from the grid to the mechanical system, and negative internal power flow in generator mode, being fed by the mechanical system into the grid.

$$\hat{U}_i = \hat{I} \cdot \frac{L_d - L_q}{\alpha} \cdot \Omega_m > 0, \quad P_\delta = \hat{U}_i \hat{I}/2 > 0 \qquad \text{motor} \qquad (2.1.4\text{-}4)$$

$$\hat{U}_i = \hat{I} \cdot \frac{L_q - L_d}{\alpha} \cdot \Omega_m < 0, \quad P_\delta = \hat{U}_i \hat{I}/2 < 0 \qquad \text{generator} \qquad (2.1.4\text{-}5)$$

With a theoretically linear change of inductance it does not make any sense to impress current longer than angle α, as in the region $\tilde{\alpha} = |\alpha_s - \alpha_r|$ the change $dL/d\gamma = 0$. So no torque is produced, but the current will generate resistive losses in the coils. In Fig.2.1.4-3 the complete pattern of changing inductance of all three phases a, b, c of a 6/4-machine is depicted. Each phase is energized with a unidirectional current pulse during the angle α. This angle is

counted in "electrical" degrees, so that $\alpha / Q_r = \Delta\gamma$ yields the mechanical angle. One rotor slot pitch corresponds with 360° electrical degrees. As the tooth width is chosen equal to the slot width, we get under these ideal conditions α = 120° el., meaning that the duration of the current impulse should be 120° el. With three phases, the three H-bridges generate current pulses with 120°el. duration and pausing for 240°el. in between. By that a theoretically smooth torque without any ripple is generated. No time overlap between different phase current occurs. From Fig.2.1.4-3 it can be seen, that the frequency of the stator current pulse is

$$f_s = n \cdot Q_r \qquad (2.1.4\text{-}6)$$

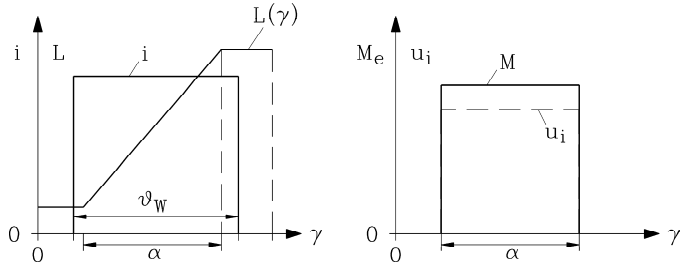

Fig.2.1.4-2: a) Unidirectional current impression into one stator phase. Duration of current impulse ϑ_W may be chosen arbitrarily by the H-bridge. With theoretically linear change of inductance ϑ_W should be equal to α. b) With constant current torque and induced voltage are also constant, if the inductance changes linear.

Conclusions:
As long as there is no current overlap between adjacent phases (like in Fig.2.1.4-3), the torque per phase is also the value of the constant torque of the SR-machine. If the "current angle" is smaller $\vartheta_W < \alpha$, then the torque shows gaps between the impulses of each phase, thus creating a torque ripple. In that case the average torque is reduced by ϑ_W/α.

2.1.5 Calculating torque in saturated SR machines

As torque rises with the square of current, high motor utilization means high current and thus saturation of iron. In order to utilize directly the saturated flux linkage characteristics $\psi(i)$ for calculating torque, the magnetic **co-energy** *W** is used (Fig.2.1.5-1). As magnetic energy is

$$W_{mag} = \int_V \int_0^B (H \cdot dB) \cdot dV = \int_0^\psi i \cdot d\psi \quad , \qquad (2.1.5\text{-}1)$$

we get in the unsaturated (linear) case $\psi = L \cdot i$

$$W_{mag} = \int_0^\psi i \cdot d\psi = L \int_0^i i \cdot di = L\frac{i^2}{2} \quad , \qquad (2.1.5\text{-}2)$$

which corresponds to the triangular area in Fig.2.1.5-1a of linear $\psi(i)$-curve. In a non-linear case W_{mag} corresponds to the area left of the non-linear $\psi(i)$-curve in Fig.2.1.5-1b.

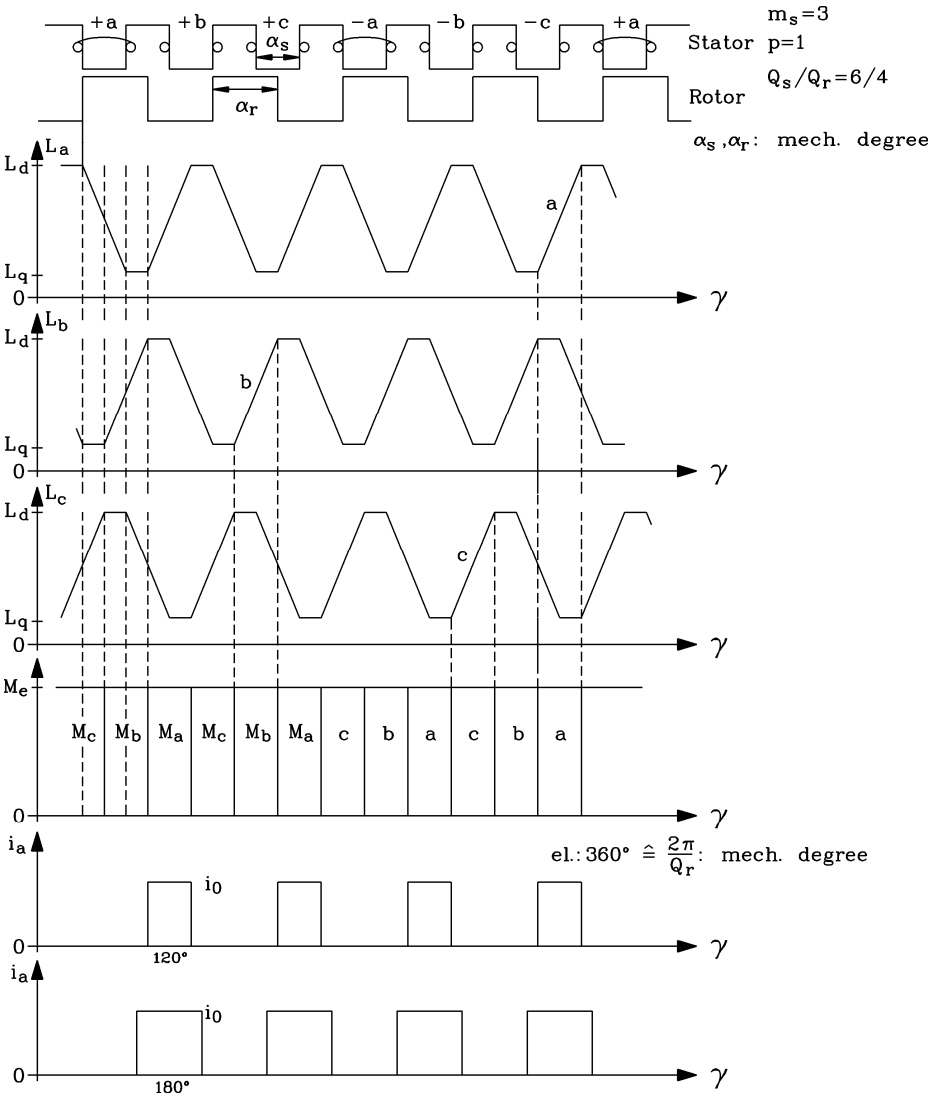

Fig.2.1.4-3: Three phase 6/4-SR machine: Unidirectional current impression is done for ϑ_w = α = 120° el. for each phase, yielding a theoretically smooth torque. A current impression of 180° at this ideal linear change of inductance will only increase resistive losses, but not torque.

Magnetic co-energy is defined as

$$W^* = \psi \cdot i - W_{mag} \qquad (2.1.5\text{-}3)$$

and corresponds to the area to the right of the $\psi(i)$-curve in Fig. 2.1.5-1.

When the rotor is turning, the magnetic flux linkage changes from one characteristic to the next (see Fig.2.1.2-2). Assuming linear characteristics in Fig.2.1.5-2 and operation with constant current i_0, a movement of the rotor towards aligned position means a changing from a lower to an upper $\psi(i)$-curve. We assume a (very small) rotor step $d\alpha$, then the change of magnetic energy and co-energy by moving from characteristic 1 to characteristic 2 yields an increase of magnetic energy and of co-energy, as the total flux linkage is now larger by the value $d\psi$. By comparing the areas in Fig.2.1.5-2 (left), we note

$$W_{mag,2} = W_{mag,1} + dW_{mag} = W_{mag,1} + i_0 \cdot d\psi - dW^* \quad . \qquad (2.1.5\text{-}4)$$

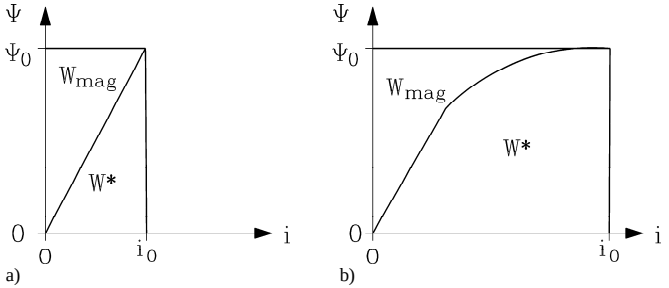

Fig.2.1.5-1: Magnetic energy W_{mag} and co-energy W^* for a) linear (unsaturated) and b) non-linear (saturated) flux linkage

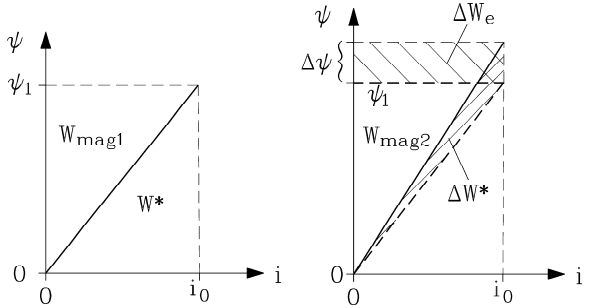

Fig.2.1.5-2: A very small rotor movement leads to a small change from flux linkage 1 (left) to flux linkage 2 (right)

From the voltage equation we get the energy balance during the very small step $d\gamma$, corresponding to the time step dt :

$$u = R \cdot i_0 + \frac{d\psi}{dt} \quad \Rightarrow \quad dW_e = u \cdot i_0 \cdot dt = R \cdot i_o^2 \cdot dt + i_0 \cdot d\psi = R \cdot i_0^2 \cdot dt + dW_{mag} + dA_m \quad (2.1.5\text{-}5)$$

A very small time step leads to an increase of loss and magnetic energy. The delivered torque produces mechanical work :

$$dA_m = M_e \cdot d\gamma = M_e \cdot \Omega_m \cdot dt \qquad (2.1.5\text{-}6)$$

By comparing (2.1.5-4) and (2.1.5-5), we see

$$i_0 \cdot d\psi = dW_{mag} + dW^* = dW_{mag} + dA_m \quad \Rightarrow \quad dW^* = dA_m \quad , \qquad (2.1.5\text{-}7)$$

thus getting the following torque equation

$$\boxed{M_e(\gamma, i) = \frac{dW^*}{d\gamma}} \qquad (2.1.5\text{-}8)$$

When changing from *q*- to *d*-position, the change in co-energy ΔW^* is the area between the $\psi_d(i)$-curve and the $\psi_q(i)$-curve. For maximizing the torque of a SR motor, this area has to be as big as possible, which demands a very high motor current. If the motor is unsaturated, the magnetic energy and co-energy are equal. This means that increase of co-energy gives the same increase to magnetic energy. As with each switch-on and switch-off of one phase the complete magnetic energy has to be put into the system and afterwards taken out, the feeding inverter must be rated for this additional amount of energy flow either by over-sizing voltage or current rating. In saturated machines, with increasing current the co-energy rises much stronger than magnetic energy (Fig.2.1.5-1b), which is very economical for inverter rating. **Therefore SR machines should be operated as highly saturated machines, which is quite contrary to many other electric machines.**

Conclusions:
Torque calculation can be done from the map of $\psi(i)$-curves, evaluating the change of co-energy with change of rotor angle γ for a given current i. SR machines shall be operated highly saturated in order to limit inverter rating by limiting switched magnetic energy.

In low current operation (no saturation) co-energy difference between *d*- and *q*-position equals a triangle area. Triangle surface is proportional to i^2. Thus torque rises with square of current. At high saturation increase of co-energy difference between *d*- and *q*-position increases linear with rising current. Therefore torque of saturated SR machines rises linear with current (Fig.2.1.5-3).

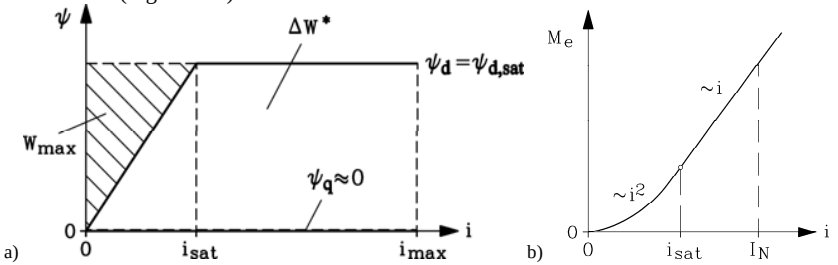

Fig.2.1.5-3: Torque-current characteristic: a) Torque is proportional to change of co-energy between *d*- and *q*-position ΔW^*, which in unsaturated case $i < i_{sat}$ is proportional i^2, in saturated case $i > i_{sat}$ tends to be proportional nearly i , b) Torque-current characteristic with unsaturated and saturated part (I_N: rated current)

2.1.6 SR machine operation at real conditions

a) Real change of inductance between unaligned and aligned position:
In Fig.2.1.6-1a the change of inductance - calculated with Finite Elements - is shown for the 8/6-motor of Fig.2.1.1-1b, being compared with the linear approximation of Section 2.1.2 and

with measurement. Thus the angle of real change of inductance is larger than the angle α. The derivative $dL/d\gamma$ is not constant, but looks like a hump (Fig.2.1.6-1b). Thus even with constant current the torque $M_e(\gamma) = (i^2/2) \cdot dL/d\gamma$ is not any longer constant, but shows a considerable **torque ripple.** In the same way induced voltage is also now hump-like shaped: $u_i(\gamma) = i \cdot dL/d\gamma \cdot \Omega_m$.

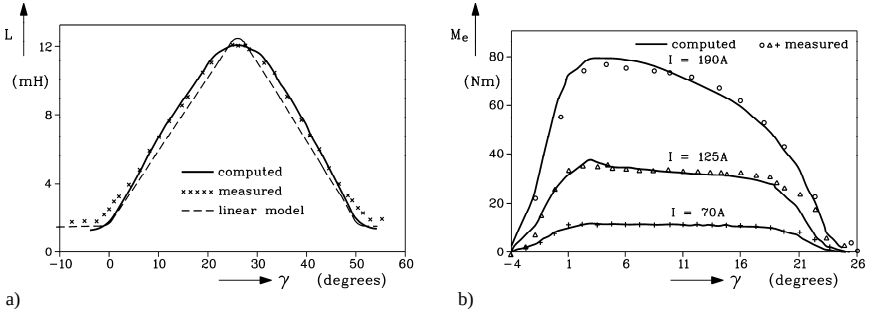

Fig.2.1.6-1: Numerical calculation of inductance and torque for the 8/6-motor of Fig.2.1.1-1b, compared with measurement. Although current is constant, torque is not, showing a considerable ripple.

This torque ripple may be reduced a little bit, if the current angle is increased: $\vartheta_W > \alpha$. Maximum possible angle is ϑ_W =180°. Bigger angle would already generate braking torque. In Fig. 2.1.6-2a the torque ripple is shown for current angle 120°. By increasing angle to 180° (Fig. 2.1.6-2b), the torque contributions of adjacent phases overlap, resulting in a smoother total torque and a slight increase in average torque on the expense of higher resistive losses.

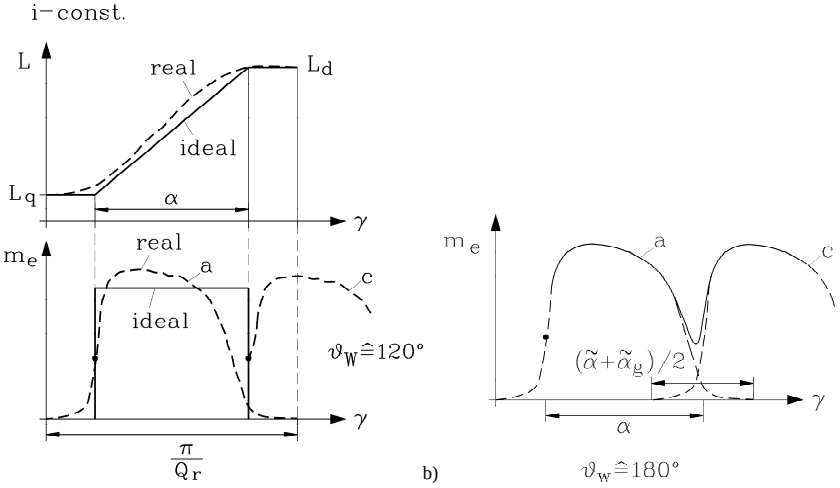

Fig.2.1.6-2: Torque ripple in SR machines: a) Due to non-linear change of inductance torque per tooth and phase shows a hump-like shape, thus reducing average torque and generating torque ripple b) If current angle is increased from 120° to 180°, torque ripple is reduced a little bit and average torque is raised.

Conclusions:
Real SR machines show considerable torque ripple already at low speed, when operated with constant current. Frequency of torque ripple is given by stator frequency $f_s = n \cdot Q_r$ per phase and number of phases m, thus $f_{puls} = n \cdot Q_r \cdot m$.

Average resistive losses per period $T = 1/f_s$ are calculated with

$$P_{Cu} = m \cdot R \cdot \frac{1}{T}\int_0^T i^2 \cdot dt = m \cdot R \cdot I^2 \quad , \qquad (2.1.6\text{-}1)$$

where r.m.s-value of unipolar current is depending on current angle, which for 120° gives a ratio of time of current flow vs. period of x_{120} = 120°/360° = 1/3 and for 180° the value x_{180} = 1/2:

$$I = \sqrt{\frac{1}{T}\int_0^T i^2 \cdot dt} = \sqrt{\frac{1}{T}\int_0^{xT} \hat{I}^2 \cdot dt} = \sqrt{\frac{1}{T} \cdot \hat{I}^2 \cdot xT} = \sqrt{x} \cdot \hat{I} \qquad (2.1.6\text{-}2)$$

Conclusions:
For 180° current angle the resistive losses are 50% higher than with 120° current angle (x_{180}/x_{120} = 3/2 = 1.5).

b) Real shape of unidirectional current:
In order to get block shaped unidirectional current, the H-bridge per phase is chopping the DC link voltage, and tries to keep by **hysteresis current control** the current amplitude within a certain small hysteresis band. The H-bridge of Fig.2.1.1-1a is chopping the DC link voltage U_d e.g. by switching upper transistor T2 on and off. Current flow continues – driven by stored magnetic energy W_{mag} - with T2 "off" by flowing through free-wheeling diode D1. Turning off current is accomplished by switching off T1 and T2. The current continues to flow via diodes D1 and D2 against the direction of DC link voltage and is therefore reduced rather quick. Stored magnetic energy is fed back to DC link. From voltage equation

$$u = R \cdot i + L \cdot \frac{di}{dt} + i \cdot \frac{dL}{d\gamma} \cdot \Omega_m = U_d \quad or \quad -U_d \quad or \quad 0 \qquad (2.1.6\text{-}3)$$

we see **at low speed** Ω_m, that induced voltage is much smaller than U_d, thus being neglected. If we also neglect resistance, current rises and decreases linear according to $u = L \cdot di/dt$ (Fig.2.1.6-3, left). Thus the ideal block shaped unipolar current is more or less well reached by the chopping operation. **At high speed** the time duration $T_W \sim 1/n$ for current pulse is very short according to high current frequency. The time constant of phase winding $T_e = L/R$ is now even larger than T_W, so current rise is much longer than the wished time duration of current pulse. No longer chopping mode is possible. It is only possible to switch DC link voltage on and off. Therefore current pulse shape is no longer of block shape, but determined by the difference of constant DC link voltage and hump-like shaped induced voltage $u_i(\gamma)$ (Fig.2.1.6-3, right). With this current shape $i(\gamma)$ the **torque ripple increases drastically**: $M_e(\gamma) = (i^2(\gamma)/2) \cdot dL/d\gamma$. In Fig.2.1.6-4 unidirectional current for very low (left) and very high (right) speed is shown. Please note, that rise and fall of current at low speed is determined mainly by inductance, which increases with time towards aligned

position. Thus current rise and fall of current ripple in hysteresis band is slowed changes is slowed down with inductance increase.

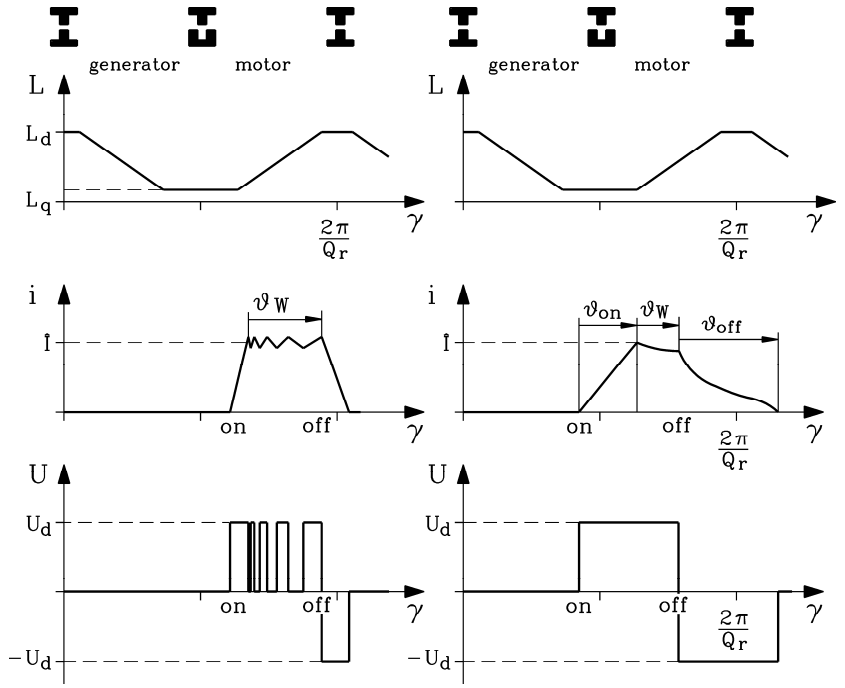

Fig.2.1.6-3: Real current shape: Left: At low speed hysteresis control of current allows generating rather block shaped unidirectional current. Right: At high speed time is too short to chop DC link voltage, so only "voltage on" and "off" is possible, leading to distorted current pulse, which generates increased torque ripple

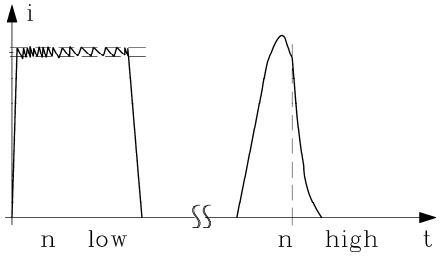

Fig.2.1.6-4: Real current shape: Left: At very low speed, Right: At very high speed time (with time scale extremely enlarged, compared to left figure)

2.1.7 SR Drive operation – torque-speed characteristic

Maximum possible torque vs. speed is called torque-speed characteristic, which is consisting of mainly two sections: **current limit** and **voltage limit**.

a) Voltage limit:
At high speed the induced voltage (back EMF), which is increasing with increasing speed, limits current flow, as stator voltage cannot surpass maximum value DC link voltage U_d. The induced voltage and the resistive and inductive voltage drop equal the DC link voltage ("**voltage limit**"). Neglecting resistance $R = 0$ and assuming constant back EMF $u_i(\gamma) = \hat{U}_i$ and constant current $i(\gamma) = \hat{I}$, the condition for voltage limit is:

$$u = U_d = R \cdot \hat{I} + L \cdot \frac{d\hat{I}}{dt} + \hat{U}_i \quad \Rightarrow \quad U_d = \hat{U}_i = \hat{I} \cdot \frac{dL}{d\gamma} \cdot \Omega_m \quad . \qquad (2.1.7\text{-}1)$$

Current flow at voltage limit is

$$\hat{I} = \frac{U_d}{dL_s/d\gamma} \cdot \frac{1}{\Omega_m} \cong \frac{U_d}{(L_d - L_q)/\alpha} \cdot \frac{1}{\Omega_m} \quad . \qquad (2.1.7\text{-}2)$$

Possible current flow rises with inverse of decreasing speed, until it reaches the inverter current limit $\hat{I}_{\max}$ at speed

$$n_g = \frac{1}{2\pi} \cdot \frac{U_d}{\hat{I}_{\max} \cdot \left((L_d - L_q)/\alpha\right)} \quad . \qquad (2.1.7\text{-}3)$$

Thus torque-speed characteristic at voltage limit is therefore

$$\boxed{M_e \cong \frac{1}{2(L_d - L_q)/\alpha} \cdot \left(\frac{U_d}{\Omega_m}\right)^2} \quad , \; n \geq n_g \qquad (2.1.7\text{-}4)$$

Conclusions:
At the voltage limit the maximum possible torque of SR drives decreases with the square of rising speed.

b) Current limit:

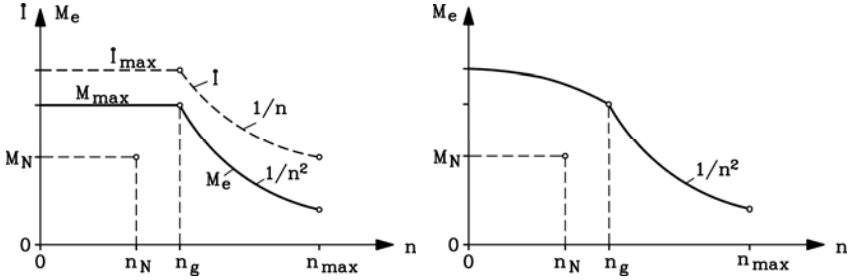

Fig.2.1.7-1: Torque-speed characteristic of SR machine, a) for ideal block-shaped current, b) considering real current shape, which deviates from block shape with rising speed

Inverter current limit is also thermal limit of inverter, as thermal time constant of semi-conductor devices is below 1 s. Motor thermal current limit (**"rated current"**) usually is 50% of this inverter current limit. So short time overload capability of machine is 100%, as its thermal time constant is - rising with motor size and depending on cooling system – about several minutes to typically half an hour. Maximum torque $M_{\max}(I_{\max})$ of drive system is available in the **base speed region** $0 \leq n \leq n_g$ (Fig.2.1.7-1a). In real SR machines with rising speed the current shape cannot be kept as ideal block. Therefore torque ripple increases with rising speed and average torque decreases. Hence real speed torque characteristics, mapping average torque versus speed, have maximum torque at low speed (Fig.2.1.7-1b).

2.1.8 Inverter rating

a) Static rating:
In each phase per switching instant the total electric energy must be put into the motor phase, not only the mechanic energy and loss energy, but also total magnetic energy. Each phase is only energized during "current angle" ϑ_W. Neglecting losses, we consider total energy per switching as

$$W_{tot} = W_{mag} + A_m = W_{mag} + \Delta W^* \qquad (2.1.8\text{-}1)$$

In Fig.2.1.5-3 a simplified flux linkage characteristic with $L_q << L_d$, assuming $L_q = 0$, and with constant saturated flux linkage $\psi_d = \psi_{d,sat}$, allows estimation of ratio

$$W_{tot}/\Delta W^* = \frac{W_{tot}}{W_{tot} - W_{mag}} = \frac{i_{\max} \cdot \psi_{d,sat}}{i_{\max} \cdot \psi_{d,sat} - (i_{sat} \cdot \psi_{d,sat}/2)} = \frac{1}{1 - (i_{sat}/(2i_{\max}))} . \qquad (2.1.8\text{-}2)$$

Example 2.1.8-1:
$i_{\max}/i_{sat} = 2 : \; W_{tot}/\Delta W^* = 4/3 = 1.33$

For static energy demand the inverter must be capable of 133% motor power rating to switch also the total amount of magnetic energy.

With three phase motors, the three H-bridge inverters need a total amount of six IGBTs and six free-wheeling diodes like three phase inverters for rotating field AC machines like induction or synchronous machines.

b) Dynamic rating:
The electric winding time constant

$$T_e = \frac{L}{R} \sim \frac{W_{mag}}{P_{Cu}} \qquad (2.1.8\text{-}3)$$

rules the current rise in simple coils. In SR machines also the back EMF must be considered, which rises with rising speed. Neglecting resistance at high speed, voltage equations yields

$$u = L \cdot \frac{di}{dt} + i \cdot \frac{dL}{d\gamma} \cdot \Omega_m = U_d \quad . \qquad (2.1.8\text{-}4)$$

The solution of this 1st order differential linear equation is

$$i = \frac{U_d}{\Omega_m \cdot dL/d\gamma} \cdot \left(1 - e^{-t/T_U}\right) \quad , \quad T_U = \frac{L}{\Omega_m \cdot dL/d\gamma} \quad , \qquad (2.1.8\text{-}5)$$

which shows that for reaching sufficient current within time T_U, a high DC link voltage is necessary. So dynamic condition demands considerable voltage and thus big inverter rating for getting rather block shaped current also at high speed.

Conclusions:
If inverter rating has to be limited because of costs, there is no sufficient surplus DC link voltage to impress block shaped unidirectional current also at high speed. Therefore current deviates from ideal block shape at high speed, causing increased torque ripple and decreased average torque, thus reducing motor power output.

c) Inverter current control:
(i) At low speed:
Block current by hysteresis control with constant current angle ϑ_W, usually 180° or 120° (increased torque ripple, decreased resistive losses). Current rise and fall time t_r and t_f very short in relation to current impulse duration T_W.
(ii) Increased speed:
Current impulse duration T_W decreases with increased speed, t_r and t_f are now significant parts of current flow duration, so current impulse gets trapezoidal shape, and average torque decreases.
(iii) At high speed:
The current impulse duration T_W is too short for chopping with hysteresis control. So only voltage "switch on – switch off" mode is possible. Current angle, determined by switch on and switch-off angle, adjusted to speed, so that average torque decreases with 1/*n* **(constant power operation).**
(iv) Voltage limit:
No adjusting of current angle possible, because of too short time T_W; average torque decreases with $1/n^2$.

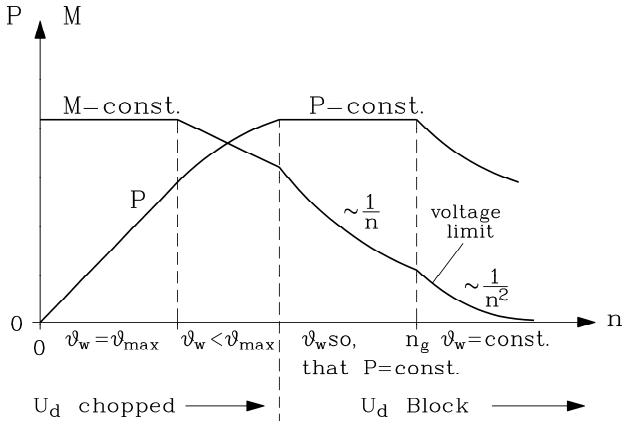

Fig.2.1.8-1: Maximum torque & power, depending on speed with inverter control according to sections (i) ... (iv), see text.

2.1.9 Motor technology and performance

a) Advantages:
- simple, low cost motor construction
- no distributed AC winding; simple tooth-wound coils; no overlap in winding overhangs
- smaller number of slots than in comparable AC machines, simple manufacturing
- robust rotor without any winding or magnets, thus well suited for high speed
- low rotor inertia
- Independent feeding of phases: if one phase fails, motor with $m \geq 3$ is still capable of self starting and running at reduced torque without overloading the "healthy" windings
- Compared with inverter fed induction machines, SR machine has increased efficiency due to lower rotor losses (Example 2.1.9-1).

b) Disadvantages:
- High torque ripple with increased speed. At very low speed current profiling by inverter current control is possible to cancel torque ripple, but not at elevated speed due to limited inverter rating.
- Increased number of phases will reduce torque ripple, but number of semiconductor switches rises (expensive !)
- No standard three phase AC inverter applicable; special H-bridge inverter is necessary.
- Danger of exciting torsion resonance vibrations by torque ripple at variable speed operation
- **Magnetically excited acoustic noise:** Pulsating radial magnetic pull with frequency $f_{puls} = n \cdot Q_r \cdot m$ causes radial vibrations of stator yoke and housing, which compresses / decompresses air with same frequency, causing acoustic sound. Acoustic sound is especially big, if frequency f_{puls} coincides with eigen-frequency of stator yoke and housing (resonance). As flux per pole is only flux per teeth, thus rather small, stator yoke is very thin and "rings like a bell" (Fig.2.1.9-1).
- Strong decrease of maximum torque with rising speed due to increased torque ripple.
- Increased inverter rating due to switching on/off of magnetic energy at each phase switching.
- Usually rotor position sensor needed for optimum inverter-motor operation

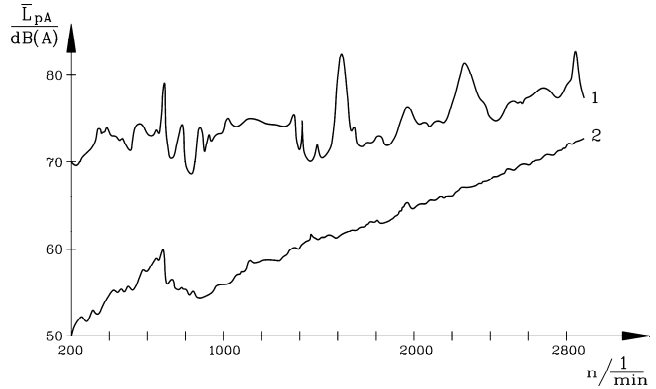

Fig.2.1.9-1: Measured sound pressure level of 7.5 kW 12/8 SR machine (Fig.2.1.1-2) in anechoic chamber (1: rated current, 2: no-load current). At no-load torque and current is very small, so air gap flux density $B_\delta \sim i$ and exciting radial magnetic pull $f_r \sim B_\delta^2 \sim i^2$ is small, leading to low magnetic noise. At rated load noise is rather big, showing sharp maximum when exciting frequency coincides with stator resonance frequencies.

c) Electromagnetic motor utilization:
Torque per motor active volume may be compared with standard induction machines. For the same cooling system about 80% of utilization of induction machine is reached.
In spite of small flux per pole (tooth flux = pole flux) this can be achieved by
- high slot fill factor due to tooth-wound coils,
- short winding overhangs due to tooth-wound coils, thus decreasing resistive losses
- reduced iron losses in rotor especially at low speed.

Example 2.1.9-1:
Comparison of inverter fed induction and SR motor (see Fig.2.1.1-2) for the same rated power and speed at identical cooling (totally enclosed, fan mounted on shaft):
Data: 7.5 kW, shaft height 132 mm, base speed 1500/min, top speed 3000/min, Thermal Class F, three-phase four-pole machines

Motor data	*Switched Reluctance Machine*	*Induction Machine*	SRD/IM Ratio
Outer/inner stator diameter d_{sa}/d_{si} (mm)	**210** / 120.9	**200** / 122.6	**+5%** /-1%
Outer rotor diameter/ air gap d_{ra}/δ (mm)	120 / 0.45	122 / 0.3	-1%/+50%
Tooth number: Stator/ Rotor Q_s/Q_r	12 / 8 unskewed	48 / 36 skewed	
Yoke height stator/rotor h_{ys}/h_{yr} (mm)	14 / 17.5	21.5 / 16	
Tooth width stator/ rotor b_{ts}/b_{tr} (mm)	16 / 16.7	4.3 / 6	
Stack length l_{Fe} (mm)	193	135	+42%
Stack length + end winding overhangs (mm)	193 + 2x18 = **229**	135 + 2x47 = **229**	**0%**
Stator resistance per phase (20 °C) R_s (Ohm)	0.85	0.512 Y	+64%
Armature winding / slot space factor	One coil per stator tooth / 0.44	Single-layer, full-pitched / 0.38	--/+16%
Number of turns per phase N_s	244	112	+118%
Stator frequency f_s for n = 0..3000/min	0 ... 400 Hz	0 ... 100 Hz	+300%
Cylindrical rotor volume $d_{ra}^2 \pi l_{Fe}/4$	2.18 dm^3	1.58 dm^3	+ 38%
Rotor moment of inertia (measured)	0.0195 kgm^2	0.024 kgm^2	-19%

Table 2.1.9-1: Some basic design data for the Switched Reluctance Machine and the Induction Machine.

Comparison of measured loss balance at rated speed:

	Switched Reluctance Machine	*Induction Machine*
Input / Output power P_{in} / P_{out}	9440 W/ 8480 W	9950 W/ 8480 W
Phase current $I/\hat{I}$	13.3 A/ 27.5 A	17.45 A/ 30 A
Stator frequency f_s	200 Hz	52 Hz ($U_{s,k=1}$ = 225.5V)
Armature temperature rise	110 K	101 K
Iron losses / friction & windage losses	200 W/ 165 W	265 W/ 55 W
Stator copper losses/cage losses	595 W/ 0 W	650 W/ 350 W
Additional losses	0 W	150 W
Stator current density J_s	5.25 A/mm^2	8.23 A/mm^2
Current loading $A = 2mN_sI_s/(d_{si}\pi)$	513 A/cm	305 A/cm
Motor efficiency η_{mot}	**89.8 %**	**85.2 %**
Inverter efficiency η_{inv}	96.6 %	97.0%
Drive efficiency η	**86.7 %**	**82.6 %**

Table 2.1.9-2: Measured results of thermal load run for 1500/min, 54 Nm and U_d = 540 V. Cooling was performed with a shaft-mounted fan of 230mm outer diameter and 7 radial fan blades.

Conclusions:
Short winding overhangs allow increased iron stack length, so for the same outer motor dimensions inverter fed induction machine and SR machine have nearly the same power output at same motor size. At low speed due to lower motor losses SR torque may be

increased (high starting torque). SR motor shows increased efficiency when compared with induction machine due to lack of cage losses.

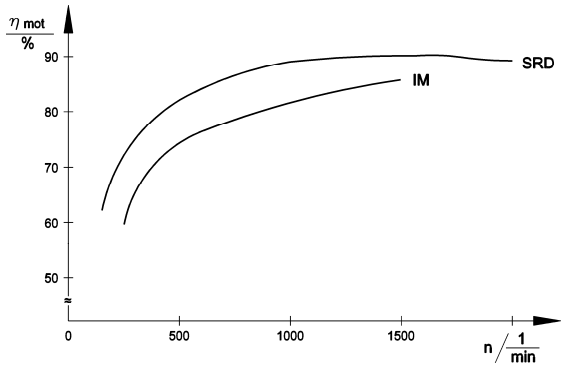

Fig.2.1.9-2: Comparison of measured motor efficiency of 7.5 kW, four-pole 12/8 SR machine (SRD) and inverter-fed standard induction machine (IM) at 54 Nm, 100 K armature temperature rise for different motor speed. Inverter efficiency of about 97% has to be added in both cases.

2.1.10 Applications of SR drives

Standard variable speed SR drives have been designed and manufactured to compete with inverter-fed variable speed induction machines. More importance was gained by using the SR drive in special applications, where variable speed drives for
- cheap mass production (e.g. drive in electric cars, pump and compressor drives),
- special purpose in rough environment (e.g. mills in coal mines, explosion hazard utilities such as oil fields)
- robust high speed drives (e.g. starter-generator for air craft engine)

are needed.

For some of these cases the magnetic noise of motor is not of interest, as the driven load is already noisy (e.g. air craft engine).

Example 2.1.10-1:
Starter-generator for military aircraft jet (*US Air Force*, manufacturer GE)

- Rated power: 250 kW, rated speed 13 500/min, rated torque 177 Nm, rated current 750 A, DC link voltage 270 V
- Maximum speed 22200/min, overspeed 26000/min, overall system efficiency: 90%
- Three phase four pole 12/8 SR machine,

For reliability two independent three phase systems are arranged with each 125 kW power.
In case of failure motor is “fail-silent” = no current = no force = no induced voltage, so risk of fire due to short circuit is minimized.
In order to decrease motor size and mass, motor is intensively cooled by oil. So motor mass is only 70 kg, yielding “power weight” of P/m = 3.6 kW/kg.

In low speed region 0 ... 13500/min SR machine is used to start compressor of air craft engine with constant torque 177 Nm.

In high speed region 13500 ... 26000/min SR machine is driven by air craft engine as generator with constant power output 250 kW (Fig.2.1.10-1).

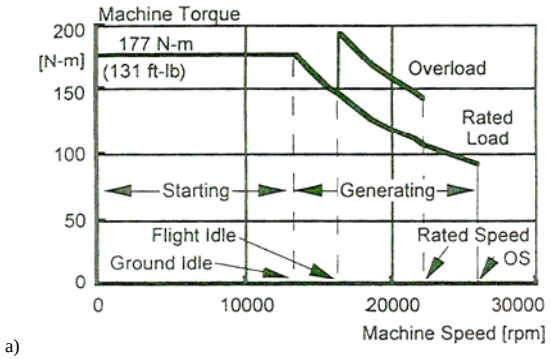

a)

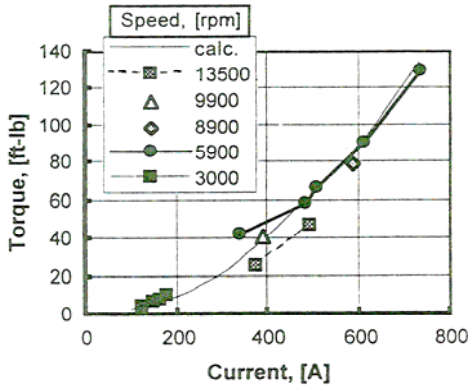

b)

Fig.2.1.10-1: 250 kW four-pole SR machine as starter-generator for aircraft; a) Torque-speed characteristic, b) Measured and calculated torque-current-curve (above 400 A the SR machine is saturated).

2.2 Synchronous reluctance machines

2.2.1 Basic function of synchronous reluctance machine

The stator of the synchronous reluctance machine is slotted, with a distributed AC winding like a PM synchronous machine. So stator winding is usually fed from sinus three-phase voltage system; current in winding is also three-phase sinus system. The rotor is consisting of deep slots between the poles in the *q*-axis ("inter-pole gaps"), whereas with the *d*-axis the air gap is as small as possible. Fig.2.2.1-1a shows a typical 4 pole rotor with slot width of 36° and pole width 54°, with resulting pole pitch 90°. In the pole region slots containing squirrel cage segments for asynchronous starting at fixed stator voltage ("line start") are arranged. After asynchronous starting, when the rotor has accelerated up to synchronous speed of stator rotating magnet field, this stator field exerts tangential magnetic pull on the rotor, if the rotor poles are not in *d*- or *q*-position (Fig.2.2.1-2). In *d*- and *q*-position total tangential magnetic

pull on rotor is zero, so no torque is generated. In positions between *d*- and *q*-position asymmetric flow of flux across rotor and air gap generates resulting tangential pull and therefore **synchronous reluctance torque**. This torque tries to align rotor in *d*-position against load torque, thus generating mechanical power output (**motor mode**).

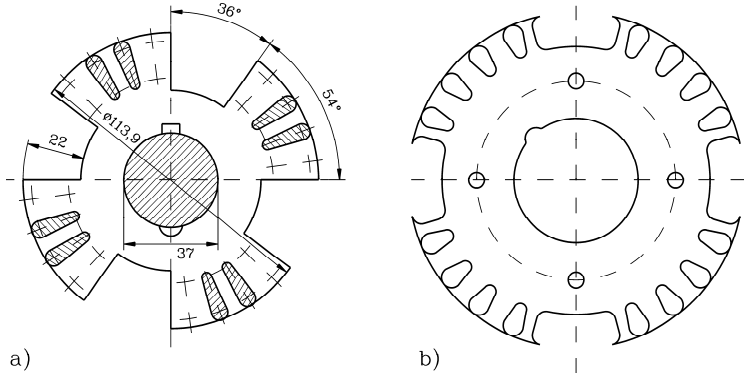

Fig.2.2.1-1: Different shapes (at different scale) of rotor cross section of 4-pole, 3-phase synchronous reluctance machines (Steady state power at Thermal Class F, totally enclosed, shaft-mounted fan, 50 Hz, synchronous speed 1500/min). Rotor a) 2.2 kW, shaft height 112 mm, rotor b) 550 W, shaft height 80 mm (*Siemens AG, Germany*).

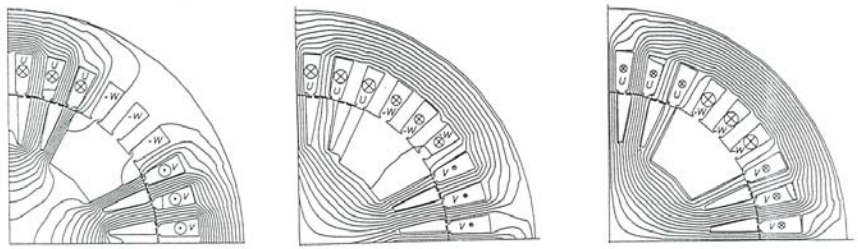

Fig.2.2.1-2: Numerically calculated flux lines per pole for rated current for motor a) of Fig.2.2.1-1: Rotor is a) in *q*-position (current angle $\beta = 90°$), b) half between *q*- and *d*-position, $\beta = 45°$, c) in *d*-position, $\beta = 0°$

If rotor is driven mechanically, and rotor is leading ahead *d*-position of stator field, polarity of torque is reversed, thus operating as generator with power flow from shaft to grid. But always **magnetizing current** from grid is needed to excite air gap flux, so always current will be lagging behind voltage.

Conclusions:
Synchronous reluctance machine is fed by three-phase sinus voltage system, and may be operated as motor or generator. Due to magnetizing current the stator current is always lagging (inductive current).

No position sensor is needed, but **load angle** ϑ between rotor axis and stator field (Fig.2.2.2-1) increases with increased torque demand up to maximum torque at 45° load angle. This maximum torque is **static pull-out torque** M_{p0}. By surpassing this angle and torque, the rotor

is pulled out of synchronism and runs asynchronously with the starting cage segments being induced and producing **asynchronous torque**.

Rotor is very robust and cheap, as it contains neither winding and magnets nor position sensor. Rotor speed in synchronism is exactly **synchronous speed** according to Section 1.1.1

$$n_{syn} = f_s / p \qquad (2.2.1\text{-}1)$$

Example 2.2.1-1:

Pole count	-		2	4	6	8
Speed	1/min	at 50 Hz	3000	1500	1000	750
Speed	1/min	at 60 Hz	3600	1800	1200	900

2.2.2 Voltage and torque equation of synchronous reluctance machine

Comparing synchronous reluctance machine with PM synchronous machine of section 1, we see that back EMF U_p is zero, as no rotor excitation exists. On the other hand stator main inductance L_h for *d*-axis with small air gap is much bigger than for *q*-axis with big air gap of rotor inter-pole gap: $L_{hd} > L_{hq}$. When each phase of stator winding is fed by stator voltage U_s, the stator current I_s will be lagging by phase angle φ. By decomposing stator current in two components with 90° phase shift, we get *d*-component of current I_d, magnetizing the rotor along *d*-axis, and *q*-component of current I_q, magnetizing current along *q*-axis. Air gap field of *d*-component experiences small air gap and therefore self-induced voltage $\omega_s L_{hd} I_d$ of that stator field component is big according to self-inductance L_{hd}, whereas in *q*-axis only smaller L_{hq} will result in smaller self-induced voltage $\omega_s L_{hq} I_q$.

Thus total voltage per phase is given by these two components of **self-induced voltage of air gap field** and of self-induced voltage due to stator **stray flux** in slots and winding overhangs and **resistive voltage** drop. As voltages and currents are sinusoidal, complex phasor calculation may be used. The real axis of complex co-ordinate system is chosen to coincide with rotor *d*-axis, and imaginary axis with rotor *q*-axis.

$$\underline{I}_s = I_d + jI_q = \underline{I}_d + \underline{I}_q \qquad (2.2.2\text{-}1)$$

Voltage equation:

$$\underline{U}_s = R_s \underline{I}_s + j\omega_s L_{s\sigma} \underline{I}_s + j\omega_s L_{hd} \underline{I}_d + j\omega_s L_{hq} \underline{I}_q = R_s \underline{I}_s + j\omega_s L_{s\sigma} \underline{I}_s + \underline{U}_h \qquad (2.2.2\text{-}2)$$

With defining **synchronous *d*- and *q*-axis inductance**

$$\boxed{L_d = L_{s\sigma} + L_{hd}\,, \quad L_q = L_{s\sigma} + L_{hq}} \qquad (2.2.2\text{-}3)$$

and **synchronous *d*- and *q*-axis reactance** $X_d = \omega_s L_d$, $X_q = \omega_s L_q$ and neglecting resistive losses, voltage equation is

$$\underline{U}_s = jX_d \underline{I}_d + jX_q \underline{I}_q = jX_d I_d - X_q I_q \quad . \qquad (2.2.2\text{-}4)$$

In Fig.2.2.2-1 for a two-pole synchronous reluctance machine this voltage equation is depicted as complex phasor diagram, showing

a) lagging stator current with **phase angle** φ,
b) decomposition of current in *d*- and *q*-component,
c) **current angle** β between direction of current phasor and *d*-axis,
d) **load angle** ϑ between stator voltage phasor and *q*-axis
e) **motor operation,** as $\cos\varphi$ is positive ($|\varphi| < \pi/2$).

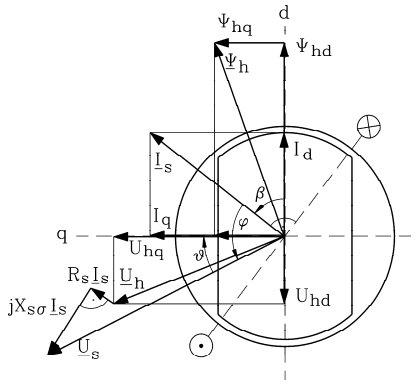

Fig.2.2.2-1: Phasor diagram for synchronous reluctance machine for motor operation. Flux linkage phasors may be taken as direction of air gap flux components.

In addition, the values of air gap flux linkages

$$\underline{\Psi}_{hd} = L_{hd} \cdot \underline{I}_d \cdot \sqrt{2}\,, \quad \underline{\Psi}_{hq} = L_{hq} \cdot \underline{I}_q \cdot \sqrt{2} \qquad (2.2.2\text{-}5)$$

indicate, that resulting air gap flux

$$\underline{\Psi}_h = \underline{\Psi}_{hd} + \underline{\Psi}_{hq} \qquad (2.2.2\text{-}6)$$

has its direction much closer to *d*-axis than current phasor. Note, that if $L_{hd} = L_{hq}$, then direction of resulting flux would be the direction of current phasor, so reluctance rotor directs flux into *d*-axis direction, thus generating reluctance torque.

Electrical real P_e is converted in motor mode into mechanical power. Neglecting losses, voltage equation (2.2.2-4) yields

$$P_e = m \cdot U_s \cdot I_s \cdot \cos\varphi = m \cdot \left(U_{s,\mathrm{Re}} \cdot I_{s,\mathrm{Re}} + U_{s,\mathrm{Im}} \cdot I_{s,\mathrm{Im}}\right) = m \cdot \left(-X_q I_d I_q + X_d I_d I_q\right) = \Omega_m M_e \Rightarrow$$

$$\Rightarrow \qquad \boxed{M_e = \frac{p \cdot m}{\omega_s} \cdot \left(X_d - X_q\right) \cdot I_d I_q} \qquad (2.2.2\text{-}7)$$

Conclusions:
A big difference between d- and q-axis inductance is needed to generate sufficient torque (typically $L_d/L_q \sim 5$). Current component I_d may be taken as magnetizing current, exciting the

"main" flux in d-direction, whereas perpendicular current component I_q may be taken as torque-delivering current.

If synchronous reluctance machine is fed from inverter with field oriented torque and current control, *d*- and *q*-current may be controlled independently, using equ. (2.2.2-7). When fed from grid with constant voltage amplitude, current is not available for control. From Fig.2.2.2-1 we take for $R_s = 0$, considering positive angle ϑ in mathematical positive direction (counter-clockwise direction), being counted from stator voltage to *q*-axis:

$$U_s \cos\vartheta = I_d X_d \;,\; -U_s \sin\vartheta = I_q X_q$$

Thus load angle is negative for motor mode and positive for generator mode. Substituting this in (2.2.2-7), and using $\sin 2\vartheta = 2\sin\vartheta\cos\vartheta$, torque equation for impressed voltage is derived:

$$M_e = -\frac{p \cdot m}{\omega_s} \cdot \frac{U_s^2}{2} \cdot \left(\frac{1}{X_q} - \frac{1}{X_d} \right) \cdot \sin(2\vartheta) \qquad (2.2.2\text{-}8)$$

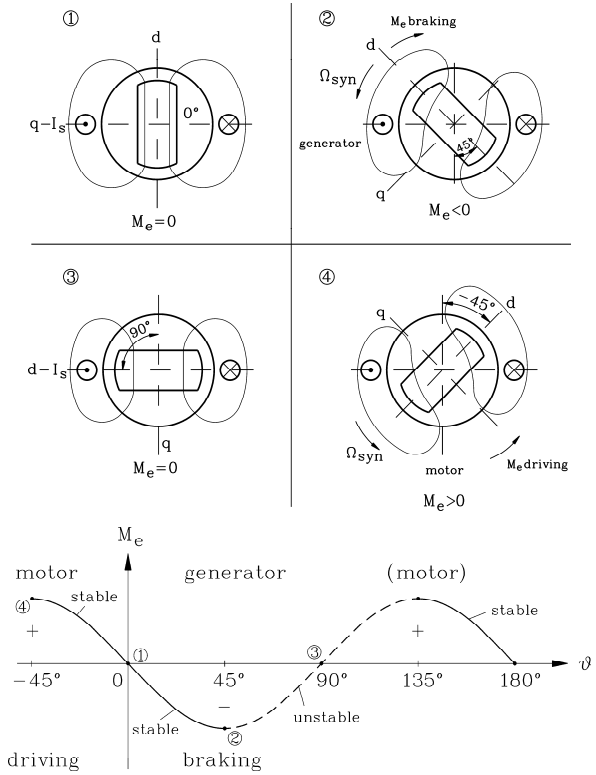

Fig.2.2.2-2: Torque vs. load angle of synchronous reluctance machine and schematic view of rotor position vs. stator field for no-load (*d*-position: $\vartheta = 0$), maximum torque (pull out torque) in generator ($\vartheta = 45°$) and motor mode ($\vartheta = -45°$) and unstable operation at *q*-position no-load ($\vartheta = 90°$)

Conclusions:
At no-load load angle is zero ($\vartheta = 0°$). Maximum torque is delivered at ($\vartheta = \pm 45°$, generator/motor), whereas q-position ($\vartheta = 90°$, zero torque) is unstable. A slight movement of rotor would snap the rotor into d-position, where flux is maximum. So only for $-45° \le \vartheta \le 45°$ stable operation for impressed stator voltage is possible.

2.2.3 Operation of synchronous reluctance machine at constant voltage and frequency

a) Phasor diagram and reluctance circle diagram ($R_s = 0$):
Line operated synchronous reluctance machine operates at constant voltage and frequency. Neglecting resistance and iron losses, voltage and torque equation (2.2.2-4), (2.2.2-7) have to be used. In Fig.2.2.3-1 phasor diagram for generator and motor mode is shown with voltage phasor $\underline{U}_s$ put in real axis. Note that *d*-axis current (**magnetizing current**) is always directed in positive *d*-axis $I_d > 0$. It is necessary to excite the magnetic air gap field of *d*-axis, which in PM machine is done by the rotor magnets. In **generator** mode *q*-axis is leading the voltage phasor, thus defining **positive** load angle ϑ. In that case *q*-axis current is directed in negative *q*-axis $I_q < 0$, yielding negative (braking) torque according to (2.2.2-7). In **motor** mode *q*-axis is lagging the voltage phasor, thus defining **negative** load angle ϑ. In that case *q*-axis current is directed in positive *q*-axis $I_q > 0$, yielding positive (driving) torque according to (2.2.2-7). The phase shift between voltage and current φ is always lagging, as machine is needing inductive reactive power to be magnetized. The power factor $\cos\varphi$ is positive in motor mode, thus showing a positive electric power. That means, machine is consuming electric power, converting it into mechanical power as a motor. The power factor $\cos\varphi$ is **negative** in generator mode, yielding negative electric power. That means, machine is delivering power as a generator.

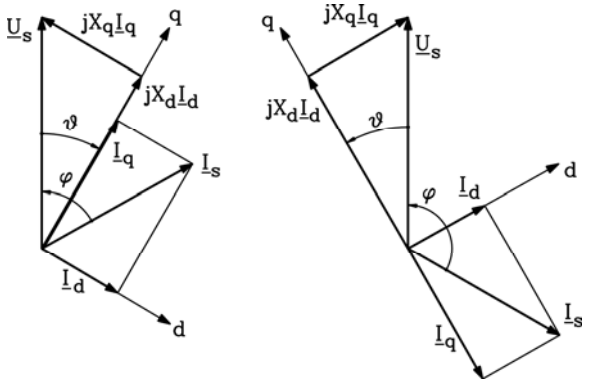

Fig.2.2.3-1: Simplified phasor diagram for neglected stator resistance: left: motor, right: generator

	Motor	**Generator**
Load angle ϑ	< 0	> 0
Phase shift φ	0 ... 90°	90° ... 180°
d-current	> 0	> 0
q-current	> 0	< 0
Electric power	> 0	< 0
Torque and mechanical power	> 0	< 0

Table 2.2.3-1: Basic electric quantities of synchronous reluctance machine

We ask: How does current input of synchronous reluctance change with changing load ? The answer is: The current phasor locus for changing load (torque or load angle) is a circle, the so-called **reluctance circle diagram** (Fig.2.2.3-2).

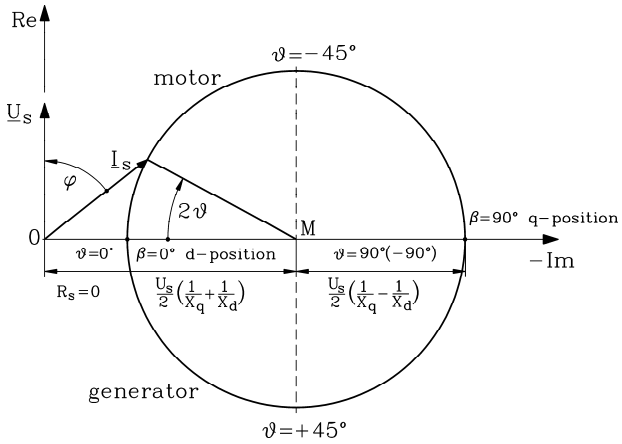

Fig.2.2.3-2: Reluctance circle diagram for neglected stator resistance: lower half circle: generator, upper half circle: motor

Proof:
With voltage phasor put in real axis we get: $\underline{U}_s = U_s$
Then we get for *q*- and *d*-current: $\underline{I}_q = I_q \cdot e^{j\vartheta}$, $\underline{I}_d = -jI_d \cdot e^{j\vartheta}$ or
$\underline{I}_q = I_q \cdot (\cos\vartheta + j\sin\vartheta)$, $\underline{I}_d = I_d \cdot (\sin\vartheta - j\cos\vartheta)$
We decompose stator phasor into real and imaginary part: $\underline{I}_s = \underline{I}_d + \underline{I}_q = I_{s,\mathrm{Re}} + j \cdot I_{s,\mathrm{Im}}$
Thus we get: $I_{s,\mathrm{Re}} = I_q \cos\vartheta + I_d \sin\vartheta$, $I_{s,\mathrm{Im}} = I_q \sin\vartheta - I_d \cos\vartheta$
From voltage phasor diagram we see: $U_s \cos\vartheta = X_d I_d$, $U_s \sin\vartheta = -X_q I_q$. Using this for current components we finally get (with $2\sin x\cos x = \sin 2x$, $\sin^2 x = (\cos 2x - 1)/2$, $\cos^2 x = (\cos 2x + 1)/2$):

$$I_{s,\mathrm{Re}} = -\frac{U_s}{2}\cdot\left(\frac{1}{X_q}-\frac{1}{X_d}\right)\cdot\sin 2\vartheta, \quad I_{s,\mathrm{Im}} = -\frac{U_s}{2}\cdot\left(\frac{1}{X_q}+\frac{1}{X_d}\right)+\frac{U_s}{2}\cdot\left(\frac{1}{X_q}-\frac{1}{X_d}\right)\cdot\cos 2\vartheta$$

Comparing these two components with the circle in Fig.2.2.3-2 we understand, that the centre point of circle *M* is lying on negative imaginary axis at $-\frac{U_s}{2}\cdot\left(\frac{1}{X_q}+\frac{1}{X_d}\right)$ and that circle radius is $\frac{U_s}{2}\cdot\left(\frac{1}{X_q}-\frac{1}{X_d}\right)$.

Note that real part of current yields input power, so again torque may be derived from circle diagram by

$$P_e = 3U_s I_{s,\mathrm{Re}} = \Omega_m M_e = P_m \quad \Rightarrow \quad M_e = -\frac{p}{\omega_s}\cdot 3\cdot\frac{U_s^2}{2}\cdot\left(\frac{1}{X_q}-\frac{1}{X_d}\right)\cdot\sin(2\vartheta) \quad ,$$

which is identical with (2.2.2-8). Thus real part of current is directly proportional to torque.

b) Reluctance circle diagram at $R_s > 0$:
Usually synchronous reluctance machines are built only for small power as cheap motors, because for larger machines the big amount of magnetizing current is not very economical. With small machines (typically 100 W ... 1 kW) influence of stator resistance usually may not be neglected. Of course, for detailed knowledge also iron, friction and additional losses have to be considered, but are here omitted for simplicity. Using instead of (2.2.2-4) now

$$\underline{U}_s = jX_d\underline{I}_d + jX_q\underline{I}_q + R_s(\underline{I}_d + \underline{I}_q) \qquad . \qquad (2.2.3\text{-}1)$$

again phasor diagram and reluctance circle diagram can be derived. Without proof we note that the centre of circle *M* is shifted upwards. So real part of current not only represents torque, but also copper losses in stator resistance. Therefore **motor pull out torque is reduced**, as electrical input power is partially consumed by copper losses, before the remaining part is converted into mechanical power. In generator mode (braking) pull out torque is increased, thus increasing mechanical torque demand to drive machine. Increased mechanical input power is now necessary also for feeding copper losses. Instead of (2.2.2-8) we get a rather complicated expression for torque, which for $R_s = 0$ is of course identical with (2.2.2-8):

$$M_e = -\frac{p\cdot m}{\omega_s}\cdot\frac{U_s^2\cdot(X_d - X_q)}{2(R_s^2 + X_d X_q)^2}\cdot\left(R_s\cdot(X_d - X_q) + \sqrt{(R_s^2 + X_d^2)(R_s^2 + X_q^2)}\cdot\sin(2\vartheta - 2\alpha)\right) \qquad (2.2.3\text{-}2)$$

$$2\alpha = \arctan\left(\frac{R_s(X_d + X_q)}{X_d X_q - R_s^2}\right) > 0 \qquad (2.2.3\text{-}3)$$

Example 2.2.3-1:
Shaft height 112 mm, pole count $2p = 4$, rated voltage and current: U_N = 380 V, Y, I_N = 9 A, 50 Hz, rated impedance $Z_N = U_N/(\sqrt{3}\,I_N)$ = 24.4 Ω; warm resistance: R_s/Z_N = 5%, X_d/Z_N = 165%, X_q/Z_N = 33%
Thus we get: 2α = 10.3°, $1-\varepsilon = R_s^2/(X_d X_q) = 0.995$

Due to the losses in stator resistance not only motor pull out torque is decreased, but also the motor pull out load angle is not any longer –45°, but –45°+10.3°/2 = -39.9°.

2.2.4 Stator flux linkage, Saturation of iron

In spite of this elaborate equation (2.2.3-2) the truth is, that economically designed motors have saturated iron parts. So assumption of constant reactances X_d, X_q is in reality not true, and for good calculation of machine saturation has to be considered. So theory of circle diagram is only good for basic understanding of machine performance, but NOT for telling the truth on real motor performance of saturated machines.

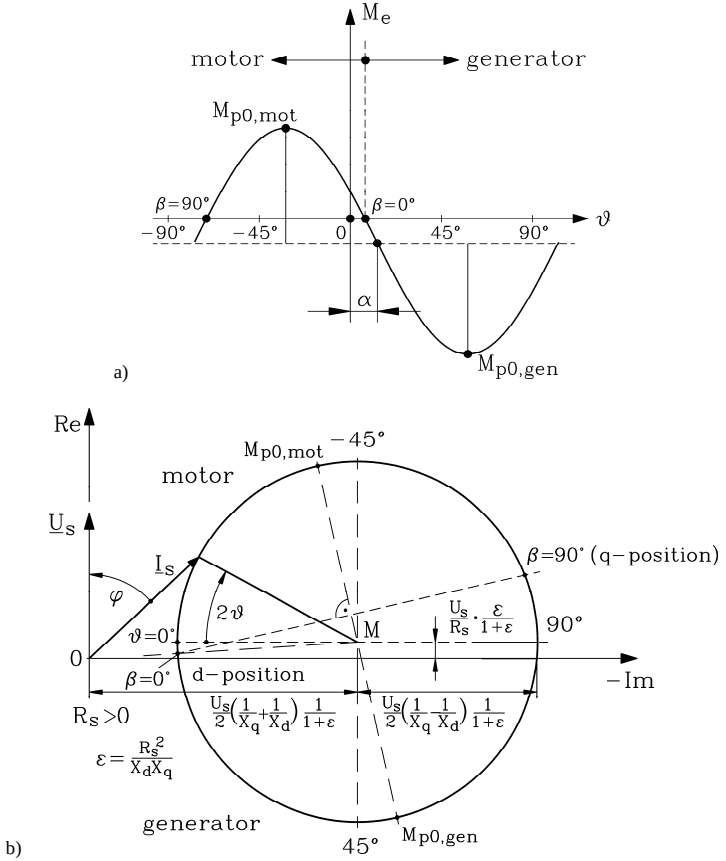

Fig.2.2.3-3: Synchronous reluctance motor, considering stator resistance: a) torque, b) reluctance circle diagram

a) NO saturation considered:

If no saturation is considered, *d*- and *q*-inductivities differ mainly due to different air gaps in pole region and gap region (Fig. 2.2.4-1). So, if we consider always constant current I_s in stator winding, but with changing angle β with respect to *d*-axis, the flux linkage components are

$$\Psi_d/\sqrt{2} = L_d I_d = L_d I_s \cos\beta, \quad \Psi_q/\sqrt{2} = L_q I_q = L_q I_s \sin\beta \qquad (2.2.4\text{-}1)$$

Thus the locus of flux linkage Ψ_s (and thus amplitude of fundamental of air gap flux density B_δ) for varying current phasor I_s on a circle is an ellipse.

$$\left(\frac{\Psi_d}{\sqrt{2}\cdot L_d I_s}\right)^2 + \left(\frac{\Psi_q}{\sqrt{2}\cdot L_q I_s}\right)^2 = 1 \qquad (2.2.4\text{-}2)$$

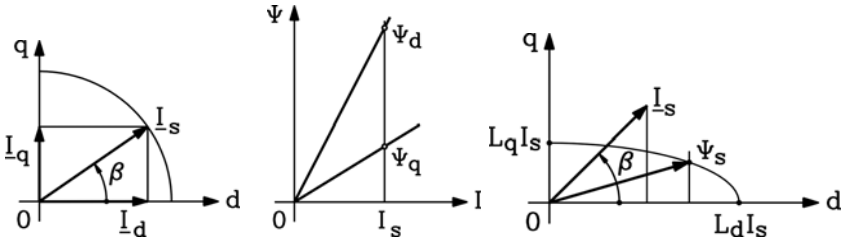

Fig.2.2.4-1: Locus of flux linkage for constant, but phase shifted stator current for unsaturated iron is an ellipse

b) WITH iron saturation considered:

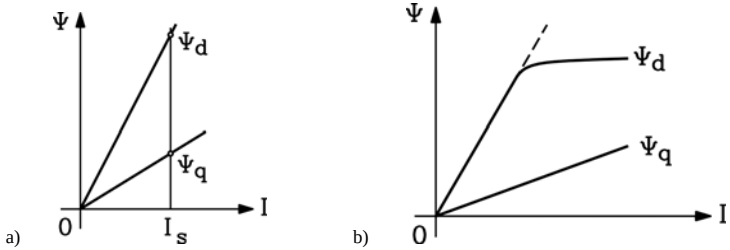

Fig.2.2.4-2: Comparison of *d*-and *q*-axis flux linkage: a) **Unsaturated iron:** Different inclination of flux linkage increase is defined by different (small and large) air gap in *d*- and *q*-axis, b) **Iron saturation** causes non-linear increase of *d*-axis flux linkage. As *q*-axis flux linkage is much smaller, iron flux density is so low, that no saturation occurs within range of rated current.

Calculating saturated flux linkage for different phase shifts β and given current amplitude is done usually numerically, as shown in Fig.2.2.1-2. Stator winding is loaded in the three phases with current in that way, that for phase shift $\beta = 0°$ the excited air gap flux lines are directed in *d*-axis, and for $\beta = 90°$ they are in *q*-axis (across the pole gap). For other angles β the direction of flux lines is in between. For each of these chosen angles the air gap flux density distribution $B_\delta(x)$ is calculated for given current. By *Fourier* analysis the fundamental amplitude $B_{\delta 1}$ is derived. With pole pitch, stack length, number of turns per phase of stator winding and winding factor of fundamental harmonic we get air gap flux linkage

$$\Psi_h = N_s k_{w1} \cdot \frac{2}{\pi} \tau_p l_{Fe} B_{\delta 1} \quad . \qquad (2.2.4\text{-}3)$$

Varying the current I_s, we get characteristics like those in Fig.2.2.4-3 (taken for the geometry of the motor of Fig.2.2.1-1a). So for each point of operation of reluctance machine (Fig.2.2.2-1) a certain current amplitude and angle β is given. Then taking the value of the flux linkage from the map of characteristics Fig.2.2.4-3 (with interpolation for angles in between the numerically calculated ones) the induced voltage is calculated, thus completing the phasor diagram. Please note, the it is NOT sufficient to take only the flux linkage characteristic for *d*- and *q*-axis by decomposing the current according $I_d = I_s \cos\beta$, $I_q = I_s \sin\beta$. If one would take these two current components, calculating with them the corresponding *d*- and *q*-flux

linkage from the two numerically derived characteristics, and composing with them the total flux linkage, one would grossly over-estimate the flux linkage. This is shown by the thus derived flux linkage locus curves Fig.2.2.4-4b. The real curves Fig.2.2.4-4a, calculated with the accurate flux linkage curves of Fig.2.2.4-3, are resembling nearly ellipses (which are depicted as dotted lines in Fig.2.2.4-4) and yield a much smaller flux for angles β between *d*- and *q*-axis. For small currents no saturation occurs and curves a and b close up to ideal ellipses, as is shown in Fig.2.2.4-4 for 50% rated current.

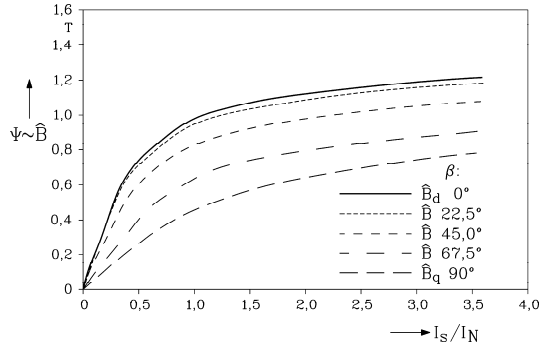

Fig.2.2.4-3: Numerically calculated flux linkage characteristics at different current angle β, rotor of Fig.2.2.1-1a

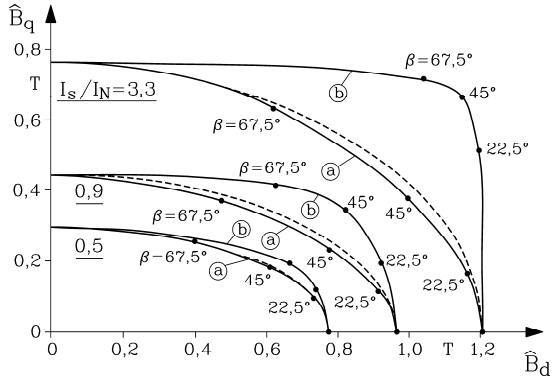

Fig.2.2.4-4: Locus of air gap flux density amplitude B_δ, which is proportional to flux linkage, for different stator current (50%, 90%, 330% of rated current) for different current angle β. Curves (a) are derived with the flux linkage characteristic of the "real" angle β, whereas curves (b) are derived only with the characteristics of *d*- and *q*-axis, which yields wrong results except for *d*- and *q*-axis. (dotted line -----: ellipses).

Example 2.2.4-1:
Four pole synchronous reluctance machine, rotor of Fig.2.2.1-1a:
Comparison of measured and calculated torque, electrical power, power factor, current, efficiency (Fig.2.2.4-5) for constant stator voltage 380 V, 50 Hz and motor and generator mode. Calculation is done using the flux linkage characteristics of Fig.2.2.4-3.

The corresponding locus of current phasor for constant voltage and frequency is depicted in Fig.2.2.4-6. Due to saturation it is **no longer a circle.** Good coincidence between calculation and measurement is only given up to rated load.

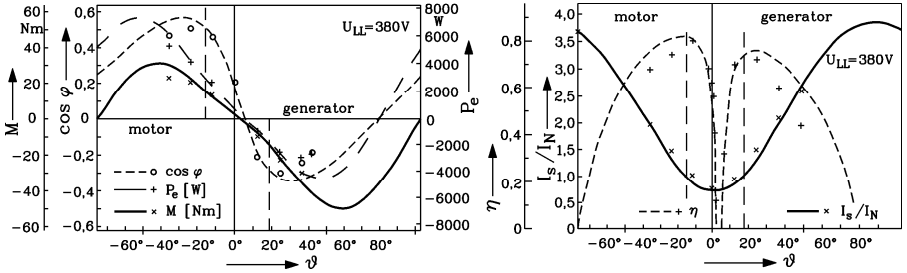

Fig.2.2.4-5: Comparison of measured (points) and calculated torque, electrical power, power factor, current, efficiency; four pole synchronous reluctance machine, rotor of Fig.2.2.1-1a

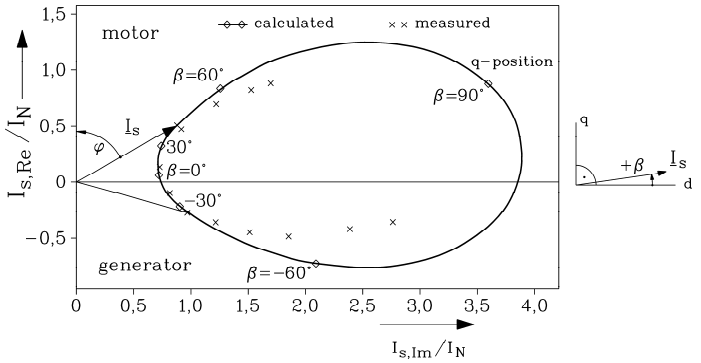

Fig.2.2.4-6: Comparison of measured (points) and calculated locus of stator phasor current; four pole synchronous reluctance machine, rotor of Fig.2.2.1-1a

Conclusions:
Saturation and two-dimensional flux density distribution has to be taken into account for reliable calculation results, so usually numerical field calculation is needed for calculating reluctance machines. Due magnetic coupling of d- and q-axis by common flux in stator yoke – which adds to total saturation - it is necessary to calculate the total flux linkage for each current phasor. Considering d- and q-flux independently would not take into account this additional saturation effect in stator yoke, thus yielding too big flux for positions between d- and q-axis.

2.2.5 Synchronous reluctance machine performance and application

a) Features and performance:
Due to low power factor (e.g. below 0.6 in Example 2.2.4-1) synchronous reluctance motors are only built for smaller power range typically below 5 kW at 1500/min. The rotor iron sheets are often taken from induction motor series any are punched out to get the gaps. Thus the small pole air gap of induction machines can be used to get big *d*-inductance, whereas for small *q*-inductance the parameter ratios
- Gap width / pole pitch,
- Gap depth / Gap width

have to be optimized to get a big ratio X_d/X_q. This is done often empirically for small motors.

Pull out torque must be at least 1.35-faches M_N to satisfy international standard IEC 60034-1. The rotor slots of the motor are used to form a cage for asynchronous line-starting of the machine. Often the rotor gaps are filled with aluminium for die-cast aluminium cage reluctance rotors to increase asynchronous **starting torque at slip $s = 1$**. Being operated from the grid with impressed stator voltage system, rotor may start speed slow oscillations at load steps like any synchronous machine, which is operated with independent voltage system. Rotor cage in that case acts as a **damper** (amortisseur winding), where currents are induced during these oscillations, causing an additional braking torque, which damps the oscillations rather quickly.

Good **synchronizing** must be achieved by big ratio X_d/X_q to ensure, that after asynchronous starting the rotor is pulled from slip $s > 0$ into synchronism $s = 0$ also, when the motor is already loaded. The **product of rated efficiency and power factor** $\eta \cdot \cos\varphi$ is shown in Fig.2.2.5-1 in comparison with line-operated induction motors and is lower du to the increased demand of magnetizing current, caused by the larger air gap of the pole gaps.

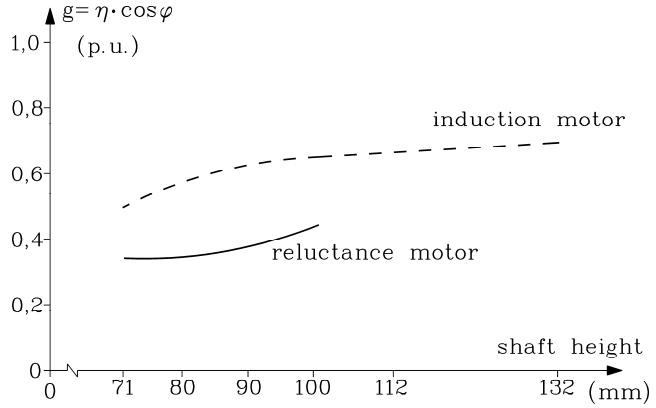

Fig.2.2.5-1: Product of measured rated efficiency and power factor for different motors: Comparison of 4-pole synchronous reluctance machine with line-operated induction motors

Example 2.2.5-1:
Comparison of 4-pole induction and synchronous reluctance machine, identical stator (shaft height 112 mm, 36 stator slots), totally enclosed, fan cooled (TEFC), 380 V Y, 9 A, 50 Hz

	Induction motor	*Reluctance motor*
Output power	4 kW	2.2 kW
Power factor	0.83	0.46
Efficiency	84 %	78 %
Rotational speed	1447 /min	1500 /min

Table 2.2.5-1: Comparison of 4-pole induction and synchronous reluctance machine with identical stator

Conclusions:
Steady state torque per volume for a certain temperature rise of stator winding is by 30% to 50% lower for synchronous reluctance machines, when compared with induction machines.

b) Inverter operation:
Usually synchronous reluctance machines are operated with inverter without any speed control due to synchronous capability of motor. Thus again rotor oscillations may happen, which have to be damped by rotor cage. With changing speed and frequency it may happen, that at certain speed the cage damping is much weaker than at other speed levels. So some **rules** were found to ensure stable non-oscillating operation for a wide speed range:
- reduction of ratio X_d/X_q (which of course is decreasing motor utilization),
- aim a ratio of rotor cage resistance in *d*- and *q*-axis of about $R_{rd}/R_{rq} = 0.5$,
- reduce rotor cage *d*-axis resistance R_{rd},
- increase stator and rotor *d*-axis stray inductance $L_{s\sigma}$, $L_{r\sigma d}$
- decrease stator resistance and rotor *q*-axis stray inductance R_s, $L_{r\sigma q}$

Often these oscillations occur for machines with rated frequency 50 Hz at lower stator frequencies below 30 Hz. By increasing the ratio of $U_s / f_s \sim \Psi$, which means increase of flux and thus saturation, the *d*-axis reactance is saturated and therefore the ratio X_d/X_q is reduced, as mentioned above. Usually the oscillations vanish.

c) Applications:
Synchronous reluctance machines are special drives, which are used often in **textile industry**, where e.g. acryl threads for synthetic textiles are manufactured. Many threads are taken from one big lump of molten acryl mass and are cooled and wound up synchronously by synchronous machines. Often more than 100 machines are working in parallel. So often cheap synchronous reluctance machines are used, fed from one main inverter at variable speed.

The synchronous reluctance machine is a **"fail-silent" machine**. In case of failure it can be switched off without further harming the system, in contrary to PM synchronous machines, where switched off, but still turning machines induce back EMF, causing losses.

Conclusions:
The synchronous reluctance machine is a special cheap, low power machine for special purposes, where synchronous speed is necessary.

2.2.6 Asynchronous starting of reluctance machines

a) Asynchronous starting torque:
Due to the rotor gaps the asynchronous starting torque is not constant for a certain slip. The stator air gap flux is rotating faster with the speed difference

$$\Delta n = n_{syn} - n = n_{syn} - (1-s) \cdot n_{syn} = s \cdot n_{syn} = s \cdot f_s / p \quad . \qquad (2.2.6\text{-}1)$$

Therefore the asynchronous torque is changing twice its value, when the stator wave passes on rotor pole pair, as two rotor gaps are passed, where the flux and thus the torque are decreased. So asynchronous torque during start up has an average value and a component, pulsating with double slip frequency $2s \cdot f_s$.

b) Asynchronous reluctance torque:
We assume for simplicity that the inverse air gap is varying along rotor co-ordinate x_r sinusoidal:

$$\frac{1}{\delta(x_r)} = \frac{1}{\delta_0} + \frac{1}{\delta_1} \cdot \cos\left(\frac{2x_r\pi}{\tau_p}\right) \qquad \delta_0 > \delta_1 \qquad \text{(2.2.6-2)}$$

yielding air gap in *d*-axis $\delta_d = \frac{\delta_0\delta_1}{\delta_0 + \delta_1}$ and in *q*-axis $\delta_q = \frac{\delta_0\delta_1}{\delta_0 - \delta_1}$. This "air gap distribution" is moving synchronously with rotor speed *n*, thus with respect to stator co-ordinate x_s we note

$$x_s = x_r + v \cdot t = x_r + 2p\tau_p \cdot n \cdot t = x_r + (1-s) \cdot 2 f_s \tau_p \cdot t \quad . \qquad \text{(2.2.6-3)}$$

The stator air gap flux density wave, excited by sinusoidal distributed stator ampere turns with amplitude $V_s = \frac{m}{\pi p} \cdot N_s k_{w1} \sqrt{2} I_s$

$$V_s(x_s, t) = V_s \cdot \cos\left(\frac{x_s\pi}{\tau_p} - \omega_s t\right) \quad , \qquad \text{(2.2.6-4)}$$

is modulated by air gap. With abbreviation $\gamma = x_s \cdot \pi / \tau_p$ we get

$$B_\delta(\gamma, t) = \mu_0 V_s(\gamma, t) / \delta(\gamma, t) = \mu_0 V_s \cos(\gamma - \omega_s t) \cdot \left[\frac{1}{\delta_0} + \frac{1}{\delta_1} \cdot \cos(2\gamma - 2(1-s)\omega_s t)\right] . \quad \text{(2.2.6-5)}$$

By using $\cos\alpha \cos\beta = (\cos(\alpha+\beta) + \cos(\alpha-\beta))/2$, three field components are distinguished by modulation:

- the stator fundamental with average air gap: $B_{s,1} = (\mu_0 V_s / \delta_0)\cos(\gamma - \omega_s t)$
- a field of same pole number, but different frequency: $B_{s,3} = (\mu_0 V_s / 2\delta_1)\cos(\gamma - (1-2s)\omega_s t)$
- a field of 3-times pole number and different frequency: $(\mu_0 V_s / 2\delta_1)\cos(3\gamma - (3-2s)\omega_s t)$.

The three-fold pole pair field induces in the three phase windings voltage, which are IN phase. So, in three phase star connected stator winding systems with insulated star point, no currents can be driven by these voltages. Hence the influence of this wave is neglected. The second field induces in the stator windings a voltage system U_3 with frequency $f_3 = (1-2s) f_s$, which causes **an additional (small) stator current** I_3. The corresponding sinusoidal distributed current ampere turns $V_3 = \frac{m}{\pi p} \cdot N_s k_{w1} \sqrt{2} I_3$ excite an additional air gap field $B_{\delta 3}(\gamma, t) = \mu_0 V_3(\gamma, t) / \delta(\gamma, t) = B_{3,1}\cos(\gamma - \omega_s t) + B_{3,2}\cos(\gamma - (1-2s)\omega_s t) + \ldots$,

which again contains – with the same calculation as above - a field with three-fold pole pair (neglected here) and two field components $B_{3,1}$, $B_{3,2}$.

The two waves $B_{s,1}$, $B_{3,1}$ have the same wave length and frequency, thus the same velocity, so they produce a constant torque $M_1 \sim B_{s,1} \cdot B_{3,1} \sim I_s \cdot I_3$. The same holds true for $B_{s,2}$, $B_{3,2}$, again resulting in a constant torque $M_2 \sim B_{s,2} \cdot B_{3,2} \sim I_s \cdot I_3$. Therefore the **constant part of asynchronous reluctance torque** is formed by the sum of these to components:

$$M_a = M_1 + M_2 \sim I_s I_3 \quad . \qquad \text{(2.2.6-6)}$$

On the other hand, the two waves $B_{s,1}$, $B_{3,2}$ have the same wave length, but not the same frequency and velocity, so they produce a pulsating torque $M_{1P} \sim B_{s,1} \cdot B_{3,2} \sim I_s \cdot I_3$. Difference of frequencies is $f_s - (1-2s) f_s = 2s \cdot f_s$, so frequency of pulsating torque is again double slip frequency. The same holds true for $B_{s,2}$, $B_{3,1}$, again resulting in a pulsating torque $M_{2P} \sim B_{s,2} \cdot B_{3,1} \sim I_s \cdot I_3$, and also for $M_{3P} \sim B_{s,1} \cdot B_{s,3} \sim I_s^2$, $M_{4P} \sim B_{3,1} \cdot B_{3,2} \sim I_3^2$, all pulsating with double slip frequency. So the **pulsating torque amplitude** (Fig.2.2.6-2) is constituted of four parts

$$M_P = M_{1P} + M_{2P} + M_{3P} + M_{4P} \sim I_s I_3, I_s^2, I_3^2 \quad . \qquad \text{(2.2.6-7)}$$

Please note that **at half synchronous speed**

$$n = n_{syn}/2 \quad \Leftrightarrow \quad s = 0.5 \qquad \text{(2.2.6-8)}$$

the frequency $(1-2s) \cdot f_s$ is zero, so **in that special point no current I_3 is induced in stator: $I_3 = 0$.** At that special point the asynchronous reluctance torque M_a vanishes and the pulsating torque has a minimum, now depending only on I_s^2 **(*Goerges*-phenomenon, Fig.2.2.6-1b).**

$$M_a(s = 0.5) = 0, \quad M_P = Min. \quad . \qquad \text{(2.2.6-9)}$$

The current $i_3(t) = \hat{I}_3 \cdot \sin((1-2s)\omega_s t)$ changes also sign at s = 0.5, therefore the real power flow of this current is also changing direction, being motor at $n < n_{syn}/2$ and generator at $n > n_{syn}/2$. Therefore the asynchronous reluctance torque is a driving (positive) torque for $n < n_{syn}/2$ and a braking (negative) torque for $n > n_{syn}/2$.

Example 2.2.6-1:
Asynchronous operation of a small synchronous reluctance torque without rotor cage in order to measure the asynchronous reluctance torque. The motor was driven by coupled external DC machine asynchronously, while stator was fed by the grid with 50 Hz constant voltage. Stator current I_s ranges between 0.35 A and 0.4 A, whereas additional current I_3 is smaller with about 0.18 A and zero at half synchronous speed (Fig.2.2.6-1a). Pulsating torque is much bigger as asynchronous reluctance torque, as it is composed by four, and not only by to components (Fig.2.2.6-1b).

Conclusions:
*During asynchronous start up the machine not only produces an **asynchronous starting torque**, but also an additional **asynchronous reluctance torque**, which is caused by the difference of d- and q-axis inductance. Both torque components consist of a constant and a pulsating value, causing the machine to vibrate. So asynchronous starting is usually much more noisy than starting of three phase induction motors.*

2.2.7 Special rotor designs for increased ratio X_d/X_q

By using flux barriers in the rotor the value of X_q may be reduced further without influencing X_d substantially (Fig.2.2.7-1). By increasing the ratio X_d/X_q the locus of stator current

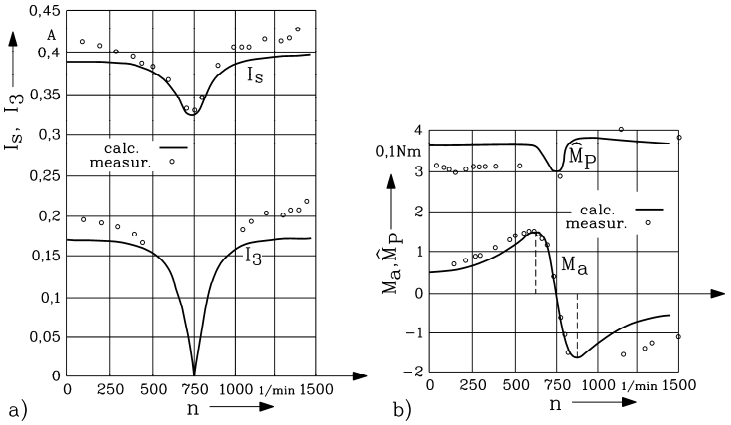

Fig.2.2.6-1: Asynchronous operation of small synchronous reluctance machine: (a) Calculated and measured (dots) stator and additional stator current I_3 , (b) asynchronous reluctance torque M_a and pulsating torque amplitude M_P (Source: *Bausch, Jordan et al, ETZ-A*)

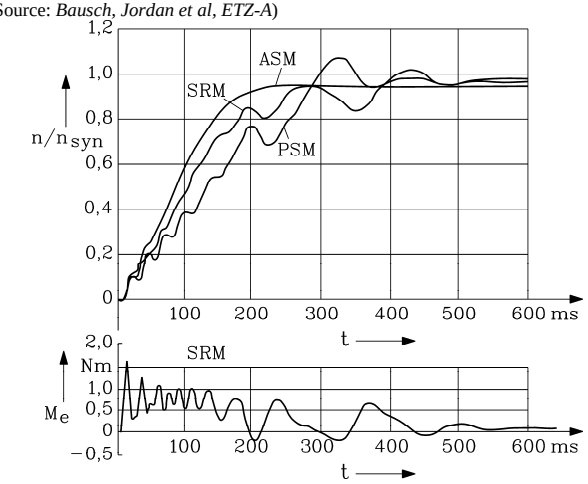

Fig.2.2.6-2: Calculated asynchronous starting: Comparison of induction machines (ASM), Synchronous reluctance machine (SRM), Permanent magnet synchronous machines with rotor cage (PSM, see Chapter 3). Above: speed, below: starting torque of SRM. Pulsating torque with decreasing frequency clearly visible (Source*: Bunzel, E., elektrie*).

becomes more like a circle. The power factor increases, which reduces the amount of magnetizing current. Therefore the copper losses are reduced, as for the same torque a lower current is needed. Thus efficiency is increased. A lot of patents have been issued on this topic of the “best” rotor configuration. With the rotors of Fig.2.2.6-1 X_d/X_q could be increased from about 5 to 10. Power factor increased up to 0.7 ... 0.8, thus nearly reaching the value of induction machines and efficiency of 0.85 ... 0.9 was possible. With these values also bigger synchronous reluctance machines with rated power at 1500/min between 20 ... 50 kW and more may be economical solutions, especially with rotor a) of Fig.2.2.6-1, whereas rotor b) and c) are rather expensive in manufacturing. The magnetic barriers of rotor c), which reach

the rotor surface, act like additional rotor slots. As it is explained in Chapter 4, the slot openings cause a local reduction in magnetic field. This distortion acts like an additional field harmonic, causing pulsating radial magnetic forces, which not only excite stator vibrations, but also acoustic noise.

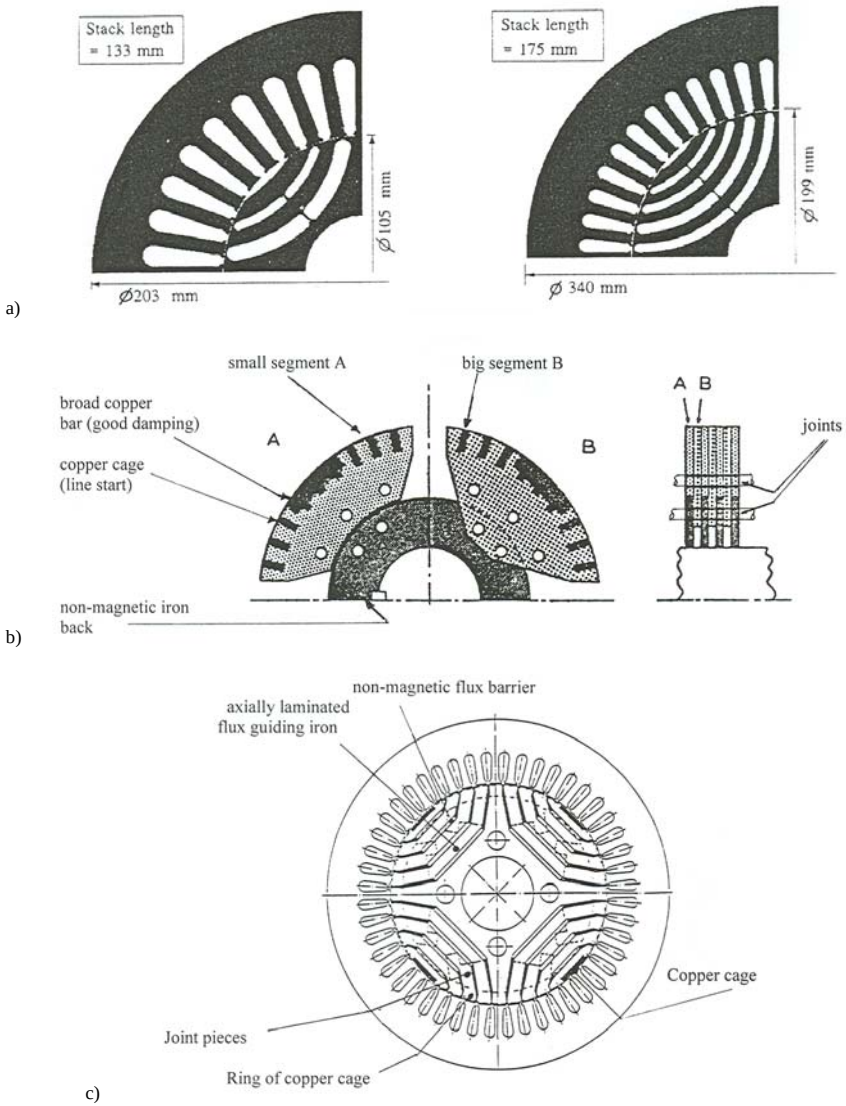

Fig.2.2.7-1: Different special rotor designs to increase ratio X_d/X_q : a) Flux barrier rotors with punched-out barriers (left: Rated torque/speed 58 Nm / 1500/min, right: 265 Nm / 1500/min (Source: *M. Kamper*), b) segmented rotor with non-magnetic shaft (*P. Lawrenson, S. Gupta*), c) axially laminated rotor, containing of different stack sections (Source: *F. Taegen, 1990, Archiv f. Elektrotechnik*)

3. PM synchronous machines with cage rotor

3.1 Basic motor function and rotor design

a) Basic motor function:
Compared with the PM brushless DC drives of Chapter 1, the PM synchronous machines with cage rotor do not operate with a rotor position sensor. They consist – like the brushless DC machine – of a slotted stator with a three phase distributed AC winding, but the rotor is containing not only permanent magnets, but also a s**quirrel cage for asynchronous starting** like the synchronous reluctance machine. Like the synchronous reluctance machines, the rotor may oscillate in speed against the stator field, which is rotating with synchronous speed, defined by stator frequency. Therefore the rotor cage, which in that case is induced by stator field, will generate cage currents, which will create reaction *Lorentz* forces with stator field, thus damping the oscillations very quickly (**amortisseur**). Rotor cage must be near air-gap to get a good flux linkage with stator field, therefore no surface mounted permanent magnets can be used (Fig.3.1-1). Permanent magnets are "buried" below the cage in the rotor.

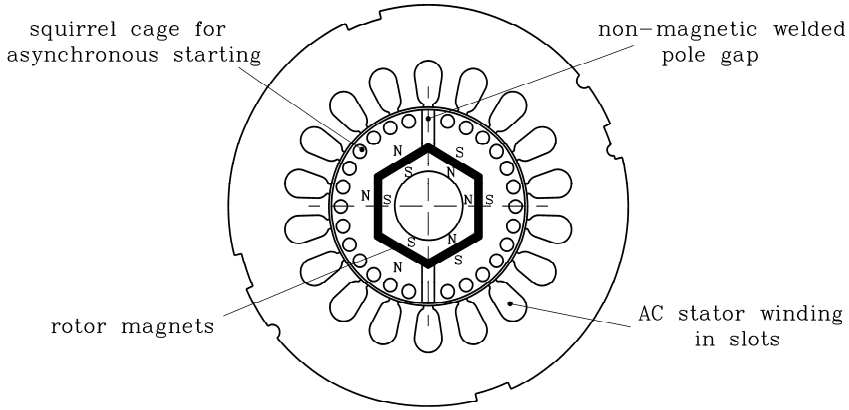

Fig.3.1-1: Two pole PM synchronous machine with cage rotor and rare earth permanent magnets. Note non-magnetic (welded with non-magnetic steel) gap between N- and S-pole to reduce PM stray flux *(Source: Siemens AG, Germany*)

PM synchronous machine may be therefore operated **at grid** (fixed voltage and frequency), **starting asynchronously** via the rotor cage, and after being pulled into synchronous speed by rotor permanent magnets, will run with synchronously rotating rotor like the previously discussed synchronous reluctance machine. No inverter is needed in that case. On the other hand, group drive with one big inverter feeding several PM machines in parallel, is also possible. They are started with variable frequency from zero to rated speed. Load steps at single motors will cause them to oscillate, but oscillations will be damped by rotor cage. If one motor is overloaded and pulled out of synchronism, it will be decelerated down to standstill by the load. Then, without changing inverter voltage and frequency, this single motor can be started up asynchronously again by the rotor cage.

Conclusions:
PM synchronous motor with squirrel cage operates without rotor position sensor, and may be operated also directly at the grid without any inverter.

b) Rotor design:
Buried magnets will cause a big part of magnetic flux to stay within the rotor iron, thus not reaching the air gap and the stator winding (**PM stray flux**). This means a waste of expensive PM magnetic material. Therefore in Fig.3.1-1 a non-magnetic gap between rotor N- and S-pole is designed, increasing the magnetic resistance, thus reducing the rotor PM stray flux considerably. Buried magnets allow the advantage of flux concentration (Fig.3.1-2) with the **flux concentration factor k_M**

$$k_M = 2b_M / \tau_p \quad . \tag{3.1-1}$$

In most simple case, rotor magnets are put with their direction of magnetization perpendicular to radial direction. Then, the maximum of rotor magnet breadth b_M is theoretically given by the difference of rotor outer and inner diameter

$$b_M < (d_{ra} - d_{ri})/2 \quad , \tag{3.1-2}$$

yielding a flux concentration of

$$k_M = \frac{2b_M}{\tau_p} = \frac{d_{ra} - d_{ri}}{\frac{d_{ra}\pi}{2p}} = \frac{2p}{\pi} \cdot \left(1 - \frac{d_{ri}}{d_{ra}}\right) \quad . \tag{3.1-3}$$

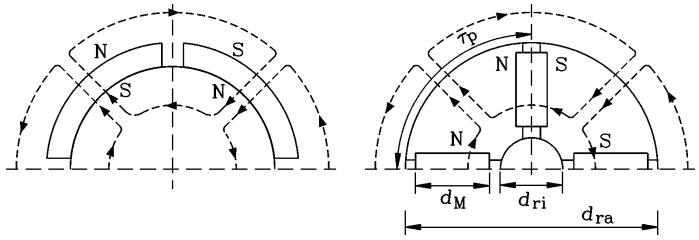

Fig.3.1-2: Comparison of rotor PM arrangement for (left) surface mounted and (right) buried magnets

Example 3.1-1:
Buried magnets: Flux concentration of radially inserted magnets: We assume $d_{ri}/d_{ra} = 0.3$.
In order to get a flux concentration, this corresponds to the demand $k_M > 1$.

Pole count 2*p*	2	4	6	8
k_M	0.45 < 1	0.9 < 1	1.34 > 1	1.78 > 1

Table 3.1-1: Flux concentration with radial inserted rotor magnets is only possible for high pole count (at least 6 poles)

Conclusions:
Effective flux concentration with radial inserted magnets needs a high pole count (of at least six poles).

By special arrangement of magnets not exactly in radial direction (Fig.3.1-3a), one gets increased breadth of magnets also four 4 pole machines, reaching values of $b_M \cong d_{ra}/2$. Now, also flux concentration for 4 pole machines is possible (Fig.3.1-4):

$$k_M = \frac{2b_M}{\tau_p} = \frac{d_{ra}}{\frac{d_{ra}\pi}{2p}} = \frac{2p}{\pi} \quad . \tag{3.1-4}$$

Pole count 2p	4	6
k_M	1.27 > 1	1.9 > 1

Table 3.1-2: Flux concentration with special arrangement of rotor magnets is also possible for 4 pole machines

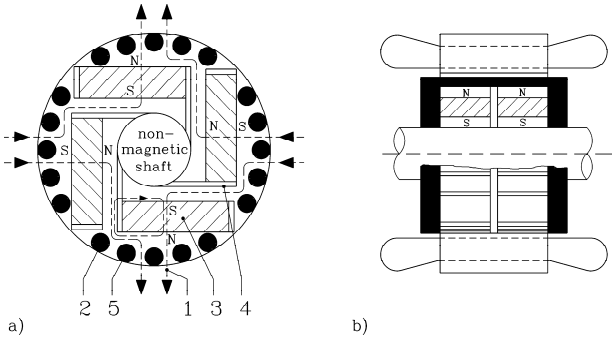

Fig.3.1-3: Flux concentration with special arrangement of rotor magnets is also possible for 4 pole machines: a) Axial cross section: 1: PM main flux, 2: PM stray flux, 3: permanent magnets (PM), 4: non-magnetic flux barrier to reduce PM stray flux, 5: rotor cage, b) side view. (*Siemens AG*)

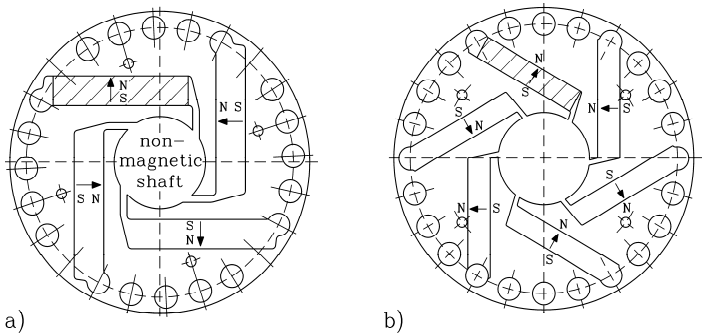

Fig.3.1-4: Flux concentration with special arrangement of rotor magnets: a) 4-pole rotor, b) 6-pole rotor (*Siemens AG*)

Example 3.1-2:

4- and 6-pole machine with buried **ferrite** magnets: B_R = 0.4 T, H_C = 300 kA/m at 20°C, magnet height 15 mm, air gap 1mm, $\mu_M / \mu_0 = (B_R / H_C) / \mu_0 = 1.06$.

Air gap flux density at no-load is calculated with (1.5.3-7), assuming ideal iron with $\mu_{Fe} \to \infty$. Note that according to Fig.3.1.3b the closed loops of flux lines pass one magnet (height h_M) and two times the air gap δ.

$$B_\delta = \frac{B_R}{\frac{1}{k_M} + \frac{\mu_M \cdot 2\delta}{\mu_0 \cdot h_M}}$$

Pole count 2p	4	6
k_M	1.27	1.9
B_δ / T	0.43	0.6

Table 3.1-2: Air gap flux density with ferrite magnets at 20°C, flux concentration for ratio h_M/δ = 15/1.

Conclusions:

Cheap PM synchronous machines can be built with ferrite magnets with pole count ≥ 4 with no-load air gap flux density amplitudes ≥ 0.4 T. Non-magnetic flux barriers are necessary to keep permanent magnet stray flux within limits. For the same reason also the rotor shaft is manufactured from non-magnetic steel, which more expensive than standard magnetic steel such as St37 or St60 material.

3.2 Motor performance at synchronous speed

At synchronous speed of rotor $n = n_{syn}$, the stator fundamental flux wave and the rotor move with identical speed, so the rotor cage is not induced, as flux linkage of stator field with rotor cage is constant. Relative position of stator field to rotor d-axis depends on phase angle of stator current I_s with respect to back EMF U_p in stator winding, induced by rotor permanent magnets. If we decompose stator current in to by 90° phase shifted components I_d and I_q, the stator field components, excited by them, will find **different rotor magnetic paths**, as shown in Fig. 3.2-1, where a very simple buried magnet rotor arrangement is depicted. It fits to the real buried magnet arrangement of Fig.3.1-3 and Fig.3.1-4, where we can see, that the magnets lie in the flux paths of *d*-axis. As magnet permeability is nearly equal to that of air $\mu_M = (B_R / H_C) \cong \mu_0$ (Example 3.1-2), the *d*-flux has to cross air gap and magnet, which both have a big "magnetic resistance". The *q*-flux only has to cross the air gap, because the rotor iron, where the cage is arranged, allows guidance of the flux lines with high iron permeability. Typical values are $L_d/L_q = 0.5$.

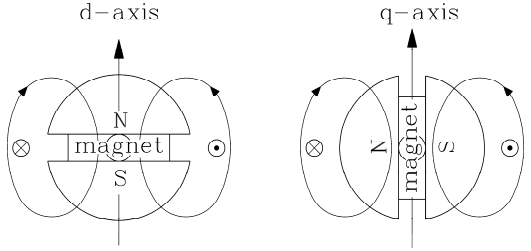

Fig.3.2-1: Simplified 2-pole arrangement with buried rotor magnets: The stator *d*-flux has to cross the rotor magnets, thus yielding a lower *d*-inductance (left). The stator *q*-flux can avoid the rotor magnets, which results in a higher *q*-inductance (right).

Conclusions:

*In PM machines with buried rotor magnets the d-inductance L_d is usually **lower** than the q-inductance L_q : $L_d < L_q$. Thus is **opposite** to the relationships in synchronous reluctance machines, where $L_d > L_q$.*

Voltage equation per phase is

$$\underline{U}_s = R_s \underline{I}_s + jX_d \underline{I}_{sd} + jX_q \underline{I}_{sq} + \underline{U}_p \quad . \tag{3.2-1}$$

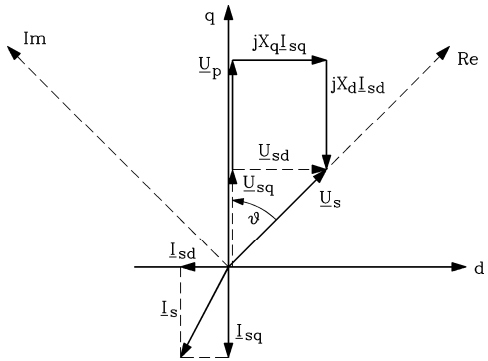

Fig.3.2-2: Phasor diagram of PM machine with buried magnets ($L_d \neq L_q$) with neglected stator resistance for generator operation (negative real part of stator current phasor). In this example also I_d and I_q are negative, whereas load angle ϑ is positive.

Neglecting stator resistance and assuming $L_d = L_q$, voltage equation is $\underline{U}_s = jX_d\underline{I}_s + \underline{U}_p$. Electrical input power is equal to mechanical output power:

$$P_e = mU_sI_s\cos\varphi = mU_sI_{s,\mathrm{Re}} = m\cdot\mathrm{Re}\left\{U_s\underline{I}_s^*\right\}, \tag{3.2-2}$$

as $\underline{U}_s$ phasor was considered to be real. Therefore it is according to Fig.3.2-2

$$\underline{U}_p = U_p(\cos\vartheta + j\cdot\sin\vartheta) \quad . \tag{3.2-3}$$

From voltage equation we get

$$\underline{I}_s = \frac{U_s - \underline{U}_p}{jX_d} \qquad \Rightarrow \qquad \underline{I}^*_s = \frac{U_s - \underline{U}^*_p}{-jX_d} \tag{3.2-4}$$

and for electrical power

$$P_e = m\cdot\mathrm{Re}\left\{U_s\cdot\frac{U_s - U_p(\cos\vartheta - j\cdot\sin\vartheta)}{-jX_d}\right\} = -m\frac{U_sU_p}{X_d}\sin\vartheta \quad , \tag{3.2-5}$$

yielding electromagnetic torque due to permanent magnets – depending on impressed stator voltage - as

$$M_e = \frac{P_m}{\Omega_{syn}} = \frac{P_e}{\Omega_{syn}} = -\frac{m}{\Omega_{syn}}\cdot\frac{U_sU_p}{X_d}\sin\vartheta \quad . \tag{3.2-6}$$

In fact, due to $L_d \neq L_q$ an additional reluctance torque is generated, as explained in Section 2.2, resulting in total torque

$$\boxed{M_e = -\frac{p\cdot m}{\omega_s}\left(\frac{U_sU_p}{X_d}\sin\vartheta + \frac{U_s^2}{2}\left(\frac{1}{X_q} - \frac{1}{X_d}\right)\sin 2\vartheta\right)} \tag{3.2-7}$$

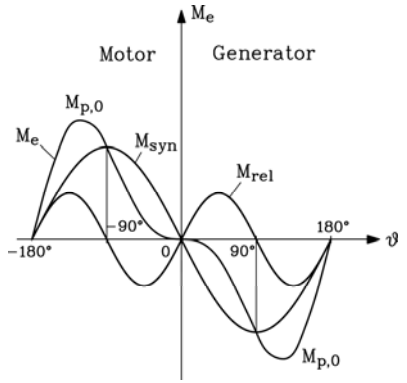

Fig.3.2-3: The torque M_e of synchronous PM machine, operated from grid with fixed voltage and frequency, is determined by permanent magnet torque M_{syn}, which depends linear on stator voltage, and by reluctance torque M_{rel}, which depends on square of stator voltage ($L_d < L_q$).

Reluctance torque is **negative** due to $L_d < L_q$. In order to avoid negative total torque, the permanent magnet material must be strong enough to yield positive inclination of torque versus load angle in motor operation at $\vartheta = 0$:

$$\left.\frac{dM_e}{d\vartheta}\right|_{\vartheta=0} \geq 0: \quad \frac{U_p}{X_d} + U_s\cdot\left(\frac{1}{X_q} - \frac{1}{X_d}\right) \geq 0 \tag{3.2-8}$$

With typical value $X_q = 2X_d$ the demand for **minimum magnet strength** is

$$U_p \geq U_s/2 \quad . \tag{3.2-9}$$

The negative reluctance torque causes a rather big load angle at rated torque. The absolute value of load angle at pull-out torque **is larger than 90°**.

Conclusions:
The torque of synchronous PM machine, operated from grid with fixed voltage and frequency, is determined by permanent magnet torque, which depends linear on stator voltage, and by reluctance torque, which depends on square of stator voltage. A certain minimum permanent magnetic flux is necessary to overcome negative reluctance torque.

Example 3.2-1:
Small ferrite permanent magnet 4-pole motor: 50 Hz, 130 V Y, 3.8 A, 340 W, efficiency 63%, power factor 0.63, shaft height 71 mm, totally enclosed, shaft-mounted fan:
$U_s = 130/\sqrt{3} = 75\,\mathrm{V}$, $U_p = 30$ V, $R_s = 3.9\,\Omega$, $X_d = 15.7\,\Omega$

Rated torque: $M_N = \dfrac{P_N}{\Omega_{syn}} = \dfrac{340}{(2\pi\cdot 1500/60)} = 2.16\,\mathrm{Nm}$

Estimated efficiency: $\eta = \dfrac{P_{out}}{P_{out} + 3R_sI_s^2} = \dfrac{340}{340+170} = 66.8\%$

Synchronous pull-out torque: $M_{p0} = \frac{m}{\Omega_{syn}} \cdot \frac{U_s U_p}{X_d} = \frac{3}{(2\pi \cdot 1500/60)} \cdot \frac{75 \cdot 30}{15.7} = 2.75\,\mathrm{Nm}$

Overload capability: $M_{p0} / M_N = 2.75 / 2.16 = 1.27$

3.3 Stress of permanent magnets at failures

a) Asynchronous operation due to pull-out:
When machine is loaded higher than maximum electromagnetic torque M_{p0} (pull-out torque), rotor is pulled out of synchronism by load torque. Rotor is running asynchronously, rotor currents are induced in rotor cage, generating an asynchronous torque. In motor operation stator field, running at synchronous speed, is now faster than turning rotor. So stator field will oppose rotor permanent magnet flux a certain instants ("**phase opposition**", Fig.3.3-1), causing danger of irreversible demagnetization of rotor magnets.

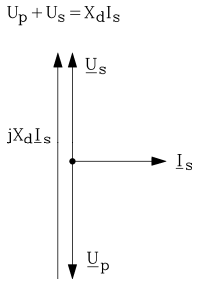

Fig.3.3-1: Phasor diagram at asynchronous operation at phase opposition (stator resistance neglected)

At that moment stator voltage and back EMF, induced by rotor magnets, are in phase opposition, causing a larger stator current flow than at rated condition:

$$I_s = \frac{U_s + U_p}{X_d} > I_N \qquad (3.3\text{-}1)$$

Permanent magnet flux consists of stray flux and air gap flux:

$$\Phi_M = \Phi_\sigma + \Phi_p \qquad (3.3\text{-}2)$$

Demagnetizing stator flux Φ_s acts opposite to air gap flux Φ_p, penetrating the magnets. In order to completely demagnetize the magnets $\Phi_{M,res} = \Phi_M - \Phi_s = 0$, the stator flux must overcome not only Φ_p, but also the permanent magnet stray flux Φ_σ. So, the unavoidable magnet´s stray flux has also its benefit. Comparing with surface mounted magnets, where this stray flux is rather small, the demagnetizing stator flux must be bigger by the ratio

$$\frac{\Phi_p + \Phi_\sigma}{\Phi_p} = 1 + \frac{\Phi_\sigma}{\Phi_p}$$

to cancel permanent magnet flux completely.

Conclusions:
Buried rotor magnets have a larger capability to withstand demagnetization by stator flux by the ratio of permanent magnet stray flux versus no-load air-gap flux.

In the same way the stray flux also protects the rotor magnets from demagnetization, when rotor is dismounted from stator, as stray flux is closing over rotor iron parts, independent of the rotor being in stator bore or not.

b) Sudden short circuit:
At sudden short circuit of stator winding the current in stator winding may become rather big. The flux linkage of stator field – excited by this transient current flow – with rotor cage changes suddenly and is inducing the rotor cage. Due to *Faraday´*s law $u_i = -d\psi/dt$ the rotor cage currents are in phase opposition with stator current, hence exciting an additional rotor flux, which opposes the stator flux. Therefore stator and rotor flux are more or less cancelling. The rotor magnets, lying below the rotor cage, are therefore protected from big flux penetration of stator flux due to the **screening effect of rotor cage**.

Conclusions:
Rotor cage acts as an electromagnetic screen for the underlying buried magnets in case of stator current transients.

3.4 Torque at asynchronous starting

Three torque components of different origin act together during asynchronous start-up. Two of these components have been already explained at start-up of synchronous reluctance machine with rotor squirrel cage. All three components consist of a constant torque component and an oscillating one.

a) Asynchronous starting torque:
Constant component is **average** asynchronous starting torque due to rotor cage currents with rotor frequency $f_r = s \cdot f_s$ (s: rotor slip) according to average stator inductance ($L_d + L_q$)/2. Due to difference ($L_q - L_d$) an oscillating part with frequency $2s \cdot f_s$ is added, as explained in Section 2.2. When reaching synchronous speed, both constant and oscillating torque vanish, as rotor cage is induced no longer, leading to vanishing rotor cage currents. Due to this asynchronous starting torque, the stator current also increases like in induction motors.

Example 3.4-1:
Permanent magnet synchronous six-pole motor, Ferrite magnets: Rated power at 50 Hz, 1000/min: 5.2 kW, rated current: 42 A, starting current: 220 A (524% !)

b) Asynchronous reluctance torque:
Rotor reluctance $L_q \neq L_d$ causes modulation of stator field, thus changing stator flux linkage with frequency $(2s-1) \cdot f_s$, leading to additional induced stator voltage of that frequency and additional stator current I_3. Fundamental space harmonics of air gap fields of stator currents I_s and I_3 produce constant asynchronous reluctance torque, which vanishes at $s = 0.5$ (***Goerges*-phenomenon**), as at this speed no current I_3 is induced. Both fields produce also an oscillating torque with rotor reluctance $L_q \neq L_d$ with frequency $2s \cdot f_s$, which is minimum at s = 0.5 due to vanishing current I_3.

At synchronism the frequency of I_3 is also f_s, therefore I_s and I_3 unite to one total resulting current I_s. Oscillating torque vanishes, and constant part of asynchronous reluctance torque become constant synchronous reluctance torque

$$M_{rel} = -\frac{p \cdot m}{\omega_s} \cdot \frac{U_s^2}{2} \left(\frac{1}{X_q} - \frac{1}{X_d}\right) \cdot \sin 2\vartheta \quad . \tag{3.4-1}$$

c) Permanent magnet braking torque during asynchronous start-up

The rotor permanent magnets induce the stator winding with frequency $f = n \cdot p$ (different to stator frequency f_s, as long as speed $n < n_{syn}$!), causing additional stator voltage $U_p = \omega \Psi_p / \sqrt{2}$. This voltage causes an additional stator current flow I_p, limited only by stator winding impedance, as no other voltage of this frequency is available on stator side. This current excites an additional fundamental air gap flux density which – along with the flux of the rotor magnets – generates a **constant braking torque** M_p. Further, this additional flux fundamental and the rotor magnets, rotating with speed n, generate with stator flux of stator current I_s, which rotates with n_{syn}, an **oscillating torque** with slip frequency $\Delta f = p \cdot (n_{syn} - n) = s \cdot f_s$. Constant braking torque is calculated by stator voltage equation for angular frequency $\omega = 2\pi \cdot f = 2\pi \cdot n \cdot p$:

$$0 = R_s \underline{I}_p + j\omega \underline{\Psi}_s / \sqrt{2} \tag{3.4-2}$$

With decomposition in *d*- and *q*-components due to $L_q \neq L_d$: $\underline{I}_p = I_{pd} + jI_{pq}$,

$\underline{\Psi}_s = \Psi_{sd} + j\Psi_{sq}$ we get

$$0 = R_s I_{pd} - \omega \Psi_{sq} / \sqrt{2} \qquad 0 = R_s I_{pq} + \omega \Psi_{sd} / \sqrt{2} \tag{3.4-3}$$

and flux linkage

$$\Psi_{sd} = \sqrt{2} \cdot L_d I_{pd} + \Psi_p \qquad \Psi_{sq} = \sqrt{2} \cdot L_q I_{pq} \quad . \tag{3.4-4}$$

Substituting flux linkages in (3.4-3) by the expressions (3.4-4), the *d*- and *q*-current components of that additional stator current are derived:

$$I_{pd} = -\frac{\omega L_q \cdot U_p}{R_s^2 + \omega L_d \cdot \omega L_q} \qquad I_{pq} = -\frac{R_s \cdot U_p}{R_s^2 + \omega L_d \cdot \omega L_q} \quad . \tag{3.4-5}$$

The losses in stator winding caused by this current have to be equal to the braking power acting on rotor due the braking torque M_p, generated by this current along with the rotor magnets.

$$P_{Cu} = 3R_s I_p^2 = 3R_s (I_{pd}^2 + I_{pq}^2) = \frac{3R_s U_p^2 \cdot (R_s^2 + \omega^2 L_q^2)}{(R_s^2 + \omega L_d \omega L_q)^2} = -\Omega_m M_p \tag{3.4-6}$$

$$\boxed{M_p = -\frac{3p \cdot R_s \cdot \omega \Psi_p^2 \cdot (R_s^2 + \omega^2 L_q^2)}{2 \cdot (R_s^2 + \omega L_d \omega L_q)^2} \qquad \omega = 2\pi \cdot n \cdot p < \omega_s} \tag{3.4-7}$$

Assuming for simplification $L_q = L_d$, maximum braking torque is derived by $dM_p / d\omega = 0$, occurring at speed

$$n^* = \omega^* / (2\pi p) = R_s / (2\pi p \cdot L_d) \tag{3.4-8}$$

with maximum value

$$M_{p,\max} = M_p(\omega^*) = \frac{3p}{2} \cdot \frac{\Psi_p^2}{2L_d} = \frac{3p}{2} \cdot \frac{U_{pN}^2}{\omega_N^2 L_d} \quad . \tag{3.4-9}$$

This maximum braking torque causes a reduction of asynchronous starting torque in saddle shape (Fig.3.4-1).

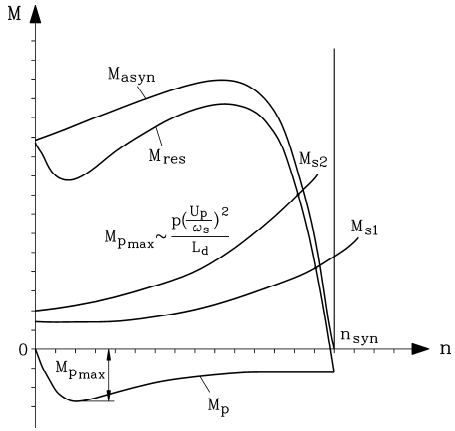

Fig.3.4-1: Average asynchronous starting torque M_{asyn} and permanent magnet braking torque M_p, yielding saddle shaped resulting torque M_{res}

Conclusions:

Permanent magnets cause a considerable decrease of asynchronous starting torque. Reduction of starting torque increases with increasing strength of permanent magnets. This choice of magnets is an optimum between necessary pull-out torque (strong magnets) and sufficient starting torque (weak magnets).

At synchronism frequency of additional stator current I_p is also frequency f_s, so I_p and I_s unite to total stator current. Due to $s = 0$ at synchronism oscillation vanishes and oscillating torque becomes constant synchronous torque

$$M_{syn} = -\frac{p \cdot m}{\omega_s} \cdot \frac{U_s U_p}{X_d} \sin \vartheta \quad . \tag{3.4-10}$$

Comparing all three torque components a), b), c), their constant values are dominated by a), which is reduced by c), whereas b) is rather small and may be often neglected. Oscillating torque with slip frequency of component c) is usually dominating, whereas components a) and

b) are much smaller. Thus, when measuring start-up torque with torque meter, this slip-frequent component is seen quite well (Fig.3.4-2).

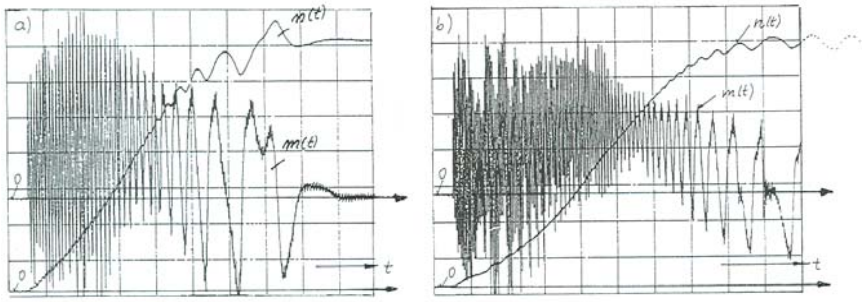

Fig.3.4-2: Measured time function of starting torque of PM synchronous machine with squirrel cage rotor at fixed stator voltage and frequency: a) Synchronisation of motor visible, b) Increased load inertia by factor 2.4: No synchronisation is possible (*Siemens AG*)

3.5 Synchronisation of machine after start-up

a) Synchronization process:
After start-up the rotor speed increases and will reach nearly synchronous speed. If only the asynchronous torque is acting, the load and inevitable friction torque will prevent the rotor to come into synchronism. It will operate at that load slip *s*. If that slip is low enough $s < s_{cr}$ ("critical slip"), it is possible that the rotating stator field "catches" the rotor either by force interaction with the rotor permanent magnets or due to the saliency of the rotor via the reluctance torque. Thus rotor is pulled into synchronism; then the slip is zero, the asynchronous torque vanishes and synchronous torque is moving the rotor.

b) Maximum pull-in slip (critical slip):
Below which critical slip the rotor will be pulled into synchronism? *Newton´*s law for calculating the rotor movement with the rotor angle γ_r (in electrical degrees) depend on the total inertia $J = J_L + J_M$ and the difference of electromagnetic and load torque.

$$\frac{J_M + J_L}{p} \cdot \frac{d^2\gamma_r}{dt^2} = M_e - M_s \qquad (3.5\text{-}1)$$

The electromagnetic torque $M_e = M_{syn} + M_{rel} + M_{asyn}$ consists of the synchronous torque M_{syn}, the reluctance torque M_{rel}, and the asynchronous torque due to the starting cage M_{asyn}. The asynchronous torque varies between *d*- and *q*-axis due to the saliency $L_d < L_q$ and has therefore two components: the average torque $M_{asyn,av}$ and the pulsating torque $M_{asyn,\sim}$ .The difference of stator and rotor angle $\Delta\gamma = \gamma_s - \gamma_r = \vartheta$ may be taken as time-varying load angle ϑ. At slipping rotor with small slip, passing the load angle from –180° to 180°, we can use the expressions for synchronous and reluctance torque (3.2-7) depending on ϑ (Fig.3.5-1).

$$\Delta\dot{\gamma} = \dot{\gamma}_s - \dot{\gamma}_r = (\Omega_{syn} - \Omega_m(t)) \cdot p = s(t) \cdot \omega_s \qquad (3.5\text{-}2)$$

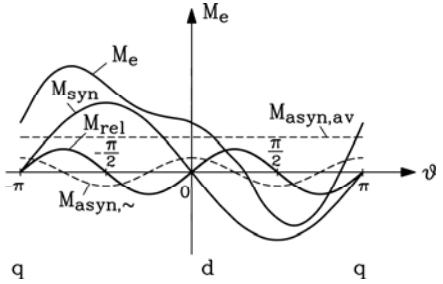

Fig. 3.5-1: Torque at low slip, rotor passing from –180° to 180°, when slipping by one pole pair

We get from (3.5-1) with $\Delta\ddot{\gamma} = \ddot{\gamma}_s - \ddot{\gamma}_r = \dot{s}(t) \cdot \omega_s$ and $\ddot{\gamma}_s = \dot{\Omega}_{syn} \cdot p = 0$:

$$-J \cdot \frac{\omega_s}{p} \cdot \frac{ds}{dt} = M_e(\vartheta(t)) - M_s \qquad . \qquad (3.5\text{-}3)$$

In the best case no load torque is applied: $M_s = 0$. We neglect the reluctance effect: $L_d = L_q$, so $M_{rel} = 0$, $M_{asyn,\sim} = 0$. At small slip $s << 1$ according to *Kloss´* function we can approximate with the asynchronous break-down torque and slip M_b, s_b (Chapter 4), that $M_{asyn,av}$ is nearly zero: $M_{asyn,av} \approx 2s \cdot M_b / s_b \cong 0$, so $M_e = M_{syn} + M_{rel} + M_{asyn} \approx M_{syn} = -M_{p0} \cdot \sin\vartheta$. At the time $t = 0$ the rotor position relative to the stator field is at $\vartheta_1 = -\pi$ and the rotor load slip $s_1 << 1$. The rotor passes from $\vartheta_1 = -\pi$ to $\vartheta_2 = 0$ during the time $t_s = 1/(2s_{av} \cdot f_s)$, being accelerated by M_{syn}, and will have then the smaller slip $s_2 < s_1$. So the average slip during that time interval is $s_{av} = (s_1 + s_2)/2$. The final chance to be pulled into synchronism is at $t = t_s$, because afterwards M_{syn} becomes negative (Fig. 3.5-1). So if $s_2 = 0$, the rotor synchronizes. The corresponding slip s_1 is then the maximum admissible slip s_{cr} for synchronization. At lower slip values $s < s_{cr}$ at $t = 0$ the rotor will synchronize already before the load angle reaches the position $\vartheta_2 = 0$. We assume the variation of ϑ from $-\pi$ to 0 linear with time *t* according to $\vartheta = -\pi + t \cdot \pi / t_s$.

$$\int_0^{t_s} -J \cdot \frac{\omega_s}{p} \cdot \frac{ds}{dt} \cdot dt = \int_{s_1}^{s_2} -J \cdot \frac{\omega_s}{p} \cdot ds = J \cdot \frac{\omega_s}{p} \cdot (s_1 - s_2) = J \cdot \frac{\omega_s}{p} \cdot s_1 = \int_0^{t_s} M_{syn}(\vartheta(t)) \cdot dt =$$

$$= \frac{t_s}{\pi} \int_{-\pi}^{0} -M_{p0} \cdot \sin(\vartheta) \cdot d\vartheta = \frac{t_s}{\pi} \cdot 2M_{p0} = \frac{1}{\pi \cdot 2s_{av} f_s} \cdot 2M_{p0} = \frac{1}{2\pi \cdot (s_1/2) \cdot f_s} \cdot 2M_{p0}$$

$$J \cdot \frac{\omega_s}{p} \cdot s_1 = \frac{1}{2\pi \cdot (s_1/2) \cdot f_s} \cdot 2M_{p0} \qquad (3.5\text{-}4)$$

From that condition with introduction of the synchronous pull-out torque

$$M_{p0} = \frac{3U_s U_p}{\Omega_{syn} X_d} = \frac{P_{p0}}{\Omega_{syn}} \qquad (3.5\text{-}5)$$

for $M_s = 0$ the **critical slip s_{cr}** is found, below which the rotor will synchronize. The condition for synchronization is therefore: $s < s_{cr}$.

$$s_1 = s_{cr} = \frac{1}{\Omega_{syn}} \cdot \sqrt{\frac{4M_{p0}}{J \cdot p}} = \frac{1}{\omega_s / p} \cdot \sqrt{\frac{2P_{p0}}{\pi \cdot (J_M + J_L) \cdot f_s}} \qquad (3.5\text{-}6)$$

With $M_s > 0$ this slip decreases according to $s_{cr} = s_{cr}\big|_{M_s=0} \cdot \sqrt{\zeta}$, with $\zeta(M_s = 0) = 1$. At a small load torque its influence is negligible. At $M_s/M_{p0} = 0.9$ critical slip has to be decreased already by 20 %. Then the critical slip rapidly decreases towards $s_{cr,min}$ with $\zeta(M_s = M_{p0}) = 0.22$ at $M_s/M_{p0} = 1$.

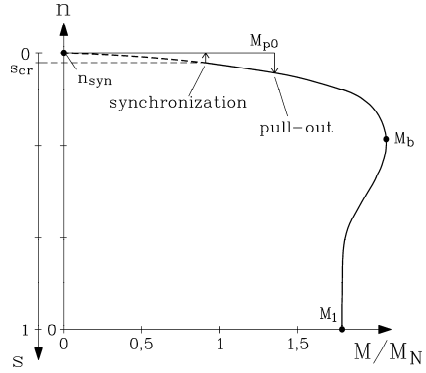

Fig.3.5-2: Start-up torque with pull-in slip and pull-out torque

Example 3.5-1:
Barium ferrite six-pole synchronous permanent magnet motor, shaft height 160mm, totally enclosed, fan-cooled: 50 ... 150 Hz, 1000 ... 3000/min, 125 ... 380 V Y, 42 A, rated torque 49.7 Nm, overload capability 150%.

Critical slip at 50 Hz and total momentum of inertia (motor and load): 1.5 kgm^2
- Rated power at 50 Hz: $P_N = (2\pi f_s / p) \cdot M_N = (2\pi \cdot 50/3) \cdot 49.7 = 5.2\,\text{kW}$
- Pull-out power: $P_{p0} = 1.5 P_N = 7.8\,\text{kW}$
- Critical slip at $M_s = 0$: $s_{cr} = \frac{1}{2\pi \cdot 50/3} \cdot \sqrt{\frac{2}{\pi} \cdot \frac{7800}{50 \cdot 1.5}} = 0.078 = 7.8\%$

Example 3.5-2:
Measured no-load start-up of barium ferrite synchronous motor with squirrel cage rotor (Fig.3.4-2) and additional momentum of inertia:
a) Motor synchronizes, b) Increase of moment of inertia by factor 2.4: no synchronization possible.

Note: The simplified calculation with critical slip will only reduce critical slip by factor $1/\sqrt{2.4} = 0.64$, whereas in reality no synchronization is possible. This can also be shown by numerical solution of dynamic equation (3.5-3).

Conclusions:
After start-up motor will synchronize within certain limits of maximum load torque and inertia at critical slip. Once running at synchronism, motor will be stable until static pull-out torque is surpassed. Hence, a "hysteresis" between pull-in and pull-out exists (Fig. 3.5-2).

3.6 Permanent magnet synchronous motor features and application

a) Motor features:
Motors are usually designed with pole counts 2, 4, 6, buried magnets and squirrel cage, utilizing flux concentration at 4 and 6 poles. Many parts such as stator housings etc. may be used form induction motor mass production. This and the cheap ferrite magnets should yield rather low motor manufacturing costs. No rotor position encoder is necessary, so often inverter is operating with fixed ratio "voltage/frequency" *U/f* without any additional motor control. At low speed voltage has to be increased above that ratio to consider voltage drop $R_s I_s$, which dominates at low speed.

- Motors must have sufficient overload capability (usually $M_{p0} \geq 1.35 M_N$ according to IEC 34-1)
- Machines are usually totally enclosed with shaft mounted fan or even without any cooling (Fig. 3.6-2)
- Quick braking of all motors is usually done by feeding stored kinetic energy in generator mode back to inverter, where it is usually transferred to dissipated heat in braking resistance, which is connected to DC link via chopping transistor.
- If only one motor of group drive has to brake, it is short-circuited by additional switch, using the braking torque M_p for slowing down the machine. Another possibility is the use of DC current injection in two phases of motor winding to brake the motor (**DC brake**).
- Asynchronous starting heats up the rotor, as for each no-load start up the same amount of energy is transferred into rotor as heat as is stored in rotor mass as kinetic energy (3.6-1). Under load conditions the thermal energy, transferred to the rotor during start up, even surpasses the amount of stored kinetic energy.

$$W_{r,thermal} = W_{r,kin} = J \frac{\Omega_m^2}{2} \qquad (3.6\text{-}1)$$

- Usually three asynchronous starts immediately one after the other must be possible. For thermal protection of stator winding temperature sensors such as PTC elements are used.
- At high speed asynchronous starting would take too long time, overheating the machine. In that case synchronous starting with variable stator frequency of inverter is used.

High speed application:
High speed is possible, typically up to 400 Hz with inverter supply.

Example 3.6-1:
Typical maximum speed of PM synchronous machines:
Shaft height 80 mm: 400 Hz, 2-pole: 24000/min

Shaft height 112 mm: 200 Hz, 2-pole: 12000/min,
4-pole: 6000/min,
6-pole: 4000/min

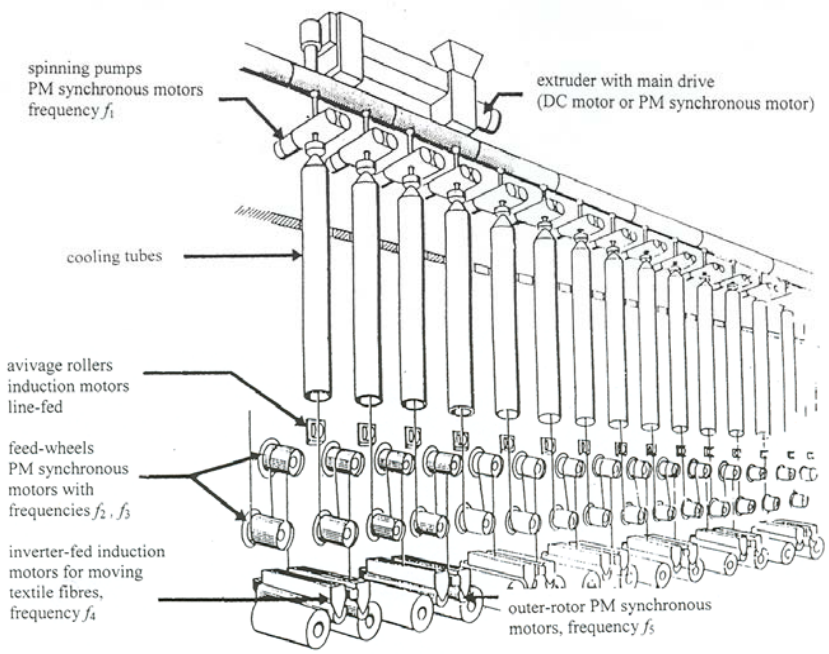

Fig. 3.6-1: PM synchronous motor group drives for synthetic thread fabrication (*Siemens AG*)

- High speed application needs reduction in motor power to keep bearing temperature below 80°C ... 90°C (average value between outer and inner race temperature). Otherwise lubrication grease will deteriorate very quickly. Demands are at least 20 000 h of life time for greased bearings. In order to avoid too much grease, which would increase friction losses in bearing, sometimes mechanical grease control is used at high speed 24000/min.
- First natural shaft bending frequency must be above maximum speed to avoid resonance excitation by rotor unbalance. In these cases shaft diameter is rather big to increase shaft stiffness.
- Iron losses increase with frequency, so special low loss iron sheets are used with e.g. 1.3 W/kg at 1 T, 50 Hz.
- Shaft-mounted fan would produce too much noise at high speed, so fan outer diameter is reduced for high speed applications.
- Additional eddy current losses in ferrite magnets are rather small, as electric conductivity of ferrite magnets is low.

b) Applications:
Main application is **synthetics textile industry**, where many parallel operating motors, fed from one inverter, pull thin threads (Fig. 3.6-1). Motors are operated as "group drive", running synchronously. From big extruder with molten plastic material is flowing to many parallel synchronously running spinning pumps, driven by PM synchronous motors at frequency f_1. The fibres are then pulled through cooling channels, where the synthetic fibres cool and get solid. Due to the pull the fibres are lengthening and therefore the pulling feed-wheel motors of next group drive have to run with a lower speed. Assuming same pole count of motors,

frequency has to be $f_2 < f_1$ and the next group with $f_3 < f_2$. Finally the fibres are wound up on cylindrical shafts, which are driven by friction via the surface of outer rotor PM motors (Fig. 3.6-2), running at lower speed $f_5 < f_3$. In between line-operated asynchronous motors are driving "avivage" rollers to smoothen the surface of the fibres, and others (operating at frequency f_4) are used to move the fibres on the outer rotor.

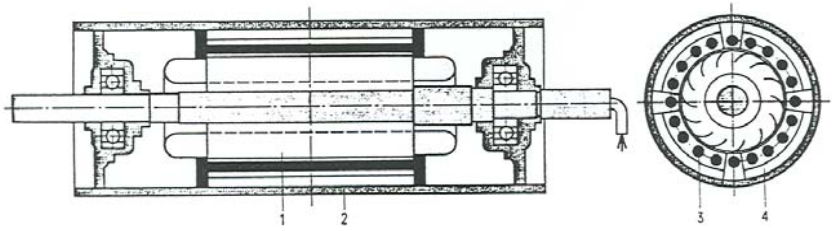

Fig. 3.6-2: Cross section of outer rotor 4-pole PM synchronous motor with ferrite surface mounted magnets and squirrel cage: 1: inner stator AC three-phase winding, 2: outer rotor iron back, 3: squirrel cage, 4: ferrite magnets (*Siemens AG*)

Other similar application is glass tube production, when tubes of glass are pulled out of the molten glass mass. In food production and packaging these motors are also used for moving transporting belts etc.

Advantages of PM synchronous motors:
Compared with induction motors:
- Constant speed without any motor control, no speed sensor and speed controller necessary
Compared with synchronous reluctance motors:
- 50 % ... 80 % increased value $\eta \cdot \cos\varphi$, thus inverter rating is reduced for same shaft power

4. Induction machines

4.1 Significance and features of induction machines

a) Basic function and different types of machines:
Induction machines are in the power range of 100 W up to several MW the most prominent motor applications, being the "working horse" of industrial drive systems, but also in domestic applications and in traction drives. Recently many induction machines are used as generators in wind-mill applications in the power range of several 100 kW up to about 5 MW in off-shore plants. Induction machines are built usually in low power range up to about 3 kW with single-phase and for increased power with three-phase AC windings. Rotor winding is always short-circuited. Synchronously rotating stator field – excited by the stator current, which is driven by stator voltage supply - will induce according to *Faraday´*s law in short-circuited rotor winding rotor currents, as long as rotor rotates asynchronously to stator field: $n \neq n_{syn}$. Rotor currents produce with stator field tangential *Lorentz* forces, thus generating **driving torque**, if $n < n_{syn}$ (sub-synchronous operation = **motor**) and **braking torque**, if $n > n_{syn}$ (super-synchronous operation = **generator**). That means that from stand-still n = 0 up to synchronous speed machine will rotate by itself as motor, whereas for generator a mechanical drive (turbine) has to drive the rotor faster than the rotating stator field. Ideal no-load is at $n = n_{syn}$, a because in that case no flux change in rotor occurs and therefore no voltage is induced in rotor, thus no rotor currents flow, hence yielding zero torque. Inevitable friction causes always some small load torque, so rotor will also at no-load rotate slightly below synchronous speed. Difference in speed is normalized as **slip**

$$\boxed{s = \frac{n_{syn} - n}{n_{syn}}} \quad , \qquad (4.1\text{-}1)$$

which at stand still equals 1 and at synchronous speed is zero, being negative in generator operation.

Rotor winding is most often a short circuited **squirrel cage** (Fig.4.1-1), which is cheap and robust, or sometimes a **short circuited three-phase wire-wound rotor winding**. Latter winding is usually star-connected with the three terminals connected to slip rings, being short circuited there. With these slip rings it is possible via sliding carbon brushes as contacts to connect additional rotor phase resistors. With this artificial increase of rotor resistance it is possible to raise motor starting torque at s = 1.

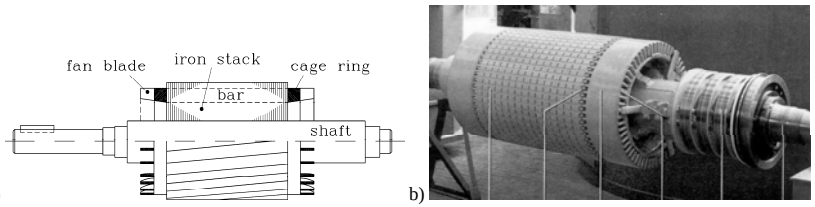

Fig.4.1-1: Rotor of induction machine: a) Squirrel cage, consisting of (here skewed) rotor bars and two outer rings, short circuiting the bars. Bars are inserted in slots in rotor iron stack. Here cage consists of die-cast aluminium. Note the additional "fan blades" on the outside of the cage rings to generate additional circulating air flow for rotor cage cooling. b) Wire-wound three phase winding with slip-ring per phase: 1: Rotor iron stack, 2: rotor winding, 3: bandage fixing winding overhang, 4: winding connection to slip rings, 5: slip rings, 6: shaft *(Siemens AG).*

Single-phase induction motors have stator windings, which consist of **two** phases a and b, displaced by half pole pitch, which are fed by currents i_a and i_b, phase shifted by 90°. Thus again a rotating stator field is generated, in the same way as it is done with three-phase winding, where the phases U, V, W are phase shifted by third of pole pair pitch, fed by three currents i_U , i_V and i_W, phase shifted by 120°. So this machine in reality is a two-phase machine. As no two-phase grid exists, motors are operated from single phase grid $U_N = U_a$. Second phase voltage U_b is generated by additional capacitor C, which is shifting current i_b by 90° with respect to i_a (Fig.4.1-2). As capacitor C is connected in series to stator phase winding b, this phase shift is only possible at certain slip (usually rated slip). At other speed values (e.g. no-load or starting) phase shift differs from 90°, so rotating field is not an ideal one. It changes amplitude during one revolution, thus causing additional losses due to eddy currents in stator and rotor iron stack, and additional pulsating torque, which causes the motor to vibrate with twice line frequency (e.g. at 50 Hz line frequency this is 100 Hz). For this reason this so-called "capacitor motor" is used only at low power below typically 3 kW due to the rather low efficiency of about 70% ... 75% in best case and due to the vibrations, mostly as 2- and 4-pole machines.

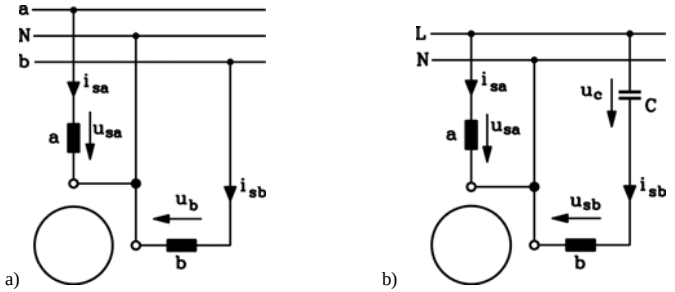

Fig.4.1-2: Two-phase induction motor: a) Operated from ideal two phase grid (which usually is not available in real world), b) operated from single phase grid, used for domestic application at low power below typically 3 kW

b) Features of standard motors:
As induction motors are widely used, these low voltage three-phase induction machines with squirrel cage rotor are **standardized**, independently from manufacturers, concerning
- shaft height (= motor size),
- distance of feet of motor housing or motor flange dimensions,
- rated power,
- shaft dimensions

between shaft height 56 mm and 315 mm (see standard IEC 72). Low voltage is defined as less than 1000 V and is standardized 230 V, 400 V, 690 V. These motors are totally enclosed, surface cooled with air by shaft mounted fan (TEFC: totally enclosed fan cooled, Fig.4.1-3). Pole numbers are usually 2, 4, 6, 8. Motors with higher pole counts are already considered special machines.

Example 4.1-1:
Standardized shaft heights (mm):

56	63	71	80	90	100	112	132	160	180	200	225	250	280	315

Standardized motor power (= mechanical shaft power = output power) (kW):

...	11	15	18.5	22	30	37	45	55	75	90	110	132	146	...

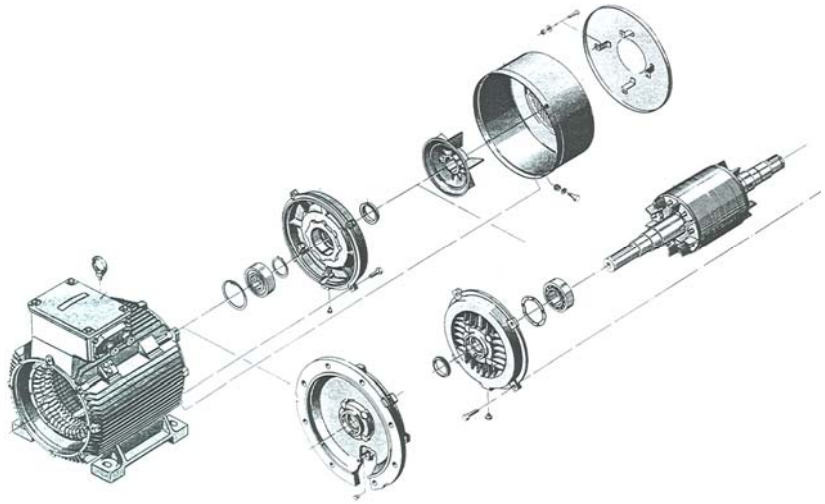

Fig.4.1-3: Standard induction motor: Motor elements for foot and flange type totally enclosed fan cooled squirrel cage machine (*Siemens AG*)

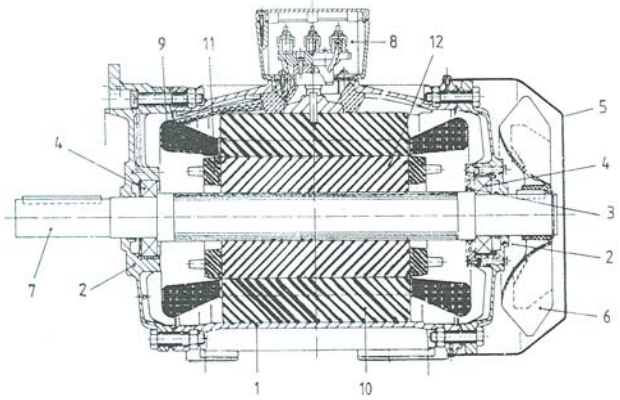

Fig.4.1-4: Cross section of standard induction machine (totally enclosed fan cooled squirrel cage machine), showing the main elements for foot (lower half of drawing) and flange type (upper half): 1: housing, 2: end-shield, 3: bearing lubrication, 4: bearing, 5: fan hood, 6: shaft-mounted fan, 7: shaft, 8: terminal box, 9: stator winding overhang, 10: stator iron stack, 11: rotor cage, 12: rotor iron stack (*Siemens AG*)

Example 4.1-2:
Standard induction motor (TEFC):
Rated data: 7.5 kW, 230 / 400 V, D/Y, 26.5 / 15.2 A, 50 Hz, 1455/min, $\cos\varphi$ = 0.82
Shaft height 132 mm, four poles $2p = 4$
Synchronous speed: $n_{syn} = f / p = 50/2 = 25/s = 1500/\min$
Rated slip: $s_N = (n_{syn} - n_N)/n_{syn} = (1500 - 1455)/1500 = 3\%$

Above motor frame size 315 mm still main dimensions of motor housings are standardized in IEC72 with shaft height 355 mm, 400 mm, 450 mm, but corresponding power ratings vary with different manufacturers, lying in the range of 355 kW ... 1000 kW for 4-pole machines. Most of the induction machines in the world are operated directly from the grid. Rotor is running with rated slip, which is usually only several percent, so speed is near synchronous speed at load and nearly synchronous speed at no-load (only friction is then loading the rotor).

Conclusions:
Line operated induction motors are regarded as fixes speed drives, as rated speed is only a few percentages below synchronous speed, so speed variation between no-load and load is small.

c) Stator winding features:
Note that on motor plate always rated voltage is line-to-line voltage and rated current is line current in motor cables. For **delta connection** line-to-line voltage is identical with phase voltage, but line current is larger by $\sqrt{3}$ than phase current. For **star connection** line-to-line voltage is larger by $\sqrt{3}$ than phase voltage, but line current and phase current are identical (Fig.4.1-5).

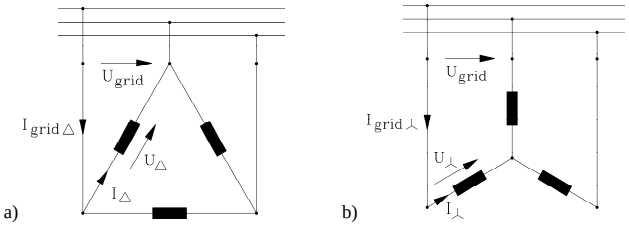

Fig.4.1-5: Three-phase stator winding can be connected either in a) delta connection or b) star connection

Example 4.1-2:
Standard induction motor (TEFC):
Rated data: 7.5 kW, 230 / 400 V, D/Y, 26.5 / 15.2 A, 50 Hz, 1455/min, $\cos\varphi$ = 0.82

Winding connection	*delta*	*star*
Phase voltage	230 V	230 V
line-to-line voltage	230 V	400 V
Phase current	15.2 A	15.2 A
Line current	26.5 A	15.2 A

From that data we can calculate electric input power for motor operation at rated slip with line values. Of course this input power is the **same** for delta or star connected stator winding.

Delta connection (D): $P_e = \sqrt{3} U_N I_N \cos\varphi = \sqrt{3} \cdot 230 \cdot 26.5 \cdot 0.82 = 8656\,\mathrm{W}$
Star connection (Y): $P_e = \sqrt{3} U_N I_N \cos\varphi = \sqrt{3} \cdot 400 \cdot 15.2 \cdot 0.82 = 8656\,\mathrm{W}$

Electric input power can also be calculated with phase values, which are identical for delta and star connection: $P_e = 3 U_s I_s \cos\varphi = 3 \cdot 231 \cdot 15.2 \cdot 0.82 = 8656\,\mathrm{W}$.

Motor rated efficiency: $\eta_N = \frac{P_{out}}{P_{in}} = \frac{P_m}{P_e} = \frac{7500}{8656} = 86.6\%$

In order to **change speed** at line operation (fixed frequency), according to $n \approx n_{syn} = f / p$, number of pole pairs has to be changed. This is accomplished either by two (or three) different windings in stator slots with different coil span and coil arrangement, thus generating stator fields with different pole pitch and therefore different pole numbers (e.g. 2 poles and 6 poles). Some **special windings** allow by changing coil connections operation with different pole count with one and the same winding, e.g. *Dahlander*-winding: $2p_1 : 2p_2 = 1:2$.

Stator winding itself is usually **single layer round wire winding**, as it is cheap. Thermal overload capability of winding is described by service factor SF, which gives the additional steady state power of the machine at the cost of an additional temperature rise of 10 K.

Example 4.1-3:
Service factor SF = 1.15, rated power 7.5 kW, winding has Thermal Class F, which means that average temperature of stator winding does not exceed 105 K at maximum 40°C ambient temperature according to IEC60034-1.
Measured temperature rise at 7.5 kW: 90 K < 105 K.
Temperature rise at $SF \cdot P_N = 1.15 \cdot 7.5 = 8.625$ kW: 100 K < 105 K.

d) Applications of line-fed induction machines:

d1) Line-fed machines (fixed speed drives):
Industrial drives for pumps, fans, production machines in different branches such as saw mills, mechanical tooling, applications such as sawing, drilling, milling, grinding, polishing etc. machines, so it is really a **multi-purpose drive**. In chemical plants, oil drilling platforms, oil refining (petro-chemistry), ... these motors are available as **explosion proof machines** with the following different features:

- EEx e: Motor surface temperature stays below certain temperature limit. In case of over-heating motor is switched off.
- EEx p: Air pressure in motor is slightly larger than that of ambient air. Thus no explosive gas might intrude into motor, hence avoiding explosion hazard.
- EEx d: Motor housing is very strong designed to withstand over-pressure, if explosion happens inside motor (EN50014 ... EN50020)

During asynchronous starting current of motor increases up to 5 ... 8-times rated current, which is rather big. This current is reduced (in likewise starting torque)
- by switching motor first in Y, and then in D-connection or
- by special part winding to reduce stator phase voltage,
- by thyristor-controlled voltage reduction.

d2) Inverter-fed machines (variable speed drives):
According to $n \approx n_{syn} = f / p$ speed can be changed continuously by changing stator frequency with inverters. Percentage of inverter-fed standard induction machines is steadily increasing, pushing back the thyristor-controlled classic DC drives in different applications such as extruding plastics, production of wires, even in paper and foil production, as smooth torque is also possible with inverter fed induction machines with pulse width modulation of inverter output voltage (PWM). At low speed, fan is generating only little air flow, so due to that bad cooling torque has to be reduced.

Further, special induction motors for inverter-operation are available, mostly for higher speed and for wide field weakening range, where constant output power is needed. Typically these motors are cooled by external fan, so that they can produce full rated torque also at stand still. Pole counts are 2- and mainly 4-pole, machines being used in tooling machinery and other special applications.

4.2 Fundamental wave model of line-operated induction machine

a) Fundamental stator air gap wave:
Here only the three-phase machine is considered, but by substituting stator phase count 3 by phase count m_s in the derived equations, model is valid for arbitrary phase counts. The three sinusoidal stator phase currents i_U, i_V, i_W have all the same amplitude $\hat{I}_s$ and r.m.s. value $I_s = \hat{I}_s / \sqrt{2}$, same frequency f_s, but are phase shifted by 120° each ($\omega_s = 2\pi f_s$), e.g. in phase U: $i_s = \hat{I}_s \cdot \sin(\omega_s t)$. With distributed AC winding, each phase shifted by $2\tau_p / 3$, as explained in Chapter 1, a moving air gap flux density is excited by the three phase current system. The shape of air gap flux density distribution is step-like because of the coil sides concentrated in slots and slot openings neglected (air gap width δ) (Fig.1.1.1-1). *Fourier* analysis yields a sinusoidal distributed space fundamental air gap flux density wave (x_s: stator circumference co-ordinate)

$$B_s(x_s, t) = B_s \cdot \cos(\frac{x_s \pi}{\tau_p} - \omega_s t) \quad , \tag{4.2-1}$$

moving with circumference speed

$$\frac{x_s \pi}{\tau_p} - \omega_s t = const. \quad \Rightarrow \quad v_{syn} = \frac{dx_s}{dt} \quad \Rightarrow \quad v_{syn} = 2 f_s \tau_p \quad , \tag{4.2-2}$$

which corresponds with rotational speed $n_{syn} = f_s / p$. Amplitude of that fundamental wave is - with assumed infinite iron permeability, number of turns per phase N_s and definition of stator winding factor k_{ws} according to Chapter 1 -

$$B_s = \frac{\mu_0}{\delta} \cdot \frac{m_s}{\pi \cdot p} \cdot N_s k_{ws} \hat{I}_s \quad . \tag{4.2-3}$$

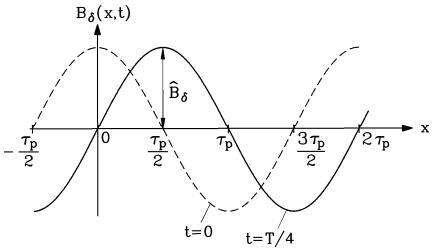

Fig.4.2-1: Fundamental air gap wave moving with speed v_{syn}. After e.g. quarter of period of stator current oscillation $T/4 = 1/(4f_s)$ wave has moved by half pole pitch: $v_{syn}T/4 = 2f_s\tau_p/(4f_s) = \tau_p/2$.

Stator flux per pole is

$$\Phi_s(t) = l_{Fe}\int_0^{\tau_p} B_s(x_s,t)\cdot dx_s = l_{Fe}\int_0^{\tau_p} B_s\cdot\cos\left(\frac{x_s\pi}{\tau_p}-\omega_s t\right)\cdot dx_s = -\frac{2}{\pi}\tau_p l_{Fe}B_s\cdot\sin(\omega_s t) \quad , \quad (4.2\text{-}4)$$

which is pulsating with stator frequency and therefore induces each phase of stator winding according to *Faraday´*s law with "self-induced" voltage

$$u_{i,ss} = -k_{ws}N_s\cdot d\Phi_s(t)/dt = \omega_s\cdot k_{ws}N_s\cdot\frac{2}{\pi}\tau_p l_{Fe}B_s\cdot\cos(\omega_s t) \quad , \quad (4.2\text{-}5)$$

which may also be described with **self-inductance L_{sh}** e.g. for phase U, as it was already described in Chapter 1 for synchronous machine, which has identical stator winding arrangement:

$$u_{i,ss} = L_{sh}\cdot di_s/dt \quad \Rightarrow \quad L_{hs} = \mu_0(N_s k_{ws})^2\cdot\frac{2m_s}{\pi^2 p}\cdot\frac{\tau_p l_{Fe}}{\delta} \quad (4.2\text{-}6)$$

As all voltages and currents vary sinusoidal, the advantage of **complex calculus** is usually used, e.g. self-induced voltage (with an arbitrarily chosen phase shift α_s)

$$u_{i,ss}(t) = \hat{U}_{i,ss}\cdot\cos(\omega_s t+\alpha_s) = \mathrm{Re}\left(\hat{U}_{i,ss}e^{j(\omega_s t+\alpha_s)}\right) = \mathrm{Re}\left(\sqrt{2}\underline{U}_{i,ss}e^{j\omega_s t}\right) \quad , \quad (4.2\text{-}7)$$

where instead of time function $u_{i,ss}(t)$ the complex number $\underline{U}_{i,ss} = U_{i,ss}e^{j\alpha_s}$ is used with r.m.s. value of $U_{i,ss}$. Thus we get instead of (4.2-6), considering the 90° phase shift from $\sin(\omega_s t)$ of current to $\cos(\omega_s t)$ of voltage by multiplication with $j=\sqrt{-1}$:

$$\underline{U}_{i,ss} = j\omega_s L_{hs}\cdot\underline{I}_s \quad . \quad (4.2\text{-}8)$$

b) Induced rotor voltage and currents:

Rotor cage may be considered as a short circuited winding system with $m_r = Q_r$ rotor phases, as each rotor bar is one independent rotor phase with its bar current as rotor phase current. Each rotor phase consists only of one bar, which is a "coil" with a half-winding: $N_r = 1/2$. Therefore distributed winding per phase is possible, hence rotor winding factor is $k_{wr} = 1$. **Induced voltage per rotor phase** (= per rotor bar) is calculated in the same way, defining **mutual inductance M_{rs}** between stator and rotor winding:

$$u_{i,rs} = -k_{wr}N_r\cdot\frac{d\Phi_s(t)}{dt} = M_{rs}\cdot di_s/dt \quad \Rightarrow \quad M_{rs} = \mu_0\cdot N_r k_{wr}N_s k_{ws}\cdot\frac{2m_s}{\pi^2 p}\cdot\frac{\tau_p l_{Fe}}{\delta} \quad (4.2\text{-}9)$$

$$\underline{U}_{i,rs} = j\omega_r M_{rs}\cdot\underline{I}_s \quad . \quad (4.2\text{-}10)$$

Note that due to rotor movement with speed n relative to stator space fundamental wave speed n_{syn} the **rotor frequency** is

$$\boxed{f_r = s\cdot f_s} \quad . \quad (4.2\text{-}11)$$

Rotor induced voltage per bar causes rotor bar currents I_r. The Q_r sinusoidal rotor bar currents $i_{r,1}, i_{r,2}, \ldots i_{r,Q_r}$ have all the same amplitude $\hat{I}_r$ and r.m.s. value $I_r = \hat{I}_r/\sqrt{2}$, same frequency f_r, but are phase shifted by $2\pi/(Q_r/p)$, because one pole pair - corresponding with Q_r/p rotor bars - is stator flux wave space period (Example 4.2-1).

Example 4.2-1:

Rotor cage with Q_r = 28 rotor bars, induced be 4 four-pole stator wave. Phase shift between adjacent rotor bar currents is therefore: $2\pi/(Q_r/p) = 2\pi/(28/2) = \pi/7$

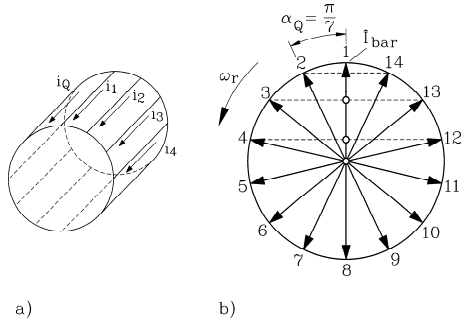

Fig. 4.2-2: Squirrel cage rotor: a) Rotor cage with Q_r = 28 rotor bars, induced by 4-pole stator wave. b) Rotor bar currents are phase shifted by $\pi/7$.

c) Fundamental rotor air gap wave:

According to (4.2-7) actual rotor current values at each time instant is given by real part of complex rotor currents, which is e.g. for Example 4.2-1 at t = 0 vertical part of current phasors $\underline{I}_r$ in Fig.4.2-2. With actual value rotor current distribution e.g. at t = 0 (Fig.4.2-3) *Ampere´*s law yields the **rotor air gap flux density** B_r and its m.m.f. $H_r\delta = (B_r/\mu_0)\cdot\delta = V_r$ again as step-like function with steps at rotor slot locations. Comparing with Fig. 1.1.1-1 we note, that step-like rotor flux density distribution fits much better to sinusoidal distribution than stator flux density step function. This is due to the much bigger phase number in rotor.

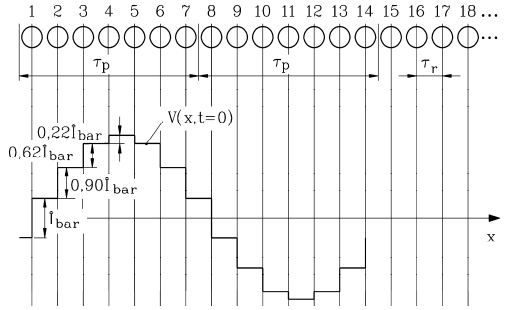

Fig. 4.2-3: Distribution of rotor bar currents and rotor m.m.f. V (proportional to air gap flux density in case of infinite iron permeability and constant air gap) along rotor circumference for example Q_r/p = 14 at t = 0

***Fourier* analysis** yields a sinusoidal distributed space fundamental air gap flux density wave (x_r: rotor circumference co-ordinate, fixed with rotor reference frame)

$$B_r(x_r,t) = B_r\cdot\cos(\frac{x_r\pi}{\tau_p}-\omega_r t) \quad , \quad (4.2\text{-}12)$$

moving with circumference speed $v_{syn,r} = 2f_r\tau_p$ or $n_{syn,r} = f_r/p$ relative to rotor, having the amplitude

$$B_r = \frac{\mu_0}{\delta} \cdot \frac{m_r}{\pi \cdot p} \cdot N_r k_{wr} \hat{I}_r \quad . \tag{4.2-13}$$

Adding rotor mechanical speed, this flux wave rotates relative to stator with synchronous speed: $n_{syn,r} + n = f_r / p + n_{syn} \cdot (1-s) = s f_s / p + f_s / p \cdot (1-s) = f_s / p = n_{syn}$. Therefore rotor fundamental induces rotor cage with rotor frequency (self-induction) $U_{i,rr}$ and stator winding with stator frequency (mutual induction) $U_{i,sr}$, calculating the corresponding inductance values in the same way as **for stator space fundamental**.

$$\underline{U}_{i,rr} = j\omega_r L_{hr} \cdot \underline{I}_r \quad \Rightarrow \quad L_{hr} = \mu_0 (N_r k_{wr})^2 \cdot \frac{2m_r}{\pi^2 p} \cdot \frac{\tau_p l_{Fe}}{\delta} \quad . \tag{4.2-14}$$

$$\underline{U}_{i,sr} = j\omega_s M_{sr} \cdot \underline{I}_r \quad \Rightarrow \quad M_{sr} = \mu_0 \cdot N_r k_{wr} N_s k_{ws} \cdot \frac{2m_r}{\pi^2 p} \cdot \frac{\tau_p l_{Fe}}{\delta} \quad . \tag{4.2-15}$$

d) Stator and rotor voltage equation:
So finally per phase a **stator and rotor voltage equation** is derived, considering also self-induced voltage by stray flux of slots and winding overhangs (inductance $L_{s\sigma}, L_{r\sigma}$) and voltage drop due to resistance R_s, R_r. Stator phase voltages are balanced by grid voltage U_s and rotor is short-circuited: $U_r = 0$.

$$\underline{U}_s = R_s \underline{I}_s + j\omega_s L_{s\sigma} \underline{I}_s + j\omega_s L_{sh} \underline{I}_s + j\omega_s M_{sr} \underline{I}_r \tag{4.2-16}$$
$$0 = R_r \underline{I}_r + j\omega_r L_{r\sigma} \underline{I}_r + j\omega_r L_{rh} \underline{I}_r + j\omega_r M_{rs} \underline{I}_s \tag{4.2-17}$$

Both voltage equations remain unchanged, if the factors $\ddot{u}_U$, $\ddot{u}_I$ are introduced in the following way:

$$\underline{U}_s = R_s \underline{I}_s + j\omega_s L_{s\sigma} \underline{I}_s + j\omega_s L_{sh} \underline{I}_s + j\omega_s (\ddot{u}_I M_{sr})(\underline{I}_r / \ddot{u}_I) \tag{4.2-18}$$
$$0 = (\ddot{u}_U \ddot{u}_I R_r) \frac{\underline{I}_r}{\ddot{u}_I} + j\omega_r (\ddot{u}_U \ddot{u}_I L_{r\sigma}) \frac{\underline{I}_r}{\ddot{u}_I} + j\omega_r (\ddot{u}_U \ddot{u}_I L_{rh}) \frac{\underline{I}_r}{\ddot{u}_I} + j\omega_r (\ddot{u}_U M_{rs}) \underline{I}_s \quad . \tag{4.2-19}$$

If these two factors are defined as

$$\ddot{u}_U = \frac{N_s k_{ws}}{N_r k_{wr}}, \quad \ddot{u}_I = \frac{m_s N_s k_{ws}}{m_r N_r k_{wr}} \quad , \tag{4.2-20}$$

a simple result is achieved (compare (4.2-9), (4.2-14), (4.2-15) !), which is called **main inductance L_h**:

$$\boxed{L_{sh} = M_{sr} \ddot{u}_I = \ddot{u}_U M_{rs} = \ddot{u}_U \ddot{u}_I L_{rh} = L_h} \tag{4.2-21}$$

With that and the abbreviations

$$I'_r = I_r / \ddot{u}_I, \; R'_r = \ddot{u}_U \ddot{u}_I R_r, \; L'_{r\sigma} = \ddot{u}_U \ddot{u}_I L_{r\sigma} \tag{4.2-22}$$

stator and rotor equations are much shorter:

$$\begin{aligned} \underline{U}_s &= R_s \underline{I}_s + j\omega_s L_{s\sigma} \underline{I}_s + j\omega_s L_h (\underline{I}_s + \underline{I}'_r) \\ 0 &= R'_r \underline{I}'_r + j\omega_r L'_{r\sigma} \underline{I}'_r + j\omega_r L_h (\underline{I}_s + \underline{I}'_r) \end{aligned} \tag{4.2-23}$$

Substituting $\omega_r = s\omega_s$ and dividing rotor voltage equation by *s*, only stator frequency remains at the cost of an **"artificial" rotor resistance R'_r / s :**

$$\begin{aligned} \underline{U}_s &= R_s \underline{I}_s + j\omega_s L_{s\sigma} \underline{I}_s + j\omega_s L_h (\underline{I}_s + \underline{I}'_r) \\ 0 &= (R'_r / s) \underline{I}'_r + j\omega_s L'_{r\sigma} \underline{I}'_r + j\omega_s L_h (\underline{I}_s + \underline{I}'_r) \end{aligned} \tag{4.2-24}$$

These two equations correspond with the **equivalent T-circuit** (Fig.4.2-4) with the **reactance** $X_{s\sigma} = \omega_s L_{s\sigma}$, $X_h = \omega_s L_h$, $X'_{r\sigma} = \omega_r L'_{r\sigma}$ and the "**magnetizing current**" $\underline{I}_m = \underline{I}_s + \underline{I}'_r$, which is given by the superposition of stator and rotor fundamental wave in air gap as resulting air gap flux density.

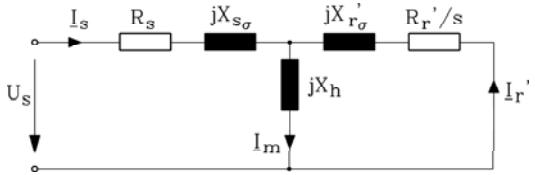

Fig.4.2-4: Equivalent circuit of induction machine, considering fundamental space harmonics and sinusoidal stator and rotor current and voltages

e) Current and torque of induction machine:
Solution of (4.2-24) for **stator and rotor current** is

$$\boxed{\underline{I}_s = \underline{U}_s \frac{R'_r + jsX'_r}{(R_s R'_r - s \cdot \sigma \cdot X_s X'_r) + j(s \cdot R_s X'_r + X_s R'_r)}} \tag{4.2-25}$$

$$\boxed{\underline{I}'_r = -\underline{I}_s \frac{jX_h}{\frac{R'_r}{s} + jX'_r}} \quad , \tag{4.2-26}$$

using as abbreviation the **stray coefficient σ**, which is the ratio of stray flux versus total flux and lies in the range of typically 8 ... 10%.

$$\boxed{\sigma = 1 - \frac{X_h^2}{X_s X'_r}} \qquad (X_s = X_h + X_{s\sigma}, \;\; X'_r = X_h + X'_{r\sigma}) \tag{4.2-27}$$

The **no-load current** at synchronous speed (s = 0) is necessary to magnetize the air gap flux completely by stator current, which induces back EMF $X_h I_{s0}$ to balance stator voltage; it ranges between 30 ... 50% of rated current, and it is nearly reactive.

$$\underline{I}_{s0} = \underline{I}_s (s=0) = \frac{\underline{U}_s}{R_s + jX_s} \approx -j \frac{\underline{U}_s}{X_s} \tag{4.2-28}$$

At starting (stand still, *s* = 1) **starting stator** current is 10 ... 12 times larger than no-load current (5 ... 6-times rated current) and nearly the same as for infinite slip (Fig.4.2-5):

$$\underline{I}_{s1} = \underline{I}_s (s=1) \approx -j \underline{U}_s \frac{1}{\sigma \cdot X_s} \tag{4.2-29}$$

Conclusions:
Stator current in induction machines is already necessary at no-load to magnetize air gap flux. At stand still (unity slip) equivalent rotor current I'_r is nearly as big as stator current, but with opposite phase. Hence rotor flux is opposite to stator flux. Therefore a very big stator current is needed to magnetize resulting air gap flux equal to the value at no-load to induce necessary back EMF to balance stator voltage. The same is true for big negative slip in generator mode.

Power balance of equivalent circuit shows for motor operation, that electrical input power

$$P_e = 3 \cdot \mathrm{Re}\left(\underline{U}_s \cdot \underline{I}_s^*\right) \quad (\underline{I}_s^*: \text{conjugate complex number of } \underline{I}_s) \tag{4.2-30}$$

minus stator copper losses $P_{Cu,s}$ must be the air gap power P_δ, transferred to rotor, where it must be equal to rotor copper losses $P_{Cu,r}$ and mechanical output power P_m.

$$P_\delta = P_e - P_{Cu,s} = P_e - m_s R_s I_s^2 = P_{Cu,r} + P_m = m_r R_r I_r^2 + P_m = m_s R'_r I'^2_r + P_m \tag{4.2-31}$$

From equivalent circuit we see that

$$P_\delta = m_s \cdot (R'_r / s) \cdot I'^2_r \quad . \tag{4.2-32}$$

Therefore we get for electromagnetic torque M_e from

$$P_m = \Omega_m M_e = (1-s)\Omega_{syn} M_e \tag{4.2-33}$$

and the comparison of (4.2-31) and (4.2-32) the following expression

$$M_e = \frac{P_m}{(1-s)\Omega_{syn}} = \frac{\left(\frac{1}{s}-1\right)\cdot m_s R'_r I'^2_r}{(1-s)\Omega_{syn}} = \frac{m_s R'_r I'^2_r}{s \cdot \Omega_{syn}} \quad . \tag{4.2-34}$$

By taking the absolute value of I'_r, I_s from (4.2-25), (4.2-26), **asynchronous torque** from (4.2-34) is derived, depending on the square of stator voltage and depending on slip s:

$$\boxed{M_e = m_s \frac{p}{\omega_s} U_s^2 \frac{s(1-\sigma) X_s X'_r R'_r}{(R_s R'_r - s\sigma X_s X'_r)^2 + (s R_s X'_r + X_s R'_r)^2}} \tag{4.2-35}$$

Conclusions:
- Asynchronous torque depends on the square of stator voltage.
- At no-load (s = 0) torque is zero.
- At infinite positive and negative slip torque is also zero.
*- Between s = 0 and s = ±∞ there exists maximum motor and generator torque (**motor break down torque $M_{b,mot}$** and **generator break down torque $M_{b,gen}$**.*
If at motor operation load torque surpasses break down torque, rotor is pulled down to stand still.

With neglected stator resistance torque equation simplifies:

$$\boxed{M_e = m_s \frac{p}{\omega_s} U_s^2 \frac{(1-\sigma)}{X_s} \frac{s R'_r X'_r}{(s\sigma X'_r)^2 + R'^2_r}} \quad (R_s = 0) \tag{4.2-36}$$

Maximum torque is derived by $dM_e / ds = 0$, yielding **break down slip**

$$s_b = \pm \frac{R'_r}{\sigma X'_r} \quad (+: \text{motor}, -: \text{generator}) \tag{4.2-37}$$

and **break down torque**

$$\boxed{R_s = 0: \quad M_b = \pm \frac{m_s}{2} \frac{p}{\omega_s} U_s^2 \frac{1-\sigma}{\sigma X_s}} \quad (+: \text{motor}, -: \text{generator}) \quad . \tag{4.2-38}$$

Using M_b and s_b, torque equation (4.2-36) looks very simple (so-called ***Kloss* function**)

$$\boxed{R_s = 0: \quad \frac{M_e}{M_b} = \frac{2}{\frac{s_b}{s} + \frac{s}{s_b}}} \tag{4.2-39}$$

With $R_s > 0$ value of generator break down torque is bigger than motor break down torque (Fig. 4.2-5), but generator and motor slip have still the same absolute value.

Example 4.2-2:
Torque-speed and stator current-speed curve of induction machine:
Data: R_s/X_s =1/100, R_r/X_r = 1.3/100, σ = 0.067, $X_s = X'_r = 3Z_N$, $Z_N = U_N/I_N$
Due to $n = (1-s)\cdot f_s / p$ torque and current may be depicted either in dependence of slip or in dependence of rotor speed n (Fig.4.2-5).

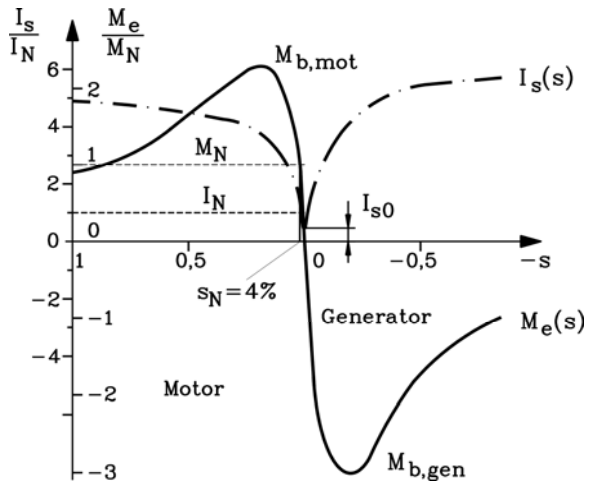

Fig.4.2-5: Torque M_e and stator current I_s depending on slip s (R_s/X_s =1/100, R_r/X_r = 1.3/100, σ = 0.067, $X_s = X'_r = 3Z_N$, $Z_N = U_{N,s}/I_{N,s}$)

f) Rotor current displacement for increased starting torque:
Fig.4.2-5 shows 5 times rated current as starting current, but starting even a little bit lower than rated torque. How to increase starting torque ? According to (4.2-34) increase of rotor resistance will increase torque at $s = 1$:

$$M_e(s=1) = \frac{m_s R'_r I'^2_r}{\Omega_{syn}} \quad . \tag{4.2-40}$$

For wire wound rotor induction machine with slip rings it is possible via sliding carbon brushes as contacts to connect additional rotor phase resistors to increase rotor resistance to raise motor starting torque at $s = 1$. But how is this possible with cage rotors ? If rotor bar is made with big bar height h_{bar} ("**deep bar**"), the rotor slot stray flux will be rather big. It oscillates with rotor frequency, which equals stator frequency at stand still.

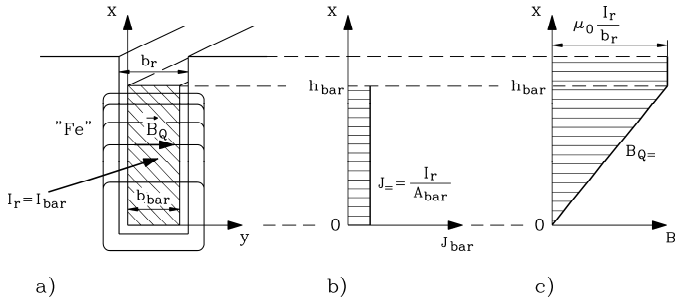

Fig. 4.2-6: Rotor deep bar : a) Rotor slot stray flux lines crossing the bar, b) rotor bar current density without current displacement, c) distribution of rotor slot stray flux density

With *Ampere´*s law we get for rotor stray flux density a linear rise within bar and constant value above bar:

$$\oint_C \vec{H} \cdot d\vec{s} = H_Q(x) \cdot b_r = J \cdot x \cdot b_{bar} \quad \Rightarrow$$

$$B_Q(x) = \mu_0 J \frac{x \cdot b_{bar}}{b_r} = \mu_0 \frac{I_r}{b_r} \cdot \frac{x}{h_{bar}} \qquad 0 \le x \le h_{bar} \tag{4.2-41}$$

$$B_Q = \mu_0 \frac{I_{bar}}{b_r} \qquad h_{bar} \le x \le h_Q \tag{4.2-42}$$

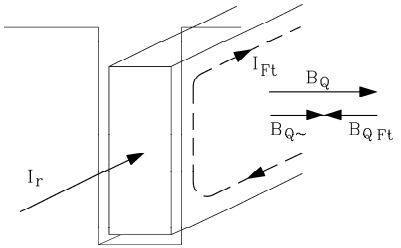

Fig. 4.2-7: Eddy current I_{Ft} in deep bar excites additional slot flux density opposite to slot stray flux B_Q, which is excited by bar current I_r

This rotor slot flux induces according to *Faraday´*s law $u_i = -d\Phi_Q / dt$ an additional voltage in the bar, which causes eddy current I_{Ft} flow (Ft: *Foucault*-current) in the bar. Due to negative sign in *Faraday´*s law direction of eddy current flow is as to excite an additional slot flux density B_{QFt} which is opposing the original slot flux density (Fig. 4.2-7). Superposition of bar current and eddy current yields increased current density at upper bar edge and reduction of current density at bottom of slot (Fig. 4.2-8).

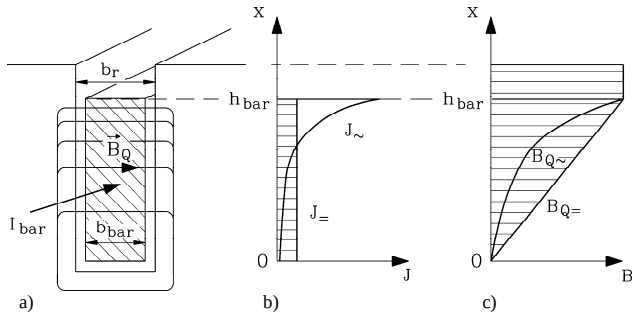

Fig. 4.2-8: **Current displacement in deep bar** at frequency f_s in comparison to DC current situation (near slip $s = 0$). a) Slot and bar cross section with slot stray flux lines, b) bar current density distribution with/without current displacement, c) slot flux density distribution with/without current displacement

As current flows mainly in upper part of deep bar, this acts like an increase of rotor resistance, which is easily understood by the following simplified current density distribution. Assume that current flows only in bar section height d_E with increased density $J_\sim$, then we get

$$I_r = b_{bar} h_{bar} J_= = b_{bar} d_E J_\sim \quad \Rightarrow \quad R_\sim = \frac{l_{Fe}}{\kappa \cdot d_E b_{bar}} = \frac{h_{bar}}{d_E} \cdot R_= \tag{4.2-43}$$

Conclusions:

Rotor bar resistance is increased from DC value $R_= = \frac{l_{Fe}}{\kappa \cdot h_{bar} b_{bar}}$ *by a factor* $k_R = \frac{h_{bar}}{d_E} > 1$.

The effect of current displacement decreases with decreasing rotor frequency. It is most prominent at stand still and vanishes at rated slip, where rotor frequency is below 2 Hz. Thus increased losses due to increased rotor resistance occur only at starting (big slip), where torque increase is needed, but NOT at rated operation.

Although total stray flux is reduced by eddy current, the deep bar causes a rather big rotor stray flux and therefore **an increased stray coefficient σ**. According to (4.2-38) break down torque is decreased by $(1-\sigma)/\sigma$, so increase of starting torque due to current displacement causes decrease of break down torque (Fig. 4.2-9). Resulting speed-torque curves are classified by so-called **rotor classes**, which defines the ratio of starting torque versus rated torque and the saddle of the torque-speed curve. Torque needs to be bigger than load torque to allow motor to run up. As voltage may vary by +/- 5% (voltage range A according to EN 60034-1), the torque may be lower by about 10% in reality (Fig.4.2-10).

Example 4.2-3:
Rotor class 16 means, that at U_N-5% the motor is capable to start against load torque of 160%M_N.

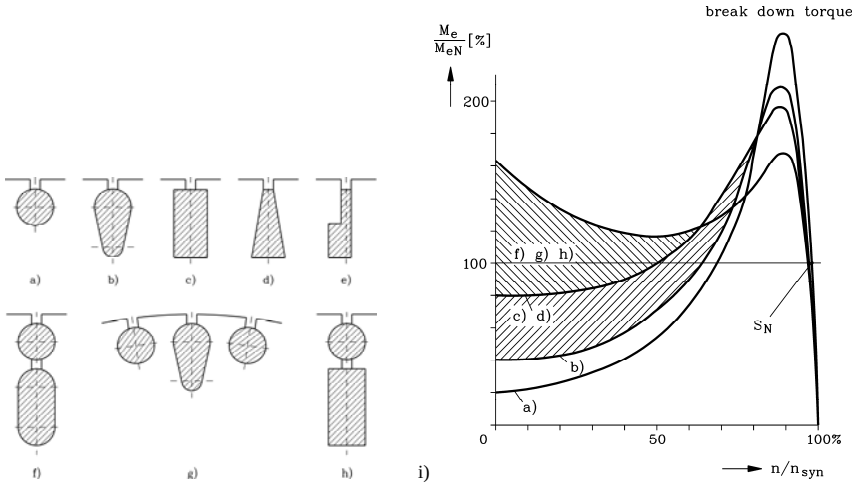

Fig. 4.2-9: Increase of starting torque and decrease of break down torque due to **current displacement:**
No or low current displacement: a) round bar, b) oval bar
Big current displacement:
c) deep bar, d) wedge bar, e) step bar, f), g) h): double cage – bronze upper cage to increase resistance
i) Corresponding torque-speed curve

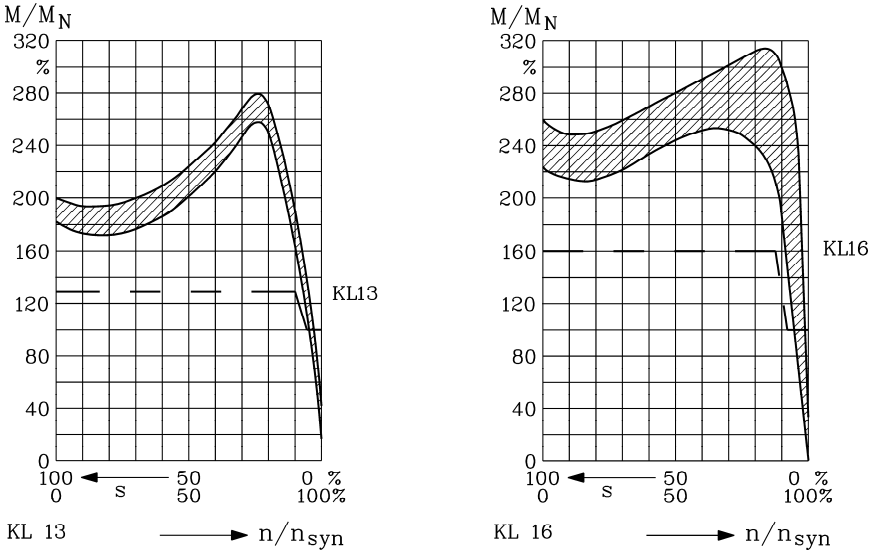

Fig. 4.2-10: Example of cage induction motors classified according to rotor classes KL

4.3 Voltage limits and premium efficiency machines

a) Voltage limits:
Induction motors operated directly from the grid shall comply with several operational demands, which are specified in standards IEC 60034-1, -2 and other parts of this international electric machinery standard. Some features are:
- sufficiently high starting torque M_1 (expressed in per unit of rated torque, see Chapter 4.2)
- sufficiently low starting current I_1 (usually 5 ... 7 times rated current)
- sufficient overload capability (breakdown torque at least 1.6-times rated torque)
- sufficient minimum start-up torque ("saddle minimum" of $M(n)$-curve)
- good efficiency (= low losses)
- low acoustic noise

Standard low voltage level, which is stator voltage, supplied by public grid, is 400 V (line-to-line), which may vary within European Community between +/- 10%.

Example 4.3-1:
Grid voltage limits: 400V+/-10%: minimum: 360 V, maximum: 440 V

If induction motor is fed **with increased voltage**, stator flux linkage is also increased according to simplified stator voltage equation ($R_s = 0$):

$$\underline{U}_s = j\omega_s L_{s\sigma}\underline{I}_s + j\omega_s L_h(\underline{I}_s + \underline{I}'_r) = j\omega_s \underline{\Psi}_s \qquad (4.3\text{-}1)$$

As flux linkage is excited by stator and rotor current, magnetizing current is increased by increased stator voltage. **Increased saturation** will occur.

$$\underline{\Psi}_s = L_{s\sigma}\underline{I}_s + L_h(\underline{I}_s + \underline{I}'_r) \approx L_h \underline{I}_m \qquad (4.3\text{-}2)$$

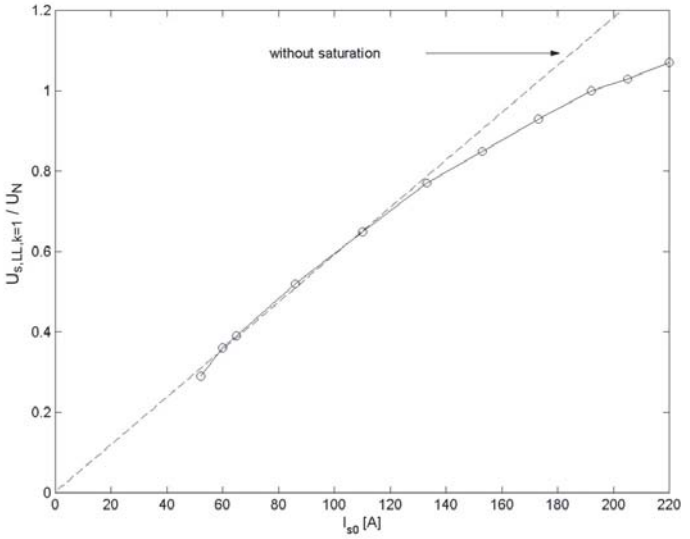

Fig.4.3-1: Measured no-load voltage *) versus no-load current, which in that special case is identical with magnetizing current (270 kW, high-speed 2 pole induction motor, inverter operation at f_s = 270 Hz, winding in delta connection. *) Fundamental harmonic line-to-line voltage versus rms-value of no-load current.

Due to iron saturation (Fig.4.3-1) an increase of 10% voltage, thus an increase of about of 10% stator flux linkage, means an increase of magnetizing current of MORE than 10%. At no load this increase of magnetizing current can easily be measured just by raising stator voltage (Fig.4.3-1) and corresponds directly with increase of stator current, as rotor current at no-load is zero. **Too low voltage** causes a drop of breakdown torque by square of voltage.

Example 4.3-2:
Rated voltage: 400V, operational voltage: 360 V, reduction in breakdown torque: $M_b / M_{bN} = (U_s / U_{sN})^2 = (360/400)^2 = 0.9^2 = 0.81$
Breakdown torque M_b is reduced by almost 20%. If motor is operated with constant rated load torque M_N, slip increases above rated slip according to *Kloss* function. *Kloss* function in range of rated (and therefore small) slip may be simplified:

$$R_s = 0: \quad \frac{M_e}{M_b} = \frac{2}{\frac{s_b}{s} + \frac{s}{s_b}} \approx \frac{2 \cdot s}{s_b} \qquad (4.3\text{-}3)$$

For constant electromagnetic torque $M_e = M_N$ a decrease of breakdown torque by 0.81 (or 19%) means an increase of slip by 1/0.81 (about +25%). Therefore stator and rotor current increase in the same way, thus increasing motor winding losses.

Conclusions:
At increased voltage stator current may rise dramatically, if machine is highly saturated. This current increase may overheat motor winding. The increase of flux causes increased iron losses. At reduced stator voltage (and therefore reduced motor flux) the motor, operated a rated torque, will consume increased current, as torque is given by product of current and flux. Increased current might overheat windings. Optimum motor design at rated voltage and rated torque is therefore minimum current consumption as a balance between flux (and therefore magnetizing current) and load current (or rotor current).

According to IEC 60034-1 motors must be capable of operating at rated voltage ±5% (**"voltage range A"**) and rated power at a maximum surplus in motor temperature rise of 10 K above the temperature rise limit of the used insulation material. At rated voltage ±10% (**"voltage range B"**) the windings will be overheated much more, therefore no long term operation at these voltage limits is recommended.

Example 4.3-3:
Rated voltage: 400V, Voltage range A: 400 V ±5% = 380 ... 420 V.
Thermal class of insulation material F (IEC 60034-1): Temperature rise limit for motors with rated power below 200 kW: 105 K over 40°C ambient temperature.
Allowable temperature rise of winding at voltage limits: 115 K.

b) Premium efficiency motors:
Industrial electric drives consume a considerable amount of energy all over the world.

Example 4.3-4:
In *Germany* is an example for an industrialized country. Power consumption in 2004 was:
a) Electrical energy consumption: 18 % of total energy consumption = 504 TWh
b) Industrial electrical energy consumption: 47 % of a) = 237 TWh
c) Conversion to mechanical energy: 69% of b) = 163 TWh

With an average efficiency increase of 4% of electromechanical energy conversion by e.g. premium efficiency motors, which could be realized for 50% of installed drive power, one gets an energy saving of $0.04 \cdot 0.5 \cdot 163\,\text{TWh} = 3.3$ TWh per year (= 8760 h), which amounts to power delivery of a power plant with 3.3 TWh / 8760 h = 377 MW. This value is increasing, as energy consumption increases. Most power plants in *Germany* are thermal power plants. New plants have an optimum efficiency of 50%, e.g. if a combined cycle plant is used. In this case saving of thermal input power is 754 MW. In reality, many of *German* thermal power plants are of older type with an average efficiency of only about 35 %. **Therefore saving would even lead to a reduction of 1077 MW thermal input power.**

Conclusions:
Efficiency improvement of industrial motors has not only an economical, but also an environmental impact.

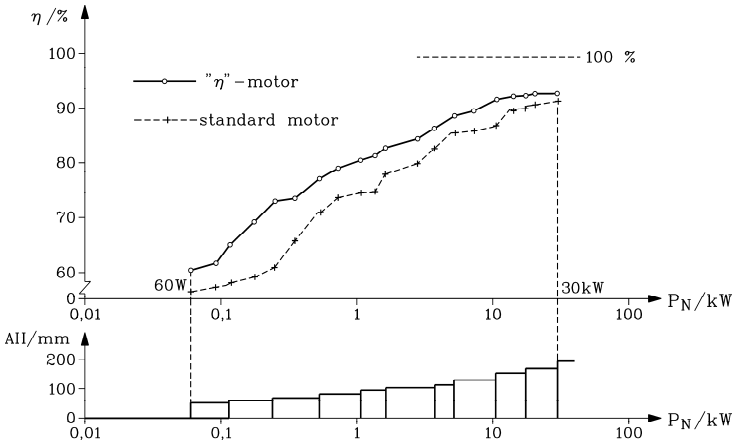

Fig.4.3-2: Typical catalogue efficiency η and shaft height AH of four pole induction motors: standard with normal efficiency (---------), motors with increased efficiency ("η-motors") (————)

In United States the **Energy Policy Act (EPACT)** was established (1997), demanding that manufacturers of standard induction motors (TEFC) selling motors on the US American market, must offer 2-pole and 4-pole squirrel-cage induction motors with increased efficiency values up to a rating of 90 h.p. with predefined values of efficiency at rated operation. By aiming at 2- and 4-pole motors in that power range the main part of standard motor applications is included. The measurement of efficiency must be done according to international standards by certified laboratory to ensure quality standard. In Europe several motor manufacturers had offered standard induction motors with increased efficiency for long (Fig. 4.3-2), but no legislative act up to now is forcing all manufacturers to do so. Shortly after the EPACT the Community of European Motor Manufacturers (CEMEP) has agreed on **a voluntary agreement with the Commission of European Community** (EC) to offer for the European market 2- and 4-pole motors with increased efficiency in a similar way as the EPACT demands. Due to the different standard power and voltage ratings in USA and Europe (e.g. USA: 460 V, 60 Hz, EC: 400 V, 50 Hz) the motor types with and their predefined increased efficiency values are slightly different from EPACT demands. According to this voluntary CEMEP agreement 2-and 4-pole motors in power range between 1 ... 100 kW are available in **three efficiency classes** (Fig. 4.3-3):

Cheap standard motors with usual efficiency values: Efficiency class eff3
Standard motors with increased efficiency: Efficiency class eff2
Premium efficiency motors at increased motor price: Efficiency class eff1

It is the long term aim that in the future only two motor classes will exist: eff2 and eff1. Since 1999 and 2003 already a considerable shift in sold motors from class eff3 to class eff2 was experienced in Western Europe.

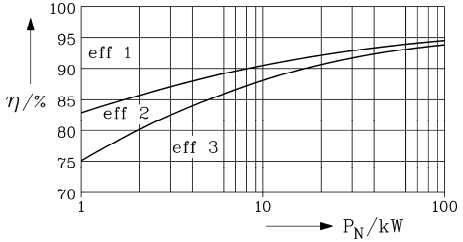

Fig.4.3-3: Definition of efficiency classes eff1, eff2, eff3 for four pole standard induction motors in power range 1 ... 100 kW according to voluntary agreement between CEMEP and commission of EC

Losses in induction machines are separated into stator and rotor losses or in no-load and load losses, mainly eddy current and hysteresis losses in the iron stack, winding and cage losses due to electric current flow, friction losses in bearings and sealing and windage losses due to power consumption of shaft mounted fan.

	No-load losses	*Load losses*
Stator losses	Copper losses in winding $P_{Cu,0}$ Iron losses in iron stack P_{Fe} Additional no-load losses	Copper losses in winding $P_{Cu,s}$ Additional load losses
Rotor losses	Friction and windage losses P_{fr+w} Additional no-load losses	Cage losses due to rotor current P_r Additional load losses

Table 4.3-1: Losses in induction machine at no-load and load (rated load)

Distortion of air gap flux density distribution by slot openings: - stator and rotor **tooth flux pulsation losses** at *no-load*, being increased *at load*
Step-like distribution of air gap flux density due to arrangement of windings in slots: - **additional harmonic rotor bar currents**, losses increased by current displacement due to the rather high frequencies, - **additional harmonic currents** in stator winding, - **eddy current losses in rotor surface**, if the rotor insulation between the iron sheets is bridged by the tooling of the rotor surface to ensure small mechanical air gap,
The additional harmonic rotor bar currents may flow as **inter-bar currents** between adjacent rotor bars, especially when the rotor is skewed, because there is usually no insulation between rotor iron stack and rotor bars.
Iron saturation causes also deviation of air gap flux density from ideal sinus, mainly by introducing an **additional third space harmonic**, which is inducing - additional harmonic rotor currents in the cage *at load* - circulating stator currents in delta connected stator winding,
Flux density leaves iron stack at the stack ends axially, penetrating the end sheets. Therefore radial stack lamination cannot suppress eddy current flow, thus - additional **iron losses in the end sheets** due to axial flux components occur
Magnetic flux is not contained only to iron stack and air gap, but a certain stray flux penetrates also massive metallic (conductive) parts such as housing and shaft, causing - additional **eddy current losses in massive metallic parts**

Table 4.3-2: Over-view on main components of additional losses.

In rotor frequency at no-load is almost zero and at load it is small (e.g. rated slip: 5%, stator frequency: 50 Hz, then rotor frequency is $f_r = s \cdot f_s = 0.05 \cdot 50 = 2.5\,\text{Hz}$), so nearly **no rotor iron losses** (eddy current losses and hysteresis losses in rotor iron stack) will occur. **Additional losses (stray load losses)** are caused mainly by the fact that the air gap flux density is not distributed like an ideal sinus flux density wave, but rather step-like due to the arrangement of winding and cage in slots. Thus additional high-frequency stator and rotor currents are induced, causing additional losses. There exist a lot of further reasons, why these additional losses may arise and can become rather significant, especially at high speed motors (Table 4.3-2).

Power flow in motor is according to Chapter 4.2 given by electric stator input power P_{in}, which feeds stator winding losses $P_{Cu,s}$ and stator core losses P_{Fe}. Stator additional losses at no-load are usually included in stator core losses in standard measurements according to IEC 60034-2. Power flow from stator to rotor via air gap $P_\delta = P_{in} - P_{Cu,s} - P_{Fe}$ is feeding rotor cage losses (slip losses) P_r and friction and windage losses P_{fr+w}. Remaining power may separated into mechanical output power P_{out}, directly measured via the shaft torque e.g. with a torque-meter and speed $P_{out} = 2\pi \cdot n \cdot M_s$ and additional load losses $P_{ad1} = P_\delta - P_r - P_{out}$.

Example 4.3-4:
Measured loss balance of a 2.55 kW, 8-pole, totally enclosed induction motor with shaft mounted fan (IEC 60034-2): ambient temperature 20°C, winding temperature rise: 61.5 K

Slip at rated power 2.55 kW	s_N = 4.44 %
Speed / torque n / M_s	860 /min / 28.4 Nm
Measured electrical input power P_{in}	3254 W
Stator copper losses $P_{Cu,s}$	385 W (55 %)
Stator iron losses P_{Fe}	133 W (19 %)
Rotor cage losses $P_r = s \cdot P_\delta$	121 W (17 %)
Additional load losses $P_{ad,1}$	47 W (7 %)
Friction and windage losses P_{fr+w}	14 W (2 %)
Total losses P_d	700 W (100 %)
Output power P_{out}	2554 W
Efficiency	**78.49 %**

Table 4.3-3: Example of measured loss balance and efficiency of a Thermal Class B 8-pole induction motor at 60 Hz, 440 V Y according to "direct" method a) of IEC 60034-2 at rated load

Please note, that efficiency of on specific motor varies with load. At no-load output power is zero, therefore efficiency is zero. Considering no-load losses P_{d0} as independent from load, and load losses P_{d1} as caused by copper losses in winding and cage: $P_{d1} \sim I_s^2$, $I_s \sim I_r'$, one gets a simple loss model for estimating change of efficiency with load (Fig.4.3-4):
- Motor flux depending on voltage and frequency, which are both fixed, so flux is constant
- No-load losses P_{d0} independent of motor load M
- Motor load M depends on flux and current I_s, so varies linear with current
- Load losses P_{d1} mainly ohmic losses in stator and rotor, depending on square of current I_s

$P_{d0} = const.$, $P_{d1} \sim I_s^2 \sim M^2$

$$\eta = \frac{P_{out}}{P_{out} + P_{d0} + P_{d1}} \qquad P_{out} = P_N \cdot (M / M_N) \tag{4.3-4}$$

$$P_{d0} = k_0 \cdot P_N, \quad P_{d1} = k_1 \cdot P_N \cdot (M / M_N)^2, \quad P_{d1N} = k_1 \cdot P_N \tag{4.3-5}$$

Optimum (maximum) efficiency is given for $d\eta / dM = 0$, yielding the result:

$$M / M_N\big|_{opt} = \sqrt{P_{d0} / P_{d1N}} \tag{4.3-6}$$

At this load point the no-load losses and the load losses are equal: $P_{d0} = P_{d1}$, yielding a maximum possible efficiency of

$$\eta_{\max} = \frac{\sqrt{P_{d0} / P_{d1N}}}{\sqrt{P_{d0} / P_{d1N}} + 2 \cdot (P_{d0} / P_N)} \quad . \tag{4.3-7}$$

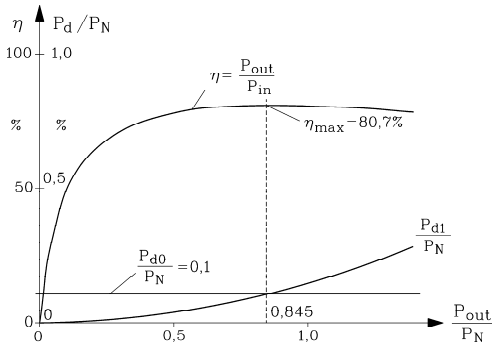

Fig.4.3-4: Variation of losses P_d and efficiency η with output power P_{out}. Here it is assumed that no-load losses are constant and $0.1P_N$, load losses at rated power are $0.14P_N$ and vary with the square of output power

Example 4.3-5:
Efficiency varies with varying load:

Motor data: $P_{d0} = 0.06 \cdot P_N, \quad P_{d1} = 0.2 \cdot P_N \cdot (M / M_N)^2, \quad k_0 = 0.06, \quad k_1 = 0.2$

$$\eta = \frac{m}{m + 0.06 + 0.2 \cdot m^2}, \quad m = M / M_N$$

Load M/M_N	0	0.25	0.5	0.75	1.0
Efficiency η	0	77.52 %	81.96 %	81.30 %	79.36 %

Table 4.3-4: Load depending efficiency at constant voltage line supply

Here: $M / M_N\big|_{opt} = \sqrt{0.06 / 0.2} = 0.55$, $P_{d0} = P_{d1} = 0.06 P_N$,

$$\eta_{\max} = \frac{\sqrt{0.06 / 0.2}}{\sqrt{0.06 / 0.2} + 2 \cdot 0.06} = 0.8203$$

Conclusions:
In order to increase motor rated efficiency, motor utilization (Power/volume) must not exceed a certain limit in order to get rated efficiency at the optimum value. At other load points (higher or lower load) efficiency will decrease.

How can **maximum efficiency** be increased for a certain motor ?
- By using low loss iron sheets iron losses are be reduced (e.g. 1.7 W/kg instead of 2.3 W/kg).
- By using copper instead of aluminium cage rotor conductivity rises by 57/34 = 167%, thus reducing rotor resistance and losses.
- By increasing slot number per pole and phase *q* (e.g. from 3 to 4) the number of steps of the air gap flux density distribution is increased by 4/3, but the steps itself get smaller by 3/4. Hence the flux density distribution is more sinusoidal, and the additional losses are reduced.
- Increase of slot number also increases the cooling surface of winding, as the winding surface towards iron is increased according to the slot surfaces. Thus the temperature rise of winding is reduced, and therefore the winding resistance is lower, leading to lower losses (and a longer life span of insulation material).

Conclusions:
A lot of rules exist to increase efficiency, but usually all these measures increase motor manufacturing costs. So motors with increased efficiency are usually more expensive.

Example 4.3-6:
Influence of winding temperature on efficiency for a 8-pole motor, 2.55 kW, 60 Hz, 440 V:

Temperature rise	**60 K**	**105 K**
Warm phase resistance	4.11 Ohm	4.7 Ohm
Slip at rated power 2.55 kW	4.44 %	5.05 %
Speed / torque	860 /min / 28.4 Nm	854 /min / 28.6 Nm
Input power	3198 W	3268 W
Stator copper losses	380 W	434 W
Iron losses	133 W	133 W
Rotor cage losses	121 W	137 W
Friction and windage losses	14 W	14 W
Output power	2550 W	2550 W
Efficiency	**79.74 %**	**78.03 %**

Table 4.3-5: Reduced efficiency due to increased temperature rise caused by inferior cooling, ambient 20°C

4.4 Space harmonic effects in induction machines

Although **time variation** of stator voltage and current is sinusoidal due sinusoidal grid supply, **spatial distribution** of flux density in air gap is NOT, as winding is located in slots. So the spatial distribution of flux density is INDEPENDENT of the kind of time variation of feeding winding currents. It depends ONLY on winding arrangement in slots and air gap geometry. In Chapters 4.1 ... 4.3 only effects of fundamental sine wave of air gap flux density distribution was considered. In reality also the higher space harmonics of stator and rotor field distribution have to be considered **to understand measured torque-speed curves** of induction machines. For simplification influence of slot openings will be neglected here. With slots with infinitesimal small slot openings the air gap flux density is step-like distributed, as explained in Chapter 1 for stator and in Chapter 4.2 for rotor field.

4.4.1 Field space harmonics and current time harmonics at sinusoidal stator voltage

a) Stator field spatial harmonics:
Sinus time-function of stator voltage U_s causes sinus time-function stator current I_s to flow in stator winding. *Fourier* analysis of stator air gap field of a m_s-phase (usually three-phase)

stator winding concentrated in $Q_s = 2p \cdot m_s \cdot q$ stator slots, fed by a time-sinusoidal m_s-phase stator current system with phase shift $2\pi / m_s$ between phases, amplitude $I_s \cdot \sqrt{2}$ and frequency f_s, yields following result: The step-like air gap flux density distribution $B_{\delta,s}(x_s, t)$ along stator circumference co-ordinate x_s can be represented by an infinite sum of sinus spatial-distributed flux density waves. Summing index is the ordinal number ν. With increasing ν wave length λ_ν, wave speed $v_\nu = \lambda_\nu \cdot f_s$ and amplitudes $B_{\delta,\nu}$ are decreasing.

$$B_{\delta,s}(x_s,t) = \sum_{\nu=1}^{\infty} B_{\delta,\nu} \cdot \cos\left(\frac{\nu\pi x_s}{\tau_p} - \omega_s t\right) \qquad \omega_s = 2\pi f_s \tag{4.4.1-1}$$

For $m_s = 3$: $\nu = 1 + 2m_s \cdot g$ = 1, -5, 7, -11, 13, -17, ... (4.4.1-2)

(g: integer number: $g = 0, \pm1, \pm2, \pm3, \ldots$)

$$B_{\delta,\nu} = \frac{\mu_0}{\delta} \cdot \frac{\sqrt{2}}{\pi} \cdot \frac{m_s}{p} \cdot N_s \frac{k_{w,\nu}}{\nu} \cdot I_s \qquad \text{(no iron saturation considered)} \tag{4.4.1-3}$$

$$\lambda_\nu = 2\tau_p / |\nu| \tag{4.4.1-4}$$

The alternatively changing sign of **ordinal numbers** ν indicates that waves move alternatively with fundamental in the same direction (clockwise) or in opposite direction (counter-clockwise). No even ordinal numbers occur, as flux density distribution is symmetrical to abscissa. This means, the shape of north and south pole of flux density distribution is identical. No odd ordinal numbers dividable by the phase number occur due to the distinct number of phases. Winding factor $k_{w,\nu}$ is defined by **distribution factor** $k_{d,\nu}$, which considers how many slots per pole q are occupied by one phase, and by **pitch factor** $k_{p,\nu}$, which considers if span per coil W equals pole pitch or not.

$$k_{w,\nu} = k_{p,\nu} \cdot k_{d,\nu} \tag{4.4.1-5}$$

$$k_{d,\nu} = \frac{\sin\left(\frac{\nu\pi}{2m_s}\right)}{q \cdot \sin\left(\frac{\nu\pi}{2m_s q}\right)} \quad , \quad k_{p,\nu} = \sin\left(\frac{W}{\tau_p} \cdot \frac{\nu\pi}{2}\right) \tag{4.4.1-6}$$

Example 4.4.1-1:

Fourier analysis of flux density distribution of a three-phase, four pole, two-layer winding with q = 2, W/τ_p = 5/6.

Winding and air gap data:

$\delta = 1$ mm; turns per coil $N_c = 5$; all coils per phase connected in series, so number of parallel winding paths is a = 1; bore diameter d_{si} = 80 mm; phase current (r.m.s): I_s = 30 A .

We get:

Q_s/p = 12 slots per pole pair, pole pitch: $\tau_p = d_{si}\pi/(2p) = 62.8$ mm and turns per phase: $N_s = 2p \cdot q \cdot N_c / a = 4 \cdot 2 \cdot 5 / 1 = \underline{\underline{40}}$.

Flux density amplitude of fundamental:

$$B_{\delta,\nu=1} = \frac{\mu_0}{\delta} \cdot \frac{\sqrt{2}}{\pi} \cdot \frac{m_s}{p} \cdot N_s \frac{k_{w,1}}{1} \cdot I_s = \frac{4\pi \cdot 10^{-7}}{0.001} \cdot \frac{\sqrt{2}}{\pi} \cdot \frac{3}{2} \cdot 40 \frac{0.933}{1} \cdot 30 = \underline{\underline{0.95}}\,\text{T}$$

ν	*Relative amplitudes* $\lvert B_{\delta\nu} / B_{\delta 1}\rvert$ (%)	*winding factor* $k_{p,\nu}$	$k_{d,\nu}$	$k_{w,\nu}$	*wave speed at f_s = 50 Hz* v_ν (m/s)
1	100	0.966	0.966	0.933	6.28
-5	1.4	0.259	0.259	0.067	- 1.26
7	1.0	0.259	-0.259	-0.067	0.9
-11	9.1	0.966	-0.966	-0.933	- 0.6
13	7.7	-0.966	-0.966	0.933	0.5
-17	0.4	-0.259	-0.259	0.067	- 0.37
19	0.38	-0.259	0.259	-0.067	0.33

Table 4.4.1-1: *Fourier* analysis of stator spatial air gap flux density distribution, excited by a three-phase, four pole, two-layer winding with q = 2, W/τ_p = 5/6, delivers a sum of travelling flux density waves in the air gap

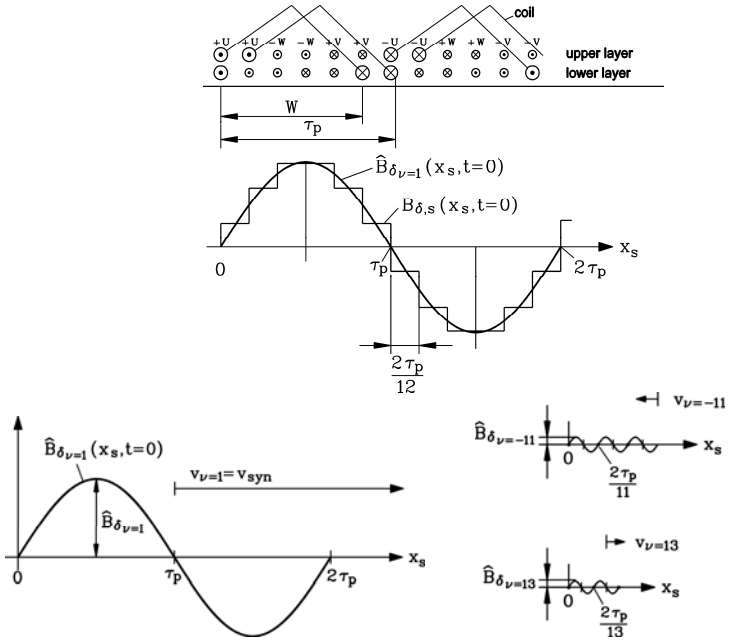

Fig. 4.4.1-1: Air gap flux density at t = 0 ($i_U = \sqrt{2}I_s$, $i_V = i_W = -\sqrt{2}I_s/2$) and fundamental and first slot harmonic waves for q = 2, W/τ_p = 5/6.

Fig. 4.4.1-1 shows the corresponding flux density distribution, Fig. 1.1.1-1 the one for q = 2, but W/τ_p = 1, which is the case for single-layer winding. Obviously Fig. 4.4.1-1 fits better to a sinus than Fig. 1.1.1-1, which is accomplished by the chording (pitching) of the coil span. Due to this chording the winding factor for 5th and 7th space harmonic is almost zero, again for 17th, 19th, and so on, whereas for 11th, 13th, 23rd, 25th, and so on, winding factor is the same as for fundamental. Therefore these wave amplitudes (so-called **"slot harmonics"**) dominate the wave spectrum. Their ordinal number is

$$\nu = 1 + \frac{Q_s}{p} \cdot g \qquad (g\text{: integer number: } g = 0, \pm1, \pm2, \pm3, \ldots) \quad , \tag{4.4.1-7}$$

yielding here ν = -11, 13, -23, 25, ... These harmonics are caused by the steps in air gap distribution (see Fig.4.4.1-1), so the average value of wave length of the first pair of slot harmonics is equal to slot pitch (step length).

Example 4.4.1-2:
Winding: q = 2, W/τ_p = 5/6, slot pitch $\tau_Q = 2\tau_p/12$.
Ordinal number of first pair of slot harmonics: ν = -11, 13
Wave length of first pair of slot harmonics: $\lambda_{-11} = 2\tau_p/11$, $\lambda_{13} = 2\tau_p/13$
Average value of wave length: $(\lambda_{-11} + \lambda_{13})/2 \cong 2\tau_p/12$

Conclusions:
Wave spectrum of air gap flux density distribution is dominated in chorded two-layer windings (apart from fundamental) by slot harmonic waves. In unchorded single-layer winding also the 5th and 7th harmonic must be considered.

b) Rotor cage field spatial harmonics, excited by rotor current I_r:
Stator fundamental field $\nu = 1$ moves with **synchronous velocity** $v_{syn} = \lambda_{\nu=1} \cdot f_s = 2 f_s \tau_p$ (or **synchronous speed** n_{syn}, respectively), whereas rotor is turning with speed n, defining slip $s = (n_{syn} - n)/n_{syn}$. Therefore stator fundamental flux linkage with rotor cage changes with rotor frequency $f_r = s \cdot f_s$, inducing sinusoidal rotor voltage $U_{i,r}$ according to *Faraday´*s law. This voltage, as shown in Chapter 4.2, causes the sinus time-function rotor current I_r, to flow in adjacent bars with phase shift $2\pi \cdot p/Q_r$, exciting also a step-like air gap flux density distribution $B_{\delta,r}(x_r, t)$ along rotor circumference co-ordinate x_r. It can in the same way be represented by an infinite sum of sinus spatial-distributed flux density waves. Summing index is the ordinal number μ. With increasing μ wave length λ_μ and wave speed $v_\mu = \lambda_\mu \cdot f_r$ is decreasing, amplitudes $B_{\delta,\mu}$ are also decreasing with $1/\mu$. As each bar represents a rotor phase ($m_r = Q_r$), consisting of 1/2 turn per phase (N_r = 1/2), winding factor is always unity ($k_{wr,\mu}$ = 1). Thus, we adopt (4.4.1-1) for rotor cage:

$$B_{\delta,r}(x_r, t) = \sum_{\mu=1}^{\infty} B_{\delta,\mu} \cdot \cos\left(\frac{\mu\pi x_r}{\tau_p} - \omega_r t\right) \qquad \omega_r = 2\pi f_r \tag{4.4.1-8}$$

$$\mu = 1 + (Q_r/p) \cdot g \quad (g\text{: integer number: } g = 0, \pm1, \pm2, \pm3, \ldots) \tag{4.4.1-9}$$

$$B_{\delta,\mu} = \frac{\mu_0}{\delta} \cdot \frac{\sqrt{2}}{\pi} \cdot \frac{Q_r}{p} \cdot \frac{1}{2} \cdot \frac{1}{\mu} \cdot I_r \quad \text{(no iron saturation considered)} \tag{4.4.1-10}$$

$$\lambda_\mu = \frac{2\tau_p}{|\mu|} \tag{4.4.1-11}$$

The alternatively changing sign of **ordinal numbers** μ indicates again that waves move alternatively with fundamental in the same direction (clockwise) or in opposite direction (counter-clockwise). As each bar represents a phase, each spatial harmonic is a slot harmonic. Equations for ordinal numbers (4.4.1-7) and (4.4.1-9) are identical. Wave velocities with respect to rotor are

$$v_{\mu,r} = \lambda_\mu \cdot f_r = 2 \cdot s \cdot f_s \cdot \tau_p / \mu = s \cdot v_{syn}/\mu \quad . \tag{4.4.1-12}$$

With respect to stator we see that rotor co-ordinate x_r plus the distance of rotor surface movement gives corresponding stator co-ordinate x_s. As rotor surface velocity v_m is given by slip s or rotor speed $n = n_{syn} \cdot (1 - s)$ respectively: $v_m = (1 - s) \cdot v_{syn} = (1 - s) \cdot 2 f_s \tau_p$, we get

$$x_s = x_r + v_m \cdot t \tag{4.4.1-13}$$

and

$$B_{\delta,\mu}(x_s, t) = B_{\delta,\mu} \cos\left(\frac{\mu\pi(x_s - v_m t)}{\tau_p} - \omega_r t\right) = B_{\delta,\mu} \cos\left(\frac{\mu\pi x_s}{\tau_p} - (\mu(1-s) + s) \cdot \omega_s t\right). \tag{4.4.1-14}$$

Therefore speed of rotor space harmonics with respect to stator is

$$v_\mu = v_{\mu,r} + v_m = v_{syn} \cdot (1 - s + s/\mu) \quad . \tag{4.4.1-15}$$

Example 4.4.1-3:
Fourier analysis of flux density distribution of a cage with 28 rotor bars, exciting a four pole field distribution. Stator frequency is 50 Hz.
Winding and air gap data:
$\delta = 1$ mm; $N_c = 1/2$; bore diameter d_{si} = 80 mm; bar current (r.m.s): I_s = 240 A, slip: s = 5%.
We get:
Q_r/p = 14 slots per pole pair, pole pitch: $\tau_p = d_{si}\pi/(2p) = 62.8$ mm, v_m = 5.97 m/s.
Flux density amplitude of fundamental:

$$B_{\delta,\mu=1} = \frac{\mu_0}{\delta} \cdot \frac{\sqrt{2}}{\pi} \cdot \frac{Q_r}{p} \cdot \frac{1}{2} \cdot \frac{1}{1} \cdot I_r = \frac{4\pi \cdot 10^{-7}}{0.001} \cdot \frac{\sqrt{2}}{\pi} \cdot \frac{28}{2} \cdot \frac{1}{2} \cdot \frac{1}{1} \cdot 240 = \underline{\underline{0.95}}\,\text{T}$$

	relative amplitudes	*winding factor*	*wave speed with respect to rotor*	*to stator*
μ	$\lvert B_{\delta\mu}/B_{\delta1}\rvert$ (%)	$k_{w,\mu}$	$v_{\mu,r}$ (m/s)	v_μ
1	100	1	0.31	6.28
-13	7.6	1	- 0.024	5.95
15	6.7	1	0.02	6.0
-27	3.7	1	- 0.011	5.96
29	3.4	1	0.01	5.98

Table 4.4.1-2: *Fourier* analysis of rotor spatial air gap flux density distribution, excited by rotor current, which is induced by four pole stator fundamental field (stator frequency f_s = *50* Hz)

Conclusions:
All rotor space harmonics – excited by rotor current I_r - are slot harmonics, containing therefore less harmonics than stator field. Rotor field fundamental runs – independently of rotor speed - synchronously with stator field fundamental, thus producing the constant asynchronous torque M_e at any speed. This is the torque described by Kloss function in Chapter 4.2. This rotor fundamental induces stator therefore with stator frequency f_s with the voltage $U_{i,sr} = \omega_s M_{sr} \cdot I_r$.

c) Stator harmonic currents, induced by rotor cage field spatial harmonics:
Rotor space harmonics $|\mu| > 1$ induce stator according to (4.4.1-14) with frequency

$$f_{r,\mu} = f_s \cdot |\mu(1-s)+s| \quad , \tag{4.4.1-16}$$

causing small additional **stator time-harmonic currents** to flow, which usually are harmless and therefore most often are neglected in further considerations. Nevertheless, if asynchronous machine is used as a generator, these currents have to be considered as they distort total stator current and may cause electromagnetic interference with tele-communication lines (***EMI***). Only rotor space harmonics $|\mu| = |\nu|$ can induce the stator winding. For $|\mu| \neq |\nu|$ the induced stator voltage is zero due to the stator winding arrangement.

Example 4.4.1-4:
Frequencies of harmonic stator currents, induced by rotor flux density space harmonics distribution: 4-pole motor with data of Example 4.4.1-3: Cage with 28 rotor bars, stator frequency: 50 Hz, slip 0.05.

	Frequency of stator current harmonics	*Is stator winding induced?*
μ	$f_{r,\mu}$ / Hz	-
1	50	Yes: $\|\mu\| = \|\nu\| = 1$
-13	615	Yes: $\|\mu\| = \|\nu\| = 13$
15	715	No: $\|\nu\| \neq 15$
-27	1280	No: $\|\nu\| \neq 27$
29	1380	Yes: $\|\mu\| = \|\nu\| = 29$

Table 4.4.1-3: Frequencies of harmonic stator currents, induced by rotor flux density space harmonics distribution (stator frequency $f_s = 50$ Hz)

Conclusions:
As operational slip is usually small ($s \approx 0$), frequency of stator harmonic current may be estimated for zero slip, showing that this frequency is proportional to rotor slot number.
$f_{r,\mu} = f_s \cdot |\mu| = f_s \cdot |1 + g \cdot Q_r / p| \approx f_s \cdot |g| \cdot Q_r / p$

Example 4.4.1-5:
Measured stator current including harmonic stator currents, induced by rotor flux density space harmonics distribution.
2-pole motor, 3 kW, 380 V Y, 50 Hz, 6.2 A, cage with 22 rotor bars, rated slip 0.05.

- Stator line-to-line peak voltage value: $\sqrt{2} \cdot 380 = \underline{\underline{537}}$ V (measured: 535 V)
- Stator current peak value: $\sqrt{2} \cdot 6.2 = \underline{\underline{8.77}}$ A (measured: 8.84 A)

Ordinal numbers of rotor space harmonics: $\mu = 1 \pm Q_r / p = 1 \pm 22/1 = \underline{\underline{-21, 23}}$

Corresponding stator current harmonic frequencies:
$\mu = -21$: $|\nu| \neq 21$: This space harmonic does not induce the stator winding!
$\mu = 23$: $|\mu| = |\nu| = 23$: $f_{r,\mu} = 50 \cdot |23 \cdot (1 - 0.05) + 0.05| = \underline{\underline{1095}}$ Hz

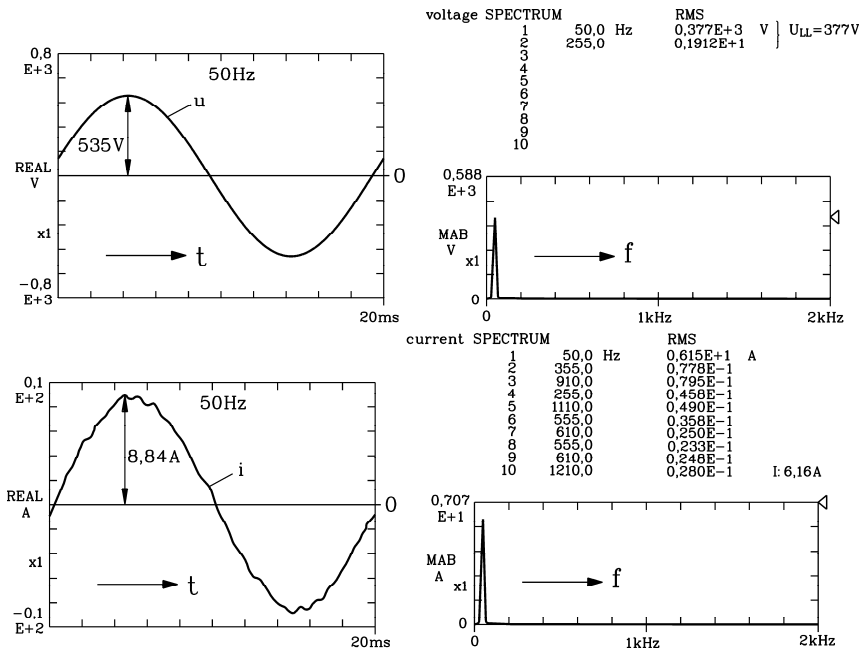

Fig. 4.4.1-2: Loaded 2-pole 3 kW cage induction motor at sinusoidal voltage supply: a) Measured stator line-to-line voltage, b) measured stator phase current, showing stator harmonic currents with 1095 Hz (roughly 22x50 Hz)

d) Harmonic rotor bar currents, induced by stator spatial field harmonics:
Stator space harmonics $|\nu| > 1$ move with velocity $v_\nu = \lambda_\nu \cdot f_s = v_{syn} / \nu$ (or speed $n_{syn,\nu} = n_{syn} / \nu$) much more slowly than rotor. Slip of these harmonics (**harmonic slip**) is

$$s_\nu = \frac{n_{syn,\nu} - n}{n_{syn,\nu}} \quad \Rightarrow \quad s_\nu = 1 - \nu \cdot (1 - s) \tag{4.4.1-17}$$

These stator space harmonics therefore induce rotor cage with frequency

$$f_{r,\nu} = s_\nu \cdot f_s = f_s \cdot |1 - \nu \cdot (1 - s)| \quad , \tag{4.4.1-18}$$

causing small additional **rotor time-harmonic bar currents $\boldsymbol{I_{r,\nu}}$** to flow.

As pole number of the stator harmonics is $2 \cdot |\nu| \cdot p$, phase shift between adjacent harmonic bar currents is $2\pi \cdot \nu \cdot p / Q_r$.

Example 4.4.1-6:
Cage induction motor, stator frequency 50 Hz, no-load s = 0. Rotor cage with 28 bars, induced by stator space harmonic ν = -5.
Harmonic slip $s_{\nu=-5} = 1-\nu\cdot(1-s) = 1+5\cdot(1-0) = \underline{6}$
Rotor cage harmonic frequency: $f_{r,\nu=-5} = s_\nu \cdot f_s = 6\cdot 50 = \underline{300}\,\text{Hz}$
Phase shift between adjacent bar currents: $\varphi_\nu = 360°\cdot\nu\cdot p/Q_r = 360\cdot(-5)\cdot 2/28 = -128.6°$.
Rotor bar currents:

Bar 1	Bar 2	Bar 3	Bar 4	etc.
$i = \hat{I}_{r\nu}\cos(\omega_{r\nu}t)$	$\hat{I}_{r\nu}\cos(\omega_{r\nu}t+\varphi_\nu)$	$\hat{I}_{r\nu}\cos(\omega_{r\nu}t+2\varphi_\nu)$	$\hat{I}_{r\nu}\cos(\omega_{r\nu}t+3\varphi_\nu)$	...

Rotor bar currents $i/\hat{I}_{r\nu}$ e.g. at t = 0:

Bar 1	2	3	4	5	6	7	8	9	10	11	12	13	14
1	-0.6	-0.2	0.9	-0.9	0.2	0.6	-1	0.6	0.2	-0.9	0.9	-0.2	0.6

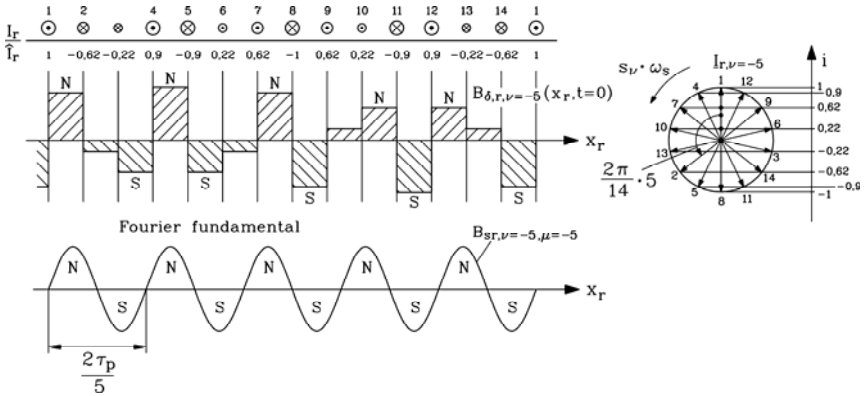

Fig. 4.4.1-3: The cage rotor reacts to 10-pole inducing stator field wave with a ten pole rotor field: The 5th stator harmonic (= 10 poles per fundamental pole pair) induces in the cage (7 bars/pole) rotor harmonic bar currents with phase shift $2\pi(5/7)$, which excite according to *Ampere´*s law a 10-pole rotor field distribution. As number of bars per 10 poles is only 1.4, the approximation of sinus curve by cage field is rather coarse, but contains a 10-pole *Fourier* fundamental, which fits to the 10-pole stator sinus field wave.

Conclusions:
Rotor harmonic bar currents $I_{r\nu}$ excite a step-like air gap field with a fundamental of the same pole number as the inducing stator field harmonic: $\mu = \nu$. Amplitude of this fundamental is calculated with the same Fourier formula (4.4.1-10), but now considering as exciting current $I_{r\nu}$.

$$B_{\delta,\mu,\nu} = \frac{\mu_0}{\delta}\cdot\frac{\sqrt{2}}{\pi}\cdot\frac{Q_r}{p}\cdot\frac{1}{2}\cdot\frac{1}{\mu}\cdot I_{r\nu} \quad \text{(no iron saturation considered)} \qquad (4.4.1\text{-}19)$$

$$\mu = \nu + \frac{Q_r}{p}\cdot g \qquad g = 0,\pm1,\pm2,...$$

Rotor bar harmonic currents $I_{r\nu}$ can be calculated by taking the same rotor voltage equation of Chapter 4.2, but considering now the parameters of the ν-th stator space harmonic.

$$u_{i,rs\nu} = -k_{wr}N_r\cdot\frac{d\Phi_{s,\nu}(t)}{dt} = M_{rs\nu}\cdot di_s/dt \qquad (4.4.1\text{-}20)$$

Flux per pole of ν-th stator space harmonic is small,
- as pole pitch is smaller by $1/\nu$ than fundamental,
- as flux density amplitude is smaller by $k_{ws,\nu}/\nu$ instead of k_{ws} than fundamental amplitude.

Thus harmonic flux per pole $\Phi_{s,\nu}$ is smaller by factor $k_{ws,\nu}/(k_{ws}\cdot\nu^2)$ than fundamental flux, therefore also mutual and self inductance of air gap field is decreased by this factor.

$$M_{rs\nu} = \mu_0\cdot N_r k_{wr} N_s k_{ws,\nu}\cdot\frac{2m_s}{\pi^2\cdot\nu^2\cdot p}\cdot\frac{\tau_p l_{Fe}}{\delta} \qquad (4.4.1\text{-}21)$$

$$\underline{U}_{i,rs\nu} = js_\nu\omega_s M_{rs\nu}\cdot\underline{I}_s \qquad . \qquad (4.4.1\text{-}22)$$

The *Fourier* space fundamental of rotor flux density distribution $\mu = \nu = -5$ (Fig.4.4.1-3) induces rotor cage with rotor frequency $s_\nu\omega_s$ due to self-induction with voltage $U_{i,r\nu}$.

$$\underline{U}_{i,rr\nu} = js_\nu\omega_s L_{rh\nu}\cdot\underline{I}_{r\nu} \qquad \Rightarrow \qquad L_{rh\nu} = \mu_0(N_r k_{wr})^2\cdot\frac{2m_r}{\pi^2\cdot\nu^2\cdot p}\cdot\frac{\tau_p l_{Fe}}{\delta} \quad . \qquad (4.4.1\text{-}23)$$

So finally rotor voltage equation is derived, considering also self-induced voltage by stray flux of slots and winding overhangs (inductance $L_{r\sigma}$), voltage drop due to resistance R_r, and that rotor is short-circuited: $U_{r\nu} = 0$.

$$0 = R_r\underline{I}_{r\nu} + js_\nu\omega_s L_{r\sigma}\underline{I}_{r\nu} + js_\nu\omega_s L_{rh\nu}\underline{I}_{r\nu} + js_\nu\omega_s M_{rs\nu}\underline{I}_s \qquad (4.4.1\text{-}24)$$

With $m_r = Q_r$, $N_r = 1/2$ and $(2m_s\cdot N_s k_{ws\nu}/Q_r)\cdot L_{rh\nu} = M_{rs\nu}$ we get for the **rotor harmonic current**

$$\underline{I}_{r\nu} = -j\frac{(2m_s\cdot N_s k_{ws\nu}/Q_r)\cdot\omega_s L_{rh\nu}}{R_r/s_\nu + j\cdot\omega_s(L_{r\sigma}+L_{rh\nu})}\cdot\underline{I}_s \qquad , \qquad (4.4.1\text{-}25)$$

which corresponds with an equivalent circuit Fig.4.4.1-4a for rotor cage, which closely resembles to T-equivalent circuit, but where now harmonic slip s_ν is introduced. But note: Fig. 4.4.1-3 shows, that the actual step-like field distribution differs considerably from the fundamental, so a more thorough analysis considers also the self-induction in the rotor cage not only from the rotor fundamental $\mu = \nu$, but also the self-induction from all other *Fourier* space harmonics of the rotor field. Thus the self-induction voltage (4.4.1-23) is enlarged by a factor $1/\eta_\nu^2$ (which is not proven here):

$$\eta_\nu = \frac{\sin(\nu\cdot p\cdot\pi/Q_r)}{\nu\cdot p\cdot\pi/Q_r} \qquad (4.4.1\text{-}26)$$

This additional **harmonic self-induction voltage** $\Delta\underline{U}_{i,rr\nu} = js_\nu\omega_s L_{rh\nu}\cdot(1/\eta_\nu^2 - 1)\cdot\underline{I}_{r\nu}$ is usually considered in (4.4.1-25) by adding it to the stray inductance (Fig. 4.4.1-4b):

$$L_{r\sigma\nu} = \left(1/\eta_\nu^2 - 1\right)\cdot L_{rh\nu} + L_{r\sigma} \quad . \quad \textbf{ν^{th} harmonic "leakage":} \ \left(1/\eta_\nu^2 - 1\right)\cdot L_{rh\nu} \qquad (4.4.1\text{-}27)$$

$$\underline{I}_{r\nu} = -j\,\frac{(2m_s\cdot N_s k_{ws\nu}/Q_r)\cdot\omega_s L_{rh\nu}}{R_r/s_\nu + j\cdot\omega_s(L_{r\sigma\nu}+L_{rh\nu})}\cdot\underline{I}_s \quad , \qquad (4.4.1\text{-}28)$$

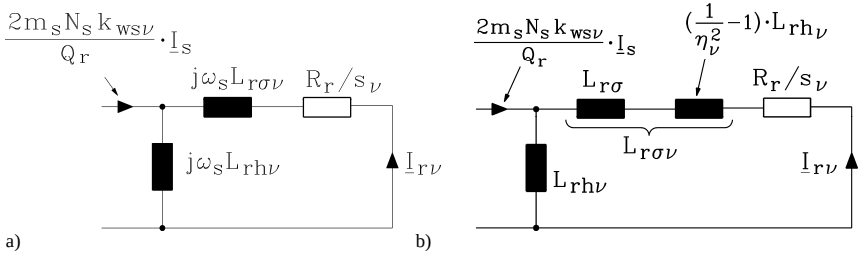

Fig. 4.4.1-4: Equivalent circuit for rotor cage for ν-th stator space harmonic, to calculate rotor current time harmonic $I_{r\nu}$ a) without and b) with considering self induction of all rotor space harmonics excited by $I_{r\nu}$

Example 4.4.1-7: ν^{th} harmonic "leakage":
Four-pole cage induction motor, f_s = 50 Hz, rotor cage with 28 bars, n_{syn} = 1500/min
(i) How big is the increase of rotor self induction voltage due to all rotor space harmonics?

ν	1	-5	7	-11	13
$1/\eta_\nu^2$	1.017	1.55	2.47	15.67	171.87

(ii) At which rotor speed n is the rotor cage NOT induced by ν-th stator space harmonic?

$$f_{r,\nu} = s_\nu\cdot f_s = f_s\cdot\left|1-\nu\cdot(1-s)\right| = 0 \quad\Rightarrow\quad s = 1-1/\nu \quad\Rightarrow\quad n = n_{syn}/\nu$$

ν	1	-5	7	-11	13
s	0	1.2	0.86	1.09	0.92
n /1/min	1500	- 300	214	- 136	115

Conclusions:
Neglecting self induction of rotor space harmonics for calculating rotor harmonic currents yields nearly no error for fundamental rotor current I_r of basic theory Chapter 4.2, but considerable error for higher harmonics; so it must be considered.
In the low speed region between +/ 20% synchronous speed for each stator field harmonic there exists a rotor speed, where rotor cage is not induced by that harmonic.

f) Influence of main flux saturation on stator field spatial harmonics:
Up to now influence of saturation of iron on harmonics has been neglected. Unsaturated sinus space-function of stator fundamental $B_{\delta s,\nu=1}(x)$ is proportional $1/\delta$. Magnetic field strength is $H_{\delta s} = B_{\delta s}/\mu_0$. When iron is unsaturated, H_{Fe} is zero, so total ampere turns of stator are needed only to magnetize air gap, yielding m.m.f. $V_s = H_{\delta s}\cdot\delta$. In case of iron saturation at high $B_{\delta s}$ magnetic field strength in iron along iron path s_{Fe} is not any longer zero, yielding $V_s = H_{\delta s}\cdot\delta + H_{Fe}\cdot s_{Fe}$. So air gap field strength and air gap flux density do not rise any longer linear with increasing V_s (Fig. 4.4.1-5). So if we consider only fundamental of stator air gap field, corresponding with sinusoidal distributed m.m.f. $V_s(x_s) = V_s\cos(x_s\pi/\tau_p - \omega_s t)$,

the air gap flux density distribution is flat-topped, which may be described by a sum of a first and 3rd harmonic.

Conclusions:
Iron saturation causes a distortion of air gap flux density distribution, generating a third harmonic field wave.

$$B_{\delta s,\nu=3}(x_s,t) = B_{\delta s,\nu=3}\cdot\cos\left(\frac{3x_s\pi}{\tau_p} - 3\omega_s t\right) \qquad (4.4.1\text{-}29)$$

Third "saturation harmonic" moves with synchronous speed as fundamental, therefore it induces stator winding with 3-times stator frequency, which is IN PHASE in all three phases. In star connected winding only phase voltage will show a $3f_s$ voltage component, whereas in line-to-line voltage this component is cancelling (see Chapter 1). Current with $3f_s$ cannot flow in star connected winding, but in delta winding it will flow as a circling current within then delta, causing additional winding losses.

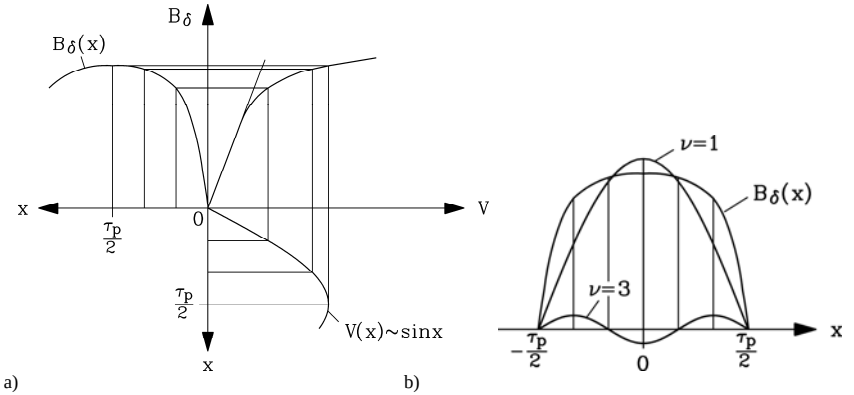

Fig. 4.4.1-5: Generation of third space harmonic of air gap field distribution due to iron saturation

With respect to rotor ($x_s = x_r + 2f_s\tau_p(1-s)t$) this wave is moving with

$$B_{\delta s,\nu=3}(x_r,t) = B_{\delta s,\nu=3}\cdot\cos\left(\frac{3x_r\pi}{\tau_p} - s\cdot 3\omega_s t\right) \quad , \qquad (4.4.1\text{-}30)$$

inducing the rotor with $s\cdot 3f_s$, causing additional rotor harmonic current $I_{r\nu=3}$ with additional losses.

4.4.2 Harmonic torques

a) Asynchronous harmonic torques:
Rotor harmonic currents $I_{r\nu}$ produce not only additional cage losses, but also due to *Lorentz* forces with stator field harmonic $B_{\delta s\nu}$ additional torque, which is called "**asynchronous**

harmonic torque". For the special case $\nu = 1$ this is the asynchronous torque of *Kloss* function. With the same mechanism of
- stator (harmonic) field inducing rotor (harmonic) current and
- rotor (harmonic) producing torque with stator (harmonic) field

the asynchronous harmonic torque is calculated. **Power balance** of equivalent circuit Fig.4.4.1-4 yields harmonic air gap power $P_{\delta\nu}$, transferred to rotor, must be equal to rotor harmonic cage losses $P_{\mathrm{Cu},r\nu}$ and mechanical power $P_{m\nu}$ due to asynchronous harmonic torque $M_{e\nu}$.

$$P_{\delta\nu} = P_{Cu,r\nu} + P_{m\nu} \tag{4.4.2-1}$$

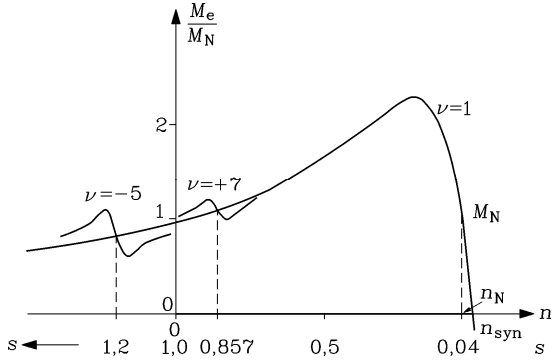

Fig. 4.4.2-1: Asynchronous harmonic of 5th and 7th stator field harmonic, which are superimposed on fundamental asynchronous torque. Data: R_s/X_s =1/100, R_r/X_r = 1.3/100, σ = 0.067, $X_s = X'_r = 3Z_N$, $Z_N = U_N/I_N$, 36 stator and 28 rotor slots, 4 pole machine, single layer winding (unchorded coils), unskewed slots

From equivalent circuit Fig. 4.4.1-4 we see:

$$P_{\delta\nu} = Q_r \cdot (R_r / s_\nu) \cdot I_{r\nu}^2 \quad , \quad P_{Cu,r\nu} = Q_r \cdot R_r \cdot I_{r\nu}^2 \tag{4.4.2-2}$$

Therefore we get for asynchronous harmonic torque $M_{e\nu}$ from

$$P_{m\nu} = \Omega_m M_{e\nu} = (1 - s_\nu)\Omega_{syn,\nu} M_{e\nu} \tag{4.4.2-3}$$

and by comparison of (4.4.2-2), (4.4.2-3) finally the torque itself:

$$M_{e\nu} = \frac{P_{m\nu}}{(1-s_\nu)\Omega_{syn,\nu}} = \frac{\left(\frac{1}{s_\nu} - 1\right) \cdot Q_r R_r I_{r\nu}^2}{(1-s_\nu)\Omega_{syn,\nu}} = \frac{Q_r R_r I_{r\nu}^2}{s_\nu \cdot \Omega_{syn,\nu}} \quad . \tag{4.4.2-4}$$

By taking the absolute value of $I_{r\nu}, I_s$ from (4.4.1-26), **asynchronous harmonic torque** is given depending on the square of stator current and on slip s:

$$\boxed{M_{e\nu} = \frac{(2m_s \cdot N_s k_{ws\nu})^2 \cdot (\omega_s L_{rh\nu})^2}{Q_r \cdot \Omega_{syn,\nu}} \cdot \frac{s_\nu \cdot R_r}{R_r^2 + (s_\nu \cdot \omega_s (L_{r\sigma\nu} + L_{rh\nu}))^2} \cdot I_s^2} \tag{4.4.2-5}$$

Asynchronous harmonic torque follows a *Kloss* function, depending in harmonic slip s_ν. At $s_\nu = 0$ this torque is zero. At $s_\nu > 0$ torque is positive and adds to fundamental torque. At $s_\nu < 0$ the torque is negative and is braking the machine. At **harmonic break down slip**

$$s_{\nu b} = \pm \frac{R_r}{\omega_s (L_{r\sigma\nu} + L_{rh\nu})} \tag{4.4.2-6}$$

torque reaches positive and negative maximum value. As $L_{r\sigma\nu} + L_{rh\nu} >> R_r$ harmonic breakdown slip is small, maximum torque values are nearby the zero value. Harmonic asynchronous torques are excited by each stator field harmonic ν and are superimposed the fundamental asynchronous torque (Fig.4.4.2-1).

b) Synchronous harmonic torques:
Rotor field harmonic of step-like air gap flux density distribution (4.4.1-10), excited by rotor fundamental current I_r, will also produce parasitic torque with stator field harmonics. Like asynchronous harmonic torque, the condition for constant torque generation is
(i) same wave length,
(ii) same velocity (means also: same direction of movement) of stator and rotor field wave.
For asynchronous harmonic these two conditions were always fulfilled, as rotor current distribution and its excited rotor field wave were induced (generated) by stator field wave, thus having the same wave length and velocity. For higher harmonics of rotor field Fig. 4.2-3 these conditions **are only fulfilled at certain rotor slip *s* = *s****:

Stator harmonic field (excited by I_s) : $B_{\delta,\nu} \cdot \cos(\frac{\nu\pi x_s}{\tau_p} - \omega_s t)$ $\quad B_{\delta,\nu} \sim I_s$

Rotor harmonic field (excited by I_r) : $B_{\delta,\mu} \cdot \cos(\frac{\mu\pi x_r}{\tau_p} - s \cdot \omega_s t)$ $\quad B_{\delta,\mu} \sim I_r$

(i) Identical wave lengths: $\lambda_\nu = \lambda_\mu \Rightarrow |\nu| = |\mu| \Rightarrow \underline{\underline{\nu = \mu}}$ or $\underline{\underline{\nu = -\mu}}$

(ii) Identical velocity: $v_\nu = v_{syn} / \nu$ $\quad v_\mu = v_{syn} \cdot (1 - s + s/\mu)$
(with respect to stator)

From $v_\nu = v_\mu$ one gets: $v_{syn} / \nu = v_{syn} \cdot (1 - s^* + s^*/\mu) \Rightarrow s^* = \frac{1/\nu - 1}{1/\mu - 1}$, resulting in the condition for slip where synchronous harmonic torque occurs:

$$\boxed{\begin{aligned} &\nu = \mu: \quad s^* = 1 \\ &\nu = -\mu: \quad s^* = \frac{\nu - 1}{\nu + 1} \end{aligned}} \tag{4.4.2-7}$$

If stator and rotor slot number is the same, then slot harmonics of stator and rotor have IDENTICAL ordinal number $\nu = \mu$, yielding to big synchronous harmonic torque at stand still of motor $s = 1$, which is known as **stand still cogging** (Fig. 4.4.2-2a). Therefore for electric motors usually it must be $Q_s \neq Q_r$. But even in this case for certain harmonics (4.4.2-7) is fulfilled. At certain slip $s^* \neq 1$ and therefore only at certain motor speed n^* stator and rotor field harmonic will create a constant torque $M_{e,\nu\nu}$ with its amplitude proportional to amplitudes of the two reacting field waves: $M_{e\nu\nu} \sim B_{\delta s,\nu} \cdot B_{\delta r,\mu} \sim I_s I_r$. As this harmonic torque occurs only a certain speed where stator and rotor field harmonic move with identical

speed (moving "synchronously"), this kind of harmonic torque is called **synchronous harmonic torque**. If the phase shift $\vartheta_{\nu\mu}$ (Fig. 4.4.2-2b) between the two waves is 0° or 180°, both waves have aligned N- and S-poles, so no torque will occur. This is the same rule as with synchronous machines. Thus phase shift angle may be regarded as load angle, yielding for synchronous harmonic torque

$$M_{e\nu\nu} \sim I_s I_r \cdot \sin \vartheta_{\nu\mu} \qquad (4.4.2\text{-}8)$$

At $\vartheta_{\nu\mu}$ = 90° torque is maximum positive, so torque will add to asynchronous torque, at $\vartheta_{\nu\mu}$ = -90° torque is maximum negative and acts as a brake. As phase shift is an arbitrary value, depending from which position of rotor relative to stator the machine was started, all possible torque values between $-M_{e\nu\nu,\max} ... M_{e\nu\nu,\max}$ may occur.

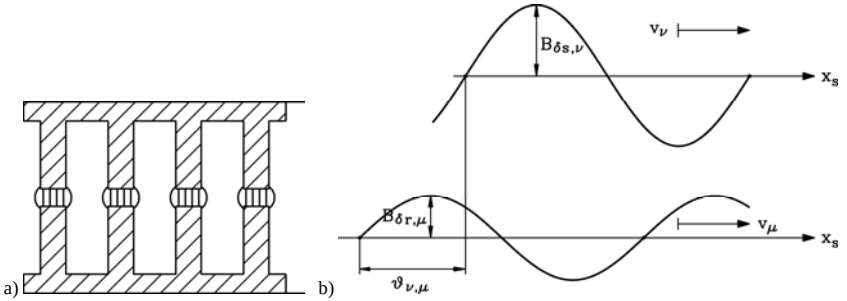

Fig. 4.4.2-2: a) If stator and rotor teeth number is the same, cogging will occur, representing a synchronous torque $\nu = \mu$, b) Generation of synchronous harmonic torque by a ν-th stator and μ-th rotor field harmonic, travelling in air gap with same speed and having same wave length

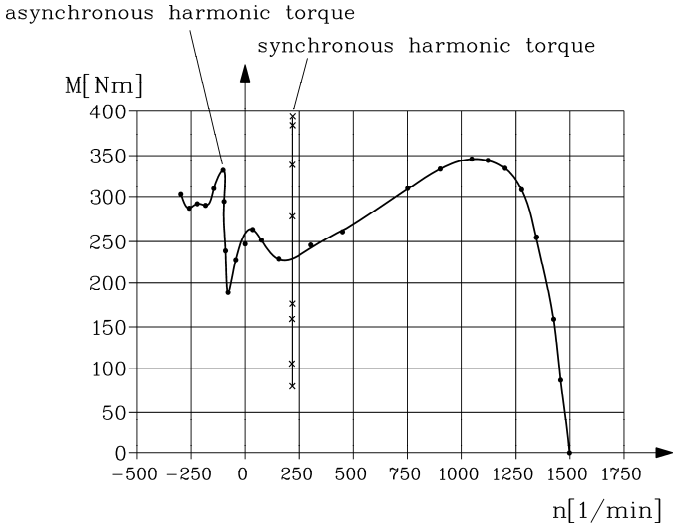

Fig. 4.4.2-3: Induction motor 15 kW, 4-pole, 36/28 slot number ratio: With finite elements calculated *M(n)*-characteristic with asynchronous torque at –136/min and synchronous torque at 215/min

Example 4.4.2-1:
4-pole cage induction motor, 380 V, D, 50 Hz, 15 kW, rated torque M_N = 100 Nm, unskewed slots, Q_s/Q_r = 36/28, air gap 0.45 mm, iron stack length 195 mm, stator bore diameter 145 mm, two-layer winding.
Torque calculated with finite elements:
(i) Asynchronous harmonic torque due to ν = -11 stator field harmonic with synchronous harmonic slip $s_\nu = 0$ at slip $s = 1 - 1/\nu = 1 + 1/11 = 1.09$, corresponding with speed $n = (1-s) \cdot n_{syn} = (1 - 1.09) \cdot 1500 = \underline{\underline{-136/\min}}$.
(ii) Synchronous harmonic torque at slip 0.86. Which field harmonics generate this torque ?
Analysis:
Stator ordinal numbers: $\nu = 1 + 2m_s g = 1 + 6g = 1, -5, 7, -11, 13, -17, 19, ...$
Rotor ordinal numbers: $\mu = 1 + (Q_r / p)g = 1 + 14g = 1, -13, 15, -27, 29, ...$
Condition fulfilled for $\nu = -\mu = 13$: $s^* = \frac{\nu - 1}{\nu + 1} = \frac{12}{14} = 0.857$ $n^* = (1 - s^*) \cdot 1500 = 215/\min$

c) Saturation causes additional harmonic torque:
The 3rd stator harmonic saturation wave caused an additional rotor harmonic current to flow $I_{r\nu=3}$ with frequency $s \cdot 3f_s$, which excites itself a rotor field with rotor harmonic with ordinal numbers

$$\mu = \nu + \frac{Q_r}{p} \cdot g, \quad g = 0, \pm 1, \pm 2, ... \qquad . \qquad (4.4.2\text{-}9)$$

These additional rotor harmonics may be sufficient big to generate with stator field harmonics additional synchronous harmonic torque. Conditions are again:

Stator harmonic field (excited by I_s) : Rotor harmonic field (excited by $I_{r,\nu=3}$) :

$B_{\delta,\nu} \cdot \cos(\frac{\nu \pi x_s}{\tau_p} - \omega_s t)$ $B_{\delta,\nu} \sim I_s$ $B_{\delta,\mu} \cdot \cos(\frac{\mu \pi x_r}{\tau_p} - s \cdot 3\omega_s t)$ $B_{\delta,\mu} \sim I_{r,\nu=3}$

(i) Identical wave lengths: $\lambda_\nu = \lambda_\mu \Rightarrow |\nu| = |\mu| \Rightarrow \underline{\underline{\nu = \mu}}$ or $\underline{\underline{\nu = -\mu}}$
(ii) Identical velocity: $v_\nu = v_{syn} / \nu$ $v_\mu = v_{syn} \cdot (1 - s + 3s/\mu)$
(with respect to stator)

From $v_\nu = v_\mu$ one gets for slip, where harmonic synchronous torque occurs, caused by saturation harmonics:

$$\nu = \mu, \ \nu = -\mu: \qquad s^* = \frac{1/\nu - 1}{3/\mu - 1} \qquad (4.4.2\text{-}10)$$

Example 4.4.2-2:
2-pole cage induction motor, 380 V, D, 50 Hz, 11 kW, rated torque M_N = 37 Nm, skewed slots, Q_s/Q_r = 36/28, insulated copper cage to avoid flow of inter-bar currents, two-layer stator winding, winding pitch 1/2.
Shaft torque measured with accelerometer (Fig. 4.4.2-4a); motor with additional inertia mounted to shaft was reversed from –3000/min to 3000/min by changing two phase connections, thus allowing to measure motor torque in slip range 2 ... 0.

(i) Asynchronous harmonic torque due to ν = -5 stator field harmonic with synchronous harmonic slip $s_\nu = 0$ at slip $s = 1 - 1/\nu = 1 + 1/5 = 1.2$, corresponding with speed:

$n = (1-s)\cdot n_{syn} = (1-1.2)\cdot 3000 = \underline{\underline{-600/\min}}$.

(ii) Synchronous harmonic torque at slip 1.07 and 0.86. Which field harmonics generate these torque components?

Stator ordinal number: $\nu = 1 + 2m_s g = 1 + 6g = 1, -5, 7, -11, 13, -17, 19, -23, 25, -29, 31, -35, 37, ...$

Rotor ordinal numbers of I_r: $\mu = 1 + (Q_r / p)g = 1 + 28g = 1, -27, 29, ...$

Rotor ordinal numbers of $I_{r,\nu=3}$: $\mu = 3 + (Q_r / p)g = 3 + 28g = 3, -25, 31, ...$

Condition fulfilled: $\nu = -\mu = 25 : s^* = \dfrac{1-1/25}{1+3/25} = \underline{\underline{0.857}}$, $\nu = -\mu = -29 : s^* = \dfrac{1+1/29}{1-1/29} = \underline{\underline{1.071}}$

$$\nu = \mu = 31 : s^* = \frac{1-1/31}{1-3/31} = \underline{\underline{1.071}}$$

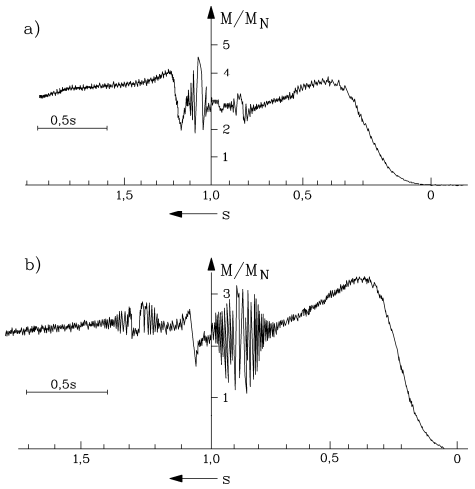

Fig. 4.4.2-4: Measured starting torque with accelerometer of induction machine with insulated copper cage, f_s = 50 Hz, 380 V: a) 2-pole motor, 11 kW, M_N = 37 Nm, 36/28 stator/rotor slots, b) 4-pole motor, 9.5 kW, M_N = 64 Nm, 36/28 stator/rotor slots

Example 4.4.2-3:

4-pole cage induction motor, 380 VD, 50 Hz/9.5 kW, rated torque M_N = 64 Nm, skewed slots, Q_s/Q_r = 36/28, insulated copper cage (= no inter-bar currents), unchorded stator winding. Shaft torque measured with accelerometer like in Example 4.4.2-2 (Fig. 4.4.2-4b).

(i) Asynchronous harmonic torque due to ν = -17 stator field harmonic with synchronous harmonic slip $s_\nu = 0$ at slip $s = 1 - 1/\nu = 1 + 1/17 = \underline{1.058}$.

(ii) Synchronous harmonic torque at slip 1.29 and 0.86. From which field harmonics are these torque components generated ?

Stator ordinal number: $\nu = 1 + 2m_s g = 1 + 6g = 1, -5, 7, -11, 13, -17, 19, -23, 25, -29, 31, -35, 37, ...$

Rotor ordinal numbers of I_r: $\mu = 1 + (Q_r / p)g = 1 + 14g = 1, -13, 15, -27, 29...$

Rotor ordinal numbers of $I_{r,\nu=3}$: $\mu = 3 + (Q_r / p)g = 3 + 14g = 3, -11, 17, -25, 31...$

Condition fulfilled for: $\nu = \mu = -11 : s^* = \dfrac{1+1/11}{1+3/11} = \underline{\underline{0.857}}$

$$\nu = -\mu = 25 : s^* = \frac{1-1/25}{1+3/25} = \underline{\underline{0.857}}$$

$$\nu = -\mu = -17 : s^* = \frac{1+1/17}{1-3/17} = \underline{\underline{1.29}}$$

The synchronous harmonic torques in this example can only be explained by considering iron saturation.

4.4.3 Rotor skew and inter-bar currents

a) Skewing of rotor cage

Slot harmonic effects can be suppressed or reduced by

- two-layer stator winding with chorded coils. If e.g. a chording of 5/6 of coil span is used, then 5th and 7th stator harmonic are reduced strongly.
- semi-closed stator and rotor slots, magnetic wedges in open stator slots or closed rotor slots.
- skewing of slots. As stator skew is expensive, usually rotor cage is skewed.

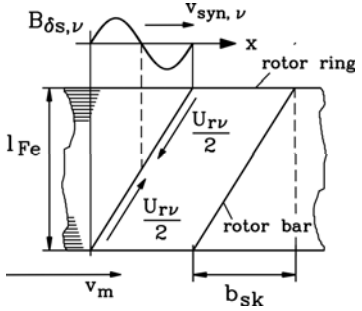

Fig. 4.4.3-1: Due to skew of rotor bar b_{sk} certain stator field harmonic cannot induce rotor

According to *Faraday´*s law induced voltage U_i in a bar with length l, moving in an external magnetic field B perpendicular to field direction with velocity $\Delta v = v_{syn,\nu} - v_m$ is given by

$$U_i = \Delta v \cdot B \cdot l \quad . \tag{4.4.3-1}$$

If skew of rotor bar b_{sk} is equal to wave length $2\tau_p / |\nu|$ of stator field harmonic, the first half of rotor bar will be induced by positive field with positive voltage $U_{r\nu}/2$, and second half by negative field and therefore with voltage $-U_{r\nu}/2$, resulting in zero voltage for whole bar. Thus no harmonic current $I_{r\nu}$ for that ν-th harmonic will be generated. This may be expressed by **skewing factor**

$$\boxed{\chi_\nu = \frac{\sin(S_\nu)}{S_\nu} \quad , \quad S_\nu = \frac{\nu \pi b_{sk}}{2\tau_p}} \quad , \tag{4.4.3-2}$$

which is zero for $\dfrac{2\tau_p}{\nu} = b_{sk}$ and multiples of it. Thus rotor harmonic currents are calculated by taking the formula of Chapter 4.4.1 and multiply it with skewing factor:

$$\underline{I}_{r\nu} = -j\frac{(2m_s \cdot N_s k_{ws\nu} / Q_r)\cdot \omega_s L_{rh\nu}}{R_r / s_\nu + j\cdot\omega_s(L_{r\sigma\nu} + L_{rh\nu})} \cdot \chi_\nu \cdot \underline{I}_s \qquad (4.4.3\text{-}3)$$

Conclusions:
If the rotor cage is skewed by one stator slot pitch $b_{sk} = \tau_s$, then all stator slot harmonics will induce the rotor only negligibly.

Example 4.4.3-1:
4-pole induction motor with 36/28 stator/rotor slots. Rotor cage skewed by one stator slot pitch: $b_{sk} = \tau_p / 9$
Stator field harmonics:
Ordinal numbers: $\nu = 1 + 6g = 1, -5, 7, -11, 13, -17, 19, -23, 25, -29, 31, -35, 37, ...$
Slot harmonics: $\nu = 1 + (36/2)g = 1, -17, 19, -35, 37, ...$

ν	1	-17	19	-35	37
χ_ν	0.9949	0.0585	-0.0523	-0.0284	0.0267

Table 4.4.3-1: Skewing factor for stator slot harmonics, if rotor cage is skewed by one stator slot

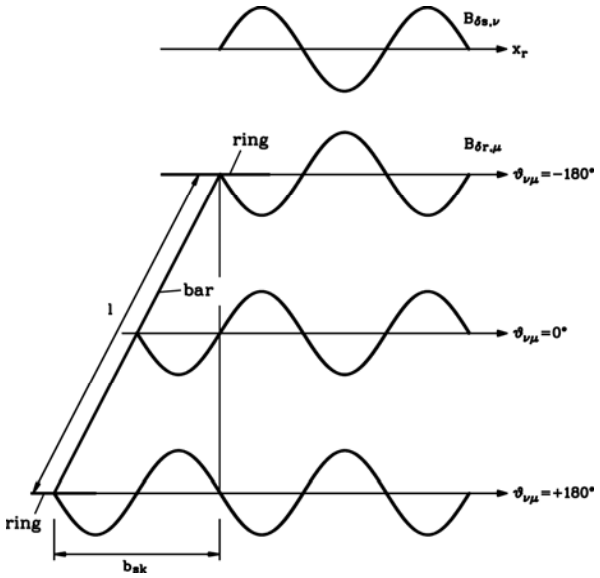

Fig. 4.4.3-2: Skewing of rotor bars b_{sk} leads also to skew of rotor field harmonics, excited by rotor current I_r. So phase shift between stator and rotor field harmonic varies along bar length and leads to cancelling of synchronous slot harmonic torque.

Harmonic synchronous torque is also reduced strongly by skewing. The rotor field harmonics of the rotor field, excited by rotor current, are – as explained – all of slot harmonic order. If rotor is skewed by one stator slot pitch, also the rotor slot harmonic flux waves are skewed in the same way (Fig. 4.4.3-2). For stator slot harmonics therefore phase shift angle $\vartheta_{\nu\mu}$ varies between –180° ... 180° along rotor bar length. Average harmonic torque production is therefore zero.

$$M_{e\nu\nu} \sim I_s I_r \cdot \int_{-180°}^{180°} \sin\vartheta_{\nu\mu}\cdot d\vartheta_{\nu\mu} = 0 \qquad (4.4.3\text{-}4)$$

Conclusions:
Skewing by one stator slot pitch leaves the fundamental field almost unaffected, but nearly cancels the inducing effect of stator slot harmonics. Therefore asynchronous harmonic torque components due to stator slot harmonics are minimized effectively. Skewing generates also variable phase shift between stator and rotor field wave, thus allowing cancelling of synchronous harmonic torque.
In order to avoid distortion of fundamental asynchronous torque M(n)-characteristic by harmonic torque effect, cage rotors of line-starting induction machines are always skewed, usually by one stator slot pitch.

b) Losses due to inter-bar currents:
Rotor bars are usually not insulated, but have electrical contact to iron stack. As number of turns per winding (= per bar) is only 1/2, induced voltage is low, so no big voltage difference between cage and iron occurs. Along rotor circumference induced voltage varies sinusoidal, so total rotor potential as average value of voltage sinus distribution is zero. Moreover, only with copper bars, inserted manually in rotor slots, cage insulation is possible, whereas with aluminium die cast cage usually not. By the way, between iron stack and copper or aluminium bar, oxidation of iron will cause additional contact resistance, which can be measured as **inter-bar resistance** R_q between adjacent bars according to Fig. 4.4.3-3. So by nature itself, rotor bars are insulated to a certain extent. If A denotes the half-surface of a rotor bar, the inter-bar resistance is smaller, if A is bigger.

$$R_q = \frac{\Delta l_{ox}}{\kappa_{ox}\cdot A} \qquad (4.4.3\text{-}5)$$

Neglecting the good conducting iron and copper or aluminium part, inter-bar resistance is determined by thickness of oxidation layer Δl_{ox} between bar and iron and conductivity of this oxide κ_{ox}. A typical value for aluminium die cast cages is

$$r_q = \Delta l_{ox} / \kappa_{ox} = 10^{-6}\,\Omega\cdot m^2 \quad , \qquad (4.4.3\text{-}6)$$

from which inter-bar resistance is calculated by $R_q = r_q / A$.

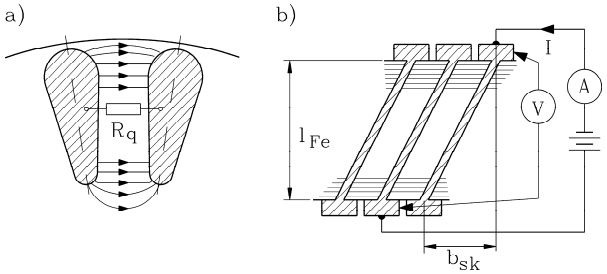

Fig. 4.4.3-3: Inter-bar resistance between adjacent bars R_q is much bigger than bar or ring resistance, as it is determined by oxidation of iron stack and bar surface. a) Inter-bar current flow via half bar-surface A during operation, b) During measurement current flows via $2A$, hence we obtain: $R_q = 2(U/I - R_{bar} - \Delta R_{ring})$.

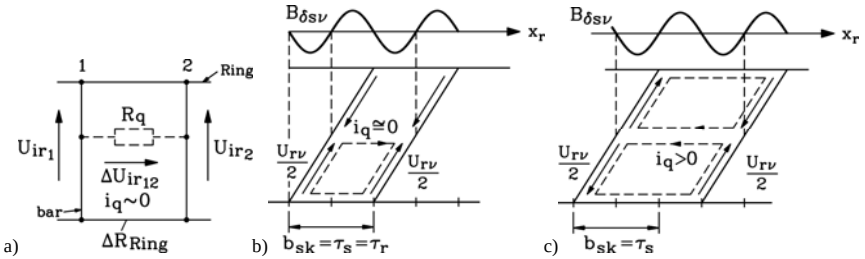

Fig. 4.4.3-4: Effect of inter-bar resistance due to oxidation R_q : a) Unskewed cage: inter-bar current is almost zero, b) Rotor cage skewed by one stator slot, stator and rotor slot number equal $Q_r = Q_s$: harmonic inter-bar current almost zero, c) as b), but $Q_r = Q_s/1.5$; harmonic inter-bar current may flow, as harmonic voltage adds up.

In unskewed rotor cages voltage difference ΔU_{ir12} along the rotor bar is constant. So the two low-ohmic ring segment resistances ΔR_{ring} are in parallel with high-ohmic inter-bar resistance R_q. Current will flow from one bar to next nearly only by ring segments as ring current. Nearly no **inter-bar current** via R_q will occur (Fig. 4.4.3-4a).
In skewed rotors with $b_{sk} = \tau_s$ harmonic voltage – induced by ν-th stator slot harmonics - considered along the loop of two bars and two ring segments, is zero. No harmonic bar or ring current will flow. In presence of finite inter-bar resistance an additional current flow along dashed line in Fig. 4.4.3-4 b, c is possible. If stator and rotor slot number is the same (which is forbidden to avoid stand still cogging, of course), total voltage along dashed loop is zero, so again no inter-bar current will flow even at low inter-bar resistance (Fig. 4.4.3-4b). Under real conditions with $Q_r < Q_s$ in Fig. 4.4.3-4c harmonic induced bar voltage along dashed loop sums up to maximum value, so considerable inter-bar current flow is possible, causing additional **inter-bar losses**

$$P_{Q\nu} = Q_r \cdot R_q I_{q\nu}^2 \quad . \tag{4.4.3-7}$$

Conclusions:
Skewing (in non-insulated rotor cages) may give rise to inter-bar currents, which cause additional losses and may increase asynchronous harmonic torque.

In case of $R_q = 0$ inter-bar losses are zero, but also for $R_q \to \infty$, as in that case rotor cage is insulated ideally. Therefore **additional rotor cage losses**, given by ohmic losses in bar and ring due to rotor harmonic current $I_{r\nu}$ and in inter-bar resistance due to inter-bar current $I_{q\nu}$

$$P_{ad,r} = Q_r \cdot \sum_{\nu>1}^{\infty} (R_r I_{r\nu}^2 + R_q I_{q\nu}^2) \quad . \tag{4.4.3-8}$$

varies with varying inter-bar resistance according to Fig. 4.4.3-5 with a maximum value for certain inter-bar resistance, which must be avoided by motor design to keep additional losses low.

Example 4.4.3-2:
Motor data: 200 kW, 50 Hz, 2 poles, stator/rotor slot number 36/28, closed rotor slots, Aluminium cage, skewed by one stator slot pitch.
Half-surface of rotor bar: A = 28570 mm^2, yielding "nominal" inter-bar resistance with $r_q = 10^{-6}\,\Omega \cdot m^2$: $R_{qN} = r_q / A = 10^{-6} / (28570 \cdot 10^{-6}) = \underline{\underline{0.035}}\,\mathrm{m\Omega}$ (Fig.4.4.3-5).

At "nominal" inter-bar resistance additional rotor cage losses are only 350 W (= 0.18% rated power). In worst case at R^*_q = 2 mΩ these losses may reach 1 kW (= 0.5% of rated power).

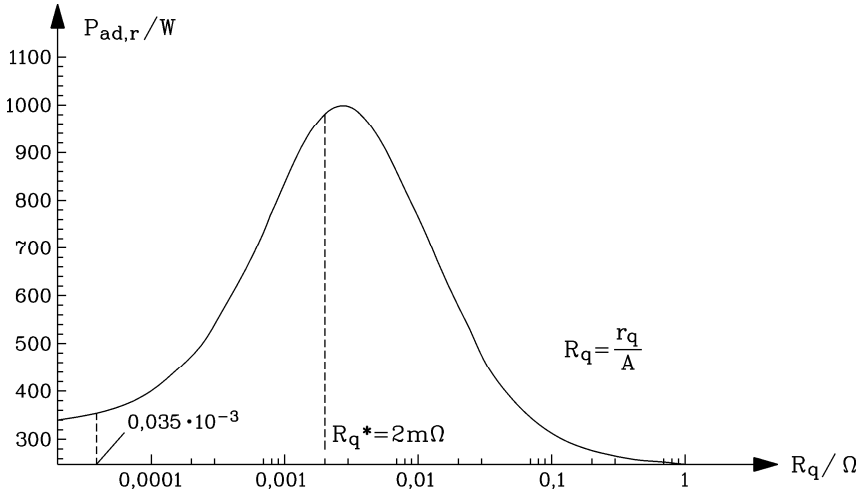

Fig. 4.4.3-5: Calculated influence of inter-bar resistance on additional rotor cage losses due to rotor harmonic currents at rated motor slip s = 0.01 (Motor data: 200 kW, 50 Hz, 2 poles, stator/rotor slot number 36/28, closed rotor slots, Aluminium cage, skewed by one stator slot pitch)

Conclusions:
In the above example due to $R_{qN} < R^*_q$ an increase of inter-bar resistance will increase inter-bar losses, which none would have expected. With small motors (below 5 kW) usually "nominal" inter-bar resistance is $R_{qN} > R^*_q$. Therefore an increase of inter-bar resistance by e.g. heating up of rotor in the oven to increase oxide thickness usually decreases rotor losses. This is especially essential for single phase induction motors, where rotor cage losses are increased due to inverse fundamental air gap field component.

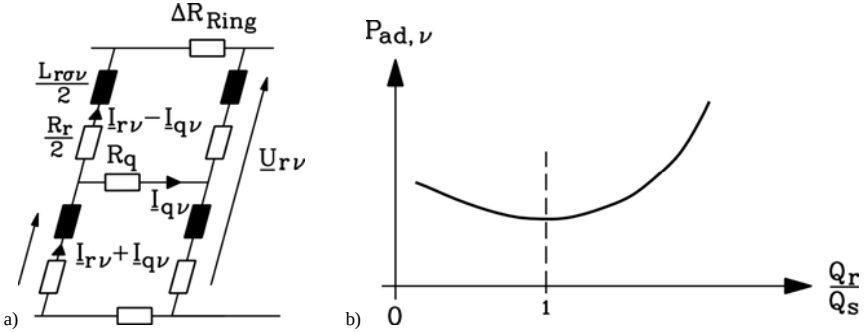

Fig. 4.4.3-6: a) Simplified equivalent circuit of one rotor loop with bar and ring resistance and loop stray inductance, considering inter-bar resistance to be concentrated in middle of bar, b) Variation of additional rotor cage losses with variation of stator-rotor slot ratio.

$Q_s = Q_r$ **:**
Unskewed rotors have nearly no inter-bar losses (Fig. 4.4.3-4a). With skewed rotors, inter-bar losses vary also with ratio Q_r/Q_s. At $Q_r/Q_s = 1$ these losses are minimum (Fig. 4.4.3-4b).
$Q_s > Q_r$:
The rather low rotor slot number causes a big deviation of step-like rotor flux density distribution, excited by $I_{r\nu}$, from sine wave fundamental, thus $L_{r\sigma\nu} = (1/\eta_\nu - 1)\cdot L_{rh\nu} + L_{r\sigma}$ is rather big and limits rotor harmonic and inter-bar current (Fig. 4.4.3-6a).
$Q_s < Q_r$:
High rotor slot number yields causes a smaller deviation of step-like rotor flux density distribution, excited by $I_{r\nu}$, from sine wave fundamental, so factor η_ν is closer to unity, $L_{r\sigma\nu}$ is small and harmonic currents and related losses will increase (Fig. 4.4.3-6b).

Conclusions:
Line-starting cage induction motors have skewed rotor cage to reduce harmonic torque influence on start-up torque. Rotor slot number is chosen SMALLER than stator slot number to reduce additional inter-bar losses.

Example 4.4.3-3:
Explosion proof induction motor (EExeII): Data: Motor size 80 mm, pole number $2p = 2$, slot numbers $Q_s / Q_r = 18 / 23$, $Q_s < Q_r$ (!), rotor skewed by one rotor slot pitch.
Motor was operated on test-bench at rated load. Rotor cage temperature was too high due to increased inter-bar losses, also heating up stator winding too much.
After changing rotor against a new one with $Q_r = 14$ (skewed), $Q_s > Q_r$ (!) with the same bar and ring resistance losses went down significantly, so that stator winding temperature stayed within thermal limits.

c) Additional asynchronous harmonic torque due to inter-bar currents:
Considering simplified equivalent circuit Fig. 4.4.3-6 a), one can solve this mesh equation, getting the inter-bar current $I_{q\nu}$ per harmonic induced rotor voltage $U_{r\nu}$. So in rotor bars flows the superposition of $I_{r\nu}$ (valid for infinite R_q) and of $I_{q\nu}$. For **unskewed** cage induced voltage in upper and lower mesh half is simply $U_{r\nu}/2$, so $I_{q\nu}$ in this simplified equivalent circuit is exactly zero.
For skewed cage one gets inter-bar current $I_{q\nu}$ flow, so the bar harmonic currents $\underline{I}_{r\nu} \pm \underline{I}_{q\nu}$ generate not only the harmonic asynchronous torque due to $I_{r\nu}$, as explained in Chapter 4.4.2,

$$M_{e\nu} = \frac{(2m_s N_s k_{ws\nu})^2 (\omega_s L_{rh\nu})^2}{Q_r \cdot \Omega_{syn,\nu}} \cdot \frac{s_\nu \cdot R_r}{R_r^2 + (s_\nu \cdot \omega_s (L_{r\sigma\nu} + L_{rh\nu}))^2} \cdot I_s^2 \cdot \chi_\nu^2 \qquad (4.4.3\text{-}9)$$

but also an additional harmonic torque due to $I_{q\nu}$

$$M_{eq\nu} = \frac{(2m_s N_s k_{ws\nu})^2 (\omega_s L_{rh\nu})^2}{Q_r \cdot \Omega_{syn,\nu}} \cdot \frac{s_\nu \cdot (R_r + 4R_q)}{(R_r + 4R_q)^2 + (s_\nu \cdot \omega_s (L_{r\sigma\nu} + L_{rh\nu}))^2} \cdot I_s^2 \cdot \chi_{q\nu}^2 \quad , \qquad (4.4.3\text{-}10)$$

depending on factor $\chi_{q\nu}$ instead of χ_ν .

$$\chi_{q\nu} = \frac{\sin^2(S_\nu / 2)}{S_\nu / 2} \quad S_\nu = \frac{\nu \pi b_{sk}}{2\tau_p} \quad . \qquad (4.4.3\text{-}11)$$

Break down slip, where maximum harmonic torque occurs, is much bigger for $M_{eq\nu}$ than for $M_{e\nu}$ (Fig. 4.4.3-7):

$$s_{\nu b} = \pm \frac{R_r + 4R_q}{\omega_s (L_{r\sigma\nu} + L_{rh\nu})} \quad \text{instead of} \quad s_{\nu b} = \pm \frac{R_r}{\omega_s (L_{r\sigma\nu} + L_{rh\nu})} \quad . \qquad (4.4.3\text{-}12)$$

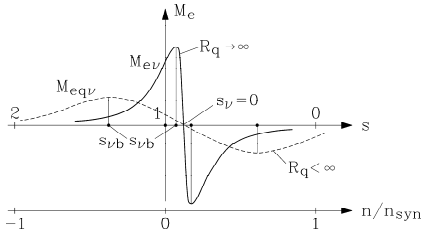

Fig. 4.4.3-7: Qualitative characteristic of asynchronous harmonic torque $M_{e\nu}$ (at infinite inter-bar resistance) and additional torque $M_{eq\nu}$ due to inter-bar current with its much bigger break-down slip

Example 4.4.3-4:
With rotor cage skewed by one stator slot pitch, skewing factor χ_ν is almost zero, so asynchronous harmonic torques disappear. But on the other hand factor $\chi_{q\nu}$ differs from zero for first / third / fifth ... pair of slot harmonics, so **additional asynchronous torque** $M_{eq\nu}$ appear.
Motor data: 4-pole induction motor with 36/28 stator/rotor slots. Rotor cage skewed by one stator slot pitch: $b_{sk} = \tau_p / 9$
Stator slot harmonics: $\nu = 1 + (36/2)g = 1, -17, 19, -35, 37, ...$

ν	1	-17	19	-35	37
χ_ν	0.9949	0.0585	-0.0523	-0.0284	0.0267
$\chi_{q\nu}$	0.0871	-0.669	0.598	-0.0025	0.0024

Table 4.4.3-2: Skewing factor and influence of inter-bar resistance for stator slot harmonics, if rotor cage is skewed by one stator slot

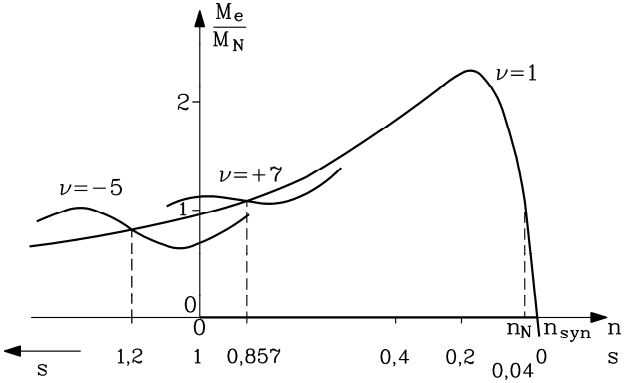

Fig. 4.4.3-8: Qualitative characteristic of total asynchronous torque as superposition of the fundamental and of the harmonic torque $M_{eq\nu}$ (here: 5th and 7th harmonic) due to inter-bar currents

According to Table 4.4.3-2 inter-bar current leaves fundamental asynchronous torque almost unaffected, as $\chi_{qv=1}$ is small. Resulting asynchronous start-up torque of induction motor with skewed rotor cage is a super-position of fundamental torque and harmonic torques M_{eqv}. Therefore the $M(n)$-characteristic shows **a broad and deep saddle** in the region $1 \le s \le 0$ and an increased braking torque at $s > 1$.

Example 4.4.3-5:
Experimental comparison of **insulated copper cage and non-insulated aluminium cage** with same bar and ring resistance (see Examples 4.4.2-2 and 4.4.2-3). Cage skewed by one stator slot pitch. Stator voltage 380 V, D, 50 Hz, Q_s/Q_r = 36/28.

a) 2-pole motor, 11 kW, M_N = 37 Nm Fig. 4.4.3-9	b) 4-pole motor, 9.5 kW, M_N = 64 Nm Fig. 4.4.3-10

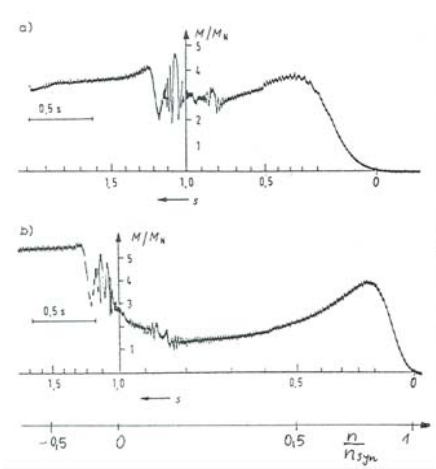

Fig. 4.4.3-9

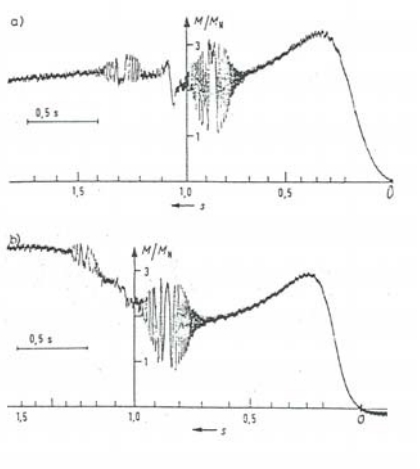

Fig. 4.4.3-10

Fig. 4.4.3-9: 2-pole induction motor, f_s = 50 Hz, 380 V, 11 kW, M_N = 37 Nm, 36/28 stator/rotor slots

Fig. 4.4.3-10: 4-pole induction motor, f_s = 50 Hz, 380 V, 9.5 kW, M_N = 64 Nm, 36/28 stator/rotor slots

Measured starting torque of cage induction motor: a) insulated copper cage, b) non-insulated aluminium cage of same resistance. Additional asynchronous harmonics torque due to inter-bar currents decrease starting torque for 1...s...0 and increase braking torque at s > 1. Note that due to increased braking and reduced starting torque at b) decelerating time from s = 2 to s = 1 is much smaller and start-up time from s = 1 to s = 0 takes longer than at a).

In 2-pole motor the rotor slot number per pole pair is with 28 twice of that of 4-pole motor. So factor η_v for 2-pole machine is closer to unity than for 4-pole machine, yielding a lower $L_{r\sigma\nu} = \left(1/\eta_\nu^2 - 1\right) \cdot L_{rh\nu} + L_{r\sigma}$. Therefore rotor harmonic and inter-bar current is bigger in 2-pole machine, yielding bigger harmonic torque M_{eqv} . Therefore the saddle shaped torque reduction of start-up torque of 2-pole machine is bigger than for 4-pole machine.

Influence of slot number ratio determines not only losses, but also harmonic torque. With $Q_s > Q_r$ the rather big rotor harmonic and inter-bar current will distort $M(n)$-characteristic much stronger than for $Q_s < Q_r$.

Example 4.4.3-6:
Influence of slot number ratio on $M(n)$-characteristic:
Motor data: Motor size 160 mm, 11 kW, 380 V, D, 50 Hz, 2p = 6, air gap 0.35 mm, iron stack length l_{Fe} = 170 mm, Q_s = 36, Single layer winding, semi-closed stator and rotor slots, rotor aluminium die cast cage.
Comparison of calculated ($r_q = 10^{-6}\ \Omega \cdot m^2$) and measured torque for two different rotors:

a) $Q_s > Q_r$	b) $Q_s < Q_r$
Q_r = 33	Q_r = 42

Rotor bar skew: 1 rotor slot pitch. Calculated and mesured results are shown in Fig. 4.4.3-11.

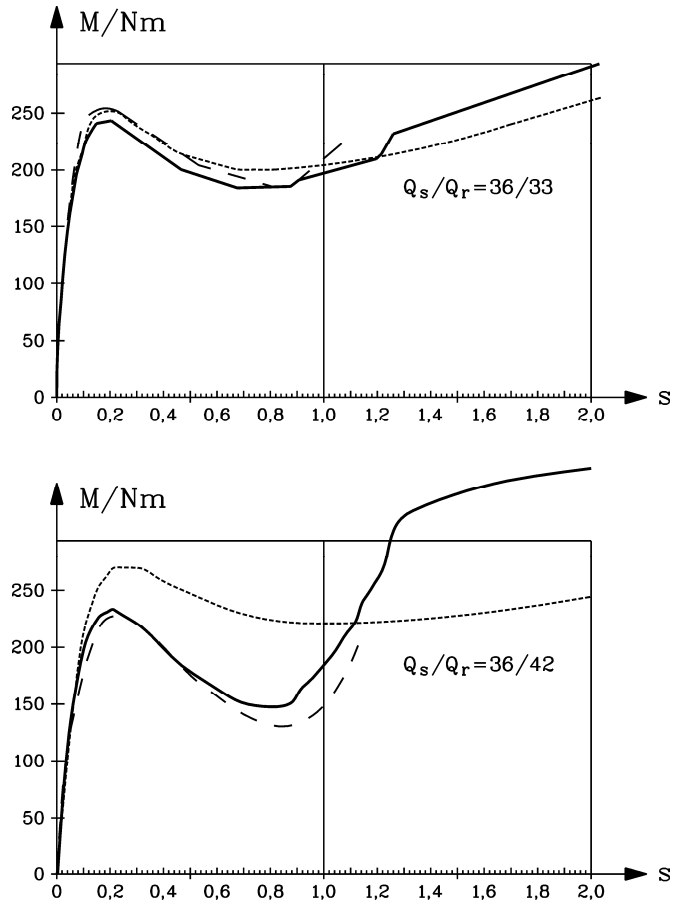

Fig. 4.4.3-11: Measured and calculated torque characteristic between stand still and no-load of 6-pole induction motor, f_s = 50 Hz, 380 V, 11 kW, M_N = 110 Nm, 36 stator slots, non-insulated aluminium cage: above: Q_r = 33, below: Q_r = 42
--------- calculated fundamental asynchronous torque
——— calculated total torque including asynchronous harmonic torque
-.-.-.-.-.- measured total torque

4.4.4 Electromagnetic acoustic noise

The harmonic field waves of stator and rotor do not only interact as tangential forces, leading to harmonic torque, but also as radial forces due to the magnetic pull between stator and rotor iron surface. Magnetic pull F_n between two parallel iron surfaces (surface *A*), with magnetic field B_n crossing the gap in between perpendicular, is according to *Maxwell* (Fig.4.4.4-1)

$$f_n = \frac{F_n}{A} = \frac{B_n^2}{2\mu_0} \quad . \tag{4.4.4-1}$$

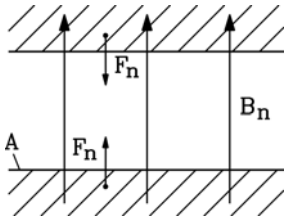

Fig. 4.4.4-1: Magnetic field B_n crossing the gap between two parallel iron surfaces (surface *A*) leads to an attracting force, the magnetic pull F_n

The space harmonic air gap field waves of stator and rotor must be considered as the total radial magnetic field, which exerts a time-varying magnetic pull on stator and rotor iron surface.

- Stator harmonic field wave, excited by stator current I_s with stator frequency f_s :

$$B_{\delta s\nu}(x_s,t) = B_{\delta s\nu} \cdot \cos\left(\frac{\nu\pi x_s}{\tau_p} - 2\pi f_s t\right), \qquad \nu = 1 + 2m_s g\ ,\ g = 0,\pm1,\pm2,... \tag{4.4.4-2}$$

- Rotor harmonic field wave, excited by rotor fundamental bar current I_r with rotor frequency $f_r = s \cdot f_s$:

$$B_{\delta r\mu}(x_r,t) = B_{\delta r\mu} \cdot \cos\left(\frac{\mu\pi x_r}{\tau_p} - 2\pi \cdot s \cdot f_s t\right),\ \ \mu = 1 + g \cdot Q_r / p\ ,\ \ g = 0,\pm1,\pm2,... \tag{4.4.4-3}$$

Considering rotor wave in stator fixed reference frame, that means instead of rotor co-ordinate x_r in terms of stator co-ordinate x_s:

$$x_r = x_s - v_m t = x_s - (1-s)\cdot v_{syn} \cdot t = x_s - (1-s)\cdot 2 f_s \tau_p \cdot t \tag{4.4.4-4}$$

yields

$$B_{\delta r\mu}(x_s,t) = B_{\delta r\mu} \cdot \cos\left(\frac{\mu\pi x_s}{\tau_p} - 2\pi f_s t \cdot (s + \mu(1-s))\right) \quad . \tag{4.4.4-5}$$

The magnetic pull due the harmonic waves is

$$f_n(x_s,t) = \frac{B^2(x_s,t)}{2\mu_0} \sim (\sum_{\nu} B_{\delta s\nu} + \sum_{\mu} B_{\delta r\mu})^2 \quad \Rightarrow \quad f_{n,\mu\nu} \sim \sum_{\nu,\mu} B_\nu^2 + 2B_\nu B_\mu + B_\mu^2 \quad . \tag{4.4.4-6}$$

Mainly the mixed products $B_\nu B_\mu$ result in radial forces, whose pulsating frequencies are in audible region of about 100 Hz to 16 kHz. We abbreviate

$$\alpha = \frac{\nu\pi x_s}{\tau_p} - 2\pi f_s t\ , \qquad \beta = \frac{\mu\pi x_s}{\tau_p} - 2\pi f_s t \cdot (s + \mu(1-s)) \tag{4.4.4-7}$$

and use the trigonometric formula

$$B_{\delta s\nu}\cos\alpha \cdot B_{\delta r\mu}\cos\beta = B_{\delta s\nu}B_{\delta r\mu} \cdot \frac{1}{2} \cdot \left[\cos(\alpha+\beta) + \cos(\alpha-\beta)\right] \ ,$$

getting

$$\begin{aligned} \alpha + \beta &= 2(\nu+\mu)p \cdot \frac{\pi x_s}{2p\tau_p} - 2\pi f_s t\left[(\mu-1)\cdot(1-s) + 2\right] \\ \alpha - \beta &= 2(\nu-\mu)p \cdot \frac{\pi x_s}{2p\tau_p} - 2\pi f_s t\left[(\mu-1)\cdot(1-s) - 0\right] \end{aligned} \quad . \tag{4.4.4-8}$$

As a result, **radial force density waves** are derived, which exert an oscillating pull on stator and rotor iron stack.

$$\boxed{f_{n,\nu\mu}(x_s,t) = \frac{B_{\delta s\nu}B_{\delta r\mu}}{2\mu_0} \cdot \cos(2r \cdot \frac{\pi x_s}{2p\tau_p} - 2\pi f_{Ton} t)} \tag{4.4.4-9}$$

The number of positive and negative half-waves of force density along machine circumference equals **the number of nodes 2*r*** in between:

$$\boxed{2r = 2p \cdot |\nu \pm \mu|} \tag{4.4.4-10}$$

The **tonal frequency** f_{Ton} of force wave variation is

$$f_{Ton} = f \cdot |(\mu-1)\cdot(1-s) + 2| \qquad \text{for} \qquad 2r = 2p \cdot |\nu + \mu| \tag{4.4.4-11}$$

$$f_{Ton} = f \cdot |(\mu-1)\cdot(1-s) - 0| \qquad \text{for} \qquad 2r = 2p \cdot |\nu - \mu| \quad . \tag{4.4.4-12}$$

The stator iron may be regarded as a steel ring, whereas the rotor is a steel cylinder. Therefore the stator is less stiff than the rotor and is bent by the force waves. As the iron surface is shaken with this frequency, the surrounding air is compressed and de-compressed with the same frequency. So acoustic sound waves are generated with tonal frequencies, which may be heard by e.g. human beings. In Fig. 4.4.4-2 the force density distribution along the air gap circumference is shown for force waves with different numbers of nodes. Nodes occur always in pairs

$$2r = 0,\ 2,\ 4,\ 6,\ 8,... \quad . \tag{4.4.4-13}$$

At **2*r* = 0** no nodes occur. The whole stator ring is expanded and shrunken with tonal frequency. All surface elements of stator oscillate in phase, so air is compressed / de-compressed in phase along stator circumference. Therefore stator surface acts like a loud-speaker membrane and **acoustic sound wave is far reaching** (Fig. 4.4.4-3a).

At **2*r* = 2** the whole geometry is oscillating in a certain direction. Therefore the rotor is bent. If tonal frequency coincides with natural **bending frequency of rotor**, resonance with big bending amplitude may occur.
At **2*r* > 2** mainly the stator ring-like geometry is bent. With increased node number zones of compressed and de-compressed air alternate along stator circumference, thus helping to equalize sound pressure. Therefore with increasing node number sound waves decrease rather rapidly in amplitude with increasing distance from motor surface (Fig. 4.4.4-3b).

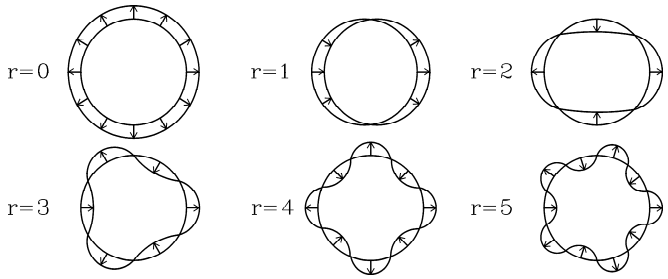

Fig. 4.4.4-2: Force distribution along air gap circumference for different force waves with different node numbers

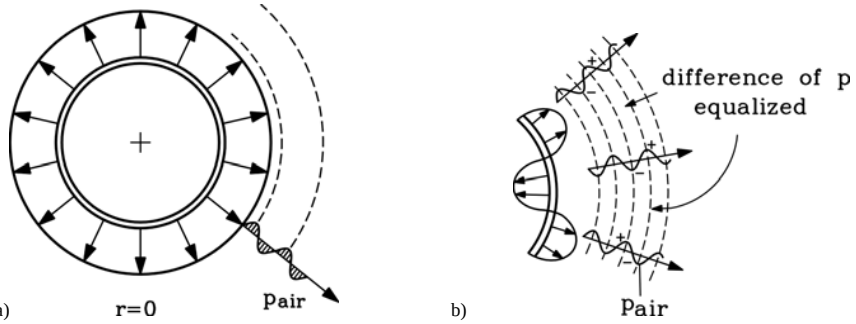

Fig. 4.4.4-3: Oscillating stator surface compresses / de-compresses air and generates acoustic sound waves.
a) For 2*r* = 0 stator surface oscillates in phase along stator circumference, so far reaching sound wave is generated.
b) With increased node number zones of compressed and de-compressed air alternate along stator circumference, thus helping to equalize sound pressure. Therefore with increasing node number sound waves decrease rather rapidly in amplitude with increasing distance from motor surface.

Stiffness of stator is defined mainly by stator yoke thickness and by stator housing stiffness. Motors with high pole count and therefore small flux per pole usually have thin stator yokes and therefore are not very stiff. So the natural bending frequency is low.

Conclusions:
Magnetic excited acoustic noise of line-operated induction machines occurs mainly, if
a) *tonal frequency of exciting force wave coincides with natural bending frequency of stator yoke,*
b) *the number of nodes of exciting force wave coincides with number of oscillation nodes of natural bending mode of stator yoke.*

Example 4.4.4-1:
Experimental modal analysis to detect natural bending mode and frequencies of induction motor:
Data: 6-pole 11 kW induction motor, motor size 160 mm, 36 stator slots, foot-mounted housing (international mounting IM B3)
a) Motor was excited with electromagnetic shaker with radial vibration with frequency varying from 250 Hz to 2750 Hz. Measured oscillation amplitude, expressed as per unit value *R* (Fig. 4.4.4-4), showed **resonance behaviour** at 390 Hz, 650 Hz, 975 Hz, 1495 Hz, 1820 Hz.
b) In second step rotor was removed and natural bending mode was examined at resonace frequencies 650 and 1820 Hz. Due to rotor removal resonance frequency decreased to 592 Hz and 1739 Hz. Exciting stator and housing with that frequency, a four-node bending mode was found at to be the natural bending mode at 592 Hz and a six-node bending mode at 1739 Hz. An additional resonance was found at 2704 Hz with 8-node bending mode (Fig. 4.4.4-5).

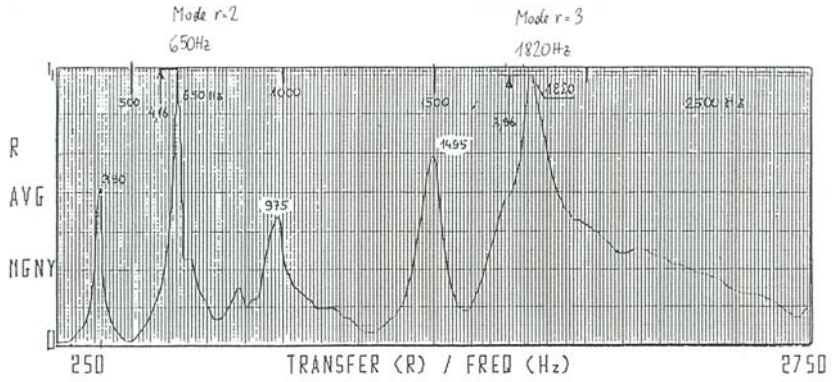

Fig. 4.4.4-4: 6-pole 11 kW induction motor, motor size 160 mm, foot-mounted housing, fan hood removed. Measured relative radial oscillation amplitude *R* of stator surface under sinusoidal radial force excitation **with varying frequency**, which is exhibiting several resonance states.

Example 4.4.4-2:
Calculation of tonal frequencies and measurement of sound pressure level for 6-pole motor of Example 4.4.4-1 (36 stator slots) for two different rotors, operated from 50 Hz grid.
a) rotor with 33 slots,
b) rotor with 42 slots

• Ordinal number of stator field harmonics:
$\nu = 1 + 6g =$ 1,-5,+7,-11,+13,-17,+19,-23,+25,-29,+31,-35,+37,..
Slot harmonics are underlined.

• Ordinal number sof rotor field harmonics, excited by rotor current I_r under load:
a) $\mu = 1 + (Q_r / p)g = 1 + 11g =$ 1,-10,+12,-21,+23,-32,+34,..
b) $\mu = 1 + (Q_r / p)g = 1 + 14g =$ 1,-13,+15,-27,+29,-41,+43,...

• Node number and tonal frequency of radial force waves at rated slip s = 0.03:
Only stator slot harmonics will be considered, as they have considerable amplitude.

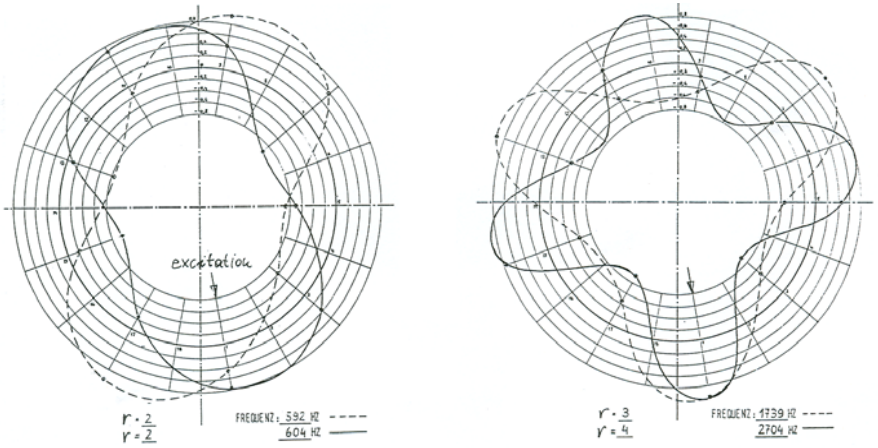

a) b)

Fig. 4.4.4-5: 6-pole 11 kW induction motor, stator iron stack and housing, rotor removed (data see Fig. 4.4.4-4). Measured relative radial oscillation amplitude *R* of stator surface under sinusoidal radial force **excitation at fixed excitation frequency** to investigate natural bending modes., resulting in

a) at excitation frequency: 592 Hz and 604 Hz, four-node bending mode as natural bending mode
b) at excitation frequency: 1739 Hz: 6-node bending mode
2704 Hz: 8-node bending mode

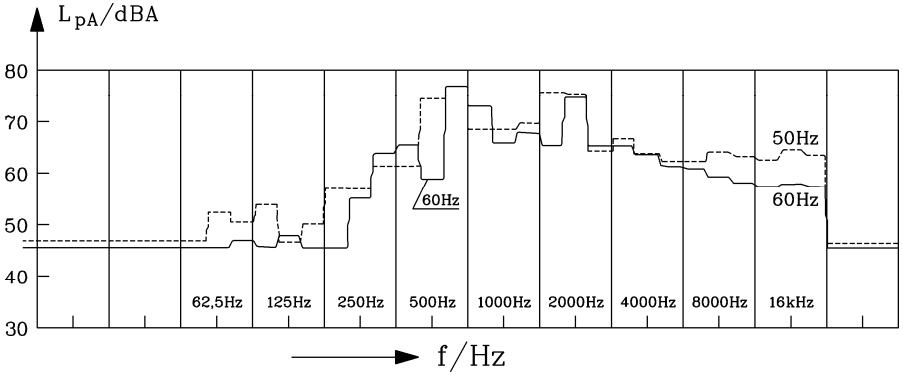

Fig. 4.4.4-6: Measured sound pressure level of 6-pole 11 kW induction motor at rated load, removed fan hood, operated at 50 Hz (--------) and 60 Hz (————) alternatively. Maximum sound pressure occurs in 500 Hz and 2000 Hz band with up to 78 dB(A). Graphs shows sound pressure level at loudest point (= aside of motor in 1 m distance of motor surface).

Rotor a):

ν = -11, μ = -10: $r = |p(\nu-\mu)| = |3(-11+10)| = 3$, $f_{Ton} = 50|(-10-1)(1-0.03)+0| = \underline{\underline{533.5}}$ Hz

ν = 13, μ = 12 : $r = |p(\nu-\mu)| = |3(13-12)| = 3$, $f_{Ton} = 50|(12-1)(1-0.03)+0| = \underline{\underline{533.5}}$ Hz

ν = -23, μ = 23 : $r = |p(\nu+\mu)| = |3(-23+23)| = 0$, $f_{Ton} = 50|(23-1)(1-0.03)+2| = \underline{\underline{1167}}$ Hz

ν = -35, μ = 34 : $r = |p(\nu+\mu)| = |3(-35+34)| = 3$, $f_{Ton} = 50|(34-1)(1-0.03)+2| = \underline{\underline{1700.5}}$ Hz

From modal analysis natural bending modes and frequencies are known:
r = 2, *f* = 592Hz; *r* = 3, *f* = 1739 Hz.
Therefore oscillation with 533.5 Hz and 1700.5 Hz is amplified. Measured sound pressure level L_{pA} was frequency analysed within frequency bands (Fig. 4.4.4-6). Frequency band centred at 500 Hz and that centred at 2000 Hz showed sound pressure level up to 78 dB(A), which for a 11 kW motor is already rather noisy. These noise peaks are due to the resonance at 592 Hz and 1739 Hz, which are excited by the force waves 533.5 Hz and 1700.5 Hz.

Operation of motor at 60 Hz grid yields a 120% shift in exciting frequency. So also measured acoustic sound spectrum is shifted by that 120% to higher frequencies (Fig. 4.4.4-6).

Rotor b):

ν = 13, μ = -13: $r = |p(\nu+\mu)| = |3(13-13)| = 0$, $f_{Ton} = 50|(-13-1)(1-0.03)+2| = \underline{\underline{579.5}}$ Hz

ν = -29, μ = 29 : $r = |p(\nu+\mu)| = |3(-29+29)| = 0$, $f_{Ton} = 50|(29-1)(1-0.03)+2| = \underline{\underline{1458}}$ Hz

With rotor b) the exciting vibration modes differ considerably from the natural vibration modes (*r* = 0 instead of *r* = 2 or 3). Thus no resonance excitation occurs. Measured sound pressure level is much lower: the dominating value occurs in the 500 Hz band with only 62dB(A)).

Conclusions:
In that example the same stator delivers a much lower magnetic acoustic sound with rotor b) instead of rotor a). So the stator-rotor slot combination and mechanical resonance determine mainly magnetic acoustic performance.

Please note, that the same motor was already treated in Example 4.4.3-6. The low noise motor with slot combination 36/42 delivered a rather bad *M(n)*-curve due to inter-bar currents. So to develop an overall good motor, it is necessary to **consider all different motor attributes** such as thermal performance, starting torque, overload capability, noise. For this motor it would be necessary to use a chorded two-layer winding (which is more expensive than an unchorded single layer winding) to reduce 5th and 7th stator field harmonic in the 36/42 slot combination to get a satisfying *M(n)*-curve.

5. Inverter-fed induction machines

5.1 Basic performance of variable-speed induction machines

Induction machines operate at fixed stator frequency between no-load (synchronous speed) and rated slip, so speed differs only a few percent ("fixed speed drive"). Cage induction machine with continuously varying speed is possible with frequency inverter, which generates a three-phase voltage system with variable frequency, which yields variable synchronous speed and therefore variable speed induction machine. Most inverters are **voltage-source inverters** with DC voltage link. (Current source inverters with a big choke in the DC current link are used only for bigger power and are nowadays rather rare in use). Grid input with its fixed frequency and voltage is rectified and smoothened by a DC link capacitor. Most of the smaller inverters operate with diode rectifier, getting as DC link voltage

$$U_d = (3/\pi)\cdot\sqrt{2}U_{LL} \tag{5.1-1}$$

Example 5.1-1:
400 V grid, $U_d = (3/\pi)\cdot\sqrt{2}\cdot 400 = \underline{\underline{540}}$ V

From this DC link voltage a new variable frequency voltage system is generated by pulse width modulation (PWM). Output line-to-line voltage is a series of pulses of $+U_d$ or $-U_d$, which may be *Fourier*-analyzed.

$$u_{LL}(t) = \sum_{k=1}^{\infty}\hat{U}_{LL,k}\cdot\cos(k\cdot\omega_s t) \tag{5.1-2}$$

Fourier fundamental line-to-line sinus voltage $\hat{U}_{LL,k=1}$ and its corresponding phase voltage $\hat{U}_{s,k=1} = \hat{U}_{LL,k=1}/\sqrt{3}$ (if motor stator winding is star-connected) is the necessary input for variable speed motor operation. Higher time harmonics $\hat{U}_{LL,k>1}$ cause additional motor current with higher frequency $f_{sk} = kf_s$, which cause additional losses, pulsating torque and generate audible magnetic noise. Neglecting these parasitic effects, variable speed motor operation is determined by variable $U_s = \hat{U}_{s,k=1}/\sqrt{2}$ and variable f_s.

a) Influence of stator resistance R_s neglected:

Stator voltage equation yields

$$\underline{U}_s = j\omega_s L_{s\sigma}\underline{I}_s + j\omega_s L_h(\underline{I}_s + \underline{I}'_r) = j\omega_s\underline{\Psi}_s/\sqrt{2} \quad , \tag{5.1-3}$$

so **constant flux linkage** in the machine at variable frequency is only possible for **voltage change proportional to frequency**:

$$\boxed{U_s \sim f_s} \tag{5.1-4}$$

Torque-speed characteristic for $R_s = 0$ is *Kloss* function, which can also be expressed in terms of rotor frequency $f_r = s\cdot f_s$:

$$\boxed{R_s = 0: \quad \frac{M_e}{M_b} = \frac{2}{\frac{s_b}{s}+\frac{s}{s_b}} = \frac{2}{\frac{\omega_b}{\omega_r}+\frac{\omega_r}{\omega_b}}} \tag{5.1-5}$$

Breakdown torque M_b occurs at **rotor breakdown frequency**

$$\omega_b = \pm\frac{R'_r}{\sigma X'_r}\cdot\omega_s = \pm\frac{R'_r}{\sigma L'_r} \quad \text{(+: motor, -: generator)} \quad , \tag{5.1-6}$$

which is independent of stator frequency. Note that also breakdown torque is independent of stator frequency, if $U_s \sim f_s$. With $U_s = \omega_s\Psi_s/\sqrt{2}$ we get

$$\boxed{R_s = 0: \quad M_b = \pm\frac{m_s}{2}\frac{p}{\omega_s}U_s^2\frac{1-\sigma}{\sigma X_s} = \pm\frac{m_s}{2}\frac{p}{2}\Psi_s^2\frac{1-\sigma}{\sigma L_s}} \quad \text{(+: motor, -: generator)} \quad . \tag{5.1-7}$$

Therefore variable stator frequency means shifting of torque-speed characteristic parallel to abscissa with unchanged shape of characteristic (Fig. 5.1-1). Motor operation range is always for each of these characteristics between $0 \le \omega_r \le \omega_b$, if maximum torque (breakdown torque) with its overload current is possible due to sufficient inverter current limit.

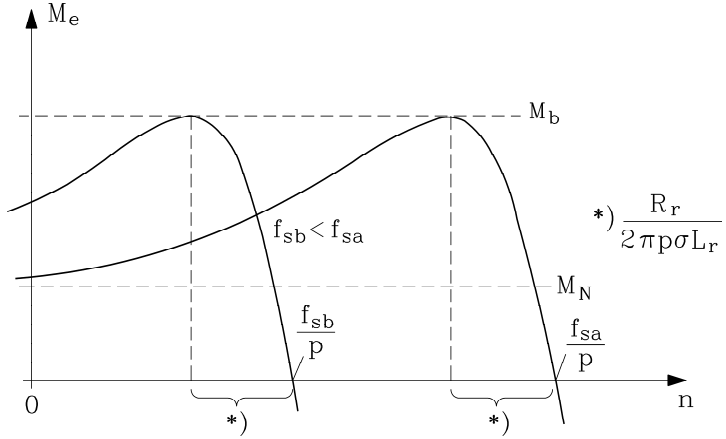

Fig. 5.1-1: Inverter operated induction motor, stator resistance neglected, only voltage fundamental of PWM inverter output voltage pattern considered: Parallel shift of torque-speed characteristic with variable stator frequency f_s and U_s/f_s = const.

With rising frequency f_s stator voltage must rise, too. By broadening the voltage impulses and narrowing the voltage gaps (zero voltage) in between, the fundamental amplitude increases. Thus the **modulation degree**

$$m = (2/\sqrt{3})\cdot\hat{U}_{LL,k=1}/U_d \tag{5.1-8}$$

rises with increased frequency up to unity, where usually **rated frequency** is defined: $f_s = f_N$. If $m > 1$ (over-modulation), maximum inverter output voltage is reached, if the voltage pulses

of PWM are united in one positive and one negative impulse per period with duration of impulses equal to 1/3 of period each ("**six step mode**").

$$\hat{U}_{LL,k=1,\max} = \frac{4}{\pi} \cdot U_d \cdot \sin\left(\frac{\pi}{3}\right) = 1.1 U_d \qquad (5.1\text{-}9)$$

Further increase of frequency yields automatically a weakening of flux, as the magnetizing current in the machine decreases (**flux weakening operation**):

$$\Psi_s = \hat{U}_{s,\max} / \omega_s \sim 1/\omega_s \qquad (5.1\text{-}10)$$

As torque is proportional to product of stator flux and rotor current, torque is decreasing in field weakening range even at constant current.

$$M_e \sim \Psi_s I_r \sim 1/\omega_s \qquad (5.1\text{-}11)$$

and motor power $P = 2\pi m M_e \approx (\omega_s / p) \cdot M_e$ is constant **("constant power range").** Breakdown torque is decreasing at constant voltage operation with

$$M_b = \frac{m_s}{2} \frac{p}{\omega_s} U_{s,\max}^2 \frac{1-\sigma}{\sigma \omega_s L_s} \sim 1/\omega_s^2 \quad . \qquad (5.1\text{-}12)$$

Therefore constant rated power range is limited at that frequency, where decreasing breakdown torque reaches torque demand for rated power $M_e = P_N \cdot (p/\omega_s)$ (Fig. 5.1-2). In order to keep an overload margin, maximum frequency $f_{s,\max}$ is defined, where ratio of breakdown torque versus torque at rated current is 1.6 (60% overload margin).

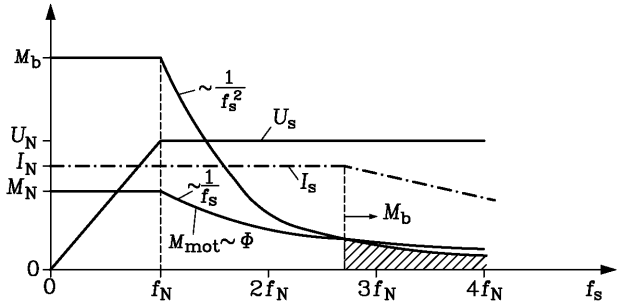

Fig. 5.1-2: Variable speed induction motor, neglected stator resistance: Torque at rated current and overload (breakdown) torque depending on variable stator frequency. Voltage linear rising with frequency below rated frequency f_N, constant maximum voltage above rated frequency.

b) Influence of stator resistance R_s considered:
Especially at low speed and therefore low stator frequency the inductive voltage drop decreases rapidly, whereas resistive voltage drop remains constant:

$$\underline{U}_s = R_s \underline{I}_s + j\omega_s L_{s\sigma} \underline{I}_s + j\omega_s L_h (\underline{I}_s + \underline{I}'_r)\big|_{\omega \to 0} \to R_s \underline{I}_s \quad , \qquad (5.1\text{-}13)$$

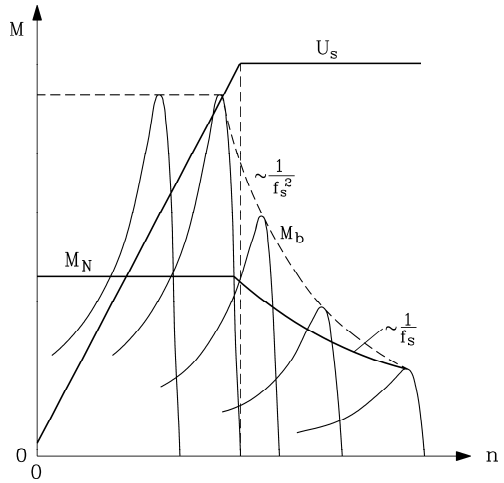

Fig. 5.1-3: Application of Fig. 5.1-2: Variable speed induction motor as traction drive of heavy loco BR120 of German railways (neglected stator resistance)

At zero frequency (DC current feeding) only resistive voltage drop remains. Therefore voltage control must consider resistive voltage drop by adding this to the U_s/f_s-characteristic. If this is not done, then breakdown torque (+: motor, -: generator)

$$M_b = \pm \frac{m_s}{2} \frac{p}{\omega_s^2} U_s^2 \frac{1}{\pm \frac{R_s}{\omega_s} + \frac{1}{(1-\sigma)\omega_s^2 L_s} \cdot \sqrt{(R_s^2 + \omega_s^2 L_s^2)(R_s^2 + \sigma^2 \omega_s^2 L_s^2)}} \qquad (5.1\text{-}14)$$

decreases rapidly with decreasing frequency (Fig. 5.1-4a). In order to keep breakdown torque constant, $U_s(\omega_s)$ is a rather complicated function, derived from (5.1-14). In commercial inverters this function is usually linear with an offset $\Delta U = R_s I_N$ at zero speed (Fig. 5.1-4b). For that simplification breakdown torque decreases also with decreasing frequency, but stays above rated torque.

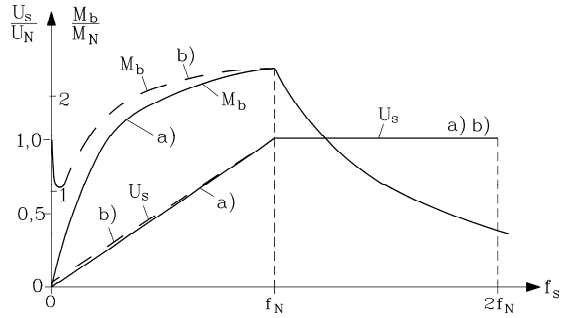

Fig. 5.1-4: Variable speed induction motor, stator resistance considered:
a) Linear rise of voltage with frequency : Breakdown torque decreases with decreasing speed
b) Additional voltage offset at zero speed to compensate resistive voltage drop: Breakdown torque decreases also with decreasing speed, but stays above rated torque

c) Drive technology:
Inverter switches are usually **insulated gate bipolar transistors** (IGBT) with free wheeling diodes, operating at voltages between 200 V and 6000 V with switching frequencies up to 20 kHz for lower and up to about 500 Hz for higher voltage rating. For higher voltage and switching power gate turn off thyristors (GTO) and thyristors with auxiliary circuit to switch current off are in use at switching frequencies below 500 Hz. Below 200 V metal oxide silicon field effect transistors (MOSFET) are used as switches with switching frequencies up to 50 kHz.

Induction motors may be operated at inverter supply without any speed sensor (**voltage control**). Speed is not constant ant constant stator frequency, but varies according to load and slip. At low frequency the short rotor time constant, which determines change of rotor flux, is rather small in comparison to voltage period $T = 1/f_s$. Therefore rotor flux may be regarded as constant during one period, thus acting like a synchronous machine rotor. Therefore **speed oscillations** may occur, if load is changed, in the same way as it is the case for synchronous machines. If the rotor is equipped with a speed sensor, **speed control** – incorporated in the inverter - is possible, thus avoiding change of speed with slip and possible speed oscillations at low speed. Speed and underlying torque control allow the inverter-fed induction machine to operate as an adjustable speed drive with high dynamic performance, if a **vector control** algorithm is used for torque control. Depending on the power of the used microprocessor (e.g. 16 bit or 32 bit), elaborate digital control is possible. Using numerical motor models with observer-assisted control, even the speed sensor may be spared, calculating the actual speed from voltage and current measurement (**speed sensorless control**).

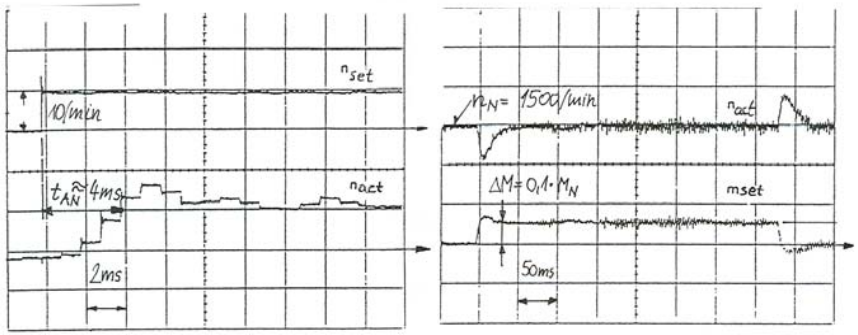

a) b)

Fig. 5.1-5: Digital speed control of inverter-fed induction machine (Data see Example 5.1-2): Actual speed response to a) step-up of set-point speed, b) step-up and step-down in load torque

Example 5.1-2:
Speed controlled inverter-fed induction motor with speed sensor and digital vector control (1 ms cycle time for measuring and calculating) :
Motor rated data: 400 V Y, 24 Nm, 1500/min, DC link voltage 600 V, inverter rated current 40 A, load inertia equal to motor inertia (each 0.011 kg.m^2)
Two examples of motor control:
a) Step in speed set-point value n_{set} for zero to 10/min: Actual speed n_{act} in Fig. 5.1-5a is shown as calculated value from microprocessor. After about 4 ms actual speed reaches set-point speed for first time and with some overshoot and damped oscillation finally after 16 ms actual speed is constant 10/min.

b) Load step from no-load to 10% of rated torque and back to no-load at set-point speed 1500/min: Actual speed (taken from speed sensor signal) dips at increased load and reaches set-point value again after 50 ms. At decreased load a speed over-shoot occurs for about 50 ms (Fig. 5.1-5b).

5.2 Drive characteristics of inverter-fed standard induction motors

a) Thermal steady state performance:
Standard motors are usually balanced for synchronous speed at 50 Hz, but are often capable of about running to twice frequency without additional measures, e.g. motor size 160 mm may be run up to 6000/min. Smaller motors may run with even elevated speed, bigger motors with less, as natural bending frequency of rotor decreases with increased motor size. Shaft mounted fan will produce increased air flow and noise at elevated speed, so often for higher speed operation fans with decreased diameter d are used. Rough estimate for change of sound pressure level of fans with speed and fan diameter is

$$\Delta L_p = 50 \cdot \lg(n_1 / n_2) + 70 \cdot \lg(d_1 / d_2) \qquad (5.2\text{-}1)$$

Example 5.2-1:
Increase of fan sound pressure level at doubled speed: $\Delta L_p = 50 \cdot \lg(2) = \underline{\underline{15}}$ dB

Cooling air flow generated by fan rises linear with speed:

$$\dot{V} \sim n / n_N \sim f_s / f_N \qquad (5.2\text{-}2)$$

Iron losses in stator rise proportional to square of flux linkage, eddy current loss component with square and hysteresis loss component linear with frequency, so an average exponent x is assumed.

$$P_{Fe} \sim (\Psi / \Psi_N)^2 \cdot (f_s / f_N)^x \quad , \quad x \cong 1.8 \qquad (5.2\text{-}3)$$

Friction losses due to bearings rise nearly linear with speed, but are usually much smaller than windage losses to due power consumption of shaft-mounted fan. Fan power consumption rises with cube of speed, so friction and windage losses rise with an exponent y = 2,5 ... 3.

$$P_{fr+w} \sim (n / n_N)^y \sim (f_s / f_N)^y \quad , \quad y \cong 2.5...3 \qquad (5.2\text{-}4)$$

Stray load losses (additional losses) due to space harmonic effects rise with speed and current:

$$P_{ad1} \sim (n / n_N)^z \cdot (I_s / I_N)^2 \quad , \quad z \cong 1.5...2 \qquad (5.2\text{-}5)$$

Considering the thermal power limit of the inverter-fed standard induction machine, we have to consider three frequency ranges (Fig. 5.2-1):
- $f_s > f_N$: Flux weakening range: Flux linkage decreases with $\Psi \sim 1/f_s$, so iron losses are nearly constant. Motor is operated at rated current, so copper losses are constant. As motor is cooled better at high speed due to increased air flow, constant rated power operation is no

thermal problem even with increased friction and stray load losses. Upper frequency limit is given, when decreasing breakdown power reaches 160% of motor rated power.

- $f_{th} < f_s < f_N$: Constant torque range: With decreasing speed at constant current iron losses decrease with square of speed, air flow only linear with speed, so down to $f_{th} \sim 0.5 f_N$ operation with rated flux and current (thus rated torque) is no thermal problem. Power decreases linear with speed.
- $f_s < f_{th}$: Reduced torque operation: Below about 50% rated speed air flow is so small, that copper losses must be reduced by reduction of stator current. Thus torque M_e is decreased. Moreover breakdown torque usually decreases also with decreasing speed (Fig. 5.1-4), so with a demanded overload margin of $M_b/M_e = 1.6$ a decrease in torque is necessary, likewise.

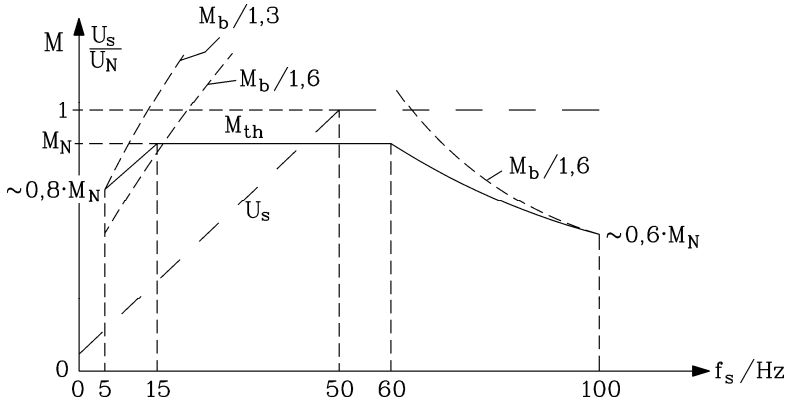

Fig. 5.2-1: Standard induction machine with shaft-mounted fan, operated at variable frequency. Steady state thermal torque versus speed and overload capability.

b) Increase of motor power with delta connected winding:

Star connected motor has phase voltage by $1/\sqrt{3}$ lower than line-to-line voltage: $U_s = U_{LL}/\sqrt{3}$. Flux linkage is $\Psi_{sN} = \hat{U}_s/\omega_s$. Operating motor with constant flux is possible up to angular frequency $\omega_s = \hat{U}_{s,\max}/\Psi_{sN} = \hat{U}_{LL,\max}/(\Psi_{sN}\cdot\sqrt{3})$. If the SAME motor is **delta** connected, line-to-line voltage of inverter is identical with motor phase voltage, so maximum angular frequency for constant flux operation is $\omega_s = \hat{U}_{s,\max}/\Psi_{sN} = \hat{U}_{LL,\max}/\Psi_{sN}$, thus being increased by factor $\sqrt{3} = 1.73$. With constant rated phase current I_{sN} and rated flux linkage operation with rated torque is therefore possible at an 173% increased speed range. Therefore motor power is raised up to 173% with the same motor (Fig. 5.2-2) due to speed increase at constant flux. At delta connection line current is $I_L = \sqrt{3}\cdot I_{sN}$, thus 173% of phase current, therefore inverter rating has to be increased by 73%.

Conclusions:

By switching winding from star to delta for the same inverter line-to-line voltage, maximum speed for rated flux is increased by 73% (e.g. 87 Hz instead of 50 Hz). Motor of same size is now capable of 73% more power, because only speed is raised, whereas torque remains constant. But inverter power has increased also, so a bigger inverter with 73% additional rating is necessary for delta operation with rated flux up to e.g. 87 Hz.

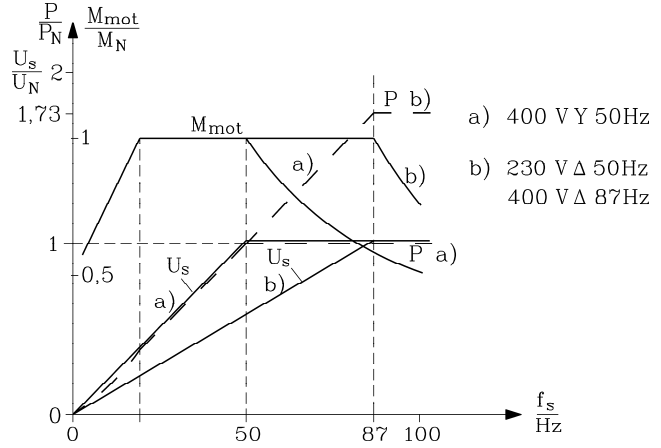

Fig. 5.2-2: Increase of constant torque range and motor output power by switching the winding from a) star to b) delta connection

Example 5.2-1:

4-pole induction motor, power factor 0.85, efficiency 90%

stator winding connection	***star***	***delta***
inverter maximum output voltage line-to-line $U_{LL,\max}$	400 V	400 V
motor maximum phase voltage $U_{s,\max}$	230 V	400 V
motor frequency f_s at $U_{s,\max}$	50 Hz	87 Hz
motor rated phase current I_{sN}	100 A	100 A
motor rated line current I_{sN}	100 A	173 A
Motor torque	336 Nm	336 Nm
motor output power	52.3 kW	90.6 kW
inverter power rating	69 kVA	119.4 kVA

Inverter voltage-frequency characteristic has to be changed, when motor is switched from star to delta:

star: $U_{LLN}/f_{sN} = 400V/50Hz = 8V/Hz$

delta: $U_{LLN}/f_{sN} = 400V/87Hz = 4.6V/Hz$

c) Drive applications:

Inverter supplied standard induction motors are used widely for many industrial purposes such as cranes, cater-pillars, mining, mills, pulp & paper machinery, wire production, extruders, woodcraft, drilling (e.g. off-shore platforms), compressors, fans, pumps.

In **fan and pump drives**, where the fluid flow and the generated pressure is adjusted via speed: $\dot{V} \sim n, \Delta p \sim n^2$, power $P = \dot{V}\Delta p \sim n^3$ increases with speed, s no flux weakening is possible at maximum speed. But with decreasing speed torque demand decreases with $M \sim n^2$, so often voltage-frequency characteristic is chosen $U_{LL} \sim f_s^2$. Thus the flux and therefore magnetizing current decrease linear with frequency. As torque is $M \sim \Psi_s I_s$, also load current I_s may decrease linear with decreasing frequency, leading to lowered motor losses.

5.3 Features of special induction motors for inverter-operation

a) Features of high-performance inverter-fed induction machines:
High performance inverter-fed induction drives must be able to produce full torque also at stand-still for continuous duty, so an **external fan, operating independent from motor speed,** is necessary for cooling. A winding temperature sensor e.g. within winding overhang such as positive temperature coefficient sensor (PTC) is often used as thermal protection against overheating. **Increased motor utilization** is often necessary to get increased power out of a given volume such as for drives for tooling machinery or electric cars. If water-jacket cooling is chosen instead of indirect air cooling, stator winding heat transfer coefficient raises up to 300%. In that case losses may increase up to 300% for the same winding temperature. Motor power may be increased by 40%.

Special attention is paid to **low inertia** and to **overload capability** (e.g. 180% for 4 min. in a 10 min. cycle, S6-40%) to get a drive with high dynamic performance. Low inertia is gained by low ratio d_{si}/l_{Fe}, but care must be taken not to get too low rotor natural bending frequency, it the rotor gets too "thin". High-performance motors are operated usually with a **high resolution speed sensor** for positioning purposes at low speed (e.g. 2048 increments per revolution), but must be capable also of high speed (e.g. motor size 100 mm up to 10 000/min, motor size 180 mm up to 6000/min). So **speed range** for operation ranges typically from 0.01 /min up to 12 000/min. If a speed sensor with sinusoidal signals is used, the 2048 sinus increments may be interpolated by sine function with 2048 interpolation points per period, yielding a **resolution** of 4 000 000 /rev. **Accuracy** of positioning is of course lower by at least factor 10, as the sinus increments differ from ideal sine wave.

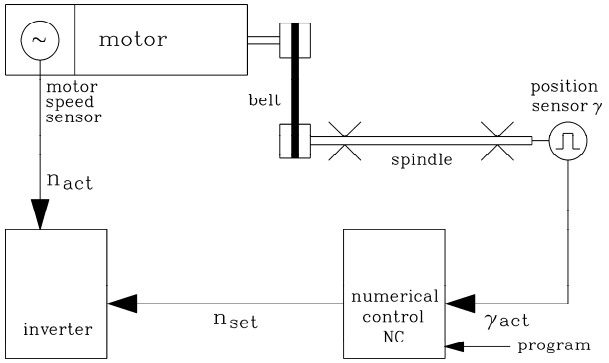

Fig. 5.3-1: Induction motor as spindle drive with positioning duty (e.g. position sensor with 1024 increments/rev.)

Especially in tooling machines a **wide constant power speed range** is necessary, as the necessary cutting power in milling or high speed cutting (HSC) process is demanded independently of speed. With low motor utilization and low stray inductance a high ratio of breakdown torque versus rated torque is possible, yielding to constant power range of $n_{max} : n_N = 5:1$ or 6:1. With star-delta switching of stator winding constant power range ratios 12:1 up to 16:1 are possible ("**wide range motors**"). By using an additional planetary gear with two stages, 1:1 and e.g. 1:4 a further extension of constant power range is possible. A 24 V-DC motor operates the gear, which needs about 400 ms to switch the gear at motor stand still form gear ratio 1:1 to gear ratio 1:4.

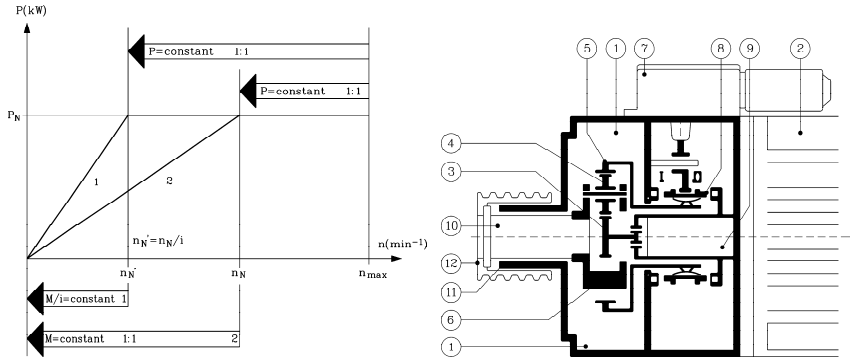

Fig. 5.3-2: Extension of constant power range (left) by use of planetary gear (right); Note logarithmic scaling of abscissa (speed axis): 1: with gear ratio 1: *i*, 2: with gear ratio 1:1 (*Siemens AG*).
Description of planetary gear:
1: gear housing, 2: motor, 3: sun wheel, 4: planetary wheel, 5: hollow wheel, 6: planetary wheel support, 7: switching unit, 8: shifting sleeve (position I: gear ratio1: *i*, position II: gear ratio1: 1), 9: motor shaft, 10: gear shaft, 11: housing, 12: belt pulley, 13: holding brake

Drive applications are mainly spindle drives in tooling machines, but also in other motion control applications, mainly production machines with high degree of automation, high dynamic performance and increased accuracy of speed and position control.

b) Induction motor design (Grid-operated vs. inverter-operated induction machines)
Grid-operated machines must start from the line at fixed frequency with slip range from 1 to zero, whereas inverter-operated machines start with variable frequency, being operated only between rated slip and zero slip. So the motor design for grid- and inverter-operated machines is quite different.

Aim	*air gap*	L_σ	R_r
Big breakdown torque	-	small [1)]	-
Small magnetizing current	small [2)]	-	-
low starting current	-	big	big
big starting torque		small	big [3)]

Table 5.3-1: Choice of equivalent circuit motor parameters for line-operated induction machines

Remarks:
[1)] many slots, no skew, no deep slots, big slot openings
[2)] low saturation
[3)] big current displacement, deep rotor slots, special rotor cage (e.g. Siluminium cage for increased resistance). For good starting performance skewing is necessary to minimize harmonic torque components

Table 5.3-1 shows that even for grid operation the different aims to optimize motor performance lead to contradicting demands for equivalent circuit parameters, so always a compromise is necessary.

Aim	*air gap*	L_σ	R_r
Big breakdown torque	-	small [1)]	-
Small magnetizing current	small [2)]	-	-
low additional losses	big [4)]	big [5)]	Small [3)]

Table 5.3-2: Choice of equivalent circuit motor parameters for inverter-operated induction machines

[1)] many slots, no skew, no deep slots, big slot openings
[2)] low saturation
[3)] small current displacement, round or oval rotor slots
[4)] low field harmonics, small slot openings
[5)] Stray inductance must limit current harmonics. Avoid skewing to avoid inter-bar currents.

Table 5.3-2 shows that also for inverter-fed induction machines the different aims to optimize motor performance lead to contradicting demands for design parameters, again making a compromise is necessary.

Pole-count for high-speed:
For high speed operation low pole count is aimed to keep stator frequency low for low iron losses, current displacement in stator winding and for limiting inverter switching frequency. High-performance induction machines for inverter-operation are usually 4-pole machines, so frequency at high speed is still low enough. Two-pole machines have only 50% of that frequency at same speed, but are used not so often, as they have some disadvantages:
- Due to big flux per pole stator and rotor yoke must be big, thus increasing motor mass.
- Coil span is – depending on chording – nearly half air gap circumference, so winding overhangs are rather big, demanding space and causing increased copper losses.
- In case of **rotor dynamic eccentricity** due to elastic rotor bending the air gap is smaller on side than on opposite side, causing an unbalanced magnetic pull on the rotor. With two pole machines this eccentricity leads to distortion of two-pole air gap field, causing a radial pulsating force in direction of minimum air gap with frequency $f = 2 \cdot n$, whereas with $2p > 2$ this frequency is usually $f = n$. So excitation of natural rotor bending frequency f_b occurs with two-pole machines already at a speed $n = f_b / 2$, which may limit speed range.

c) Design criteria for motors with wide field weakening range:
(i) Oversizing of motor:
Due to oversizing the demanded rated torque M_N of the motor is smaller than thermal possible rated torque $M_{N,th}$ of motor. Therefore increase of ratio breakdown torque / rated torque M_b/M_N is given, yielding an increased constant power (= field weakening) range, but at a cost of a bigger motor.

Example 5.3-1:
Motor with rated torque $M_{N,th}$ = 150 Nm (thermally possible), ratio $M_{bN}/M_{N,th}$ = 2.5. Field weakening range:

$$\frac{M_e / M_{N,th}}{n / n_N} = \frac{M_{bN} / M_{N,th}}{(n/n_N)^2} \Rightarrow \frac{1}{n/n_N} = \frac{2.5}{(n/n_N)^2} \quad \frac{n_{\max}}{n_N} = 2.5$$

Motor oversized by 30%: M_N = 150 Nm/1.3 = 115 Nm.

$$\frac{M_e / M_{N,th}}{n / n_N} = \frac{M_{bN} / M_{N,th}}{(n/n_N)^2} \Rightarrow \frac{1/1.3}{n/n_N} = \frac{2.5}{(n/n_N)^2} \quad \frac{n_{\max}}{n_N} = 2.5 \cdot 1.3 = 3.25$$

Field weakening range is increased by 30%.

(ii) Increase of inverter current rating:
Motor is rewound with less windings per phase: $N_{sx} = N_s / x$, so rated motor voltage is reduced to $U_{Nx} = U_N / x$. For the same power and torque current has to be increased by $I_{Nx} = I_N \cdot x$. This is thermally possible, as current density J in motor remains the same, as constant slot cross section A_Q offers increased conductor cross section q_{Cu} due to decreased number of conductors: $q_{Cu} \sim A_Q / N_s \Rightarrow q_{Cux} \sim A_Q / N_{sx} \Rightarrow q_{Cux} = x \cdot q_{Cu}$, therefore we get $J = I_{Nx} / q_{Cux} = I_N / q_{Cu}$. Inverter rated voltage remains U_N, but due to increased current I_{Nx} inverter power increases by factor *x*. Due to $L_s \sim N_s^2$ breakdown torque increases by $M_b \sim x^2$:

$$M_b = \frac{m_s}{2} \frac{p}{\omega_s^2} U_{sN}^2 \frac{1-\sigma}{\sigma L_s} \sim \frac{1}{N_s^2} \ .$$

Increase of field weakening range by factor x^2 is possible at the cost of increased inverter rating by factor *x* and increased additional motor losses due to inverter supply. This is caused
a) by decreased motor stray inductance $L_\sigma \sim N_s^2$, which limits additional motor current harmonics, caused by non-sinusoidal inverter output voltage.
b) Further, motor is operated at 1/*x* reduced modulation degree *m*. Inverter output voltage harmonic amplitudes are maximum at about *m* = 1/2, so due to decreased *m* the amplitudes of harmonic currents and their related losses are increased.

Example 5.3-2:
Motor with rated voltage 400 V is rewound to 300 V: *x* = 4/3 = 1.33. Inverter is oversizied by 33%, breakdown torque increases by 1.33^2 = 77%. Field weakening range is increased by 77%.

(iii) Star-delta switching of stator winding:
By switching from Y to D, the maximum phase voltage increases by $\sqrt{3}$, thus raising the breakdown torque by factor 3:

$$M_{bY} = \frac{m_s}{2} \frac{p}{\omega_s^2} U_{sY\max}^2 \frac{1-\sigma}{\sigma L_s} \ , \quad M_{bD} = \frac{m_s}{2} \frac{p}{\omega_s^2} (\sqrt{3} U_{sY\max})^2 \frac{1-\sigma}{\sigma L_s} = 3 M_{bY} \ .$$

Field weakening range is extended by factor, but needs now a switch with six connections for the six winding terminals U-X, V-Y, W-Z.

Example 5.3-3:
a) 4-pole Y-connected motor with $N_s = 111$ turns per phase operates with rated line-to-line voltage 400 V, rated phase current 17 A at rated speed 1500/min and power 9 kW (power factor 0.85, efficiency 0.9). Constant power operation is possible up to 4500/min, where breakdown torque is reached (Fig. 5.3-3). By switching in D-connection, full voltage 400 V is reached at $\sqrt{3} \cdot 1500 = 2600$/min. Inverter current is kept constant 17 A, so power is kept constant. Motor phase current decreases by $17 / \sqrt{3} = 10$ A, leaving the motor now oversized. But due to increased breakdown torque by factor 3 constant power operation with 9 kW is possible up to $3 \cdot 4500 = 13500$/min.

b) *For comparison:* If the same motor size 4-pole Y-connected motor without Y-D-switching should be used for the same constant power range 9 kW, 13500/min, the motor must be

equipped with $N_s = 111/\sqrt{3} = 66$ turns per phase, yielding an increase in inverter current rating of $17 \cdot \sqrt{3} = 30$ A, which usually is more expensive than the Y-D-switch for 17 A.

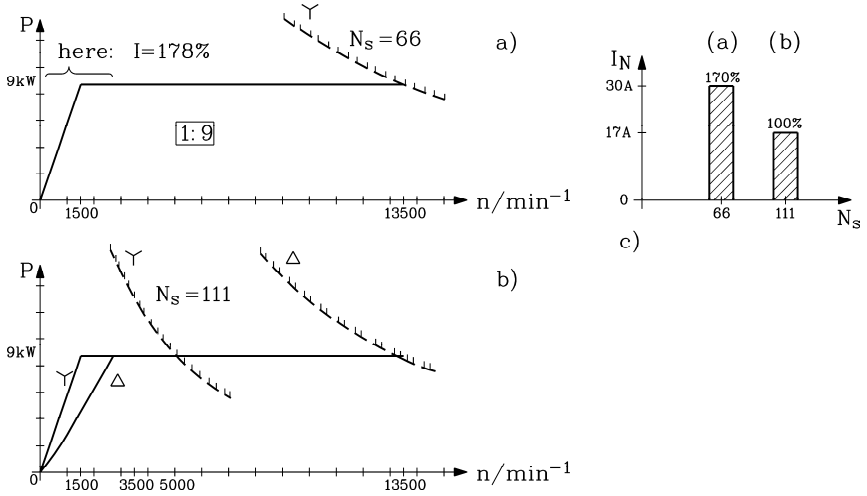

Fig. 5.3-3: Field weakening with constant power 9 kW: (a) Y-connected motor with decreased number of turns per phase, (b) Y-D-switching of winding, c) Increase of inverter current rating for b)

(iv) Series-parallel switching of stator winding:

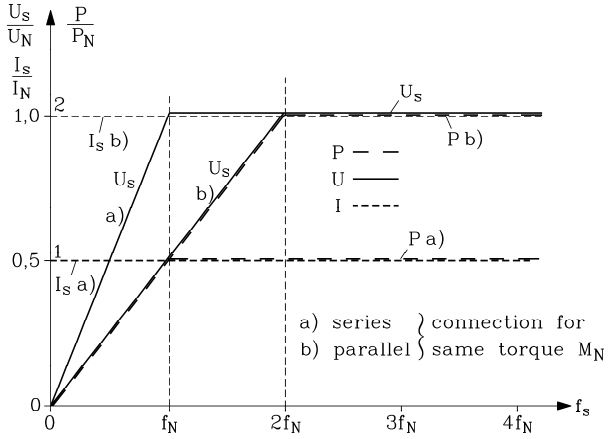

Fig. 5.3-4: Possible motor current, voltage and power rating for the same motor size and torque, but a) series and b) parallel connection of each phase: With parallel winding number of turns is only 50%, so for the same rated voltage the rated frequency and current is 200%, thus increasing motor power by factor 2

If e.g. for a four pole motor the number of turns per winding N_s is split into two halves (one for first and one for second pole pair, each $N_s/2$), one can switch those two halves either in series or in parallel. In parallel the total number of turns per phase is with $N_s/2$ only 1/2 of the

series value N_s, thus breakdown torque increases by factor $(N_s/(N_s/2))^2 = 4$, allowing 4-times larger field weakening range in parallel than in series (Fig. 5.3-5). In parallel switching mode for the SAME inverter current rating the current per parallel winding branch is only 50% of rated current, so motor is oversized in parallel winding field weakening operation by factor 2 (Fig. 5.3-4). As each phase is split into two halves, a series-parallel switch for 12 terminals is needed: U1-X1, U2-X2, V1-Y1, V2-Y2, W1-Z1, W2-Z2.

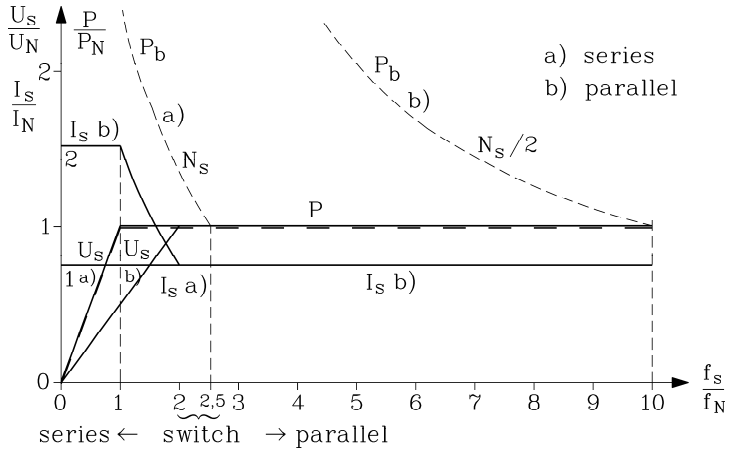

Fig. 5.3-5: Series-parallel switching for increasing constant power range by factor 4
a) Breakdown power $P_b = 2\pi m M_b \sim 1/n$, current, voltage and power for series connected winding
b) Operation with parallel connected winding allows increase of field weakening by factor 4 from 1:2.5 to 1:10

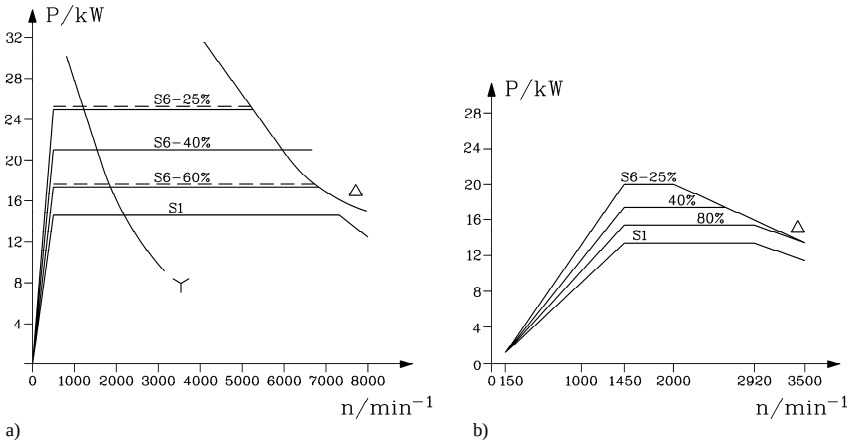

Fig. 5.3-6: Catalogue examples for maximum motor power versus speed at voltage source inverter supply for motor size 160 mm: S1: thermal steady state operation, S3-60%: intermittent operation: 6 minutes overload, 4 minutes stand still, S6-60%: intermittent operation: 6 minutes overload, 4 minutes no load
a) High performance 4-pole induction motor with star-delta switch to enlarge constant power range, rated speed at Y: 500/min, rated frequency 16.7 Hz
b) Standard induction 4-pole motor, D connected winding, rated speed 1460 /min, rated frequency 50 Hz

5.4 Influence of inverter harmonics on motor performance

a) Inverter voltage time harmonics:
Inverter line-to-line output voltage is a series of rectangular shaped voltage impulses of varying duration due to PWM (Fig. 5.4-2). *Fourier* analysis yields voltage harmonics, depending of modulation degree *m*. Usually the **switching frequency** of inverter transistors is fixed (f_T = const.), independent of fundamental frequency $f_{k=1} = f_s$ (**asynchronous switching**). For bigger power ratings e.g. with GTO-inverters the ratio f_T/f_s is fixed and an integer odd number, but may be changed for different values, e.g. 9, 15, ... (**synchronous switching**). In case of asynchronous switching usually switching frequency is high enough $f_T/f_s >> 1$ (e.g. 3 ... 10 kHz), that one can always take $f_T/f_s \cong$ integer odd number. In Fig. 5.4-2 example for synchronous switching f_T/f_s = 12000 Hz/800 Hz = 15 is given for different modulation degrees is given, yielding different fundamental line-to-line voltage amplitudes $\hat{U}_{LL,k}$ as a complete spectrum, depending on modulation degree, or – in other words – depending on fundamental voltage amplitude.

$$0...m...(5...10) \quad \Leftrightarrow \quad 0...U_{sk=1}...U_{s,k=1,\max}$$

Often in inverters upper limit is modulation degree m = 1, leaving over-modulation as additional voltage margin for current control. At over-modulation PWM converts into six-step voltage mode (compare Fig. 5.4-2a with Fig. 5.4-2c). **Phase voltage for star connected stator winding** is derived from line-to-line voltage according to Fig. 5.4-1a

$$u_{S1}(t) - u_{S2}(t) = u_{L1-L2}(t) \tag{5.4-1}$$
$$u_{S2}(t) - u_{S3}(t) = u_{L2-L3}(t) \tag{5.4-2}$$
$$u_{S1}(t) + u_{S2}(t) + u_{S3}(t) = 0 \quad . \tag{5.4-3}$$

Thus phase voltage of phase 1 ("U") is

$$u_{S1}(t) = \frac{2u_{L1-L2}(t) + u_{L2-L3}(t)}{3} \quad , \tag{5.4-4}$$

yielding in case of over-modulation a step-like time-function (Fig. 5.4-1b) with amplitude $2U_d/3$.

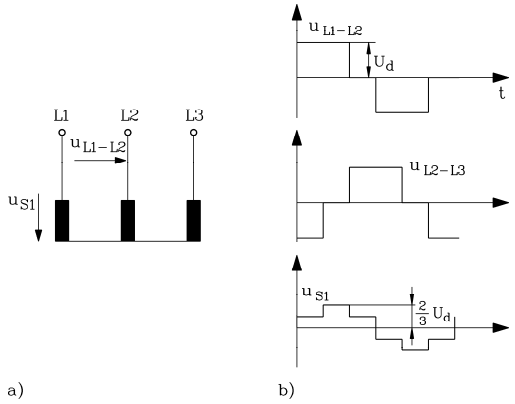

Fig. 5.4-1: Star connection of stator winding: a) Phase voltage u_S and line-to-line voltage u_L, b) Time-function of line-to-line voltage u_L and phase voltage u_S in case of six step operation

In case of delta connected winding line-to-line voltage is also phase voltage. Fig. 5.4-1b shows clearly, that in case of star connection the voltage time-function fits better to ideal sine time-function than in case of delta connection.

Conclusions:
Inverter fed machines are usually operated in star connection, as phase voltage time function fits better to ideal sine wave.

Frequencies of voltage harmonics are $f_{sk} = k \cdot f_s$, and inverter generates three phase voltage system for each time harmonic *k*.

$$\begin{aligned} u_{Uk}(t) &= \hat{U}_{Sk} \cos(k \cdot \omega_s t) \\ u_{Vk}(t) &= \hat{U}_{Sk} \cos(k \cdot (\omega_s t - 2\pi/3)) \\ u_{Wk}(t) &= \hat{U}_{Sk} \cos(k \cdot (\omega_s t - 4\pi/3)) \end{aligned} \tag{5.4-5}$$

Example 5.4-1:
k = 1: phase sequence U, V, W: **clockwise** rotating air gap field
$u_{U1}(t) = \hat{U}_{S1}\cos(\omega_s t) \quad u_{V1}(t) = \hat{U}_{S1}\cos(\omega_s t - 2\pi/3) \quad u_{W1}(t) = \hat{U}_{S1}\cos(\omega_s t - 4\pi/3)$
k = 5: phase sequence U, V, W: clockwise rotating air gap field
$u_{U5}(t) = \hat{U}_{S5}\cos(5\omega_s t) \quad u_{V5}(t) = \hat{U}_{S5}\cos(5\omega_s t - 10\pi/3) \quad u_{W5}(t) = \hat{U}_{S5}\cos(5\omega_s t - 20\pi/3)$
This can also be written as
$u_{U5}(t) = \hat{U}_{S5}\cos(5\omega_s t) \quad u_{V5}(t) = \hat{U}_{S5}\cos(5\omega_s t - 4\pi/3) \quad u_{W5}(t) = \hat{U}_{S5}\cos(5\omega_s t - 2\pi/3)$,
which means that phase V and W for 5th harmonic have changed phase shift, yielding:
k = 5: phase sequence U, W, V: **counter-clockwise** rotating air gap field.

Time-harmonic three-phase voltage system, applied to stator winding as stator voltage U_{sk} with frequency f_{sk} causes **time-harmonic** three-phase current system I_{sk}, which excites air gap flux density $B_{\delta sk}$, which may be expressed as *Fourier* sum of **space-harmonics**

$$B_{\delta sk}(x_s, t) = \sum_{\nu=1,-5,7,...}^{\infty} B_{\delta sk,\nu} \cdot \cos(\frac{\nu \pi x_s}{\tau_p} - k \cdot \omega_s t) \tag{5.4-6}$$

with wave speed of fundamental space harmonic of k^{th} current system

$$v_{syn,k,\nu=1} = 2 \cdot k f_s \cdot \tau_p \quad . \tag{5.4-7}$$

So inverse rotation of air gap field of e.g. 5th time-harmonic current system is described mathematically correct, if we define the ordinal number k as negative number k = -5. Result of *Fourier* analysis of Fig. 5.4-2 is: Line-to-line voltage spectrum contains in case of synchronous switching as **ordinal numbers *k*** all odd numbers, which are not dividable by 3 (due to the 3-phase system):

$$\boxed{k = 1 + 6g}, \qquad g = 0, \pm1, \pm2, \pm3, \pm4, ... \tag{5.4-8}$$

Negative sign means that sequence of phase voltages change their position (U, W, V instead of U, V, W), yielding current system in motor, which excites **inverse rotating** air gap magnetic fields.

Conclusions:
Do not mix up the formulas $\boxed{k = 1 + 6g}$ *for ordinal number of three-phase time-harmonic voltage and current harmonics, and* $\boxed{\nu = 1 + 6g}$ *for ordinal number of space-harmonics of air-gap field, excited by three-phase winding system. First is defined by inverter, independent of motor design, second is defined by winding arrangement in motor, independent of inverter design. In both cases negative sign of ordinal number means, that the air gap field is inverse rotating.*

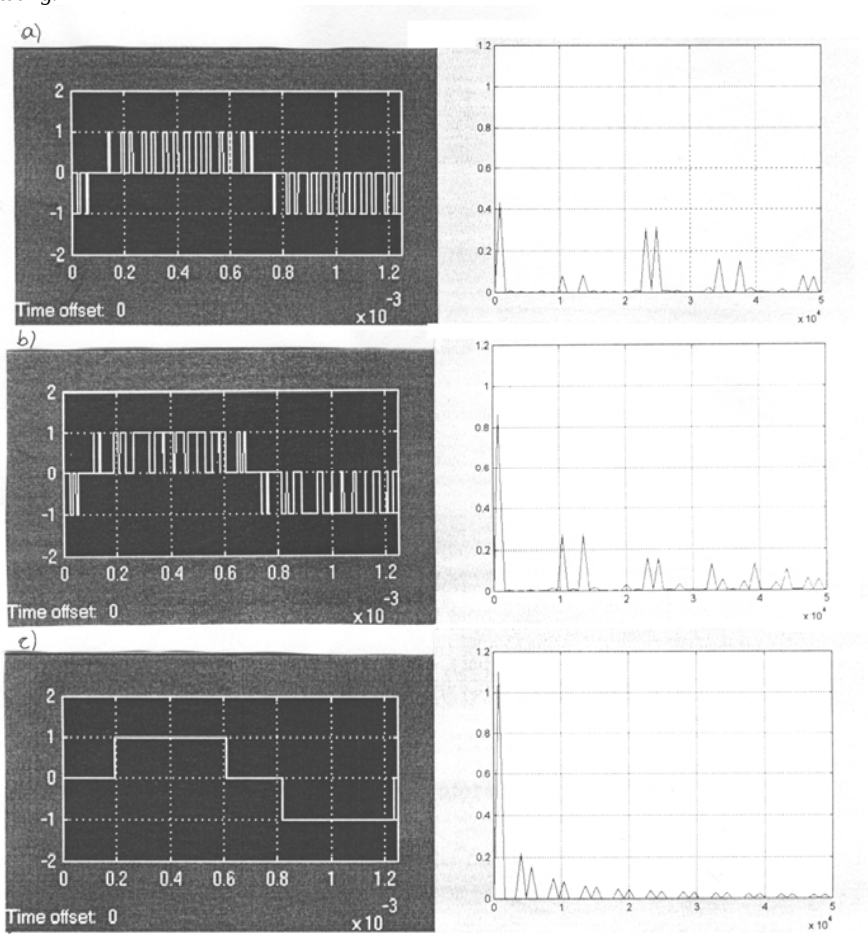

Fig. 5.4-2: Line-to-line pulse width modulated voltage in per unit of DC link voltage U_d, and its *Fourier* spectrum for synchronous switching mode f_T/f_s = 12000 Hz/800 Hz = 15 for different modulation degree *m*
a) PWM with *m* = 0.5, b) PWM with *m* = 1, c) over-modulation m = 5, which yields six step voltage supply

Fig. 5.4-2 shows that for low modulation degree dominating amplitudes of voltage time-harmonics occur at frequencies $2f_T \pm f_s \approx 2f_T$ (Fig. 5.4-2a), and therefore often $f_p = 2f_T$ is defined as pulse frequency, as number of positive and negative voltage impulses in line-to-

line voltage is given by f_p/f_s (e.g. Fig. 5.4-2: $f_T / f_s = 15 \Rightarrow f_p / f_s = 30$: 15 positive and 15 negative voltage impulses). At modulation degree near unity dominating amplitudes of voltage time-harmonics occur at switching frequency $f_T \pm 2f_s \approx f_T$ (Fig. 5.4-2b), whereas with over-modulation (six step mode) voltage harmonics decrease with inverse of ordinal number (Fig. 5.4-2c).

Conclusions:
At medium modulation degree twice switching frequency voltage harmonics ("pulse-frequent" voltage ripple) is dominating as harmonic voltage content (Fig. 5.4-3).

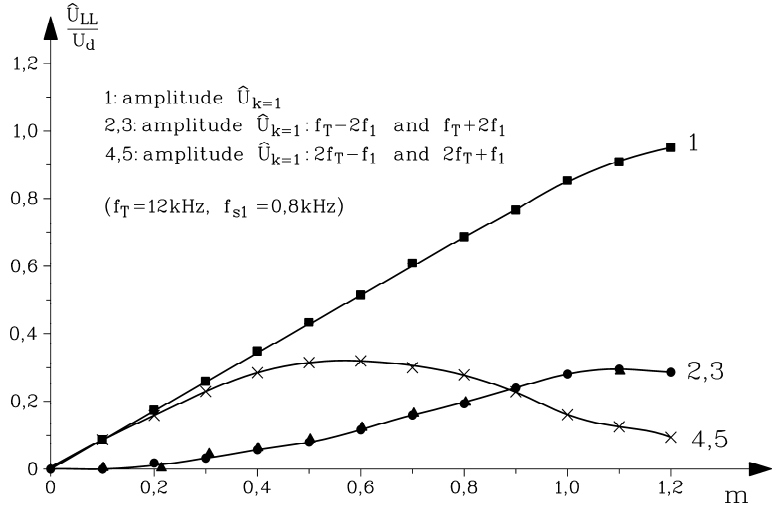

Fig. 5.4-3: Harmonic amplitudes of line-to-line PWM voltage *Fourier* analysis: (1) Fundamental *k* = 1, (2) , (3) harmonics at $k \cong f_T/f_s$, (4), (5) harmonics at $k \cong 2f_T/f_s$, depending on modulation degree *m*

Example 5.4-2:
Fourier voltage harmonics in six-step mode:

a) Line-to-line voltage:

$$u_{LL}(t) = \sum_{k=1}^{\infty} \hat{U}_{LL,k} \cdot \cos(k \cdot \omega_s t)$$
$$\hat{U}_{LL,k} = \frac{4U_d}{\pi} \cdot \frac{\sin(|k| \cdot \pi/3)}{|k|} = \frac{2U_d}{k \cdot \pi} \cdot \sqrt{3} \qquad k = 1, -5, 7, -11, 13, -17, 19, ... \tag{5.4-9}$$

b) For deriving phase voltage, one has to evaluate eq. (5.4-4) for each harmonic. If we take time co-ordinate so that like in (5.4-9) fundamental voltage amplitude occurs at *t* = 0, we get :

$$u_S(t) = \sum_{k=1}^{\infty} \hat{U}_{S,k} \cdot \cos(k \cdot \omega_s t)$$
$$\hat{U}_{S,k} = \frac{2U_d}{\pi} \cdot \frac{\sin(|k| \cdot \pi/2)}{|k|} = \frac{2U_d}{k \cdot \pi} \cdot (-1)^g \qquad k = 1 + 6g = 1, -5, 7, -11, 13, -17, 19, ... \tag{5.4-10}$$

Conclusions:

Phase voltage amplitudes are $\hat{U}_{S,k} = \hat{U}_{LL,k} / \sqrt{3}$ *in star-connected stator winding and* $\hat{U}_{S,k} = \hat{U}_{LL,k}$ *in delta connected stator winding.*

b) Current time harmonics and additional motor losses due to inverter supply:

Applying harmonic phase voltage as stator voltage U_{sk} to stator winding yields a stator harmonic current I_{sk}, which excites a step-like air gap field, that can be written as *Fourier* sum of field space harmonics (5.4-6). As I_{sk} for $|k| > 1$ is usually much smaller than $I_{s,k=1} = I_{s,1}$, for higher time-harmonics only the fundamental of excited air gap field is considered $B_{\delta sk,\nu=1}$, whereas higher space harmonics $B_{\delta sk,|\nu|>1}$ are neglected. Slip of the fundamental field wave of k^{th} current harmonic is according to (5.4-7)

$$s_k = \frac{n_{syn,k} - n}{n_{syn,k}} = \frac{n_{syn} \cdot k - n}{n_{syn} \cdot k} = 1 - \frac{1}{k} \cdot (1 - s) \quad , \tag{5.4-11}$$

inducing rotor cage with rotor harmonic frequency

$$f_{rk} = s_k \cdot f_{sk} = s_k \cdot |k| \cdot f_s \quad . \tag{5.4-12}$$

As only fundamental field wave is considered, we can use fundamental wave equivalent circuit of induction machine for deriving harmonic current I_{sk} (Fig. 5.4-4).

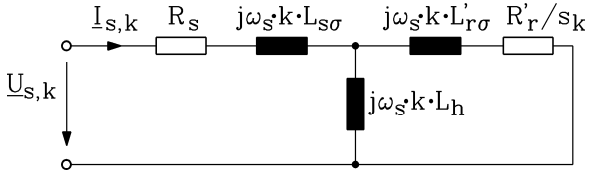

Fig. 5.4-4: Equivalent circuit for calculating time harmonic current I_{sk} with fundamental air gap field wave

As $|k| \geq 5$, slip is $s_k \cong 1$, that means: Due to high frequency space fundamental of k^{th} harmonic current moves so fast with respect to rotor, that rotor seems to be at stand-still. Therefore absolute value of $j|k|\omega_s L_h$ is much bigger than absolute value of $R'_r / s_k + j|k|\omega_s L'_{r\sigma} \approx R'_r + j|k|\omega_s L'_{r\sigma}$, so we can simplify: $\underline{I}_{s,k} \cong -\underline{I}'_{r,k}$, getting

$$s_k \approx 1 \quad \Rightarrow \quad I_{s,k} \approx \frac{U_{s,k}}{\sqrt{(R_s + R'_r)^2 + (k\omega_s)^2 \cdot (L_{s\sigma} + L'_{r\sigma})^2}} \approx \frac{U_{s,k}}{|k|\omega_s (L_{s\sigma} + L'_{r\sigma})} \tag{5.4-13}$$

Conclusions:

Harmonic currents $I_{s,k}$ *are nearly independent from load (= slip s) and are limited mainly by stray inductance. They occur already at no-load s = 0 in full extent, causing additional losses*

$$P_{ad,inv} \cong 3 \sum_{|k|>1}^{\infty} (R_s + R'_r) I^2_{s,k} \quad . \tag{5.4-14}$$

Due to high frequency considerable current displacement mainly in rotor conductors will occur, increasing AC bar resistance and additional losses $P_{ad,inv}$ due to inverter supply. Therefore rotor bars are designed especially for inverter supply. Round bars would yield lowest current displacement, but bars are as broad as high, thus leading to narrow rotor teeth with high iron saturation. Therefore **oval shaped slots** with constant width teeth in between are preferred (Fig. 5.4-5). This oval shape is usually only possible if cage is made from die-cast aluminium.

In case of **semi-closed** rotor slot opening (Fig. 5.4-5, slot A) stray inductance is lower than in case of **closed slots** (Fig. 5.4-5 B, C), as the iron bridge in case B, C has a lower magnetic resistance and therefore guides a bigger rotor stray flux. So slots B, C would limit current harmonics stronger. Further, air gap wave will induce in aluminium surface of slot opening additional eddy current, which in case of closed slots with iron stack made of insulated iron sheets is not possible.

Comparing slot B and C, one has to consider that in order to ensure small air gap, the rotor surface is often tooled. Tooling process might bridge the insulation between adjacent iron sheets, leading to a thin layer conducting iron rotor surface, where the air gap field again might induce eddy currents, causing additional rotor losses. In case of slot C, the small additional slot above the iron bridge interrupts the rotor surface and the eddy currents. Moreover it adds an additional by-pass for rotor stray flux, thus increasing rotor stray inductance and limiting stronger stator and rotor current harmonics.

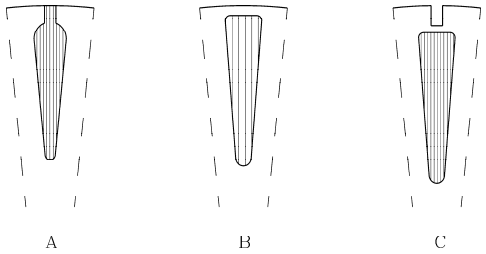

Fig. 5.4-5: Typical oval rotor slots for aluminium die cast cages, especially for inverter supplied induction machines: A: semi-closed slot, B: closed slot, C: closed slot with additional gap

Example 5.4-3:

Comparison of effect of different rotor slots A and C for three-phase unskewed motor

Data: 2*p* = 4, 15 kW, 380 V D, 30 A, air gap 0.45 mm, iron stack length 195 mm, rotor outer diameter 145 mm, slots in stator / rotor: 36 / 28.

Calculation of additional losses in bars numerically with finite elements for inverter operation at f_s = 50 Hz and 15 kW, synchronous inverter switching, f_T = 750 Hz (f_T/f_s = 15), as compared to sinusoidal operation at 50 Hz from grid:

$$P_{ad,r,inv} = Q_r \sum_{|k|>1}^{\infty} R_r \cdot I^2_{r,k}$$

Slot shape A: 190 W, slot shape C: 60 W.

Conclusions:

For inverter operation often oval shaped die cast bars are used, where bars with big stray induction reduce additional cage losses, but increased stray inductance also reduces breakdown torque. So often as compromise slot shape B is used.

Increased losses e.g. with slot shape A yield increased temperature in motor, typically in stator winding up to 5 K, which sometimes might lead to slight motor de-rating to stay within thermal limit of applied thermal motor class.

A further method to decrease current harmonics is to raise inverter switching frequency f_T. From Chapter 4.2 we know that due to current displacement AC bar resistance increases by ratio $k_{Rk} \cong h_{bar} / d_{E,k}$ with **penetration depth** (conductivity κ, permeability μ of rotor bar conductor)

$$d_{E,k} = 1/\sqrt{\mu \cdot \kappa \cdot \pi \cdot f_{rk}} \approx 1/\sqrt{\mu \cdot \kappa \cdot \pi \cdot |k| \cdot f_s} \quad . \qquad (5.4\text{-}15)$$

Losses in bar conductors are therefore for k^{th} harmonic

$$P_{ad,r,inv} = Q_r \cdot R_{r\sim} \cdot I_{r,k}^2 = Q_r \cdot k_{Rk} \cdot R_{r=} \cdot I_{r,k}^2 \cong Q_r \cdot k_{Rk} \cdot R_{r=} \cdot \frac{U_{s,k}^2}{(|k|\omega_s (L_{s\sigma} + L'_{r\sigma}))^2} \quad \text{or}$$

$$P_{ad,r,inv} \sim \sqrt{|k|} \cdot U_{s,k}^2 / |k|^2 \quad . \qquad (5.4\text{-}16)$$

Increasing switching frequency e.g. at medium modulation degree means increasing of ordinal number $|k| = 2 f_T / f_s$, where dominant voltage harmonic $U_{s,k}$ occurs. With increase of k voltage harmonic is reduced, but current harmonic is reduced much stronger by $U_{s,k}/k$, so losses in rotor bars decrease according to (5.4-16). On the other hand switching losses in power transistors of inverter rise linear with switching frequency, so optimum for minimum system losses (= overall drive efficiency) has to be found.

Example 5.4-4:
Standard 2-pole motor, 3 kW, 380 V Y is fed by voltage source inverter with asynchronous switching with rating 8.3 kVA, 12 A rated current, 400 V. Motor is operated at f_s = 50 Hz with slip s = 4.5% at 10 Nm (rated power 3 kW), loading the inverter with 54% of rated inverter current. Motor and inverter efficiency was measured by directly measuring input and output power both of motor and inverter for different inverter switching frequency.

	grid operation	***inverter operation***		
f_s / Hz	50	50	50	50
f_T / Hz	-	2 400	4 800	9 600
$f_p = 2f_T$ / kHz		4.8	9.6	19.2
Efficiency motor	81.9 %	81.3 %	81.4 %	81.4 %
Efficiency inverter	-	96.9 %	96.8 %	95.9 %
Overall efficiency	**81.9 %**	**78.8 %**	**78.8 %**	**78.1 %**

Table 5.4-1: Measured motor, inverter and overall efficiency of 3 kW motor at different inverter switching frequency

As inverter is only partially loaded, its efficiency is lower than at rated point, which is 97%. This is due to constant load independent losses such as current supply for controller electronics and fan blower.

Conclusions:
At f_P = 9.6 kHz overall motor efficiency is higher (motor heating is lower), and overall efficiency is the same as at 4.8 kHz. At 19.2 kHz current ripple reduction in motor is already negligible, but inverter losses increase considerably.

In Fig. 5.4-6 and Fig. 5.4-7 the corresponding measured time functions of line-to-line voltage and of motor phase current along with the *Fourier* spectra are shown for switching frequency 2.4 kHz and 4.8 kHz. Inverter operates at DC link voltage U_d = 525 V. Note that oscilloscope

resolution was not sufficient to display PWM pattern of line-to-line voltage for a whole period appropriate. Only in the zoomed time function the voltage pulse is visible correctly.

		$U_{LL,k}$	$I_{s,k}$	$I_{s,k} / I_{s,k=1}$
f_s	50 Hz	372 V	6.2 A	100 %
$2f_T - f_s$	4750 Hz	89.5 V	0.18 A	2.9 %
$2f_T + f_s$	4850 Hz	91.3 V	0.18 A	2.9 %
$4f_T - f_s$	9550 Hz	38.6 V	0.035 A	0.6 %
$4f_T + f_s$	9650 Hz	24.8 V	0.027 A	0.4 %

Table 5.4-1: Measured *Fourier* spectrum of line-to-line voltage and phase motor current at 2.4 kHz inverter switching frequency (see Example 5.4-4)

Note that overall r.m.s. of voltage e.g. at 2.4 kHz switching frequency

$$U_{LL,rms} = \sqrt{\sum_{k=1}^{\infty} U_{LL,k}^2} \qquad (5.4\text{-}17)$$

is with $U_{LL,rms}$ = 403 V much bigger than r.m.s.-value of fundamental (372 V) due to voltage harmonics. Current harmonics are small, so total current r.m.s. $I_{s,rms}$ = 6.25 A is nearly the same as r.m.s. of fundamental 6.2 A. Current is close to sine wave, so current measured peak 9.65 A is nearly the same as $\sqrt{2} \cdot I_{s,k=1} = \sqrt{2} \cdot 6.2 = 9.2$ A. From Table 5.4-1 we derive with (5.4-13) total motor stray inductance

$$L_{s\sigma} + L'_{r\sigma} = L_\sigma = \frac{U_{LL,k} / \sqrt{3}}{\omega_{sk} \cdot I_{sk}} = \frac{89.5 / \sqrt{3}}{2\pi \cdot 4750 \cdot 0.18} = 9.61\,\text{mH}$$

and current amplitude at e.g. 9550 Hz with

$$I_{sk} = \frac{U_{LL,k} / \sqrt{3}}{\omega_{sk} \cdot (L_{s\sigma} + L'_{r\sigma})} = \frac{38.6 / \sqrt{3}}{2\pi \cdot 9550 \cdot 0.00961} = \underline{\underline{38.6}}\,\text{mA} \ ,$$

which fits well to the measured value 35 mA, proving the value of presented theory. Measured current ripple is the sum of all current *Fourier* harmonics and is of triangular shape, as it is explained in Chapter 1. In case that voltage impulse width is the same as voltage gap in between, peak-to-peak of current ripple is maximum. Considering in Y-connection the stray inductance of two phases for line-to-line voltage value U_d and frequency of voltage impulses as double switching frequency, we get as maximum peak-to-peak current ripple 2.8 A, which fits well to the measurement Fig. 5.4-6.

$u = L \cdot di/dt \quad \Rightarrow \quad U_d = 2L_\sigma \cdot \Delta i / \Delta t$, $\quad \Delta t = T_p / 2 = 1/2 f_p$:

$$\Delta i = \frac{U_d}{4 L_\sigma f_p} = \frac{525}{4 \cdot 0.00961 \cdot 4800} = \underline{\underline{2.8}} A$$

The 5th and 7th inverter voltage harmonic are rather small at this modulation degree, e.g. 5th voltage line-to-line r.m.s. measured value is 2.9 V at $5 \cdot 50 = 250$ Hz, yielding with (5.4-13) harmonic current $I_{s,5} = 2.9/(\sqrt{3} \cdot 2\pi \cdot 250 \cdot 0.00961) = 0.11$ A; measured value is 0.09A.

Note that this motor has been already investigated at sinusoidal voltage supply (Example 4.4.1-5), showing due to **rotor slot space harmonics** additional stator current harmonics at about 950 Hz and 1150 Hz with r.m.s. current harmonics 0.08 A and 0.05 A, which are also visible in Fig. 5.4-6 and Fig. 5.4-7.

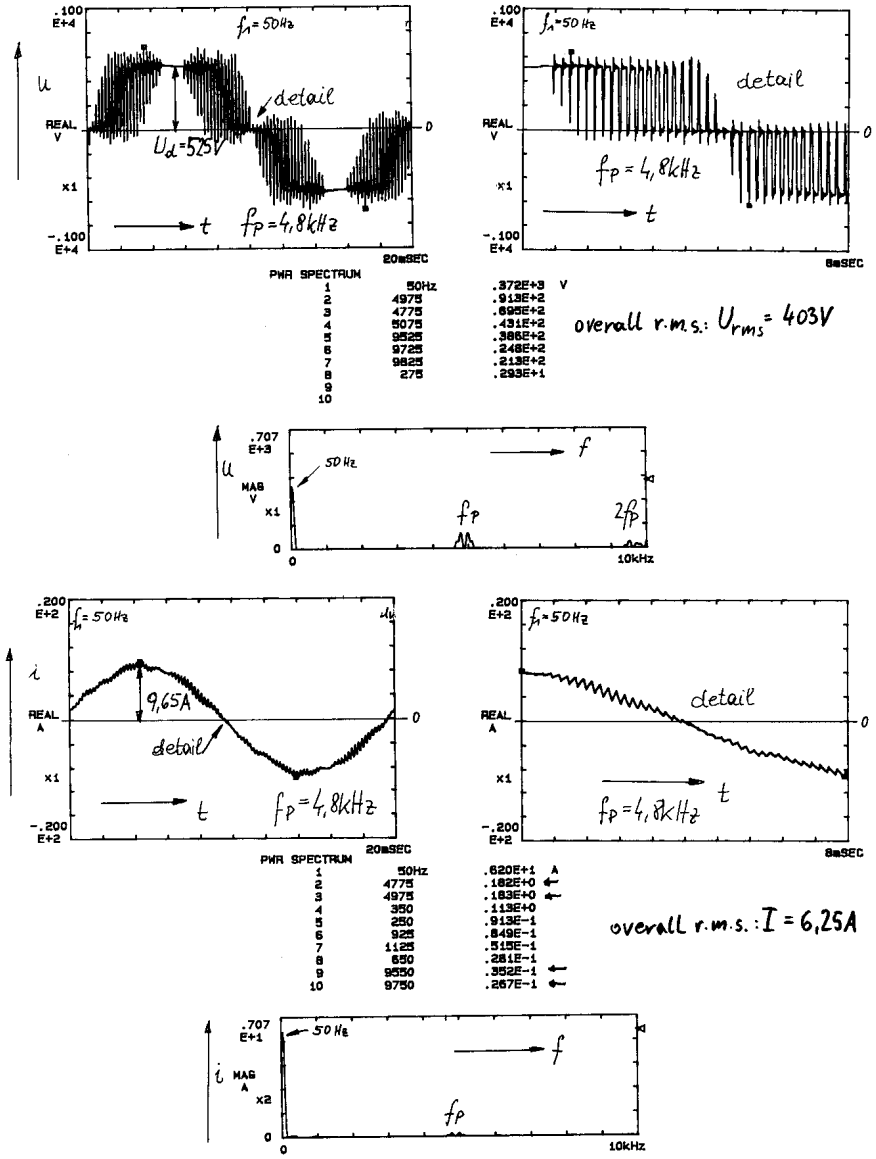

Fig. 5.4-6: Above: Measured line-to-line voltage PWM inverter output at pulse frequency 4.8 kHz (switching frequency 2.4 kHz) of example 5.4-4 and corresponding *Fourier* spectrum, showing considerable voltage harmonics at $2f_T \pm f_s$ and $4f_T \pm f_s$. Below: Motor phase current time-function, showing current ripple with frequency $f_p \cong 2f_T$ = 4.8 kHz, which is determined in corresponding *Fourier* spectrum as $2f_T \pm f_s$. Note that current harmonics decrease much stronger with increasing ordinal number, so that at $4f_T \pm f_s$ nearly no current amplitude is visible any longer.

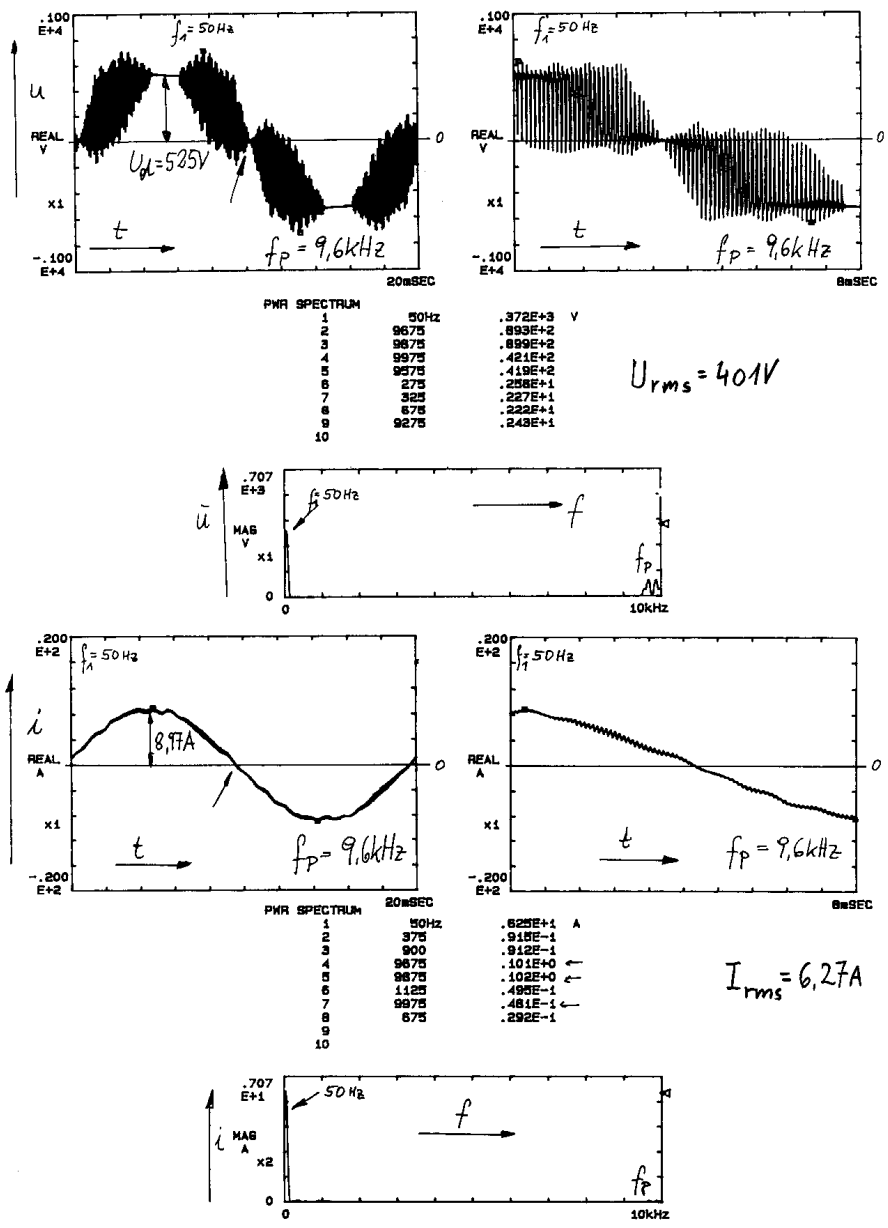

Fig. 5.4-7: As Fig. 5.4-6, but at pulse frequency 9.6 kHz (switching frequency 4.8 kHz). Note that compared with Fig. 5.4-6 due to doubling of switching frequency current ripple is reduced by 50%

c) Inverter-induced torque ripple:
Fundamental air gap field amplitudes $B_{\delta sk,v=1}$ of stator harmonic currents I_{sk} produce with rotor harmonic currents I_{rk} tangential *Lorentz*-forces, and therefore additional torque components. Space harmonics $|\nu| > 1$ are neglected, as their amplitude is much smaller.

- Stator field $B_{\delta sk,v=1}$ generates with rotor harmonic current I_{rk} of SAME ordinal number k a constant torque $M_{e,kk}$, which is proportional to product $M_{e,kk} \sim B_{\delta sk,v=1} \cdot I_{rk}$. As $B_{\delta sk,v=1} \sim I_{sk}$, this torque is $M_{e,kk} \sim I_{sk} \cdot I_{rk}$. As both amplitudes are small for $|k| > 1$, their product is very small, so these constant torque contributions $M_{e,kk}$ for $|k| > 1$ are negligible. The torque $M_{e,kk}$ for $k = 1$ is the well known fundamental torque of *Kloss* function.
- Stator field $B_{\delta sk=1,v=1}$, excited by fundamental current $I_{s,k=1}$, generates with rotor harmonic current I_{rk} of DIFFERENT ordinal number k a **pulsating** torque $M_{e,1k}$, which is proportional to product $M_{e,1k} \sim B_{\delta sk=1,v=1} \cdot I_{rk}$ or due to $B_{\delta sk=1,v=1} \sim I_{sk=1}$ it is $M_{e,1k} \sim I_{s1} \cdot I_{rk}$. Due to rather big fundamental current this torque ripple is **not negligible**.

Rotor bar current with amplitude $\hat{I}_{rk}$ and frequency $f_{rk} = s_k \cdot f_{sk}$ is distributed in the rotor bars along rotor circumference. Due to phase shift between adjacent bar currents on can describe current distribution along rotor circumference as ideal sinusoidal, so that per rotor circumference element dx_r we have the rotor current element

$$di_{rk}(x_r,t) = \frac{Q_r \cdot \hat{I}_{rk}}{2p\tau_p} \cdot dx_r \cdot \sin(\frac{x_r\pi}{\tau_p} - s_k \cdot \omega_{sk} t) \qquad (5.4\text{-}18)$$

With respect to stator co-ordinate system with $x_r = x_s - (1-s) \cdot 2 f_s \tau_p \cdot t$ and considering harmonic slip $s_k \cdot f_{sk} = (1 - \frac{1}{k}(1-s)) \cdot k \cdot f_s$ we get

$$di_{rk}(x_s,t) = \frac{Q_r \cdot \hat{I}_{rk}}{2p\tau_p} \cdot dx_s \cdot \sin(\frac{x_s\pi}{\tau_p} - k \cdot \omega_s t) \qquad . \qquad (5.4\text{-}18)$$

Tangential *Lorentz*-force $dF_{tk} = di_{rk}(x_s,t) B_{\delta\hat{s}}(x_s,t) l_{Fe}$ yields torque $dM_{e,1k} = dF_{tk} \cdot (d_{si}/2)$ and with $d_{si}/2 = p\tau_p/\pi$ torque is the summation of d$M_{e,1k}$ along rotor circumference

$$M_{e,1k} = \int dM_{e,1k} = \frac{p\tau_p l_{Fe}}{\pi} \int_0^{2p\tau_p} \frac{Q_r \cdot \hat{I}_{rk}}{2p\tau_p} \cdot \sin(\frac{x_s\pi}{\tau_p} - k \cdot \omega_s t) \cdot B_{\delta\hat{s}} \cdot \cos(\frac{x_s\pi}{\tau_p} - \omega_s t) \cdot dx_s \qquad (5.4\text{-}19)$$

$$\boxed{M_{e,1k} = \frac{p\tau_p Q_r \hat{I}_{rk} B_{\delta\hat{s}} l_{Fe}}{2\pi} \cdot \sin((1-k)\omega_s t) = \mathrm{sgn}(g) \cdot \frac{p\tau_p Q_r \hat{I}_{rk} B_{\delta\hat{s}} l_{Fe}}{2\pi} \sin(6|g|\omega_s t)} \qquad (5.4\text{-}20)$$

Conclusions:
As $f_{1k} = |1-k| f_s = 6|g| f_s$, the pulsating torque occurs with multiples of six time stator fundamental frequency. Each two harmonics, e.g. k = -5 and k = 7, contribute with their torque amplitudes e.g. $\hat{M}_{e,1,-5}$, $\hat{M}_{e,1,7}$ to one resulting pulsating torque with e.g. $6f_s$ as the sum of both torque amplitudes: $\hat{M}_{e,6f_s} = \hat{M}_{e,1,-5} + \hat{M}_{e,1,7}$.

Proof (here for six step operation):
Time-harmonic ordinal number: $k = 1 + 6g > 1, \quad g = \pm 1, \pm 2, ...$

Phase voltage amplitude: $\hat{U}_{s,k} = \frac{2U_d}{k \cdot \pi} \cdot (-1)^g$

Rotor harmonic currents: $\hat{I}_{rk} = \ddot{u}_I \hat{I}'_{rk} = -\ddot{u}_I \hat{I}_{sk} = -\frac{m_s N_s k_{ws}}{Q_r/2} \cdot \frac{\hat{U}_{s,k}}{|k|\omega_s L_\sigma}$

Torque amplitude: $\hat{M}_{e,1k} = -\mathrm{sgn}(g) \cdot \frac{p\tau_p Q_r B_{\delta\hat{s}} l_{Fe}}{2\pi} \cdot \frac{m_s N_s k_{ws}}{Q_r/2} \cdot \frac{1}{|k|\omega_s L_\sigma} \cdot \frac{2U_d}{k \cdot \pi} \cdot (-1)^g$

The sign of $\frac{\mathrm{sgn}(g)}{k} \cdot (-1)^g$ is for a harmonic pair e.g. *k* = -5, 7 always the same, so both torque amplitudes add as the sum to resulting torque amplitude.

Example 5.4-5:
Standard 8-pole induction motor, 440 V Y, 60 Hz, 2.6 kW, 5.6 A, 28.4 Nm, 860/min
fed by inverter supply at f_s = 50 Hz from 50 Hz-grid, 380 V, U_d = 525 V, PWM, switching frequency 2.4 kHz
Motor design data: m_s = 3, Q_s/Q_r = 48/44, l_{Fe} = 80 mm, L_σ = 19.6 mH, two-layer winding, q = 2, coil chording 5/6, k_{ws} = 0.933, N_s = 344, stator bore diameter 155 mm

Stator field fundamental: $B_{\delta\hat{s}} = 1\mathrm{T}$, $\hat{I}_{rk} = -\frac{m_s N_s k_{ws}}{Q_r/2} \cdot \frac{\hat{U}_{s,k}}{|k|\omega_s L_\sigma}$

$\|k\|$	f_k	$\hat{U}_{s,k}$	$\hat{I}_{rk}$	$\hat{M}_{e,1k}$	$\hat{M}_{e,6\|g\|f_s}$	f_{1k}
-	Hz	V	A	Nm	Nm	Hz
5	250	2.5	3.55	0.55		
7	350	2.5	2.54	0.39		
					0.94	**300**
95	4750	73.1	5.5	0.85		
97	4850	74.2	5.4	0.83		
					1.68	**4800**
191	9550	31.4	1.1	0.17		
193	9650	20.2	0.7	0.11		
					0.28	**9600**

Table 5.4-2: Calculated low frequency torque ripple 300 Hz at PWM is 0.94/28.4 = 3.3 % in air gap

$$f_k < f_0: \ \hat{M}_s \cong \frac{\hat{M}_{e,6|g|f_s} \cdot J_L}{J_L + J_M} \qquad f_k > f_0: \ \hat{M}_s \cong \frac{\hat{M}_{e,6|g|f_s} \cdot c}{J_M \cdot (2\pi f_k)^2} \qquad (5.4\text{-}21)$$

Shaft torque ripple is below torsion resonance determined by ratio of load versus motor inertia (Chapter 1.1), and above resonance by the inverse square of pulsation frequency. For f_0 = 200 Hz, f_s = 10 Hz we get: $6f_s$ = 60 Hz < 200 Hz, $2f_T$ = 4.8 kHz > 200 Hz. With $J_L = J_M$ we get: $\hat{M}_s / M_N \cong 0.5 \cdot \hat{M}_{e,6|g|f_s} / M_N = 1.7\%$, whereas at 4800 Hz shaft torque ripple is 0.0015 Nm.

Conclusions:
Although voltage amplitude of 5^{th} and 7^{th} voltage harmonic is low, compared to pulse frequency harmonic voltage amplitude, the $6f_s$ harmonic torque ripple is dominating, as switching frequency torque ripple is attenuated by inertia and elastic coupling. Natural torsion frequency f_0 of drive train is 20 ... 200 Hz, so torsion resonance might be excited. Note that the frequency of the 5^{th} and 7^{th} voltage harmonic vary with speed, so during speed variation torsion resonance might be hit.

Example 5.4-6:
Measured torque ripple with accelerometer:
Standard induction motor: 2 pole, 750 W, 2850/min, 2.51 Nm, 400 V D, 50 Hz, 1.6 A
Voltage-source IGBT Inverter: 1500 VA, 2.2 A, 400 V
Motor operated at f_s =1.2 Hz, n = 20/min, s = 0.72, M = 1.24 Nm = 50% rated torque
a) PWM, asynchronous switching: $k = 1+6g = 1,-5,7,-11,13,...$ $g = 0,\pm1,\pm2,...$
b) PWM only for two thirds of one period, one third no switching (zero voltage): This switching mode leads to lower inverter switching losses, but voltage output pattern is not symmetrical to abscissa, so voltage harmonics with even ordinal numbers occur: $k = 1+3g = 1,-2,4,-5,7,-8,10,-11,13,...$ $g = 0,\pm1,\pm2,...$

Calculation of lowest torque ripple frequency (Table 5.4-3) and measurement of torque ripple $\hat{w}_M$ according to Chapter 1. Load inertia is much bigger than motor inertia, so shaft torque ripple is equal to air gap torque ripple.

$$\hat{w}_M = \frac{\hat{M}_{cogging}}{M_{average}} = \frac{(M_{\max} - M_{\min})/2}{(M_{\max} + M_{\min})/2} \qquad (5.4\text{-}22)$$

	a) symmetrical PWM	b) asymmetrical PWM
Lowest torque ripple frequency	$f_{1k} = 6\lvert g\rvert f_s = 6 f_s =$ $= 6 \cdot 1.2 = 7.2Hz$	$f_{1k} = 3\lvert g\rvert f_s = 3 f_s =$ $= 3 \cdot 1.2 = 3.6Hz$
Measured torque ripple $\hat{w}_M$	14.4%	35.0%
Torque ripple amplitude	0.18 Nm	0.43 Nm

Table 5.4-3: Calculated low frequency torque ripple at PWM for different PWM feeding

Conclusions:
With asymmetrical PWM increase of voltage harmonics occurs, leading to increased current harmonics and to double torque ripple amplitude at low frequency, which might excite torsion resonance.

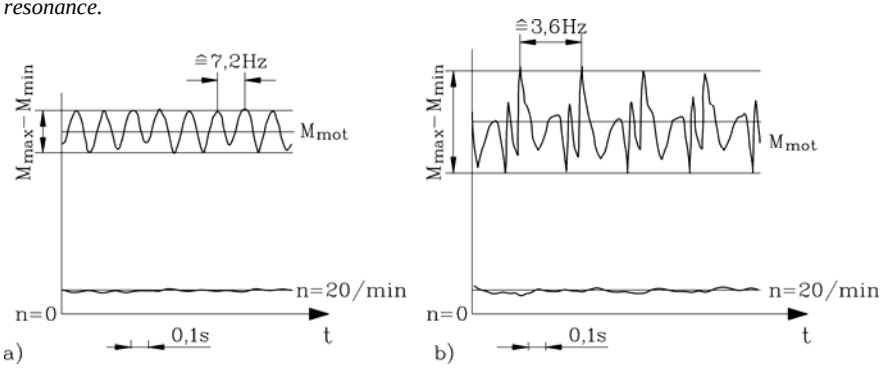

Fig. 5.4-8: Measured low frequency torque ripple at low speed with a) symmetrical PWM, b) asymmetrical PWM. High frequency torque ripple e.g. due to inverter switching is not seen, as accelerometer is low pass filter. In case b) superposition of torque ripple with 3.6 Hz and 7.2 Hz is visible.

d) Acoustic noise
In addition to the magnetically excited acoustic noise at sinus voltage supply, caused by the slot harmonics, the additional air gap waves of the current harmonics I_{sk} will add to acoustic noise with new tonal frequency, which is typically inverter pulse frequency $f_p = 2f_T$. Like for

torque ripple, also here only the fundamental wave amplitudes $B_{\delta sk,\nu=1} \sim I_{sk}$ are considered, as the space harmonics amplitudes of higher order $|\nu| > 1$ are small. So dominant field wave $B_{\delta sk=1,\nu=1} \sim I_{sk=1} = I_s$ of fundamental current is modulated by $B_{\delta sk,\nu=1} \sim I_{sk}$:

- Stator fundamental field wave, excited by magnetizing current $\underline{I}_m = \underline{I}_s + \underline{I}'_r\, I_s$ with stator frequency f_s:

$$B_{\delta sk=1,\nu=1}(x_s,t) = B_{\delta s} \cdot \cos\left(\frac{\pi x_s}{\tau_p} - 2\pi f_s t\right) = B_{\delta s} \cdot \cos\alpha \qquad . \qquad (5.4\text{-}23)$$

- Stator harmonic field wave, excited by magnetizing current $\underline{I}_{mk} = \underline{I}_{sk} + \underline{I}'_{rk}\, I_s$ with stator harmonic frequency f_{sk}:

$$B_{\delta sk,\nu=1}(x_s,t) = B_{\delta sk} \cdot \cos\left(\frac{\pi x_s}{\tau_p} - 2\pi \cdot k \cdot f_s t\right) = B_{\delta sk} \cdot \cos\beta \qquad . \qquad (5.4\text{-}24)$$

The magnetic pull due the superposition of these waves is

$$f_n(x_s,t) = \frac{B^2(x_s,t)}{2\mu_0} \sim (\sum_{k=1}^{\infty} B_{\delta sk})^2 \quad \Rightarrow \quad f_{n,1k} \sim \sum_{k=1}^{\infty} B_{\delta sk}^2 + 2B_{\delta sk}B_{\delta sk'} \qquad k \neq k' \,. \qquad (5.4\text{-}25)$$

Mainly the mixed products $B_{\delta sk}B_{\delta sk'} = B_{\delta sk}B_{\delta sk=1}$ of fields of the k^{th} harmonic and of the fundamental current are of interest, because they are big enough. The squares $B_{\delta sk}^2$ for $|k| > 1$ and the mixed products $B_{\delta sk}B_{\delta sk'}$ for $k \neq k' \neq 1$ are very small due to the small field amplitudes. With use of the trigonometric formula $2\cos\alpha \cdot \cos\beta = [\cos(\alpha+\beta) + \cos(\alpha-\beta)]$ the **radial force density waves,** exert an oscillating pull on stator and rotor iron stack, are

$$\boxed{f_{n,1k}(x_s,t) = \frac{B_{\delta s}B_{\delta sk}}{2\mu_0} \cdot \cos(2r \cdot \frac{\pi x_s}{2p\tau_p} - 2\pi f_{Ton,k} t)} \qquad . \qquad (5.4\text{-}26)$$

The number of positive and negative half-waves of force density along machine circumference equals **the number of nodes 2*r*** in between:

$$2r = 2p \cdot |1 \pm 1| = 4p \text{ ("+")} \quad \text{and} \quad 0 \text{ ("-")} \qquad (5.4\text{-}27)$$

The **tonal frequency** $f_{\text{Ton,k}}$ of force wave variation is

$$f_{Ton,k} = f_s \cdot |1+k| \qquad \text{for} \qquad 2r = 4p \qquad (5.4\text{-}28)$$

$$f_{Ton,k} = f_s \cdot |1-k| \qquad \text{for} \qquad 2r = 0 \,. \qquad (5.4\text{-}29)$$

As already explained, the deformation of stator yoke as elastic ring is small for high node force wave, and the acoustic sound wave of this multi-pole excitation is not far reaching. On the other hand, the vibration mode $2r = 0$ yields to "in-phase" vibration of the whole motor surface as a very good loud-speaker. As already shown in this chapter, the dominating current harmonic amplitudes occur at medium modulation degree with frequencies $f_{sk} = 2f_T \pm f_s$. Thus tonal frequency is $f_{Ton,k} = f_s \cdot |1-k| = f_{sk} - f_s = 2f_T$ or $f_{Ton,k} = 2f_T - 2f_s$.

Conclusions:
Inverter caused magnetic noise is usually excited with twice switching frequency ("pulse frequency").

Force amplitude is depending on motor main flux and stator current harmonics. Therefore **inverter-induced magnetic noise occurs already at no-load**, as both main flux Φ and current harmonics I_{sk} are at their full value already at no-load.

$$\hat{F}_{n,1k} = \frac{1}{2\mu_0} \cdot B_{\delta s} \cdot \frac{\mu_0}{\delta} \cdot \frac{\sqrt{2}}{\pi} \cdot \frac{m_s N_s k_{ws} I_{sk}}{p} \sim I_m \cdot I_{sk} \sim \Phi \cdot I_{sk} \qquad (5.4\text{-}30)$$

By **increasing inverter switching frequency acoustic noise may be reduced**, because
- harmonic current is reduced,
- at high frequencies beyond 6 kHz human ear is decreasingly sensitive,
- vibration amplitude of mechanical structure decreases with increased frequency.

Magnetically excited acoustic noise depends on speed range: In the constant torque range $0 \le n \le n_N$ flux is constant and big, so noise is big. In the constant power range flux is weakened by $\Phi = \Phi_N \cdot (n_N / n)$ and therefore magnetic noise decreases. In case of standard induction motors with shaft mounted fan the mechanical noise of the fan increases with speed, containing mainly the **"fan blade frequency"** $f_z = z \cdot n$ with z as number of fan blades.

Example 5.4-7:
Measurement of sound pressure level L_{pA} in 1 m distance of motor in **acoustic chamber**, where walls contain sound-absorbing glass fibre cones, so no reflections of sound waves occur. **Sound pressure level** L_p (with human audibility level $p_0 = 2 \cdot 10^{-5}$ Pa) is measured as average value of 8 microphones

$$\bar{L}_{pA} = 20 \cdot \lg(p / p_0) \cdot a \quad , \qquad (5.4\text{-}31)$$

and is weighted with factor a to simulate frequency-dependent sensitivity of human ear.
4 pole cage standard induction motor, size 71 mm (shaft height), with shaft-mounted fan and data: 250 W, 400 V D, 50 Hz, fed from IGBT-inverter with 400 VA, capable of different switching frequencies 1 kHz, 2 kHz, 4 kHz, 8 kHz, leading to audible noise with pulse frequency 2 kHz, 4 kHz, 8 kHz, 16 kHz. Fig. 5.4-9 shows, that increase of switching frequency above 2 kHz decreases $\bar{L}_{pA}$ considerably up to 25 dB(A) at low speed. With switching frequency 8 kHz the current ripple (at 16 kHz) is so small, that current is nearly sinusoidal. So no difference in noise to ideal sinusoidal voltage operation (generated from synchronous test-field generator with variable frequency) occurs. Above 1500/min flux is weakened and sound pressure level is reduced at 1 and 2 kHz switching frequency. At high speed the noise of the fan is dominating. **Noise of fan** increases theoretically with

$$\Delta L_p = 50 \cdot \lg(n_2 / n_1) \quad , \qquad (5.4\text{-}32)$$

thus between 1500/min and 6000/min by 30 dB, which is well in coincidence with measurement at 8 kHz switching frequency.

For **big motors** it is not easy to raise inverter switching frequency to reduce audible noise, as due to increased switching losses the power transistors must be oversized, which is expensive at big power. As audible tone with pulse frequency (e.g. 2 kHz) may be experienced really

nasty, some manufacturers of inverters offer a control strategy with **wobbling** of switching frequency. Switching frequency varies between e.g. 1 kHz and 2 kHz periodically with e.g. a sine function. So the tonal frequency varies also. One experiences a frequency mix instead of a tonal fixed frequency. This sound is to many people more convenient, but sometimes resembles to that kind of noise, if motor bearings were damaged.

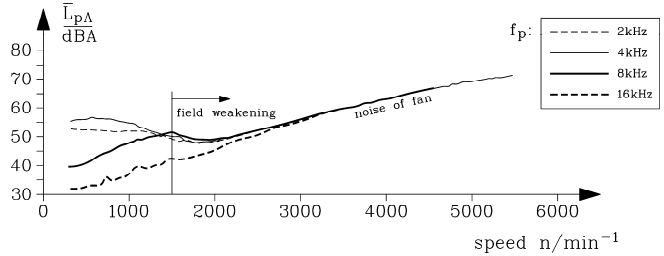

Fig. 5.4-9: Measured A-weighted sound pressure level at 1 m distance of 250 W, PWM inverter-fed induction motor, varying with speed and switching frequency f_T, corresponding with pulse frequency $f_p = 2f_T$.

e) Influence of air gap field space harmonics at inverter-operation:
Asynchronous and synchronous harmonic torque due to slotting occur at big slip (typically between s = 0.8 ... 1.2), so inverter-fed motors – being operated usually between full-load slip and zero slip – should not be influenced by these parasitic torque components. Nevertheless, at low speed, full-load slip increases up to unity, so that space harmonic torque will be in the range of motor operation. Yet, motor current is in the range of rated current and not –as with line-started induction motors – in the range o 500% rated current. So these parasitic torque components remain small and negligible (see Example 5.4-8).

Example 5.4-8:
Calculation of **space harmonic torque** with numerical finite element calculation method for unskewed 4-pole cage induction motor, 15 kW, 380 V, D, 50 Hz, 30 A, 1430/min, 100 Nm, Q_s/Q_r = 36 / 28.

a) Harmonic torque at f_s =50 Hz line-operation (This was calculated in Example 4.4.2-1):
(i) Asynchronous harmonic torque due to ν = -11 stator field harmonic with harmonic synchronous speed $n = (1-s) \cdot n_{syn} = (1-1.09) \cdot 1500 = \underline{\underline{-136 / \min}}$.

(ii) Synchronous harmonic torque at slip 0.86 due to harmonics $\nu = -\mu = 13$ occurs at 215/min with amplitude 150 Nm.

b) Harmonic torque at f_s = 1.5 Hz inverter-operation (Fig. 5.4-10):
(ii) Synchronous harmonic torque at slip 0.86 due to harmonics $\nu = -\mu = 13$ occurs at 6.3/min with amplitude 5 Nm.

	a) 50 Hz line operation	*b) 1.5 Hz inverter operation*
Synchronous speed	1500/min	45/min
speed at rated torque 98 Nm	1460/min	5/min
slip at rated torque 98 Nm	2.6 %	88.9 %
rotor frequency at 98 Nm	1.3 Hz	1.3 Hz
current at slip 0.86 (synchronous harmonic torque)	550 % rated current	100% rated current
speed at synchronous torque	215/min	6.3 /min
Synchronous torque amplitude	150 Nm	5 Nm

Table 5.4-4: Harmonic synchronous torque at inverter-operation is very small, as motor operates only up to due rated motor current, avoiding the big starting currents of line-operated machines

According to Chapter 4.4 the synchronous torque amplitude $M_{evv} \sim I_s I_r \sim I_s^2$ depends on square of stator current. At inverter operation current stays in the range of rated current, avoiding big starting currents. In our example, we get therefore only 5 Nm instead of 150 Nm as synchronous torque amplitude.

$$M_{evv,b)} = \left(\frac{I_{s,b)}}{I_{s,a)}}\right)^2 \cdot M_{e,vv,a)} = \left(\frac{1}{5.5}\right)^2 \cdot 150 = 5\ \text{Nm}$$

As asynchronous harmonic torque depends in the same manner on I_s^2, their values are reduced likewise.

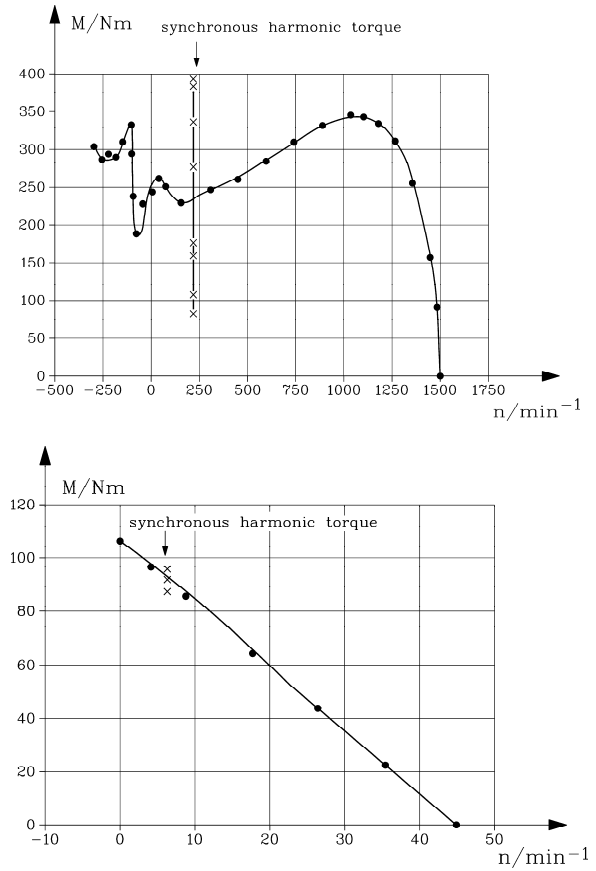

Fig. 5.4-10: Calculated torque-speed characteristic for 15 kW four pole cage induction motor
a) at 50 Hz, 400 V, b) at 1.5 Hz, voltage 12 V + $I_s R_s$ = 23 V to keep main flux constant in machine. Synchronous and asynchronous harmonic torque are strongly reduced at inverter operation due to reduction of current from starting current values (550% rated current) down to rated current range.

6. du/dt-effects in inverter-fed machines

6.1 Voltage wave reflection at motor terminals

a) Wave propagation on loss-free motor cable with reflection coefficients 1 and –1:
Fast switching IGBT inverters allow **voltage rise time** t_r between zero and dc link voltage of down to typically 100 ns. Depending on dc link voltage, a rather big **voltage change rate** d*u*/d*t* is given.

$$du/dt \cong U_d/t_r \qquad (6.1\text{-}1)$$

Example 6.1-1:
Typical values d*u*/d*t* in IGBT inverters for voltage rise time t_r = 100 ns:

Line supply	*dc link voltage*	$du/dt \cong U_d/t_r$
Single phase 230 V 50 Hz	310 V	3.1 kV/μs
Three phase 400 V 50 Hz	560 V	5.6 kV/μs
Three phase 500 V 50 Hz	700 V	7.0 kV/μs

Table 6.1-1: Typical change rate of inverter output voltage for fast switching IGBT inverters

Conclusions:
Typical voltage change rates du/dt of low voltage IGBT inverters range between 3 to 8kV/µs. High voltage IGBT inverters with voltage levels of several kV show the same rates du/dt, as high-volt IGBT switching is slower, but dc link voltage is bigger, compared with low voltage inverters. Thus du/dt is much bigger than the demand for motor insulation according to VDE0530/1, Amendment 2: U_{LL} <1000V, du/dt < 500V/µs).

Between motor and inverter the motor cable is guiding the voltage impulses from the inverter to the motor as electromagnetic wave with velocity of light. Cable consists of copper or aluminium wire with insulation (PVC, PE) in between. Voltage between two phases of cable and current in the cable conductors generates electromagnetic field *E* and *B*, which are determined by permittivity of dielectric insulation ε and magnetic permeability μ.

$$\varepsilon = \varepsilon_r \cdot \varepsilon_0\,, \quad \mu = \mu_r \cdot \mu_0 \qquad . \qquad (6.1\text{-}2)$$

Velocity of *E*- and *B*-wave propagation in material with permittivity ε and permeability μ is given by

$$v = \frac{1}{\sqrt{\varepsilon_0\mu_0}} \cdot \frac{1}{\sqrt{\varepsilon_r\mu_r}} = \frac{c_0}{\sqrt{\varepsilon_r\mu_r}} \qquad , \qquad (6.1\text{-}3)$$

where c_0 is velocity of light in vacuum. As dielectric insulation ε **defines capacitance per cable length** C'_{cable} and magnetic permeability μ defines **inductance per cable length** L'_{cable}, wave propagation velocity of **loss-free** cable may also be written as

$$v = \frac{c_0}{\sqrt{\varepsilon_r\mu_r}} = \frac{1}{\sqrt{L'_{cable}C'_{cable}}} \qquad (6.1\text{-}4)$$

Example 6.1-2:
a) c_0 : velocity of light **in vacuum**:

$$\varepsilon_0 = 8.854\cdot10^{-12}\ \text{As/(Vm)},\ \mu_0 = 4\pi\cdot10^{-7}\ \text{Vs/(Am)}:\ c_0 = \frac{1}{\sqrt{\varepsilon_0\mu_0}} = \underline{\underline{2.998\cdot10^8}}\ \text{m/s}$$

b) v : velocity of light **in motor cable**:

$$\varepsilon_r = 4\,,\ \mu_r = 1:\ v = \frac{c_0}{\sqrt{4}} = \underline{\underline{1.499\cdot10^8}}\ \text{m/s}$$

Conclusions:
Velocity of electromagnetic wave in motor cable is typically 150 km/ms, which is about half of velocity of light in vacuum.

Neglecting rise time (t_r = 0), we consider for each voltage impulse of inverter PWM output a voltage step either from 0 to U_d or from U_d to 0, which is travelling from inverter to motor with velocity *v*. The inverter may considered as a voltage source with zero internal impedance at high frequency, as the dc link capacitor stabilizes the dc link voltage and has an impedance $Z_{inv} = 1/(\omega C)$, which is small at high frequencies. The AC motors (synchronous or asynchronous machines) may be regarded as very high impedance, as their armature winding impedance $Z_{mot} = \sqrt{R_s^2 + (\omega\sigma L_s)^2} \approx \omega\sigma L_s$ is very big at high frequencies. Motor wave impedance is determined by high frequency voltage distribution within motor winding (see Chapter 6.2), so the formula presented here is only a rough estimate.

Example 6.1-3:
Three-phase four-pole standard induction motor, 400 V, Y, 50 Hz, 1.1 kW, frame size 90 mm (= shaft height), total stray inductance at 50 Hz: 50 mH,
Stray inductance at wave reflection frequency f_d = 300 kHz (see Example 6.1-4) is much smaller due to the strong current displacement in motor conductors and is estimated here with 5 mH, yielding calculated value $Z_{mot} = \omega_d \cdot L_{s\sigma} = 2\pi\cdot300\cdot10^3\cdot5\cdot10^{-3} = 9.4\,\text{k}\Omega$.
Measured motor wave impedance is smaller: Z_{mot} = 5000 Ω.
Difference is explained by the reason, that at high frequencies f_d = 300 kHz also stray capacities within motor winding have to be considered to calculate Z_{mot} . The same holds true for inverter wave impedance Z_{inv} , where at high frequencies also stray inductance of inverter cabling has to be considered. So in fact different formulas for Z_{mot}, Z_{inv} are needed for exact determination of motor and inverter wave impedance.

Conclusions:
Calculation of wave impedance of motor winding and inverter is rather complicated due to high frequency effects, taking stray capacitance in motor and stray inductance in inverter into account. Nevertheless we conclude that usually the motor wave impedance is significantly bigger and the inverter wave impedance is significantly smaller than the cable wave impedance. This is proven by measurement.

Cable as wave guide between inverter and motor has the **cable wave impedance,** which can be calculated easily for homogeneous cable as

$$Z_{cable} = \sqrt[4]{\frac{R'^2_{cable} + (\omega L'_{cable})^2}{G'^2_{cable} + (\omega C'_{cable})^2}} \approx \sqrt{\frac{L'_{cable}}{C'_{cable}}} \qquad , \qquad (6.1\text{-}5)$$

where we will neglect cable losses (resistance per cable length R'_{cable} per phase and conductance per cable length G'_{cable} of insulator between phases), yielding typical values between 50 and 100 Ohm.

Example 6.1-4:
PVC-insulated cable H05VVF4G1.5: 4 x 1.5 mm^2, (3 phases U, V, W and one PE (potential equalizer) conductor): conductor diameter *d* = 1.4 mm, $q = d^2\pi/4 = 1.5\,\text{mm}^2$, distance

between conductor centres (= conductor diameter + insulation thickness): a = 4.15 mm, average relative permittivity: $\varepsilon_r = 4$. HF current flows on conductor surface, so no inner conductor inductance to be considered.

Cable phase outer inductance per unit length: $L'_{cable} = \frac{\mu_0}{2\pi} \cdot \ln(2a/d) = 0.36\mu\,\mathrm{H/m}$

Cable phase capacitance per unit length: $C'_{cable} = 2\pi \cdot \varepsilon_r \cdot \varepsilon_0 / \ln(2a/d) = 125\,\mathrm{pF/m}$

Cable wave impedance: $Z_{cable} = \sqrt{\frac{L'_{cable}}{C'_{cable}}} = \underline{\underline{53.7}}\,\Omega$ (measured: 83 Ω)

Wave velocity : $v = \frac{1}{\sqrt{L'_{cable} C'_{cable}}} = \underline{\underline{149 \cdot 10^6}}\,\mathrm{m/s}$

The propagation path of the voltage wave is not homogenous at both ends, where impedance changes abruptly, causing wave reflection and wave refraction. Reflected part of wave is thrown back on cable, whereas refracted part of wave penetrates into connected medium with impedance Z. **Reflection coefficient** r between cable and another medium with wave impedance Z is given by ratio of amplitude of reflected wave and incoming wave:

$$\frac{u_{reflected}}{u_{incom}} = r = \frac{Z - Z_{cable}}{Z + Z_{cable}} \quad . \tag{6.1-6}$$

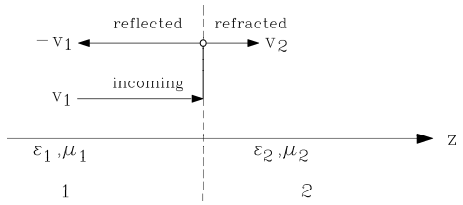

Fig. 6.1-1: Wave reflection and refraction at border between cable (1) and motor (2)

For further simplification we consider motor impedance to be infinite and inverter impedance to be zero. Then we get wave propagation between voltage source (inverter) and open cable end (motor) according to Fig. 6.1-2, yielding reflection coefficient at motor and inverter terminals +1 and –1:

$$r_{mot} = \frac{Z_{mot} - Z_{cable}}{Z_{mot} + Z_{cable}} \quad Z_{mot} \to \infty: \quad r_{mot} = 1 \quad , \tag{6.1-7}$$

$$r_{inv} = \frac{Z_{inv} - Z_{cable}}{Z_{inv} + Z_{cable}} \quad Z_{inv} \to 0: \quad r_{inv} = -1 \quad . \tag{6.1-8}$$

Reflection due to voltage wave propagation between inverter and motor with **cable length** ***l*** is as follows, if. e.g. switching from 0 to $U_d = U$ occurs.
(1): Line-to-line voltage between two cable phases rises from 0 to $U_d = U$ and travels as voltage wave from position ($z = 0$) to end of cable ($z = l$) with **propagation time**

$$t_p = l/v \quad . \tag{6.1-9}$$

There voltage reflection with $r = 1$ happens, causing due to superposition of incoming and reflecting wave for resulting voltage u_{res} a doubling of voltage amplitude $2U$:

$$u_{res}(z = l) = u + u_r = u + r \cdot u = U + r \cdot U = U + U = 2U \tag{6.1-10}$$

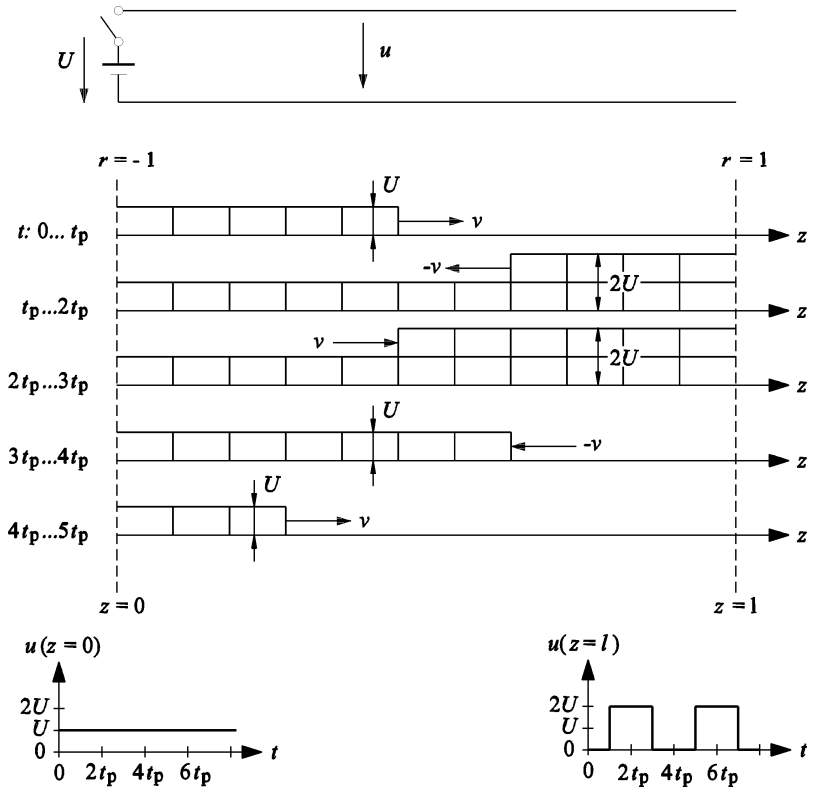

Fig. 6.1-2: Oscillation of voltage at open cable end due to wave reflection at both ends of cable (loss-free cable)
Above: cable with open end, below: voltage wave propagation along cable, bottom: voltage time function at both cable ends

(2): Reflected voltage wave travels back during time t_p towards inverter, while at the open end (motor side) voltage value $2U$ remains constant. Due to inverter internal impedance $Z_{inv} = 0$ at inverter output terminals we get wave reflection r = -1 . Thus reflected voltage inverses from $u_r = U$ to $u_{r,r} = -U$; so voltage at inverter output remains constant:

$$u_{res}(z = 0) = u + u_r + u_{r,r} = u + r_{mot} \cdot u + r_{inv} \cdot u = U + U - U = U \quad . \tag{6.1-11}$$

(3): Reflected wave $-U$ runs again forward to open end of cable (motor side) during time t_p and is reflected there again with $r_{mot} = r = 1$. As reflected wave with amplitude $-U$ wave is travelling back to inverter terminals. At open cable end (motor side) due to this reflection we get voltage $-2U$, which is superimposed on voltage $2U$ from (6.1-10). So resulting voltage at motor side is cancelled to zero: $-2U + 2U = 0$.

$$u_{res}(z = l) = u + u_r + 2U = u + r \cdot u + 2U = -U + r \cdot (-U) + 2U = -2U + 2U = 0 \tag{6.1-12}$$

(4): Voltage wave, travelling back with $-U$ during t_p, is reflected at inverter side with r = -1 from $-U$ to U , leaving resulting voltage at inverter side unchanged at U. Now the whole process starts again with section (1), leading to an oscillation of voltage at motor side with period T and frequency f_d:

$$T = 4t_p = 4 \cdot \frac{l}{v} = 4 \cdot l_c \cdot \sqrt{L_{cable}' C_{cable}'} = 4 \cdot \sqrt{L_{cable}' l_c \cdot C_{cable}' l_c} = 4 \cdot \sqrt{L_{cable} \cdot C_{cable}} \quad (6.1\text{-}13)$$

$$f_d = 1/T = \frac{1}{4\sqrt{L_{cable} C_{cable}}} \quad (6.1\text{-}14)$$

Conclusions:

*Compared with a lumped parameter model per phase of loss-free cable, consisting of one concentrated capacitance C_{cable} and one concentrated inductance L_{cable} per phase with natural frequency $f_d = 1/(2\pi\sqrt{L_{cable} C_{cable}})$, the real behaviour of the cable is that of a wave conductor. So natural frequency is $f_d = 1/(4\sqrt{L_{cable} C_{cable}})$. Motor terminal line-to-line voltage oscillates between $2U_d \ldots 0$, so **voltage overshoo**t is $\hat{U}_{LL,mot}/U_d = 1 + r_{mot} = 2$. This over-voltage leads to increased insulation stress in the motor armature.*

<u>*Example 6.1-5:*</u>

Cable length l_c = 100 m, wave velocity on cable $v = 150 \cdot 10^6$ m/s, dc link voltage 560 V, motor reflection coefficient $r_{mot} = 1$.

Line to line over-voltage at motor terminals: $\hat{U}_{LL,mot} = (1 + r_{mot})U_d = 2 \cdot 560 = \underline{\underline{1120}}\,\text{V}$

Wave propagation time: $t_p = l_c / v = 100/(150 \cdot 10^6) = 0.67\,\mu\text{s}$

Oscillation frequency: $f_d = 1/(4t_p) = \dfrac{1}{4\sqrt{L_{cable} C_{cable}}} = \underline{\underline{375}}\,\text{kHz}$

b) Wave propagation on loss-free motor cable with reflection coefficients $r < |1|$:

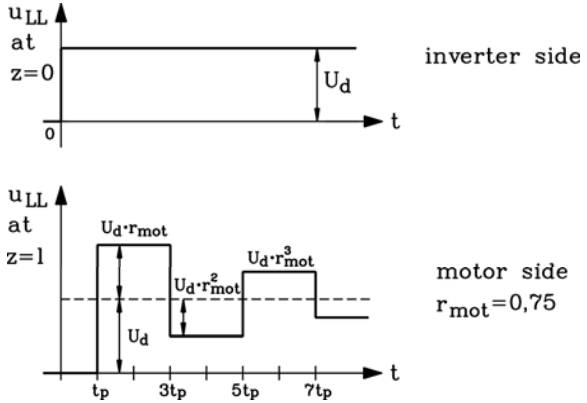

<u>Fig. 6.1-3:</u> Oscillation of voltage at motor side of open cable end due to wave reflection at both ends of cable (loss-free cable) with reflection coefficient 0.75 on motor side and –1 at inverter side. Voltage rise time neglected.

As shown in (6.1-7), (6.1-8) the real motor reflection coefficient is about $r_{mot} = 0.7 \ldots 0.9$, the inverter reflection coefficient is $r_{inv} \cong -0.9$. This influence on oscillation of motor voltage is depicted in Fig. 6.1-3, where it is assumed, that $r_{mot} = 0.75$ and $r_{inv} = -1$. Reflected voltage at motor terminals is $u_r = 0.75U_d$, voltage overshoot is $\hat{U}_{LL,mot}/U_d = 1 + r_{mot} = 1.75$. At inverter reflected voltage is $u_r = -0.75U_d$, being again reflected at motor terminals after time $3t_p$ as $u_r = -0.75 \cdot 0.75 \cdot U_d = -0.56 \cdot U_d$. After reflection at inverter terminals $u_r = -(-0.56 \cdot U_d) = 0.56U_d$, the voltage is reflected at motor terminals after time $5t_p$ as $u_r = 0.75 \cdot 0.75 \cdot 0.75 \cdot U_d = 0.42 \cdot U_d$ and so on. As a result the amplitude of oscillation of terminal voltage with frequency f_d is decreasing to reach finally the value of U_d.

Conclusions:

*With motor reflection coefficient < 1 the **voltage overshoot** $\hat{U}_{LL,mot}/U_d = 1 + r_{mot}$ is a value between 1 and 2, leading to increased insulation stress in the motor armature.*

Wave impedance of motor cables Z_{cable} is more or less independent from rated cable current, which determines conductor cross section to get a rated current density of about 2 ... 3 A/mm^2, depending on cable arrangement and cable cooling. As shown, the wave propagation of E and B occurs in the insulation layer between cable conductors. Thickness of this insulation, which also defines distance between phase conductors, is determined by voltage rating of cable and determines parameters L'_{cable}, C'_{cable}. Therefore for low voltage motors the wave impedance of motor cables for different current ratings is more or less the same.

Motor impedance is determined by $Z_{mot} = \omega\sigma L_s$. With the same voltage rating, but increased motor size (= increased motor power and motor current rating) the number of turns per phase N_s decrease due to stator voltage equation $U_s \cong \omega_s N_s k_{ws} \Phi_s / \sqrt{2}$, as flux per pole increases with motor size according to $\Phi_s = d_{si} \cdot l_{Fe} \cdot B_{\delta s} / p$. Due to $L_s \sim N_s^2$ motor impedance decreases with increased motor size.

Conclusions:

Motor reflection coefficient $r_{mot} = \dfrac{Z_{mot} - Z_{cable}}{Z_{mot} + Z_{cable}}$ is decreasing with increasing motor size, as the ratio $Z_{mot}/Z_{cable} > 1$ for same voltage rating, but increasing motor size is also decreasing. Therefore smaller motors are exposed to higher voltage overshoot than bigger motors and are therefore more endangered.

<u>*Example 6.1-6:*</u>

<u>a) Small 1.1 kW-motor:</u>

- Three-phase four-pole standard induction motor, 400 V, Y, 50 Hz, 1.1 kW, 2.1 A, frame size 90 mm (= shaft height), measured motor wave impedance 5000 Ohm.
- Motor cable 4 x 1.5 mm^2, Type H05VVF4G1.5, (3 phases U, V, W and one PE (potential equalizer) conductor): cable current density: $J = 2.1/1.5 = 1.4$ A/mm^2, wave impedance 83 Ohm.

Motor reflection coefficient: $r_{mot} = \dfrac{5000 - 83}{5000 + 83} = \underline{\underline{0.967}}$

<u>b) Bigger 18.5 kW-motor:</u>

- Three-phase four-pole standard induction motor, 400 V, Y, 50 Hz, 18.5 kW, frame size 180 mm (= shaft height), measured motor wave impedance 570 Ohm.
- Motor cable wave impedance 75 Ohm.

Motor reflection coefficient: $r_{mot} = \dfrac{570-75}{570+75} = \underline{\underline{0.77}}$

In case **of long cable connections** the oscillation frequency decreases with inverse of cable length. Considering cable resistance, which rises linear with cable length, losses along the cable will cause a certain voltage drop, thus decreasing voltage overshoot to certain extent.

Note, that if cable wave impedance is larger than motor impedance, then **no voltage overshoot** will occur, but voltage at motor terminals will steadily rise up to dc link voltage.

$$r_{mot} = \frac{Z_{mot} - Z_{cable}}{Z_{mot} + Z_{cable}} \quad Z_{mot} < Z_{cable} \quad r_{mot} < 0 \tag{6.1-15}$$

c) Critical cable length and slow switching power devices:

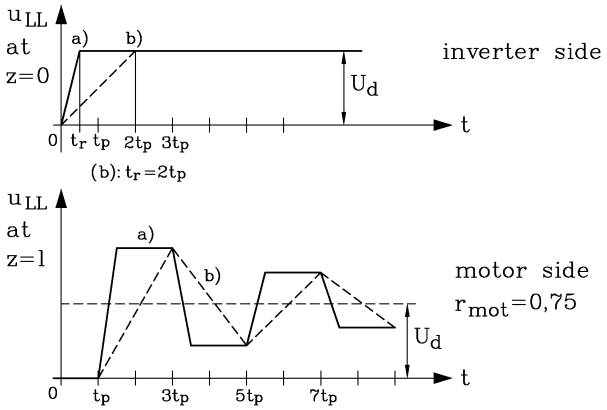

Fig. 6.1-4: Oscillation of voltage at motor side due to wave reflection at both ends of cable (loss-free cable) with reflection coefficient 0.75 on motor side and –1 at inverter side:
a) Voltage rise time $t_r = 0.5t_p$, $t_{rm} = 0.875t_p$, *b)* $t_r = 1.14t_p$, $t_{rm} = 2t_p$.

Considering finite voltage rise time t_r, the voltage rise at inverter output may be assumed as a ramp (Fig. 6.1-4). Thus reflected voltage at motor terminals is also rising according to a ramp. Thus voltage build up – measured between two motor terminals – is given from 0 to $\hat{U}_{LL,mot}$ and takes the time t_r. At the value $t_r = 2t_p$ (Fig. 6.1-4b) the motor voltage overshoot still reaches the value $\hat{U}_{LL,mot} = (1+r_{mot})\cdot U_d$, but if $t_r > 2t_p$, the voltage build up is not finished yet, when already the inverter-side reflected voltage wave comes back with opposite polarity and decreases motor terminal voltage (Fig. 6.1-5). In Fig. 6.1-5 the original voltage signal and its reflected parts are shown in detail to see, how the resulting voltage oscillation at motor terminals comes into being. Maximum over-voltage occurs after 3 propagation times instead after 2. With further increasing rise time the maximum voltage overshoot decreases further down to U_d.

For a given voltage rise time t_r, defined by the inverter, always a so called **"critical cable length"** $l_{c,crit}$ exists, where $t_r = 2t_p$. Longer cables than this length will lead to full voltage

overshoot $\hat{U}_{LL,mot} = (1+r_{mot})\cdot U_d$, as $t_r < 2t_p$, whereas shorter cable will lead to reduced voltage overshoot like in Fig. 6.1-5 due to $t_r > 2t_p$.

$$\boxed{t_r = 2t_p = 2\cdot l_c / v \quad \Rightarrow \quad l_{c,crit} = v\cdot t_r / 2} \tag{6.1-16}$$

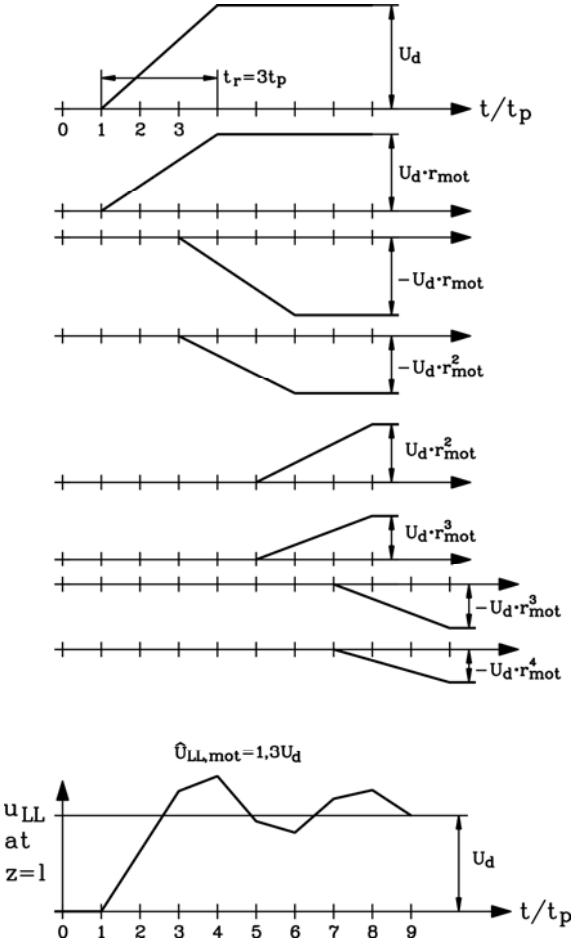

Fig. 6.1-5: Oscillating voltage overshoot at motor side due to wave reflection does not reach its worst-case maximum value $(1 + r_{mot})U_d = 1.75U_d$, but only $1.3U_d$, as $t_{rm} > 2t_p$!
Example: Motor reflection coefficient 0.75, inverter reflection coefficient –1, voltage rise time $t_r = 3t_p$

Example 6.1-7:

Wave velocity in cable $v = 150\cdot 10^6$ m/s
a) IGBT-inverter: $t_r = 200$ ns:
Critical cable length $l_{c,crit} = v\cdot t_r / 2 = 150\cdot 10^6 \cdot 200\cdot 10^{-9} / 2 = \underline{\underline{15}}$ m

b) GTO-inverter: $t_r = 5\ \mu s$:

Critical cable length $l_{c,crit} = v \cdot t_r / 2 = 150 \cdot 10^6 \cdot 5000 \cdot 10^{-9} / 2 = \underline{\underline{375}}\,\text{m}$

For **slow switching devices** like GTO or thyristors with voltage rise time in the range of several μs, this critical cable length is much bigger. That is why only with the advent of fast switching IGBT-inverters the problem of increased voltage stress even to low voltage motors came up, whereas with slow switching bipolar power transistors or GTOs etc. even with long cable connections between motor and inverter no voltage over-stress occurred. Disadvantage of these slow switching devices is of course, that motor speed and torque control is not possible with that dynamic performance. Further increased voltage and harmonic current ripple causes additional motor losses and considerable torque ripple (see Chapter 5).

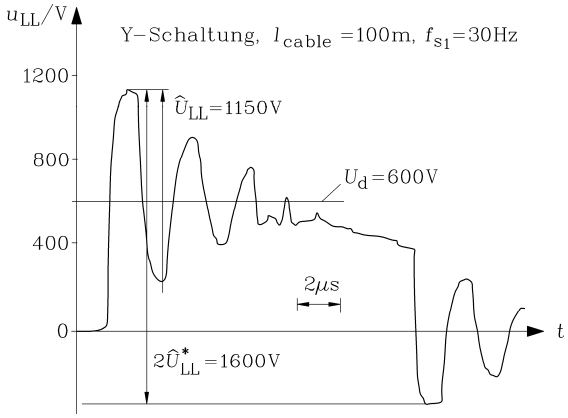

Fig. 6.1-6: Measured oscillating line-to-line voltage overshoot, 2 pole induction motor, frame size 80 mm, 400 V, Y, fed from IGBT-inverter with motor cable 100 m at fundamental frequency f_s = 30 Hz, switching frequency f_T = 8 kHz, 600 V dc link voltage

Example 6.1-8:

2 pole induction motor, frame size 80 mm, 400 V, Y, fed from IGBT-inverter with motor cable 100 m at fundamental frequency f_s = 30 Hz, 600 V dc link voltage (Fig. 6.1-6), PWM, duration of voltage impulse 14 μs. Measured oscillating line-to-line voltage overshoot $\hat{U}_{LL,mot} = (1 + r_{mot}) \cdot U_d = \underline{\underline{1150}}\,\text{V}$ yields motor reflection coefficient $r_{mot} = \underline{\underline{0.92}}$. Measured oscillation frequency $f_d = 1/(4t_p) = 375\,\text{kHz}$ leads to t_p = 666 ns and wave velocity in cable of 150 000 km/s. Voltage rise time t_r = 500 ns is obviously shorter than $2t_p$ = 1330 ns, so **full** voltage reflection occurs.

6.2 HF voltage distribution in armature winding

Motor winding can be regarded as an equivalent circuit per turn, consisting of inductance per turn ΔL, line-to-earth capacitance ΔC_E between conductor and stator iron, defined by the main insulation in slot between winding and iron, and series capacitance ΔC_s between conductors of adjacent turns in slot, spaced by the inter-turn insulation, which in low voltage machines is only the enamel of the copper wire. Due to small conductor surface, but big slot surface,

usually $\Delta C_E >> \Delta C_s$. All turns per phase in series may be therefore regarded as an equivalent circuit as shown in Fig. 6.2-1 a).

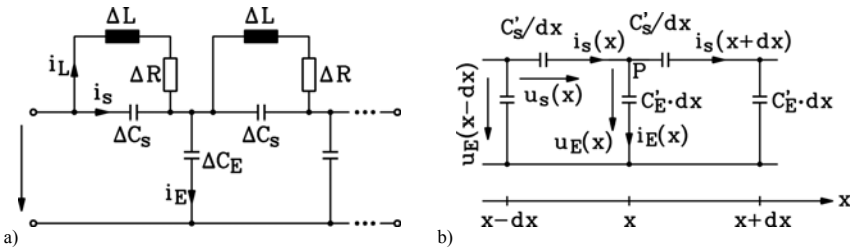

Fig. 6.2-1: a) HF (high frequency) equivalent circuit for armature winding per phase, b) *Kirchhoff*'s laws applied to one element of equivalent circuit

With N_s turns per winding (length of winding per turn is Δx) the **total line-to-earth capacitance** C_E and **total series capacitance per phase** C_s is

$$C_E = N_s \cdot \Delta C_E\,, \qquad C_s = \Delta C_s / N_s \qquad , \tag{6.2-1}$$

and with winding length $l = \Delta x \cdot N_s$ we get

$$C_E = N_s \Delta x \cdot (\Delta C_E / \Delta x) = l \cdot C'_E\,, \qquad C_s = \Delta C_s \cdot \Delta x / (N_s \Delta x) = C'_s / l \tag{6.2-2}$$

or for each turn

$$\Delta C_E = C'_E \cdot \Delta x\,, \qquad \Delta C_s = C'_s / \Delta x \qquad . \tag{6.2-3}$$

Taking infinitesimal winding section dx instead Δx allows solving the problem as differential equation: $dC_E = C'_E \cdot dx$, $dC_s = C'_s / dx$.

Considering e.g. star connected winding, a line-to-line voltage step from 0 to U_d (= rise time is assumed to be zero) between two phases can be regarded in that equivalent circuit as a step of potential of left circuit leg by U_d, whereas right leg is at zero voltage. In between are $2N_s$ turns (= phases). Due to $u_L = \Delta L \cdot di_L / dt$ the current i_L shortly before and after applying this voltage step must be zero, as a step in current would lead to infinite voltage u_L. Thus for calculating **voltage distribution in winding** shortly after applying voltage step, only the capacities need to be considered. We apply *Kirchhoff*'s laws to the equivalent circuit Fig. 6.2-1b for the capacitive currents

$$i_E(x) = C'_E \cdot dx \cdot \frac{du_E(x,t)}{dt}\,, \quad i_s(x) = \frac{C'_s}{dx} \cdot \frac{du_s(x,t)}{dt} \tag{6.2-4}$$

and consider infinitesimal calculus $i(x+dx) = i(x) + \frac{di}{dx} \cdot dx$:

$$i_s(x) = i_s(x+dx) + i_E(x) \quad \Rightarrow \quad 0 = \frac{di_s}{dx} \cdot dx + i_E(x) \tag{6.2-5}$$

$$u_E(x-dx) = u_s(x) + u_E(x) \quad \Rightarrow \quad 0 = \frac{du_E}{dx} \cdot dx + u_s(x) \quad \Rightarrow \quad 0 = \frac{d^2 u_E}{dx^2} \cdot dx + \frac{du_s}{dx} \tag{6.2-6}$$

Combining (6.2-4) and (6.2-5) by eliminating i_E, i_s we get after time integration:

$$0 = \frac{di_s}{dx}\cdot dx + i_E(x) \quad \Rightarrow \quad 0 = \frac{d}{dt}\left(\frac{du_s}{dx}\right)\cdot C'_s + C'_E \cdot dx \cdot \frac{du_E}{dt} \quad \Rightarrow \quad 0 = \frac{du_s}{dx}\cdot C'_s + C'_E \cdot dx \cdot u_E$$

which we combine with (6.2-6), thus finally deriving a **differential equation for u_E** :

$$\frac{d^2u_E(x)}{dx^2} - \frac{C'_E}{C'_s}u_E(x) = 0 \qquad (6.2\text{-}7)$$

Boundary conditions are $u_E(x=0) = U_d$, $u_E(x=l) = 0$, leading to solution of (6.2-7) as

$$\boxed{u_E(x) = U_d \cdot \frac{\sinh(\gamma\cdot(l-x))}{\sinh(\gamma\cdot l)}} \qquad \text{with} \quad \gamma = \sqrt{C'_E / C'_s} \quad \text{unit } [\gamma] = 1/m \quad . \qquad (6.2\text{-}8)$$

Voltage distribution along winding is shown in Fig. 6.2-2a for different values $\gamma\cdot l$, showing the voltage is NOT distributed linear along winding. Only for $\gamma\cdot l \to 0$ we get a linear distribution of voltage along winding, which of course is not realistic, as winding has always line-to-earth capacitance.

Conclusions:

The line-to-earth voltage distribution along the winding is non-linear. Non-linearity increases, if parameter $\gamma = \sqrt{C'_E / C'_s}$ increases, hence if line-to-earth capacity is much bigger than inter-turn capacity.

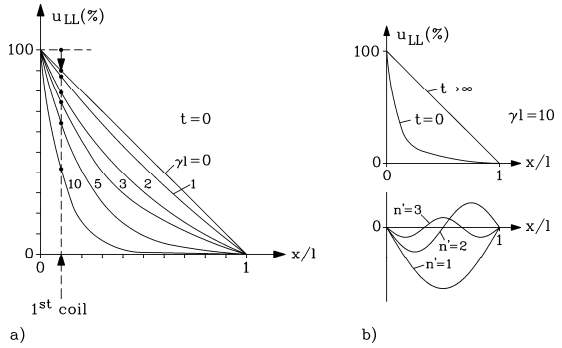

Fig. 6.2-2: Non-linear line-to-earth voltage distribution during voltage step supply of winding (= zero rise time)
a) Voltage distribution shortly after applying the voltage step is only determined by winding capacities
b) Winding inductance, capacitance and resistance per turn cause a voltage oscillation, which starts at non-linear distribution $u_E(x, t = 0)$ and ends at linear distribution $u_E(x, t \to \infty)$ (*Heller-Veverka, VEB-Verlag, 1957*)

Example 6.2-2:

Star connected winding with n = 5 coils per phase, thus $2n$ = 10 coils between line-to-line, $\gamma\cdot l = 8$.

Line-to-earth voltage distribution is calculated with (6.2-8) for U_d = 600 V at the end of each winding. Voltage difference between beginning and end of each coil gives series voltage drop along each turn (Fig. 6.2-2a):

$u_{s,12} = u_{E(1)} - u_{E(2)}$

First coil is stressed with 330/600 = 55% of total voltage instead of only 10% as in case of linear voltage distribution $U_d/(2n)/U_d = 1/(2n)$ = (600/10)/600 = 10% (Table 6.2-1).

x/l	0	0.1	0.2	0.3	0.4	0.5	0.6	0.7	0.8	0.9	1
u_E / V	600	270	121	54	24	11	5	2.2	1	0.4	0
u_s / V	-	330	149	67	30	13	6	2.8	1.2	0.6	0.4
Number of coil		1.	2.	3.	4.	5.	6.	7.	8.	9.	10.

Table 6.2-1: Non-linear voltage distribution in AC winding due to voltage step

Winding inductance ΔL, capacitance ΔC_E, ΔC_s and resistance ΔR per turn cause a damped voltage oscillation, which starts at non-linear distribution $u_E(x, t = 0)$ and ends at linear distribution $u_E(x, t \to \infty)$. Voltage distribution is oscillation with superposition of eigen-modes $n' = 1$, $n' = 2$, $n' = 3$ and so on with decreasing amplitudes per increasing mode ordinal number (Fig. 6.2-2b). For considering non-linear voltage stress the non-linear distribution at $t = 0$ gives full information, so this oscillation is not considered her further.

6.3 Insulation stress of AC winding at inverter supply

In Fig. 6.3-1 measured PWM motor terminal voltage pattern for 400V Y motor with 30 m motor cable is shown between line-to-line, line to earth and voltage drop at first coil per phase. **Line-to-line voltage overshoot** is about +70% due to voltage wave reflection, yielding maximum voltage of $1.7\cdot U_d = 1.7\cdot 600 = 1020$ V. There is no danger of flashover between terminals, as over-voltage test according to IEC34-1 must be for low voltage motors $U_{test,rms} = 2U_N + 1000\,\text{V} = 2\cdot 400 + 1000 = 1800\,\text{V}$, yielding a peak test voltage of $1800\cdot\sqrt{2} = 2545$ V. But voltage overshoot occurs at each voltage step-up and step-down of PWM, thus with pulse frequency $f_p = 2f_T$, which ranges several kHz, yielding a peak-to-peak AC voltage of

$$2\hat{U}^*_{LL} = U_d\cdot(1 + 2r_{mot}) \qquad . \qquad (6.3\text{-}1)$$

In case of Fig. 6.3-1 this is $2\hat{U}^*_{LL} = 600\cdot(1+2\cdot 0.7) = 1440$ V and is in worst case r_{mot} = 1 a value $2\hat{U}^*_{LL} = U_d\cdot(1+2r_{mot}) \cong 3U_d = 1800$ V. The additional oscillation due to wave reflection with f_d about 200 ... 400 kHz depending on cable length is super-imposed to that AC component.

In **winding overhangs** the phases U, V, W are crossing, so at these crossing points the HF AC voltage amplitude $\hat{U}^*_{LL} = 1.5U_d$ (e.g. $\hat{U}^*_{LL} = 1.5\cdot 600 = 900$ V) and the maximum voltage stress $\hat{U}_{LL.mot} = 2U_d$ (e.g. $\hat{U}_{LL.mot} = 2\cdot 600 = 1200$ V) are active. If no additional insulation is put in between the phase windings, only the enamel of the copper wire will act as insulator, which usually is designed for sinus supply $\hat{U}_{LL} = \sqrt{2}\cdot U_N = \sqrt{2}\cdot 400 = 565$ V and 50 Hz. Thus voltage amplitude stress is increased at inverter supply by 50% ... 100% in the phase-to-phase insulation due to:

$$\frac{\hat{U}^*_{LL}}{\hat{U}_N} \cong \frac{1.5U_d}{U_d} = 1.5 \qquad \frac{\hat{U}_{LL,mot}}{\hat{U}_N} \cong \frac{2U_d}{U_d} = 2.0 \qquad . \qquad (6.3\text{-}2)$$

Even worse is the large repetition rate $f_p = 2f_T$, which in comparison to grid supply is increased by typically $f_p / f_N = (2000...8000)/50 = 40...160$ and the high frequency oscillation f_d. Each voltage impulse may cause small spark ignition at weak points between

the phases. These small sparks are called **"partial discharges (PD)"**, as they are too faint to be visible, but repeated very often they will cause erosion of enamel, leading finally to a big flash or phase-to-phase short circuit.

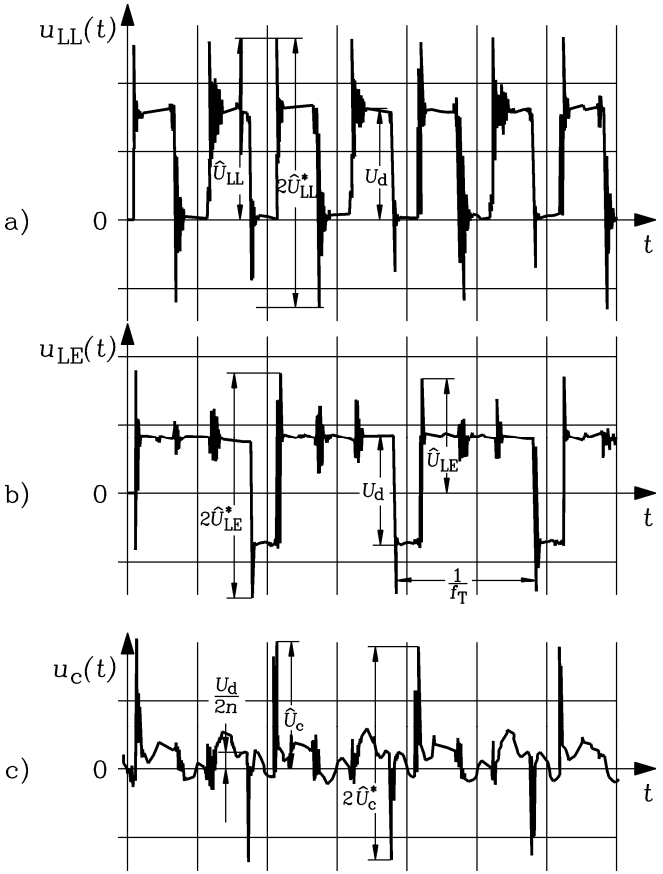

Fig. 6.3-1: Measured motor voltages at PWM IGBT-inverter operation of a 400 V Y-motor at dc link voltage 600 V and 30 m cable length between motor and inverter. a) Line-to-line voltage, b) line to earth voltage, c) voltage drop at first coil per phase (*Hentschel, E. et al. etz 114*)

Therefore only additional phase-to-phase insulation layers (inter-phase lining), which are strong enough to withstand the above noted voltage stress, can avoid partial discharges. Thus inverter-operated motors have to get an improved winding insulation, which is tested during manufacturing by the **"partial discharge test"** (Fig. 6.3-2). In the example of Fig. 6.3-2 a small synchronous reluctance motor was manufactured with – by accident - displaced inter-phase lining between phases U and V. With increasing line-to-line test voltage at 740 V (corresponding with amplitude $\sqrt{2}\cdot 740 = 1045$ V) the partial discharges began to occur at 20°C, thus the **partial inception (PD) voltage** is 740 V for this motor. This is too low for safe operation at increased temperature, as PD voltage decreases with increasing winding

temperature by about 4 V/K. Thus a Thermal Class F motor with about 150°C winding temperature needs at 20°C a PD inception voltage (r.m.s.) of about $U_{pd} = 1200$ V to be safe at 150°C.

$$20°C: U_{pd} = 1200V, \hat{U}_{pd} = 1700V \Rightarrow 150°C: U_{pd} = 1700 - 4\cdot(150-20) = 1180V \approx 2\hat{U}_{LL,mot}$$

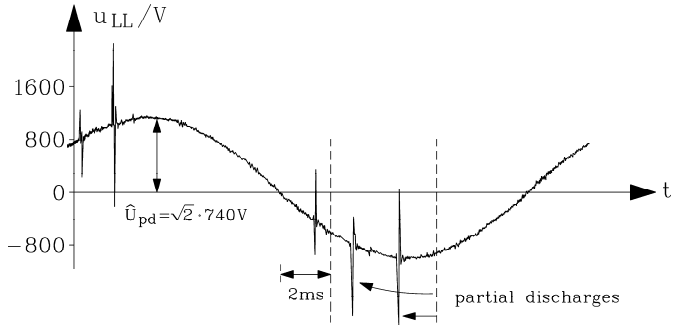

Fig. 6.3-2: Partial discharge test of stator winding of a 2-pole 400V Y, 50 Hz, synchronous reluctance motor at 20°C. A sinus 50 Hz line-to-line voltage with variable amplitude between the non-connected phases U, V, W is applied. In case of partial discharges the spark discharge currents flow as HF spikes from one phase to the other. Via a HF capacitor this current flow may be detected and is made visible as additional HF voltage, superimposed on testing voltage (*Siemens AG*).

Line-to-earth voltage stress is lower, as can be seen from Fig. 6.3-1b. Potential of each winding changes with the same AC amplitude $\hat{U}^*_{LE} = U_d/2 + r_{mot}U_d$, (e.g. at 400V-motors 900 V) like line-to-line voltage, but maximum voltage is also only $\hat{U}_{LE,mot} = U_d/2 + r_{mot}U_d$ (e.g. 900 V), which is lower than line-to-line value 1200 V. Further AC frequency is only switching frequency f_T and not pulse frequency $2f_T$.

Voltage stress of first coil is critical, if the rise time is really short (< 1 μs), as then the calculation for $t_r = 0$ in Chapter 6.2 is valid. Enforced inter-turn insulation is necessary to cope with this increased voltage stress especially for first coil per phase. In Fig. 6.3-1c the voltage peak of first coil $\hat{U}_c$ at each pulse switching instant is visible, which then is damped down to linear voltage distribution $U_d/(2n)$. Measured voltage overload in that Fig. 6.3-1c is about $\hat{U}_c/(U_d/(2n)) = 8$, so in case of $2n = 10$ first coil bears 80% of dc link voltage.

Conclusions:
At fast-switching IGBT-inverter supply low voltage AC winding insulation of AC motors is stressed with additional voltage due to voltage reflection at motor terminals and due to non-linear voltage distribution in AC winding. Therefore improved winding insulation is necessary to increase partial discharge inception voltage up to 1200 V r.m.s. at 20°C, which is sufficient for 400 V-inverter operation.

6.4 System design of inverter drives coping with big du/dt

a) Increased voltage stress of motor winding:
Apart from improving motor insulation often additional filter combination at the inverter output are used. Such **du/dt-filters** consist of chokes and small capacities to increase voltage

rise time. Thus the inverter is still fast switching, but the motor terminal voltage has an increased voltage rise time, which may decrease voltage overshoot and non-linear voltage distribution in motor winding. Moreover, high frequency voltage components on motor cable, which may cause **electromagnetic interference (EMI)** in adjacent cabling, are reduced. Best results are achieved with **sine wave filters**, which is an L-C combination with resonance frequency $f_0 = 1/(2\pi\sqrt{LC})$ lying between fundamental frequency f_s and high frequency components f_{sk} of inverter output voltage. This low-pass filter reduces high frequency voltage harmonics, so that inverter line-to-line voltage is more or less sinusoidal, but these filters are expensive.

b) Capacitive motor cable currents:
Due to high switching frequency f_T and the short voltage rise time t_r the motor cable capacitance C_{cable} causes big current spikes

$$i_C = C_{cable} \cdot \frac{du}{dt} \approx C_{cable} \cdot \frac{U_d}{t_r} \quad . \qquad (6.4\text{-}1)$$

Especially with long cables $C_{cable} = C'_{cable} \cdot l_c$ capacity and therefore current spikes are big. Thus inverter current limit may be reached even at motor no-load. By using **inverter output chokes**, which are used especially at long cable above 30 ... 50 m, these current spikes are reduced, so that no over-sizing of inverter is necessary.

c) Motor bearing currents:

c1) Bearing currents at sinusoidal voltage supply:
In case of **magnetic asymmetries** in line-fed motors under sinusoidal supply a shaft voltage may be induced with line frequency, multiples of it or slot frequency (Fig. 6.4-1). If this voltage surpasses about 0.7 V (peak), the insulating lubricant film is punctured and electric bearing currents may occur, which can damage the bearing races **("fluting")**, thus leading to increased bearing noise and finally to bearing failure. Critical bearing current densities lie above 0.1 ... 0.3 A/mm^2. Especially big motors above frame size 500 mm and then especially two-pole motors, where the flux per pole is biggest (hence also the parasitic ring-flux $\Delta\Phi$ due to magnetic asymmetries), are sensitive to bearing currents, caused by magnetic asymmetries. As the shaft voltage causes a bearing voltage drop at both bearings with opposite sign, the bearing current flows as **LF circulating current** from bearing via stator housing to the other bearing and the shaft. By insulating one bearing this kind of bearing current is interrupted.

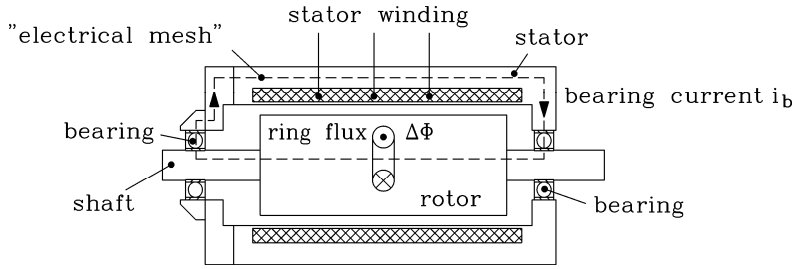

Fig. 6.4-1: Induction of an AC voltage by a magnetic AC ring flux $\Delta\Phi$. This voltage occurs as shaft voltage between the two shaft ends. This shaft voltage may cause – especially in big two-pole machines – a harmful circulating bearing current i_b.

c2) Bearing currents at inverter supply:
In addition to the effect of magnetic asymmetries, additional high-frequency bearing currents may occur at inverter supply at already much smaller motors. Under **inverter supply** the stray capacitance of the lubricant film of the bearing – in addition with the winding line-to-earth capacitance and the capacitance of the air gap between stator and rotor – acts as a capacitive voltage divider. The **"common mode voltage" u_0** as the average line-to-earth potential difference of the stator winding

$$u_0(t) = \frac{u_{UE}(t) + u_{VE}(t) + u_{WE}(t)}{3} = \frac{\varphi_U(t) + \varphi_V(t) + \varphi_W(t)}{3} - \varphi_E(t) \qquad (6.4\text{-}2)$$

changes polarity due to inverter switching with switching frequency, so very often, and with IGBT voltage rise-time, so very fast (Fig. 6.4-2) ($u_{UE}(t) = \varphi_U(t) - \varphi_E(t)$, $u_{VE}(t) = \varphi_V(t) - \varphi_E(t)$, $u_{WE}(t) = \varphi_W(t) - \varphi_E(t)$). Note that at sinusoidal symmetrical voltage supply with 120° phase shift between the phase voltages the common voltage is zero, as the star potential φ_Y is then equal to zero, so identical with earth potential $\varphi_0 = 0$.

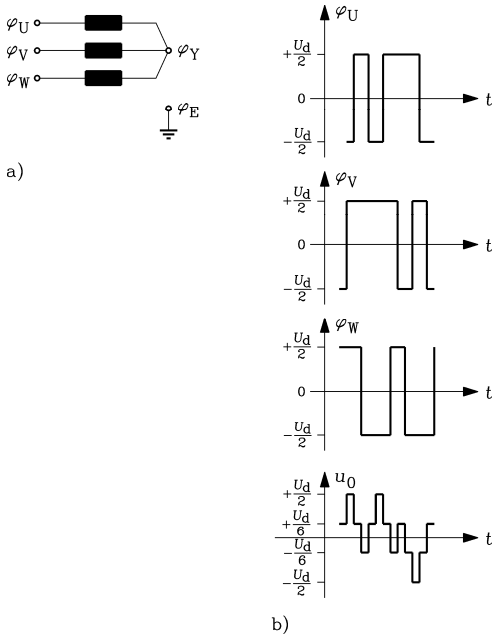

Fig. 6.4-2: Generation of common mode voltage of stator winding at inverter supply as average line-to-earth potential of the winding:
a) Star-connected three-phase stator winding with electrical potential at terminals, at star-point and earth-potential.
b) At two-level PWM inverters the common mode voltage has values $+U_d/2$, $+U_d/6$, $-U_d/6$, $-U_d/2$.

Due to the fast change rate of the common mode voltage at each switching instant the parasitic capacities of the electric motor are loaded and unloaded with a capacitive current:

The already discussed big line-to-earth capacity of the winding via the main insulation in the slots to the housing $C_E = C_{wh}$ (Fig. 6.2-1) in the range of several hundreds of nF causes a HF line-to-earth capacitive current i_E. The much smaller parasitic capacities (several pF) between winding and rotor iron C_{wr}, between rotor iron and stator housing C_{rh} and in parallel from rotor iron via the bearings (bearing capacity C_b) to the earthed housing cause very small, negligible capacitive currents, but give rise to considerable HF bearing voltage u_b via the voltage divider (Fig. 6.4-3) (**„bearing voltage ratio BVR“**):

$$BVR = \frac{u_b}{u_0} = \frac{C_{wr}}{C_{wr} + C_{rh} + 2C_b} \qquad (6.4\text{-}3)$$

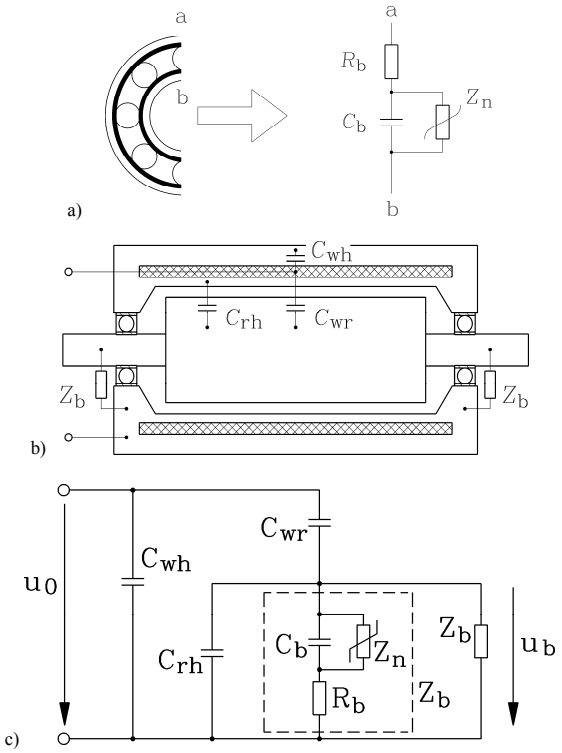

Fig. 6.4-3: Parasitic capacities in electric machines, loaded via the common mode voltage of inverter:
a) Electrical equivalent circuit of a ball bearing at HF-voltage stress. The non-linear impedance Z_n is zero, if the lubricant film is punctured either by electrical break-down or by the balls at low speed n < 100/min, and is roughly infinite at intact insulating lubricant film at elevated speed.
b) Parasitic capacities between stator winding w, rotor iron r, stator housing h,
c) Capacitive voltage divider (equivalent circuit) for arrangement b). The impedances Z_b of both bearings are acting electrically in parallel and consist acc. to a) each of the elements C_b, R_b, Z_n.

At the bearings and intact lubricant film with a typical BVR = 3 % … 10 % a bearing voltage of $u_{b,max} = BVR \cdot u_{0,max} = BVR \cdot (U_d/2) \approx 0.1 \cdot (600/2) = 30\,\text{V}$ may occur. Due to this high voltage the insulting lubricant film breaks suddenly down electrically, causing electric

discharge bearing currents $i_{b,HF}$. So due to this puncture of lubricant film harmful bearing current spikes occur with the same harmful results as at line operation bearing currents – again fluting of the baring races will lead to mechanical failure of the bearings. This effect due to discharge bearing current is called electric discharge machining (EDM) of the bearing races. The discharge bearing currents occur at both bearings with same polarity **(common-mode HF bearing current)**, so insulating the bearing might not interrupt them. Special **common mode filters** at the inverter output – which reduce u_0 to harmless small values – are needed to avoid a bearing voltage build up. Another possibility is the use of **ceramic bearings**, which reduces the electric field strength in the lubricant film even at 30 V bearing voltage, thus avoiding film discharge.

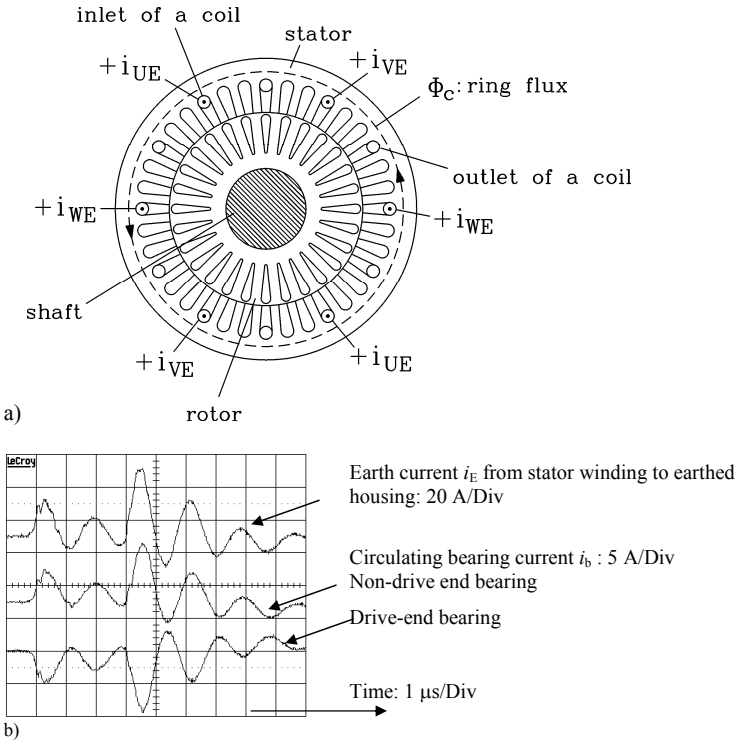

Fig. 6.4-4:
a) Generation of a HF ring-flux Φ_c, excited by the stator winding line-to-earth HF current i_E (Example: Four-pole cage induction machine: The earth current i_E – flowing from the inverter to the machine - enters the winding phases at the terminals, but does not leave at the coil ends back to the inverter, but flows via the slot insulation to the stator housing. Si in machine cross section only one current direction is active, causing via *Ampere´s* law a ring flux).
b) Measurement of circulating bearing current at no-load of an inverter fed standard cage induction motor (Frame size 400 mm, two pole, rated power 500 kW) at fundamental frequency f_s = 50 Hz, 3000/min; bearing temperature 70 °C (*Siemens AG*)

In addition to this common-mode HF bearing currents also HF circulating bearing currents may occur at inverter supply (**differential mode HF bearing currents**). The reason for this is the following: At bigger motors the capacitive winding line-to-earth current i_E is big enough

to excite an additional parasitic magnetic flux (Fig. 6.4-4a), which may induce an additional rotor shaft voltage like in the case of magnetic asymmetries, causing a **HF circular bearing current flow** (Fig. 6.4-4b**)**.
This kind of current usually is even more harmful than the discharge bearing currents, as its amplitude is bigger, especially at low speed, where the thickness of lubricant film is small or even punctured by the balls. This circulating HF bearing current may be interrupted effectively by insulating one bearing.

6.5 Combined inverter-motors

a) Basic idea of inverter integration:
By integrating the inverter into the enlarged terminal box of the motor on gets a combined inverter-motor (Fig. 6.5-1). Thus motor and inverter are a compact unity, avoiding the long cable between motor and inverter. This motor is operated below critical cable length and voltage overshoot at motor terminals is negligible. Further, EMI problems due to HF voltage on motor cable are avoided, too.

b) Design considerations and applications:
In order to get the inverter into the motor terminal box, usually dc link capacitor has to be reduced in size. Thus dc link voltage is not smoothened very well, causing a considerable voltage and current ripple due to line-side harmonics.

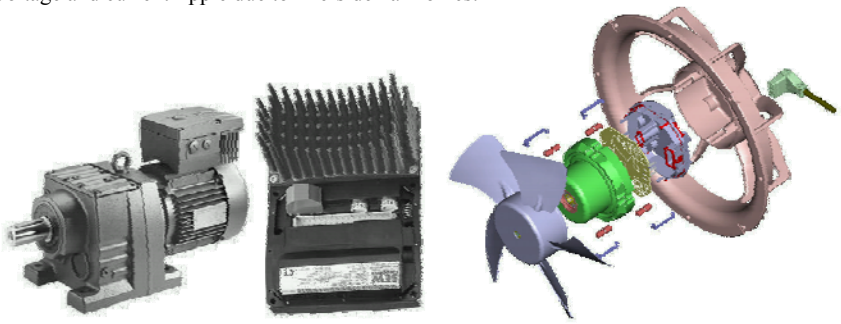

a) b)

Fig. 6.5-1: Combined inverter-motors a) left: 3 kW / 1500/min standard induction motor with gear box to increase torque and inverter integrated in terminal box of motor, right: integrated inverter bottom side with cooling fins for the IGBT power transistors (*SEWeurodrive, Bruchsal*), b) small (< 100 W) PM brushless dc synchronous motor with integrated inverter as fan drive for application in computers (*ebm Papst*)

Motor size is determined by **torque**, whereas inverter size is determined by **power**. So low speed, high torque motors are big in size, but power is small to moderate. Thus it is easy to integrate rather small inverter into big motor. For example, **low speed** PM synchronous drives in submarines, powered by fuel-cells, offer enough space within the hollow rotor bell to house the feeding inverter.
With **high speed motors** usually it is not possible to integrate inverter into motor, as power is big, but motor is small.
Medium speed motors such as 1000 ... 1500/min ... 3000/min allow inverter integration up to about 7.5 kW. At bigger power ratings dc link capacitor, power module and cooling plate of inverter are too big to be integrated easily. Thus combined inverter-motors in that speed range of 2- to 6-pole induction motors with frequency up to about 100 Hz are available on the

market with rated power between several Watt (as fan blowers in computer and other electronics) and about 7.5 kW. In that power range many drives are used as variable speed pump drives in warm water heating, drives for conveyor belts, automation of production lines e.g. transfer lines in automobile production etc.

Combined inverter-motors are most often automatically operated by remote control. Drive communication is done via the digital communication protocol of modern bus systems.

c) Pros and Cons of Combined-inverter motors:
Advantages:
- Cost reduction: No additional inverter-motor cabling, no extra purchasing of motor and inverter, motor and inverter combination already optimized by manufacturer
- No or small EMI problems

Disadvantages:
- Power electronics are exposed to motor vibration and motor heat, so high quality elements must be used, which are more expensive,
- Volume and heat at the load is increased by inverter volume and inverter losses,
- Mean time between failure (MTBF) of inverter is lower than of motor, so in case of repair one must more often have access directly to the working machine, where the combined inverter-motor is mounted
- Combined inverter-motors usually are not suited for open air operation, as electronics are sensitive to large temperature changes, humidity, salt, etc.

7. Mechanical motor design

Mechanical motor design is as vital as the electromagnetic motor design to build good motors. This comprises questions concerning the
- rotor balancing,
- motor bearing systems,
- cooling and heat transfer,
- mechanical stress of motor parts and their vibration behaviour,
- constructive design of motor parts with respect to insulation co-ordination of electric parts.

7.1 Rotor balancing

The rotating rotor body is usually not an ideal mechanical system with the centre of gravity located on the rotational axis, but under real conditions centre of gravity is dislocated from rotational axis by a certain displacement e_S. Thus **centrifugal force** F of rotor mass m_r

$$F = m_r \cdot e_S \cdot \Omega_m^2 \qquad (7.1\text{-}1)$$

at rotational angular frequency

$$\Omega_m = 2\pi \cdot n \quad , \quad n\text{: rotational speed} \qquad (7.1\text{-}2)$$

will occur as radial force in direction of dislocation of centre of gravity from rotor axis, trying to bend the elastic rotor and acting as additional forces at the rotor bearings. As direction of this force rotates with rotational speed, it may excite mechanical vibrations of the whole motor with frequency $f = n$, which – when hitting natural vibration frequency of motor system – causes resonance with increased vibration amplitude. So, **imbalance** may lead to
- increased bearing stress,
- additional rotor loading and
- increased machine vibrations.

In order to quantify imbalance, usually the real system with elastic rotor and elastic bearings is modelled by step-wise by **idealized models**. All effects of rotor vibration are included in the **theory of rotor dynamics**, which is a mathematical discipline of theoretical mechanics.

rotor model	*rotor*	*bearings*
rigid rotor model	rotor body shows no deformation under force load (= geometry does not change shape under force load)	rigid bearings show no deformation under force load
elastic rotor model	rotor body is deformed under force load (= *Young´*s modulus of elasticity E of rotor material is not infinite)	rigid bearings
elastic bearing model	elastic rotor body	bearing geometry is deformed under force load (deformation is ruled by *Young´*s modulus of elasticity E of bearing material and end shields)

Table 7.1-1: Different mathematical models for rotor system (= rotor body and bearings)

Elastic rotor is bending under radial force load, thus acting like a spring with a natural bending frequency f_{b1}. If exciting frequency $f = n$ stays below 70% of f_{b1}, no resonance effect will occur and rotor bending deformation will usually be small, and therefore is neglected. Thus with **maximum speed n_{max} below** $0.7 \cdot f_{b1}$, usually the rigid rotor model is used for calculation of mechanical vibration. Please note, that in addition to mechanical imbalance also

"unbalanced magnetic pull" may be active, which in case of 2-pole machines with eccentric rotor, as explained in Chapter 5, may excite radial forces with $f = 2n$. Then of course limit for rigid rotor model is $n_{max} \le 0.35 \cdot f_{b1}$.

Calculation of rotor dynamics and technique of balancing rotors is today fine art, which is taught in special lectures. International standardization ISO1925, ISO1940 and ISO5460 and the national *German* guide line "VDI-Richtlinie 2060" apply. Here, only the basics will be given in short to get an overview.

7.1.1 Imbalance of rigid rotor bodies

a) Disc rotor:
We assume the rotor body to be rigid as well as the bearings. Thermal influence on rotor, which leads e.g. also to axial rotor expansion (*z*-direction in Fig. 7.1.1-1), which may be different from thermal expansion of stator housing, is coped with one of the two bearings being a loose bearing. That means, that the rotor and this bearing may move in axial direction (usually axial movement is well below 1 mm) under expansion, whereas the other bearing is fixed in axial direction. The most simple model is a **disc-like rotor** (thickness l_{Fe} much smaller than diameter d_{ra} and bearing distance L) with rotor mass m_r, mounted on an infinite stiff, but very thin shaft (shaft length between bearing is bearing distance L) (Fig. 7.1.1-1). For simplification we assume disc to be centred between the bearings.

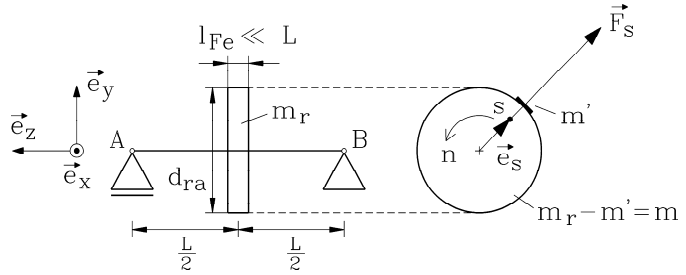

Fig. 7.1.1-1: Rigid body disc rotor on stiff shaft with centre of gravity S dislocated from rotational axis by distance e_S (left: loose bearing A, right: fixed bearing B).

Dislocation e_S of centre of gravity S from rotational axis, which is centred at geometrical centre of disc, is e.g. given by an additional mass m' at radius $d_{ra}/2$, whereas the mass $m_r - m'$ is evenly distributed on the disc. Thus centre of gravity of mass $m_r - m'$ is located on rotational axis. At standstill gravity will drag additional mass m' down right below rotational axis, thus turning the disc in that position, so one can recognize the imbalance also at standstill, hence calling it **static imbalance**. The maximum torque exerted by gravity on the disc at stand still occurs at disc position where additional mass is in horizontal plane:

$$M = m' \cdot g \cdot d_{ra}/2 = m_r \cdot g \cdot e_S \qquad \Rightarrow \quad e_S = (m'/m_r) \cdot (d_{ra}/2) \qquad (7.1.1\text{-}1)$$

Denoting the displacement as a vector, directed from centre of rotation to centre of gravity, we get under rotation the radial centrifugal force vector, which defines the **static imbalance vector** $\vec{U}_S$, which is NOT a force:

$$\vec{F}_S = m_r \cdot \vec{e}_S \cdot \Omega_m^2 \quad \Rightarrow \quad \vec{U}_S = \frac{\vec{F}_S}{\Omega_m^2} = m_r \cdot \vec{e}_S \qquad (7.1.1\text{-}2)$$

Conclusions:
Static imbalance U_S is the proportional coefficient between square of angular mechanical frequency and centrifugal force. It is independent of speed.

Example 7.1.1-1:
Rotor mass m_r = 60 kg, rotor outer diameter d_{ra} = 200 mm, m' = 2 g,

$e_S = (m'/m_r) \cdot (d_{ra}/2) = (2/60000) \cdot (0.2/2) = \underline{3.33}\mu\,\text{m}$

$U_S = m_r \cdot e_S = 60 \cdot 3.33 \cdot 10^{-6} = \underline{200}\,\text{g·mm}$

Centrifugal force at n = 2000/min:

$F_S = m_r \cdot e_S \cdot \Omega_m^2 = 60 \cdot 3.33 \cdot 10^{-6} \cdot (2\pi \cdot 2000/60)^2 = \underline{8.8}\,\text{N}$

Note: Gravity force of rotor is $m_r \cdot g = 60 \cdot 9.81 = 589$ N. Already at a small displacement of centre of gravity by 3.3 μm, a centrifugal force of 8.8/589 = 1.5% of rotor gravity force occurs at 2000/min. At 4000/min centrifugal force is already 6% of gravity force. As already such small displacements e_S cause considerable centrifugal forces, it is easily understood, that it is practically impossible to build rotors with no imbalance. A balancing process is always necessary.

The rotating force $\vec{F}_S = F_S \cdot \vec{e}_x \cdot \cos(\Omega_m t) + F_S \cdot \vec{e}_y \cdot \sin(\Omega_m t)$ may be decomposed into an *x*- and *y*-component according to Fig. 7.1.1-1. As disc is centred between bearings, the load bearing forces in A and B are identical due to symmetry: In vertical direction (*y*-direction) gravity load and imbalance load occur, whereas in horizontal direction (*x*-direction) only imbalance is acting.

$$\vec{F}_{A,x} = \vec{F}_{B,x} = F_S/2 \cdot \cos(\Omega_m t)$$
$$\vec{F}_{A,y} = \vec{F}_{B,y} = m_r \cdot g/2 + F_S/2 \cdot \sin(\Omega_m t) \qquad (7.1.1\text{-}3)$$

$$\vec{F}_{A,x\sim} = \vec{F}_{B,x\sim} = U_S \cdot \Omega_m^2/2 \cdot \cos(\Omega_m t)$$
$$\vec{F}_{A,y\sim} = \vec{F}_{B,y\sim} = U_S \cdot \Omega_m^2/2 \cdot \sin(\Omega_m t) \qquad (7.1.1\text{-}4)$$

Conclusions:
Due to static imbalance an additional oscillating bearing force occurs. With the square of increasing speed this oscillating component of the bearing load increases due to static imbalance, with oscillation frequency being rotational frequency. In both bearings this additional bearing force is IN PHASE (common mode force).

b) Finite length rotor:
Due to rotor iron stack length l_{Fe} electric motor rotors are usually not disc-like (Fig. 7.1.1-2). Let us assume an ideal cylindrical rotor with cylinder length l_{Fe}, being placed centred between bearings A and B. Ideal cylinder has its centre of gravity on cylinder axis, which is here also rotational axis. If two additional masses m'' are placed on the cylinder ends in opposite radial position at cylinder circumference, they will not shift centre of gravity from rotational axis. So at stand still rotor will NOT move under gravitational force. But if rotor is rotating, on each of the two masses a centrifugal force F'' with opposite direction will occur

$$F'' = m'' \cdot (d_{ra}/2) \cdot \Omega_m^2 \quad , \qquad (7.1.1\text{-}5)$$

resulting due to this force pair in an additional torque

$$M'' = m'' \cdot (d_{ra}/2) \cdot \Omega_m^2 \cdot l_{Fe} \quad \Rightarrow \quad M_U = \frac{M''}{\Omega_m^2} = \frac{m'' \cdot d_{ra} \cdot l_{Fe}}{2} \quad . \qquad (7.1.1\text{-}6)$$

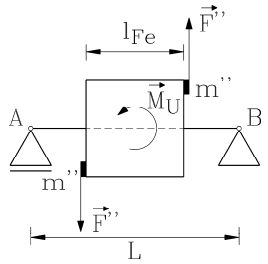

Fig. 7.1.1-2: Rigid body cylindrical rotor with centre of gravity *S* located on rotational axis, but uneven distributed mass along rotor axis, represented here by two masses *m*" , which lead to imbalance torque *M*", when rotor is rotating.

As the effect of this mass arrangement is only active at rotor rotation, whereas at stand still no effect is visible, we call this a **dynamic imbalance** M_U, which is defined as torque per square of rotational angular frequency. Note, that no total centrifugal force occurs, as the two force components are opposite, cancelling each other: $F_S = F'' - F'' = 0$. The additional torque M'' leads to reaction forces ΔF in the two bearings as a force pair with opposite direction of ΔF in the two bearings, which counter-balance this torque:

$$M'' = F'' \cdot l_{Fe} = \Delta F \cdot L \qquad \Rightarrow \Delta F = (l_{Fe}/L) \cdot F'' \qquad (7.1.1\text{-}7)$$

$$\vec{F}_{A,x\sim} = -\vec{F}_{B,x\sim} = (M_U/L) \cdot \Omega_m^2 \cdot \cos(\Omega_m t)$$
$$\vec{F}_{A,y\sim} = -\vec{F}_{B,y\sim} = (M_U/L) \cdot \Omega_m^2 \cdot \sin(\Omega_m t) \qquad (7.1.1\text{-}8)$$

Conclusions:
Dynamic imbalance M_U is the proportional coefficient between square of angular mechanical frequency and imbalance torque. It is independent of speed. It leads to additional oscillating bearing forces with opposite sign in both bearings (= 180° phase shift = differential mode force), again with oscillation frequency equal to rotational speed.

In real rotors both effects, static imbalance due to dislocation of centre of gravity from rotational axis, and dynamic imbalance due to uneven mass distribution along rotor axis, occur. Thus bearing oscillating force are containing a **common-mode component** due to static imbalance and a **differential mode component** due to dynamic imbalance.

In Fig. 7.1.1-3 examples for imbalance are given:
a) Disc rotor with static imbalance: The centre of gravity *S* turns at standstill beneath rotational axis under the influence of gravity. Thus effect of static imbalance can be experienced already at stand still (at static conditions).

b) Dynamic imbalance if disc rotor: Inertia axis of disc rotor (which is geometric of disc, if disc mass is homogenous distributed) is not aligned with rotor axis. Thus centre of gravity of upper and lower half disc is displaced axially by Δz. Under rotation, the centrifugal forces F'' lead to imbalance torque $M'' = F'' \cdot \Delta z$.

c) Superposition of static and dynamic imbalance: A cylindrical rotor with inertia axis unaligned with rotational axis in that way, that also the centre of gravity *S*, located on inertia axis, is dislocated from rotational axis.

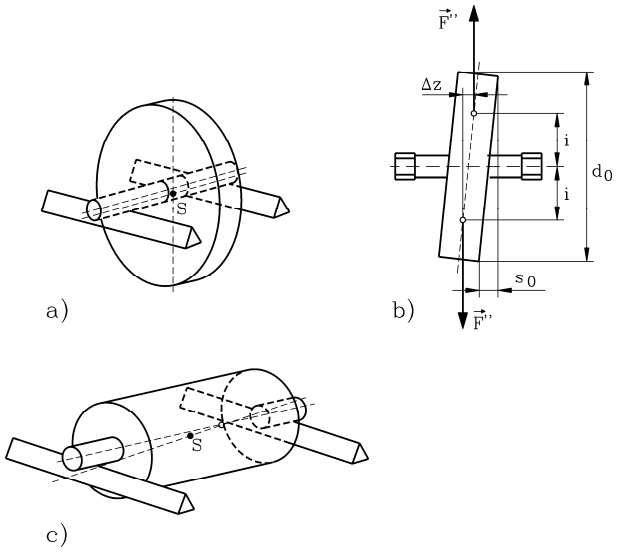

Fig. 7.1.1-3: Examples for rigid body imbalance: a) static imbalance, b) dynamic imbalance, c) static and dynamic imbalance

If we decompose the cylindrical rotor of Fig. 7.1.1-3c by thought into cylindrical thin disc slices ($l_{Fe,disc} \to 0$), each of these rotor discs will be thin enough to produce no imbalance torque ($M''_{disc} \sim l_{Fe,disc} \to 0$). Each disc has therefore only static imbalance of different amplitude and direction. In Fig. 7.1.1-4 this is shown for example for rotor decomposed in 3 disc slices. The static imbalance e.g. of disc 3 U_3 leads to centrifugal force F_{S3} at speed *n*. When disc 3 is placed at co-ordinate z_3, we get the reaction forces in the bearings A = L (left) and B = R (right):

force equilibrium: $F_{S3} = F_{L3} + F_{R3}$, torque equilibrium: $M_{S3} = F_{S3} \cdot z_3 = F_{R3} \cdot L$, yielding to

$$F_{L3} = F_{S3} \cdot \frac{L - z_3}{L}, \quad F_{R3} = F_{S3} \cdot \frac{z_3}{L} \qquad . \qquad (7.1.1\text{-}9)$$

Superposition of $\vec{F}_L = \vec{F}_{L1} + \vec{F}_{L2} + \vec{F}_{L3}$, $\vec{F}_R = \vec{F}_{R1} + \vec{F}_{R2} + \vec{F}_{R3}$ leads to resulting bearing forces $\vec{F}_L, \vec{F}_R$, corresponding with $\vec{U}_L = \vec{F}_L / \Omega_m^2, \vec{U}_R = \vec{F}_R / \Omega_m^2$ in Fig. 7.1.1-4. Bearing forces and corresponding imbalance may ALWAYS be decomposed in **common mode** (S: *symmetrical*, resultant static component) and **differential mode component** (A: *anti-symmetrical*, resultant dynamic component).

$$\vec{F}_L = \vec{F}_S + \vec{F}_A, \quad \vec{F}_R = \vec{F}_S - \vec{F}_A \quad \Rightarrow \quad \vec{F}_S = (\vec{F}_S + \vec{F}_S)/2, \quad \vec{F}_A = (\vec{F}_L - \vec{F}_R)/2 \qquad (7.1.1\text{-}10)$$

Conclusions:
In general case additional bearing force in left and right bearing are not directed in the same direction, but in arbitrary one. Nevertheless each bearing force may always be written as a sum of common and a differential mode component. This each rigid rotor imbalance is given as a superposition of a total static and dynamic imbalance.

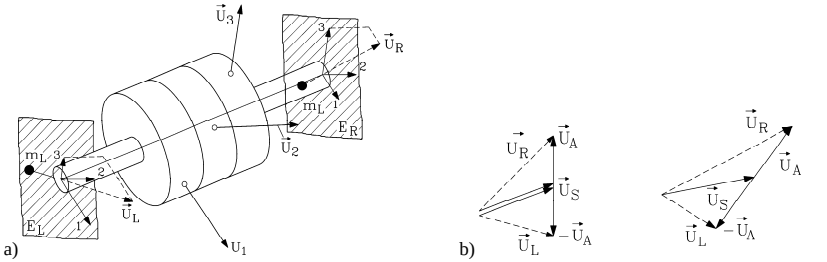

Fig. 7.1.1-4: a) A cylindrical rotor with static and dynamic imbalance is decomposed into three disc slices. For each disc slice the dynamic imbalance may be neglected. So the total imbalance is given by the sum of the static imbalances of each disc. Its components in the bearing planes (L: left, R: right) are summed up as vectors for total bearing reaction. b) The bearing reaction imbalance may be decomposed into a static and dynamic component by taking common mode (symmetrical: S) and differential mode (anti-symmetrical: A) component. This decomposition is always possible for any arbitrary imbalance component in the R and L bearing plane.

7.1.2 Balancing equation for rigid rotor bodies

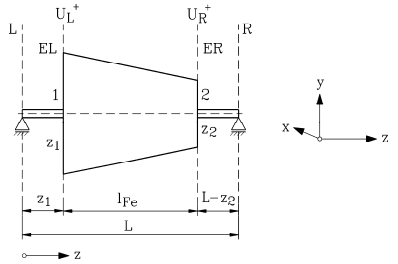

Fig. 7.1.2-1: Balancing of rotor with static and dynamic imbalance by two additional masses fixed in the planes EL and ER to compensate the additional imbalance bearing forces

If two additional masses m_L and m_R would be added in the bearings opposite to the bearing additional forces at a certain distance (Fig. 7.1.1-4), their centrifugal forces would cancel the bearing additional forces. This is the basic idea of balancing a rotor by additional masses. As in the bearings there is no space for additional masses, the idea is to use additional balancing planes at the co-ordinates z_1 and z_2, where the additional masses are fixed. In many cases the end planes of the rotor body itself are used as these balancing planes (Fig. 7.1.2-1). By fixing the two balancing masses m_1, m_2 at the radii r_1, r_2 in those two balancing planes EL and ER ($\vec{U}_1 = m_1\vec{r}_1, \vec{U}_2 = m_2\vec{r}_2$), their additional centrifugal forces $\vec{F}_1 = \vec{U}_1\Omega_m^2, \vec{F}_2 = \vec{U}_2\Omega_m^2$ must be such, that their reaction forces $\vec{F}_L^+, \vec{F}_R^+$ in the bearings compensate the imbalance bearing forces $\vec{F}_L, \vec{F}_R$ which are caused by the original rotor imbalance (Fig. 7.1.1-4). Assuming for simplification F_L, F_R directed in the same plane, we get

force equilibrium: $F_L^+ + F_R^+ = F_1 + F_2$, torque equilibrium: $F_R^+ \cdot L = F_1 \cdot z_1 + F_2 \cdot z_2$, thus

$$F_1 = F_L^+ \cdot \frac{z_2}{z_2 - z_1} - F_R^+ \cdot \frac{L - z_2}{z_2 - z_1}$$
$$F_2 = -F_L^+ \cdot \frac{z_1}{z_2 - z_1} + F_R^+ \cdot \frac{L - z_1}{z_2 - z_1} \qquad (7.1.2\text{-}1)$$

With $F_L^+ = -F_L = -U_L \Omega_m^2$, $F_R^+ = -F_R = -U_R \Omega_m^2$ we get for the balancing masses the **balance equations**

$$\boxed{U_1 = m_1 r_1 = \frac{-U_L + U_R \cdot (L / z_2 - 1)}{1 - z_1 / z_2}}$$
$$\boxed{U_2 = m_2 r_2 = \frac{U_L \cdot (z_1 / z_2) - U_R \cdot (L / z_2 - z_1 / z_2)}{1 - z_1 / z_2}} \qquad (7.1.2\text{-}2)$$

Example 7.1.2-1:
Medium sized electric motor of 75 kW, 1500/min, rotor mass m_r = 60 kg, rotor outer diameter 200 mm, balancing in two planes at $L / z_2 = 3/2$, $z_1 / z_2 = 1/2$, balancing radii:
$r_1 = r_2 = d_{ra} / 2 = 100\,\text{mm}$.
Measured imbalance bearing forces at 500 /min: $F_L = 1.6\,\text{N}$, $F_R = 1.0\,\text{N}$. We assume force direction in both bearings to be the same.
How big must be the compensating balancing masses m_1, m_2 to compensate completely rotor imbalance ?

$$U_L = F_L / \Omega_m^2 = 1.6 / (2\pi(500/60))^2 = 583.6\,\text{g·mm}$$
$$U_R = F_R / \Omega_m^2 = 1.0 / (2\pi(500/60))^2 = 364.8\,\text{g·mm}$$
$$m_1 = \frac{-U_L + U_R \cdot (L/z_2 - 1)}{1 - z_1/z_2} \cdot \frac{1}{r_1} = \frac{-583.6 + 364.8 \cdot (3/2 - 1)}{1 - 1/2} \cdot \frac{1}{100} = \underline{\underline{-8g}}$$
$$m_2 = \frac{U_L \cdot (z_1/z_2) - U_R \cdot (L/z_2 - z_1/z_2)}{1 - z_1/z_2} \cdot \frac{1}{r_2} = \frac{583.6 \cdot (1/2) - 364.8 \cdot (3/2 - 1/2)}{1 - 1/2} \cdot \frac{1}{100} = \underline{\underline{-1.46g}}$$

Balancing masses are 8 g and 1.5 g, which – due to negative sign – must be fixed opposite to direction of measured bearing forces, or this amount of mass must be removed from the rotor.

Conclusions:
From balancing equations one concludes that balancing masses for given imbalance are smaller, if the fixing radii r_1, r_2 for these masses are big, so usually outer rotor diameter is chosen. They are also small, if the distance between the two balancing planes z_2 - z_1 is big.

7.1.3 Balancing of rigid rotors

Rotor is put on to measuring bearings in the balancing machine (Fig. 7.1.3-2) and is driven by a small motor on to balancing speed *n*. The measuring bearings have a certain elasticity, which may be expressed by the stiffness c_B. Due to imbalance the rotor generates *n*-frequent force oscillation $\hat{F} \cdot \cos(\Omega_m t)$ in the bearings, which vibrate. In horizontal plane *x* no gravity force is acting, so we get

$$m_r \cdot \ddot{x} + c_B \cdot x = \hat{F} \cdot \cos(\Omega_m t) \qquad (7.1.3\text{-}1)$$

Solution of this second order linear differential equation with constant coefficients is

$$x(t) = \hat{X} \cdot \cos(\Omega_m t) \quad , \quad \hat{X} = \frac{\hat{F}}{c_B - \Omega_m^2 \cdot m_r} \quad , \quad \Omega_m = 2\pi \cdot n \quad . \qquad (7.1.3\text{-}2)$$

At resonance frequency $n = f_B$ amplitude of this (here assumed) loss-free oscillation vibration amplitude tends to infinite, thus denominator is zero, yielding for f_B

$$c_B - \Omega_m^2 \cdot m_r = 0 \quad \Rightarrow \quad n = f_B = \frac{1}{2\pi} \cdot \sqrt{\frac{c_B}{m_r}} \quad . \qquad (7.1.3\text{-}3)$$

If rotor speed *n* is operated well below or well above resonance frequency, resonance is avoided and we get

$$\underline{n << f_B}: \quad \hat{X} \approx \frac{\hat{F}}{c_B} \quad \Rightarrow \quad \hat{F} = \hat{X} \cdot c_B = U \cdot \Omega_m^2$$
$$\underline{n >> f_B}: \quad \hat{X} \approx \frac{\hat{F}}{-\Omega_m^2 \cdot m_r} = -\frac{U}{m_r} \qquad (7.1.3\text{-}4)$$

In order to operate at the same speed with $n << f_B$, one has to build stiff bearings with high stiffness c_B as shown in Fig. 7.1.3-1a. A pressure sensor (e.g. piezo-electric sensor) between a stiff basement construction and the V-shaped bearing directly measures the horizontal force amplitude $\hat{F} = U \cdot \Omega_m^2$, which is directly proportional to imbalance (**stiff measuring bearing**). If operation should be done at $n >> f_B$ for the same speed, one has to build "soft" bearings with low stiffness c_B as shown in Fig. 7.1.3-1b. The V-shaped bearing is fixed by long springs to the basement construction. The longer the spring, the lower is the value c_B. An e.g. inductive position sensors is directly measuring the horizontal movement of the measuring bearing $\hat{X} = -U / m_r$, which is directly proportional to imbalance *U* (**low stiffness measuring bearing**). Both methods are used nowadays to measure the imbalance.

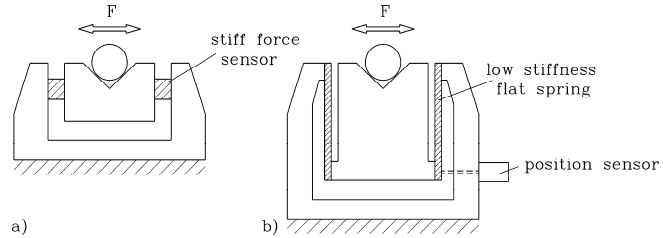

Fig. 7.1.3-1: Measuring rotor imbalance a) with bearing force measurement, b) bearing position measurement

Measurement signal of bearing force $F_R(t)$, $F_L(t)$ or bearing position $s_R(t)$, $s_L(t)$ contains not only rotational frequency, but due to other excitations like the balls of the bearings additional harmonics and also some noise due to EMI (Fig. 7.1.3-2). So signal is filtered with low pass

filter, then only getting the *n*-frequent signals $R(t), L(t)$, which have same frequency, but different amplitude and phase shift. If the signals are taken as phasors, rotating with Ω_m in the complex plane according to

$$\begin{aligned} \underline{\hat{L}} &= \hat{L} \cdot e^{j\varphi_L} \quad \Leftrightarrow \quad L(t) = \hat{L} \cdot \cos(\Omega_m t + \varphi_L) = \mathrm{Re}\left\{\underline{\hat{L}} \cdot e^{j\Omega_m t}\right\} \\ \underline{\hat{R}} &= \hat{R} \cdot e^{j\varphi_R} \quad \Leftrightarrow \quad R(t) = \hat{R} \cdot \cos(\Omega_m t + \varphi_R) \end{aligned} \quad , \qquad (7.1.3\text{-}5)$$

one can take them directly as the imbalance vectors $\vec{U}_L, \vec{U}_R$, which are used as input for the balancing equation (7.1.2-2). With the balancing masses m_1, m_2 calculated from (7.1.2-2), these masses are fixed to the rotor and measurement of bearing forces or position is repeated.

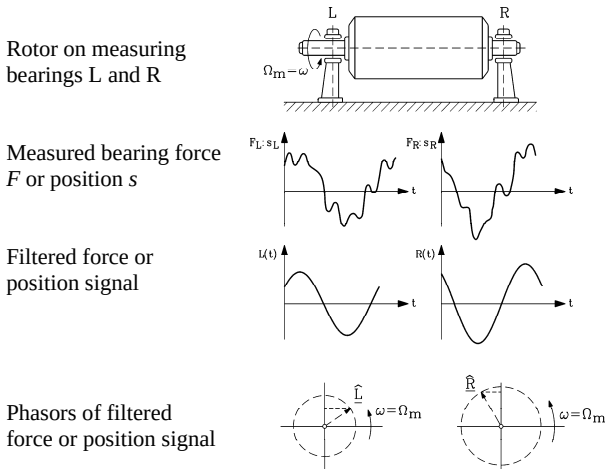

Fig. 7.1.3-2: Measuring of rotor imbalance by deducing resultant imbalance in the bearings

If balancing is ideal, now no *n*-frequent bearing forces should occur any longer. In reality of course still some small imbalance is left. This residual imbalance must stay below certain limits, whereby these limits are defined – depending on the purpose of the rotor – by standard ISO 1940. This residual imbalance is not given as imbalance value, but as **circumference speed of centre of gravity**

$$G = \Omega_m \cdot e_S \quad . \qquad (7.1.3\text{-}6)$$

In ideal case with centre of gravity on rotational axis $G = \Omega_m \cdot e_S = \Omega_m \cdot 0 = 0$, so G can also be taken as measure for residual imbalance.

Example 7.1.3-1:
Limit of residual imbalance according to ISO 1940 for electric motor, 2000/min, 100 kW, rotor mass 100 kg.
Table 7.1.3-1: $G = 2.5 mm/s \quad \Rightarrow \quad e = G/\Omega_m = 0.0025/(2\pi \cdot 2000/60) = 11.9\,\mu\mathrm{m}$
Residual imbalance: $U = 11.9 \cdot 10^{-6} \cdot 100 = \underline{\underline{1194}}\,\mathrm{g \cdot mm}$

	$\Omega_m \cdot e_S$	*Examples*
	mm/s	
G 4000	4000	Slow turning big *Diesel* engines for ships
G 1600	1600	Big two stroke combustion engines
G 630	630	Big four stroke combustion engines
G 250	250	Fast turning four stroke piston engines
G 100	100	Combustion engines for cars and locomotives
G 40	40	Wheel sets for cars
G 16	16	Cardan transmission shafts
G 6.3	6.3	Fans, pump rotors, standard electric motor rotors
G 2.5	2.5	Rotors of steam and gas turbines, big electric generators, high speed electric motors, turbo prop for air craft
G 1	1	Ultra high speed small motors, grinding spindle drives
G 0.4	0.4	Gyroscopic rotors, special high speed grinding spindle drives

Table 7.1.3-1: Limits for residual imbalance according to ISO 1940

Methods for balancing:
With wound rotors of small up to medium sized motors of DC machines, universal motors, wound rotor induction machines the balancing masses are a special fast-hardening cement, put into the winding overhangs of the rotor winding.
Cage induction rotors often have special cylindrical noses integrated into the aluminium end rings of the cage. On these noses metal rings are fixed as balancing masses.
For high speed machines these noses might cause additional friction in air, therefore often some cage mass is cut off (**" negative masse balancing"**).
Bigger machines get special additional discs on the rotor, where the balancing masses are fixed.

7.1.4 Balancing of complete motor system

After mounting the rotor into the stator housing and the end-shields, the additional imbalance might be induced by inaccuracy of bearing seats in the end shields. For high speed motors or motors for very low vibration therefore additional balancing is necessary e.g. by cutting of some mass from rotor shaft end or by cutting off some mass of special rotor discs. Thus **balancing of the complete motor** is done. This has to be done at cold motor, but has to be repeated at hot motor, because due to uneven thermal expansion of rotor additional imbalance might occur (**thermally induced imbalance**). For example, the iron sheets of rotor iron stack usually do not have exactly parallel sides, so thickness varies a little bit along the sheet plane. If all sheets are stacked on the rotor shaft with bigger thickness on one side, thermal expansion there is bigger, causing the rotor to bend, when hot. Thus centre of gravity is displaced, causing imbalance. By stacking the rotor with the rotor sheets shifted by 90° each, this effect is equalized, thus avoiding this reason for thermal imbalance.

But how to check the status of imbalance at the completed motor ?
Motor is put on an elastic test bed, e.g. beneath motor feet thick rubber pads are put (Fig. 7.1.4-1a). Another possibility is to hang the motor into springs. This method is of course only possible for smaller motors (Fig. 7.1.4-1b).

Vibration measurement in radial perpendicular direction (*x*, *y*-co-ordinate) at the bearing location (= end shields) and in axial direction (*z*-co-ordinate) is done with respect to rotational

frequency $f = n$, e.g. by measuring vibration velocity v or acceleration a. If motor housing surface position in horizontal direction is x, we get

$$x(t) = \hat{X} \cdot \cos(\omega t), \quad v(t) = \dot{x}(t) = -\omega \hat{X} \cdot \sin(\omega t), \quad a(t) = \ddot{x}(t) = -\omega^2 \hat{X} \cdot \cos(\omega t) \qquad (7.1.4\text{-}1)$$

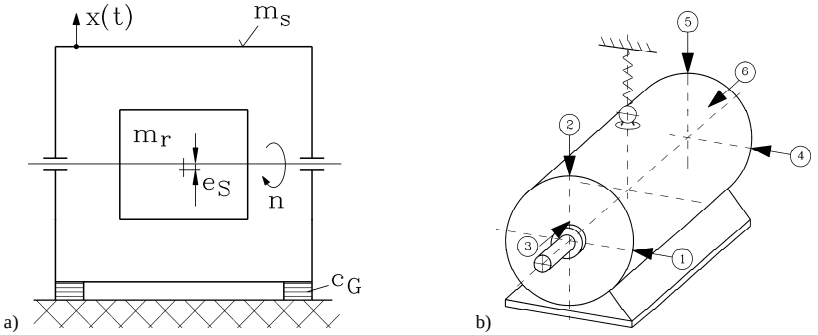

Fig. 7.1.4-1: Vibration measurement for completed motor: a) motor put on rubber pads, b) motor hung in springs

Motor with mass m, consisting of stator mass m_s and rotor mass m_r is put on rubber pads or hung in springs (with spring or pad stiffness c_G). Motor winding is connected to inverter to drive rotor at no-load with different speed n. Rotor imbalance leads to oscillating bearing forces F, which also excite the stator housing to vibrate. Vibration $x(t)$ of stator housing is measured with respect to rotational frequency. We assume static imbalance U_S, getting the x-component of centrifugal force

$$F_S = m_r \cdot e_S \cdot \Omega_m^2 \quad \Rightarrow \quad F_x(t) = F_S \cdot \cos(\Omega_m t) \qquad (7.1.4\text{-}2)$$

for exciting the vibration of the whole motor mass in x-direction:

$$(m_s + m_r) \cdot \ddot{x} + c_G \cdot x = F_S \cdot \cos(\Omega_m t) \quad . \qquad (7.1.4\text{-}3)$$

Due to the low stiffness c_G the resonance frequency f_G is much lower than rated speed. Solution of this linear second order differential equation is according to (7.1.3-2)

$$x(t) = \hat{X} \cdot \cos(\Omega_m t) \quad , \quad \hat{X} = \frac{F_S}{c_G - \Omega_m^2 \cdot m_{mot}} \quad , \quad f_G = \frac{1}{2\pi} \cdot \sqrt{\frac{c_G}{m_{mot}}} \quad . \qquad (7.1.4\text{-}4)$$

Due to the low stiffness c_G the resonance frequency f_G is much lower than rated speed.

$$\underline{n >> f_G}: \quad \hat{X} \approx \frac{F_S}{-\Omega_m^2 \cdot m_{mot}} = -\frac{U_S}{m_{mot}} \quad . \qquad (7.1.4\text{-}5)$$

$$v(t) = \dot{x}(t) = \frac{U_S}{m_{mot}} \cdot \Omega_m \cdot \sin(\Omega_m t) \quad \Rightarrow \quad \hat{v} = \frac{m_r}{m_s + m_r} \cdot e_S \cdot \Omega_m \qquad (7.1.4\text{-}6)$$

Conclusions:
Vibration velocity rises linear with speed, its inclination being directly proportional to imbalance itself. Thus it is possible by elastic mounting of motor to get access to status of imbalance by vibration measurement.

Vibration velocity is directly proportional to circumference velocity of centre of gravity:

$$\hat{v} = \frac{m_r}{m_s + m_r} \cdot e_S \cdot \Omega_m = \frac{m_r}{m_s + m_r} \cdot G \qquad (7.1.4\text{-}7)$$

The imbalance limit G is connected to the r.m.s. limit of vibration velocity by

$$v_{r.m.s} = \frac{m_r}{m_s + m_r} \cdot \frac{G}{\sqrt{2}} \quad . \qquad (7.1.4\text{-}8)$$

Example 7.1.4-1:
With a mass ratio $m_r / m_{mot} = 1/3$ and G = 6.3 mm/s a typical value for r.m.s. vibration velocity limit is $v_{r.m.s} = \frac{1}{3} \cdot \frac{6.3}{\sqrt{2}} = \underline{\underline{1.5}}$ mm/s.

For balancing complete motor system in ISO2373 limits $v_{r.m.s}$ are given, which according to (7.1.4-6) rise with speed. Depending on increased performance of drive system, which is defined by application such as motors for tooling machines, **different vibration levels** are given:
N: normal use (standard),
R, S, SR: decreased vibration level is given by levels R, S and SR (Fig. 7.1.4-2).
These values are given of course not for extremely big motors, as for them it is difficult to put them **on elastic mounting** (Fig. 7.1.4-1) for measurement. Values are defined for AC- and DC-machines with frame size 80 mm to 400 mm (shaft height), corresponding with rated power 0.5 kW up to 450 kW at 1500/min. Vibration levels are defined in IEC34-14 and more detailed in ISO2373.

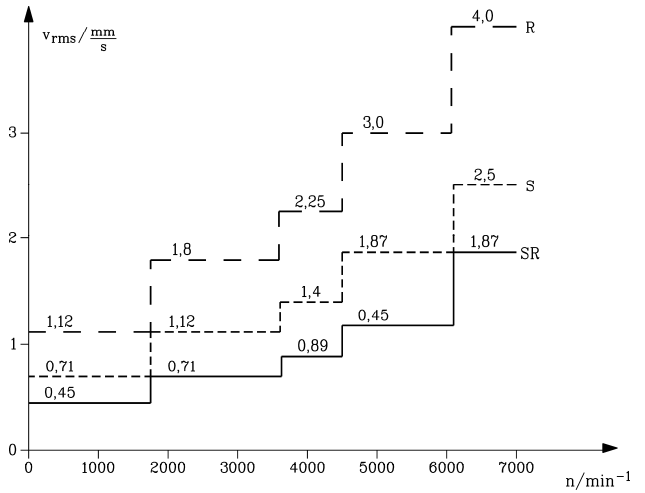

Fig. 7.1.4-2: Vibration levels (r.m.s. vibration velocity), depending on maximum speed of motor, according to ISO2373, for motor size 160 mm to 180 mm

Above frame size 400 mm the motors are too big to be measured on elastic mounting. Therefore only limits of values $v_{r.m.s.}$ for **stiff mounting** are given. In that case machine and

machine bed, where machine is mounted, are coupled, so vibration of machine causes also the bed to vibrate. This measurement method therefore does not allow access to the vibration behaviour of the machine itself, but only of the whole drive system with machine bed. So measurement values may be quite different, when compared with measurement on elastic mounting.

Example 7.1.4-2:
Limits of r.m.s. vibration level according to ISO2372 for frame size 160 mm to 180 mm:
Level N: 2.8 mm/s for variable speed drives with maximum speed 600/min ... 3600/min
Levels R, S, SR are depicted in Fig. 7.1.4-2 for extended speed range up to 7000/min.

7.1.5 Elastic rotor system - Vibrations of rotors

The rotor system is constituted by the rotor body and the bearing system, which comprises the bearings and the end shields or bearing seats. Elasticity of the rotor shaft and of the bearing system leads to natural vibrations of the rotor system, which makes it impossible to balance the rotor only in two balancing planes, as it is possible for rigid rotor body system.

a) Influence of elastic bearings :

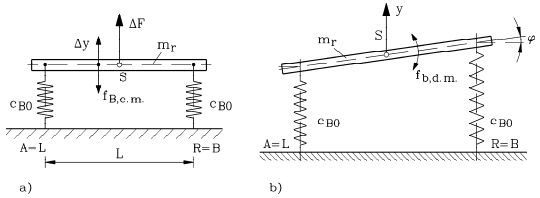

Fig. 7.1.5-1: Rigid body vibration on elastic bearings: a) common mode vibration (c.m.), b) differential mode vibration (d.m.)

The bearing stiffness of ball or roller bearings is much higher than the stiffness of the rotor body. But in case of magnetic bearings, oil sleeve bearings or air bearings the bearing stiffness is smaller. So, if a rigid rotor body is placed on elastic bearings, these bearings may be described by the bearing stiffness c_B (Fig. 7.1.5-1). We assume identical bearings, so equivalent spring systems for left and right bearing are identical: $c_{BL} = c_{BR} = c_{B0}$, yielding for bearing deformation e.g. in vertical direction Δy along with vertical force per bearing $\Delta F_{BL} = \Delta F_{BR} = \Delta F_B$:

$$\Delta F_B = c_{B0} \cdot \Delta y \quad . \tag{7.1.5-1}$$

If both bearings vibrate IN PHASE (common mode vibration) e.g. in vertical direction, the rotor body is also oscillating vertically (Fig. 7.1.5-1a). As both bearing springs act mechanically in parallel, both bearing forces add for the SAME vertical deformation, leading to resulting vertical stiffness $c_B = 2c_{B0}$.

$$\Delta F = 2\Delta F_B = c_B \cdot \Delta y = 2c_{B0} \cdot \Delta y \quad . \tag{7.1.5-2}$$

This common mode bearing vibration has been already described in Section 7.1.3, leading to common mode (c.m.) natural frequency

$$f_{B,c.m.} = \frac{1}{2\pi} \cdot \sqrt{\frac{c_B}{m_r}} \tag{7.1.5-3}$$

If both bearings vibrate with 180° PHASE SHIFT (differential mode vibration) e.g. in vertical direction due to phase shift of 180° between left and right bearing force $\Delta F_{BL} = -\Delta F_{BR}$, the rotor body is not only oscillating vertically (Fig. 7.1.5-1b), but shows also angular movement around *x*-axis with angle α, which according to $J_x \cdot d^2\varphi / dt^2 = M$ is ruled by the moment of inertia of rotor body around *x*-axis and by the torque $\Delta M = L \cdot \Delta F_B$. The resulting **differential mode natural frequency** (given without proof here)

$$f_{B,d.m.} = \frac{1}{2\pi} \cdot \frac{L}{2} \cdot \sqrt{\frac{c_B}{J_x}} > f_{B,c.m.} \tag{7.1.5-4}$$

is usually higher than the common mode natural frequency, if *L* is big enough.

Conclusions:
In the complete motor system elasticity of bearings and end shields leads to two rigid rotor body vibrations, which may influence (disturb) the balancing process of the complete motor system, if rotational speed f = n coincides with on of these two natural frequencies, leading to resonance. The balancing of the rotor alone on a balancing machine is not influenced by these bearing vibrations, as on the balancing machine the rotor runs in special measuring bearings.

b) Elastic rotor shaft with lumped mass assumption:
The rotor iron stack, consisting of the stacked iron sheets, shows no big stiffness, compared to massive cylindrical rotor body of the same dimensions. So it is mainly the massive rotor shaft (mass m_{sh}), which determines rotor stiffness ($c_{sh} = c_r$). The rotor iron stack (mass m_{stack}) acts mainly as additional mass. Here for simplicity the model of **disc rotor** (thickness l_{Fe} much smaller than diameter d_{ra} and bearing distance *L*) is considered. This model is very applicable to a one stage steam turbine rotor and was first studied by *de Laval*, thus being called *Laval* rotor. Mass of shaft is added as **lumped mass** to stack mass as total rotor mass $m_r = m_{stack} + m_{sh}$, which is mounted on elastic mass-less shaft (here for simplicity in the middle between both bearings at $z = L/2$). Elasticity of shaft is described by *Young´*s modulus *E*, which for steel is $E = 212 \cdot 10^9\ \mathrm{N/m^2}$. Shaft circular cross section with diameter d_{sh} resists to bending with area momentum of inertia $I = \pi \cdot d_{sh}^4 / 64$. Shaft length between bearing is bearing distance *L* (Fig. 7.1.5-2). For simplification we assume rotor disc to be centred between the bearings. At stand still due gravity the shaft is bent with maximum deformation y_M in the middle (Fig. 7.1.5-2)

$$F = m_r \cdot g = c_{sh} \cdot y_M \tag{7.1.5-5}$$

with

$$c_{sh} = \frac{48 \cdot E \cdot I}{L^3} \quad . \tag{7.1.5-6}$$

Example 7.1.5-1:
Electric motor with 75 kW at 1500/min:
Shaft length / diameter L = 0.7 m, d_{sh} = 80 mm, stack length l_{Fe} = 350 mm,
outer diameter d_{ra} = 190 mm, iron mass density ρ = 7850 kg/m^3:

$m_{sh} = \rho \cdot L \cdot d_{sh}^2 \pi / 4 = 27.6\,\text{kg},\ m_{stack} = \rho \cdot l_{Fe} \cdot (d_{ra}^2 - d_{sh}^2)\pi / 4 = 64.1\,\text{kg},$

$m_r = 27.6 + 64.1 = 91.7\,\text{kg},\ I = \pi \cdot d_{sh}^4 / 64 = 2.01 \cdot 10^{-6}\,\text{m}^4,\ c_{sh} = \dfrac{48 \cdot E \cdot I}{L^3} = 59.63 \cdot 10^6\,\text{N/m}$

Static rotor bending due to gravity: $y_M = m_r \cdot g / c_{sh} = 15\,\mu\text{m}$

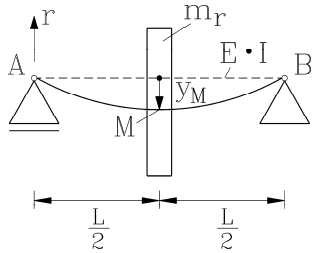

Fig. 7.1.5-2: Disc rotor on elastic shaft (*Laval* rotor)

Natural bending frequency is given by

$$m_r \cdot \ddot{y} + c_{sh} \cdot y = 0 \qquad (7.1.5\text{-}7)$$

with **natural bending frequency**

$$\boxed{f_b = \frac{1}{2\pi} \cdot \sqrt{\frac{c_{sh}}{m_r}}} \quad . \qquad (7.1.5\text{-}8)$$

Conclusions:
For getting stiff rotor the distance between the bearings must be small and the shaft diameter should be big. This and small rotor mass allow increase of rotor bending natural frequency.

Example 7.1.5-2:
Electric motor with 75 kW at 1500/min (Date of Example 7.1.5-1):
$m_r = 91.7\,\text{kg},\ c_{sh} = 59.63 \cdot 10^6\,\text{N/m}$

Natural bending frequency is $f_b = \dfrac{1}{2\pi} \cdot \sqrt{\dfrac{c_{sh}}{m_r}} = \dfrac{1}{2\pi} \cdot \sqrt{\dfrac{59631953}{91.7}} = \underline{\underline{128.3}}\,\text{Hz}$

At speed $n = f_b$ = 7700/min an imbalance will excite big motor vibrations due to resonance. Therefore maximum motor speed should stay below $n_{max} = f_b \cdot 0.7 = 5390$/min.

c) Elastic rotor shaft with distributed mass:
In reality the shaft has to be considered as cylindrical beam of diameter d_{sh} and length L with DISTRIBUTED mass along the beam. Like a vibrating guitar string, this beam has not only one bending natural frequency, but a whole spectrum of natural bending modes, which depend on the elasticity of the bearings. Assuming rigid bearings, where the *x*- and *y*-co-ordinate of the beam is always zero, but allowing the beam to change its inclination also at the bearing´s location, the natural bending frequencies of the beam (with cross section areas *A*) are derived as

$$f_{b,i} = \frac{1}{2\pi} \cdot \left(\frac{i \cdot \pi}{L}\right)^2 \cdot \sqrt{\frac{E \cdot I}{\rho \cdot A}} \quad , \quad i = 1, 2, 3, \ldots \qquad (7.1.5\text{-}9)$$

As the iron stack mass increases the total mass, this considered according to (7.1.5-8) by

$$f_{b,i,corr} = f_{b,i} \cdot \frac{1}{\sqrt{1 + \dfrac{m_{stack}}{m_{sh}}}} \quad , \quad i = 1, 2, 3, \ldots \qquad (7.1.5\text{-}10)$$

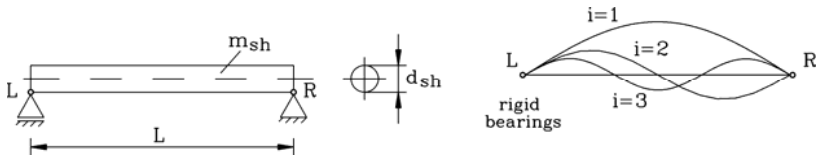

Fig. 7.1.5-3: Model of shaft as cylindrical beam, showing a spectrum of bending natural frequencies, which depend on the influence of bearing stiffness

Example 7.1.5-3:
Electric motor with 75 kW at 1500/min (data of Example 7.1.5-1) :
L = 0.7 m, d_{sh} = 80 mm, ρ = 7850 kg/m^3, $m_{sh} = 27.6\,\text{kg},\ m_{stack} = 64.1\,\text{kg},$
$1 + m_{stack} / m_{sh} = 1 + 64.1 / 27.6 = 3.32,\ A = \pi \cdot d_{sh}^2 / 4 = 5.03 \cdot 10^{-3}\,\text{m}^2$

i	1	2	3
$f_{b,i,corr}$ / Hz	182	731	1645

Compared with the simplified lumped mass model (7.1.5-6), the more detailed model (7.1.5-10) yields 40% higher first natural bending frequency and in addition also higher frequency eigen-modes.

Bigger motors have rather big distance of bearings L and rather big rotor mass. Hence, to consider influence of machine size on natural bending frequency, we take geometric dimensions $L \sim x, d_{sh} \sim x$ in (7.1.5-9), showing that frequency decreases inverse with increasing frame size: $f_{b,i} \sim 1/x$.

Conclusions:
Calculation of natural bending frequency is rather complicated, as distributed mass and geometry of rotor has to be considered. The stiffening influence of rotor iron stack is also difficult to calculate. Elasticity of bearings may reduce the natural bending frequencies by about 10 % to 20 %. Further, big machines have low natural bending frequency.

d) Influence of "unbalanced magnetic pull" on natural bending frequency:
When the rotor shaft is bent by *y*, this leads to an air gap eccentricity $e = -y$. The electric machine air gap is reduced on side by $\delta - e$ and increased on the other side by $\delta + e$. Thus radial magnetic flux density, which is excited by m.m.f. in air gap V_δ, in case of machines with pole numbers $2p \geq 4$ is increased on side by $B_{\delta+} = \mu_0 \cdot V_\delta / (\delta - e)$ and reduced on the opposite side by $B_{\delta-} = \mu_0 \cdot V_\delta / (\delta + e)$. Thus radial magnetic pull per unit rotor surface $A_r = 2p \cdot \tau_p \cdot l_{Fe}$ with $B_\delta = \mu_0 \cdot V_\delta / \delta$ as air gap flux density amplitude of non-eccentric rotor

$$f_{n+} = \frac{B_{\delta+}^2}{2\mu_0} > f_{n-} = \frac{B_{\delta-}^2}{2\mu_0} \qquad (7.1.5\text{-}11)$$

is no longer in equilibrium, but residual ("unbalanced") magnetic pull in direction of decreased air gap remains (formula given without proof):

$$F_M = (f_{n+} - f_{n-}) \cdot A_r = \frac{p \cdot \tau_p \cdot l_{Fe}}{2\mu_0} \cdot B_\delta^2 \cdot \frac{e}{\delta} \quad , \quad 2p \geq 4 \qquad (7.1.5\text{-}12)$$

For **two-pole machines** this unbalanced magnetic pull is only 50%.
Note: At zero eccentricity $e = 0$ this residual pull is also zero.

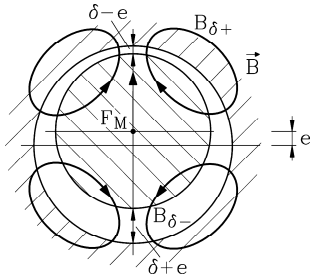

Fig. 7.1.5-4: "Unbalanced magnetic pull" F_M in four pole motor due to air gap eccentricity e

This residual radial magnetic force tends to decrease the reduced air gap further. Comparing with the elastic bending of the shaft, where a bending by value y increases elastic force $F_{c_{sh}} = c_{sh} \cdot y$, acting against the bending force, the unbalanced magnetic pull acts in direction of bending force, thus opposite to elastic force:

$$F_M = -c_M \cdot y \quad . \qquad (7.1.5\text{-}13)$$

Considering $y = -e$, the "magnetic stiffness"

$$c_M = \frac{p \cdot \tau_p \cdot l_{Fe}}{2\mu_0} \cdot B_\delta^2 \cdot \frac{1}{\delta} \qquad (7.1.5\text{-}14)$$

has to be considered in the model of elastic rotor. It **reduces the resulting stiffness** by

$$c_{res} = c_{sh} - c_M \quad , \qquad (7.1.5\text{-}15)$$

leading to decrease of natural bending frequency by

$$\boxed{f_{b,M} = \frac{1}{2\pi} \cdot \sqrt{\frac{c_{sh} - c_M}{m_r}} = f_b \cdot \sqrt{1 - \frac{c_M}{c_{sh}}}} \quad . \qquad (7.1.5\text{-}16)$$

Example 7.1.5-4:
4-pole electric motor with 75 kW at 1500/min (data of example 7.1.5-3):
L = 0.7 m, d_{sh} = 80 mm, l_{Fe} = 350 mm, d_{ra} = 190 mm, $m_r = 91.7\,\text{kg}$, air gap flux density amplitude B_δ = 0.9 T, air gap δ = 1.0 mm, pole pitch: $\tau_p = 149\,\text{mm}$

Rotor gravity force: $m_r \cdot g = 900\,\text{N}$
Unbalanced magnetic pull at 10% eccentricity: $e/\delta = 0.1$:

$$F_M = \frac{p \cdot \tau_p \cdot l_{Fe}}{2\mu_0} \cdot B_\delta^2 \cdot \frac{e}{\delta} = \frac{2 \cdot 0.149 \cdot 0.35}{2 \cdot 4\pi \cdot 10^{-7}} \cdot 0.9^2 \cdot 0.1 = \underline{\underline{3360}}\,\text{N}$$

Depending on air gap eccentricity, the unbalanced magnetic pull can reach considerable values (here: 225 % of rotor gravity force).

Calculated first natural bending frequency without influence of magnetic pull: $f_{b1} = 183\,\text{Hz}$:

equivalent shaft stiffness: $c_{sh} = (2\pi f_{b1})^2 \cdot m_r = 121.4 \cdot 10^6\,\text{N/m}$,

magnetic stiffness: $c_M = \frac{p \cdot \tau_p \cdot l_{Fe}}{2\mu_0} \cdot B_\delta^2 \cdot \frac{1}{\delta} = 33.6 \cdot 10^6\,\text{N/m}$

Calculated first natural bending frequency with influence of unbalanced magnetic pull:
$f_{b1,M} = f_{b1} \cdot \sqrt{1 - c_M / c_{sh}} = 183 \cdot \sqrt{1 - 33.6/121.4} = \underline{\underline{155.6}}\,\text{Hz}$:

Conclusions:
Unbalanced magnetic pull leads to a considerable decrease of natural bending frequency by about 10% ... 20%, depending on utilization of magnetic circuit.

7.1.6 Balancing of elastic rotors

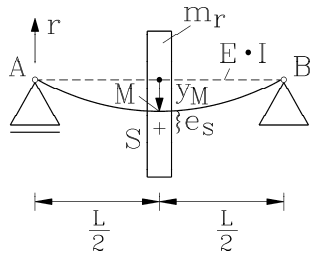

Fig. 7.1.6-1: Static imbalance due to dislocation of centre of gravity S by e_S from rotational axis. Additional dislocation of centre of rotation from geometrical axis of unbent shaft (here: Example of disc rotor on elastic shaft (*Laval* rotor))

We assume static imbalance due to dislocation of centre of gravity S by e_S from rotational axis (Fig. 7.1.6-1). Neglecting the bending due to gravity, we here consider only bending due to centrifugal force caused by imbalance, which causes in y-direction additional dislocation y_M of centre of rotation M from geometrical axis of unbent shaft. In x-direction dislocation x_M occurs. With resulting radial dislocation $r_M = \sqrt{x_M^2 + y_M^2}$ due to bending the centre of gravity is displaced from geometrical axis by $r_S = e_S + r_M$, causing centrifugal force

$$F_S = m_r \cdot (e_S + r_M) \cdot \Omega_m^2 = m_r \cdot r_S \cdot \Omega_m^2 \quad . \qquad (7.1.6\text{-}1)$$

The shaft bends until equilibrium between centrifugal force and elastic force is reached,

$$F_S = F_{c_{sh}} \quad \Rightarrow \quad m_r \cdot (e_S + r_M) \cdot \Omega_m^2 = c_{sh} \cdot r_M \quad , \qquad (7.1.6\text{-}2)$$

yielding for the displacement r_M of centre of rotation *M* from geometrical axis in dependence of speed

$$r_M = e_S \cdot \frac{\Omega_m^2}{\omega_b^2 - \Omega_m^2} \quad , \qquad \omega_b = 2\pi \cdot f_b \tag{7.1.6-3}$$

and for the displacement r_S of centre of gravity *S* from geometrical axis in dependence of speed (Fig. 7.1.6-2)

$$\boxed{r_S = e_S \cdot \frac{\omega_b^2}{\omega_b^2 - \Omega_m^2}} \quad . \tag{7.1.6-4}$$

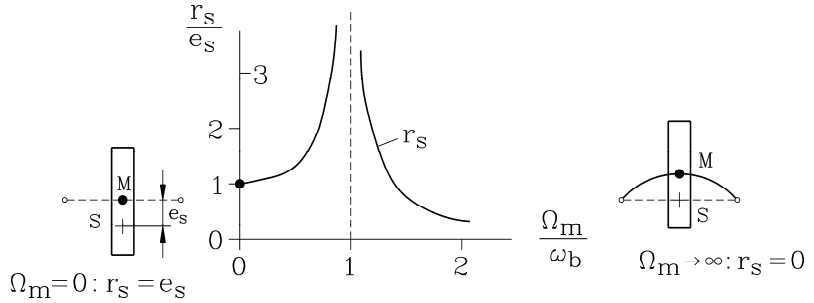

Fig. 7.1.6-2: Displacement r_S of centre of gravity *S* from geometrical axis in dependence of speed

After passing through the resonance region, the centre of gravity is centring itself on the geometrical axis at high speed ($r_S \to 0$); hence the centrifugal force will vanish at high speed. Centrifugal force is depending not only on U_S and Ω_m^2, but also on the ratio of Ω_m / ω_b, so rigid body balancing is not possible any longer.

$$\boxed{F_S = m_r \cdot e_S \cdot \frac{\omega_b^2}{\omega_b^2 - \Omega_m^2} \cdot \Omega_m^2 = U_S \cdot \frac{1}{1 - (\Omega_m / \omega_b)^2} \cdot \Omega_m^2} \tag{7.1.6-5}$$

In order to minimize the increase of centrifugal force and the related bearing forces

$$\begin{aligned} \vec{F}_{A,x\sim} &= \vec{F}_{B,x\sim} = F_S / 2 \cdot \cos(\Omega_m t) \\ \vec{F}_{A,y\sim} &= \vec{F}_{B,y\sim} = F_S / 2 \cdot \sin(\Omega_m t) \end{aligned} \tag{7.1.6-6}$$

near resonance $\Omega_m \approx \omega_b$, **special balancing techniques** for elastic rotors have been developed. In a third plane additional balancing masses are fixed. This third plane should be located at the rotor near the location of maximum rotor bending. The centrifugal force of this added imbalance shall act opposite to the centrifugal force of the bent shaft.

Small and medium sized motors are operated even with high speed application usually below first natural bending frequency. So the rigid body balancing is sufficient. But bigger motors

have their first natural bending frequency already **below** their rated speed, so **elastic balancing** is necessary. Big 2-pole turbo generators for steam power plants with bearing distances *L* of several meters, being operated at 3000/min = 50 Hz, have typically 2 or 3 natural bending frequencies below 50 Hz. Elastic balancing needs for each natural bending frequency, which is below maximum machine operating speed, an additional balancing plane to fix further balancing masses. The centrifugal forces of these added imbalances shall counter-act to the bending modes of the rotor at each of the natural bending frequencies.

Example 7.1.6-1:
a) 2-pole standard induction motor, 50 Hz, 500 kW:
1st natural bending frequency at f_{b1} = 35 Hz.
Elastic balancing with 3 balancing planes is necessary.
b) 2-pole large synchronous turbo generator, 50 Hz, 1000 MW (power plant *Lippendorf, Germany*): 3 natural bending frequencies lie in the frequency range 5 ... 40 Hz:
Elastic balancing with 5 balancing planes is necessary.

8. Stepper motors

Electromechanical actuators, which transform electrical impulses into mechanical steps, are called **stepper motors**. A complete **stepper drive** consists of
- an electronic control unit,
- a power amplifier, including a grid-side front end, and
- a stepper motor.

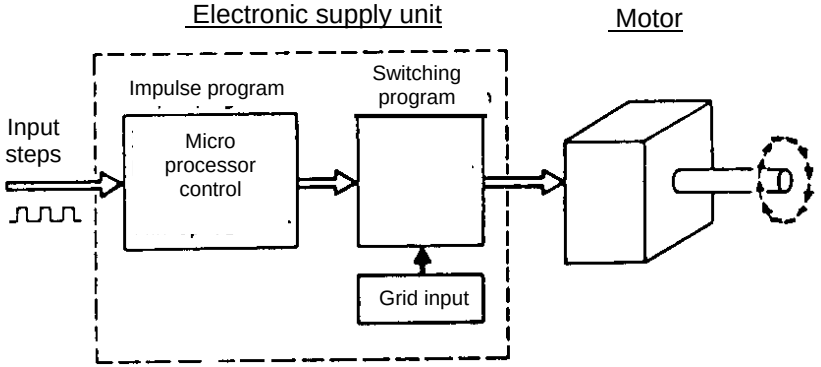

Fig. 8-1: Basic scheme of a stepper drive (*Stölting et al., El. Kleinmaschinen, Teubner,* 1987)

In order to keep the cost for a stepper drive as low as possible, the stepper motor is operated in a **feed forward control**, without any use of a position feed-back. Hence the condition, that the number of electrical impulses is always identical with the number of mechanical steps, must be guaranteed under all circumstances. Stepper motors usually operate according to the **synchronous motor** principle in three different variants (Table 8-1):
- Variable reluctance stepper motors (**VR-motor**)
- Permanent magnet stepper motors (**PM-motor**)
- **Hybrid** stepper motors, which operate on a combination of the PM and VR stepper principle

Therefore stepper motors, like grid-operated synchronous motors, have a **static pull-out torque**, which is the maximum available electromagnetic torque at steady state operation. If the load torque at the shaft is bigger than the pull-out torque, the rotor is pulled out of synchronism and falls behind the stator magnetic field; the motor is **losing steps**. During acceleration and deceleration the rotor tends **to oscillate** like grid-operated synchronous machines due to the elastic attributes of the magnetic field forces and the rotor and load inertia. Hence stepper motors are usually manufactured only up to a rated power of about 1 kW. For bigger power the position-controlled synchronous servo drives („brushless DC drives“), which are not endangered by pull-out torque and intrinsic oscillation, are the more economical solution.

Type of stepper motor	**PM-motor**	**VR-motor**	**Hybrid motor**
Electromagnetic utilization	high	low	medium
Damping of oscillations	good	bad	good
Detent torque (= at open circuit) ?	yes	no	yes
Minimum necessary phase count	2	3	2
Cost	low	high	high

Table 8-1: Three variants of stepper motor principles

8.1 Basic principle of operation of steppers

The multi-phase stator winding may be arranged in the stepper motors either
- in one plane (Fig. 8.1-1a) or
- in different planes along the rotating axis (Fig. 8.1-1b).

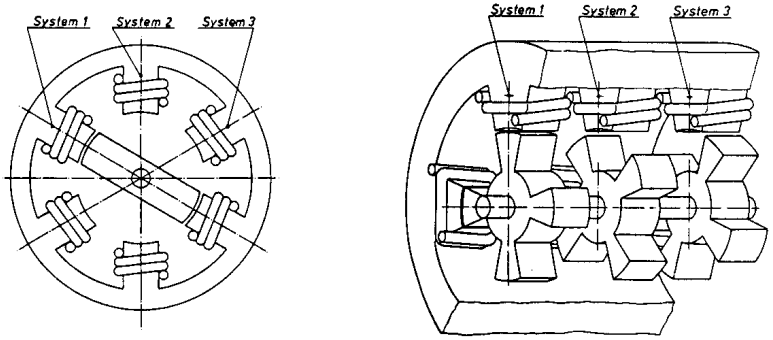

a) b)

Fig. 8.1-1: Design examples of the multi-phase stator winding of a VR-motor with m phases and Q_r rotor teeth
a) stator winding phases in one plane: $m = 3$, $Q_r = 2$
b) stator winding phases in three planes along the axis: $m = 3$, $Q_r = 4$

We assume that each stator phase is fed independently by an impulse voltage, so each phase is energized separately. If the feeding leads to block currents (impulses) per phase, the stator magnetic field is directed into the axis of phase U, if phase U is energized only. A PM rotor of the same pole count as the stator winding or a reluctance rotor of $Q_r/p = 2$ rotor teeth per pole pair (like a conventional synchronous reluctance machine) will be aligned into the stator field direction due to the magnetic tangential drag. By feeding afterwards phase W with a negative block current (**bipolar feeding**) the stator field performs a step of 60°el., which the above described rotors will follow due to the magnetic tangential drag. In case of **uni-polar feeding** (= always positive phase current) the next phase to be energized may e.g. phase V, which is shifted spatially by 1/3 of $2\tau_p$ to phase U. Hence the stator field will make a step of 120°el.. A PM will have to move also by 120°, whereas the VR rotor moves only by 60°, because it is magnetized in the opposite direction and aligns like that into the direction of phase V. Energizing next phase W with positive phase current moves the PM rotor by another 120°, and the VR rotor by another 60°, being now magnetized again into the same direction as before in case of phase U. According to Fig. 8.1-1a the number of mechanical steps z_p during one stator period $T_s = 1/f_s$ for a VR-rotor is given with m stator phases and Q_r/p rotor teeth per pole pair as

$$z_p = (Q_r / p) \cdot m \qquad (8.1\text{-}1)$$

At each step the rotor is shifted by the **rated stepping angle** (in electrical degrees, as a shift by 2π is a movement per one pole pair)

$$\alpha_e = 2\pi / z_p \quad . \qquad (8.1\text{-}2)$$

The number of steps per rotor revolution is p-times bigger:

$$z = p \cdot z_p = Q_r \cdot m \qquad (8.1\text{-}3)$$

Hence the possibility to increase z acc. to (8.1-3) is increasing
- the number of poles $2p$ and/or
- the number of teeth per pole Q_r/p.

The **rated stepping angle** in mechanical degrees is the fraction $1/p$ of the value in electrical degrees:

$$\alpha = \alpha_e / p = 2\pi /(z_p \cdot p) = 2\pi / z \quad . \qquad (8.1\text{-}4)$$

In case of $2p = 2$ there are the following identities: $\alpha = \alpha_e, \quad z = z_p$.

By increasing the number of rotor teeth per pole by the factor 2, getting $Q_r/p = 4$, the VR-rotor moves only by 30° (electrically), if the stator three-phase winding is energized with uni-polar block current first in phase U and then in phase V. If first teeth 1 and 3 have been magnetized by the magnetic field of phase U, at the next step the teeth 2 and 4 are magnetized by the magnetic field of phase V. Comparing the cases $Q_r/p = 2$ and $Q_r/p = 4$, the rotor movement is opposite for the two cases, if the stator phases are energized in the same way, e.g. U-V-W-U-V-W-…

Example 8.1-1: $2p = 2$ stepper motor
a) VR-motor: Fig. 8.1-1a: $Q_r = 2$, $m = 3$, $z = 6$, $\alpha = 360°/6 = 60°$
b) VR-motor: Fig. 8.1-1b: $Q_r = 4$, $m = 3$, $z = 12$, $\alpha = 360°/12 = 30°$

In case of PM stepper motors the rotor teeth number Q_r is replaced by the rotor pole pair number p. Instead of Q_r/p we put 1 and get

$$z = p \cdot z_p = p \cdot m \quad . \qquad (8.1\text{-}5)$$

Facit:
Whereas in conventional synchronous machines the m-phase, 2p-pole stator winding is fed with m sinusoidal phase voltages of the frequency f_s, which are phase shift by $2\pi/m$, resulting in a rotational stator magnetic field with rotational speed $n_{syn} = f_s / p$, the movement of the stator field in stepper motors is not continuous, but step-wise. The stator winding is fed by impulse e.g. block voltages, resulting in case of neglected stator inductances, considering only the stator winding resistance, in block currents and block flux linkages.

8.1.1 Full-step and half-step operation

Full step operation:
If each phase a, b, c, d, … is energized separately by its phase voltage, the stator field moves from phase axis to phase axis, hence by the angle $2\pi/m$ (in electrical degrees). The mechanical step of the rotor depends on the type of rotor, as explained before.
In order to increase z by a factor of 2 we introduce the half-step operation.

Half step operation:
If after a single phase excitation two adjacent phases are energized at the same time (e.g. a, a-b, b, b-c, c, c-d, ….) both with the same current polarity e. g. due to uni-polar feeding, the resulting field is positioned along the axis between the two phases. Hence the angle of stator

field movement is halved, resulting in an electrical angle π/m. Independent of the type of rotor the number of rotor steps therefore is doubled in comparison to full step operation and the mechanical stepping angle is halved. In case of VR-rotors we get for the number of steps per rotor revolution:

$$\text{VR: } z = Q_r \cdot m / k_B \quad , \qquad \text{PM: } z = p \cdot m / k_B \qquad (8.1.1\text{-}1)$$

($k_B = 1$: Full step operation, $k_B = 0.5$: Half step operation)

In this mode of operation alternatively one or two phases are magnetized. As the phase current amplitude i is always the same, the magnetic field amplitude may change its amplitude. For easy understanding we punt in the cross section of the machine a complex coordinate system and describe the magnetic field per phase as a vector of flux linkage (a complex phasor), that is aligned in direction of the phase axis. In case of $m = 3$ and uni-polar feeding the field amplitude should not change, being first e.g. $\underline{\psi}_U$ and then $\underline{\psi}_U + \underline{\psi}_V = \underline{\psi}_U + \underline{\psi}_U \cdot e^{j\cdot 2\pi/3} = \underline{\psi}_U \cdot e^{j\cdot \pi/3}$. But already in case of $m = 4$ the field is bigger in case of two energized adjacent phases, leading first e.g. to a flux linkage $\underline{\psi}_a$ and then to $\underline{\psi}_a + \underline{\psi}_b = \underline{\psi}_a + \underline{\psi}_a \cdot e^{j\cdot 2\pi/4} = \sqrt{2} \cdot \underline{\psi}_U \cdot e^{j\cdot \pi/4}$. Due to the changing magnetic field also the electromagnetic torque $m \sim i \cdot \psi$ is changed, being smaller with only one phase energized. The stepping torque changes step by step between a small and a big torque, hence between a hard and a soft step.
- **Hard** step: Two adjacent phases are energized, big torque
- **Soft** step: One phase energized, small torque.

8.1.2 Variable reluctance with additional stator teeth (*Vernier* machine)

In Fig. 8.1.2-1 a VR-motor is shown, where the pole surface of the stator and rotor is toothed with stator and rotor teeth of different tooth count or slot pitch, respectively. The condition $Q_r \neq Q_s$ is essential to avoid a big magnetic cogging torque, which would fix the rotor position with stator teeth and rotor teeth aligned. Due to the additional slot openings of the stator the resulting magnetic air gap field is modulated. The air gap δ is varying due to the stator slotting roughly with the stator tooth count Q_s.

$$\delta(x_s) = \delta \cdot (1 + \lambda \cdot \cos((Q_s / p) \cdot (x_s \pi / \tau_p))) \qquad (8.1.2\text{-}1)$$

The parameter λ increases with increasing stator slot opening and decreasing air gap. The stator m.m.f. per phase may be expanded into a FOURIER series. Its fundamental is a m.m.f. wave of pole count $2p$, which – together with the air gap – gives the resulting magnetic air gap field.

$$V_{phase,\nu=1}(x_s) = \hat{V} \cdot \cos(x_s \pi / \tau_p) \qquad (8.1.2\text{-}2)$$

$$B(x_s) = \mu_0 \hat{V} \cdot \cos(x_s \pi / \tau_p) / \delta(x_s) = B \cdot \cos(x_s \pi / \tau_p) + (\lambda / 2) \cdot B \cdot \cos((1 \pm Q_s / p) \cdot x_s \pi / \tau_p)$$

By the modulation of the stator field due to the stator pole slotting an additional magnetic field wave pair $(\lambda/2) \cdot B \cdot \left(\cos((1 + Q_s/p) \cdot x_s \pi/\tau_p) + \cos((1 - Q_s/p) \cdot x_s \pi/\tau_p)\right)$ appears with the average pole count $2p' = 2p \cdot \left((Q_s/p - 1) + (Q_s/p + 1)\right)/2 = 2Q_s$. The stator slotting gives

by modulation of the stator field an additional harmonic field wave of the pole count $2p' = 2Q_s$. The rotor teeth are interacting with this space harmonic field wave and experience a much higher pole count $2p' = 2Q_s >> 2p$, which now defines the number of steps per revolution. Hence the rotor teeth per pole Q_r / p' are of interest to define the number of mechanical steps z_p during one stator period $T = 1/f_s$ for a VR-rotor. Therefore the number of rotor teeth must be refined with respect to the number of stator teeth. With m stator phases and Q_r/p' rotor teeth per "new" pole pair the number of steps per electrical period is $z_p = (Q_r / p') \cdot m$. The number of steps per rotor revolution is p'-times bigger, resulting again in $z = p' \cdot z_p = Q_r \cdot m$ (*Vernier* principle), but now with a much bigger number of rotor teeth with small slot openings and small slot depth.

Facit:
The stator slotting gives by modulation of the stator field an additional harmonic field wave of the pole count $2p' = 2Q_s$. The rotor teeth are interacting with this space harmonic field wave and experience a much higher pole count $2p' = 2Q_s >> 2p$, which now defines the number of steps per revolution.

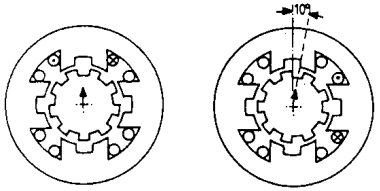

a) Phase 1 energized b) Phase 2 energized

Fig. 8.1.2-1: 2-pole VR-motor with stator and rotor slotting: $Q_s = 8$, $Q_r = 9$, $m = 4$

Example 8.1.2-1:
Vernier VR-motor acc. to Fig. 8.1.2-1: $2p = 2$, $Q_s = 8$, $Q_r = 9$, $m = 4$:
$2p' = 2Q_s = 16$, $Q_r / p' = 9/8$, $z_p = (Q_r / p') \cdot m = (9/8) \cdot 4 = 9/2$
$z = p' \cdot z_p = 8 \cdot (9/2) = Q_r \cdot m = 9 \cdot 4 = 36$, $\alpha = 360°/36 = 10°$

8.1.3 Comparison of basic stepper motor functionality

VR stepper motors:
According to Chapter 2 a switched reluctance motor, which is the special case of a VR-motor with position encoder feed back, cannot self-start, if it is only manufactured with 2 phases and symmetrical rotor. In order to get a defined direction of self-starting, at minimum three phases are necessary. In open circuit (= zero stator current) the torque is zero. Hence at switched off motor no torque is supplied to keep the motor in the wanted position. On the other hand a very fine slotting can be manufactured with problems, so with the *Vernier* principle a rather high number of steps per revolution is possible.

PM stepper motors:
PM-motors have due to the rotor permanent magnet field also in 2-phase stators a defined starting torque and starting direction, so the minimum phase number for stepper operation is 2. At open circuit the cogging torque of the rotor permanent magnet field with the stator

slotting provides sufficient torque to keep the rotor at the desired position before switch-off. On the other hand it is very difficult to magnetize a cylindrical rotor permanent magnet material with a high pole count, as the magnetization coils for a N-S-N-S-polarization with a very small pole width are difficult manufacture. Hence the number of steps per revolution is considerably smaller than in VR-motors. So rotors for a high number of steps per revolution must be VR-rotors with a very accurate manufacturing in order to keep the relative error of the individual stepping angle below 3% ... 5%.

Hybrid stepper motors:
In hybrid motors a rotor PM excitation is combined with toothed rotor ring structures to generate a variable reluctance in the air gap. Hence the advantages of PM stepper motors with minimum phase count 2 and open circuit torque are combined with the advantages of VR stepper motors with a high number of steps per revolution (Table 8.1-3-1).

type of motor	VR/H	VR/H	VR/H	VR/H/PM	PM	PM	PM	PM	PM
rotor teeth Q_r	100	90	50	24					
rotor poles $2p$				24	20	16	12	6	4
z (at $m = 2$)	200	180	100	48	40	32	24	12	8
α / ° (mech.)	1.8	2	3.6	7.5	9	11.25	15	30	45

Table 8.1.3-1: Typical numbers of rotor teeth for different kinds of stepper motors
(VR: variable reluctance stepper motor, H: hybrid stepper motor, PM: permanent magnet stepper motor)

8.1.4 Micro stepping
If the stator winding of the 3-phase, 2-pole VR-motor with 2 rotor teeth of Fig. 8.1-1a is fed with uni-polar phase currents according to Fig. 8.1.4-1, the rotor will need for one revolution two electrical periods $2T_s$ and will perform six steps per revolution. During one electrical period the rotor performs 3 mechanical steps.

Electrical stator frequency $f_s = 1/T_s$, stepping frequency $f = 1/T = 3f_s$

By applying a **bipolar current feeding** with e.g. $k_z = 20$ current steps per period T_s (Fig. 8.1.4-2), where the stepped current curve approximates a sine wave, the rotor will perform instead of 3 steps per period T_s now 20 "micro" steps. This can be understood easily, if the magnetic field per phase is regarded as a vector, which is aligned into positive phase axis, when fed with positive phase current. Due to *Ampere´*s law the length of the vector is directly proportional to the phase current, e.g. $\underline{\psi}_U \sim i_U$. Hence the vector of the resulting magnetic field is a superposition of the phase magnetic field vectors. In a three-phase system ($m = 3$) the direction of the three phase axes is shifted in space by 120° (electrically). Hence the phase magnetic field vector of V is shifted with respect to U by $2\pi/3$ or $\underline{a} = e^{j \cdot 2\pi/3}$, and the phase vector of W by 240° or $\underline{a}^2 = e^{j \cdot 4\pi/3}$. The resulting magnetic field vector, expressed as the resulting magnetic flux linkage, is given as superposition of the three phase flux linkage vectors.

$$\underline{\psi} = \underline{\psi}_U + \underline{\psi}_V + \underline{\psi}_W \sim i_U + \underline{a} \cdot i_V + \underline{a}^2 \cdot i_W \qquad (8.1.4\text{-}1)$$

Hence the position of the resulting field my be adjusted by the current values i_U, i_V, i_W nearly continuously. If these values approximate a sine wave function with e.g. 20 steps per period $2\pi/20$, the resulting field will take 20 positions per period with almost constant amplitude ψ.

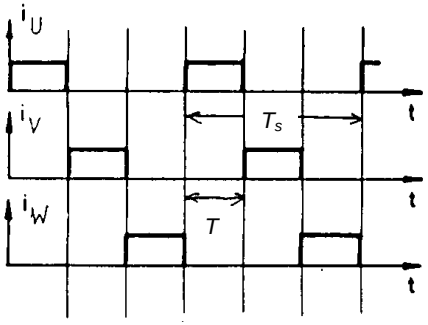

Fig. 8.1.4-1:
Uni-polar current feeding of a three-phase stator winding

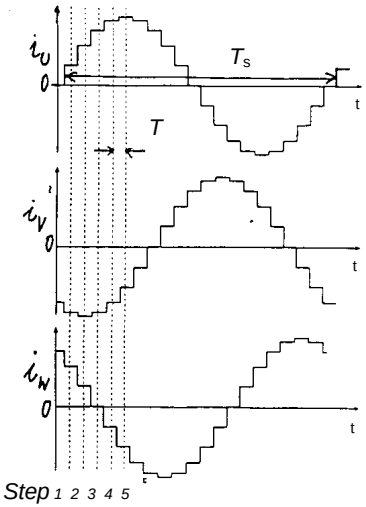

Fig. 8.1.4-2:
Bipolar current feeding of a three-phase stator winding with **micro-stepping** (here: $T_s/T = 20$)

Proof:

$\Omega_s = 2\pi / T_s$, $k_z = 20$, $t_i = 0, T_s/20, 2T_s/20, 3T_s/20, \ldots$:

$$i_U(t_i) = \hat{I} \cdot \cos(\Omega \cdot t_i),\ i_V(t_i) = \hat{I} \cdot \cos(\Omega \cdot t_i - 2\pi/3),\ i_W(t_i) = \hat{I} \cdot \cos(\Omega \cdot t_i - 4\pi/3)$$

With $i_U(t_i) = \hat{I} \cdot \dfrac{e^{j\Omega_s \cdot t_i} + e^{-j\Omega_s \cdot t_i}}{2}$, $i_V(t_i) = \hat{I} \cdot \dfrac{e^{j(\Omega_s \cdot t_i - 2\pi/3)} + e^{-j(\Omega_s \cdot t_i - 2\pi/3)}}{2}$

and $i_W(t_i) = \hat{I} \cdot \dfrac{e^{j(\Omega_s \cdot t_i - 4\pi/3)} + e^{-j(\Omega_s \cdot t_i - 4\pi/3)}}{2}$ one gets

$$\underline{\psi}(t_i) \sim \hat{I} \cdot \left[\frac{e^{j\Omega_s \cdot t_i} + e^{-j\Omega_s \cdot t_i}}{2} + e^{j\frac{2\pi}{3}} \cdot \frac{e^{j(\Omega_s \cdot t_i - 2\pi/3)} + e^{-j(\Omega_s \cdot t_i - 2\pi/3)}}{2} + \right.$$

$$\left. + e^{j\frac{4\pi}{3}} \cdot \frac{e^{j(\Omega_s \cdot t_i - 4\pi/3)} + e^{-j(\Omega_s \cdot t_i - 4\pi/3)}}{2} \right] = \hat{I} \cdot \left[\frac{3e^{j\Omega_s t_i}}{2} + \frac{3e^{-j\Omega_s t_i}}{2} \cdot \left(1 + e^{j\frac{4\pi}{3}} + e^{j\frac{8\pi}{3}} \right) \right] =$$

$$= \underline{\underline{(3\hat{I}/2) \cdot e^{j\Omega_s \cdot t_i}}}$$

The length of the resulting field vector remains constant. The angle of the field vector position is changing in steps $\Omega_s t_i = 2\pi \cdot t_i / T_s = 0, 2\pi/20, 2 \cdot 2\pi/20, \ldots$ The stepping angle is therefore refined by k_z.

VR: $\alpha = 2\pi/(Q_r \cdot k_z)$ PM: $z = 2\pi/(p \cdot k_z)$ (8.1.4-2)

The driving electronic equipment is more complicated fort the micro stepping operation than for the conventional half step operation.

Example 8.1.4-1:

VR stepper motor: $m = 3$, $Q_r = 50$

a) Full step operation, uni-polar current feeding: $\alpha = 2\pi/(Q_r m) = 360°/(50x3) = 2.4°$

b) Micro step operation $k_z = 20$: $\alpha = 2\pi/(Q_r k_z) = 360°/(50x20) = 0.36°$

Facit:

By increasing phase count, pole count and half-step or micro-step operation the number of steps may be increased for all kinds of stepper motors. In addition in VR- and hybrid stepper motors the number of steps per revolution may be increased by increasing number of rotor teeth.

8.2 Stepper motor design

8.2.1 Hetero-polar motors

The polarity of the air gap flux changes its sign along the motor air gap circumference (Fig. 8.1-1) as north and south poles. Most of the VR- and PM-stepper motors are built as hetero-polar motors. A low cost design for the stator winding is the **claw pole stator winding**. Each phase of the stator winding is manufactured as a ring coil, which is surrounded by an iron yoke made of claws, which alternatively enclose the ring coil from the left and the right side. The ring coil field with closed field lines preferably passes in this iron yoke, but is forced at the end of the claws to cross the air via the air gap. Hence the field lines leave at e.g. positive current polarity the left claw tips and enter the right claw tips. Thus the left claws may be regarded as north poles and the right ones as south poles. Thus an alternating ("hetero-polar") air gap field distribution is generated. The number of claws per ring coil therefore is even and equals the number of poles. The different phases are arranged in different planes along the motor axis.

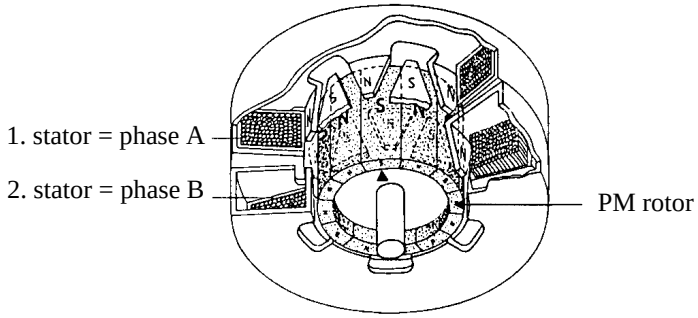

Fig. 8.2.1-1: PM-claw pole stepper motor, $m = 2$, $2p = 12$ (*Stölting et al., El. Kleinmaschinen, Teubner,* 1987)

In Fig. 8.2.1-1 a two-phase motor with 2 ring coils is depicted. Each ring coil is surrounded by 6 right and 6 left claws, fitting to a 12-pole PM cylindrical rotor. The necessary 90° el. shift between the two phases is realized by shifting the second phase claws by half claw pitch (= half pole pitch), whereas the rotor is magnetized without any axial skew. Of course it would be also possible to arrange the claws of the two phases aligned and shift the

rotor magnetization of the second half (beneath the second phase) by half pole pitch. But this kind of magnetization is difficult to realize and is therefore not in use.

Note, that this kind of motor very closely resembles to a two-phase transversal flux motor, where the stator U-yokes are replaced by the stator claws!

Example 8.2.1-1:
PM-claw pole stepper motor (Fig. 8.2.1-1):
Number of steps per revolution $z = 2p.m = 12x2 = 24$, stepping angle $\alpha = 360°/24 = 15°$ (mech. degrees)

In Fig. 8.2.1-2 the bipolar current feeding for the two phases A and B is shown for the motor of Fig. 8.2.1-1 for full step operation step by step. The current polarity in A is reversed prior to the current in B. The direction of rotation is reversed by changing the sequence of current reversal; the current polarity in B is then reversed before the current in A changes its polarity. It is clearly visible, that two phases are sufficient in PM motors to define the direction of motion at starting.

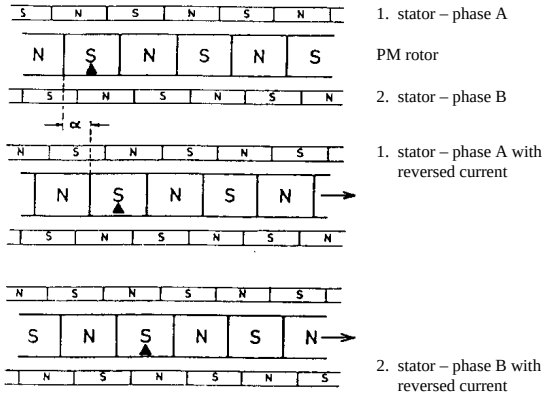

Fig. 8.2.1-2: Current feeding sequence of a two-phase claw pole PM stepper motor

8.2.2 Homo-polar motors

Rotor permanent magnets:
The flux polarity does not change along the motor air gap circumference, but it is changing in axial direction. Hence the air gap flux density along the rotor circumference is called homo-polar. Mainly **hybrid stepper motors** are designed as homo-polar machines. In Fig. 8.2.2-1a the two-phase stator winding ($m = 2$) is unskewed. The permanent magnet rotor has at its outer side two additional toothed iron rings, which are shifted by half tooth pitch in circumference direction. The rotor shaft is made of non-magnetic iron to keep the permanent magnet inner stray flux as small as possible. The homo-polar permanent magnet flux leaves the first rotor half with positive polarity and enters the second half, hence defining there negative polarity. So all teeth of the first ring are north poles, and the teeth of the second ring are south poles. If the rotor magnet is omitted, only the iron tooth rings remain and we get a VR-motor in homo-polar design. For the same stator *Ampere*-turns this VR-motor produces a smaller torque than the hybrid stepper motor due to the missing PM flux.

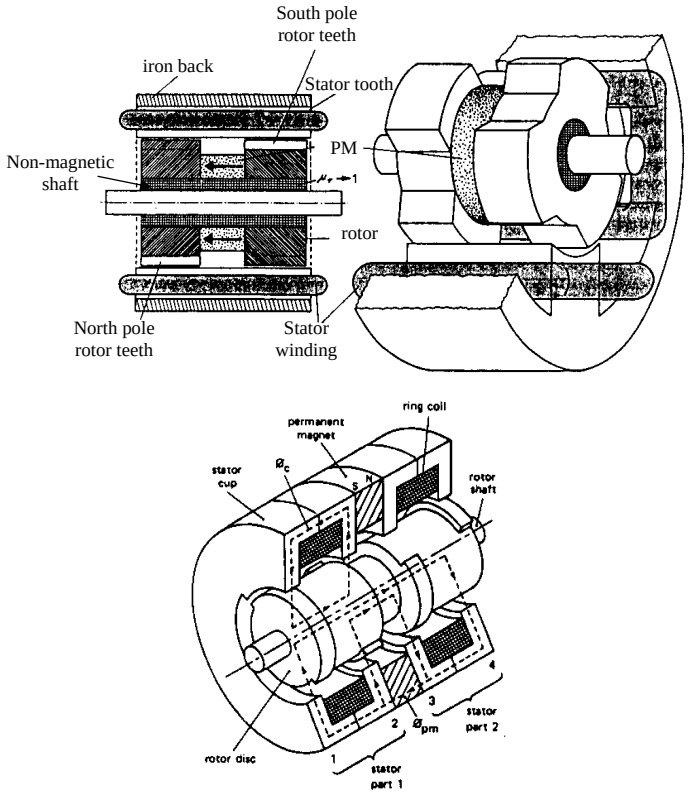

Fig. 8.2.2-1: 2-phase hybrid stepper motors with homo-polar flux arrangement and bipolar current operation:
a) Permanent magnet in the rotor, 3 rotor teeth per half machine, 4 stator teeth (*Stölting et al., El. Kleinmaschinen, Teubner*, 1987), b) Permanent magnet in the stator, claw pole stator, 1 tooth in stator and rotor per radial plane: Φ_c: coil flux, Φ_{PM}: PM flux (*Philips Comp.*)

The bipolar current operation for the stator winding of the motor of Fig. 8.2.2-1a is shown in Fig. 8.2.2-2 for

(i) full step operation with one excited stator phase,
(ii) full step operation with two excited stator phases (increased torque),
(iii) half step operation, exciting alternatively $m = 2$ and $m - 1 = 1$ phases.

Stator permanent magnets:
In the same way the permanent magnet may be also arranged **in the stator** as e.g. a ring magnet with axial direction of magnetization to guide the flux Φ_{PM} with positive polarity in the first axial half of the machine (here: first phase) and with negative polarity in the second half (= second phase) (Fig. 8.2.2-1b, stator claw pole arrangement with one claw per half side (cup)). If the first phase is magnetized with positive current, resulting in a positive coil flux Φ_c, Φ_{PM} and Φ_c add on the left stator cup of phase 1 and substract on the right cup. Hence the rotor moves in aligned tooth position on the left cup (plane 1). For the next step phase 1 is switched off and phase 2 is magnetized (full step operation) e.g. with positive current,

aligning stator and rotor tooth in plane 4, where Φ_{PM} and Φ_c add. A step of 90° is performed in counter-clockwise operation. Then phase 2 is turned off and phase 1 is energized with negative coil current. Due to negative Φ_c the fluxes Φ_{PM} and Φ_c add on the right stator cup of phase 1 (plane 2), where the teeth align. In total 2x90° =180° rotational angle have been performed. Then phase 2 is energized with negative current and so on.

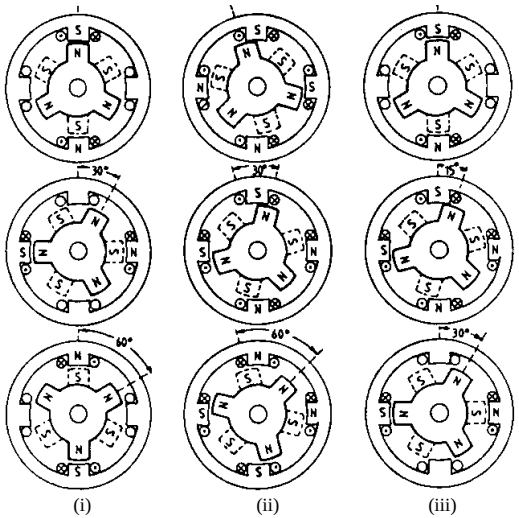

Fig. 8.2.2-2: Current pattern in the stator winding of the hybrid stepper motor of Fig. 8.2.2-1: full step operation with (i) one excited stator phase, (ii) with two excited stator phases, (iii) half step operation (*Stölting et al., El. Kleinmaschinen, Teubner*, 1987)

Example 8.2.2-1:
Hybrid stepper motor of Fig. 8.2.2-1a: $m = 2$. Sum of the teeth of both tooth rings: $Q_r = 6$
$k_B = 1$: Full step operation (Fig. 8.2.2-2 (i) and (ii)): $z = Q_r m / k_B = 12, \alpha = 360°/12 = 30°$
$k_B = 0.5$: Half step operation: $z = Q_r m / k_B = 24, \alpha = 360°/24 = 15°$

Example 8.2.2-2:
Hybrid stepper motor of Fig. 8.2.2-1b: $m = 2$. Sum of the teeth of the two tooth rings per phase: $Q_r = 2$
$k_B = 1$: Full step operation: $z = Q_r m / k_B = 4, \alpha = 360°/4 = 90°$

8.2.3 Single phase stepper motors

Single phase stepper motors are used e.g. as drives for watches and are very simple and low cost motors. They are PM stepper motors with a PM rotor and asymmetric stator poles (teeth) to define a direction of motion.

a) In Fig. 8.2.3-1 the single phase ($m = 1$) stator winding carries no current at the time instant *a*. The rotor is positioned according the cogging torque, which is generated by the PM rotor flux and the stator teeth.
b) At time instant *b* the stator coil is energized with positive current (voltage U_c), exciting a flux Φ_c. Hence the left pole shoe (tooth) is magnetized as north-pole and the right one as south-pole. Due to that magnet field the rotor is turned anti-clockwise.

c) At time instant *c* the current is again zero and the rotor is fixed due to the cogging torque.
d) At time instant d the stator winding is energized with reversed current (voltage $-U_c$), exciting a flux $-\Phi_c$. The left pole shoe (tooth) is magnetized as south-pole and the right one as north-pole. Hence the rotor continues its anti-clockwise rotation.

Note: If the stator winding is energized at time instant b with negative current (left pole shoe is south-pole), the rotor would not have moved at all. Only positive current allows rotation, which shows that it is possible to get **a defined sense of rotation** also with single phase

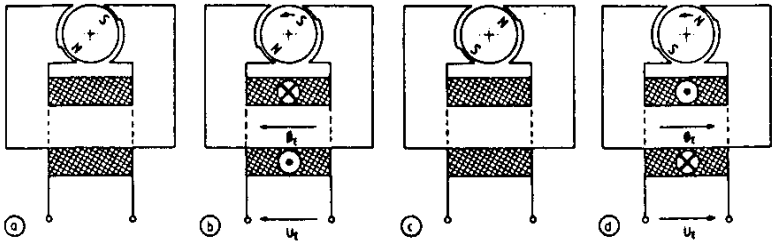

Fig. 8.2.3-1: Single phase PM stepper motor with asymmetric poles by narrower air gap at one pole side (*Stölting et al., El. Kleinmaschinen, Teubner*, 1987)

Facit:
VR- and PM-stepper motors are mainly manufactured as hetero-polar motors, whereas hybrid steppers are mainly homo-polar machines. Single phase steppers need an asymmetric magnetic circuit and are manufactured as PM machines.

8.3 Driving circuits of stepper motors

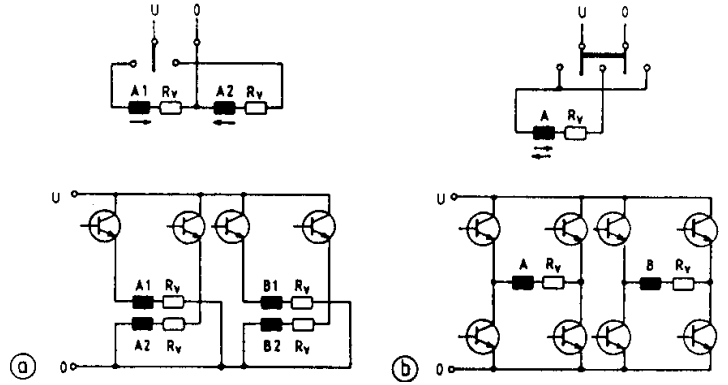

Fig. 8.3-1: Driving circuits for stepper motors with a) uni-polar, b) bipolar current. Free-wheeling diodes are omitted here for clarity. The resistance R_v are used to reduce the electric time constant (*Stölting et al., El. Kleinmaschinen, Teubner*, 1987)
a) The two branches A1, A2 of phase A and B1, B2 of phase B are energized subsequently always with positive current, so always one branch per phase is without current, which gives only 50% motor winding utilization.
b) By using four switches instead of two per phase the phases A and B may be energized with bi-polar current, so always the complete phase winding is energized, yielding a high motor utilization at the expense of double amount of power switches.

The electronic driving circuits for stepper motors work either with **uni-polar** current impulses (current impulses of one polarity) or with **bipolar** current (AC current) (Fig. 8.3-1).

Kind of winding current	**uni-polar**	**Bipolar**
Number of winding branches	two per phase	one per phase
Number of power switches	two per phase	four per phase
Polarity of current	positive	positive and negative
Amount of circuit elements	low	high
Motor utilization	low	high

Table 8.3-1: Uni-polar and bipolar current feeding for stepper motor windings

The ideal current wave form is the rectangular impulse, but the current rise at voltage turn-on is limited by the **electrical time constant** $T_e = L_s/R_s$, which is defined by the winding resistance R_s and inductance L_s per phase (Fig. 8.3-2). Hence the electrical switching frequency f_s cannot be shorter than $1/T_e$: $f_{s,\max} < 1/T_e$.

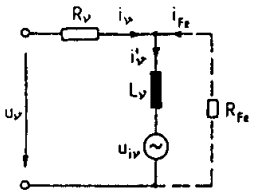

Fig. 8.3-2: Electrical equivalent circuit of the ν^{th} stator phase (R_ν, L_ν: phase resistance and inductance, $u_{i\nu}$: back EMF per phase, R_{Fe}: equivalent resistance for considering the iron losses per phase) (*Stölting et al., El. Kleinmaschinen, Teubner*, 1987)

Measures to raise the switching frequency:

Constant voltage operation – serial resistance:
By adding an additional serial resistance per phase R_v the electrical time constant is reduced $T_e = L_s/(R_s + R_v)$, which allows an increase of $f_{s,\max} < 1/T_e$. This may be used for operation with constant supply voltage U (which has to be increased for constant current: $U = I \cdot (R_s + R_v)$), but the losses are increased by R_v/R_s (Fig. 8.3-1).

Constant current operation – chopping mode:
By raising the supply voltage U the inclination of current slope is increased: $di/dt = U/L_s$. Hence the rise time t_r to reach the rated value I is decreased: $t_r = I/(di/dt) = L_s \cdot I/U$. As $I << U/R_s$, the supply voltage must be chopped to adjust the average voltage $U_{av} = R_s \cdot I < U$ to keep the current at its rated value (Fig. 8.3-3a). The switching losses have to be covered in the power converter, and slightly higher losses in the stator winding due to the switching-frequent current ripple.

Bi-level voltage operation:
The winding is switched on with a high voltage U_{HW} to reduce the current rise time according to $t_r = L_s \cdot I/U_{HW}$. After reaching the rated current, the voltage is lowered to the value $U_{NW} = R_s \cdot I < U_{HW}$ (Fig. 8.3-3b).

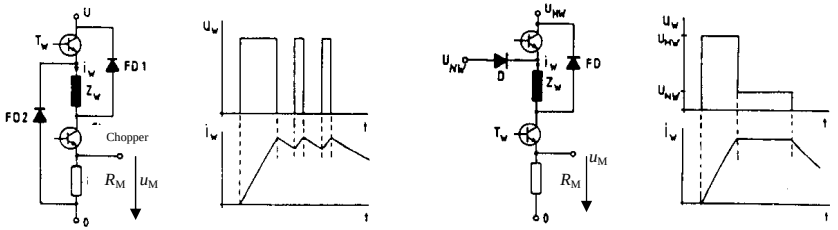

Fig. 8.3-3: Driving circuits for stepper motors (winding impedance Z_w) (*Stölting et al., El. Kleinmaschinen, Teubner*, 1987)
a) Chopping mode: The phase is turned on and off with the upper transistor T_w to the DC link voltage U. The lower transistor is chopping. The current with its ripple is measured at the measuring resistance R_M, (shunt), delivering the voltage u_M. The free-wheeling diode FD1 takes over the current during chopping and FD2 after final turn-off of the phase.
b) Bi-level-mode for stepper motor current feeding: The upper transistor switches the phase to the high voltage U_{HW}. During that time the diode D blocks the current not to enter the low voltage circuit U_{NW}. After the upper transistor is switched off, the winding is operated with $U_{NW} < U_{HW}$. The phase is turned off with the transistor T_w, and the free-wheeling diode FD takes over the residual winding current to decay via U_{HW}.

Due to the inertia of the rotor the motor tends to overshoot the last step, where it should come to a stand still. Hence this over-shooting must be damped effectively.

Measures to damp the over-shoot at the last step:

Mechanical damper unit:
Mechanical damper units have been used in the earlier days of stepper motors, but are nowadays practically out of use.

Short circuit damper:
If those winding phases, which are not energized at the last steps, are short circuited by the power electronics supply, the voltage, which is induced there by the moving rotor, will cause a short circuit current. The short circuit currents produce with rotor a braking torque, that damps the overshoot. As the stepper motors are usually of small power rating, their winding resistance per phase R_s is rather big. Hence the short circuit current is not very big, compared to the rated current, so the braking and damping usually is weak.

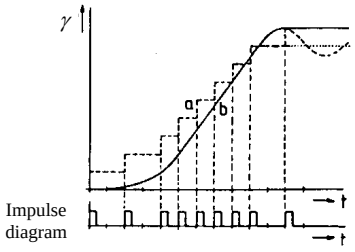

Fig. 8.3-4: Delayed last step: According to the current impulses (below) the wanted rotor position (dashed line *a*), expressed as rotational angleγ, is followed by the real motion (solid line b). At the maximum overshoot of step *N*-1 the last current impulse is commanded, hence avoiding the overshoot at step *N* (*Stölting et al., El. Kleinmaschinen, Teubner*, 1987).

Electronic damping:
a) Delayed last step:
If the current impulse for the last step is given delayed during the maximum overshoot of the step before, the rotor will have lost already a part of its kinetic energy and will come to rest without further overshoot (Fig. 8.3-4).
b) Back phase damping:
The final step N+1 is a step into opposite direction of motion to brake the rotor at the step N.

Facit:
Uni-polar and bipolar impulse current feeding is used to operate the stepper motors stepwise, but always in open-loop. The drive unit must avoid overshoot at the last step and should be able to realize high switching frequencies.

8.4 Torque characteristics of stepper motors

8.4.1 Static torque characteristic

Like in conventional feed-forward operated synchronous machines, operated by voltage supply, there exist two kinds of static torque components:

a) **synchronous torque M_{syn}** (interaction of rotor magnetic field with stator current in the stator winding),
b) **reluctance torque M_{rel}** (interaction of stator magnetic field of stator currents, which is modulated by rotor reluctance, with stator currents in the stator winding).

Cogging torque:
In Fig. 8.4.1-1 for a **PM-stepper motor** the synchronous torque due to the interaction of the rotor PM field with the stator currents is depicted. The reluctance torque in this case is given by the interaction of the rotor PM field with its modulated field component due to the stator slotting. This cogging torque occurs already at no load (= stator open circuit) and is an unwanted effect. The resulting torque of the PM stepper motor is therefore a superposition of both torque components. The stator field is not modulated by the rotor, as the rare earth rotor PM material has a permeability of nearly unity, so there is no rotor reluctance active for the stator field.

Holding torque M_H:
The holding torque is the maximum torque, with which an excited stepper motor can be loaded without performing a continuous motion. In Fig. 8.4.1-1 this torque corresponds with the static pull out torque M_{p0} of an electrically excited synchronous machine, which occurs at a load angle ϑ of ±90° (el.). The disturbing influence of the cogging torque increases M_H slightly and shifts this value to $|\vartheta| < 90°$. If the stator slot openings are small, this influence may be neglected.

Detent torque M_D:
The detent torque is the maximum torque, with which an un-excited stepper motor can be loaded without performing a continuous motion. Like in Fig. 8.4.1-1, this torque corresponds in PM and hybrid stepper motors with the cogging torque.

The stable operation range for PM stepper motors without VR or cogging effect is given as $-90° \le \vartheta \le 90°$ (Fig. 8.4.1-2a).
In **VR motors** only the reluctance torque M_{rel} exists, when the stator winding is excited. This torque is essentially determined by rotor slot width and depth. No detent torque exists.

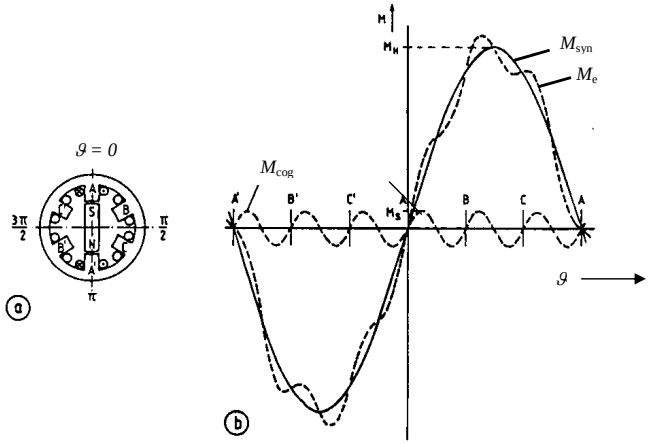

Fig. 8.4.1-1: Three-phase, 2-pole PM-stepper motor (m = 3, 2p = 2): a) cross section: Rotor S-pole at position A, load angle is zero, b) static torque for increasing/decreasing load angle. For the cogging torque six periods with the positions A, B, C, A´, B´, C´ exist. (*Stölting et al., El. Kleinmaschinen, Teubner,* 1987)

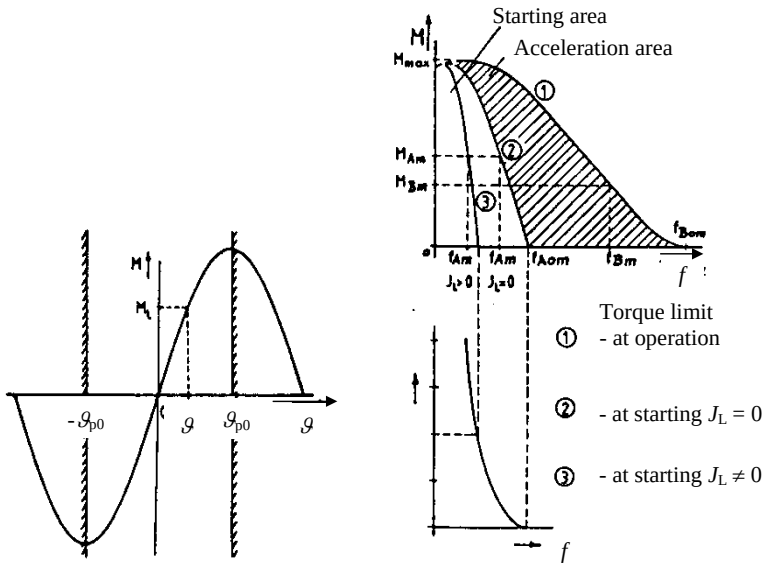

Fig. 8.4.1-2: a) Static load angle ϑ of a stepper motor, that is loaded at the shaft with a torque M_s, b) dynamic torque characteristic of a stepper motor in dependence of the stepping frequency f : 1: Torque limit at operation with constant f, 2: Torque limit at no-load starting (no load coupled: J_L = 0), 3: as 2, but with coupled load inertia $J_L > 0$ (J_L, J_M: Load and motor rotor inertia)
below: Admissible load inertia for starting with zero load torque
(*Stölting et al., El. Kleinmaschinen, Teubner,* 1987)

8.4.2 Dynamic torque characteristics

Torque limit at operation:
The holding torque can only be produced, if the stator current rises to the rated value. As this needs some time due to the electric time constant of the winding, the holding torque can be only produced at **stand still** (n = 0). When the stator winding of the rotating motor (rotational speed n) is supplied with current impulses with the stepping frequency

$$f = z \cdot n \quad , \qquad (8.4.2\text{-}1)$$

the average current per phase is smaller than the maximum (rated) value at constant voltage operation due to the current rise time. Hence the average motor torque is also smaller and so the admissible load torque decreases, too (curve 1 in Fig. 8.4.1-2b). It decreases with increasing stepping frequency, as due to the rising speed the duration of the current impulses decrease ~ 1/n. The current rise time t_r becomes a more dominating part of the duration of the current impulse, and the average current per impulse decreases with 1/n or with 1/f.

Torque limit at starting:
Starting the motor means to synchronize the rotor movement with the stepwise movement of the stator field. In Chapter 3 for asynchronously starting PM-machines it was stated, that the slip of the rotor with respect to the moving stator field must get smaller than a critical slip to allow synchronization of the rotor movement with the moving stator field. That critical slip decreased with increasing inertia and stator frequency.
Here the starting torque M_e is either the synchronous or the reluctance torque or both. According to *Newton´*s equation $(J_L + J_M) \cdot d(2\pi n)/dt = M_e - M_s$ (J_L, J_M: load and motor rotor inertia) the motor can start at a certain load inertia J_L with only a certain upper limit of the stepping frequency. This stepping frequency, supplied by the driving electronics, must be sufficiently low to allow safe motor synchronization. Hence for a given load inertia the maximum possible loading torque M_s at a given stepping frequency f for safe synchronization is given as a torque limit at starting (Fig. 8.4.1-2b, curve 3). The lower the load inertia, the higher the load torque at starting may be.
The maximum admissible load torque occurs at J_L = 0 (Fig. 8.4.1-2b, curve 2). From curves 2 and 3 for zero load torque the admissible load inertia in relation to the motor inertia for starting is determined in dependence of the starting frequency (Fig. 8.4.1-2b: $J_L/J_M(f)$).

Acceleration operation:
Once the motor is synchronized, it may be operated for a certain load torque also at higher stepping frequencies without losing steps (shaded area in Fig. 8.4.1-2b), hence with a faster rotor movement.

Example 8.4.2-1:
Dynamic torque curve of Fig. 8.4.1-2b): With the load torque M_{Am} and the load inertia J_L a starting frequency of $f_{Am}(J_L>0)$ is possible. This frequency may be increased to $f_{Am}(J_L=0)$, if no additional load inertia is acting. The maximum starting frequency is at zero load torque: f_{A0m}. With the load torque M_{Bm} during operation a maximum frequency f_{Bm} may be reached. The maximum operational frequency is at zero load torque: f_{B0m}.

Example 8.4.2-2:
Hybrid stepper motor (Fig. 8.4.2-1): m = 3, delta connected, dc link voltage 325 V, Q_r = 50, micro-step-operation, 1000 steps per revolution, motor inertia J_M = 0.00022 kgm^2. The holding torque is M_H = 4.0 Nm at I_{rms} = 2.0A per phase.

- Stepping angle: $\alpha = 360°/1000 = 0.36°$
- At J_L = 0 (= no load torque) the maximum admissible stepping frequency at starting is acc. to Fig. 8.4.2-1 (ii) b) f_{max} = 5.3 kHz. The corresponding speed is $n = f/z = (5300/1000) \cdot 60 = 318/\text{min}$.

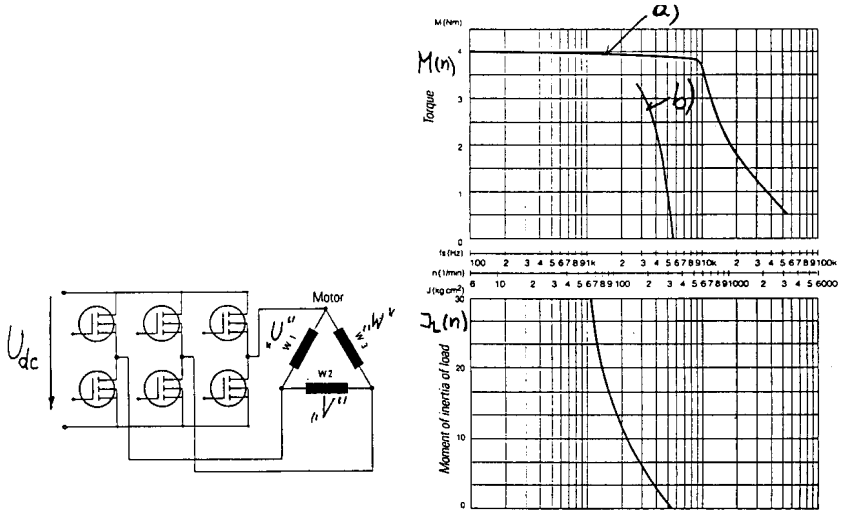

(i) (ii)

Fig. 8.4.2-1: Hybrid stepper motor: (i) Three-phase bipolar power electronic circuit and delta-connected stator winding, (ii) dynamic torque characteristic: a) Torque limit at operation with constant f, b: Torque limit at no-load starting (no load coupled: J_L = 0), below: admissible load inertia for starting with zero load torque (*Berger-Lahr*, 1994)